Energies Renouvelables

Proceedings of Engineering & Technology
-PET-

Editor :
Dr. Ahmed Rhif (Tunisia)

International Centre for Innovation & Development
- ICID -

ISSN: 1737-9334
-PET- Vol-71

ICID

International Centre for Innovation& Development

Proceedings of Engineering & Technology

-PET-

Les Petites et les Moyennes Entreprises

Editor :
Dr. Ahmed Rhif (Tunisia)

International Centre for Innovation & Development
- ICID -

Présidents d'honneurs

- Djamila Rekioua (ALG)
- Georges Descombes (FR)
- Rachid Benchrifa (MAR)

Présidents Généraux

- Ahmed Rhif (TUN)
- Benzeroual Tarek (ALG)
- El Mati Khoumri (MAR)
- Kasbadji Merzouk Nachida (ALG)

Comité International

- Abdelkrim KHIREDDINE (ALG)
- Djeghlal Mohammed Elamine (ALG)
- Gasmi Ines (FR)
- Haitham Saad MOHAMED RAMADAN (FR)
-Jaafar Gaber (FR)
- KAMAL REKLAOUI (MAR)
- Madiha Yessari (MAR)
- Meriem HAYANI MECHKOURI (MAR)
- Mimi Belatel (ALG)
- Mohamed GHERBI (ALG)
- Nawel Seddiki (ALG)
- Rafika Boudries (ALG)
- Sara Zatir (ALG)
- Selma Rabhi (ALG)
- Souad Tayane (MAR)
- Soukaina Akrouch (MAR)
- Youssef Errami (MAR)
- Zohra Ameur (ALG)

Sommaire

CREATION D'UNE NOUVELLE STRATEGIE D'OXYDATION POUR le TRAITEMENT des EFFLUENTS AQUEUX CONTAMINES PAR des AGENTS REFRACTAIRES

Rayene kolai[#1], Slimane Merouani[*2], Mohamed Larbi Djaballah [#3]

[#] *Département de Génie des Procédés, Ecole Nationale Polytechnique de Constantine, Constantine, Algérie*
[1]korayene6@gmail.com
[3]mohameddjaballa@gmail.com

[*] *Faculté de Génie des Procédés, Université Salah Boubnider Constantine 3, Constantine, Algérie*
[2] s.merouani@yahoo.fr

***Abstract*— En raison de la stabilité exceptionnelle des colorants synthétiques et de leur résistance à la biodégradation. Cette étude a donc été menée pour évaluer la dégradation du H-3G, un polluant textile de type azoïque, à l'aide d'un système UV/Chlore/Pi (PI : periodate de sodium), qui s'est avéré plus performant que les systèmes binaires UV/Chlore et UV/Pi. Le système combiné a complètement éliminé le H-3G en 10 minutes à un taux de dégradation 11 fois plus rapide que les UV seuls, alors que les systèmes autonomes UV/Chlore, UV/PI et PI ont éliminé 67 %, 59 % et 10 % du H-3G, respectivement. En outre, la combinaison des systèmes UV/Chlore et UV/PI a démontré un impact synergique. L'influence des paramètres opérationnels a été évaluée dans une étude systématique complète de l'élimination du H-3G par le système UV/Chlore/Périodate. À pH5 et à une concentration de H-3G (20 mg/l), le taux de dégradation initial a augmenté de façon spectaculaire avec l'augmentation des concentrations initiales de PI ; en outre, une bonne efficacité a été obtenue à de faibles concentrations de polluant. Par conséquent, lorsque cette étude a été réalisée dans des matrices réelles, l'efficacité de la conversion de le H-3G par le procédé UV/Chlore/Périodate a été améliorée, faisant de ce procédé une technique potentielle pour le traitement des eaux naturelles réellement contaminées.**

***Keywords*— Colorants Synthétiques ; Biodégradation ; UV/Chlore/PI ; Polluant azoïque.**

I. INTRODUCTION

L'eau sert de récepteur à une variété de rejets et de déchets qui contiennent des quantités importantes de polluants organiques émergents (PEE) produits par des opérations industrielles et agricoles intensives. Parmi les différents EOP identifiés dans le milieu aquatique figurent les hydrocarbures aromatiques polycycliques (HAP), les polychlorobiphényles (PCB) et les colorants synthétiques[1].Les colorants azoïques sont les plus populaires et les plus utilisés dans l'environnement. Ils sont principalement formés d'entités aromatiques reliées entre elles par une liaison N=N. Ils sont chimiquement stables, non biodégradables, et peuvent être toxiques et cancérigènes[2]. Le rejet d'une quantité même infime de colorant (de l'ordre de 1 mg/L) est inacceptable et peut mettre en danger la santé humaine et l'environnement. Pour préserver et améliorer la qualité de ces eaux, des méthodes d'oxydation avancée sont utilisées pour traiter chimiquement les eaux usées afin de garantir une minéralisation complète des contaminants ou les convertir en composés biodégradables Ce phénomène est basé sur la formation de radicaux hydroxyles (OH), qui ont une réactivité spécifique contre la plupart des composés organiques[3]. Par conséquent, notre objectif est d'éliminer les polluants réfractaires dans l'environnement aquatique à l'aide de nouvel approche UV/Chlore/PI.

II. MATERIEL ET METHODE

Toutes les solutions ont été préparées avec des produits chimiques de qualitéréactif et de l'eau dés ionisée.

Le H-3G a été obtenu à partir d'une usine textile locale située dans la ville de Constantine, en Algérie. Les solutions d'hypochlorite de sodium (NaOCl) et de periodate de sodium (NaIO4) ont été fournies par Sigma-Aldrich. Tous les autres réactifs (NaOH et H2SO4) étaient des produits commerciaux de la plus pure qualité disponible (Sigma- Aldrich). Le réacteur photochimique était constitué d'une cuve à eau à double paroi en verre cylindrique de 500 ml. Une lampe à mercure basse pression (Oriel 6035, 15 mW cm-2, émission maximale à 253,7 nm) fixée dans un type de quartz (ϕ = 1 cm) était placée verticalement au centre du réacteur. La solution irradiée (250 ml) était agitée magnétiquement et sa température, affichée par un thermocouple, était contrôlée par la circulation d'eau, fournie par un thermo cryostat RC6 Lauda, à travers l'enveloppe de la cellule à débit contrôlé. Des aliquotes d'échantillons (3 ml) ont été prélevés à différents intervalles de temps à l'aide d'une seringue en verre et transférés dans une cellule en quartz (1 cm de chemin optique) d'un appareil UV-vis.

ISSN: 1737-9334

III. RESULATS ET DISCUTION

A. *Dégradation du H-3G dans différents systèmes*

Préliminaire

Des travaux préliminaires ont été réalisés pour tester le degré de dégradation du H-3G (C0 = 20mg L-1) dans quatre systèmes différents, à savoir (i) photolyse, (ii) photolyse en présence de Periodate (0.5mM), (iii) photolyse avec (0.2 mM) de Chlore (iv) photolyse en présence de Chlore (0.2 mM) et de (0.5mM) de Periodate.

Aucune perte significative de H-3G n'a été observée dans le cas du UV seul. Le rendement de dégradation par photolyse seule a été déterminé comme étant d'environ 27% après 10 min. Cependant, dans le cas de la photo dégradation en présence de periodate, une dégradation rapide du H-3G s'est produite, c'est-à-dire que 59% du H-3G a été éliminé après 10 min, ce qui est probablement dû à l'implication des espèces radicalaires dans le processus de dégradation.de plus le système UV/chlore a un effet plus significatif sur la dégradation du colorant que le système UV/periodate. 67% du H-3G a été éliminé après 10 min avec le système UV/ Chlore.

Il faut mentionner que la combinaison UV/Chlore /periodate a donné lieu à un taux de dégradation beaucoup plus élevé que celui obtenu pour les systèmes individuels UV/Chlore et UV/periodate.

B. *Effet des paramètres de fonctionnement*

Nous avons étudié l'effet des paramètres de fonctionnement affectaient la capacité du système UV/chlore /periodate à dégrader rapidement le polluant. La dégradation photolytique du H-3G (C0 = 20 mg/L, 0,2 mM de chlore) dans une gamme de périodate de 0,05 à 0,5 mM a été étudiée à 20 °C et à un pH initial de 5. À des concentrations supérieures à 0,5 mM, le periodate peut se photodissocier plus facilement, produisant plus de radicaux et accélérant la vitesse de dégradation. Des travaux supplémentaires de dégradation À diverses concentrations de polluants ont été menés en présence de 0.2 mM de Chlore et de 0,5 mM de periodate. Il a été observé que la concentration du substrat diminue exponentiellement avec le temps. L'étendue de la dégradation s'est avérée être inversement proportionnelle à la concentration initiale du colorant. L'élimination du H-3G a été complètement accomplie après seulement 10 min pour une concentration initiale de substrat de 5 mg/L, mais le pourcentage d'élimination a diminué à 97% pour 10 mg L-1 H-3G, 83% pour 20 mg L-1 H-3G, 53% pour 50 mg L-1 H-3G et 37% pour 100 mg L-1 H-3G. d'une autre façon l'augmentation de C0 augmente la densité optique interne et rend la solution plus opaque à la transmission de la lumière. Cela réduit l'efficacité de dégradation. En outre Le test de dégradation dans l'eau minérale naturelle a montré une amélioration significative du taux d'élimination du colorant. Cependant, une variation de la vitesse de dégradation a été observée dans l'eau de mer.

IV. CONCLUSIONS

La présente étude a démontré que le traitement intégré UV/chlore /Periodate est plus efficace que les systèmes binaires UV/Chlore et UV/Periodate pour la dégradation du H-3G en phase aqueuse et que l'avantage du système intégré est d'éviter l'utilisation de quantités excessives de réactifs (chlore, periodate) et les pertes d'énergie pour le chauffage.

REFERENCES

[1] A. Malik and E. Grohmann, *Environmental protection strategies for sustainable development*. 2012.

[2] S. C. DeVito, "Predicting Azo Dye Toxicity," *Crit. Rev. Environ. Sci. Technol.*, vol. 23, no. 3, pp. 249–324, 1993, doi: 10.1080/10643389309388453.

[3] H. Bendjama, S. Merouani, O. Hamdaoui, and M. Bouhelassa, "Efficient degradation method of emerging organic pollutants in marine environment using UV/periodate process: Case of chlorazol black," *Mar. Pollut. Bull.*, vol. 126, no. August, pp. 557–564, 2018, doi: 10.1016/j.marpolbul.2017.09.059.

Influence of Alignment of Information Systems with Business Strategy in the Performance of Small Medium Enterprises in Gaborone, Botswana

Keneilwe Zuva[#1], TranosZuva[*2], Trust Tshepo Mapoka[#3]

[#]*First-Third Department of Computer Science, First-Third University of Botswana*
P/Bag 0022 Gaborone Botswana
[1]zuvak@ub.ac.bw
[3]mapokat@ub.ac.bw

[*]*Vaal University of Technology*
Private Bag X021, Vanderbijlpark, 1990
[2]tranosz@vut.ac.za

***Abstract*—According to studies that have been reviewed information technology/systems strategy (IT/IS) and business strategy has become a major subject matter and researchers worked to develop frameworks and instruments so that they may measure alignment. Aligning of IT/IS with business strategies in an organization is important, therefore for IS/IT to attain its business objectives it requires the alignment of IT/IS and business in organizations. This study aims to look at the alignment of business strategy and information technology/systems strategy in organizations using the model introduced by Henderson &Venkatraman. The purpose of this study is to measure the alignment between IT/IS and business strategy in Small and Medium Enterprises and to study how alignment affects the performance of the company. A model was used to measure the alignment between Business and Information Technology/Systems Strategy and its impact on the business performance. Data was collected using a questionnaire. A sample of ninety-nine (99) individuals from a variety of SMEs was used. SPSS was used to analysis the data. The results showed the variables of the model were all positively correlated to one another. Therefore, alignment of Information Systems (IS) and Business Strategy (BS) was confirmed. The overall performance of the business was influenced positively (0.459, 0001) by alignment.**

Keywords—information systems, information technology, SME's, alignment, business strategy.

I. INTRODUCTION

An organisationutilises Information Technology (IT)to performbusiness goals. This makes the alignment of Information Systems(IS) with business processes in an organisation to be in a dynamic state. The alignment of IT exist when objectives, operations and procedures of a company are in coherence with the Information Systems which are backing them. Several years ago, IT has been a technological way of implementing business goals. IT and ISis key to the procedure of business planning, design analysis, operations management and strategic decision making[1].

IS ties together the organisation goals, information needed to support the goals and the implementation of computer systems to provide information that will assist in meeting the organisation's demands in supporting those goals [2]. Effective alignment of IT and Business Strategy usually does not happen automatically, organisation's need to continuously keep evaluating themselves and minimize the behaviors that inhabit alignment and start to maximize the behaviors that increase alignment. For an organisation to stay competitive in the business world they must make sure that they have an efficient and effective IS strategy aligned and supporting their business strategy and processes. The alignment between business strategy and IT strategy thus remains a recognizable subject of concern.

Many researches on IT and business alignment have adopted the framework of Henderson &Venkatraman. An important contribution of Henderson &Venkatraman was their identification of numerable types of alignment, namely strategic level and functional level alignment. They joined the two alignment, whereby the strategic alignment is the match between business strategy and IT strategy and the functional alignment is the match between business infrastructure and IT infrastructure. The purpose of this study is to:

- Identify whether IT and business strategy has an impact on the performance of SMEs

This paper is arranged as follows. Section 2 we give a brief outline of the Literature Review showing the concepts that are relevant for this study, Section 3 is the brief outline of the Methodology that has been used in the study. Section 4 results are summarized and conclusion presented.

II. LITERATURE REVIEW

Inorganisations, alignment of IS/IT and business process is becoming the key issue. The objectives of the IT department must be in line with those of the businessfor the IS/IT business strategies to be aligned. Otherwise there will be a misalignment which leads tounproductive business. Business strategic alignment has been viewed as a vital missing link between IT and the organisation's performance[2]. Organizations mostly achieve alignment of their IT with their corporate objectives through three levels of alignment which are awareness, integration and alignment [3].

Information systems are the key components in defining the framework assuring the alignment between the information system and the business strategy. In order to

ISSN: 1737-9334

achieve alignment, the sources of misalignment must first be identified, an effective business-IT alignment requires the analyses of business problems and the changes that take place from market perspective to IT issues, the required interface between IT and business must be based on a clear and continuous of the business requirements into information [4].

Increasing dynamics in markets and organisation's results in a continuous adapting of change in their environment. This leads to organisations facing recurringissueof aligning IT to business strategy. The role of IT has changed over the past years, the assessment of IT strategy and business strategy alignment is pivot in that IT is used appropriately IT in the organisation and ensuring that the organisation's objectives are met [5].

Several models have been proposed over the years which addressed specific aspects on alignment, the models can be analyzed and classified according to different perspectives. Cataledo et al.classifies them into two main categories by means of following the scope of alignment: which are Strategic Alignment, Operational or Process Alignment[6].

Many researchers studied the idea of alignment from different perspectives. The studies revealed the different types of alignment; namely "Strategic Alignment", "Structural Alignment", "Business Alignment", 'Information System Alignment" and Cross-dimensional Alignment. Looking into the assessment of alignment, many at-tempts have been made to measure the alignment between business and IT on a strategic level[7].Recent study by [8] argues that the operational level of an organisation has direct impact on the organisation's overall performance, as this is where the organisation's strategy and IT strategy is performed.

A. Small Medium Enterprise's(SMEs)

According to the European Commission in 2003[9], SMEs are "enterprises which employ people fewer than 250 and which have an annual turnover not exceeding 50 million euros, and/or an annual balance sheet total not exceeding 43 million euro". The United States definition of SMEs vary depending on industry, ownership structure, revenue, and number of employees. Generally, however, the number of employees must be less than 500. Furthermore, according to [10]SMEs usually don't have a widely spread IT infrastructure.

In Botswana 'SME' is a term that is used interchangeably. The National Small Business Act 102 of 1996, p 17, defines SME as small business meaning a separate and distinct business entity, which includes corporative enterprises and non-governmental organisation's, managed by a single owner or more including its branches or subsidiaries. If any it is predominately carried over to any sector or sub-sector of the economy. The economic growth and development of SME sector in Botswana continues to be affected by various challenging factors. The study by [11] substantiates that the rate in which an SME can survive the economy is still one of the lowest in the world. Growth rates of small businesses in Botswana are showing as low with an average of 50% of fail to grow. A lot of factors increase their influence and causing a huge effect on the success of SMEs [12].

TABLE I. ILLUSTRATION HOW THE NATIONAL SMALL BUSINESS ACT USESTHE NUMBER OF EMPLOYEES COMBINED WITH THE ANNUAL

Definitions of SMEs given in the National Small Business Act			
Enterprise size	**Number of employees**	**Annual turnover**	**Gross assets, excluding fixed property**
Medium	Fewer than 100 to 200, depending on industry	Less than R4 million to R50 million, depending upon industry	Less than R2 million to R18 million, depending on industry
Small	Fewer than 50	Less than R2 million to R25 million, depending on industry	Less than R2 million to R4,5 million, depending on industry
Very small	Fewer than 10 to 20, depending on industry	Less than R200 000 to R500 000, depending on industry	Less than R150 000 to R500 000, depending on industry
Micro	Fewer than 5	Less than R150 000	Less than R100 000

TURNOVER PER ENTERPRISE SIZE CATEGORY TO DEFINE SMES

Alignment refers to the use of IS in a way that is appropriate to support business needs, strategies and objectives. Alignment requires an intense communication procedure whereby the organisation's strategic and IT goals are shared with the members[13]

Alignment allows organisations to apply ISand IT to the business delivery tasks and operational activities [14], this requires co-operation between the business and the IT department and it is uppermost important to consider the business and IT objectives together[15]. Alignment within an organisationcertifies that operationsacross the organisation are channeled towards the accomplishments of shared objectives[16].

B. Challenges in Achieving Alignment

Failure in achieving alignment causes major problems includingthe inability to maintain internal and external business, and IT relationships, failure to implement change, lack of senior management support, and a culture that refuses to shift [17]. Organizations that have accomplished a high degree of alignment are often associated with better business efficiency and effectiveness performance[18].Within many organisation'sITis no longer regarded as just a support function for core business processes, it is also an enabler of internal efficiencies and competitive advantages. As the role of IT continues to expand, enterprises increasingly require greater alignment between their business and IT strategies, as well as the means to constantly measure the value ITgives.

Although IT is the core, it also faces several challenges along the waywhen trying toalign IT to business strategies.

III. RESEARCH METHODOLOGY

The proposed model suggests that strategy and IT developments must be coherent. The strategic alignment between business strategy and IT strategy is derived from two main relations:

1) The strategic match between the external and internal scopes of the firm.

2) The functional integration of IT within the organisation.

These links are drawn between four elements: Business Strategy, Business Infrastructure and Processes, IT Strategy and IT Infrastructure and Processes.

Business Strategy: This domain is defined by the choices pertaining to the positioning of the business in the product-market [19].

IS Strategy: The domain defines the choices pertaining to the positioning of the business in the information technology marketplace and looking at the applications and technologies which are set in place [20].

Business Infrastructure & Processes: This domain is defined by the choices pertaining to an internal arrangement within the organisation, including the layout of management structure and work processes (work performed by employee's) [19].

IS Infrastructure & Processes: The domain consists of components which are related to the IT Infrastructure and the applications being used within the organisation. The IS Infrastructure & Processes is defined in terms of choices pertaining to internal arrangement and processes which determine the types of Information Systems (IS) products and services provided to the organization [20].

[19] argued that neither strategic integration nor functional integration alone is enough to effectively align an organisation. The linkage between strategy and infrastructure and processes is observed in terms of the processes, structure and people in the organisation. Therefore, change can't take place in one domain without impacting the other three domains in some way.

In this study the proposed model was adapted from the strategic alignment model (SAM) [21]. The model consists of four variables which is "Business Strategy", "IT Strategy", "Business Infrastructure/Processes and IT Infrastructure/Processes. A quantitative approach was chosen in this study to examine the alignment of the variables and their impact on the firm's performance.

As discussed in a previous study on the Alignment of IS with business strategy literature associated with SMEs. When Information Systems is aligned with business strategy what are the factors that will lead to the firm's performance. Four factors are chosen from the strategic alignment model (SAM) to apply in this research. The research model used for this study was derived and adopted from the Strategic Alignment Model proposed by[22] and[20]See figure 1 below.

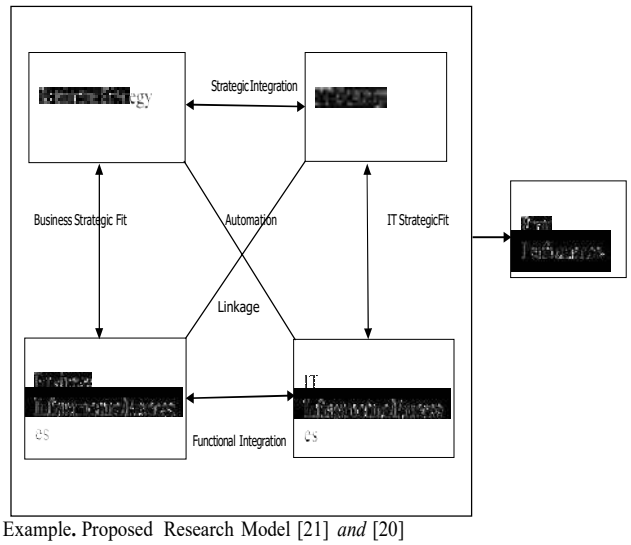

Fig. 1. Example. Proposed Research Model [21] *and* [20]

B. Sampling Procedures

To examine the alignment and firm performance, a survey was conducted on Small Medium Enterprises in Gaborone, Botswana. Data for this research was collected through a form of a questionnaire which had 7 questions that were broken up into 44 sub-questions. The questions are based on literature and previous studies. The questionnaire consists of 7 parts, covering the areas including the Background, Business Strategy and IT Strategy (Strategic Integration), Business Infrastructure/Processes and IT Infrastructure/Processes (Functional Integration), Business Strategy and IT Infrastructure/Processes (Automation), IT Strategy and Business Infrastructure/Processes (Linkage), IT Strategy and IT Infrastructure/Processes (IT Strategic Fit), Business strategy and Business Infrastructure/Processes (Business Strategic Fit).The respondents had to rate the questions on a 5-point Likert scale.

120 questionnaires were sent out and distributed to the participants by email. 92 completed questionnaires were received back which resulted in a responserate of76%.

C. Data Processing and Analysis

SPSS version 24.0 was used to analyse the data received from the participants. Validity test was used to access whether the research tool used(survey) measured what it was intended to measure using Kaiser-Meyer-Olkin (KMO), Bartlett's test of sphericity and the principal component analysis (PCA) using the varimax rotation, this was followed by factor analysis between the constructs to test and verify scale construction and operational.

In this study, we examine the impact of Business Strategic Fit, Strategic Integration, Functional Integration, IT Strategic Fit collectively as independent variable on the firm performance as the dependent variable

IV. RESULTS

The result of the survey is presented according to the main section of the surveyquestionnaire.

A. Participants Demographic Information

The first section of the questionnaire requested for background information including Gender, Age and Ethic Group of the participants. From the 99 respondent completed ***the questionnaire 54(54.5%) were Female and 45(45.5%)*** were Male. The Respondents were from different ethnic groups 50%(White), 39%(Black), 5%(Coloured) and 5%(Indian).

TABLE II. PARTICIPANT DEMOGRAPHIC INFORMATION

		Frequency	Percent	Valid Percent	Cumulative Percent
Valid	**Female**	54	54.5	54.5	54.5
	Male	45	45.5	45.5	100.0
	Total	99	100.0	100.0	

TABLE III. CORRELATION COEFFICIENT BETWEEN THE ALIGNMENT LINES

Correlations

		Strategic Integration	Functional Integration	Automation	Linkage	IT Strategic Fit	Business Strategic Fit
Strategic Integration	Pearson Correlation	1	.669**	.561**	.288**	.289**	
	Sig. (2-tailed)		0.000	0.000	0.003	0.000	
	N	99	99	99	99	99	
Functional Integration	Pearson Correlation	.669**	1	.555**	.365**	.365**	
	Sig. (2-tailed)	0.000		0.000	0.003	0.000	
	N	99	99	99	99	99	
Automation	Pearson Correlation	.561**	.555**	1	.379**	.379**	
	Sig. (2-tailed)	0.000	0.000		0.000	0.000	
	N	99	99	99	99	99	
Linkage	Pearson Correlation	.288**	.365**	.379**	1	1.000**	
	Sig. (2-tailed)	0.003	0.000	0.000		0.000	
	N	99	99	99	99	99	
IT Strategic Fit	Pearson Correlation	.289**	.365**	.379**	1.000**	1	
	Sig. (2-tailed)	0.000	0.000	0.000	0.000		
	N	99	99	99	99	99	
Business Strategic Fit	Pearson Correlation	.287**	.366**	.393**	.394**	.394**	
	Sig. (2-tailed)	0.000	0.000	0.000	0.000	0.000	
	N	99	99	99	99	99	

** Correlation is significant at the 0.01 level (2-tailed).

The above results show that Functional Integration between Businesses with a correlation coefficient of .220 is confirmed and with a significance level of .000 is supported. The Functional Integration influences Firms performance. Linkage with a correlation coefficient of .561 is confirmed and with a significance level of .000 is supported. Linkage between IT strategy and Business Infrastructure/Processes influences Firms performance.

Model Summary

Model	R	R Square	Adjusted R Square	Std. Error of the Estimate	Change Statistics				
					R Square Change	*F Change*	*df1*	*df2*	*Sig. F Change*
1	.571a	0.326	0.298	0.2979	0.326	11.39	4	94	0

a. Predictors: (Constant), Business Strategic Fit, Strategic Integration, Functional Integration, IT Strategic Fit

b. Dependent: Firm Performance

Model		*Unstandardized Coefficients*		*Standardized Coefficients*	*t*	*Sig.*
		B	*Std. Error*	*Beta*		
1	(Constant)	2,21	0,227		9,741	0,001
	Total A	0,521	0,426	0,958	1,222	0,001

a. Dependent Variable: Firms Performance

TABLE IV. REGRESSION ESTIMATION AND MODEL TESTING RESULT

V. CONCLUSION AND FUTUREWORK

This paper focused on the alignment of Information Systems with business processes within SME's (Small Medium Enterprises). IS has been commonly used by many companies to automate and integrate their business operations. Previous researches have shown that information system adoption does increases firm's performance and operations efficiency. This study contributed in examining the connection between Business Strategy, IT Strategy, Business infrastructure/Processes and IT Infrastructure/Processes. The research was conducted on SME within Botswana, it also covered the participants with diverse age group, race and background on alignment of IS with business processes. The results concluded that the four variables influence an increase in Firm's performance.

The results indicate that the correlation between Business Strategic Fit, Strategic Integration, Functional Integration and IT Strategic Fit combined are significant predictors of firm performance. The positive relationships established between the different methods of alignment and the firm's performance show's that attaining alignment between IT and the business is important for firm's success.

As previous studies show aligning IS and business processes showed that issues pertaining alignment within SME's exists, and that if an organisation is successfully aligned this will lead to an increase in the firm's performance. In this paper we observed IS Alignment, focusing on thealignment of IS with business processes.

However, alignment is not something that can only be implemented once and think that all is done it is anendless procedure. Therefore, we recommend as IT/IS becomes an

important factor in the development and delivery of business strategy, further research in looking at an alignment model which is IS driven. Further studies can be undertaken on accounting software implementation within SME's to assist in identifying areas of successful implementation and observe whysome SME's succeed or fail.

REFERENCES

[1] Sarhandi, " Business-IT Alignment," *Stockholm University & Royal Institute of Technology, Department of Computer and Systems Sciences* vol. , 2011.

[2] R. Sabherwal and Y. Chan, "Alignment between Business and IS Strategies," *A study of prospectors, analyzers and defenders* vol. 12, pp. 11-33, 2001.

[3] Y. E. Chan and B. H. Reich, "IT alignment what have we learned?," *Journal of Information Technology,* vol. 22, pp. 297-315, 2007.

[4] C. Consortium, "Achieving Strategic Business " *IT Integration and Alignment,* pp. 18-25, 2001.

[5] J. Luftman, "Business-IT Strategic Alignment Concept in theory " *Business-IT Strategic Alignment Concept in theory,* vol. 3, pp. 89-104, 2004.

[6] A. Cataldo, R. J.McQueen, and Hardings, "Comparing Strategic IT Alignment versus Process IT Alignment," *Journal of Research and Practice in Information Technology,* vol. 44, pp. 43-57, 2012.

[7] R. S. Chen and C. M. Sun, "Aligning Information Technology and business strategy with dynamic capabilities perspective," *International Journal of Information Management* vol. 28, pp. 366-378, 2008.

[8] F. Schlosser, D. Beimborn, T. Weitzel, and H. Y. Wagner, "Achieving social alignment between Business and IT," *Journal of Information Technology,* vol. 30, pp. 119-135 2015.

[9] F. Perrini, "SMEs and CSR Theory: Evidence and Implications from an Italian Perspective. ," *J Bus Ethics https://doi.org/10.1007/s10551-006-9186-2,* vol. 67, pp. 305–316, 2006.

[10] E. Fernely and F. Bell, "Using bricolage to integrate business and information technology innovation in SME's," *Technovation https://doi.org/10.1016/j.technovation.2005.03.005,* vol. 26, pp. 232-241, 2006.

[11] M. Herrington, "Entrepreneurship in South Africa," *UCT: Graduate School of Business.,* vol. 1, pp. 15-25, 2010.

[12] G. Cacciotti, "Fear and Entrepreneurship: A Review and Research Agenda," *International Journal of Management Reviews,* vol. 17, pp. 165-190, 2015.

[13] D. Avison, J. Jones, P. Powell, and D. Wilson, "Using and validating the strategic alignment model," *The Journal of Strategic Information Systems,* vol. 13, pp. 223-246, 2004.

[14] S. Gregory, Hart, D. & Martin, N., "Enablers of business strategy and IS/IT alignment " *Information Technologyand People,* vol. 20, pp. 96-120, 2007.

[15] K. Bruce, "Can you align IT with Business Strategies?," *Strategy and Leadership,* vol. 26, pp. 16-20, 1998.

[16] G. Puth, "The communicating leader. Second Edition, South Africa " *Van Schaik Publishers,* 2002.

[17] J. W. Weiss, "Aligning Technology and Business Strategy," *Field of study of 15 Companies,* 2004.

[18] E. Silva, "Strategic Business and IT Alignment," *A Prioritized Theory Diagram,* 2006.

[19] T. Coltman, P. Tallon, and R. e. a. Sharma, "Strategic IT alignment: twenty-five years on," *J Inf Technol https://doi.org/10.1057/jit.2014.3,* vol. 30, pp. 91–100, 2015.

[20] P. Cragg, T. Marco, and A. Mills., "Evaluating the alignment of IT with business processes in SMEs " *ACIS 2007 Proceedings https://aisel.aisnet.org/acis2007/10,* vol. 10, 2007.

[21] J. C. Henderson and N. Venkatraman, "Strategic Alignment: Leveraging Information Technology for Transforming Organizations," *IBM Systems Journal (Volume: 32, Issue: 1, 1993),* vol. 32, 1993.

[22] J. C. Henderson and N. Venkatraman, "IBM Systems Journal " *IBM Systems Journal https://doi.org/10.1147/SJ.1999.5387096,* vol. 38, pp. 472–484, 1999

Current state of research on microbial fuel cells: transfer mechanism, biofilm development, electrodes materials and architecture

Maryam Khadim Mbacké[#1], Mouhamed Ndong[*2], Babacar Ngom[#3]

[#] *Laboratoire des Sciences, Technologies Avancées et Développement Durable*
University Amadou Mahtar Mbow, Lot No75R VDN, Cité Keur Gorgui, BP 45 927, Dakar (Sénégal)

[1] maryam.mbacke@uam.edu.sn

[3] babacar.ngom@uam.edu.sn

[*] *Laboratoire eau, énergie, environnement, procedés industriels*
École Supérieure Polytechnique de Dakar, Université Cheikh Anta Diop de Dakar, Corniche Ouest, BP 5085, Dakar (Sénégal)

[2]mouhamed.ndong@esp.sn

***Abstract*— Microbial fuel cells are an alternative for the production of clean energy. The power provided by this system depends on several factors including the nature of the biofilm formed, the mechanisms of electron transfer within the bacterium and from the biofilm to the anode, the electrode materials and the configuration of the cell. This review aims to highlight the advances in research in this field over the past two years in order to identify the technical challenges, the proposed solutions and the possible synergies for obtaining better efficienciesintheconversionofenergy.**

Keywords: microorganisms, biofilm, anode, cathode, bacteria, electricity.

I. INTRODUCTION

In 2021, the concentration of the atmosphere in carbon dioxide amounted to 415.7 (ppm), that of methane to 1,908 (ppb) and that of nitrous oxide to 334.5 ppb, an increase of 149%, 262% and 124%, respectively, compared to pre-industrial times [1]. These greenhouse gases resulting mainly from the use of fossil fuels lead to strong impacts on the environment through climate change.

It is therefore urgent to move towards the energy mix through using renewable energies to achieve an energy intensity of 3.2% in accordance with objective 7 of sustainable development [2].

Microbial fuel cells are an energy source that has received scientific interest in recent years due to their dual utility in effluent treatment and energy production, but also their market share estimated at 33.09 billion. USD by2027 [3].

Given the complexity of the system which involves microbiological, electrochemical and transfer phenomena within a reactor, it is important to analyze the performance of microbial fuel cells under various experimental conditions.

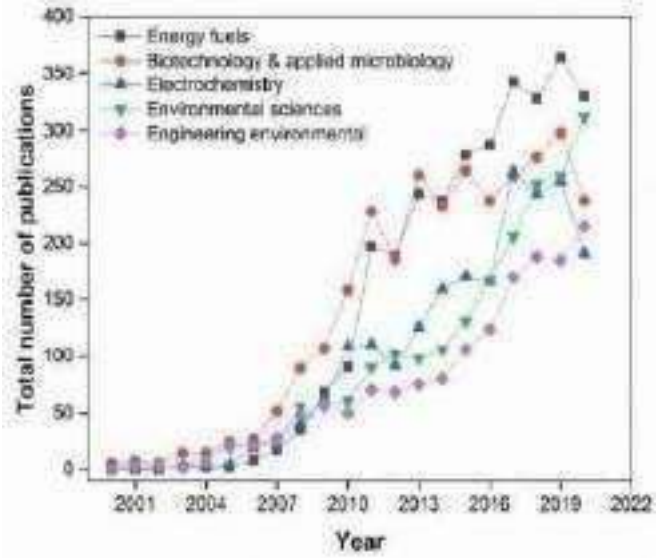

Fig. 1 Evolution of MFC subject categories [4].

II. OPERATING PRINCIPLE OF PCMS

The microbial fuel cell is a device consisting of an anode and a cathode separated or not by a membrane. At the anode, bacteria are used as a catalyst through the formation of a biofilm to oxidize the organic matter present in a substrate. The electrons thus released pass from the anode to the cathode through an electrical circuit while the

protons cross the membrane towards the cathode to close the circuit.

The anodic oxidation reactions involved depend on the type of substrate used. In the case of acetate, the reaction is such that [5]:

$$CH_3COO^- + 4H_2O \rightarrow 2HCO_3^- + 9H^+ + 8e^- \quad (1)$$

The reduction reaction at the cathode is ensured by a supply of oxygen in the case of an air cathode. Oxygen is used as an oxidant in many cases, due to its availability and high reduction potential. Indeed, an ideal electron acceptor is necessary and must be durable, without interference or toxic effect on the microbial community or any other element of the system [6].

$$O_2 + 4H^+ + 4e^- \rightarrow 2H_2O \quad (2)$$

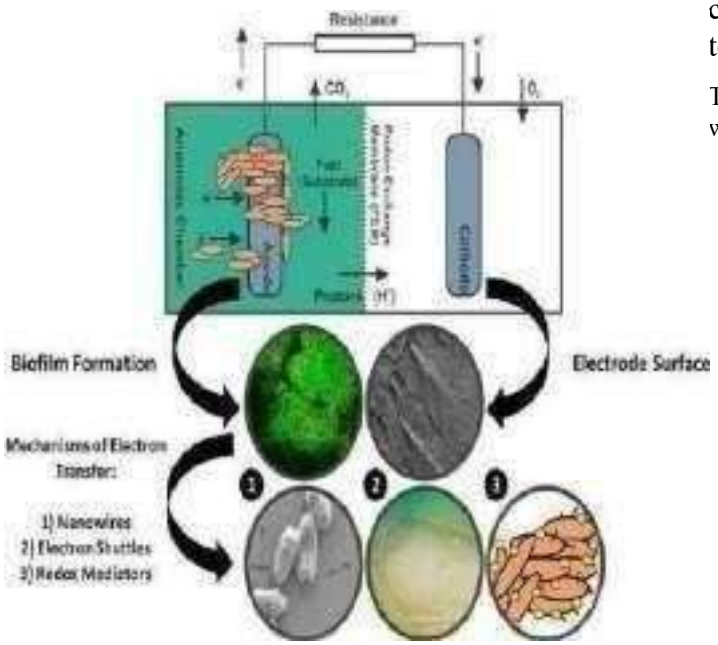

Fig. 2. Schematic of a typically employed two-chamber microbial fuel cell highlighting the various electrochemical and electro-microbiological processes [5]

III. THE KEY PARAMETERS

MFC configuration is a key factor in determining the power production to achieve greater efficiencies and reduced costs for industrial applications. A distinction is thus made between various configurations such as MFCs without membrane with a single chamber, MFCs with a double chamber separated by a membrane, tubular or cylindrical MFCs with a single compartment with a membrane and MFCs with a single chamber with a configuration with several anodes [10].

A. The configuration

Due to the complexity of the phenomena involved (electrochemistry, microbiology), the operation of a microbial fuel cell depends on various factors such as the configuration of the cell, the nature of the electrodes, the type of substrate and the bacteria present.

From the point of view of the configuration, a distinction can be made between single-chamber batteries and double-chamber batteries [6]. Dual chamber configurations are typically used for pilot testing.

Table 1 gives the advantages and disadvantages associated with each of them.

TABLE I

ADVANTAGES AND DISADVANTAGES OF MFCS BY CONFIGURATION

Configuration	MFC single chamber	MFC double chamber	Reference
Advantages	low implementation cost	Ability to track system behavior in each compartment	8
		Low fouling of electrodes	7
Disadvantages	oxygen backscatter	separator (pem) and aeration costs	7
		increase in internal resistance due to inter-electrode distance	7
		slow oxygen reduction reaction (ORR).	8
		Cathode chamber fed regularlywith fresh electrolytes or with a continuous air sparge	8

Different configurations based on key parameters have been proposed to improve electricity production.

Related to the separator, PEEK membranes (polyether ether ketone) are an alternative to Nafion.

Indeed, it is a low-cost polymer with good thermal stabilityand good mechanical properties [9].

The configuration of MFCs can vary widely to optimize power outputs. We thus distinguish various configurations such as MFC without membrane with single chamber, MFC with double chamber separated by a membrane, tubular or cylindrical MFC with a single compartment with membrane and MFC with single chamber with a configuration with several anodes [10].

There are different arrangements of MFC (a) MFC with two compartments and a membrane (b) Single-compartment MFC (c) Single-compartment multi-anode MFC (d) Single-compartment tubular MFC with membrane (e) Single-compartment cylindrical MFC with membrane (f) Single-chamber membrane-less cylindrical MFC [10].

TABLE II
MFC PERFORMANCE BY CONFIGURATION

Configuration	Performances	Reference
four reactors (28 mL x4) connected in parallel configuration	volumetric power density of 1248.5 mW/m^3 (139.8 µW) at 0.291mA	11
reactor with multiple tin-coated copper mesh (TCCM) anodes and a platinum-coated titanium mesh cathode	Power density of 2965 mW/m^2	12
cylindrical reactor	power density of 3322 ± 38 mWm^{-2}	13

B. The electrodes

Electrodes can be classified mainly into two groups, namely metal-based electrodes and carbon-based electrodes.

Mostly used anode electrodes are carbon paper, carbon cloth, carbon fibre, reticulated vitrified carbon, carbon mesh, graphitic granular, carbon brushes, graphite rod, polycrystalline graphite, carbon felt, platinum mesh, different metal electrode strips, conductive polymer-based strips.[14]

The anode material must combine good conductivity and biocompatibility with bacteria. Metals such as copper, platinum and stainless steel are good conductors and therefore ideal for electrochemical activity but have poor compatibility for microbial activity. Some metals such as platinum and titanium have shown a strong ability to transport electrons over long distances but have limitations related to their high cost. Research then turns to alternative materials when scaling.

Cathode performance is rated based on high electrical conductivity, high mechanical strength, and catalytic efficiency. The main constraint identified in the functioning of the cathode is related to slow oxygen reduction (ORR).

Table 3 shows the rated performance as a function of electrode material.

TABLE III
PERFORMANCE ACCORDING TO ELECTRODE MATERIAL

Anode	Cathode	Separator	Performances	Reference
lignin-based electrospun carbon fiber	air cathode consisting of macrocyclic catalysts pyrolyzed on carbon bound by polytetrafluoroethylene (PTFE)	fiberglass	maximum current densityof 0.59 Am^{-2} and a power densityof 0.12 Wm-2	15
graphite activated carbon cloth	graphite activated carbon cloth		power density of 904 mW/m^2	16
activated carbon derived from coffee waste (CWAC)			power density of 3927 mW m^{-2}	17
stainless steel disc coated with candle soot			power density of 1650 ± 50 mW/m^2	18
	Activated carbon from Balsa wood chips by pyrolysis at 800 ˚C		power density of 200 mW/m^2	19

The analysis of research results on cathode materials shows that biocathodes can be a good alternative to the use of expensive materials. In effect, when working with a membrane less SMFC, the likely development of a biofilm at the cathode can be leveraged in the form of a biocatalyst to accept electrons from the cathode substrate. The challenge will then be to optimize the starting of the cathode.

C. Substrate, biofilm and transfer mechanism

Biodegradable substrates can be of different types ranging from pure constituents such as acetate, glucose, cysteine, ethanol and bovine serum albumin, to complex mixtures of organic substances such as wastewater, garden or agricultural waste.

The development of an efficient anodic biofilm has a significant impact on the energy performance of MFCs. It depends on the nature of the microorganisms, the nature of the substrate and the affinity with the electrodes. The electroactive organisms present in the anode chamber often consist of Geobacter, Rhodobacter and Turicibacter [20] which are powerful electrogens. Other species were detected depending on the characteristics of the substrate.

Table 4 indicates the performances noted according to the type of substrate and the bacteria constituting the biofilm.

TABLE IV

PERFORMANCES DEPENDING ON THE TYPE OF SUBSTRATE AND BACTERIA

Substrate	Biofilm	Performances	Reference
soil+poultrywaste		power density of 904 mW/m^2	16
algal biomass		power density of 2965 mW/m^2	12
acetate	Geobacter sulfurreduce ns	maximum current density of 0.59 Am^{-2} and a power densityof 0.12 Wm^{-2}	15
	Pseudomon as aeruginosa	power density of 3322 ± 38 mWm^{-2}	13

Depending on the biocompatibility between the bacteria and the anode, a biofilm is formed. Bacteria release electrons by oxidation of organic matter in the substrate. Electrons must be transferred from the living microbial cell membrane inside the outer membrane. This extracellular electron transfer must result in a redox active species that can electronically link the bacterial cell to the electrode. The transfer of extracellular electrons (EET) between living microorganisms and the electrodes can therefore be direct (DET) or indirect or mediated (MET).

The analysis of the different works show that the optimization of the power density depends on several factors. Researchers' approaches remain targeted on each parameter separately. Table 5 translates the parameters which gave the best performance.

TABLE V

Parameter	Proposed Solution	Impact
Configuration	cylindrical	Increased power density
Anode	carbon-based materials modified by techniques such as: acid treatment, electrochemical treatment, polymer coating	low cost, biocompatible, good conductivity
Cathode	mixed transition metal oxides of nickel and copper (Ni and Cu), supported on a graphene (G) electrocatalyst (NiO–CuO/G)	profitable for ORR
	air cathode obtained from Balsa wood chips bypyrolysis at 800 ˚C	low cost
Substrate	Organic waste	biodegradable, high population of electricity-causing bacteria
Biofilm and Transfer Mechanisms	pure strains	Bacteria with anodic exo-electrogenic metabolism, the best known and studied are Geobacter sulfurreducens and Shewanella oneidensis

Observed performance can be attributed to single parameters or a combination of different factors. It is then relevant to carryout an experimental plan to

optimize the operating parameters. A 7-factor HADAMARD Matrix can be used.

Scaling MFCs involves controlling the impact of different parameters. Multi-factor modeling can be used.

In this sense, work has been initiated on the use of aluminum hydroxide sludge from the effluent treatment process by electrocoagulation as a source of bacteria.

Conclusions

MFCs are an innovative and sustainable technology for energy production. The objective of this review is to take stock of research on MFCs for energy production to see the limits, the solutions proposed, the possible synergies and the challenges for scaling up. We have seen that for most researchers, the objective was to combine the production of energy with the elimination of a pollutant. The results are therefore more focused on the effectiveness of the MFC according to different parameters. Parameters such as configuration, electrode materials, substrate, microorganisms, biofilm and transfer mechanisms have been investigated. It is then necessary to push more research towards the optimization of these parameters. Effective operation of the MFC system depends on a stable internal and external environment. Scaling of MFC systems should be supported by proper control of operating conditions. The operating parameters can be optimized through experimentaldesigns and modelling.

ACKNOWLEDGMENT

Our thanks go to Dr. Malick Mbengue and Dr. Cheikhou Kane of the Ecole Supérieure Polytechnique of Dakar (Senegal) for their respective contributions in the interpretation of microbiological and electrochemical phenomena.

REFERENCES

[1] Organisation mondiale de la métrologie, Bilan des gaz à effet de serre présents dans l'atmosphère, d'après les observations effectuées à l'échelle du globe en 2020, Bulletin de l'OMM sur les gaz à effet de serre N° 17 | 25 octobre 2021, ISSN 2078-0796

[2] Rapport sur les objectifs de développement durable 2022, ISSN :2521-7216, Copyright © Nations Unies, page 40-42, 2022.

[3] Resources market research reports, Fuel Cell Market Size, Share & Trends Analysis Report by Raw Material, by Product (PEMFC, PEFC, SOFC, MCFC), by Application (Stationary, Transportation, Portable), and Segment Forecasts, 2020 – 2027, February 2020

[4] Muhammad Nihal Naseer and al. Mapping the field of microbial fuel cell: A quantitative literature review (1970-2020), Energy Reports 7:4126-4138 DOI: 10.1016/j.egyr.2021.06.082, July 2021.

[5] Anthony J. Slatea, , Kathryn A. Whiteheada, , Dale A.C. Brownsona, , Craig E. Banks. Microbial fuel cells: An overview of current technology. Renewable and Sustainable Energy Reviews Volume 101, Pages60-81, March 2019.

[6] Flimban SGA, Ismail IMI, Kim T, Oh S-E. Review overview of recent advancements in the microbial fuel cell from fundamentals to applications, Energies;12:1-20, 2019

[7] Shams Forruque Ahmed et al. Insights into the development of microbial fuel cells for generating biohydrogen, bioelectricity, and treating wastewater, Energy · May 2022

[8] Timothé PHILIPPON, Développement et étude des bio-cathodes dénitrifiantes dans le contexte de la dépollution des zones humides, these de doctorat de l'universite de rennes 1, pages 29-35, (2021)

[9] Aritro Banerjee and al. Role and Important Properties of a Membrane with Its Recent Advancement in a Microbial Fuel Cell, Fuel Cell. Energies, 15, 444. https://doi.org/10.3390/en15020444, 2022

[10] Jeetendra Prasad, Ramesh Kumar Tripathi, Review on improving microbial fuel cell power management systems for consumer applications, Energy Reports 8 10418–10433, (2022)

[11] Simona Di Micco and al. Performance assessment of stacked air-cathode microbial fuel cells under series and parallel electrical connections, E3S Web of Conferences 334, 08011 (2022)

[12] Taşkan, B., Bakır, M., Taşkan, E.,. Enhanced power generation from algal biomass using multi-anode membrane-less sediment microbial fuel cell. Int. J. Energy Res. 45 (2), 2021.

[13] Zhang, M., Ma, Z., Zhao, N., Zhang, K., Song, H.,. Increased power generation from cylindrical microbial fuel cell inoculated with p. aeruginosa. Biosens. Bioelectron. 141, 111394, June 2019.

[14] Yaqoob AA, Ibrahim MNM, Rafatullah M, Chua YS, Ahmad A, Umar K. Recent advances in anodes for microbial fuel cells: An Overview. Materials 13(9): 2078, 2020,

[15] Masoom Fatima, Yohannes Kiros, Robina Farooq, Rakel W. Lindström, Low-Cost Single Chamber MFC Integrated With Novel Lignin-Based Carbon Fiber Felt Bioanode for Treatment of Recalcitrant Azo Dye, Front. Energy Res., 21 Sec. Fuel Cells, Electrolyzers and Membrane Reactors, June 2021.

[16] Siti Kudnie Sahari et al., Fabrication of Single Chamber Microbial Fuel Cell (SMFC) Using Soil as a Substrate, Pertanika J. Sci. & Technol. 30 (2): 1103 -1114 (2022)

[17] Hung, Y.—H.; Liu, T.—Y.; Chen, H.—Y. Renewable Coffee Waste—Derived Porous Carbons as Anode Materials for High - Perfor - mance Sustainable Microbial Fuel Cells. ACS Sustain. Chem. Eng. 7, 16991–16999, 2019.

[18] Singh S., Bairagi P.K., Verma N. Candle soot-derived carbon nanoparticles: An inexpensive and efficient electrode for microbial fuel cells. Electrochim. Acta;264:119–127. doi: 10.1016/j.electacta.2018.01.110, 2018.

[19] Chang H-C, Gustave W, Yuan Z-F, Xiao Y and Chen Z One-step fabrication of binder-free air cathode for microbial fuel cells by using balsa wood biochar Environ. Technol. Innov. 18 100615,2020

[20] Merin Grace Baby and M. Mansoor Ahammed, Nutrient removal and recovery from wastewater by microbial fuel cell-based systems – A review, Water Science & Technology Vol 86 No 1, 29, (2022)

Control of an Isolated Photovoltaic System Based on Artificial Neural Network Approach

Noureddine Akoubi[#1], Jamel Ben Salem[#2], Lilia El Amraoui[#3]

[#] *Research Laboratory Smart Electricity & ICT, SE&ICT Lab, LR18ES44,*
National Engineering School of Carthage, University of Carthage
45 Entrepreneurs Street, 2035 Charguia II Tunisia
[1]yaakoubi.n@gmail.com
[2]bsj_jamel@yahoo.fr
[3]lilia.elamraoui@gmail.com

Abstract— **This paper proposes a study on the structure of the artificial neural network (ANN) dedicated to the control of a photovoltaic system. Indeed, the prediction capacity of the ANN varies according to the number of hidden layers and the number of neurons per layer. Moreover, a short learning base affects the accuracy of the ANN. The restructuration of the ANN allows to overcome this problem. This paper proposes, thus, a methodology to design an ANN-based control system with the best performance. MATLAB software is used to design the control model, design the artificial neural network, and visualize the simulation results.**

Keywords— **Photovoltaic system, Maximum Power Point Tracking, Artificial Neural Network, Supervised learning, Neural Net Fitting.**

I. Introduction

The application of the Maximum Power Point Tracking (MPPT) technique by artificial neural network in the control of photovoltaic systems has shown its effectiveness compared to the traditional control method [1]-[5]. Indeed, the artificial neural network has a reduced oscillation rate with a high detection and tracking speed of the maximum power point [4]-[6]. The stability of the control system based on artificial neural networks is due to the use of climate data as inputs. These climatic variables are characterized by a slow evolution compared to the electrical variables that disturb the control system.

The artificial neural network also marks a good level of accuracy in case a large training database is available. The establishment of this database is done in two ways. The first is based on generating data from a model and the second method is based on collecting data online from a working PV system [4]-[5]. In both cases, the correct choice of the structure and size of the artificial neural network and the proper distribution of the training data are the main elements that influence the accuracy of the artificial neural network. This study treats the impact of the choice of the structure and size of the artificial neural network on the control performance of a photovoltaic system [4].

The paper is composed of 4 sections. In the first, the studied PV system is presented. The second deals with the structural analysis of the neural network for the prediction of the control voltage of the DC-DC converter. The next section discusses the performance of the optimal neural network in tracking the maximum power point and we end with a conclusion.

II. Presentation of the Studied System

The studied system, which is given in Fig. 1, is composed of a photovoltaic panel of reference ASUN Energy ASM190PCA0G101, a DC-DC boost converter and a resistive load equal to 20 Ω [7]. The photovoltaic panel, which consists of three paralleled strings of two modules, produces 1 kW of power. The PV system is controlled by an artificial neural network through a PI voltage regulator with a proportional gain Kp=0.015 and an integral gain Ki=0.001 [8]. Themodel is implemented on MATLAB/Simulink.

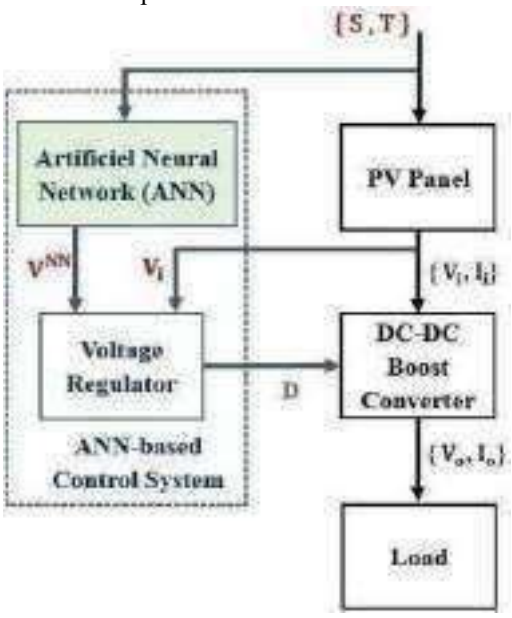

Fig. 1 Studied photovoltaic system

The voltage V^{NN}, that is generated by the artificial neural network, is the prediction of the voltage V^{MPP} that corresponds to the maximum power point (MPP) [8]. The efficiency of the ANN depends on its ability to converge to the V^{MPP} value with the smallest deviation for each value of the solar irradiation S and the temperature T.

The internal construction of the DC-DC boost converter is shown in Fig. 2.

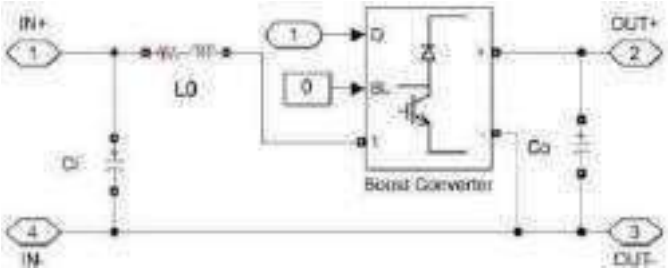

Fig. 2 Studied photovoltaic system

Where Ci=100µF, L0=2mH and Co=100µF.

III. Formalization of the Training data and Design of Artificial Neural Networks

The training data of the artificial neural network is produced from the P-V curves of the photovoltaic panel. Indeed, for each couple (S, T), we identify the value of the maximum power as well as the value of the associated voltage V^{MPP}. For example, Fig. 3 shows a value of V^{MPP} corresponding to solar irradiance level S and temperature T.

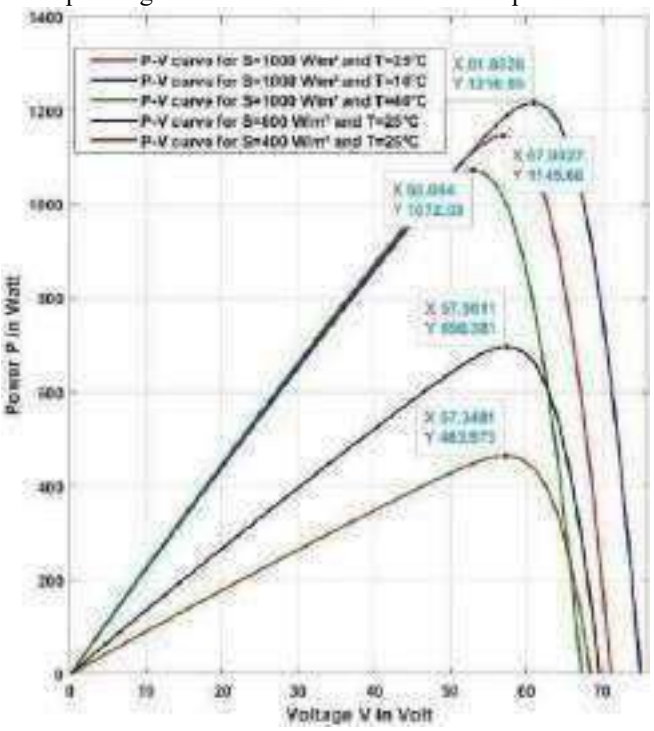

Fig. 3 Identification of the value of the voltage V^{MPP} from the P-V curves for different levels of irradiation S and temperature T

The triplet (S, T and V_{MPP}) forms a record of the training database of the artificial neural network. The training data generation program is developed in MATLAB/Simulink, which allows to form a training database. The association of the couple (S, T) with the value V^{MPP} is shown in Fig. 4.

The ANN controller has the climate variables as input. The output is the value of maximum power voltage. The ANN controller is synthesized through the "nntool" application on the MATLAB software. The study is performed on six artificial neural network structures which are described in Table I. In the following paragraph, a

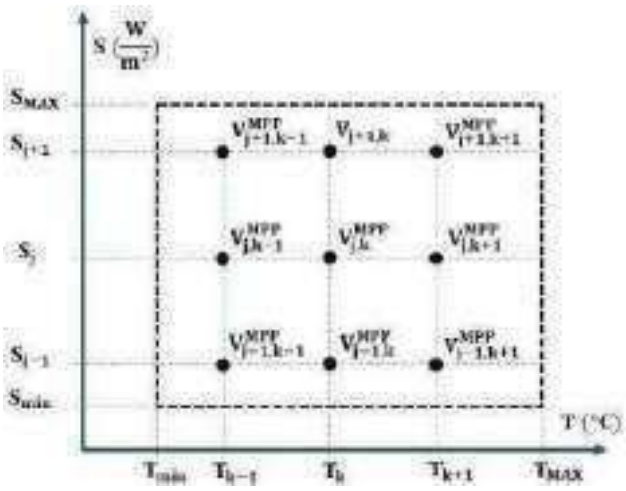

Fig. 4 Distribution of the voltage V^{MPP} as a function of the climate variables

The irradiation levels vary from 100 W/m² to 1000 W/m² with a step of 100 W/m² and the temperature varies from 5°C to 50 with a step of 5°C.

IV. Structural Analysis of the ANN

Based on the approach proposed in Section III, six artificial neural network structures have been synthesized in this study, as shown in Table I. For a series of 100 value samples of the climate variables S and T, the value of the voltage V generated by the six artificial neural networks is compared to the exact value V_{MPP} which is identified from the P-V curves of the PV panel.

TABLE I
Structure of the studied ANNs

Designation of the ANN	Number of HiddenLayer	Neurone Number per Hidden Layer
ANN1L2N	1	2
ANN1L4N	1	4
ANN1L6N	1	6
ANN1L10N	1	10
ANN2L2N	2	2
ANN2L4N	2	4

The relative error Er between the voltage V_{MPP} and the voltage generated by the neural network which is given by equation (1), is used as a criterion to evaluate the accuracy of each structure of the artificial neural network.

$$Er = \left|\frac{V_{MPP} - V_{NN}}{V_{MPP}}\right| . 100 \qquad \text{Equation 1}$$

detailed analysis of the performance of each ANN is carried out to evaluate the different structures.

Fig. 5 shows the relative error value Er for each ANN structure over the 100 climate state samples. The maximum and average value of the relative error Er for each structure of the ANN are illustrated in the histogram presented by the Fig. 6. According to the histogram, the value of the average relative error and the average relative error decrease with the increase of the number of neurons on the hidden layer. It is certainly possible to obtain better performance when the structure is divided into two hidden layers instead of one. This is clearly seen by comparing NN1L10N with NN2L4N. Thus, NN2L4N has a number of neurons equal to 8, which is lower than NN1L10N with 10 neurons and offers better performance in terms of accuracy. Indeed, the value of the average relative error is equal to 0.0632% for the NN2L4N artificial neural network against 0.0821% for the NN1L10N

artificial neural network. The maximum relative error is 0.4843% for the NN2L4N neural network and 0.5087% for the NN1L10N artificial neural network.

Fig. 5 Error variation of an A

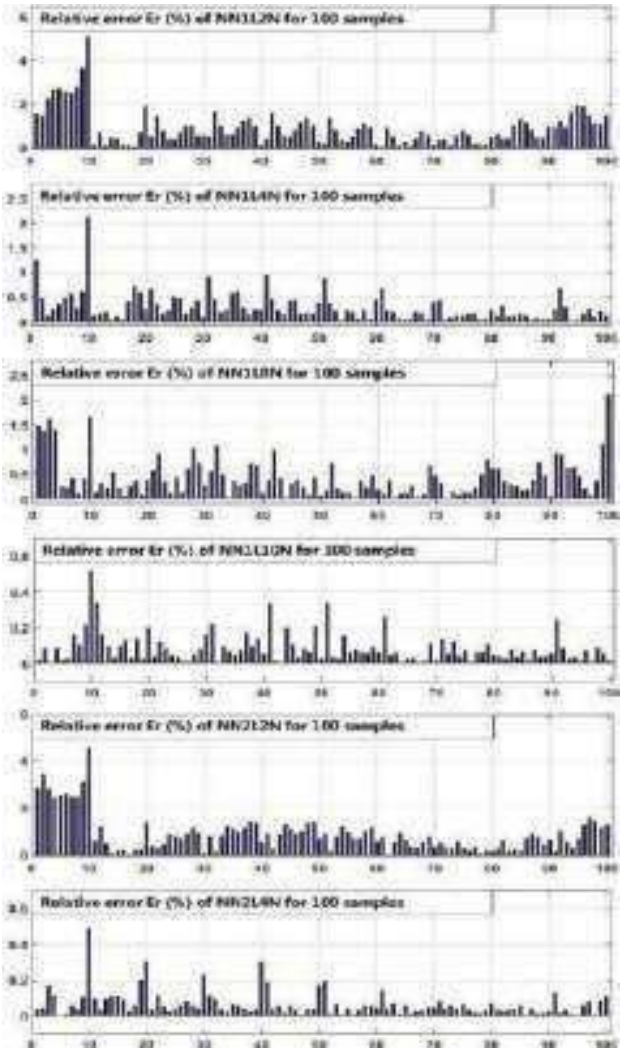

Fig. 6 Analysis of the relative error Er for each artificial neural network

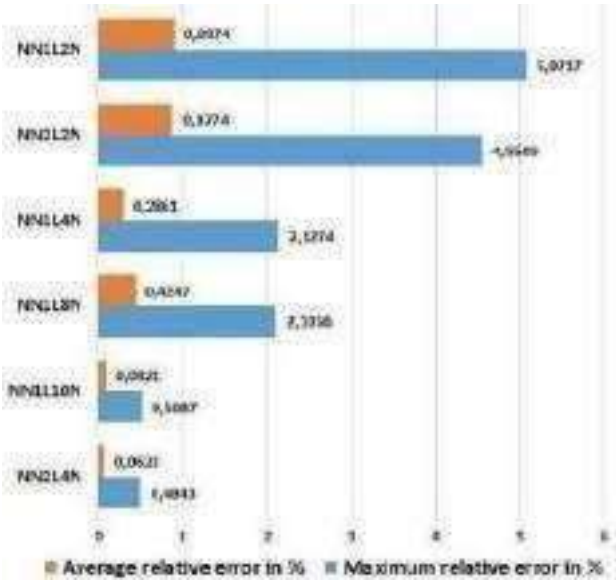

V. Simulation Result

In this section, the PV system model is implemented using the optimal artificial neural network, defined as ANN2L4N. The evolution scenario of the climate variablesS and T is given in Fig. 7 and Fig. 8, respectively.

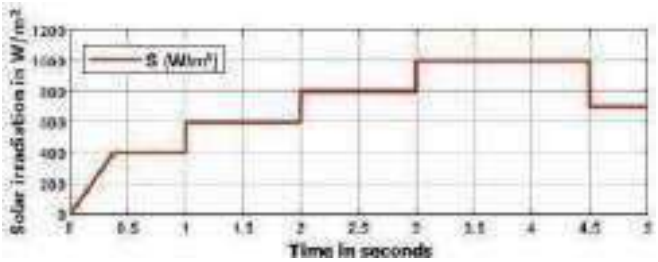

Fig. 7 Evolution of solar irradiation

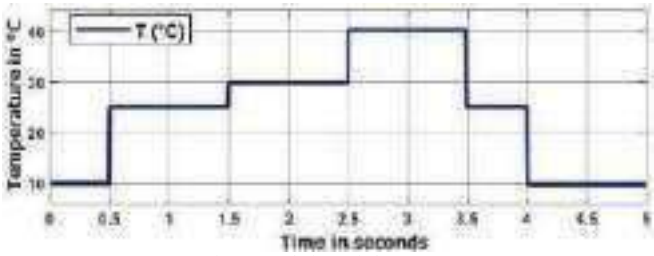

Fig. 8 Evolution of the temperature

Fig. 9 shows the variation of the amount of energy supplied bythe photovoltaic panel over the time.

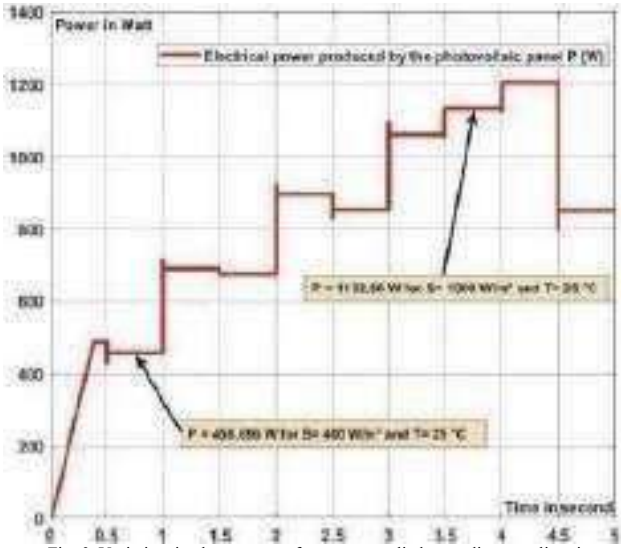

Fig. 9 Variation in the amount of energy supplied according to climatic conditions

Based on the P-V curve of the photovoltaic panel, shown in Fig. 3, Table II presents an evaluation of the accuracy of the ANN in tracking the maximum power point MPP for different levels ofsolar irradiance S and temperature T.

TABLE III
Evaluation of the accuracy of the selected ANN

S (W/m²)	T (°C)	MPP (W)	P	Gap (%)
400	25	463.973	458.696	1.13
600	25	696.381	689.07	1.04
1000	25	1145.66	1132.66	1.14
1000	40	1072.53	1059.29	1.23
1000	10	1216.95	1203.59	1.09

It can be seen that the error does not exceed 1.25%. Hence, the accuracy of the proposed model is about 98.75%. The artificial neural network correctly tracks the value of the maximum power. The small difference between the maximum power and the maximum power point is due to the electrical energyabsorbed bythe electronic component.

VI. CONCLUSION

In order to synthesize a controller based on an artificial neural network, the first step is to specify its structure and size. It turns out that the choice of the structure and size of the artificial neural network has a significant impact on the prediction accuracy of the ANN. Indeed, in this study, it is clearly demonstrated that increasing the number of layers of the ANN improves its accuracy.

Similarly, the size of the training data plays, in a second step, a key role on the prediction quality of the artificial neural network.

REFERENCES

[1] Mohammad Sarvi and Ahmad Azadian, "A comprehensive review and classifed comparison of MPPT algorithms in PV system", Energy Systems Vol. 13, pp 281–320 ,March 18, 2021.

[2] M. Mao, L. Cui, Q. Zhang, K. Guo, L. Zhou, and H. Huang, "Classification and summarization of solar photovoltaic MPPT techniques" A review based on traditional and intelligent control strategies, Energy Reports, volume 6, pp. 1312–1327, November 2020.

[3] César G. Villegas-Mier, Juvenal Rodriguez-Resendiz, José M. Álvarez-Alvarado, Hugo Rodriguez-Resendiz, Ana Marcela Herrera-Navarro, and Omar Rodríguez-Abreo, "Artificial Neural Networks in MPPT Algorithms for Optimization of Photovoltaic Power Systems: A Review", Micromachines 2021, October 17, 2021.

[4] Noureddine Akoubi , Jamel Ben Salem and Lilia El Amraoui, "Contribution on the Combination of Artificial Neural Network and Incremental Conductance Method to MPPT Control Approach", 2022 5th International Conference on Advanced Systems and Emergent Technologies (IC_ASET), IEEE, May 25, 2022.

[5] S. D. Al-Majidi, M. F. Abbod, and H. S. Al-Raweshidy, "Design of an intelligent MPPT based on ANN using a real photovoltaic system data,", 54th International UPEC, IEEE, 2019

[6] J. P. Ram, T. S. Babu, and N. Rajasekar, "A comprehensive review on solar PV maximum power point tracking techniques," Renewable and Sustainable Energy Reviews, vol. 67, pp. 826–847, January 2017.

[7] V. Kumar, S. Ghosh, N. K. S. Naidu, S. Kamal, R. K. Saket, and S. K. Nagar, "Load voltage-based MPPT technique for standalone PV systems using adaptive step," JEPE, vol. 128, June 2021.

[8] Hajar Doubabi, Issam Salhi, Mohammed Chennani, Najib Essounbouli, "High Performance MPPT based on TS Fuzzy–integral backstepping control for PV system under rapid varying irradiance—Experimental validation", ISA Transactions, Vol. 118, pages 247-259, December 2021

[9] M. R. Benzidane, R. Melati, M. Benyamina, S. Meskine, P. Spiteri, A. Boukortt, and T. A. Benattia, "Miniaturization and Optimization of a DC–DC Boost Converter for Photovoltaic Application by Designing an Integrated Dual-Layer Inductor Model, " Transactions on Electrical and Electronic Materials, October 2021.

[10] R.Divyasharon, R.N. Banu, and D.Devaraj, "Artificial Neural Network based MPPT with CUK Converter Topology for PV Systems Under Varying Climatic Conditions," IEEE International Conference on Intelligent Techniques in Control, Optimization and Signal Processing (INCOS), April 2019.

[11] Unal Yilmaz, Omer Turksoy, Ahmet Teke, "Improved MPPT method to increase accuracy and speed in photovoltaic systems under variable atmospheric conditions", International Journal of Electrical Power & Energy Systems Vol. 113 pp. 634-651,December 2019,

[12] R. Palanisamy, K. Vijayakumar, V. Venkatachalam, R. M. Narayanan, D. Saravanakumar, and K. Saravanan, "Simulation of various DC-DC converters for photovoltaic system," IJECE, vol. 9, pp.917–925, April 2019.

[13] Shaowu Li, "A variable-weather-parameter MPPT control strategy based on MPPT constraint conditions of PV system with inverter", Energy Conversion and Management Vol. 197, October 1, 2019.

[14] CH Hussaian Basha and C Rani, "Different Conventional and Soft Computing MPPT Techniques for Solar PV Systems with High Step-Up Boost Converters: A Comprehensive Analysis", Energies Vol. 13, January 12, 2020.

[15] M. R. Benzidane, R. Melati, M. Benyamina, S. Meskine, P. Spiteri, A. Boukortt, and T. A. Benattia, "Miniaturization and Optimization of a DC–DC Boost Converter for Photovoltaic Application by Designing an Integrated Dual-Layer Inductor Model, " Transactions on Electrical and Electronic Materials, October 2021.

[16] M. Fathi, and J. Amiri Parian, "Intelligent MPPT for photovoltaic panels using a novel fuzzy logic and artificial neural networks based on evolutionary algorithms," Energy Reports, volume 7, pp. 1338–1348 November 2021.

[17] S. Bhattacharyya, D. S. Kumar P, S. Samanta, and S. Mishra, "Steady Output and Fast Tracking MPPT (SOFT-MPPT) for P&O and InC Algorithms," IEEE Transactions on Sustainable Energy, vol. 12, , pp. 293–302, January 2021.

[18] Indresh Yadav, Sanjay Kumar Maurya and Gaurav Kumar Gupta, "A literature review on industrially accepted MPPT techniques for solar PV system", International Journal of Electrical and Computer Engineering (IJECE) Vol. 10, No. 2, pp. 2117-2127, April 20, 2020.

[19] Mazen Abdel-Salam, Mohamed-Tharwat EL-Mohandes and Mohamed Goda, "History of Maximum Power Point Tracking", , Modern Maximum Power Point Tracking Techniques for Photovoltaic Energy Systems pp 1-19, Green Energy and Technology, July 31, 2019.

[20] D. Gielena, F. Boshella, D. Sayginb, M. D. Bazilianc, N. Wagnera, and R. Gorinia, "The role of renewable energy in the global energy transformation," Energy Strategy Reviews Volume 24, pp. 38-50, April 2019.

[21] C. Vimalarani, N. Kamaraj, and B. Chitti Babuc, "Improved method of maximum power point tracking of photovoltaic (PV) array using hybrid intelligent controller," Optik, Volume 168, pp. 403-415, September 2018.

[22] M. N. Ali, "Improved Design of Artificial Neural Network for MPPT of Grid-Connected PV Systems," Twentieth International Middle East Power Systems Conference (MEPCON), Cairo University, Egypt, December 2018.

[23] Q. Qi, D. Ghaderi, and J. M. Guerrero, "Sliding mode controller-based switched-capacitor-based high DC gain and low voltage stress DC-DC boost converter for photovoltaic applications," International Journal of Electrical Power & Energy Systems, vol. 125, February 2021.

[24] K. Y. Yap, C. R. Sarimuthu, and J. Mun-Yee Lim, "Artificial Intelligence Based MPPT Techniques for Solar Power System: A review," Journal of Modern Power Systems and Clean Energy, vol. 8, pp. 1043–1059, November 2020.

[25] I. Chtouki, P. Wira, and M. Zazi, "Comparison of several neural network perturb and observe MPPT methods for photovoltaic applications," IEEE International Conference on Industrial Technology (ICIT), Lyon, France, February 2018.

Removal of some organics compounds present in wastewater by activated carbon prepared from Algerian sidr nabak

Oumessaâd Benturki*[1], Asma Benturki[1.2], Nadj Moulai Mostefa[2], Saliha Benturki[3]

*[1] *Laboratory of Physical and Chemical Study of Materials and Applications in the Environment, Faculty of Chemistry (USTHB), BP 32-16111 EL-Alia, Algeria.*

oum_saad@yahoo.fr; ben.asma.2019.2@gmail.com.

[2]*Materials and Environmental Laboratory, Faculty of Sciences and Technology, University of Medea, Ain D'Heb, 2001 Medea, Algeria*

moulai.nadji@univ-medea.dz

[3]*Faculté of engineering of mechanics and processes*

benturkisali22@gmail.com

***Abstract*— This study investigates the use of activated carbon prepared from an agricultural solid waste based Algerian Sidr Nabak shells by chemical activation with zin chloride($ZnCl_2$), followed by pyrolysis at 650°C for the removal of some organics compounds from aqueous solution. Batch studies were conducted for kinetic, thermodynamic and equilibrium studies on the adsorption of phenol (P) and 2-4 dichlorophenol (2-4 DCP) from aqueous solution, using activated carbon prepared (ACNS). The adsorption kinetics has been studied pertaining to various initial concentrations. The rates of adsorption were found to conform to the second-order kinetics with good correlation. Boyd plot confirmed that external mass transfer was the rate-limiting step in the sorption process. Regardless of temperature, the capacity of the activated carbon used to adsorb these compounds presented the following order: 2, 4 *Dichlorophenol* > *phenol*. The increase of temperature slightly defavoured the adsorption capacity of the organics compounds.. The maximum organics compounds removal of 92% was obtained at a pH of 6.5. The maximum adsorption efficiency of phenol and 2-4 dichlorophenol was 122.48 mg.g−1 and 277.77 mg.g−1, respectively. The results of the study show that the activated carbons derived from Sidr Nabak shells can be used as potential adsorbent for organics compounds inwater/wastewater.**

Keyword: **Activated carbon, adsorption, isotherm, organic compounds, Sidr Nabakshells.**

I. INTRODUCTION

The contamination of waterways by phenolic compounds resulting from, for example, petroleum refining and plastics and ink production, is currently a serious environmental problem. In this work we explored one of the more effective techniques for removing these compounds, namely adsorption from the liquid phase. Both powdered activated carbon is widely used in this application. However, they have the inconvenience of high cost. Hence we decided to use activated carbon produced from cork wastes (a product extre mely abundant in our region) with advantages in terms of low cost and adsorption characteristics. As one type of the most hazardous materials [1], [2], they are carcinogenic, mutagenic and resistant to biodegradation, and thus have to be decomposed before discharging into receiving waters, in order to avoid the biomagnified toxicity to aquatic flora and fauna through various food chains. Many efforts have been made for the physicochemical and/or biological t reatments of chlorophenol-rich wastewaters.

For instance, they could be removed effectively through adsorption process by using a variety of adsorbents. Among various adsorbents, activated carbon is most commonly used in wastewater treatment, attributed to its vast surface area and great affinity for organics [3].A large numbers of studies have been carried out to investigate the adsorption of phenols by activated carbon [4]–[15].Reference [12] studied the adsorption equilibrium of phenol, 4-nitrophenol, 4-chlorophenol and 2-chlorophenol onto commercial activated carbon before and after the oxidation of activated carbon at various pHs. Reference [15] investigated the adsorption isotherms of phenol, 4-chlorophenol and 4-nitrophenol from aqueous solutions using activated carbon at adsorbate concentration and solution pH on the adsorption efficiency. However, at the present time little information is available concerning the adsorption of phenols onto powder activated carbon, a new exce llent adsorbent. The objective of this study was the elaboration and characterization of carbon materials

ISSN: 1737-9334

with great adsorption power for liquids and gases; this material is basis of a biomass, an abundant agricultural product, the Sidr Nabak shells.

The activated carbon was prepared by chemical activation with zinc chloride and carbonisation at 650°C and it was to investigate the adsorption of phenol (P) and 2,4-dichlorophenol (2-4DCP) as a typical phenols, onto granular activated carbon from aqueous solutions, and to evaluate the adsorption efficiency of as a new type of adsorbent. We have concentrated on the characterization of the porosity by the B.E.T method for adsorption of N^2 [25], elementary analyses, analysis by FT-IR spectroscopy. In this work, two isotherm models, Langmuir and Freundlich, equations, were compared for describing the adsorption isotherms. In addition, the adsorption kinetics was e xplored using three kinetic models. With the e xperimental data of adsorption isotherms and kinetics, the thermodynamics of the adsorption process was also analyzed.

II. EXPERIMENTAL

A. Adsorbent

The Sidr Nabak shells as the precursor material obtained from an agricultural waste product were well washed with water several times for the removal of dust and dried at 110◦C for 6h. The dried samples were then used for the preparation of carbons. The powder activated carbon noted (ACNS) used in this work. The activated carbon was prepared by chemical activation of The Sidr Nabak shells with zinc chloride and carbonisation at 650°C at the rate of 5◦C/ min, for about 1 h under nitrogen atmosphere and cooled down to room temperature at the same rate at 650 ◦C for 2 h. The textual properties of ACNS are given in Table I. In addition to the micropores, there were many mesopores with a diameter around 2.54 nm in the ACNS, which was beneficial to facilitating the transportation of P and 2-4 DCP in the adsorption process. The ACNS was washed in boiling water for three times to remove impurities and then dried at 120 ◦C for 24 h prior to adsorption.

B. Chemicals

The chemicals used in this study, zinc chloride noted $ZnCl_2$. Phenol noted P and 2,4-dichlorophenolnoted 2-4DCP in this work and there were purchased from Fluka Chemical Reagent.

All the reagents were of analytical reagent grade and were used without further purification. Table I shows some characteristics of the phenols.

C. Analysis

1. Determination of Porous Characteristics

This was performed by the adsorption of Nitrogen at 77 K using Micrometrics Surface Area Analyzer (ASAP2010, Micromeritics Inc., USA). Before measurement, the samples were dried in the range 100-110°C and degassed at 150°C under vacuum pression 10^{-4} Pa, during 15 hours. The specific surface areas were calculated for activated carbons by the BET. The total pore volumes were estimated to be the liquid volume of N_2 at relative pressure(P/Po) of0.95.

2. Surface Characterization

The FT-IR spectrum of activated carbon was obtained by transmission with a Perkin Elmer 2000 spectrophotometer. The spectra of the samples were recorded between 4000 and 400 cm^{-1}. About 1% of carbon was dispersed in a 0.25 g KBr pellet. The pellet are immediately used and compressed at 10 tons for 3 min in a hydraulic press.

3. Batch Mode Adsorption Studies

Adsorption experiments were conducted in flasks by allowing an accurately weighted amount of ACNS to reach equilibrium with 100 mL of P or 2-4 DCP solution and 0.1g of activated carbon at temperatures of 298, 303, 313 and 333 K initial phenols concentration(2-150mg/ L) and contact time (5–2880 min). These flasks were then agitated in a temperature controlled shaker at 110 rpm. At equilibrium, the supernatant were sampled for analysis. The e xperiments of adsorption kinetics were carried out at 25C°or 298 K. Samples were analyzed at given time intervals. Each run of the e xperiments was replicated at least three times. The concentration of P and 2-4DCPwas determined using a UV– Vis spectrophotometer (Jasco 560), at an absorbance wavelength of 269 nm and 287 nm. The surface area and pore structure of the ACNS were determined bythe Nitrogen-BET method.

The amount of adsorption at equilibrium, q_e (mg/g), was calculated using. (1):

$$qe = \frac{(C_0 - C_e)V}{W} \quad (1)$$

where C_0 a*nd* C_e are the initial equilibrium concentrations (mg/L), respectively of phenol and 2-4DCP in solution, V is the volume (L), and W is the weight (g) of adsorbent.

TABLE I
PHYSICAL CHARACTERISTICS OF PHENOLIC COMPOUNDS

Compound	Molecular Mass (g/mol)	Molecular Formula	Purity	Solubility at 293 K g/100g H_2O	pK_a 298 K
Phenol (P)	94.11	C_6H_5OH	73%	9.3	9.96
2.4-DCP	163	$Cl_3C_6H_3OH$	98%	4.9	7.80

III. RESULTS AND DISCUSSION

A. General Characterization of the Activated Carbon

Nitrogen adsorption, because the relatively s mall molecule diameter of nitrogen is frequently used at 77 K to probe porosity and surface area and to be a standard procedure for the characterization of porosity texture of carbonaceous adsorbents also, the adsorption isotherm is the information source about the porous structure of adsorbent ,heat of adsorption, characteristic of physic and chemistry. As illustrated in Fig. 1, N_2 adsorption at 77 K is standard method used in characterization of the adsorbents. ACNS exhibited

ISSN: 1737-9334

adsorption isotherm of type IV according to IUPAC.

The type I isotherm represents the micro-mesoporous structure of adsorbents. The initial part of isotherm follows the same path as corresponding type II isotherm and therefore the results of monolayer-multilayer adsorption on mesopore [21], [22]. Characterization of activated carbon used in this study, the BET surface area (S_{BET}), total pore volume (V), micropore volume (V_{micro}) and mesopore volume (V_{meso}) are listed in Table II.

TABLE II
CHARACTERISTICS OF THE ACTIVATED CARBON PREPARED

Characteristics	ACNS
S_{BET} (m^2/g)	1184
V (cm^3/g)	0.560
V_{micro}(cm^3/g)	0.372
V_{meso}(cm^3/g)	0.188

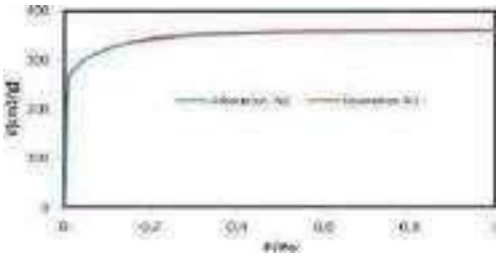

Fig.1 N_2 adsorption–desorption isotherms of activated carbon ACNS

This activated carbon is highly microporous , with a BET surface area of 1184 m^2/g, V = 0.560 c m^3/g, V_{micro} = 0.372 cm^3/g (derived from the D–R equation) and V_{meso} = 0.188 cm^3/g. It appears that activated carbons ACNS include microporesand mesopores. The IR spectrum of the activated carbons, Fig. 2, showed weak and broad peaks in the region of 3853-453 cm^{-1}. Appro ximate FT-IR band assignment indicated the presence of carbonyls, carboxyl, lactones, phenol, olefin, and aromatic structures. The 1800-1540 cm^{-1} , band is associated to C=O stretching mode in carbonyls, carboxy lic acids and lactones and C=C bonds in olefin and aromatic structures whereas the 1440-1000 cm^{-1} band was assigned to the C-O and O-H bending modes. Further, a presence of relatively weak peak/band of the hydro xyl group (centred around 3400 cm^{-1}) can be observed but slightly differs for both adsorbents.

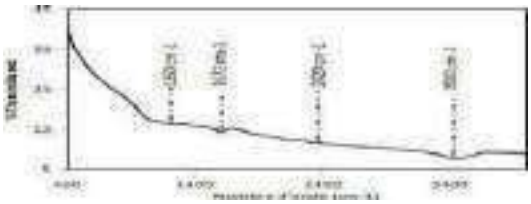

Fig.2 FT-IR spectrum ofactivated carbon ACNS

B. Effect of pH

The effect of pH of the solution on the adsorption capacity of activated carbon ACNS for substituted phenols is shown in Fig.3. At low p H, the amount of phenols adsorbed increases slightlywith the pH and at certain value of pH, there is a decrease in the value of qe while pH increases. The results indicate that the phenolic compounds are preferentially adsorbed on surface of the activated carbons in molecular form. At low pH values, they are not dissociated. The activated carbons used continue progressively acquiring negative charge from the external to the internal surface of the pores as the solution pH increases from 4 to 11 for ACNS activated carbon, the amount of phen lic compound adsorbed depends alsoon thesurface charge [20].

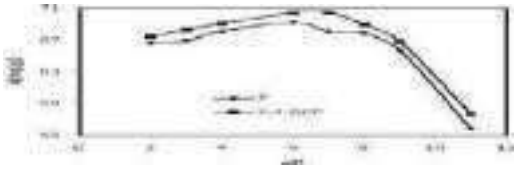

Fig. 3 Effect of pH on the adsorption of P and 2-4 DCP by activated carbon ACNS (Time =48 h, adsorbate concentration=75 $mg.L^{-1}$ and temperature=(25 ± 1°C))

C. Adsorption Isotherms

In order to understand the adsorption mechanisms of P and 2-4DCP onto ACNS, two adsorption isotherm models, Langmuir and Freundlich, were used to fit the adsorption e xperimental results. The Langmuir model is usually used with an ideal assumption of an entirely homogeneous adsorption surface, whereas the Freundlich model is appropriate for a heterogeneous surface.

The Langmuir and Freundlich isotherms, which have two parameters, could be respectivelylinearized as follows:

$$\frac{C_e}{q_e} = \frac{C_e}{q_{max}} + \frac{1}{q_{max}.K_L} \quad (2)$$

$$\ln q_e = \ln K_F + \frac{1}{n} .C_e \quad (3)$$

The parameters in the equations above could be graphically determined through linear regression. Different adsorption isotherms obtained at 25°C or 298K are illustrated in Figs. 4, 5. Application of Langmuir model and Freundlich model to adsorption isotherms, provide satisfactory linearization of the data and the values of the parameters estimated from the plots along with the correlation coefficients are listed in Table III. The high regression correlation coefficients were obtained, suggesting that all these adsorption isotherm models were applicable to describing the P and 2-4DCP adsorption onto ACNS

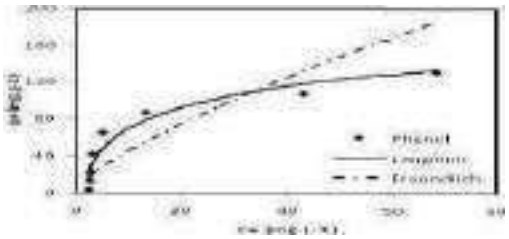

Fig. 4 Isotherm of adsorption of P onto ACNS (Time=48h, Temperature= (25 ± 1°C))

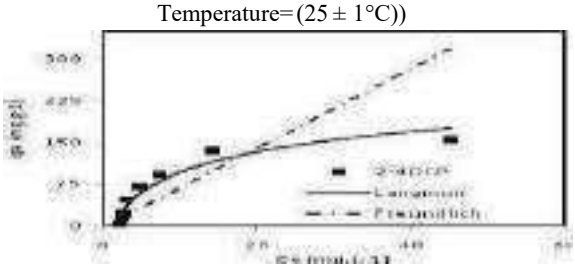

Fig.5 Isotherms of adsorption of 2-4 DCP onto ACNS (Time=48h, Temperature=(25 ± 1°C))

The isotherms for the adsorption of P and 2-4DCP onto activated carbons developed from Sidr nabak shells materials are shown in Figs. 4,5.

The maximum amount adsorbed by ACNS was observed 250 mg/g for 2-4DCP and 142.85 mg/g for P. The substituted phenol is higher removal byactivated carbon ACNS.

As shown in Table III, the isotherm models fitted to the e xperimental data in the order of: Langmuir >Freundlich and indicating that, at lower temperatures, the adsorption higher and the sorption energy was lower. This result was in consistent with the experimental observation. The magnitude of the e xponent 1/n in the Freundlich model usually gives an indication of the favorability and capacity of the adsorbent/adsorbate system. In these e xperiments, the n values greater than 1 suggest that the P and 2-4DCPcould be readily adsorbed byACNS at all the temperatures studied. In addition, the values of n were all in the range of 1–10, showing that the adsorption was beneficial for P and 2-4 DCP.

TABLE III
PARAMETERS OF THE LANGMUIR AND FREUNDLICH ISOTHERMS

	P	2-4 DCP
Langmuir		
q_{max}(mg/g)	120.48	277.77
K_L (L/mg)	0.009	0.0094
R^2	0.973	0.996
Freundlich		
1-1/n 1/n 1/n		
n	1.172	1.040
R^2	0.999	0.980

D. Adsorption Kinetics

Adsorption experiments were carried out for different contact time at 25C° with a fixed adsorbent dosage at pH=6. . The results are presented in Fig 6. Similar plots we re determined for P and 2-4 DCP. It was observed that amount of phenol adsorbed gets increased with increase in contact time. Also maximum of phenolic compound was observed at 120 min (2h) (89% for P and 90% for 2-4DCP, of total phenols adsorbed) and there after the adsorption proceeds at slower rate till equilibrium and steadystatewas after equilibrium.

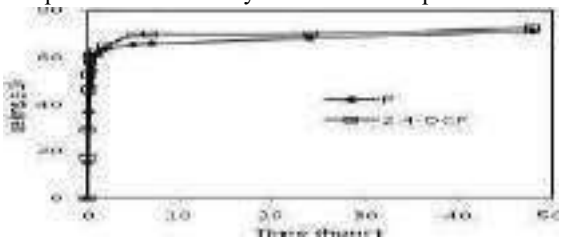

Fig.6 Effect of contact time on the adsorption of P and 2-4DCP.by activated carbon ACNS (Time =48 h, adsorbate concentration=75 mg.L^{-1} and temperature= (25±1°C))

Two kinetic models, pseudo first-order and pseudo second order models, were used to evaluate the P and 2-4DCP adsorption kinetics by ACNS at 25C°, are presented in Table IV. The linearized form of the pseudo first-order model could be expressed as following:

$$\log(q_e - q_t) = \log q_e - \frac{k_1}{2.303}.t \qquad (4)$$

However, the value of q_e (equilibriu m adsorption capacity) had to be pre-estimated by e xt rapolating the e xperimental data to t =∞. In addition, in most cases, the first-order rate equation of the Lagergren model is usually applicable over the initial 30–50 min of the adsorption process [16]. The linear relationships were observed only for the in itial 30min adsorption, and after this short period the experimental data deviated considerablyfrom the theoretical ones (not shown). The rate constants k_1 and theoretical values of q_e calculated from theslope and intercept ofthe linear plots are summarized in be given as:

$$\frac{t}{q_e} = \frac{1}{k_2.q_e^2} + \frac{t}{q_e} \qquad (5)$$

By plotting t/q against t for different adsorbats, slight lines were obtained. The values of the second-order rate constants k_2 and qe, determined from the slopes and intercepts of the plots in Fig.7, are given in Table IV.

The rate constants k_1, k_2 and theoretical values of qe calculated from the slope and intercept of the linear plots are summarized in Table IV, along with the corresponding correlation coefficients.

TABLE IV
FIRST AND SECOND-ORDER ADSORPTION RATE CONSTANTS, CALCULATED AND EXPERIMENTAL Q_E VALUES

	$q_{e(exp)}$	First-Order			Second-Order		
		k_1	$q_{e(cal)}$	R^2	k_2	q_e (cal)	R^2
	(mg/g)	(h^{-1})	(mg/g)		($mg^{-1}.g.h^{-1}$)	(mg/g)	
p	50.25	3.360	46.87	0.939	0.180	50.50	1

2-4 DCP	68.85	3.17	44.25	0.954	0.098	70.92	1

The equilibrium sorption capacities q_e(cal) determined using the pseudo-first-order model does not agree with the experimental q_e(exp) values. This shows that the adsorption of P and 2-4DCP onto activated carbon prepared from Sidr Nabak shells does not follow first order kinetics. The equilibrium sorption capacities determined q_e(cal) using the pseudo-second-order plots (Fig. 7) by the method of Ho and Wang [26] is in good agreement with the experimental q_e(exp) values. The correlation coefficients for the second order kinetic model indicate that the system under study is more appropriately described by the pseudo-second-order model. The confirmation of pseudo-second-order kinetics indicates that in the adsorption process, concentrations of both adsorbate (phenols) and adsorbent (activated carbon) are involved in rate determining step.

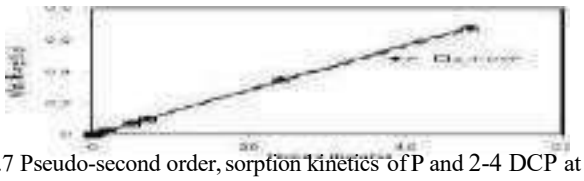

Fig.7 Pseudo-second order, sorption kinetics of P and 2-4 DCP at (pH= 6.5; adsorbent dose 0.1g, temperature (25 ± 1°C))

For all the cases, the correlation coefficients for the second-order kinetic model were close to 1.0 and the theoretical values of q_e were consistent with the experimental data. The correlation coefficients for the pseudo first order kinetics were lower than those of the pseudo second-order one [17].

The adsorption of adsorbate onto the adsorbent surface from the solution phase occurs in several steps, such as film or external diffusion, pore diffusion, surface diffusion and adsorption on the pore surface [18]. The overall adsorption process may be controlled by one or more steps. This implies that the diffusion of P and 2-4 DCP into the pores of ACNS was not the sole rate-controlling step. These results also show that the pseudo second-order adsorption model was better to describe the adsorption data than the pseudo first-order model.

E. Thermodynamic Analysis

The concept of thermodynamic assumes that in an isolated system, where energy can't be gained or lost, the entropy change is the driving force [23], [24]. The thermodynamic parameters that must be considered to determine the process are changes in standard enthalpy (ΔH^0) standard entropy (ΔS^0) and standard free energy (ΔG^0) due to transfer of unit mole of solute from solution onto the solid–liquid interface.

The value of ΔH^0 and ΔS^0 were computed using:

$$LnK_C = \frac{-\Delta H^0}{R.T} + \frac{\Delta S^0}{R} \quad (6)$$

where R (8.314 J/ mol.K) is the universal gas constant, T(K) the absolute solution temperature and K_C, the equilibrium constant which can be calculated as:

$$K_C = \frac{C_0 - C_e}{C_e} \quad (7)$$

plots between Ln K_C versus $1/T$ and also from Van't Hoff equation. The Gibbs free energy change ΔG^0 indicates the degree of the spontaneity of the adsorption process, is defined as:

$$\Delta G^0 = -RTLnK_C \quad (8)$$

with C_0: Initial concentration (mg/L), C_e: Equilibrium concentration (mg/ L) The values of ΔH^0 and ΔS^0 were calculated from the slope and intercept point of the plots between Ln K_C versus $1/T$ and also from Van't Hoff equation 6.

The ΔG^0 values were calculated at 298K and thermodynamic parameters for the adsorption are summarized in Table V.

TABLE V
THERMODYNAMIC PARAMETERS OF P AND 2-4 DCP ADSORBED BY ACNS

Adsorbant	Phenols	ΔH^0 (kJ/mol)	ΔS^0 (J/mol)	ΔG^0(kJ/mol) 298	303	313	333
ACNS	P	-18.64	-60004	-1,745	-1.144	-0.54	0.356
	2-4DCP	-26.00	-67.450	-5.95	-5.275	-4.60	-3.59

The negative ΔG^0 values indicate that the adsorption process led to a decrease in Gibbs free energy and that the adsorption process was feasible and spontaneous. The change of Gibbs free energy for the physical adsorption is generally in the range of 0 to −20 kJ/ mol, and that for the chemical adsorption is in the range of −80 to −400 kJ/ mol [19]. The values of ΔG^0 at different temperatures in this study were in the range between those of physical and chemical adsorptions. Thus, the adsorption of P and 2-4 DCP onto ACNS could be considered as a physical adsorption enhanced by the electrostatic effect. On the other hand, the adsorption enthalpy for the physical adsorption is usually in the range of nil to −60 kJ/ mol, and that for the chemical adsorption is in the range of −60 to −125 kJ/mol. Hence, based on a ΔH^0 value of −18.64 kJ/ mol for P and -26.00 kJ/ mol for 2-4 DCP, in this study, the adsorption of 2-4 DCP and P onto ACNS could also be considered as a physical adsorption. In addition, the negative ΔH^0 value implies that the adsorption process was exothermic, which was in good agreement with the experimental observations.

The positive value of ΔS^0 suggests that the randomness increased in the liquid/solid interface in the adsorption of P and 2-4 DCP onto ACNS. The adsorbed water molecules, which were displaced by the P and 2-4DCP species, gained more translational entropy than that which the P and 2-4DCP molecules lost, thus allowing the prevalence of randomness in the system. The increase in entropy of P and 2-4DCPadsorption process might be associated with the configuration changes in P and 2-4 DCP in adsorption process and/or the changes of ACNS surfaces caused byadsorption.

The experimental results above demonstrate that the ACNS activated by air was a highly efficient and cost-effective adsorbent for removal of phenolic compounds from wastewater.

IV CONCLUSION

The study indicated that activated carbon prepared from Sidr nabak (*Zizyphus jujuba*) ACNS can be summarized as follows:

The Nitrogen adsorption show, that activated carbon ACNS includes mesopores and micropores. The adsorption capacities of phenols onto ACNS, decreases in the order 2-4DCP >P. The maximal amount can be adsorbed for ACNS activated carbon is 277.77 mg/g and for P is 120 mg/g for 2-4 DCP. The preparation of activated carbon from Sidr Nabak shells by chemical activation with potassium hydroxide is efficient and gave an activated carbon with high performance of adsorption. The pH of the solutions has an important role on the adsorption performance; since it influences the surface charge of activated carbons and consequently the intensity of electrostatic interaction between metalions and activated carbons. The negative values of ΔG^0 indicate the feasibility and spontaneity of the adsorption process. The thermodynamic parameters, $\Delta H^0$and ΔS^0, were suggesting that the adsorption was exothermic. The material under consideration is not only economical, but also an agricultural waste product. Hence activated carbon prepared would be useful for economical treatment of wastewater containing phenols.

REFERENCES

[1] E. T utem, R. Apak and C.F. Unal, " Adsorptive removal of chlorophenols from water by bituminous shale,"*Wat. Res.* vol. 32, n°. 8, pp 2315-2324,Apr. 1998.

[2] Y. Fu and U.M. Diwekar and J. Adv. " Cost effective environmental control technology for utilities", *Environ. Res.* vol 18, pp 173–196, Jan, 2004.

[3] C.L. Z.R. Yue, J. Economy, S. Maloney, P. Kemme and D. Cropek, "Adsorption of organic contaminants from water using tailored ACFs",*Chem.Mater*,vol. 13, n° 7,pp 2356–2360. June. 2001,

[4] P.E. Diaz-Flores, R. Leyva-Ramos, R.M. Guerrero-Coronado and J.Mendoza-Barron, " Adsorption of Pentachlorophenol from Aqueous Solution onto Activated Carbon Fiber ",*Ind. Eng. Chem. Res.*, vol. 45, n°, pp 330–336,**2006**

[5] O.S.Benturki and F.Addoun, "Use of Activated Carbons for Treatment of Water Polluted by the Phenolic Substances", *Asian. J. Chem* , vol. 19, n°6, pp4523-4532, June.2007.

[6] Z.G. Yue, C. Mangun and J. Ecomomy, "Removal of chemical contaminants from water to below USEPA MCL using fiber glass supported activated carbon filters," *Environ. Sci. Technol.* vol.35, n°13, pp 2844–2848, July. 2001.

[7] C. BrasquetandP. Le Cloirec, "Effects of activated carbon cloth surface on organic adsorption in aqueous solutions, use of statistical methods to describe mechanisms" *Langmuir,* vol. 15, n° 18, pp 5906–5912, March. 1999.

[8] C.L. Mangun, Z.R. Yue, J. Economy, S. Maloney, P. Kemme and D. Cropek, " Adsorption of organic contaminants from water using tailored ACFs ",*Chem. Mater*,vol 13, n° 7,pp 2356–2360, 2001.

[9] J.W. Park, S.S. Lee, D.K. Choi, Y.W. Lee, *J. Chem. Eng. Data,* vol 47, pp980–983,May, 2002.

[10] M. El-Merraoui, M. Aoshimaand K. Kaneko, " Micropore size distribution of activated carbon fiber using the density functional theory and other methods", *Langmuir*, vol 16, n° 9, pp 4300–4304.March, 2000.

[11] F.C. Wu and R.L. Tseng, "Preparation of highly porous carbon from fir wood by KOH etching and CO_2 gasification for adsorption of dyes and phenols from water", *J. Colloid Interf. Sci*. vol 294, pp 21–30, Apr. 2006.

[12] P.J.M. Carrott, P.A.M. Mourão, M.M.L. Ribeiro Carrott and E.M. Gonçalves, " Separating surface and solvent effects and the notion of critical adsorption energy in the adsorption of phenolic compounds by activated carbons", *Langmuir*, vol 21, n° 25, pp 11863–11869, Oct. 2005.

[13] C. Namasivayam and D. Kavitha, "Adsorptive removal of 2 - chlorophenol by low-cost coir pith carbon", *J. Hazard. Mater.*vol 98 pp 257-274,Jan.2003.

[14] B. Okolo, C. Park and M.A. Keane, "Interaction of phenol and chlorophenols with activated carbon and synthetic zeolites in aqueous media", *J. Colloid,Interf. Sci.*vol *226*, pp 308–317, Oct. 2000.

[15] A.R. Khan, R. Ataullah, A. Alhaddad "Equilibrium Adsorption Studies of Some Aromatic Pollutants from Dilute Aqueous Solutions on Activated Carbon at Different Temperatures",*J. Colloid Interf. Sci.* vol 194, n°1, pp 154–165, Oct. 1997.

[16] S.J. Zhang, H.Q. Yu and H.M. Feng, "PVA-based activated carbon fibers with lotus root-like axially porous structure", *Carbon* vol. 44, n° 10, pp 2059-2068,Aug. 2006.

[17] Z. Aksu, " Biosorption of reactive dyes by dried activated sludge: Equilibrium and kinetic modeling", *Biochem. Eng. J*. vol. 7, pp 79–84, Dec. 2001.

[18] *M.* S. Bilgili, "Adsorption of 4-chlorophenol from aqueous solutions by xad-4 resin: Isotherm, kinetic and thermodynamic analysis", *J. Hazard. Mater,* vol. 137 *pp* 157–164,Nov. 2006.

[19] Y. Wang, Y. Mu, Q.B. Zhao and H.Q. Yu, " Isotherms, kinetics and thermodynamics of dye biosorption by anaerobic sludge", *Sep. Purif. Technol.* vol. 50, pp 1–7, June. 2006.

[20] O. S. Benturki, A. Donnot, S. Molina, A. Merlin, F. Addoun, " Synthesis and characterization of activated carbons obtained from jujube shells «nebka»",*J. Soc. Alg. Chim,* vol. 18,n° 1, pp 7-23, 2008.

[21] T.H. Usmani, W.A. Tamour,S.ZafarAhmed, A. H. K. Yousufzai," Preparation and characterization of activated carbon from a low rank coal", *Carbon*vol. 34, n° 1, pp 77-82, May.1996.

[22] K. K. W. Sing, D. H. Everett, R. A. W. Haul, L. Moscou, R. A. Pierotti, J. Rouquero and T. Siemieniewasa, "Physical and biophysical chemistry division commission on colloid and surface chemistry including catalysis",*Pure Appl. Chem.* vol.**5, pp** 603-619, 1985.

[23] Z.Ryu, J. Zheng, M. Wang, B. zhang, " Characterization of pore size distributions on carbonaceous adsorbents by DFT", Carbon. vol. 37, n 8, pp 1257-1264,Jun. 1999.

[24] K.V. Kumar and A. Kumaran, " Removal of methylene blue by mango seed kernel powder", *Biochem. Eng. J*. vol. 27, pp83-85, Nov. 2005.

[25] S.J. Gregg, K.S.W. Sing, " Adsorption, Surface Area and Porosity", *Academic Press,* New York, 1982.

[26] Y.S. Ho, C.C. Wang, "Pseudo-isotherms for the sorption of cadmium ion onto tree fern ",Process Biochemistry, vol, 39, pp 759 –763, Jan. 2004.

ÉVALUATION de L'ACTIVITE ANTIBACTERIENNE de la *GLOBULARIA ALYPUM*

Meriem Slama [#1]

[#] *Département de Génie des Procédés, Ecole Nationale Polytechnique de Constantine, Constantine, Algérie*

[1] meriemslama95@gmail.com

Abstract—L'espèce *Globularia Alypum* est connue pour son usagealimentaireen tant que tisane dans le but de traiter les troubles de la digestion et la constipation.Notre travail consiste à évaluerl'activité antibactérienne d'un extrait hydrométhanolique de cette plante. L'extraction par macération classique, à partir desfeuilles de cette plante, a donné un rendement d'extraction considérable de 47.50 %.

L'évaluation de l'activité antibactérienne a été déterminée à partir des bactéries à gram positif (bacillus subtilis, Staphylococcus) et des bactéries à gram négatif (Enterobacteriaceae) selon la méthode de diffusion sur un disque d'agar, L'extrait présente un effet antibactérien contre*Staphylococcus*(20 mm), suivi de *B. subtilis* et *Enterobacteriaceae* (15 mm).

***Keywords*—*Globularia Alypum* ;Rendement ; activité antibactérienne ; *Staphylococcus* ;bacillus subtilis ; *Enterobacteriaceae*.**

I. INTRODUCTION

L'usage des plantes pour des fins médicales a été utilisé depuis la nuit des temps par la médecine traditionnelle dite aussi non-conventionnelle. Cette dernière est basée sur l'expérience séculaire transmise par compagnonnage[1].

Généralement les plantes comprennent une ample variété de molécules chimiques (terpènes, polyphénols, alcaloïdes, etc.). Elles sont aussi une source de molécules bioactives ayant une large variété d'activités biologiques (antitumorale, antivirale, antimicrobienne, antioxydantes, etc.) [2].

Le choix de notre étude se porte sur une plante appelée *Globularia Alypum*, cette dernièreest fortement utilisée en médecine traditionnelle d'où la nécessité d'évaluer son potentiel antimicrobien.

II. MATERIEL ET METHODES

A. Matériel végétalet méthode d'extraction

L'espèce Globularia Alypum a été récoltée durant la période du mois de Décembre 2017, dans la région de Béni Ouartilene, wilaya de Sétif, région montagnarde loin de toute pollution. Les feuilles de cette plante, séparées des tiges et des fruits, ont été séchées au laboratoire, à température ambiante et à l'air libre. Elles ont été broyées, jusqu'à l'obtention d'une poudre fine. Ensuite 25 g de la poudre a été extraite avec un mélange de méthanol/eau (80/20 : V/ V) dont le rapport utilisé est (1 g de matière végétale pour 10 ml de solvant) pendant 24 h sous agitation à température ambiante. Après filtration, lemélange a été évaporé sous vide et l'extrait obtenu a été pesé,récupéré en le faisant dissoudre dans le méthanolet stocké à 4°C pour l'évaluation de l'activité antibactérienne.

B. L'activité antibactérienne

L'activité antibactériennede l'extrait méthanoïque a été déterminé par la méthode de diffusion sur disque. Trois souches bactériennes ont été utilisées : Staphylococcus, Bacillus subtilis et Enterobacteriaceae. Les souches bactériennes ont été cultivées sur gélose Mueller-Hinton. A partir d'une culture microbienne de 24 h, les inoculums microbiens ont été préparés dans une solution saline stérile. Ensuite, des plaques de gélose stériles ont été inoculées avec la suspension microbienne et des disques de papier filtre stériles ont été déposés sur les surfaces des plaques de gélose. Chaque disque a été imprégné de 100 µL de la solution d'extrait méthanoïque. Après incubation à 37°C pendant 24h, les diamètres des zones d'inhibition de croissance ont été mesurés[3].

III. RESULATS ET DISCUTION

A. Rendements d'extraction

L'extrait hydrométhanoliqueobtenu par macération des feuilles broyées en fine poudrede l'espèce Globularia Alypum nous a donné un rendement d'extraction de 47,50 %.

Une étude menée par[4] sur le rendement d'extraction de la *Globularia Alypum* a enregistré une valeur de 42,40 % pour une extraction hydrométhanolique (75% méthanol, 25% eau, V/V) dans un système soxhet pendant 48 h à 65 ° C. Une autre étude réalisée par[5] a enregistré un rendement d'extraction 30,40% pour une macération éthanoïque pendant 72 h.

La variation des rendements d'extraction dépend de plusieurs paramètres tels que : type et concentration du

solvant, rapport solide / solvant, temps, température, pH, etc[6].

B. Evaluation de l'activité antibactérienne

Les résultats montrent que notre extrait méthanoïque de la plante Globularia Alypum a un effet contre les bactéries Bacillus subtilis, Staphylococcus et Enterobacteriaceae avec des diamètres de 15, 20 et 15 (mm) respectivement.

Une étude sur l'effet antimicrobien d'extrait méthanoïque des feuilles de l'espèce Globularia Alypum montre des zones d'inhibition de croissance bactérienne pour les S. aureus et B. subtilis (gram positive) avec des diamètres de 6.67±0.33 et 10.67±0.33, respectivement En revanche aucun effet n'a été constaté pour les bactéries E. coli et P. aeruginosa (gram négative) [3]. Il existe d'autres études sur l'activité antibactérienne des substances actives d'origine végétale, montrant la dépendance de cette dernière de la nature des bactéries Gram+ ou Gram–. Dans le sens où la paroi des bactéries Gram– est assemblée enlipopolysaccharides (LPS), la membrane extérieure de ces dernières constitue une barrière de perméabilité efficace alors que les bactéries Gram + sont moins protégées contre les agents antibactériens, le peptidoglycane n'entrave que ladiffusion des molécules supérieures à plus de 50000 Da [7].

Par ailleurs, la diffusion des molécules antibactériennes contenues dans l'extrait vers les bactéries, dépend de plusieurs paramètres tels que la température, le pH, l'aération, le pourcentage en NaCl, la concentration du glucose, et le temps d'incubation sur les différentes souches microbiennes [8].

IV. CONCLUSIONS

Lamacération hydrométhanolique nous a permis d'obtenir un rendementd'extraction de 47.50%. Cette méthodes'estrévélée très efficace pour puiser le contenu bioactif des plantes médicinales, entre autres Globularia Alypum.

L'étude biologique de cette plante montre que le pouvoir antimicrobien de l'extrait hydrométhanolique est plus important contre la bactérie de Staphylococcus (20 mm), suivi de B. subtilis et Enterobacteriaceae (15 mm).

REFERENCES

[1] A. Lengani, L. Fulbert lompo, I. Pierre guissou, and J. Nikiema, "Médecine traditionnelle et maladies des reins au Burkina Faso," *Néphrologie & Thérapeutique*, vol. 6, no. 1, pp. 35–39, 2010.

[2] T. Michel, "Nouvelles méthodologies d ' extraction , de fractionnement et d' identification : application aux molécules bioactives de l' argousier (Hippophae rhamnoides)," Université d'Orléans, 2011.

[3] O. K. Taghzouti, M. Balouiri, W. Ouedrhiri, A. Ech chahad, and A. Romane, "In vitro evaluation of the antioxidant and antimicrobial effects of Globularia alypum L. extracts," *J. Mater. Environ. Sci.*, vol. 7, no. 6, pp. 1988–1995, 2016.

[4] D. Khlifi *et al.*, "Global Chemical Composition and Antioxidant and Anti-Tuberculosis Activities of Various Extracts of Globularia alypum L. (Globulariaceae) Leaves," *Molecules*, vol. 16, no. 12, pp. 10592–10603, 2011.

[5] M. Touaibia and F. Z. Chaouch, "Global chemical composition and antioxidative effect of the ethanol extracts prepared from Globularia alypum leaves," *Nat. Technol.*, vol. 14, pp. 2–6, 2016.

[6] N. C'ujic, K. Šavikin, T. Jankovic, D. Pljevljakušic, G. Zdunic, and S. Ibric, "Optimization of polyphenols extraction from dried chokeberry using maceration as traditional technique," *Food Chem.*, vol. 194, pp. 135–142, 2016.

[7] A. Basli, M. Chibane, K. Madani, and N. Oukil, "Activité antibactérienne des polyphénols extraits d 'une plante médicinale de la flore d ' Algérie : Origanum glandulosum Desf," *Phytothérapie*, vol. 10, pp. 2–9, 2012.

[8] M. Jafarzade, N. A. Yahya, F. Shayesteh, G. Usup, and A. Ahmed, "Influence of Culture Conditions and Medium Composition on the Production of Antibacterial Compounds by Marine Serratia sp .," *J. Microbiol.*, vol. 51, no. 3, pp. 373–379, 2013.

Compression effect on permeability of gas diffusion layer of polymer electrolyte fuel cells

Ben Amara Mohamed Amine[#1], Talbi Sondes [*2]

[#] *Laboratoire d'Études des Systèmes Thermiques et Énergétique,*
École Nationale d'Ingénieurs de Monastir,
Monastir 5019 Tunisia.
[1] *medamine.benamara@fsb.u-carthage.tn*

[*] *Institut Supérieur des Etudes Technologiques de Bizerte,*
Route Menzel Abderrahmen – Zarzouna 7021 Bizerte. Tunisia.
[2]talbi.sondes2@gmail.com

Abstract— **This work deals with numerical modeling of compression effect on permeability of gas diffusion layer of polymer electrolyte fuel cells based on lattice Boltzmann method for fluid flow and linear elastic stress-strain model for GDL deformation. A thresholding and binarization step is required to transform the obtained gas diffusion layer data from the micro tomography scans into a two level grayscale image; the method used for the segmentation of three-dimensional data is based on Otsu threshold segmentation algorithm. A brief overview of the different methods used in this work is presented. The permeability is numerically estimated and reported as a function of compression ratio. It was shown that the permeability of the GDL under mechanical compression was decreased which will stronglyaffect water management through the fuel cell.**

Keywords— **PEM fuel cell, gas diffusion layer, permeability, latticeBoltzmann method.**

I. INTRODUCTION

Much of the research done on polymer electrolyte fuel cells relates to improving the water management which is the product of the oxygen reduction reaction at the cathode of PEFC. Indeed, this is often the cause of many performance degradations that fuel cells can undergo. One of the crucial components regarding flooding in PEFC is the Gas diffusion layer which is placed between bipolar plate and catalyst layer and made from a carbon porous material treated with polytetrafluoroethylene to ensure hydrophobic character on the surfaces to improve its water removal properties. GDLs are generally porous materials about 100 to 300 µm thick [2], prepared from carbon in the form of fibers, woven or not which gives them an atypical mechanical behavior. The stress-strain relation is non-linear [19].

The GDL performs many functions such as ensuring the diffusion of the reactants to the active layer and the transport of electrons between the active layer and the bipolar plate. Another of its functions is to evacuate liquid water because if water accumulates in the active layer, a large proportion of the catalyst is no longer accessible to the reactive gas. During assembly of a cell, a certain clamping pressure is recommended for the Membrane-Electrode (AME) assembly, GDL and bipolar plates in order to avoid gas leaks and minimize contact resistance. GDL is the fuel cell element most sensitive to these mechanical stresses, due to its high porosity. The mechanical compressions that the GDL undergoes will influence the performance of the PEFC since theyaffect the water evacuation.

During the last few years, experimental and numerical studies have been devoted to investigating the interaction between mechanical behaviors and multiphysics couplings and have contributed toa better understanding ofthe fuel cell. Park et al [6] show that excessive compression can have a detrimental effect if excessive clamping pressure is applied. Indeed, excessive tightening of the entire fuel cell can irreversibly damage its components: it is likely to reduce the capacities of the GDL, and damage the GDL/catalytic layer interface and bipolar plates interfaces. According to Radhakrishnan et al [15] and Kumar et al [5], compression leads to change in structure and properties of GDL such as surface morphology, roughness, pore size and distribution, thickness , electrical resistance, contact angle and permeability. Yuan et al [17] showed that excessive compressive forces cause geometric distortion of GDL thickness as well as its intrusion into transport channels. This irreversible local degradation of the GDL leads to a non-uniform distribution of the reactive flux as well as a significant increase in the pressure drops in the GDL. In addition, the loss of hydrophobicity was observed after pressing. This loss comes from the breakage of the carbon fibers as well as the detachment of the PTFE from the surface of the GDL. In addition to structural change and deformation of GDL, the effect of compression was also observed in the significant variation of its physical properties including permeability.

Nitta et al investigated the effects of compression on different GDL thicknesses. They found that compressing the gas diffusion layer reduces permeability, while improving electrical conductivity. Zhou et al [14] investigated the effect of clamping force on the interface contact resistance and porosity of gas GDL in a PEMFC [13]. Lee et al [16] studied the performance of fuel cells as a function of the compression pressure with different types of gas diffusion layers and the gasket. Their studies showed that changes in cell performance maybe due to changes in GDL permeability and water

ISSN: 1737-9334

saturation in the membrane. Using the finite element method and finite volume method, Zhou et al [8] studied the GDL elastic deformation, the mass transport of reactants and products, their results showed that there is an optimum clamping force to achieve the highest electrical and thermal power density as a function of electrical current for the PEMFC. The effect of the clamping force on the interface contact resistance and the GDL porosity was also investigated. Berning et al [12] presented a three-dimensional, computational model of PEM fuel cells and found that GDL permeability is a crucial parameter, and liquid water saturation in theelectrode increase with decreasing permeability.
GDL permeability have been studied by many authors and several methods, such as lattice Boltzmann method and Pore network modelling [7].

In the present work, a lattice Boltzmann model was applied to simulate single phase flow through a 3D reconstruction obtained from segmented microtomography data of gas diffusion layer and the permeability was calculated using Darcy's law.

II. METHODOLOGY

A. Lattice Boltzmann method

The fluid mechanics problems and more generally the resolution of partial differential equations lead us to use direct methods of resolution (finite differences, finite elements, finite volume ...). This is consist on a spatial and temporal discretization of macroscopic equations (Euler, Navier Stokes ...). However, a different approach is based on direct simulation at the microscopic level of particles evolution making the fluid. Simplified versions of this microscopic approach has been developed to study the flows in rarefied gases, other types of simplifications have been proposed to allow the simulation of viscous fluid flow in particular the Lattice Boltzmann method which is a relatively recent numerical method used in fluid flow computations based on microscopic models and mesoscopic kinetic equation. This method has made enormous progress in last years because of it's ability to simulate transport problems in complex geometry with complex boundary conditions such flow in porous media, multiphase fluid systems and microflows. Instead of solving the Navier–Stokes equations bytraditional techniques , the Boltzmann equation which describes the statistical distribution of particles in a fluid is solved in phase space, in this method historicallyemerged from the Lattice Gas cellular automata models [1], the system is described bya probability distribution function $f_i(x,t)$representing the number of particles with velocity c_i at the site **x** and time t, i represent a finite number of directions in which the group of particles are allowed to move along the bonds of a regular lattice, each lattice point has an assigned set of velocity vectors with specified magnitudes. The lattice Boltzmann approach models the fluid at the microscopic level and considers that the macroscopic dynamics results from collective behavior of microscopic particles. At the microscopic level, the gases are described by a cloud of particles (molecules) subject to shocks. The statistical approach is then to express all physical variables (macroscopic) from the characteristic of the trajectory of particle length, speed and time. Thereby, the local macroscopic parameters such density, velocity and momentum can be obtained from the distribution function $f(x,t)$ by using $\rho = \int f dc$ and $\rho u = \int c f dc$.

B. Lattice Boltzmann equation

The Boltzmann equation which gives information regarding the single particle distribution function *f* takes the following form: $\frac{\partial f}{\partial t} + v.\nabla f = \Omega(f)$ Where v is the speed of a particle at a position x and time t and $\Omega(f)$ is the collision operator controlling the rate of change in the distribution function *f* during the collision, the term $v.\nabla f$ models the change in the distribution function due to the spread of the particles during their movement. The collision term $\Omega(f)$ is usually represented by a complex integral form, in most applications dealing with the kinetic theory of fluid dynamics; this term is approximated by simple expressions. One of these approximations is the approximation so-called "BGK" proposed by Bhatnagar, Gross and Krook, which was integrated by Qian and al [18], consequently the integral term is replaced by a simpler one given by:

$$\Omega(f) = \frac{1}{\tau_c}[f^{eq}(x,v,t) - f(x,v,t)]$$

This operator models the effect of the collision as a relaxation of the distribution function *f* to a Maxwellian steady state$f^{eq}(x, v, t)$, the parameter τ represents a characteristic time that controls the frequency of relaxation of the distribution function toward the equilibrium. BGK approximation is sometimes called Single relaxation time model and it is the most popular in the literature. Other forms of the collision operator are used as the multiple relaxation timemodel [4].

C. LBGK equation

Generally, the velocity space is continuous i.e., a particle can move freely at random speed. A first step towards the discretization of the Boltzmann equation is the restriction of the velocity continuous space into a finite set of velocities $V \{c_0, c_1, \ldots, c_{n-1}\}$, this means that a particle located at a point *x* must have one of the n speeds c_i. Thus the distribution function $f(x, v, t)$ is reduced to $f_i(x, t)$ which describes the distribution along a finite lattice. The Boltzmann equation under the BGK approximation becomes the discrete Boltzmann equation [15] given by:

$$\frac{\partial f_i}{\partial t} + c_i \cdot \nabla f_i = \frac{1}{\tau}(f_i^{eq} - f_i)$$

This equation is discretized with a space step Δx and a time step Δt which are linked by the following relation: $\frac{\Delta x}{\Delta t} = c_i$, this discretization ensures that the particles in a node x move while Δt to a neighbor node $x + c_i\Delta t$ along the vector c_i. If we take the time step Δt =1, the LBGK equation becomes:

$$f_i(x + c_i, t + 1) - f_i(x, t) = \frac{1}{\tau}(f_i^{eq}(x, t) - f_i(x, t))$$

Thismethod consists of the following two steps:

· **Collision**: the arriving particles at the points interact with another and change their velocity directions, thus, at time t, particles at node x come into collision with each other which changes the distribution function from $f_i(x,t)$ to

$$f_i^*(x,t) = f_i(x,t) + \frac{1}{\tau}(f_i^{eq}(x,t) - f_i(x,t))$$

· **Streaming**: particles move during the time step Δt, along lattice bonds to the neighbouring lattice nodes; the distribution function $f_i(x,t)$ spreads along the vector c_i, more formally:

$$f_i(x + c_i, t+1) = f_i^*(x,t)$$

Both collision and streaming process used in cellular automata are applied to the case of the LBGK equation on a network (1-D, 2-D or 3-D).

The macroscopic variable ρ and u are given by some linear combinaison of the distribution function thus: $\rho(x) = \sum_i f_i$ and $\rho(x)u(x) = \sum_i c_i f_i$.

D. Lattice pattern

In the lattice Boltzmann method many type of lattice are used, theyhave all the same naming scheme D_nQ_m, where n denote the dimension of the lattice model and m is the number of the discrete velocities, for example we have the D_1Q_3 and D_1Q_5 in one dimension configuration, in 2-D systems we find the D_2Q_5, D_2Q_7 and D_2Q_9 in three dimensions we can cite the D_3Q_{15}, D_3Q_{19} and D_3Q_{27} [3]. In three-dimensional problems, the most popular scheme is the D_3Q_{19} model.(See Fig. 2).

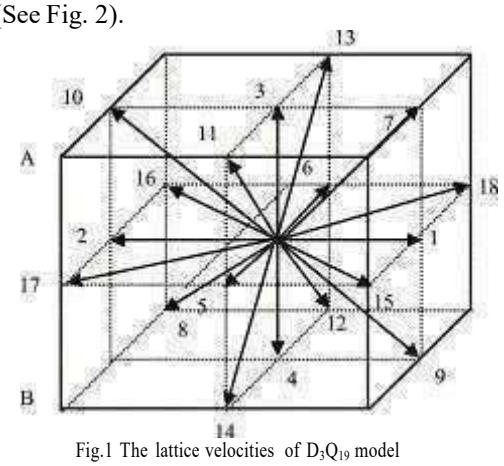

Fig.1 The lattice velocities of D_3Q_{19} model

In thismodel, thelattice velocities are defined as:

$$c_i = \begin{cases} 0, & i = 0 \\ (\pm1,0,0),(0,\pm1,0),(0,0,\pm1), & i = 1\ to\ 6 \\ (\pm1,\pm1,0),(\pm1,0,\pm1),(0,\pm1,\pm1) & i = 7\ to\ 18 \end{cases}$$

We attribute to each direction a weighting factor while respecting the isotropy of the system, thus we set the weighting factor of the speed c_i, also we assume that these factors are the same for directions having the same velocity, these variables satisfy the following relationship: $\sum_i w_i = 1$

For D_3Q_{19}, the weighting factors are defined by:

$$w_i = \begin{cases} 1/3, & i = 0 \\ 1/18, & i = 1\ to\ 6 \\ 1/36, & i = 7\ to\ 18 \end{cases}$$

E. Equilibrium distribution function

The equilibrium distribution function f_i^{eq} depends on the density and the local fluid velocity, it can be written under the following implicit form: $f_i^{eq}(\rho, u)$

A general form of the equilibrium distribution function is obtained bya Taylor expansion of Maxwell Boltzmann equilibrium function: $F(\xi) = \frac{\rho}{(2\pi RT)^{3/2}} exp\left[-\frac{|\xi-u|^2}{2RT}\right]$

With R the specific gas constant, T the static temperature, ρ the particle density, ξ the molecular velocity components and u themacroscopic velocityvector . Thus f_i^{eq}can be written as [11,18]:

$$f_i^{eq} = \rho w_i\left[1 + \frac{c_i.u}{c_s^2} + \frac{(c_i.u)^2}{2c_s^4} - \frac{u^2}{2c_s^2}\right]$$

Where $c_s$is the isothermal speed of sound, it's obtained by Chapman-Enskog expansion [11] of the Boltzmann equation near incompressible limit ($|u|/c_s \ll 1$) which make the relation between the Navier Stokes equation and the Boltzmann equation. This development gives us the relation between the sound speed and the collision frequency through $\nu = c^2(2\tau - 1)$, the positivity of the kinematic viscosity requires that $\tau > 1/2$. The pressure in D_3Q_{19} model is determined by the equation of state $p = \frac{\rho}{3}$ and the sound speed is $c_s = \frac{1}{\sqrt{3}}c$.

F. Initial and boundary conditions

Boundary conditions are a quite complex problem in LBM. The difficulties arise from the fact that there exists no physical intuition on the behaviour of the velocities distribution function on boundaries. Usually we only have macroscopic information (e.g. no slip BC on walls for fluid flows). We therefore have to translate this macroscopic information on the microscopic distribution functions. There is no unique way of doing this translation and many authors propose their own solution. One should be aware that the BC chosen is of primary importance since it affects greatly the numerical accuracy of the simulation but also its stability.

1) *Initial condition:* The determination of the macroscopic quantities (density and velocity) requires the knowledge of initial condition; in LBGK method, the initial distribution function must be known to be able to handle these quantities. In the Lattice Boltzmann method for incompressible flows, the general approach used to determine the initial value, is to equalize the initial distribution function with the equilibrium distribution function: $f_i^0(x) = f_i^{eq}(\rho_0(x), u_0(x))$. With u_0 is the initial velocity field and $\rho_0$is theinitial density.

2) *Solid boundary condition:* In the lattice Boltzmann method, the solid boundary condition is called "the bounce back boundary conditions" [11]. It is considered as the most attractive advantage of the LBM which mimic the particle-wall interaction that, when a particle collides with a

solid wall, it is reversed as it shown in Fig.3 This condition ensures thenon-slip boundarycondition at the walls.

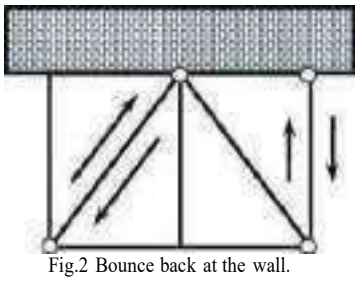

Fig.2 Bounce back at the wall.

3) *Boundary condition with known velocity:* It is very common in practical applications that we know the velocity at the boundary. In LBM method we need to specify inward distribution functions at the boundaries. From the streaming process the distribution functions streaming away from the fluid domain are know. The distribution functions streaming toward the fluid need to be calculated. Zou and He [10] described a method to calculate the unknown distributions functions based on the formulas of macroscopic quantities with equilibrium assumption normal to the boundary.

G. Permeability

Permeability is a physical characteristic that represents how easily a material allows fluid transfer through a connected network. Darcy's law makes it possible to link a flow to a pressure gradient applied to the fluid thanks to a characteristic parameter of the medium crossed: the permeability *k*. Darcy's law, and therefore permeability, is defined for laminar flow conditions in a homogeneous, isotropic and continuous medium; the fluid not interacting with the medium. In one dimensional case when the pressure gradient is only applied along the x-direction, permeability can be defined byDarcy's lawas follow: $Q = -\frac{k}{\mu}\frac{dp}{dx}$, μ is the dynamic viscosity of the fluid and Q is the volumetric flow rate. Empirical relations are often used to predict the permeability of simple pore structure. The Kozeny-Carman relation is one of the widely used permeability correlations for porous media which is derived from the models with pipes. The classical solution for laminar flow through pipe with a radius r gives: $Q = -\frac{\pi r^4}{8\mu}\frac{dp}{dx}$, comparing with Darcy's law permeabilitybecomes: $k = \frac{\pi R^4}{8A}$. This model is used to validate the LB model.

H. X-raymicro-tomographyand segmentation

Three-dimensional x-ray micro-tomography is a technique for obtaining representation of an object from 2D images produced by transmission electron microscopy (TEM). The principle of transmission electron microscopy is to bombard the sample with a beam of electrons which will interact with the material. The beam transmitted and diffracted through the sample. The transmitted beam is detected and makes it possible to obtain a 2D projection of the observed 3D object. Electron tomographyconsists in acquiring several 2D projections to reconstruct the 3D volume. The projections are obtained in gray levels but they must be converted into 1/0 images to determine where the solid is and where are the pores. This step called segmentation is carried out using the Otsu method which is an automatic thresholding segmentation method. We then obtain a binary segmented figure 1/0 where 1 corresponds to the solid and 0 to the pores. This technique, developed by Nobuyuki Otsu [9] is used to perform automatic thresholding or reduction of a grayscale image to a binary image based on the image's histogram shape which is a function that gives the frequency of occurrence of each level of gray in the image. It can be used to improve the quality of an image (image enhancement) by introducing some modifications. The method used consists in dividing the pixels of the image into two classes. The threshold is calculated based on the histogram of the image and the selection of a minimum between two pixels. This makes it possible to find a threshold level that minimizes the weighted intraclass variance.

I. GDL Deformation

Rigorous modeling of gas diffusion layer deformation is a very difficult challenge because of its elastic and plastic behaviour. In this work, a simple model was applied in which the plastic nature of GDL is not taken into account andalso theneglecting of transverse strain.

The height, h of the compressed GDL is linked to the initial thickness H by the following relation: $h = (1-\beta)H$, β is the compression ratio. To facilitate the mechanical modelling, we consider that the change of the GDL thickness is due to the change of pores volume but the solid part does not change. therefore, the GDL porosityis given bythe following relation: $s = 1 - (1 - s_0)\frac{H}{h}$ where s_0 is the initial porosity. Another physical parameter describing the porous media is the tortuosity given by $\tau = 1 - 0.49\ln(v)$. GDL deformation was carried out using the commercial software ANSYS APDL based on finite element analysis. The deformed geometry of the GDL will be implemented in the LBM code.

III. Simulation

The first step in this study was the acquisition of a 3D image of a porous carbon gas diffusion layer (GDL) for polymer electrolyte fuel cells (PEFC), a sample carbon fibrous material of 128x128x128 array of voxels can be seen from Fig. 3. Otsu algorithm was applied for the thresholding of acquired data, since it generates good and consistent binary images. Fig.4 show micro-tomographic data with automatic Otsu thresholding. Fig.5 shows the GDL samples according to the compression ratio. The compression ratios are respectively $\beta = \{50\%, 39.0625\%, 25\%, 12.5\%\}$.

The permeability of various compressed samples is calculated using LB method with Darcy's law.

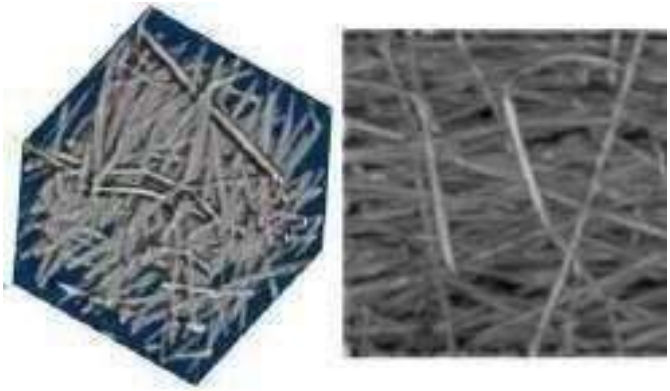

Fig.3 3D and 2D images of a GDL carbon paper sample from microtomography.

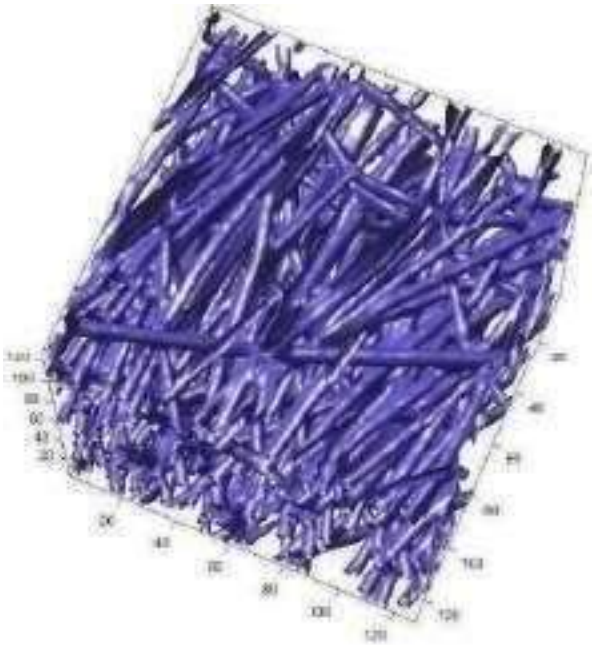

Fig.4: Binary image obtained by Otsu segmentation.

Permeability vs compression ratio was plotted in Fig.6 which shows that compression can cause a significant increase in permeability. The dependence of permeability on compression ratio was expressed by polynomial regression. The relation between permeabilityand compression ratio given by:

$$k = -8.4.\,10^{6}.\,\beta^{2} - 1.5.\,10^{7}.\,\beta + 2.8.\,10^{7}$$

Chart of permeability vs porosity was also created(Fig.7), porosity and permeability increase simultaneously but not linearly. From this, a third order polynomial interpolation can be applied to the permeability porosity crossplot to give the followingrelation:

$$k = 6.7.\,10^{9}.\,c^{3} - 1.7.\,10^{10}.\,c^{2} + 1.4.\,10^{10}.\,c - 3.8.\,10^{9}$$

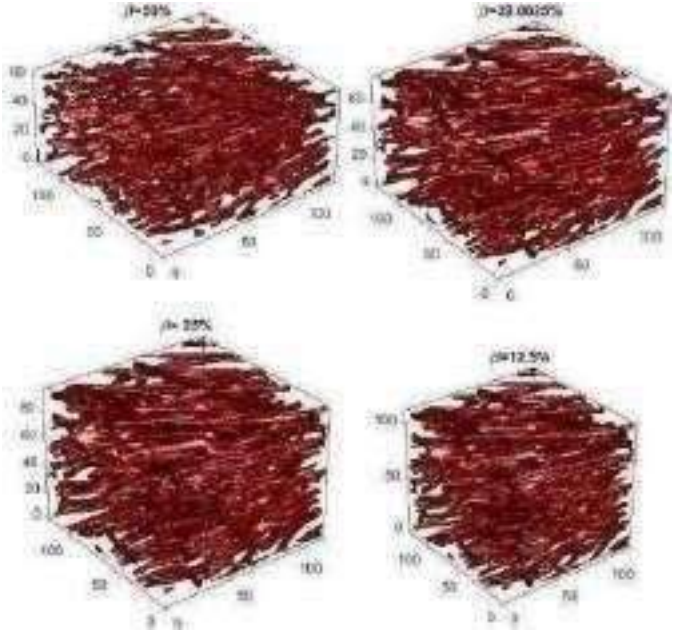

Fig.5 Schematic of the GDL deformation: (1) 50% compressed GDL model; (2) 39.0625% compressed GDL model; (3) 25% compressed GDL model; (4) 12.5% compressed GDL model.

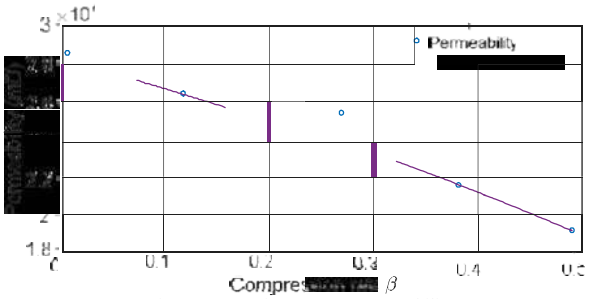

Fig.6 Compression rate vs permeability

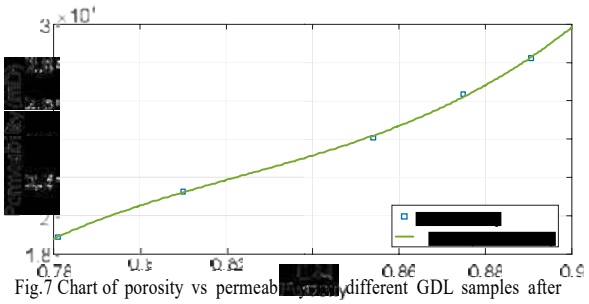

Fig.7 Chart of porosity vs permeability different GDL samples after compression

IV. Conclusions

In this work, a numerical model based on the lattice Boltzmann method for predicting the effect of mechanical compression on the permeability of gas diffusion layer of polymer electrolyte fuel cells was established. The sample from X ray micro-tomography was firstly segmented using Otsu method, binary microstructure was thus obtained in

which 0 and 1 represent void space and solid space. The single phase permeability of the compressed GDL samples was calculated with Darcy's Law from lattice Boltzmann simulations of fluid flow. For the mechanical model, the GDL deformation was predicted under simplifying assumptions using ANSYS APDL based on finite elements method. It was shown that the permeability decreases as a result of the reduced pore size caused by compression. Two regression relations between permeability, compression ratio and porosity are established. The effects of thresholding and mechanical compression modeling on gas diffusion layer microstructuremorphologyneed more attention.

REFERENCES

[1]. B. Chopard, and M. Droz, Cellular Automata Modeling of Physical Systems University Press, Cambridge, 1998.

[2]. B.G. Pollet, A.A. Franco, H. Su, H. Liang, and S. Pasupathi, *Proton exchange membrane fuel cells*, [in] F. Barbir, A. Basile, and T.N. Veziroğlu, eds., Compendium of Hydrogen Energy. Volume 3: Hydrogen Energy Conversion, Woodhead Publishing, Cambridge, p. 3, 2016.

[3]. D. A. Wolf-Gladrow, *Lattice-Gas Cellular Automata and lattice Boltzmann Models*, Lecture Notes in Mathematics, 1725, Springer-Verlag Berlin/Heidelberg, 2000.

[4]. D. d'Humières, I. Ginzburg, M. Krafczyk, P. Lallemand, L. Luo, *Multiple-Relaxation-Time Lattice Boltzmann Models in Three Dimensions,* Phil. Trans. R. Soc. A, 2002 360, 437-451.

[5]. *J. F. R. Kumar , V. Radhakrishnan , P. Haridoss, Effect of electrochemical aging on the interaction between gas diffusion layers and the flow field in a proton exchange membrane fuel cell, Int J Hydrog Energy. 2011, 36(12):7207-11.*

[6]. J. Park, H. Oh, T. Ha, Y.I. Lee, K. Min, *A review of the gas diffusion layer in proton exchange membrane fuel cells: durability and degradation*, Applied Energy 155, 866-880,2015.

[7]. J. T. Gostick, M. W. Fowler, M. D. Pritzker, M. A. Ioannidis, and L. M. Behra, *In-plane and through-plane gas permeability of carbon fiber electrode backing layers*, J. of Power Sources, 2006, 162,228-238.

[8]. K, Zhou., T. Li., Y. Han., J. Wang., J. Chen., K. Wang, *Optimizing the hydrophobicity of GDL to improve the fuel cell performance,* RSC Advances 2021, 11(4).

[9]. N. Otsu, A Threshold Selection Method from Gray-Level Histograms, IEEE Transactions on Systems, Man and Cybernetics, 1979,9,62--66.

[10]. Q. Zou, X. He, *On pressure and velocity boundary conditions for the lattice Boltzmann BGK model,* Phys. Fluids, 1997, 9, 1592-1598.

[11]. S. Chen, G. D. Doolen, *Lattice Boltzmann Method for Fluid Flows,* Ann. Rev. Fluid Mech., 1998, 30, 329-364.

[12]. T. Berning , N. Djilali, *A 3D, multiphase, multicomponent model of the cathode and anode of a pem fuel cell*, J Electrochem Soc, 2003,150:A1589e98.

[13]. T. Hottinen, O. Himanen, S. Karvonen, I. Nitta, *Inhomogeneous compression of PEMFC gas diffusion layer—Part II: modeling the effect*, J. Power Sources 2007, 171, 113–121.

[14]. T. Zhou, H. Liu, *Effects of the electrical resistances of the GDL in a PEM fuel cell*, J Power Sources ,2006, 161:444–53.

[15]. V. Radhakrishnan, P. Haridoss , *Effect of cyclic compression on structure and properties of a Gas Diffusion Layer used in PEM fuel cells*, Int J Hydrog Energy. 2010, 35(20):11107–18.

[16]. W. K. Lee, C.H. Ho, J. W. V. Zee, M. Murthy. *The effects of compression and gas diffusion layers on the performance of a PEM fuel cell*, J. Power Sources, 1999, 84(1):45–51.

[17]. *X. Z. Yuan , S. Zhang , J. C. Sun, H. Wang, A review of accelerated conditioning for a polymer electrolyte membrane fuel cell, Journal of Power Sources, 2011,196(22):9097-06*

[18]. Y.H. Qian, D. d'Humières, P. Lallemand, *Lattice BGK Models for Navier-Stokes Equation*, Europhys. Lett., 1992, 17, 479-484.

[19]. Z. Zhang, P. He, Y. J. Dai, P.H. Jin, W.Q. Tao, *Study of the mechanical behavior of paper-type GDL in PEMFC based on microstructure morphology,* International Journal of Hydrogen Energy 45 (53),2020, 29379-29394.

Etude thermorhéologique de la solution Xanthane-Crosslinker

MELLAL Mounir[#1], CHEKIR Nadia[*2], KHEDRAOUI Sofiane[#3]

[#]*First-Third Department, First-Third University*
Address Including Country Name

[1]m_rinmou@yahoo.fr
[3]third.author@first-third.edu

[*]*Second Company*
Address Including Country Name

[2]second.author@second.com

Résumé*—L'objectif de cette étude est la caractérisation des propriétés rhéologiques d'un fluide de fracturation à base de gomme de xanthane et de crosslinker à différentes concentrations [0.1%, 0.3%, 0.5%, 0.7%, 1%]. Etudier l'influence des différents paramètres tels que la concentration, la température [à 25°C, 40°C, 55°C, 70°C] et le breaker sur le comportement rhéologique de ce fluide. Les résultats obtenus nous ont permis de conclure que le crosslinker augmente les interactions entres les chaines moléculaires ce qui se traduit par une augmentation de la viscosité. La température détruit les chaines du polymère ce qui induit la diminution de la viscosité. Le breaker brise les chaines du polymère ce qui affirme sa fiabilité.

Keywords— **Thermorhéologie. Xanthane, Crosslinker, Fracturation, rhéologie.**

I. Introduction

Les fluides de fracturations utilisés pour l'extraction des hydrocarbures non conventionnels piégés dans des roches peu perméable doivent avoir un profil rhéologique particulier. De ce fait, la détermination des propriétés rhéologiques de ces fluides est primordiale pour les adapter aux conditions géologiques du réservoir et éviter tout problème lors de l'exploitation.

II. Matériels et Méthodes

L'analyse rhéologique des échantillons est réalisée par un rhéomètre KINEXUS ultra + destiné à la caractérisation des dispersions, des fluides complexes et des solides mous.

A. Xanthane

- Dans cette étude, nous avons choisi deux concentrations de solution de polymère (gomme de xanthane): 4000ppm (0.4% en masse) et 2000ppm (0.2% en masse), selon la littérature les concentrations optimales de xanthane utilisées dans les fluides de fracturation varient entre 2000ppm et 10000ppm.

B. Crosslinker

Une fois la quantité du crosslinker mesurée selon la concentration souhaitée: 0,1 %, 0,3%, 0.5 %, 0.7% et 1 % massiques, elle est versée dans un des cinq échantillons de solution de xanthane, et laissée sous agitation à l'aide d'un agitateur magnétique pendant 10 à 15 minutes. Les différentes solutions préparées sont ensuite conservés à température ambiante au repos pendant quelques heures avant leurs utilisations, afin d'éliminer les bulles d'air.

III. Resultats

All paragraphs must be indented. All paragraphs must be justified, i.e. both left-justified andright-justified.

A. Text Font of Entire Document

The entire document should be in Times New Roman or Times font. Type 3 fonts must not be used. Other font types may be used if needed for special purposes.

Recommended font sizes are shown in Table 1.

B. Title and Author Details

Title must be in 24 pt Regular font. Author name must be in 11 pt Regular font. Author affiliation must be in 10 pt Italic. Email address must be in 9 pt Courier Regular font.

TABLE I
Font Sizes for Papers

Font Size	Appearance (in Time New Roman or Times)		
	Regular	**Bold**	**Italic**
8	table caption (in Small Caps), figure caption, reference item		reference item (partial)
9	author email address (in Courier), cell in a table	abstract body	abstract heading (also in Bold)
10	level-1 heading (in Small Caps), paragraph		level-2 heading, level-3 heading, author affiliation
11	author name		
24	title		

All title and author details must be in single-column format and must be centered.

Every word in a title must be capitalized except for short minor words such as “a”, “an”, “and”, “as”, “at”, “by”, “for”, “from”, “if”, “in”, “into”, “on”, “or”, “of”, “the”, “to”, “with”.

Author details must not show any professional title (e.g. Managing Director), any academic title (e.g. Dr.) or any membership of any professional organization (e.g. Senior Member IEEE).

To avoid confusion, the family name must be written as the last part of each author name (e.g. John A.K. Smith).

Each affiliation must include, at the very least, the name of the company and the name of the country where the author is based (e.g. Causal Productions PtyLtd, Australia).

Email address is compulsory for the corresponding author.

C. *Section Headings*

No more than 3 levels of headings should be used. All headings must be in 10pt font. Every word in a heading must be capitalized except for short minor words as listed in Section III-B.

1) Level-1 Heading: A level-1 heading must be in Small Caps, centered and numbered using uppercase Roman numerals. For example, see heading “III. Page Style” of this document. The two level-1 headings which must not be numbered are “Acknowledgment” and “References”.

2) Level-2 Heading: A level-2 heading must be in Italic, left-justified and numbered using an uppercase alphabetic letter followed by a period. For example, see heading “C. Section Headings” above.

3) Level-3 Heading: A level-3 heading must be indented, in Italic and numbered with an Arabic numeral followed by a right parenthesis. The level-3 heading must end with a colon. The body of the level-3 section immediately follows the level-3 heading in the same paragraph. For example, this paragraph begins with a level-3 heading.

D. *Figures and Tables*

Figures and tables must be centered in the column. Large figures and tables may span across both columns. Any table or figure that takes up more than 1 column width must be positioned either at the top or at the bottom of the page.

Graphics may be full color. All colors will be retained on the CDROM. Graphics must not use stipple fill patterns because they may not be reproduced properly. Please use only *SOLID FILL* colors which contrast well both on screen and on a black-and-whitehardcopy, as shown in Fig. 1.

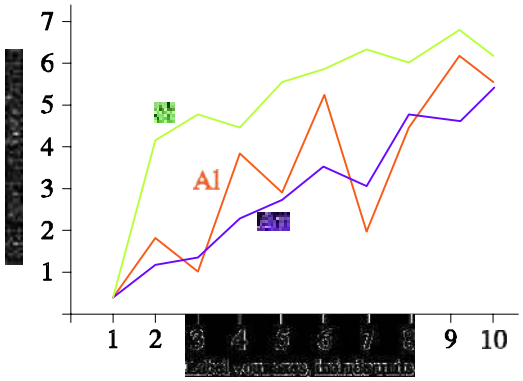

Fig. 1 A sample line graph using colors which contrast well both on screen and ona black-and-white hardcopy

Fig. 2 shows an example of a low-resolution image which would not be acceptable, whereas Fig. 3 shows an example of an image with adequate resolution. Check that the resolution is adequate to reveal the important detail in the figure.

Please check all figures in your paper both on screen and on a black-and-white hardcopy. When you check your paper on a black-and-whitehardcopy, please ensure that:

- the colors used in each figure contrast well,
- the image used in each figure is clear,
- all text labels in each figure arelegible.

E. *Figure Captions*

Figures must be numbered using Arabic numerals. Figure captions must be in 8 pt Regular font. Captions of a single line (e.g. Fig. 2) must be centered whereas multi-line captions must be justified (e.g. Fig. 1). Captions with figure numbers must be placed after their associated figures, as shown in Fig. 1.

Fig. 2 Example of an unacceptable low-resolution image

Fig. 3 Example of an image with acceptable resolution

F. Table Captions

Tables must be numbered using uppercase Roman numerals. Table captions must be centred and in 8 pt Regular font with Small Caps. Every word in a table caption must be capitalized except for short minor words as listed in Section III-B. Captions with table numbers must be placed before their associated tables, as shown in Table 1.

G. Page Numbers, Headers and Footers

Pagenumbers, headers and footers must not be used.

H. Links and Bookmarks

All hypertext links and section bookmarks will be removed from papers during the processing of papers for publication. If you need to refer to an Internet email address or URL in your paper, you must type out the address or URL fully in Regular font.

I. References

The heading of the References section must not be numbered. All reference items must be in 8 pt font. Please use Regular and Italic styles to distinguish different fields as shown in the References section. Number the reference items consecutively in square brackets (e.g. [1]).

When referring to a reference item, please simply use the reference number, as in [2]. Do not use "Ref. [3]" or "Reference [3]" except at the beginning of a sentence, e.g. "Reference [3] shows …". Multiple references are each numbered with separate brackets (e.g. [2], [3], [4]–[6]).

Examples of reference items of different categories shown in the References section include:

- example of a book in [1]
- example of a book in a series in [2]
- example of a journal article in [3]
- example of a conference paper in [4]
- example of a patent in [5]
- example of a website in [6]
- example of a web page in [7]
- example of a databook as a manual in [8]
- example of a datasheet in [9]
- example of a master's thesis in [10]
- example of a technical report in [11]
- example of a standard in [12]

IV. Conclusions

The version of this template is V2. Most of the formatting instructions in this document have been compiled by Causal Productions from the IEEE LaTeX style files. Causal Productions offers both A4 templates and US Letter templates for LaTeX and Microsoft Word. The LaTeX templates depend on the official IEEEtran.cls and IEEEtran.bst files, whereas the Microsoft Word templates are self-contained. Causal Productions has used its best efforts to ensure that the templates have the same appearance.

Causal Productions permits the distribution and revision of these templates on the condition that Causal Productions is credited in the revised template as follows: "original version of this template was provided by courtesy of Causal Productions (www.causalproductions.com)".

Acknowledgment

The heading of the Acknowledgment section and the References section must not be numbered.

Causal Productions wishes to acknowledge Michael Shell and other contributors for developing and maintaining the IEEE LaTeX style files which have been used in the preparation of this template. To see the list of contributors, please refer to the top of file IEEETran.cls in the IEEE LaTeX distribution.

References

[l] S. M. Metev and V. P. Veiko, *Laser Assisted Microtechnology*, 2nd ed., R. M. Osgood, Jr., Ed. Berlin, Germany: Springer-Verlag, 1998.

[2] J. Breckling, Ed., *The Analysis of Directional Time Series: Applications to Wind Speed and Direction*, ser. Lecture Notes in Statistics. Berlin, Germany: Springer, 1989, vol. 61.

[3] S. Zhang, C. Zhu, J. K. O. Sin, and P. K. T. Mok, "A novel ultrathin elevated channel low-temperature poly-Si TFT," *IEEE Electron Device Lett.*, vol. 20, pp. 569–571, Nov. 1999.

[4] M. Wegmuller, J. P. von der Weid, P. Oberson, and N. Gisin, "High resolution fiber distributed measurements with coherent OFDR," in *Proc. ECOC'00*, 2000, paper 11.3.4, p. 109.

[5] R. E. Sorace, V. S. Reinhardt, and S. A. Vaughn, "High-speed digital-to-RF converter," U.S. Patent 5 668 842, Sept. 16, 1997.

[6] (2002) The IEEE website. [Online]. Available: http://www.ieee.org/

[7] M. Shell. (2002) IEEEtran homepage on CTAN. [Online]. Available: http://www.ctan.org/tex-archive/macros/latex/contrib/supported/IEEEtran/

[8] *FLEXChip Signal Processor (MC68175/D)*, Motorola, 1996.

[9] "PDCA12-70 data sheet," Opto Speed SA, Mezzovico, Switzerland.

[10] A. Karnik, "Performance of TCP congestion control with rate feedback: TCP/ABR and rate adaptive TCP/IP," M. Eng. thesis, Indian Institute of Science, Bangalore, India, Jan. 1999.

[11] J. Padhye, V. Firoiu, and D. Towsley, "A stochastic model of TCP Reno congestion avoidance and control," Univ. of Massachusetts, Amherst, MA, CMPSCI Tech. Rep. 99-02, 1999.

[12] *Wireless LAN Medium Access Control (MAC) and Physical Layer (PHY) Specification*, IEEE Std. 802.11, 1997.

ISSN: 1737-9334

Traitement des Eaux de l'Industrie de Textile par une Suspension de Nanoparticules

Nadia Chekir[*1], Djilali Tassalit[2], Ouassila Benhabiles[2], Mehdi Nebbache[1] and Nassila Sabba[1]

1. Laboratoire de Valorisation et Recyclage de la Matière pour le Developpement Durable, Faculté de Génie Mécanique et deGénie des Procédés, Université des Sciences et de la Technologie Houari Boumediene (USTHB), Bab-Ezzouar, 16111 Alger,Algérie

1,2Unité de Développement des Equipements Solaires. UDES /Centre de Développement des Energies Renouvelables CDER, Bou- Ismail, 42004, W. Tipaza, Algérie.

[*]nchekir@yahoo.fr

***Résumé*— L'augmentation des activités industrielles engendre une pression grandissante sur les réserves en eau douce de la planète. En effet, ces activités génèrent une grande diversité de produits chimiques qui se déversent dans le cycle de l'eau, mettant en péril l'équilibre naturel. L'application des nouvelles techniques pour le traitement des eaux prend une ampleur considérable. Parmi ces technique se distingue l'une des plus répandue actuellement la photocatalyse hétérogène. Par l'action jumelée d'un semi-conducteur et d'une irradiation ultraviolette, ce procédé induit a la décomposition des polluants organiques donnant lieux à une eau propre et du CO2. L'objectif de ce travail est d'appliquer cette nouvelle technique pour la dégradation des colorants de textiles qu'on peut retrouver dans les rejets de l'industrie textile plus précisément le bleu suprantine BWL 300%. L'influence de certains paramètres (quantité de catalyseur utilisé , concentration initial en polluant) a été étudiée à l'aide d'un photoréacteur tubulaire dans le but d'optimiser ces derniers.**

***Mot clés*— photocatalyse, colorant, oxyde de zinc, dioxyde de titane.**

I. INTRODUCTION

Nous vivons dans un monde où tout est coloré, nos vêtements, nos produits cosmétiques, nos aliments et même nos produits pharmaceutiques, …etc. Ces colorants sont de plus en plus des colorants de synthèse, en raison de leur fabrication facile, de leur production rapide et de leur grande variété de couleurs si on les compare aux colorants naturels. Aujourd'hui, les colorants de synthèse constituent une véritable industrie et un capital de la chimie moderne. Les vêtements que nous portons sont fabriqués à partir de fibres textiles colorées à l'aide de différentes teintures leur donnant leur couleur définitive. Nous sommes loin d'imaginer que la fabrication de ces mêmes vêtements engendre une pollution de plus en plus importante et dangereuse pour les êtres humains. Ces colorants sont pour la plupart synthétiques et représentent aujourd'hui un large groupe de composés chimiques. La production mondiale de ces colorants de synthèse est évaluée à 800 000 tonne/an. Une partie de ces colorants, (approximativement 140 000 tonne/an), est rejetée lors des étapes de fabrication et coloration des tissus **[1]**. Les industries textiles, et plus particulièrement les phases de teinture et d'ennoblissement, utilisent principalement des produits chimiques, nuisibles pour la santé, comme certains colorants azoïques cancérogènes, et engendrent une pollution des eaux de surface et des nappes phréatiques.

Parmi les nombreuses familles de colorants synthétiques, les colorants azoïques sont les plus largement utilisés (60 à 70 %). Ces colorants sont très stables et relativement peu biodégradables. L'industrie des colorants constitue aujourd'hui un domaine capital de la chimie. Les colorants sont employés pour l'impression et la teinture des fibres textiles, des papiers, des cuirs, des fourrures, des bois, des matières plastiques et des élastomères. Ils servent aussi à préparer des peintures, des encres d'imprimerie, des vernis et, comme additifs, à colorer des produits alimentaires et pharmaceutiques. Ils sont utilisés dans l'industrie des cosmétiques, la coloration des métaux (aluminium anodisé), la photographie (sensibilisateurs), la biologie (coloration des préparations microscopiques), les indicateurs colorés, et certains d'entre eux sont employés en thérapeutique (antiseptiques, antimalariques, etc.) **[2]**

En raison de leurs effets toxiques et/ou carcinogènes, les fabricants et les industries utilisant ces colorants tentent cependant de réduire l'incidence négative de ces molécules sur l'environnement. La stratégie générale consiste, d'une part, à améliorer le pouvoir colorant intrinsèque des molécules et leur fixation chimique sur la matrice receveuse afin de réduire les doses employées, et, d'autre part, à augmenter leur dégradation. L'évaluation des risques liés à ces molécules colorantes repose sur une approche globale ne permettant pas de situer avec exactitude la nature des toxicités induites. Si les molécules colorantes ne sont pas elles-mêmes nécessairement toxiques à l'origine, leurs dérivés issus des processus de biodégradation pourraient l'être.

Le traitement des eaux polluées par ces types de colorants est donc devenu une priorité dans notre monde moderne. La mise au point de méthodes et l'optimisation des procédés existants, qui doivent être aussi efficaces que peu coûteux, font donc l'objet d'un nombre considérable de travaux. La photocatalyse se présente donc comme une technologie de choix pour la dépollution et l'intégration de ces eaux usées, car il s'agit d'un système performant, simple et économique **[3, 4]**. Ces différentes caractéristiques attractives ont engendré un grand intérêt de la part des chercheurs pour la compréhension, l'optimisation et l'application industrielle de ce procédé.

La photocatalyse est une nouvelle technique qui a été introduite dans les années 1930 **[5]**, elle implique des photoréactions qui se produisent à la surface du catalyseur solide. D'après l'IUPAC (Union Internationale de Chimie Pure et Appliquée), la photocatalyse est le domaine de la catalyse qui fait intervenir la lumière comme moyen d'activation du catalyseur. Plus généralement il est possible de définir le concept de photocatalyse à travers les réactions chimiques dites photocatalytiques induites par l'absorption de photons (énergie lumineuse) par un photocatalyseur. Ces derniers sont des nanoparticules (matériaux semi-conducteurs) dont l'absorption de photons permet de promouvoir un électron depuis la bande de valence vers la bande de conduction alors séparées énergétiquement par une bande interdite ou band gap. Plusieurs semi-conducteurs ont été testés dans la photocatalyse comme TiO2, ZnO, ZnS, WO3, GaP, Fe2O3 et CdS **[6 , 7].**

Pendant les trois dernières décennies, la photocatalyse hétérogène est passée des réactions douces en milieux gaz et liquide, à une oxydation totale et à une dégradation de divers composés organiques et polluants dans l'eau ou dans l'air humide. Le processus photocatalytique repose sur l'excitation du photocatalyseur par un rayonnement lumineux.

La présente étude porte sur l'optimisation et la modélisation de la photodégradation d'un colorant qui est le bleu BWL 300%, une nouvelle molécule utilisée dans l'industrie textile de Blida (TEXALG- l'Algérienne des textiles-Boufarik).

II. MATERIEL ET METHODE

Dispositif expérimental

Afin de traiter les eaux polluées par photocatalyse nous avons utilisé un réacteur photocatalytique tubulaire dimensionné pour le traitement d'un volume de 2 litres d'eau polluée en circuit fermé. Ce réacteur tubulaire se compose d'un collecteur parabolique dit CPC (compound parabolic collector) soutenu par une armature d'aluminium (fig.1). Le collecteur est constitué de 06 tubes en verre sous forme d'un serpentin de 30 cm de longueur et 2,6 cm de diamètre interne placé sur une armature en aluminium avec des réflecteurs placés sous les tubes afin d'augmenter l'intensité du flux lumineux. Pour maintenir les mêmes conditions opératoires, un réservoir de deux (02) litres a été utilisé ainsi qu'un agitateur magnétique afin d'assurer l'homogénéisation de la solution à traiter. Ce mélange est recyclé au moyen d'une pompe péristaltique permettant ainsi la recirculation du mélange réactionnel. La solution a été irradiée par une source de rayonnement artificiel en utilisant des lampes U.V. Philips PL-L 24W/10/4P de 24W de puissance chacune et avec un maximum d'émission à 365nm.

Fig.1. Schéma de l'installation expérimentale.

Réactifschimiques utilisés

Dans le cadre de ce travail, nous avons utilisé un colorant azoïque comme molécule organique biorécalcitrante. Le polluant utilisé lors de cette étude est le bleu suprrantine BWL 300%, c'est un colorant textile utilisé dans l'industrie textile de Blida.

Le phptocatalyseur utilisé lors de cette étude est l'oxyde de zinc ZnO. Il est sous forme d'une poudre blanche utilisé en suspension dans la solution à traiter. L'oxyde de zinc (ZnO) a été fourni par Sigma Aldrich ChemicalCompany avec une pureté de 99%, une surface spécifique de $9m^2/g$ et une taille moyenne des particules de 30nm.

Avant de se fixer sur le ZnO comme photocatalyseur, nous avons effectué une comparaison avec le dioxyde de tutitane P-25 et commercial de Biochem.

le dioxyde de titane (TiO_2) de type P-25, commercialisé par la société Dégussa, contient 80 % d'anatase et 20% rutile, une surface spécifique (BET) de 50 m^2/g et une taille des particules de 20 nm.

Le dioxyde de titane (TiO_2) commercial est fourni par *BIOCHEM ChemoPharma* (*Quebec, Canada*), contient 90 % d'anatase et 10% rutile, une surface spécifique (BET) de 4,61 m^2/g et un diamètre de particules de 48 nm.

III. RÉSULTATS ET DISCUSSION

Etude préliminaire

Le dioxyde de titane TiO_2 est le photocatalyseur le plus utilisé lors de la dégradation des polluants organiques en général. Afin de déterminer le type de photocatalyseur le plus performant, une étude préliminaire a été menée pour la dégradation du notre colorant en présence de différents types de photocatalyseurs à savoir le TiO_2 P25, le TiO_2 commercial Biochem et un autre semi-conducteur qui est l'oxyde de zinc ZnO.

Une série d'expérience a été réalisée en batch dans différents milieux réactionnels neutres et sous irradiation par deux lampes de 24 watt de puissante chacune. La

photodégradation du polluant a été évaluée en maintenant les conditions opératoires suivantes :

- Une quantité dephotocatalyseur (TiO2, ZnO): 0,25 g/L ;
- Une concentration initiale du colorant : 10 mg/l ;

Les courbes illustrées dans la figure 2 représentent l'évolution temporelle de la concentration réduite pour différents types de suspension de nanoparticules. Les courbes montrent que pour tous les cas étudiés, le polluant a été oxydé de façon appréciable à l'exception de la solution avec le TiO_2commercial de Biochem.

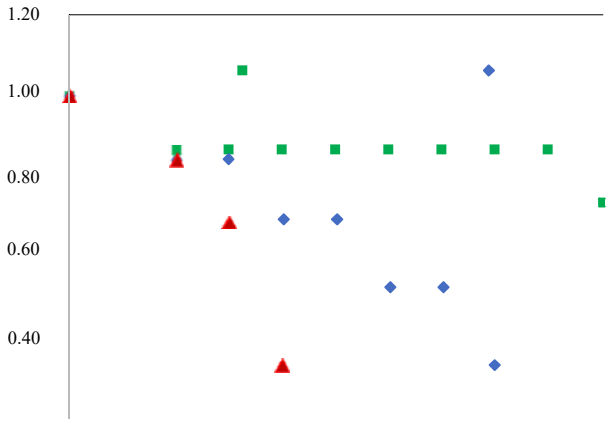

Fig. 2. Evolution temporelle de la concentration réduite du colorant en utilisant différents types de photocatalyseurs.

L'allure des courbes est de forme exponentielle laissant prédire que la cinétique de la dégradation du colorant est de pseudo-premier ordre. Les constantes de vitesses de pseudo-premier ordre k_{app}, les taux de dégradation déterminés après 60 min de traitement ainsi que les temps de demi-réaction sont regroupés dans le tableau 1.

Tableau 1. Valeurs des constantes de vitesse apparente, vitesses initiales, le temps de demi-réaction et le taux de dégradation.

	X % à 60min	k_{app} (min^{-1})	r_0 (mg. l^{-1}.min^{-1})	$t_{1/2}$ min	R^2
TiO_2 Comm	16	0,0109	0,109	64	0.70
TiO_2 P25	100	0,0195	0,195	36	0.93
ZnO	100	0,0243	0,243	29	0.92

Les valeurs du tableau 1, montrent qu'une dégradation totale est observée pour le TiO_2 P25 et le ZnO avec un taux de dégradation qui a atteint 100% au bout de 50 et 30 minutes de traitement respectivement. En tenant compte des constantes des vitesses apparentes, le ZnO présente une performance plus importante avec une constante k_{app} égale à 0,0956 min^{-1} comparativement à celle de TiO_2 P25 avec k_{app}de 0,0365 min^{-1}, d'où vient notre choix pour la suite denotre travail **[8, 9]**.

Effet de la concentration en catalyseur ZnO

Afin d'étudier l'influence de la concentration d'oxyde de zinc ZnO sur la photodégradation de notre colorant, nous avons fait varier les concentrations du catalyseur dans la gamme allant de 0,01 à 0,25 g/l.
Une série d'expériences a été réalisée en maintenant constantes les conditions opératoires suivantes :

- Un débit derecirculation de la solution 0,3 L/min
- Une concentration initiale de polluant 10 mg/L
- Une puissance de la lampe 24 W
- Un pH libre (7, 3-7,8)
- Une température du mélange réactionnel ambiante 24°C
- Volume réactionnel 2L

Les courbes illustrées dans la figure 3, représentent la variation temporelle de la concentration réduites en colorant en fonction du temps pour différentes concentration en ZnO.

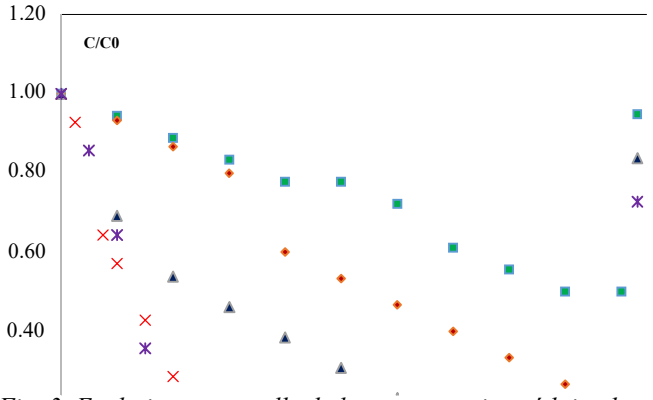

Fig. 3. Evolution temporelle de la concentration réduite du bleu suprantine pour différentes concentration en ZnO. C_0=10 mg/L, Q=0,3L/min, V=2L, T = 24°C, PH libre.

Les courbes de la figure 3 montrent que la dégradation du colorant augmente avec la concentration d'oxyde de zinc jusqu'à ce qu'il atteigne une concentration maximum de 0,125g/L.

Au-delà de cette valeur, la dégradation diminue, ce comportement s'explique par le fait qu'au-dessus de la concentration optimale les particules de ZnO provoquent un effet écran vis à vis de la lumière UV et réduisent ainsi la formation de radicaux hydroxyles responsable de la réaction d'oxydation du polluant Notre choix s'est porté sur la concentration en d'oxyde de zinc de 0,125g/L pour son performance pour l'élimination de ce polluant.

Les constantes apparents de vitesse relatives à chaque concentration ont été déterminées par régression linéaire à partir du trace de l'évolution de $-\ln(C/C_0)$ en fonction du temps. Les résultats sont regroupés dans le tableau 2.

Tableau 2. Valeurs des constantes de vitesse apparente, vitesses initiales, le temps de demi-réaction et le taux de dégradation pour les différentes concentrations en ZnO.

ISSN: 1737-9334

[ZnO] (g/L)	X % 40 mn	K_{app} (min^{-1})	$t_{1/2}$ (min)	R^2	r_0 ($mg.l^{-1}.mn^{-1}$)
0.01	22.22	0.0061	114	0,99	0.072
0.03	39.99	0.0073	95	0,99	0.072
0.06	61.54	0.0258	27	0,98	0.221
0.125	100	0.0602	11.5	0,99	0.554
0.250	92.85	0.0673	9.5	0,98	0.599

D'après les valeurs de tableau 2, le taux d'abattement augmentent avec la quantité du d'oxyde de zinc ZnO jusqu'à atteindre un optimum correspondant à la valeur 0,125g/L.

Pour des quantités plus élevées en catalyseur, la vitesse de réaction diminue à cause de la saturation ou par perte de la lumière par diffusion. Les résultats obtenus montrent que :

- Si [ZnO] > 0,125 g/L : l'efficacité de la dégradation diminue à cause de l'excès en catalyseur qui va empêcher la pénétration des rayons UV.
- Si [ZnO] < 0,125 g/L : la dégradation du colorant devient plus lente à cause dune grande quantité du colorant et la quantité du catalyseur ne suffit pas pour l'éliminer complètement.

Effet de la concentration initiale en polluant

L'effet de la concentration initiale en bleu suprantine a été étudié pour des valeurs variant de 5 à 40 mg/L, les expériences ont été effectuées selon les conditions opératoires suivantes :

- Un débit derecirculation dela solution 0,3 L/min
- Une quantité de ZnO de 0,125 g/L
- Une puissance de la lampe 24 W
- Un pH libre (7, 3-7,8)
- Volume réactionnel 2L
- Une température du mélange réactionnel ambiante 24°C.

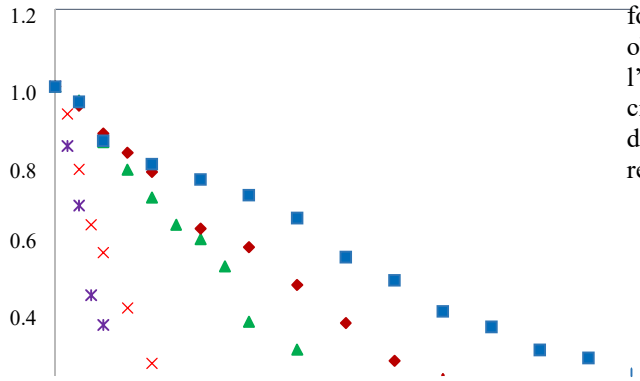

Fig. 4. Évolution temporelle de la concentration réduite en colorant pour différents concentration initiales en polluant C^{ZnO}=0,125g/L, Q=0,3L/min, pH libre, T= 24°C

Les courbes illustres dans la figure 4 représentant l'évolution temporelle de la concentration réduite pour différents concentrations en polluant, montrent que la dégradation du bleu suprantine est plus importante lorsque sa concentration diminue.

Ce phénomène peut être expliqué par la disponibilité d'un plus grand nombre de sites actifs qui conduisent à l'adsorption des molécules du bleu surrantine et d'eau sur les particules de ZnO qui produisent ainsi des radicaux hydroxyles et menant un processus rapide d'oxydation. L'allure exponentielle des courbes laisse présager une cinétique de pseudo-premier ordre.

Le tableau 3 illustre les valeurs des constantes de vitesse K_{app}, des vitesses initiales r_0, des taux de dégradation après 60min d'irradiation et des temps de demi-réaction, pour les différentes concentrations initiales en colorant.

Tableau 3. Valeur des constantes cinétiques, vitesses initiales, taux de dégradation et temps de demi-réaction pour les différentes concentrations en bleu surrantine.

$[C_0]$ (mg/L)	X % 60 mn	K_{app} (min^{-1})	$t_{1/2}$ (min)	R^2	r_0 ($mg.l^{-1}.mn^{-1}$)
0.01	100	0.096	7	0,98	0.8211
0.03	100	0.0602	12	0,99	0.5545
0.06	40	0.0171	41	0,98	0.3150
0.125	36	0.0146	47	0,99	0.3938
0.250	28	0.0109	64	0,98	0.3586

Le tableau 3 montre que la constante de vitesse diminue avec l'augmentation de la concentration initiale en polluant. Un taux de dégradation optimale 100% est obtenu pour les concentrations 5 et 10mg/L. Les constante cinétiques augmentent lorsque la concentration en colorant diminue, ceci peut être expliqué par la disponibilité des sites actifs et par l'absence d'interactions entre les molécules.

Vérification du modèle de langmuir-hinshelwood

Afin de vérifier le modèle de langmuir-hinshelwood, nous avons représenté $1/K_{app}$ en fonction de C_0. La courbe de la figure 5 représente l'inverse de la constante apparente en fonction de la concertation initiale en colorant. La courbe obtenue est une droite, la pente correspond a (1/k*K) et l'ordonnée a l'origine correspond a l'inverse de la constante cinétique, la constante d'équilibre d'adsorption K est déterminée a partir de la pente de la droite. Les résultats sont reportes dans le tableau 4.

ISSN: 1737-9334

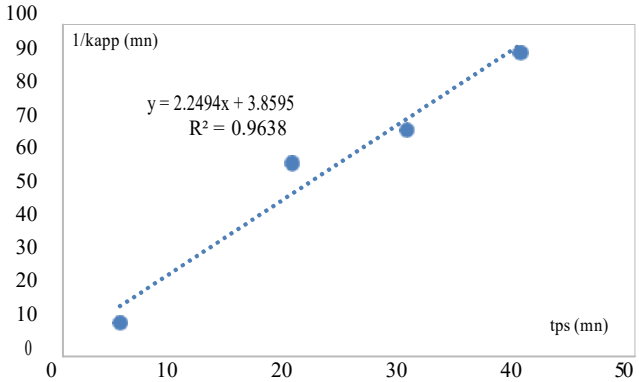

Figure III.5. Détermination des constantes cinétiques et d'équilibre par linéarisation du modèle de langmuir-hinshelwood.

Tableau III.5. Constantes cinétiques de réaction et d'adsorption du colorant

k (mg /L .min)	K (mg^{-1} .L^{-1})	R^2
0.26	1.71	0.991

Le tableau 5 rassemble les valeurs des constantes cinétiques et d'équilibre d'adsorption la cinétique de dégradation du bleu suprantine obéit au modèle de Langmuir-hinshelwood vu la valeur du coefficient de corrélation

IV. CONCLUSIONS

Tout au longue de notre travail, nous nous sommes fixés comme objectif la dégradation d'une solution aqueuse synthétisée au laboratoire à base d'une quantité variante de colorant d'origine de l'industrie textile (TEXALG-l'Algérienne des textiles-Boufarik) dans un réacteur tubulaire sous irradiation artificiel (lampe UV) et en présence de ZnO en suspension comme catalyseur.

Afin d'étudier l'influence de certains paramètres sur l'efficacité du procédé photocatalytique UV/ZnO, pour la dégradation de notre colorant des expériences ont été réalisées en faisant varier les paramètres physico-chimiques tel que : la concentration initiale en polluant et la quantité de catalyseur. Les résultats de l'étude ont montré que :

- L'augmentation de la concentration en ZnO accélère la dégradation photocatalytique de bleu BWL jusqu'à la valeur optimale qui est 0,125g/L. Au-delà de cette valeur nous remarquons une diminution de la vitesse traduite par l'effet écran causé par l'excès en catalyseur ; La vitesse initiale de dégradation de notre colorant augmente avec la concentration initiale tandis que la constante de vitesse apparente diminue.

Un taux d'abattement de 100% est obtenu lors du traitement de 2L de solution à une concentration de 0,125 g/L de catalyseur et une quantité de 10mg/L de pollution au bout de 40min de traitement seulement ;

- La cinétique de dégradation de bleu BWL 300% est décrite par le modèle de Langmuir-Hinshelwood et la réaction est de pseudo-premier ordre, les valeurs des constantes cinétique d'adsorption K et de réaction k sont respectivement égales à1,71mg^{-1} /L^{-1} , k=0,26 mg /L/min.

REFERENCES

[1] Ben Mansour H., R. Mosrati, D. Corroler, K. Ghedira, D. Bariller et L. Chekir . Genotoxic and anti-butyrylcholinesterasic activities of acid violet 7 and its biodegradation products. Drug Chem. Toxicol., 32, 230-237,2009

[2] BENBLIDIA M. L'efficience d'utilisation de l'eau et approche économique. Plan Bleu, Centre d'Activités Régionales PNUE/PAM, Etude nationale, Algérie, 2011, 9-12

[3] A.G.S. Prado, E.A. Faria, J.R. SouzaDe, J.D. Torres. Ammonium complex of niobium as a precursor for the hydrothermal preparation of cellulose acetate/Nb_2O_5 photocatalyst, J. Mol. Catal. A 237 (2005) 115–119.

[4] **J**.D.Torres, E.A. Faria, J.R. SouzaDe, A.G.S. Prado. Preparation of photoactive chitosan–niobium (V) oxide composites for dye degradation, *J.* Photochem. Photobiol. A 182 (2006) 202–206.

[5] HADDOU Ménana: Dégradation de dérivés de l'acide benzoïque par les procédés d'oxydation avancée en phase homogène et hétérogène: procédés Fenton, photo-Fenton et photocatalyse. Thèse de doctorat, Université de Toulouse III, France (2010)

[6] S. Chatterjee, S. Sarkar, S.N. Bhattacharyya, Photodegradation of phenol by visible light in the presence of colloidal Fe2O3, Journal of Photochemistry and Photobiology A: Chemistry 81 (3), 1994, 199-203.

[7] J.-M. Herrmann, M.-N.l. Mozzanega, P. Pichat. Oxidation of oxalic acid in aqueous suspensions of semiconductors illuminated with UV or visible light, Journal of Photochemistry 22 (4), 1983, 333-343.

[8] N. Chekir, Ouassila Benhabiles, Djilali Tassalit, Nadia Aicha Laoufi and Fatiha Bentahar. Photocatalytic degradation of methylene blue in aqueous suspensions using TiO2 and ZnO. Desalination and Water Treatment. 57 (2016) 6141–6147.

[9] Lizama C., Freer J., Baeza J., Mansilla H.D., Optimized photodegradation of reactive blue 19 on TiO2 and ZnO suspensions, Catal. Today, 76, (2002), 235–246.

Biosorption of reactive basic Red 5 dye by Local agricultural waste: kinetic and equilibrium studies.

Oumessaâd Benturki*[1], Asma Benturki[1.2], Nadj Moulai Mostefa[2], Saliha Benturki[3]

*[1] *Laboratory of Physical and Chemical Study of Materials and Applications in the Environment, Faculty of Chemistry (USTHB), BP 32-16111 EL-Alia, Algeria.*
oum_saad@yahoo.fr, ben.asma.2019.2@gmail.com

[2]*Materials and Environmental Laboratory, Faculty of Sciences and Technology, University of Medea, Ain D'Heb, 2001 Medea, Algeria*
moulai.nadji@univ-medea.dz

[3]*Faculté of engineering of mechanics and processes , (USTHB), BP 32-16111 EL-Alia, Algeria*
benturkisali22@gmail.com

Abstract— **The use of agricultural waste in effluent treatment is interesting due to its low cost and high availability. In this study the potential of biomass, a by-product of brewing process, was evaluated as biosorbent of reactive basic Red 5 dye. The wild jujupe (nabak) shells was characterized by point of zero charge (pH_{PZC}). Batch experiments were carried out to investigate: effect of, dye solution, effect of pH, kinetics, biosorption isotherm. The pH_{PZC} of the biosorbent was determinedat 6. The results showed that reactive basic Red 5, biosorption optimum conditions were obtained using biosorbent dosage of 1 g L^{-1} and at pH 2. The pseudo-second order model and the Langmuir isotherm model (qmax = 17.01 mg g-1) best represented the kinetic and equilibrium biosorption data, respectively. The results indicated that the wild jujupe (nabak) shells can be used as an alternative and promising biosorbent to be applied in the treatment of effluents containing the reactive basic Red 5 dye.**

Keywords— **Bisorption, Isotherm, Dye, Agricultural waste,**

I INTRODUCTION

Bisorption, Isotherm, dye agricultural waste

The modification of natural environments by anthropic actions is one of the most relevant issues today. Pollution from effluents, especially those containing dyes, is a worldwide concern, because they come from various industrial segments such as food, cos metics, paper, and textiles. However, the source of the largest residues of dyes comes from the textile industry, the expansion of this sector caused serious problems of environmental contamination due to the excessive generation ofliquid effluents [1].

During the process of tissue dyeing the effluent is enriched with colored compounds, which did not attach to the fiber [2 ,3]. This effluent is inappropriate for human consumption and its discharge into rivers is unacceptable due to large amount of dyes. Besides the strong coloration, theyare non-biodegradable.

Reactive dyes are used because they present advantages, such as easily application and result in bright colors and stable coloration [4]. The coloration present in the water due to the inappropriate dyes discard damages the aquatic ecosystem, because it inhibits the entrance of solar radiation, hindering the photosynthetic activity and altering the solubility of gases in water [5]. In addition, the dyes may be carcinogenic, toxic and have mutagenic effects [1].

Therefore, methods for treating effluents have been developed in order to reduce environmental impacts. Among these methods stand out techniques of adsorption, biodegradation, electroflocculation, coagulation/flocculation, ozonation, photochemical

ISSN: 1737-9334

degradation and chemical degradation. The adsorption technique is superior to other techniques due to easily biosorbent regeneration and for not generating a secondary chemical sludge. In addition, it has other advantages such as being a low cost technique, has practical operation mechanism and allows the use of biosorbents, which are easy to obtain and do not need anyhigh cost pretreatment to be used [6, 15].

Biosorbents are natural materials or mostly agriculturalby-products, which have purpose to replace activated carbon, an effective adsorbent, but that at large scale presents high cost. Some biosorbents have already been studied as cotton stalk and sugarcane bagasse [7, 8]. The use of by-products in effluent treatment is interesting due to its low cost and high availability. Therefore, the aim of the present study is to examine the potential of as biosorbent of the reactive blue BF-5 G dye, and evaluate the best operating conditions of the process, such as: particle size, dosage, pH, contact time and also investigate the kinetic, equilibrium isotherm and desorption.

II. MATERIALS AND METHODS

A. Biosorbent and Dye Solution

The The wild jujube sidr nabak shells as the precursor material obtained from an agricultural waste product, theywere well washed with water several times for the removal of dust and dried at 110◦C for 24h. Dye was donated by Textill company. The dye solution was prepared using distilled water. All used reagents were of analytical grade. The pH value of the dye solution was adjusted using 0.1 mol L^{-1} of HCl and NaOH solution.

B.. Characterization of the wild jujupe (nabak) shells

To determine the point of zero charge (pH_{PZC}), which is the pH that the surface of the biosorbent has a neutral charge ([12], [13]), it was followed the methodology of Regalbuto & Robles [14], called the "11 point scale". The experiments were performed in triplicate. A biosorbent mass of 50 mg material was placed in contact with 50 mL of aqueous solution with different initial pH (2, 4, 6, 8, 10, 12) and kept under shaking at 150 rpm and 25 °C. After 24 hours the final pH of the aqueous solution was measured. The pH_{PZC} corresponds to the range where the final pH remains constant regardless ofinitial pH.

C. Biosorption Experiments

In biosorption experiments, the measurements of dye ultraviolet-visible UV–Vis spectrophotometer (Jasco 560 Model), at wavelength of 525nm, where the maximum absorbance was observed. The Erlenmeyer flasks were agitated in a shaker-incubator (Tecnal Incubator,). After the biosorption process, the biomass was separated using domestic sieve and the fluid was subjected to absorbance reading. Control experiments were conducted without the addition of biosorbent in the dye solution, maintaining the same experimental biosorption conditions. The Erlenmeyer flasks are stirred in a stirrer-incubator After the biosorption process, the biomass was separated. Control experiments were carried out without adding biosorbent to the dye solution, maintaining the same experimental conditions of biosorption. Samples were collected and the amount of dye adsorbed on the biosorbent at equilibrium (q_{eq}, mg g^{-1}) bythe malt bagasse was calculated according to Equation (1).

$$q_e = (C_0 - C_e)\frac{V}{m} \quad (1).$$

concentration in solution were quantified by where Co and Ce are the initial equilibrium concentrations (mg/L), of Reactive basic Red 5 (NR) in solution, V is the volume (L), and W is the weight (g)ofadsorbent..

In order to determine the equilibrium time, wstudied the effect of contact time between the adsorbents and the colored solution. For this purpose, we prepared a series of 250 ml vials containing 50 mg of adsorbent and 50 ml of the solution at concentrations of: 5, 10 and 20 mg/l of the dye RN. These bottles were placedin a thermo regulator fixed at 25° C. with stirring at 150 rpm for 3 hours with a pitch of 20 minutes. The samples taken were then placed in a centrifuge for 10 minutes, the supernatants were taken and then analyzed by a UV-visible spectrometer to measure the residual concentrations of the solution of the dye RN.

In order to assess the influence of solution temperature on the adsorption of the RN dye by the grains of jujube nuclei and date nuclei, we examined the evolution of the amount adsorbed at different temperatures by varying the initial concentrations of5, 10, 15, 20, 25, 30, 35, 40 and 50 mg/l, bypreparing a series of vials containing a mass of 50 mg of adsorbent with 50 ml of each concentration. The solutions are stirred for 24 hours at a speed of 150 rpm. The residual concentrations of the dye were determined byUV spectrometry.

ISSN: 1737-9334

III-RESULTS AND DISCUSSION

A .Determination of pH zero charge (pHpzc)

The pHpzc values obtained make it possible to determine the acidic or basic character ofan adsorbent and to know, according to the pH of the solution, its netsurface charge.

Fig 1.Shows the curves used to determine the pHpzcvalue.

The pHpzc values of the two adsorbents can be derived from the intersection of the pH variation curves with the bisector. The NJB is characterized by pHpzc=6.81, the dye is anionic, which makes adsorption favored bypHs<pHpzc

B. Study of the effect of pH.

The pH-dependent adsorption results are showngraphicallyin Fig 2

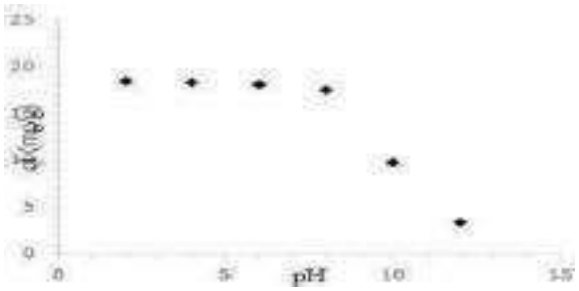

Fig2: Effect of pH on the adsorption of RN dye byNJB grains

to studythe influence of the pH of the solution on the adsorption capacities of the dye RN under equilibriumconditions, we varied the pH of the solution from 2 - 12.

C. Study of bisorption kinitics:

The results obtained illustrated by the figure 3, show that the amount adsorbed increases over the contact time as well as with the increase in the content of the solution of the dye RN; indeed, the increase in the concentration induces the change in the driving force of the concentration gradient, and therefore the increase inthe diffusion of the molecules of the dye in solution through the surface of the adsorbent

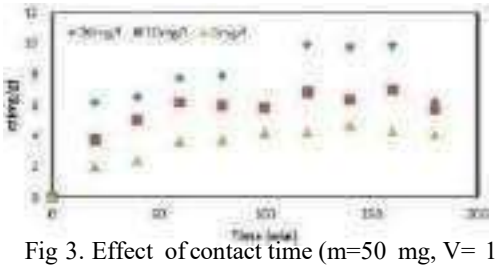

Fig 3. Effect of contact time (m=50 mg, V= 150 rpm,pH = 6, T=25°C)

The results obtained (Table I.) show that the pseudo second order model is the most reliable kinetic model for determining the order of the adsorption kinetics of the dye RN on the grains of the NJB a. In fact, the best model established is chosen according to thecorrelation factor, the higher the value of the factor, the better the model is for the study of the adsorption process (R^2>0.98) [15]. This model characterizes the adsorption kinetics by assuming that rapid solute adsorption occurs primarily at high energy sites and relatively slow adsorption at low energy sites. Based on

the reported qe values in Table I, we note that they are closer to those determined experimentally using the second-order pseudo model, this table also shows that for the second-order pseudo model, the rate constant depends on the initial concentration of RN dye since the increase in the initial concentration from 5 to 20 mg/L results in an increase in the rate constant from 4,479 to 65,673 for NJB grains.

B. Study of bisorption isotherms

The experimental results obtained from the adsorbents(NJB) are illustrated in figure 4. Isotherms of the biosorption of the dye RN by NJB.The pattern of isotherms of NJB grains indicates thatq_e is low at low concentrations, e.g. at T=45°C,increasing concentrations leads to an increase in theadsorption capacity of NJB grains. The attraction forces between the adsorbed molecules are thereforelow, so according to the Giles AL classification theisotherms are of type L [18]. The increase in thetemperature of the medium promotes the mobility anddiffusion of the dye RN through the outer boundarylayer of the adsorbent surface and consequentlyincreases the maximum amount of adsorption, for NJBgrains.

TABLE I: FIRST AND SECOND-ORDER BIOSORPTION RATE CONSTANTS,CALCULATED AND EXPERIMENTAL Q_EVALUESIn order

Pseudopremier ordre : $\ln(q_e - q_t) = \ln q_e - K_1 t$ (2)

Co (mg/L)	qe(exp) (mg.g-1)	qecal (mg.g-1)	K1 (min−1)	R²
5	4.740	1.493	0.004	0.760
10	6.996	1.477	0.002	0.507
20	9.980	2.863	0.0114	0.971

Pseudo second ordre : $\frac{t}{q_t} = \frac{K_1 . q_e^2}{} + \frac{}{q_e}$ (3)

Co (mg/L)	qe(exp) (mg.g-1)	qe cal (mg.g-1)	K2 (g/min .mg)	R²
5	4.741	5	4.479	0.982
10	6.996	7.633	22.28	0.983
20	9.980	11.90	65.67	0.984

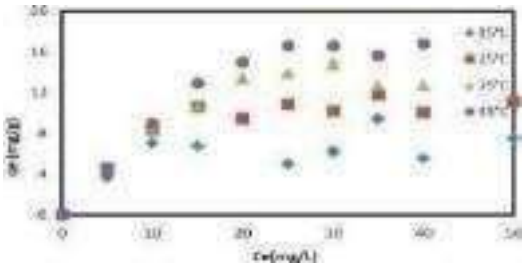

Fig 4. effect ofinitial concentration on the ofreactive basic red 5 dye (m=50mg, pH 6, 150 rpm, 24 h,,) .

TABLE II : PARAMETERS OF THE LANGMUIR AND FREUNDLICH ISOTHERMS

Langmuir Model : $\frac{C_e}{q_e} = \frac{C_e}{q_m} + \frac{1}{b \times q_m}$ (4)

T(°C)	q_{max} (mg/g)	K_L (L/mg)	R_L	R²
15	5,567	-4,402	-0,011	0,984
25	11,074	1,292	0,037	0,990
35	13,228	3,857	0,013	0,990
45	17,090	1,229	0,039	0,996

Freundlich Model : $\ln q_e = \ln K_F + \frac{1}{n} \ln C_e$ (5)

T(°C)	n	K_F (L/mg)	R²
15	9,166	4,935	0,180
25	5,705	6,361	0,707
35	4,237	7,146	0,831
45	3,029	7,929	0,729

Based on the results obtained and grouped in Table II, we find that the Langmuir model gave a good correlation (R^2>0.99) for the adsorption of the dye RN on the two adsorbents, which indicates that the adsorption is carried out with the formation of a molecular monolayer on energy-equivalent adsorption sites and that there is no interaction between the adsorbed molecules [17]. In accordance with this model, the maximum capacities adsorbed by NJB grains is 17.1 mg/g. In the range of initial concentrations used, the dimensional factor R_L varies from 0.01 to 0.09 indicating that the adsorption process is favorable. We also note that the values of n are between 1 and 10, which confirms that the adsorbent used have a good affinity for the dye used [16].

IV CONCLUSIONS

In this study, the biosorption of the reactive basic Red 5 (RN) dye was favored at pH 2, fact associated with the electrostatic interactions between the positive charge of the biosorbent surface and anionic dye (pH < pHPZC = 6). The equilibrium time of the system was reached with 2 hours of biosorbent and dye contact, being the biosorption data better adjusted by the pseudo-second order kinetic model. The equilibrium experimental data were better described by the Langmuir isotherm model (qmax = 17.01 mg $g^{-1.}$., The increase in biosorption temperature results an increase in adsorption capacity . The results of the thermodynamic study showed that the adsorption process is endothermic and that the adsorption works mainly by physical adsorption. The The wild jujube sidr nabak shells revealed to be an effective biosorbent in theremoval of the reactive basic R d 5 dye with the advantage of having low cost, be of a renewable source.

REFERENCES

[1]. M. Alkan, M. Dogan, Y. Turhan, O. Demirbas, P. TuranAdsorption kinetics and mechanism of maxilon blue 5G dye on sepiolite from aqueous solutionsChemical Engineering Journal, 139 (2)(2008),pp.213.
[2]. M.V.B. Zanoni, P.A. Carneiro O descarte dos corantes têxteis Ciência Hoje, 29 (174) (2001), pp. 61.
[3]. S. Ledakowicz, M. Solecka, R. Zylla Biodegradation, decolourisation and detoxification of textile wastewater enhanced by advanced oxidation processes Journal of Biotechnology, 89 (2-3) (2001),pp.175.
[4]. T.E.M. Carvalho, D.A. Fungaro, J.C. IzidoroAdsorção do corante reativo laranja 16 de soluções aquosas por zeólita sintética Química Nova, 33 (2) (2010), pp. 358.

[5]. C.R.L.S. Souza, P.P. Zamora « Degradação de corantes reativos pelo sistema ferro metálico/peróxido de hidrogênio ; Química Nova, 28 (2) (2005), pp. 226. [6] R. Han, W. Zou, W. Yu, S. Cheng, Y. Wang, J. Shi Biosorption of methylene blue from aqueous solution by fallen phoenix tree's leaves Journal of Hazardous Materials, 141 (1)(2007),pp.156

[7] H. Deng, J. Lu, G. Li, G. Zhang, X. Wang Adsorption of methylene blue on adsorbent materials produced from cotton stalk Chemical Engineering Journal, 172 (1)(2011), pp. 326

[8] K.A.G. Gusmão, L.V.A. Gurgel, T.M.S. Melo, L.F. Gil Adsorption studies of methylene blue and gentian violet on sugarcane bagasse modified with EDTA dianhydride (EDTAD) in aqueous solutions: Kinetic and equilibrium aspects ,Journal of [9]. Environmental Management, 118 (2013), pp. 135 [9]. L.M. Mendonça ,Utilização de resíduo úmido de cervejaria na alimentação de cabras anglo nubiana em final de lactaçãoMaster's Thesis). Retrieved from Repositório Institucional UFS(2012)

[10]. K.M. Lynch, E.J. Steffen, E.K. Arendt Brewers' spent grain: a review with an emphasis on food and health ,Journal of the Institute ofBrewing,122(2016),pp.553.

[11]. L.G. Cordeiro, A.A. El-Aouar, C.V.B. Araújo Energetic characterization of malt bagasse by calorimetry and thermal analysis. Journal of Thermal Analysis and Calorimetry, 112 (2) (2013), pp. 71.3

[12]. C. Qin, L. Liu, Y. Han, C. Chen, Y. Lan « Mesoporous Magnetic Ferrum-Yttrium Binary Oxide: a Novel Adsorbent for Efficient Arsenic Removal from Aqueous Solution », Water Air Soil Pollution, 227 (2016), p. 337,

[13]. J.F. Honorio, M.T. Veit, G.C. Gonçalves, E.A. Campos, M.R. Fagundes-Klen « Adsorption of reactive blue BF-5G dye by soybean hulls: kinetics, equilibrium and influencing factors Water Science and Technology, 73 (5)(2016), pp. 116.

[14] . J.R. Regalbuto, J. Robles, The engineering of Pt/Carbon catalyst preparation – For application on proton exchange fuel cell membrane (PEFCM), University of Illinois at Chicago, USA (2004)REU 2004 Summer Program. Final Report.

[15] . O. S. Benturki, A. Donnot, S. Molina, A. Merlin, F. Addoun, " Synthesis and characterization of activated carbons obtained from jujube shells «nebka»",*J. Soc. Alg. Chim,* vol. 18,n° 1, pp 7-23, 2008.

[16]. A. Mittal, J. Mittal, A. Malviya, V.K. Gupta ,Adsorptive removal of hazardous anionic dye "Congo red" from wastewater using waste materials and recovery by desorption, Journal of Colloid and Interface Science, 340 (1)(2009), pp. 16-

[17]. Saeed, M. Sharif, M. Iqbal, Application potential of grapefruit peel as dye sorbent: Kinetics, equilibrium and mechanism of crystal violet adsorption,, Journal of Hazardous Materials, 179 (1-3) (2010), pp. 564-[18] C. H. Giles, D. Smith and A. Huitson, ―A General « Treatment and Classification of the Solute Adsorption Isotherm». I. Theoretical,‖ Journal of Colloid and Interface Science, Vol. 47(1974) 755-

Numerical Simulation of Multiphase Flow in T-junction

Imene Laalaibia [#1], Omar Kholai [*2]

Department of transport engineering, University of Frère Mentouri-Constantine
Transport and Environment Engineering Laboratory, Street 325 Ain El Bey Constantine, 25017, Algiers
[1]imene.laalaibia@student.umc.edu.dz
[2]kholai.omar@googlemail.com

***Abstract*— the article presents the results of a computational fluid dynamics (CFD) analysis of gas-liquid multiphase flow. The simulation was conducted using CFD code and the Euler–Euler approach. The present study relates to the turbulent flow of water and carbon dioxide mixture in a 2D pipe. Separation phenomenon between phases is observed. The solution was obtained using a mixture model. Different values of carbon dioxide volume fraction were taken into account in the analysis of the results. The analysed cases were compared grace to the obtained calculations results. The main purpose of the simulations was to show streamlines, velocity, pressure, and volume fraction distribution that could be useful in developing pipeline systems in many industrial applications, especially for CO2 separators.**

***Keywords*— CFD, Computational Fluid Dynamics, Multiphase Flow, Numerical Simulations, T-junction**

I. INTRODUCTION

Multiphase flow is a phenomenon that occurs in many industrial processes, including the oil and gas industry. Due to the complexity of multiphase flows, the development of a reliable analysis tool is difficult. Computational fluid dynamics (CFD) has been a well-established tool for monophasic flow analysis for over 25 years, but has only begun to prove itself in the multiphase domain. To be able to use CFD in a meaningful way, it is important to study, understand and validate the many models offered in commercial codes such as CFX, Fluent ANSYS, and COMSOL Simulation has increased enormously in recent decades at the center of this thesis by studying the basic CFD techniques that are used to simulate gas-liquid flow. This job is to perform simulations using the different multiphase models available in CFD software and to compare these models. The simulations are based on a study of the flow of a gas-liquid mixture in a horizontal junction.

The objective of Simulations is to find the most reliable models that predict accurately.

The two-dimensional problem is modeled by the basic equations of classical fluid mechanics (continuity and momentum), accompanied by the volume fraction equation for each phase of the mixture.

The T-junctions problem are found in a large number of pipe systems, mainly used to direct the flow from the main branch to several ducts, which leads to the flow being divided. They can vary in the number of ducts and shapes.

The water-carbon dioxide mixes flows upwards in a junction and then splits near the horizontal arm. This phenomenon of separation between the phases is observed, the solution was obtained using a model mixture.

The Euler-Euler approach for multiphase flow modelling was used. The solution was obtained using a mixing model. After performing the calculations, the results were analyzed taking into account different values of the volume fraction of carbon dioxide.

The results are presented by the current lines, the velocity vector field, and the volume fraction distribution of the phases. Different carbon dioxide volume fraction values were taken into account in the analysis of the results.

II. CATEGORIZATION OF MULTIPHASE FLOW REGIMES

The flow regime typically is defined by a classification of flow pattern or a description of the morphological arrangement of the phases **[1]**. In addition, multiphase flow regimes are categorized into four classes, which are gas-solid flows, liquid-solid flows, gas-liquid or liquid-liquid flows (ANSYS FLUENT 12.1 Theory Guide, 2010) **[2]**). In this work two–phase, gas-liquid only is presented. Figure (1) shows a schematic chart of the multiphase flowregimes.

CLASSIFICATION OF GAZ-LIQUID FLOW PATTERNS

The flow patterns are utilized to illustrate the interface distribution of two phases. In two-phase gas-liquid flow, the interface can take different configurations based on different parameters, such as the two-phase velocities, two-phase fluid properties, and the pipeline geometry. Three basic flow patterns are proposed by (Hubbard and Dukler, 1966namely, separated, intermittent, and distributed flow) [**3**].

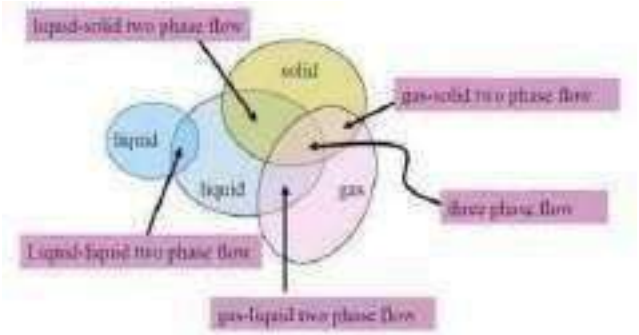

Fig 1.Multiphase flowregimes **[2]**.

FLOW PATTERNS IN HORIZONTAL PIPES

The two-phase flow in a pipeline can take various physical distributions of the interface known as flow patterns or flow regimes **[4]**. These flow patterns can be identified using different techniques which are categorized into traditional approaches, such as photography in transparent pipes or direct observation, and objective indicator approaches, that include x-rays, gamma-rays, fluorescent light, void fraction variations, pressure variations, tomography etc. [**4**].

The typical flow patterns in horizontal circular pipes are demonstrated in Figure (2). The two-phase in this pipe geometry tends to separate out because of the asymmetry which is affected by the gravity acceleration. The flow patternsthat can be observed are:

a) **Bubbly flow**: In horizontal flow the gas bubbles are created due to the turbulence of the liquid phase and tend to come together to flow at the top of the pipeline. Higher liquid velocities are likely to form identical bubbles, which are distributed and appear as froth **[5]**.
b) **Plug flow**: This forms when large bubbles develop due to an increase of gas velocity. The formed bubbles coalesce to create long bubbles, which are recognized as plugs, and which keep travelling along the top side of the pipeline **[5]**.
c) **Stratified flow**: This also generates when the gas velocity is higher than the liquid phase that is specified by low flow rate. The gas phase separates out and flows separately on the top of the pipe with liquid flowing at the bottom due to the density difference **[5]**.
d) **Slug flow**: This generates when the wave amplitude has become so big that the wave touches the top of the pipe, creating gas pockets in the pipe that are smooth from the front but keep on shedding gas bubbles from the tail area while flowing **[5].**
e) **Annular flow**: This is most likely to occur when the gas velocity has increased to a high value that is sufficient to push the liquid away at the same flow direction. In annular flow, the gas phase occupies the pipe core; while the liquid exists in two forms, as film around the pipe circumference and also as droplets in the core **[5]**.

Fig 2. Flowregimes in horizontal gas–liquid **[5]**.

FLOW PATTERNS IN VERTICALE PIPES

The flow regimes in vertical upward flows can be categorized into four typical flow patterns that are slug, churn, bubbly, and annular flow **[9]**. These classes have been further differentiated by several investigators. The flow regimes that can be identified in vertical upward, co-current flows at various gas-liquid velocities are demonstrated in Figure (3). These are listed in order as the gas velocity is increased **[6]**.

a) **Bubbly flow**: This flow is generated when the gas phase is dispersed in the continuous liquid phase. Further categorizing of this flow pattern has been made as: low liquid loading bubbly flow and dispersed bubbly flow **[6] [7]**.

· Low liquid loading bubbly flow: This occurs when the liquid superficial velocity is low, and tends to form some gas bubbles, which are roughly the same size. They are presented and spread uniformly in the core phase of liquid where the coalescence mechanism can take place **[6]**.

· Dispersed bubbly flow: This flow is obtained over the entire pipe diameter variety and inclination **[8]**. The feature of

this flow is that the gas phase is dispersed as small separate bubbles in the continuous phase of liquid **[8]**.

b) **Slug flow**: This generates as the gas superficial velocity is increased, in consequence of that, more gas bubbles are created and adhere together to form a long smooth bubble with a front cap as a bullet shape (also called nose). These bubbles are referred to as Taylor bubbles, which have a cross section that is comparable to the pipe. These bubbles are typically attached to the wall via a thin liquid film. Moreover, the two successive Taylor bubbles are separated by a liquid slug that may have small gas bubbles that are being shed from the tail of the leading Taylor bubble**[6] [7]**.

c) **Churn flow**: This flow can be obtained as a result of increasing the gas superficial velocity in previous flow patterns (slug), where the Taylor bubble develops and becomes more distorted near the interface of liquid-gas. This distorted bubble moves in a motion which is similar to a churn motion, and this leads to it growing into irregular shaped portions of gas and liquid. This flow is identified as froth slug, dispersed slug, churn–turbulent flow, and pulsating annular **[7]**.

d) **Annular flow**: This flow is described by the gas phase existence in the core of the pipe, which is surrounded by liquid film around its diameter. Some of the liquid also exists in the core phase as droplets. This flow can be distinguished by two different flows, namely (Hewitt, 1982**[10]**)

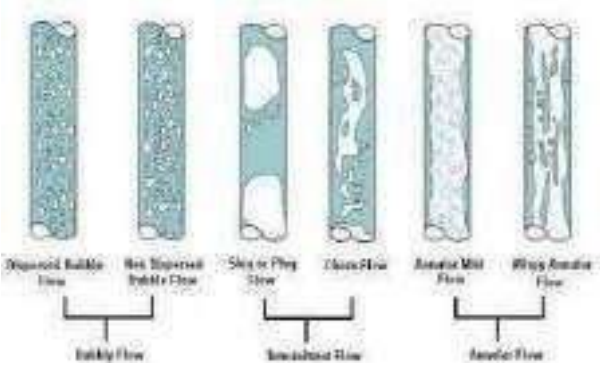

Fig 3. Flowregimes in vertical gas–liquid up-flow**[5]**.

III. MATHEMATICAL PROBLEM

The mathematical modeling of the transport of petroleum products with horizontal pipes is very difficult given the complexity of the thermo-physical properties of these products. The multiphase flows in the pipes were pressure drop and the control of fluid behavior is very important. The coupling of the partial differential equations modeling these phenomena makes the numerical solution very expensive and painful.

The use of computational fluid dynamics (CFD) methods using commercial software, (fluent, CFX, ANSYS).

The work requested is studied numerically these flows of turbulent nature using several models such as (k-Ɛ, k-Ꞷ and its variants).

In ANSYS FLUENT, three different Euler-Euler multiphase models are available: the Fluid Volume Model (VOF), the Mixture Model and the Eulerian Model. The Eulerian model is the most complex of ANSYS FLUENT's multiphase models.

IV. THE EULER-EULER APPROACH TO MULTIPHASE MODELLING

The dynamics of multiphase flows has been provided by the progressive increase of computer power and advances in computational fluid mechanics. There are two ways to perform numerical simulations of multiphase flows: based on either the Euler–Lagrange approach or the Euler–Euler approach [**11**].

In the Euler–Euler approach the dispersed phase is treated mathematically as a continuum. Conservation equations for each phase are derived to obtain a set of equations which have a similar structure for all phases. The constitutive equations close the equation system by taking into account the structure of the flow field and the material properties by experimental correlations. Eulerian averaging uses spatial, statistical or temporal averages taken in the spatial coordinate system [**11**]. The Euler–Euler approach introduces the concept of volume fractions, which are assumed to be continuous functions of space and time, and their sum is equal to one, which is shown in Equation **[12]**.

THE MIXTURE MODEL

To investigate the effect of phase separation in analyzed pipe, the mixture model was used. In general, the mixture model solves the momentum equation for the mixture of any number of phases. The dispersed phase may consist of bubbles, droplets or particulates, and in order to describe that, the model specifies relative velocities. However, the mixture model can also be used without relative velocities for the dispersed phases to model homogeneous multiphase flows. The mixture model has a wide range of applications, including horizontal or vertical flows of gas–liquid mixtures in pipes, bubbly flows, sedimentation and cyclone separators, but it is also applied on particle–fluid mixtures, like fluidized beds. In the mixture model, the volume fraction equation for the secondary phase can be obtained using Equation (4), which comes from the continuity equation for the secondary phase it solves a set of momentum and continuity equations for each phase this problem is modeled by:

Continuityand momentum equations

$$\frac{\partial}{\partial t}(\quad) + div\left(\quad V\right) = 0 \qquad (1)$$

$$\frac{v}{t} + V \, grad \, V = \frac{1}{} grad P + \, V \quad (2)$$

Volume fraction equation

$$\frac{q}{t} + u_i \frac{q}{x_i} = 0 \quad (3)$$

$$\text{With} \quad q = 1 \quad (4)$$

V. METHODOLOGY

Description of the problem:

T-junctions are commonly encountered in pipeline systems. In this study, a vertical T-junction with a horizontal junction the upper arm branch and lateral branch is used with a length of 5 m and lower branch is used with 3 m having a diameter of 0.5 m. When multiphase flow enters a T-junction, phase redistribution often occurs. This redistribution may be desirable for a phase separation is necessary.

In some situations, this can lead to a reduction in the efficiency of pipeline systems. Where it is necessary to study the phenomenon of separation of phase.

Geometry

The fluid domain geometry of the T junction was created on ANSYS FLUENT to study phase separation the phenomenon occurring on the fluid when multiphase flow enters a T-junction. The cross-section of the running for arm was named as the inlet and the cross-sections of the branch arm and the upper part of the running arm were named as outlet_2 and outlet_1 respectively.

The geometry of the fluid domain is shown in Fig.**4**. To study, pipe geometry was also created with the fluid domain using ANSYS FLUENT 16.0 and Structural Static.

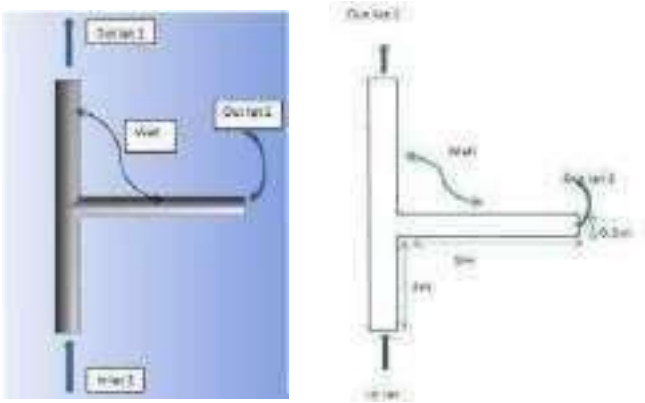

Fig 4.Schematic of the problem geometry.

Boundary conditions

For phase materials, the primaryphase was taken as water and the secondaryphase as carbon-dioxide. For inlet, carbon-dioxide and water velocities must be indicated. The carbon-dioxideand water velocities at the inlet were given at 2.5 m/s. At the outlet since the pressure value was unknown, the condition at the outlet limits was given for both outlets. The flow rate weighting for outlet 1 and 2 was given as 0.68and 0.32 respectively.

VI. RESULTS AND DISCUSSION

Simulations were performed on the geometry created as mentioned above by applying the boundaryconditions.

The solutions were obtained using third-order discretization for momentum and turbulence quantities.

Different values of carbon-dioxide volume fraction were taken into account: 0.05, 0.1, and 0.2. It is necessary to set some conditions separately for individual phases, while other conditions are shared by the mixture. For a velocity inlet,2.5 m/s for each phase was specified; the bubble diameter was equal to 1 mm. Here it is assumed that carbon dioxide at the inlet is moving at the same physical speed as the water.

TABLE I
SIMULATION PARAMETERS

case	CO2 volume fraction	Flow velocity [m/s]	Inlet density [kg/m3]	Inlet viscosity [kg/m. s]
1	0.05	2.5	948.65	0.0009538097
2	0.1	2.5	898.53	0.000904044
3	0.15	2.5	848.37	0.0008542428

Velocity Magnitude

Figures **5** through **7** shows the velocity magnitude distributions for each case, which are presented as a cross-section of the 2D geometrical model.

In general, increasing the value of volume fraction leads to a reduction in the velocity magnitude (**Figs. 5–7**).

The interaction between the flux and the sharp corner leads to the creation of a recirculation pattern, which can be better observed in Figure **8**.

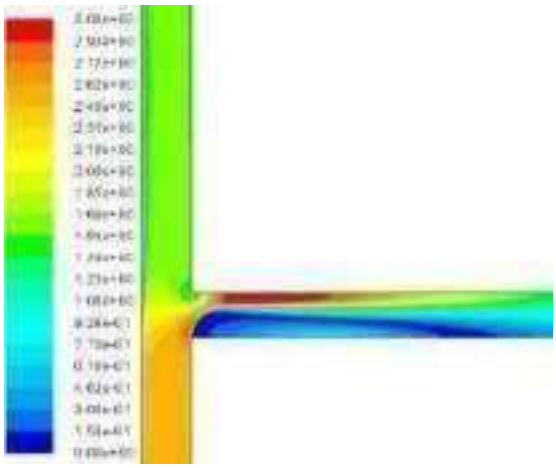

Fig 5.Contours of velocity magnitude v (m/s) – Case 1.

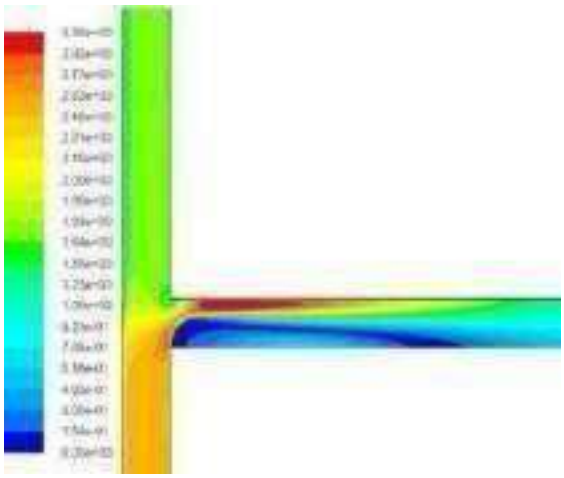

Fig 6.Contours of velocity magnitude v (m/s) – Case 2.

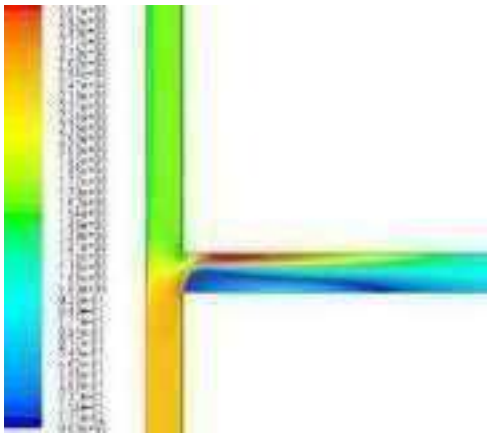

Fig 7.Contours of velocity magnitude v (m/s) – Case 3.

Fig 8.Contours of particle path-lines, coloured by particle ID.

Volume fraction

From the results of performed simulations contour of carbon-dioxide volume fraction are obtained Fig. shows the contour of volume fraction obtained from each case. In figures it can be observed that the gravity acts against the inertia that tends to concentrate gas on the lower pressure side and create gas pockets. In the vertical arm, both the gas and the water have velocities in the same direction, and therefore there is no separation because the force of gravity influences identically.

When gravity acts downwards, it induces stratification in the side arm of the T-junction like vertical section.

The outflow split greatly modifies the relation between inertia forces and gravity and has an important role in flow distribution and the gas concentration.

As the dispersed phase bubbles move along the lateral armwith the flow.

This velocity gradient induces lift force, inferring buoyancy force, thus delaying the accumulation of carbon dioxide concentration along the upper surface of the side arm.

In these cases, the carbon dioxide volume concentration is relatively small, so the mixture turbulence model is sufficient to capture the important features ofthe turbulent flow.

ISSN: 1737-9334

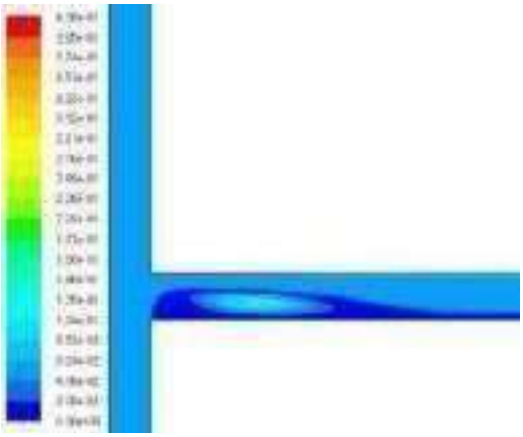

Fig 9.Contours of CO2 volume Fraction– Case 1.

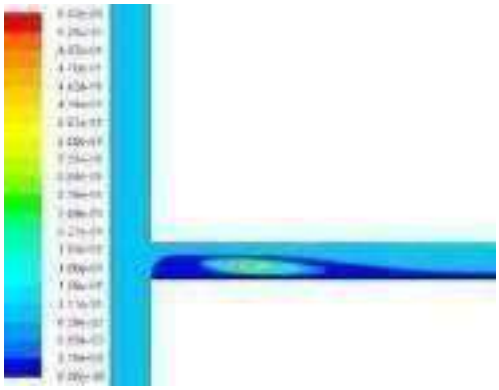

Fig 10.Contours of CO2 volume fraction – Case 2.

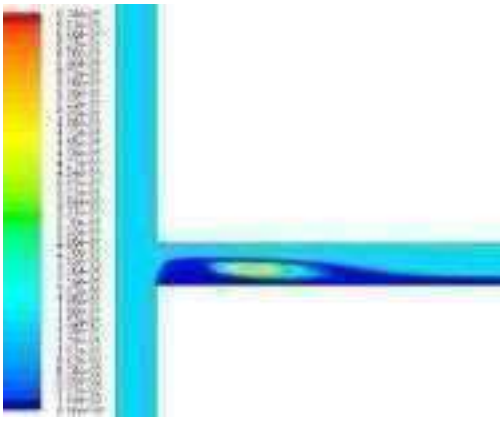

Fig 11.Contours of CO2 volume fraction – Case 3.

Pressure field

The dynamic pressure is obtained from the kinetic energy of the particles in motion. In the case of dynamic pressure, its increases and decreases are also influenced by increasing or decreasing friction.

Due to the Operating Density parameter being set to 0, which is necessary when one of the fluid phases is compressible, a hydrostatic pressure gradient is observable in the vertical arm.

This pressure gradient is reduced while the value of volume fraction increases. Figure (**12, 13 and 14**).

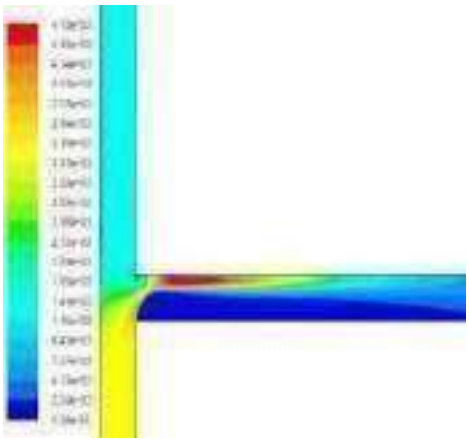

Fig 12.Contours of dynamic pressure p (Pa) – Case 1.

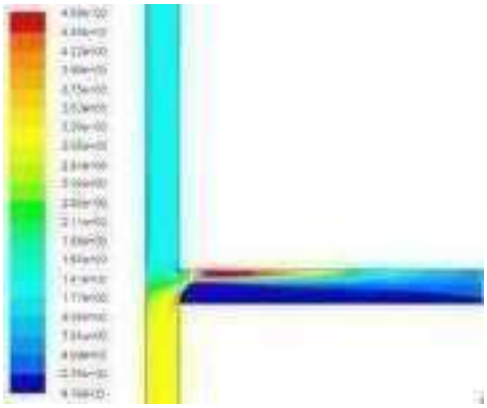

Fig 13.Contours of dynamic pressure p (Pa) – Case 2.

ISSN: 1737-9334

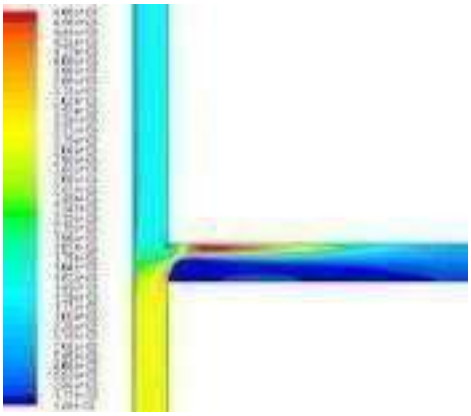

Fig 14.Contours of dynamic pressure p (Pa) – Case 3.

VII. CONCLUSIONS

In this article, the multiphase flow of water – a carbon dioxide mixture in a 2D duct was studied. The solution was obtained using a mixture model.

Taking into account the three different values of volume fraction of the secondary phase made it possible to observe the flow phenomena in the T-junctions and the nature of the multiphase water-carbon dioxide flow to better understood.

When multiphase flow enters a T junction, a redistribution of phases often occurs. In this paper, this phase separation phenomenon was studied by applying suitable boundary conditions in terms of carbon-dioxide volume fraction and carbon-dioxide velocity.

The studybased on:

From the contours of the volume fraction of carbon-dioxide obtained after the analysis, it can be seen that a greater amount of dioxide carbon are formed in all parts of the junction, hence the phase separation is higher at the branch arm but negligible ofthe running arm due to the effect of gravity

Grace to the model, the volume fractions, and pressure fields and velocity fields can be determined, Furthermore, in order to separate gas from liquids more efficiently.

REFERENCES

[1] Wallis, 1969 One-dimensional two-phase flow. McGraw-Hill Book Company, New York.

[2] ANSYS FLUENT 12.1 Theory Guide, 2010.

[3] Dukler, 1966 A. E. Frictional pressure drop and holdup in two-phase flow, Part A- A comparison of existing correlations for pressure drop and holdup, Part B- An approach through similarity analysis. AIChE Journal, 10, 38-51.

[4] Ferziger J. H., Perić M., Computational Methods for Fluid Dynamics, Springer, 3rd Edition, 2002.

[5] Ali, S. F. (2009). Two phase flow in large diameter vertical riser. PhD thesis, Cranfield University.

[6] Taitel et al, 1980 Modelling flow pattern transitions for steady upward gas-liquid flow in vertical tubes. AIChE Journal, 26(3), 345- 354.

[7] Taitel et al., 1980; Weisman and Kang, 1981; McQuillan and Whalley, 1985; Barnea and Brauner, 1986 and Barnea 1987 Flow patterns in vertical two phase flow. International Journal of Multiphase Flow, 11, 161-175.

[8] (2002) The IEEE website. [Online]. Available: http://www.ieee.org/

[9] Hewitt and Roberts, 1969; Speeding and Nguyen, 1980; Matsui, 1984; and Mishmi and Ishii, 1984 *FLEXChip* 1996 Two-phase co current flow in inclined pipe. International Journal of Heat Mass Transfer, 41, 4205-4228.

[10] Hewitt, G. F. (1982). Chapter 2: flow regimes and Chapter 10: Measurement of Two Phase Flow Parameters. In: Handbook of Multiphase Systems, Edited by Hetsroni, G. Publisher: Hemisphere/McGraw Hill, Washington.

[11] ANSYS®, Academic Research Mechanical and CFD, Release 19.0, 2019.

[12] Crowe C. T., Multiphase Flow Handbook, CRC Press, 2006.

Monitoring plant status: Experimental evaluation of a novel night heating method and its relevance in the physiological study of tomato

Sellami Douja[#1], Salwa Bouadila[*2], Asma Ben Salem-Fnayou[#3]

[#]*Research and technology Centre of energy-Biotechnology Centre, Technoparpark Borj-cedria*
BP: 95, Hammam-Lif 2050, Tunisia

[1]sellami.douja@gmail.com

[3]bensalem_f@yahoo.com

[*] *Research and technology Centre of energy*
BP: 95, Hammam-Lif 2050, Tunisia

[2]salwa.bouadila@crten.rnrt.tn

***Abstract*— Regarding climate change issues, the use of solar energy is becoming more and more important worldwide. In Tunisia, the sustainable availability of this renewable resource highly encouraged its use in agriculture. In this context, we studied the effect of a heating mode (a solar air collector with latent heat storage-SACLHS) on greenhouse-cultivated tomatoes. Tomato plants were grown under different greenhouses (Conventional CG, and thermally insulated and heated with the solar air collector IGHSC). Comparative physical, physiological and agronomic studies were carried out in order to highlight the effect of greenhouse climatic conditions on tomato growth and development. The results show better plant growth under IGHSC as compared to other greenhouse conditions. Besides, tomato plants had a significantly higher number of flowers and 14 day-early maturity under IGHSC conditions compared to the conventional greenhouse' conditions. In addition, IGHSC conditions allowed an average total yield more than 5 kg plant-1 with a high percentage of marketable fruits (Class A). On the other hand, night heating using the solar air collector allowed a better photosynthetic activity of tomato plants.**

Finally, our results demonstrate the efficiency of the solar air collector for greenhouse heating and suggest the large-scale use of such an ecological and inexpensive heating technique for sustainable agriculture.

***Keywords*— Tomato, Heating, Greenhouse, Fruit, Temperature**

I. INTRODUCTION

Among the horticultural crops, tomato (Solanum Lycopersicum) is widely grown in fields and under protected cultivation. Reference [1] demonstrated that optimum temperatures are 22–26°C during the day and 13–18°C at night, with an average optimum daily temperature between 21 and 25°C, depending on stage development. Therefore, in the greenhouse, supplemental night heating is often required to enhance seedling growth and to obtain year-round high production and good quality.

Tomato yield is not an isolated characteristic and depends on the growth of the whole plant. Therefore, the interaction between plant morphology, physiology, and growth conditions determined the yield. Low night temperature is known to adversely affect the vegetative and generative growth of tomato plants. It induces stomata closing leading to reduced transpiration and photosynthesis [2], whereas respiration processes are enhanced [3].

Thus, the objective of this study is to determine whether the proposed new heating system is able to ensure optimal night heating in order to provide favourable conditions for plant growth. Therefore, a close study of the relationship between night-time heating and solar energy, gas exchange parameters, chlorophyll fluorescence, and yield can provide clues.

II. MATERIALS AND METHODS

The experiments were carried out in two greenhouses located in the Research and Technology Center of Energy in Borj Cédria, in Tunisia. The structure of both greenhouses is all galvanized steel fixed to the ground with stones and concrete. The conventional greenhouse is all covered by a 3 mm of thick glass (CG). The insulated greenhouse has sidewalls and the northern roof built with 0.4 m and 0.6 m of thick sandwich panels respectively. This greenhouse was equipped with a solar air heating system with latent storage (IGHSC).

The Solar Air Heater with Latent Storage Collector (SAHLSC) is used as a means of heating the interior environment of the greenhouse during night time. The experimental device consists of a packed bed absorber formed of spherical capsules; with a black coating and fixed with a steel matrix. The PCM was confined inside those capsules. The packed bed role consists in absorbing the sun's radiations and storing the solar thermal energy as sensible and latent heat.

The climatic parameters were measured with different sensors (Scientific Campbell) and the samples were recorded every10 min using a CR5000 data logger.

ISSN: 1737-9334

The number of clusters is followed every two days. Chlorophyll fluorescence parameters were carried out with a pulse-modulated fluorometer (OS1-FL Chlorophyll Fluorometer Pulse Modulated, Hand Held).

Fruits of tomato plants grown under the three greenhouses were harvested every 3 days and weighed immediately. The dates of each harvest are noted in order to determine the rate ofprecocitybetween the different greenhouses.

III. RESULTS

A. Supplied Heat of SAHLSC

When the solar radiation is maximal, the indoor day temperature of IGHSC was at average 13.2°C higher than the ambient temperature, 7.5 °C than the indoor temperature of CG and 5.7°Cthan that in the insulated greenhouse.

The global solar radiation profile inside the greenhouses corresponded to this outside (Fig. 3A). The maximal intensity of incoming radiation, over the entire observation period outside the greenhouse, was 649 Wm^{-2}. The inside radiation both greenhouses was a similar view that the southern front wall is made of the same glass plates.

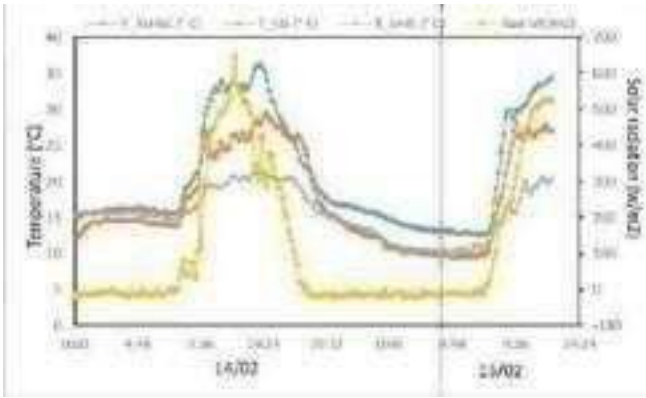

Fig. 1 Variation of solar radiation and temperature in different greenhouses on one day.

B. Effect in photosynthesis

Our experimental results showed that night heating with a solar air collector increased the net photosynthesis (A) in tomato plants (Table I). The increase in the (A) was one of the reasons which improved the growth of tomato.

TABLE I
GAS EXCHANGE OF PLANTS IN IGHSC AND CG, THE COMPARISONS OF AVERAGE S WE RE CALCULATE D USING ONE- AND TWO-WAY ANALYSES OF VARIANCE (ANOVA) (P < 0.05).

	ci	E	gs	A	WUEI
IGHSC	389,8 a	3,322 c	0,462 a	14,46 a	4,47 a
CG	367 c	5,8 a	0,49 a	11,78 b	2,05 c

The photosynthetic capacities and transpiration of the tomato plants under the microclimatic conditions of both experimental greenhouses. When grown under IGHSC, a significant stimulation in net photosynthesis (A) (14.46 mol CO_2 m^2 s^{-1}) accompanied by a decrease in transpiration (E) was observed resulting in a high level of water use efficiency (WUEI). A drop in stomatal in the intercellular CO_2 (Ci) was showed for the plants under this greenhouse in comparison with CG. Under this later, the net photosynthesis and the water use efficiencyhave lower values.

A. Assessment of energy performance on crops

1) *Precocity of maturity's fruits:* The number of flower clusters is higher in the heated greenhouse than in that of the conventional greenhouse (Fig.2 a). This obviously affects the fruit set rate, which is more pronounced in IGHSC (Fig.2 b). The dates noted for the onset of fruit maturity were 08/4 for the IGHSC plants and 22/4 for the CG plants. Therefore, a precocity of about 14 days is recorded.

So, providing heat at night during the treatment period had a positive effect in earliness maturity of fruits. The earliness of maturity was associated with an increased rate of mature fruitsper plant always in favour ofplants grown under IGHSC.

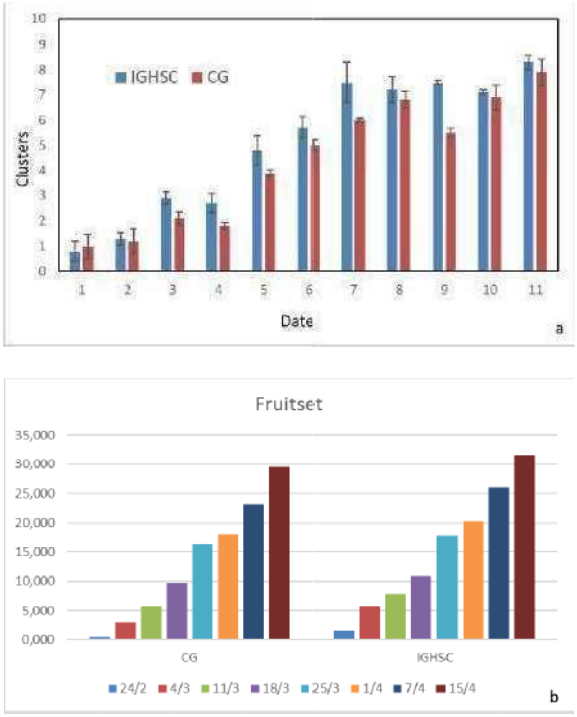

Fig.2 Clusters number and fruit set of tomato plants grown under CG and IGHSC.

2) *Yield:* The average fresh fruit weights per tomato plant in the two greenhouses were determined as the harvest progressed (Fig.3). The results show that there is a significant difference in yield between greenhouses in favour of IGHSC in the different harvest periods. The total weight of tomatoes per greenhouse ranged from the size of the fruit.

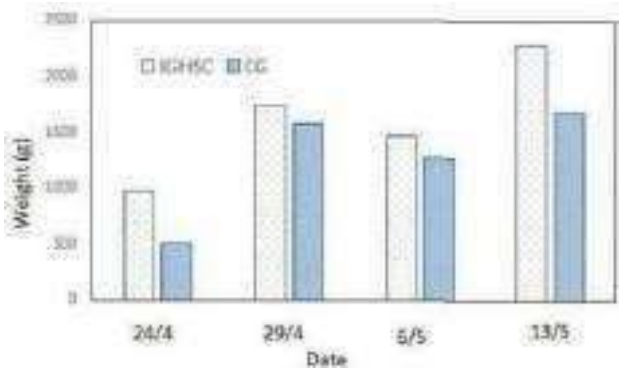

Fig. 3 Different harvest of tomato plants grown under different greenhouses: CG and IGHSC.

Fig.4 shows that throughout the harvest time, the highest weight of class-A tomatoes was recorded under IGHSC. Furthermore, monitoring of culture proved a resemblance between the two greenhouses considering medium-sized fruit (class-B). Significantly higher yields of class-C fruits were obtained under CG conditions.

The mentioned microclimatic changes in the present studycan also be used to explain changes in the volume of fruit growth in the IGHSC.

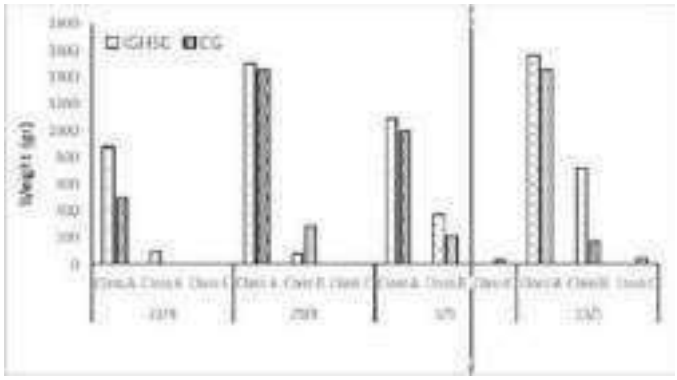

Fig.4 The weight of different fruit classes in both CG and IGHSC greenhouses.

IV. DISCUSSION

There is a general consensus that the growth and development of plants are based on the synthesis and accumulation of organic substances which depend on the photosynthesis of plants.

Reference [4] demonstrated that the (A) is the most representative photosynthetic parameter, and it can reflect directly the photosynthetic ability of plants. Our experimental results showed that night heating with a solar air collector increased the photosynthesis in tomato plants (Table 1), and this increase was one of the reasons which improved the growth of tomato.

According to [5] chlorophyll fluorescence emitted by higher plants can reflect photosynthetic activities in a complex manner. Chlorophyll is the parameter that allows plants to obtain energy from light, and thus chlorophyll is vital for photosynthesis [6]. As proved by [7], the photosynthesis depends on the ability to capture light and the efficiency of conversion of intercepted light into biomass. Our results from experiments indicated that one reason of the increase in photosynthesis is the increase in the content of Chlorophyll induced bynight heating.

It's well known that plant yield is the result of the interaction of various environmental factors under which plants are grown. The present study examined the effects of different microclimatic conditions on the yield of tomato plants grown under greenhouses.

According to [8], high temperature causes significant losses in tomato production due to reduced fruit set and lower quality fruits.

Our results are in agreement with [9], who reported that the use of a solar water heater enhanced the productivity of tomato by46.67 %.

In this study, we investigated the effects of different temperature and relative humidity levels on the plant growth of tomatoes under greenhouse conditions. The strongly reduced night temperature and high relative humidity in CG (Fig.1) lowered the growth rate of the plants inside the greenhouse and thus the number of clusters (Fig.2a)). This is in agreement with [10] who documented that variations in relative humidity exert influences on plant growth, leaf CO_2 assimilation rate, stomatal aperture, transpiration, and nutrient uptake. However, other reports showed that humidity had no alleviation effect on the growth ofplants [11].

V. CONCLUSION

By investigating the effects of different climatic conditions on yield of tomato, we have demonstrated that the prosperous conditions for tomato crop were under IGHSC. Accompanied with a high night temperature and a low relative humidity, the plant chlorophyll Fluorescence characteristics of the plants grown under this greenhouse was the better.

The experimental results indicate that the SAHLSC can be used in Tunisia for greenhouse optimal heating and for providing high production. Overall, it is concluded that the latent heat system allowing an increase in night temperature and a dehumidification without harming the plant will improve protected tomato crops.

ACKNOWLEDGMENT

I would like to thank all the other contributors for the development of this work such as the technicians of the laboratories of the two centers of biotechnology and research and technologies of Borj Cedria, Tunisia.

REFERENCES

[1] E. Heuvelink, "Dry Matter Production in a Tomato Crop: Measurements and Simulation," *Ann. Bot.*, vol.75, pp. 369–379, 1995. http://dx.doi.org/10.1006/anbo.1995.1035.

[2] Y. F. Liu, T. L. Li, T. Xu, M. F. Qi, C. Q. Xu, H. Y. Qi, "Effect of low night temperature treatment and recovery on photosynthesis and the allocation of absorbed light energy in tomato (Lycopersicon esculentum Mill.) leaves," *J Hortic Sci Biotechnol.*, vol. 86, pp. 91–96, 2011. https://doi.org/10.1080/14620316.2011.11512731

[3] D. Morales, P. Rodriguez, J. Dell'Amico, E. Nicolas, A. Torrecillas, M. J. Sanchez-Blanco, "High-temperature preconditioning and thermal shock imposition affects water relations, gas exchange and root hydraulic conductivity in Tomato," *Biol Planta*., vol. 47, pp. 6–12, 2003.

[4] K. A. Khatib, G. M. Paulsen, "Enhancement of thermal injury to photosynthesis in wheat plants and thylakoids by high light intensity," *J. Plant Physiol*., vol. 90, pp. 1041–1048, Jul. 1989.

[5] D. R. Calatayud, P.F. Martinez, "Spatial–temporal variations in rose leaves under water stress conditions studied by chlorophyll fluorescence imaging," *Plant Physiol Biochem*., vol. 44, pp. 564–573, 2006.

[6] W. Fu, P. Li, Y. Wu, "Effects of different light intensities on chlorophyll fluorescence characteristics and yield in lettuce," *Sci Hortic*., vol. 135, pp. 45–51, Feb. 2012.

[7] H. Jiang, J. Yang, J. Zhang, "Effects of external phosphorus on the cell ultrastructure and the chlorophyll content of maize under cadmium and zinc stress," *Environ Pollut*., vol. 147, pp. 750–756, Jul. 2007.

[8] N. Garg, D. S. Cheema, "Assessment of fruit quality conditions," *Sci Hortic*., vol. 131, pp. 29-38, 2011.

[9] A. M. S. Al-Amri, "Solar energy utilization in greenhouse tomato production," *J. King Saud University, Agri Sci.*, vol. 9, pp. 21–38, 1997.

[10] S. Cha-um, B. Ulziibat, C. Kirdmanee, "Effects of temperature and relative humidity during in vitro acclimatization: on physiological changes and growth characters of Phalaenopsis adapted to in vivo," *Aust J Crop Sci*, vol. 4, pp. 750–756, 2010.

[11] J. R. Torres-García, J. A. Escalante-Estrada, M. T. Rodríguez-González, C. Ramírez-Ayala, D. Martínez-Moreno, "Exogenous application of growth regulators in snap bean under water and salinity stress," *J stress physiol biochem,* vol. 5, pp. 13–21, 2009.

A numerical study of the stabilization of the CAF method in heavy oil pipeline transport

Rima Klaa#, Omar Kholai*2

Department of transport engineering,University of Frére Mentouri-Constantine

Transport and Environment Engineering Laboratory, Street 325 Ain El Bey Constantine, 25017, Algiers

[1]Rima_klaa@doc_umc_edu_dz
[2]Kholai_omar@googlemail_com

***Abstract*—** The study of the description and the physical understanding of poly-phasic flows in pipes, form a fundamental research topic in fluid mechanics, whose industrial applications are very numerous. Transporting heavy oil from the production site to refineries is very difficult due to their high viscosity and also characterized by low API below 20°. There are several methods to reduce viscosity and facilitate transportation: pipeline heating method, emulsification method, dilution method, drag reducing additive method andlubrication method.
In this work, we will attempt to describe a two-phase (2D) flow in a horizontal pipe composed of two non-miscible fluids (figure 1), separated by an interface using the CAF (Core Annular Flow) lubrication method. The flow considered is formed by: a hydrocarbon (oil) located in the center of the pipe and water at the circumferential part and enveloping the oil.

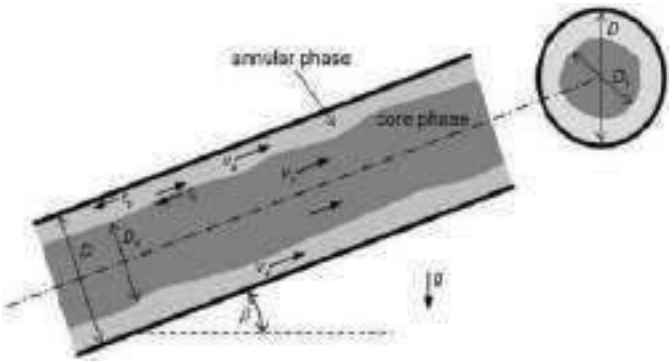

Fig. 1 schematic of the geometry problem

This two-dimensional problem can be modelled by, the basic equations of the mechanics of conventional fluids (continuity and momentum equations of motion), accompanied by an equation of the volume fraction of phases, in order to model the multiphase aspect of the problem. We chose the finite volume method under the Fluent ANSYS software for the discretization of partial differential equations of the mathematical model. The problem of turbulence was overcome using two statistical models: k-ε standard and k-ω. We applied the VOF (Volume Of Fluid) method to track and locate theinterface between the phases studied.

The results are presented by the stream lines, the velocity vector field, andthe densityfraction distribution of the phases.

The continuityand momentum equations are:

$$\frac{\partial \rho}{\partial t} + div\left(\rho \vec{V}\right) = 0$$

$$\frac{\partial \vec{v}}{\partial t} + \vec{V}\,grad\,\vec{V} = \frac{1}{\rho}\,grad\,P + \vec{V}$$

And the volume fraction equations are:

$$\frac{\partial \alpha_q}{\partial t} + u_i \frac{\partial \alpha_q}{\partial x_i} = 0$$

With $\sum_{q=1}^{n} \alpha_q = 1$

This work is divided into two parts, in the first part; we study the impact of the velocity of water on the stabilization of the interface water - heavy oil and the skin friction near the wall and also on the interface water-heavy oil. As a result, we obtained in this part that the velocity of water has a significant role for the stabilization in the CAF method.

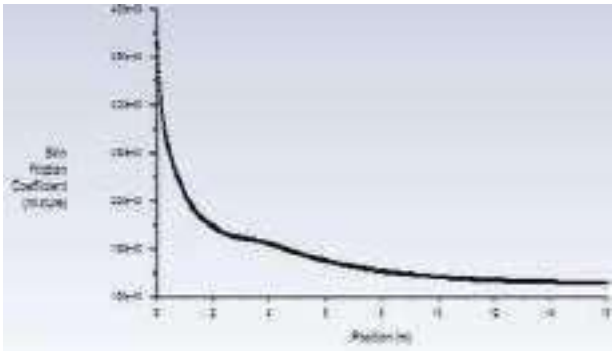

Fig. 2 skin friction near the wall (velocity of water 0.6 m/s)

In the second part, we change the viscosity of heavy oil to see on which velocity of water the method CAF (core annular flow) is stationary. As a result, we obtained in the second part that the viscosity also has a role for the stabilization of the method CAF.

Finally, for the stability of this method it must choose the velocity of water according to the viscosity of our fluid.

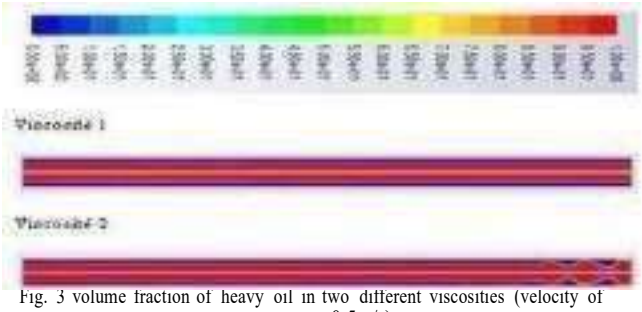

Fig. 3 volume fraction of heavy oil in two different viscosities (velocity of water 0.5m/s)

***Keywords*— Core Annular Flow; Horizontal pipeline; Heavy oil transport; Interface; Two - phase flow.**

Experimental investigation on the effect of the working fluid inventory on the performance of the two-phase closed thermosyphon

M.S. Elmosbahi[#1], M. Hazami[#2]

[#]*Laboratory of Thermal Process, Research and Technologies Center of Energy, Ecoparck of Borj-Cedria , BP 95 Hammam lif 2050, Tunisia*

[1]elmosbahi_mohamed@gmail.com

[2]hazamdi321@yahoo.fr

***Abstract*— This paper reports a study on the effect of the heat flux and the filling rate of the working fluid on the performance of the gravity assisted solar heat pipe. During the experimental period, the following measurements were carried out on daily basis in summer months. Eight fluid loadings were investigated, that varies from 7 ml to 14 ml corresponding to approximately halffilled and overfilled evaporator section.**

The parameters affecting the thermal hydraulic characteristics are the input power (the solar radiation intensity), the working fluids, namely Methanol, the filling rate of the working fluid varying from 50% to100%

Results prove that the optimum performance is observed when the 2/3 of evaporator volume is filled with methanol.

***Keywords*— Heat pipe, Heat input, Solarenergy, performance, Working fluidinventory**

I. INTRODUCTION

The heat transfer is an integral part of many industrial processes. Moreover, there is large quantities of thermal energy that are being exhausted and only the heat exchangers can be used to recover this heat and put it to use by heating or cooling a fluid in the process. Among the devices that can transport relatively large quantities of heat over a small temperature gradient between its ends, is heat pipe [1]. The heat pipe technology is widely used for various heat transfer equipments and variety of industrial applications. It offers many advantages in electronics cooling [2], chemical engineering [3], air conditioning systems [4], solar heating systems [5] and, recently, in light water nuclear reactors [3]. Particularly, the heat pipes are currently utilized in many energy systems according to their needs, in industrial applications including the solar system considered in the present analysis. For example, the heat pipes are suitable for domestic solar water heating [6], solar swimming pool heating [7] and solar space heating systems [8].

However, the first area that appears most appropriate for heat pipe application is domestic hot water heating. Hot water is an essential requirement in industry as well as in the domestic sector and it accounts for about 35% of the nation's energy consumption in the residential sector.

The object of the present work was to develop a prototype of a solar domestic hot water system using a gravity assisted heat pipe. This paper reports a study on the effect of working fluid inventory on the performance of gravity assisted solar heat pipe. the results of an experimental investigation of the energy behaviour of this system employing a heat-pipe are presented.

II. THEORY OF OPERATION

The heat exchanger with heat pipes occurs by phase change, in the evaporator and in the condenser. The evaporator is positioned lower than the condenser, in order to allow the condensed fluid return to the evaporator region through gravity ([2], [9]). This type of heat pipe is known as a closed, gravity assisted, two-phase thermosyphon. This paper introduces a heat pipe in which there is no wick and the flow of the condensed fluid is accomplished bygravityas shown in Fig. 1.

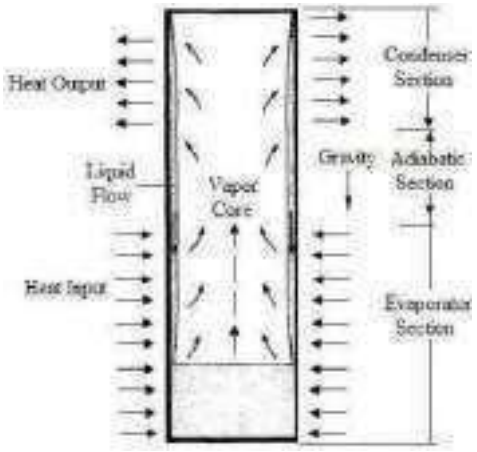

Fig. 1 A simple gravity-assisted two-phase closed thermosyphon

III. THE EXPERIMENTAL SETUP

A schematic diagram of the experimental set-up is shown in Fig. 2. The prototype is mounted on a metal support with inclination angle ranging from 0 ° to 90 ° to the horizontal. In the test, the inclination of the system set at an angle 45°. The system employs a heat pipe assisted by gravity, where the condenser and the evaporator were placed respectively in the upper and lower part of the heat pipe. To evaluate the thermal performance of gravity-assisted, two-phase thermosyphon with methanol as working fluid under same working conditions such as inclination angle and liquid fill charge, the solar radiation measurements obtained with the Kipp & Zonen CM11 pyranometer which was integrated to a computer based data-logger, mounted on a surface parallel to the plane of the collector was used to measure the intensity of the global solar irradiation on the collector surface.

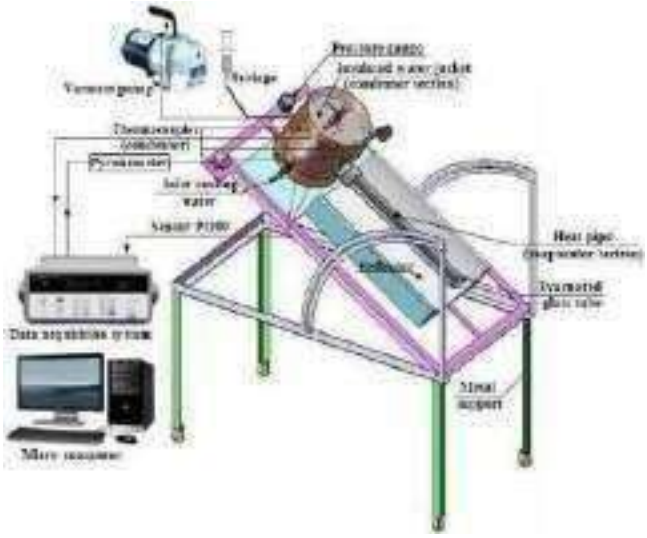

Fig. 2 Experimental setup

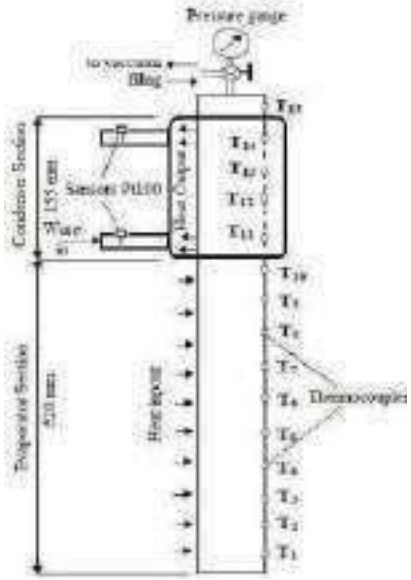

Fig. 3 Temperature measurement locations

To measure temperature along the heat pipe, fifteen J-type thermocouples are fixed at each portion. As shown in Fig. 3, Ten thermocouples and four thermocouples were uniformly spaced on the circumference of the evaporator and condenser respectively. The number of thermocouples that were used was limited by mounting difficulties.

Three thermocouples were fixed at three levels inside the storage tank while and two temperature sensors Pt100 were placed at the inlet and the exit of the water jacket. The thermocouples are connected through a twenty point selector switch

and the output is displayed on a data acquisition system.

IV. METHODS

Heat transfer rate between the heat pipe and the cooling liquid Qw can be calculated using water temperature variation dTw/dt taking into account the water quantity Mw and its specific heat Cpw and may be expressed as ([6]):

$$Qw=Mw.Cpw.dTw/dt \qquad (1)$$

The later relation called heat pipe performance has been proposed in order to illustrate the effect of the fill charge on thermosyphon performance, as shown in Fig. 2. The measurements have been performed, under favourable radiation conditions and low tank water temperature to predict the maximum useful energy gained.

The overall heat transfer coefficient can be optimum and secondly, when the energy transported to the cooling water is maximum for a given fill charge.

The overall heat transfer coefficient is used to evaluate the performance of the heat pipe, and is calculated from experimental data by the following equation introduced byChi ([10], [11]):

$$Q=A.U.(Te-Tc) \qquad (2)$$

where U is an overall heat transfer coefficient, A is an inside surface area of the evaporator or the condenser, Te and Tc are the mean temperatures on the outside surfaces of the evaporator and the condenser, respectively and Q is the power transported by the heat pipe. The value of Q can be calculated either by the heat removed at the condenser section or by the power dissipated on the heat pipe with taking into account the heat losses ([12]).

V. RESULTS

The results indicate that adding more working fluid inventory in the heat pipe can have a significant effect on its performance as shown in Fig. 4. As can be seen in this figure, the maximum heat transfer rate Qw occurred at the fill charge of 10 ml and reaches with a maximum value of 215,1W. The period after which the heat rate maximum is attained depends on the fill charge. and comparing the results data for a filling volume of 10 ml, there is a heat gained in watts of 12.9%, 1.9%, 22.9% and 45.1% over the respective volumes of8 ml, 9 ml, 11 mland 14 ml.

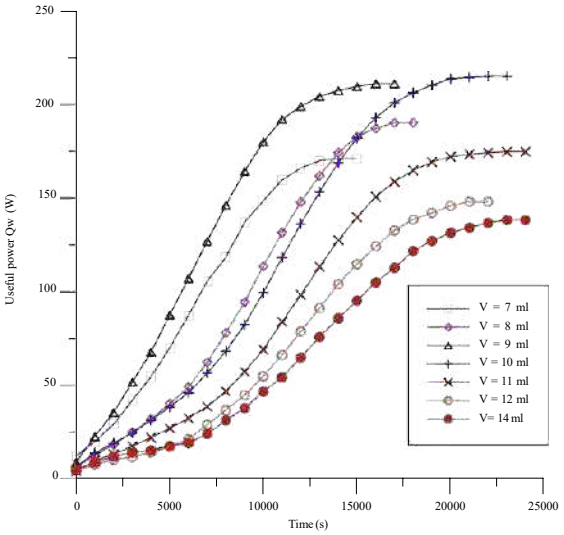

Fig. 4 Effect of liquid fill charge on useful power Q_w transferred to the cooling water

The results show that the overall temperature difference between evaporator and condenser section across the heat pipe, was affected by the values of liquid fill charge. The results show also that increasing the fill charge can increase or decrease the overall temperature difference as shown in Fig. 5.

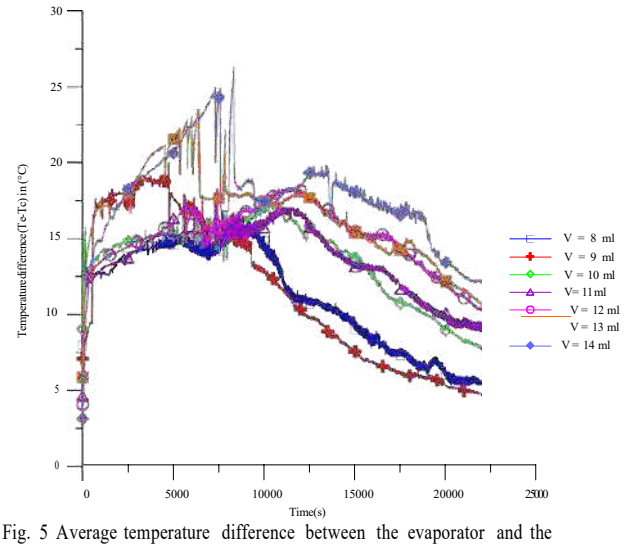

Fig. 5 Average temperature difference between the evaporator and the

condenser wall vs. time for different liquid filling charges

After several sets of experiments, it was observed that the effective heat transfer rate of the methanol filled the gravity assisted heat pipe strongly depends on fill ratio of working fluid of volume of evaporator. Fig. 6 shows that the maximum heat transfer rateoccurred when the filling ratio is 70%.

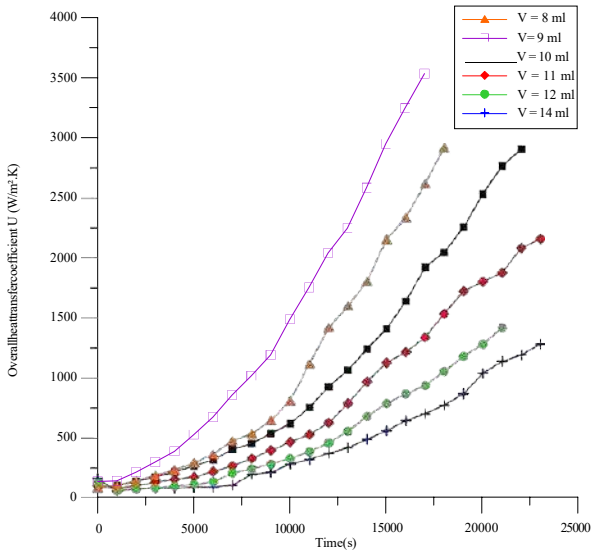

Fig. 6 Variation of overall heat transfer coefficient as a function of the time for different liquid fill charges

VI. CONCLUSION

In this study, we developed a new prototype of a solar domestic hot water system using a gravity assisted heat pipe in CRTEn. The maximum performance was obtained, in the optimum evaporator volume filled with liquid range between 9 and 10 ml which corresponds to 2/3 of evaporator volume is filled with methanol. The better results have been obtained in terms of increased useful power Qw transferred to the cooling water and overall heat transfer coefficient of the heat pipe with reduced average temperature difference between the evaporator and the condenser wall. An analysis of thermal performances of the system using Tunisian meteorological data reveals that filling the evaporator between 64% and 71% gives optimum performances and heat transfer coefficient. The actual system can be developed and used efficiently in domestic hot water production in similar countries with weather conditions like Tunisia.

ACKNOWLEDGMENT

In this section, give credit to those who helped in this study by contributing advice, permission, technical assistance, funds for conducting the actual work, and help with preparation ofthe paper.

REFERENCES

[1] D. Reay, and P. Kew, *Heat Pipes: Theory, Design and Applications*, 4nd ed, Linacre House, Jordan Hill, Ed. Oxford, 2006.

[2] M. Groll, M. Schneider, V. Sartre, M.C. Zaghdoudi, and M. Lallemand, "Thermal control of electronic equipment by heat pipes," Revue Generale de Thermique., vol. 37, pp. 323-352, 1998.

[3] P. Sabharwall, and F. Gunnerson, "Engineering design elements of a two-phase thermosyphon for the purpose of transferring NGNP thermal energy to a hvdrogen plant," Department of Mechanical Engineering, Nuclear Engineering Program, University of Idaho, Science Center Drive, Idaho Falls, ID 83402, Etats-Unis, 2009.

[4] P.W. Xiao, P. Johnson, and A. Akbarzadeh, "Application of heat pipe heat exchanger to humidity control in air-conditioning systems", Applied thermal Engineering., vol. 17, pp. 561-568, 1997.

[5] C. I. Ezekwe, "Thermal performance of heat pipe solar energy systems," Solar & wind technology., vol. 7, pp. 349-354, 1990.

[6] E. Mathioulakis, and V. Belessiotis, "A new heat-pipe type solar domestic hot water system," Solar Energy., vol. 72, pp. 13–20, 2002.

[7] Reiner Croy, and Felix A. Peuser, "Experience with solar systems for heating swimming pools in Germany," Solar Energy., vol. 53, pp. 47 - 52, July, 1994.

[8] C.Hoa, B. Demolder, and A. Alexandre, "Roadmap for developing heat pipes for ALCATEL SPACE's satellites," Appl. Therm. Eng., vol. 23, pp. 1099–1108, 2003.

[9] M.S. El-Genk, and H.H. Saber, "Flooding limit in closed, two-phase flow thermosyphons," Int. Journal of Heat and Mass Transfer., vol. 40, pp. 2147-2164, 1997.

[10] K. Negishi, and T. Sawada, "Heat transfer performance of an inclined two-phase closed thermosyphon," International Journal of Heat and Mass Transfer., vol. 26, pp. 1207–1213, 1983.

[11] S. W. Chi, Heat pipe theory and practice: McGraw Hill, Ed. New York, 1976.

[12] L.A. Samuel, and Sergio Colle, "Experimental investigation of two-phase closed thermosyphons with a liquid retention structure for SDHWS," in Solar World Congress. ISES, Orlando, 2005.

Structural, Microstructural and Optical Properties of 5%-doped ZnO (M = Al, Mg, Co and Ni) Thin Films

H.Benzerouk#[1], M.Mekhnache[1], F. Chouit[1] , T. Souier [2], M. Bououdina [3,4], M. Emziane [2] and A. Drici[5]
[1] *Department of* technology, *Faculty of technology, Skikda University, Algeria*
[2]*Masdar Institute of Science and Technology, PO Box 54224, Abu Dhabi, United Arab Emirates*
[3]*Nanotechnology Centre, University of Bahrain, P.O. Box 32038, Kingdom of Bahrain*
[4]*Department of Physics, College of Science, University of Bahrain, P.O. Box 32038, Kingdom of Bahrain*
[5] *LEREC, Department of Physics, Badji-Mokhtar University, Annaba, Algeria*
Corresponding author:
E-mail : h.benzerouk@univ-skikda.dz
b_hanin08@yahoo.fr

***Abstract*— In this study, 5% doped ZnO (M = Al, Mg, Co and Ni) thin films were prepared using spray pyrolysis method. ZnO:Al, ZnO:Mg, ZnO:Ni and ZnO:Co film were deposited by chemical spray pyrolysis (CSP) on slide glass substrates at atmospheric pressure in air gas at a flow rate of (5ml/min). Doped ZnO film was produced by spraying aqueous solutions using a zinc acetate dihydrate (Zn(CH3COO)2·2H2O) dissolved in ethanol to obtain a starting solution with a 0.2 mol/l concentration.**

X-ray diffraction showed that films have a wurtzite structure with a preferential orientation along the (002) direction for Mg, Ni and Co doped ZnO when a preferential orientation along the (101) direction for Al doped ZnO. The smallest average grain size was 11.7 nm, obtained with 5 wt% Al doping..

***Keywords*— Zinc oxide, spray pyrolysis, semiconductors, XRD, doped ZnO, Nanostructure**

I. INTRODUCTION

In recent years, considerable attention has been given to wide gap materials with optical transparency and metallic conductivity in the development of transparent electrodes in liquid crystal displays and solar cells. . Recently, they have received greater attention because of their various technological applications such as solar cells [1], optoelectronics [2], heat mirrors [3], gas sensors [4], wear resistant applications [5], and thin-film resistors [6].

ZnO thin films received extensive attention due to their excellent optical and electrical properties [7]. Zinc oxide is a semiconductor considered promising for optoelectronic and solar cell applications. The wurtzite-structured ZnO has become one of the most promising materials for the fabrication of high-technology applications such as photonic crystals, light-emitting diodes, sensors, electro- and photo-luminescent materials [8, 9].

However, the wide band-gap nature of the materials has been a limitation in producing devices for certain applications. Doping has been considered as one of the ways to alter the band gap [10]. The key requirements for these applications are that ZnO materials have the good electrical, optical, and magnetic properties and that the control of the shape and crystal structure is important. It is well known that the addition of impurities into a wide gap semiconductor can often induce dramatic changes in the optical, electrical, and magnetic properties [11, 12]. Therefore, doping a selective element into ZnO has become an important route for enhancing and controlling its optical, electrical, and magnetic performance, which is crucial for their practical applications.

Theoretical calculations have showed that transition-metal (TM)-doped ZnO would be a good candidate to achieve Curie temperature above room temperature [13, 14]. Since then, great efforts have been devoted to the investigation of magnetic-metal/ZnO one-dimensional (1D) structure materials hetero-structures due to its new functionality in memory devices, detectors and light-emitting sources [15,16]. Of the many magnetic-metal, Ni is an important dopant to achieve Curie temperature above room temperature, Co-doped ZnO [17, 18], Mn-doped ZnO [19, 20], F-doped ZnO [21, 22], In-doped ZnO [23] among others. Al doped ZnO coatings exhibit high transparency and low resistivity which is suitable for device applications. Recently, 1D

ISSN: 1737-9334

nanostructures of ZnO, such as nanowires, nanorods, nanobelts, and nanotubes, have been reported [23, 25],

The preparation techniques for un-doped and doped ZnO thin film are many such as chemical vapour deposition (CVD) [26], pulsed laser deposition (PLD) [27], radio frequency magnetron sputtering [28], electrochemical bath deposition [29], sol–gel spin-coating method [30] and chemical spray process [31]. However, all these techniques require sophisticated instruments and/or a high temperature of deposition. Among the thin film deposition methods, chemical spray deposition (SP) from aqueous solutions is the simplest and most economical.

In this study, 5% doped ZnO (M = Al, Mg, Co and Ni) thin films were prepared using pyrolysis method. Structure and microstructural analyses were carried out using X-ray diffraction and atomic force microscopy (AFM). Hall measurements were also carried out to determine the electrical properties. The results were discussed according to the effect ofthe nature ofthe transition metal.

II. Experiment part

A. *Materials and Synthesis*

Zinc acetate dihydrate (Zn(CH3COO)2·2H2O), ethanol (C2H5OH),Aluminum (III) chloride(AlCl3), magnesium(II) chloride (MgCl2), Nickel(II) chloride(NiCl2) and Cobalt(II) chloride(CoCl2) were used as a starting material, a solvent and a dopants source respectively.

ZnO:Al, ZnO:Mg, ZnO:Ni and ZnO:Co film were deposited by chemical spray pyrolysis (CSP) on slide glass substrates at atmospheric pressure in air gas at a flow rate of (5ml/min). A soda lime glass was used as substrate material washed with absolute acetone and methanol in an ultrasonic bath and then washed with deionized water. Doped ZnO film was produced by spraying aqueous solutions using a zinc acetate dihydrate (Zn(CH3COO)2·2H2O) dissolved in ethanol to obtain a starting solution with a 0.2 mol/l concentration, Doping of zinc oxide thin films with aluminum, magnesium, Nickel and cobalt were carried out by adding the compound source in the starting solution with a atomic percentage(5at.%). A small amount of acetic acid was added into the solution to avoid forming milky precipitate of Hydroxides.

The mixture was stirred around 30 min until total dissolution was observed using a magnetic stirrer. The resulting solution was sprayed onto the heated substrates at a constant temperature of 350°C which was measured using electronically controlled Cr–Al thermocouple positioned under the substrate.:

B. Characterizations Techniques

The phase identification of the films deposited on glass substrates was investigated using Rigaku Ultima IV high resolution X-ray diffractometer in thin mode equipped with Cu-Kα radiation (λ = 0.15418 nm). Microstructural and lattice parameters were determined using peak profile analysis programs provided with the equipment.

The structural properties of doped ZnO film were characterized by means of scanning probe and electron microscopy. QuantaTM 250 FEG scanning electron microscope (SEM) from FIE company was employed for high resolution imaging. Both Secondary Electron (SE) detector and Backscatter Electron detector (BSE) were used for structural and chemical contrast imaging. Moreover, the SEM is equipped by Genesis Apex Energy-dispersive X-ray (EDX) spectroscopy system used for chemical content microanalysis.

A complementary structural and surface topography of the films were studied by means of atomic force microscopy AFM. The experiments were performed on MFP-3D Stand Alone AFM microscope from Asylum Research. AC 240TS silicon tips have been used for tapping mode AFM imaging. The resonance frequency of the tip is 78 kHz and the spring constant is 2 N/m measured by thermal tuning. The AFM was used for both morphology analysis and to film thickness measurements.

III. Results and Discussion

ISSN: 1737-9334

The X-ray diffraction pattern of the 5% doped ZnO (M = Al, Mg, Co and Ni) thin films (Fig. 1) reveal the existence of a ZnO single-phase with a hexagonal wurtzite structure. The X-ray diffraction patterns for Mg, Ni and Co doped ZnO thin films exhibited a strong orientation towards (002) plane or c-axis, whereas there was no preferred orientation in case of AZO thin film when the (101) direction as the preferred growing orientation for the AZO thin film. Fig. 1 shows that doping changes the orientation of the growing film which is related to the nucleation process of the films. There are many explanations about the formation of c-axis orientation; for example, the c-axis orientation occurs due to a minimization of the internal stress and surface energy [32] and c-axis orientation could also result from an easy growth because of the high atomic density along (002) plane [33]. The lattice parameters (a and c) and the crystallite size were determined by using peak profile analysis programs provided with the equipment. In addition, the ratio of lattice constants c/a was found to be around 1.60 for all doped layers. The films were in good agreement with those reported in JCPDS data cards [36-1451]. The crystallite size was estimated by Halder-Wagner method. Theresults are shown in Table 1.

TABLE I. STRUCTURAL PARAMETER DEDUCED FROM XRD STUDY OF ZNO THIN FILMS (BRAGG' ANGLE (2Θ), LATTICE PARAMETERS (A AND C), CRYSTALLITE SIZE (C) AND VOLUME (V)).

	ZnO :Al	ZnO :Mg	ZnO :Ni	ZnO :Co
a(nm)	**0.3264**	**0.3260**	**0.3258**	**3.259**
C(nm)	0.5221	0.5214	0.5220	5.221
c/a	1.59	1.59	1.6	1.6
Cs(nm)	11.7	15.8	16.5	17.0
V(Å3)	55.623	55.412	55.408	55.453

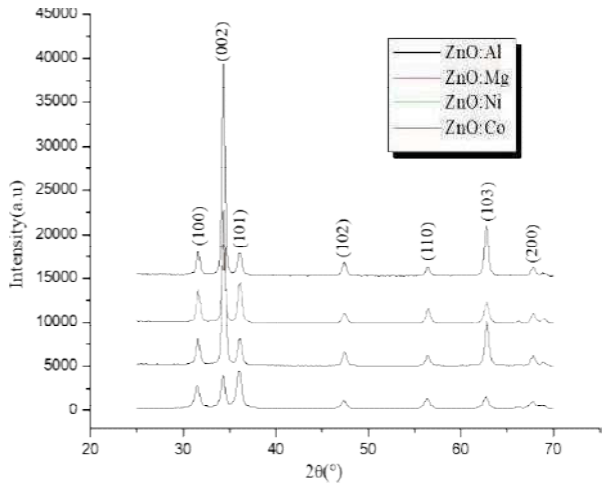

Fig. 1 X-ray diffraction patterns of 5%-doped ZnO (M = Al, Mg, Co and Ni)

REFERENCES

[1] D.P. Norton, Y.W. Heo, M.P. Ivill, S.J. Pearton, M.F. Chisholm, T. Steiner, Mater. Today 7 (2004) 34–40.
[2] X.W. Sun, H.S. Kwok, J. Appl. Phys. 86 (1999) 408–411.
[3] C.X. Xu, X.W. Sun, B.J. Chen, P. Shum, S. Li, X. Hu, J. Appl. Phys. 95 (2004) 661–666.
[4] F. Ruske, M. Roczen, K. Lee, M. Wimmer, S. Gall, J. Hüpkes, D. Hrunski, B. Rech, J. Appl. Phys. 107 (2010) 013708.
[5] R. Martins, E. Fortunato, P. Nunes, I. Ferreira, A. Marques, M. Bender, N. Katsarakis, V. Cimalla, G. Kiriakidis, J. Appl. Phys. 96 (2004) 01398.
[6] C. Jin, A. Tiwari, R.J. Narayan, J. Appl. Phys. 98 (2005) 083707.
[7] O. Kluth, B. Rech, L. Houben, S. Wieder, G. Schope, C. Beneking, H. Wagner, A. Loffl, H.W. Schock, Thin Solid Films 351 (1999) 247–253.
[8] T.F. Chung, L.B. Luo, Y.H. He, I. Leung, Appl. Phys. Lett. 91 (2007) 233112.
[9] H.J. Choi, H.K. Seong, J.Y. Chang, K. Lee, Y.J. Park, J.J. Kim, S.K. lee, R.R. He, T. Kuykendall, Adv. Mater. 17 (2005) 14479.
[10] D. Raviendra, J.K. Sharma, J. Appl. Phys. 58 (1985) 838.
[11] B.B. Lia, X.Q. Xiua, R. Zhanga, Z.K. Taoa, L. Chena, Z.L. Xie, Y.D. Zheng, Mater. Sci. Semicond. Proc. 9 (2006) 141.
[12] G. Sanon, R. Rup, A. Mansingh, A. Phys. Rev. B 44 (1991) 5672.
[13] K. Sato, H. Katayama-Yoshida, Jpn. J. Appl. Phys. 39 (2000) L555.
[14] K. Sato, H. Katayama-Yoshida, Jpn. J. Appl. Phys. 40 (2001) L334.
[15] Y. Wu, R. Fan, P. Yang, Nano Lett. 2 (2002) 83.
[16] M.S. Gudiksen, L.J. Lauhon, J. Wang, D.C. Smith, C.M. Lieber, Nature415 (2002) 617.
[17] M. Wei, D. Zhi, J.L. McManus-Driscoll, Scr. Mater. 54 (2006) 817.
[18] K. Ando, H. Saito, Z. Jin, T. Fukumura, M. Kawasaki, Y. Matsumoto, J. Appl. Phys. 89 (2001) 7284.
[19] P. Sharma, A. Gupta, K.V. Rao, F.J. Owens, R. Sharma, R. Ahuja, Nat. Mater. 2 (2003) 673.
[20] V.R. Shinde, T.P. Gujar, C.D. Lokhande, R.S. Mane, S.-H. Han, Mater. Chem. Phys. 96 (2006) 326.
[21] M. de la L. Olvera, A. Maldonado, R. Asomoza, Sol. Energy Mater. Sol. Cells 73 (2002) 425.
[22] A. Guille´ n-Santiago, M. de la L. Olvera, A. Maldonado, R. Asomoza, D.R. Acosta, Phys. Status Solidi A 201 (2004) 952.
[23] M.A. Lucio-Lo´ pez, A. Maldonado, R. Castanedo-Pe´ rez, G. Torres-Delgado, M. de la L. Olvera, Sol. Energy Mater. Sol. Cells 90 (2006) 2362.

[24] M.H. Huang, S. Mao, H. Feick, H. Yan, Y. Wu, H. Kind, E. Webber, R. Russo, P. Yang, Science 292 (2001) 1897.
[25] M.T. Bjork, B.J. Ohlsson, C. Thelander, A.I. Perssom, K. Deppert, L.R. Wellenberg, L. Samuelson, Appl. Phys. Lett. 81 (2002) 4458.
[26] X. Meng, B. Lin, Z. Fu, J. Lumin. 126 (2007) 203–204.
[27] F.K. Shan, Y.S. Yu, J. Eur. Ceram. Soc. 24 (2004) 1869–1870.
[28] B.H. Kong, D.C. Kim, Y.Y. Kim,H. Koun, J. Korean Phys. Soc. 49 (2006) S741–S744.
[29] R.E. Marotti, P. Giorgi, G. Machado, E.A. Dalchiele, Sol. Energy Mater. Sol. Cells 90 (2006) 2357–2361.
[30] Y. Natsume, H. Sakata, Thin Solid Films 372 (2000) 30–36.
[31] H. Gómez, A. Maldonado, R. Castanedo-Pérez, G. Torres-Delgado, M. de la, L. Olvera, Mater. Charact. 58 (2007) 708–714.
[32] D. Bao, H. Gu, A. Kuang, Thin Solid Films 312 (1998) 9-37.
[33] S. Amirhaghi, V. Craciun, D. Craciun, J. Elders , I.W. Bord, Microelectron. Eng. 25 (1994) 321-6.
[34] P. Singh, A. Kumar, A. Kaushal, D. Kaur, A. Pandey, R.N. Goyal, Bull. Mater. Sci. 31 (2008) 573–577.
[35] S. Lemlikchi, S. Abdelli-Messaci, S. Lafane, T. Kerdja, A. Guittoum, M. Saad, Applied Surface Science 256 (2010) 5650–5655.
[36] J.H. Lee, K.H. Ko, B.O. Park, J. Cryst. Growth 247 (2003) 119.
[37] S. Kasap, P. Capper, Springer Handbook of Electronic Materials, Springer, (2006) 47–77.
[38] B.L. Zhu, X.Z. Zhao, S. Xu, F.H. Su, G.H. Li, , Jpn. J. Appl. Phys. 47 (2008) 2225–2229.

Synthesis and Study of Structural, Morphological and Electrochemical Properties of $Ce_{1-x}M_xO_{2-\delta}$ (M=Gd,Y) for SOFC applications

Fatima Melit*[1],Nedjemeddine Bounar *[2]

* *LIME Laboratory, University of Jijel, BP 98 Ouled Aissa, 18000, Algeria*

[1]fatima.melit@univ-jijel.dz
[2]nedjemeddine.bounar@univ-jijel.dz

Abstract— Polycrystalline samples of $Ce_{1-x}M_xO_{2-\delta}$ (x=0.1, 0.15, 0.2)(M=Gd, Y) were prepared by the solid-state chemical reaction from mixtures of pre-dried oxides powders of CeO_2, Gd_2O_3 and Y_2O_3 in the appropriate stochiometric ratio to explore their use as solid electrolytes for intermediate temperature solid oxide fuel cells (IT-SOFCs). Their crystal structures and ionic conductivities were characterized by X-ray powder diffraction (XRD) and AC complex impedance spectroscopy (EIS). The XRD analyses confirm that all the resulting synthetized co-doped cerium oxide powders are single-phase and crystallize in the cubic structure system with the space group Fm3m. On the one hand, the lattice parameter (a) of the phases increases with increasing Gd content, on the other hand, with increasing Y-substitution rate, the latter decreases. The results of complex impedance conductivity measurements have shown that doping has a remarkable effect on conductivity. The co-doped cerium phases showed significant ionic conductivity values, making these materials excellent candidates for solid oxide electrolytes at intermediate temperatures.

Keywords— Electrolyte, X-ray diffraction, EIS, SEM, SOFC etc.

I. INTRODUCTION

Solid oxide fuel cells (SOFCs) are a desirable technology due to their environmentally friendly nature, high energy conversion performance, andhigh fuel compatibility[1-5].

A typical high-temperature SOFC uses yttrium-stabilized zirconia (YSZ) as the electrolyte, which has to operate at a temperature of about 1000° C; to obtain sufficient current density; such high operating temperature causes some disadvantages for commercialization: Thermal degradation of the different parts of the cell, and high manufacturing cost, etc...[6-9]

To reduce the operating temperature the most impotent solution is using alternative materials with higher conductivity at lower temperatures; doped ceria has been considered to be a candidate for use as an electrolyte İn comparison to YSZ, Ceria-based ceramic has a high oxygen-conductivity. The fact of being a potential electrolyte, inner layer, and electrode for SOFCs at low temperatures. [10, 11].

Pure CeO_2 has a fluorite structure having a (Vo++) oxygen vacancy as the predominant ionic defect; It is considered to have a low ionic conductivity [12, 13]. To ameliorate their performances many studies have been based on the effects of of their mixing with metallic oxides on the electrical properties of ceria-based ceramics on their electrical properties. [14-16].Some singly doped electrolytes, such as $Ce_{1-x}Gd_xO_{2-}$(GDC), $Ce_{1-x}Sm_xO_{2-\delta}$(SDC), $Ce_{1-x}Y_xO_{2-\delta}$ (YDC)etc, show high oxide ion conductivity at intermediate temperatures (500–700 °C) [17-20].

Another possible way to increase, the ionic oxide conductivity of ceria–based electrolytes in the intermediate temperature range (500-700° C) is their Structural modification by co-doping with Gd2O3 or Sm2O3 and other trivalent cations such as La^{3+}, Nd^{3+}, Y^{3+}, Bi^{3+}, Nd^{3+} or divalent cations Ca^{2+}, Mg^{2+}, Sr^{2+}, these Materials, have generally improved ionic conductivities, but in some cases a deterioration in ionic conductivity or increased electronic conductivityhave been observed [21-26]

In this work, Gd^{3+} and Y^{3+} co-doped ceria materials were prepared and characterized. The effect of co-doping on structure and conductivity was studied.

The synthesis samples were denoted with codes such that the initial four letters CGYO indicated the chemical name, followed by a number representing the element amount in the sample.

II. EXPERIMENTAL

Polycrystalline samples of $Ce_{1-x}M_xO_{2-\delta}$ (x=0.1, 0.15, 0.2)(M=Gd, Y) were prepared by solid-state chemical reaction from pre-dried powder mixtures of CeO_2(sigma Aldrich 99.9%),(sigma Aldrich 99.9%) and Y_2O_3 (sigma Aldrich 99.9%) in the proper stochiometric proportions. Powders were ground in an agate mortar and then pressed with a uniaxial press under a pressure of 200MPa into cylindrical pellets (13mm diameter and 0.5mm thick). The samples were finely heated at 1473 (K) for 48h.

X-ray diffraction patterns were recorded at room temperature on a Bruker AXS D8-Advance diffractometer (CuKa radiation) equipped with a curved graphite

ISSN: 1737-9334

monochromator in the secondary beam. Collect data in 0.04° increments and 16-second count times per step over the range 10°-90°(2Θ).

The surface morphologies of the pellets were observed using an SEM apparatus (PHILIPS XL 30) to study the structure of the prepared samples. Before SEM, the sintered pellets were coated with a thin layer of gold to avoid the charging effect during the measurement.

For complex impedance, measurements were made using a Solartron 1260 impedance analyser with a dielectric interface. Measurements were carried out over a temperature range of 500°C to 700°C and a frequency range of 5 Hz to 20 MHz.

III. Result and Discussions

A. X-ray Diffraction Analysis (XRD)

Fig1 shows the XRD patterns obtained for all samples prepared by sintering at 1200 ºC. Eight symmetrical diffraction peaks were observed in the XRD spectra (111, 200, 220, 311, 222, 400, 331, and 420). X-ray diffraction analysis shows that all the co-doped cerium oxide powders obtained contain only the fluorite phase of cubic structure with space group Fm3m (JCPDS File No:34-0394)[27-29].

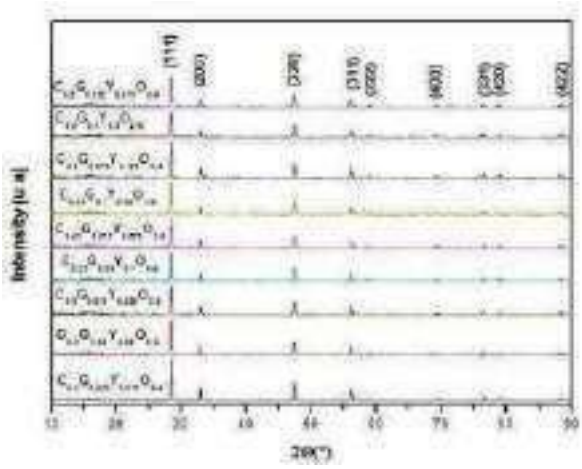

Fig.1: X-ray diffraction patterns of different samples prepared $Ce_{1-x}M_xO_{2-\delta}$ (x=0.1, 0.15, 0.2)(M=Gd, Y), with varying doping compostion .

Substitution of Ce for Gd and Y has caused a slight shift in the cerium oxide peaks. This shift indicates changes in the crystal structure which is reflected in the variation of the lattice parameters.

Lattice parameters were calculated using Reitica[30]software by performing a full deconvolution of the obtained XRD spectra. Fig 2 shows the variation of lattice parameters as a function of the Y and Gd content in $Ce_{1-x}M_xO_{2-\delta}$ (x=0.1, 0.15, 0.2)(M=Gd, Y), as can be seen; cell parameters increase with increasing of the Gd content, on the other hand; with increasing of Y substitution rate, the latter decrease, this is due to the difference between the ionic radii[29, 31, 32]; Previous researches have shown that the ionic radius r_c=1.038Å is defined as the critical ionic radius which causes no change in lattice parameters of the host fluorite[31, 33]. In our case; the ionic radius of Gd^{3+} ($r_{Gd^{3+}}$=1.053Å)[34] is larger than the critical ionic radius which results in lattice expansion, while the ionic radius of Y^{3+} ($r_{Y^{3+}}$=1.019Å)[34] is smaller than the critical ionic radius, which causes contraction of the lattice constant. The results in the figure follow Vegard'srule [12, 31] , which proves that gadolinium and yttrium are considerably integrated on the crystal lattice of cerium oxide.

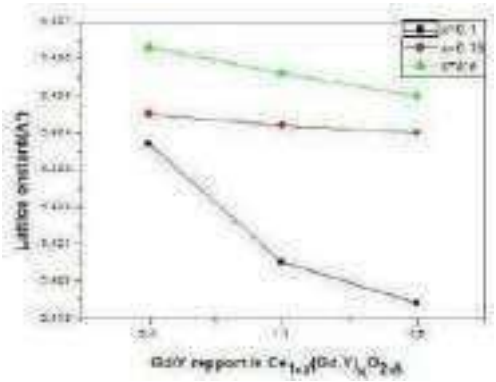

Fig.2: The lattice parameters as a function of Y and Gd concentration

B. Scanning ElectronMicroscopy (SEM)

Fig 3 shows an example of SEM micrographs of our samples. The SEM images show the presence of porosity in our samples. For such materials, it is very important to minimize the porosity; their densification requires hot sintering under pressure or changing the synthesis method.

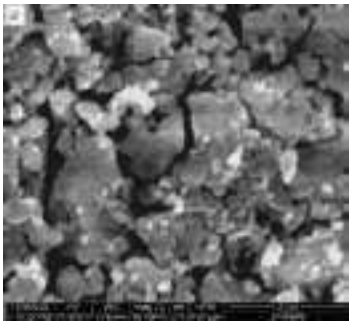

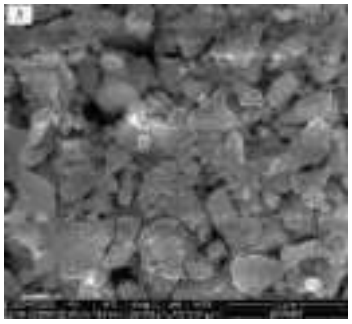

Fig.3: SEMimages of prepared electrolyte(a) $Ce_{1.85}Gd_{0.075}Y_{0.075}0_{7-\delta}$ *(b)* $Ce_{1.8}Gd_{0.1}Y_{0.1}0_{7-\delta}$

C. Electrochemical Impedance Spectroscopy(EIS)

To measure the electrical conductivities of solid ionic materials the AC impedance technique is commonly used. In the general case at low temperatures, three successive semicircles can be resolved in the complex impedance spectra, the first one at high frequencies corresponding to the grain polarisation, the second one at medium frequencies representing the contribution of the grain boundary, and a last one at low frequencies corresponding to the electrode polarisation[31, 35].

AC impedance plots of $Ce_{1-x}M_xO_{2-\delta}$ (x=0.1, 0.15, 0.2)(M=Gd,Y) specimen obtained for temperatures of 500° C, to 700° C in the air are shown in Fig 4 . As can be seen, the pattern consists of one semi-circle. As the semicircles in the impedance spectrum shift to higher frequencies with increasing temperatures[21, 36], the semicircle that appears on the impedance curve correspond to the contribution of polarisation at the electrolyte-electrode interface.

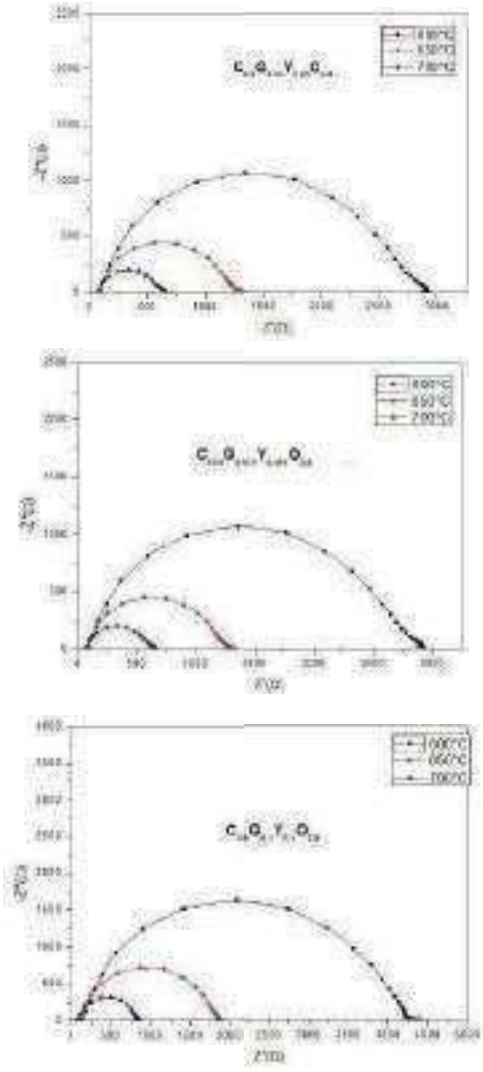

Fig.4: Impedance spectra of $Ce_{1-x}M_xO_{2-\delta}$ *(x=0.1, 0.15, 0.2)(M=Gd, Y)at 650°C and 700°C*

Electrical conductivity (σ_{ac}) was calculated based on the observed resistance values from the complex impedance plots fitting using equation[31]:

$$\sigma_{ac} = \frac{l}{RA}$$

Where 'l' is the thickness of the pellet , 'A' is the cross-section of the pellet and 'R' is theresistance electrolyte .

The conductivity results are presented in Table 1. Codoping has a considerable effect on the electrolyte conductivity $Ce_{1-x}M_xO_{2-\delta}$ (x=0.1, 0.15, 0.2)(M=Gd, Y). In ionic conductors, charge transport is achieved by the jumping of charged O^{2-} ions to neighboring vacancies in the crystal structure, in a

process whose probability of success is thermally increased[37].

Table.1 : Comparative study conductivity and activation energy of Gd and Y co-doped CeO.

X	Composition	Conductivity at 700°C ($S.cm^{-1}$)	Activation energy (eV)
0.1	$Ce_{1.9}Gd_{0.025}Y_{0.075}O_{7-\delta}$	0.0030	0.815
	$Ce_{1.9}Gd_{0.05}Y_{0.05}O_{7-\delta}$	0.0032	0.839
	$Ce_{1.9}Gd_{0.075}Y_{0.025}O_{7-\delta}$	0.0031	0.816
0.15	$Ce_{1.85}Gd_{0.05}Y_{0.1}O_{7-\delta}$	0.0028	0.910
	$Ce_{1.85}Gd_{0.075}Y_{0.075}O_{7-\delta}$	0.0042	0.881
	$Ce_{1.85}Gd_{0.1}Y_{0.05}O_{7-\delta}$	0.0039	0.899
0.2	$Ce_{1.8}Gd_{0.075}Y_{0.125}O_{7-\delta}$	0.0033	0.820
	$Ce_{1.8}Gd_{0.1}Y_{0.1}O_{7-\delta}$	0.0040	0.829
	$Ce_{1.8}Gd_{0.125}Y_{0.075}O_{7-\delta}$	0.0038	0.856

As can be seen in the table, the best conductivity results were obtained for the composition $Ce_{0.85}Y_{0.075}Gd_{0.075}O2._{\delta}$These results are similar wit with previous studies [31, 35, 38].

The activation energy can be calculated from the Arrhenius pattern, as shown in Fig 5. From the patterns obtained, we found activation energies about 0.8eV and these results are in good agreement with the research reported in the literature [16, 21, 31, 35, 38]

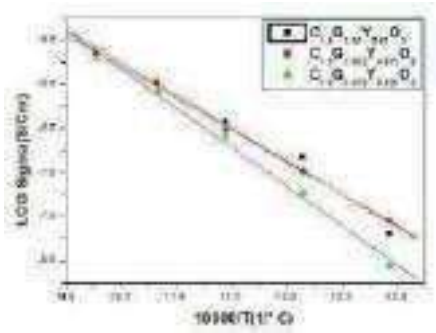

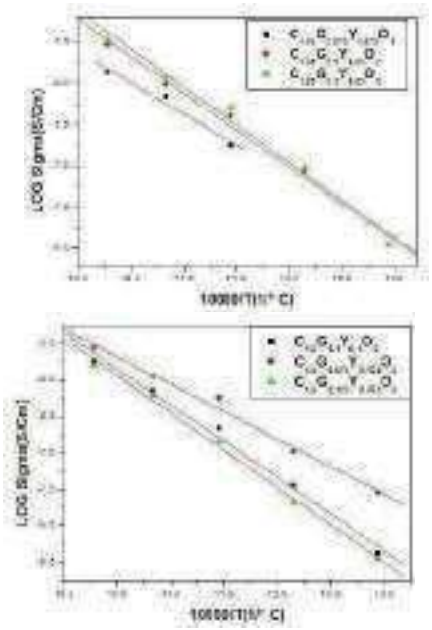

Fig 5: Arrhenius plots of conductivity for different prepared samples

IV. Conclusions

Polycrystalline Co-doped ceria $Ce_{1-x}M_xO_{2-\delta}$ (x=0.1, 0.15, 0.2)(M=Gd, Y) fluorite structure was prepared by using conventional solid-state reaction. The substitution of Ce^{4+} by Gd^{3+} and Y^{3+} in CeO_2 has shown a remarkable effect on the electrolyte material studied.

On the one hand, the substitution by a cation (Gd) larger than the critical radius r_c causes an expansion of the lattice, on the other hand, the contraction of the lattice is due to the doping by Y which is smaller than the radius r_c this phenomenon causes a nonlinear variation of the crystal parameters. This modification caused an improvement in their ionic conductivity.

The highest ionic conductivity for $Ce_{1-x}M_xO_{2-\delta}$ (x=0.1, 0.15, 0.2)(M=Gd, Y) studied for x = 0.15 and was found to be 4.2×10^{-3} $S.cm^{-1}$ at 700°C with an activation energy of 0.88 eV. Thus, from the detailed characterization study and structural, morphological, and electrochemical analysis of prepared $Ce_{1-x}M_xO_{2-\delta}$ (x=0.1, 0.15, 0.2)(M=Gd, Y), it is concluded that the synthesized materials can be one of the emerging potential candidates as a highly concentrated electrolyte material for SOFC applications.

References

[1] G. M. Mustafa, S. Atiq, S. K. Abbas, S. Riaz, and S. Naseem, "Tunable structural and electrical impedance properties of pyrochlores based Nd doped lanthanum zirconate nanoparticles for capacitive applications," *Ceramics International,* vol. 44, pp. 2170-2177, 2018.

[2] F. Yang, Y. Wang, X. Zhao, and P. Xiao, "Enhanced ionic conductivity in pyrochlore and fluorite mixed phase yttrium-doped lanthanum zirconate," *Journal of Power Sources,* vol. 273, pp. 290-297, 2015.

[3] J. S. Gardner, M. J. Gingras, and J. E. Greedan, "Magnetic pyrochlore oxides," *Reviews of Modern Physics,* vol. 82, p. 53, 2010.

[4] W. Pan, S. R. Phillpot, C. Wan, A. Chernatynskiy, and Z. Qu, "Low thermal conductivity oxides," *MRS bulletin,* vol. 37, pp. 917-922, 2012.

[5] H. Zhang, K. Haule, and D. Vanderbilt, "Metal-insulator transition and topological properties of pyrochlore iridates," *Physical review letters,* vol. 118, p. 026404, 2017.
[6] Y.-P. Fu, S.-H. Chen, and J.-J. Huang, "Preparation and characterization of Ce0. 8M0. 2O2− δ (M= Y, Gd, Sm, Nd, La) solid electrolyte materials for solid oxide fuel cells," *International journal of hydrogen energy,* vol. 35, pp. 745-752, 2010.
[7] T. Horita, T. Kawada, N. Sakai, H. Yokokawa, and M. Dokiya, "Low temperature fabrication of (Y, Gd, Sm)-doped ceria electrolyte," *Solid State Ionics,* vol. 86, pp. 1255-1258, 1996.
[8] B. Huang, X. Ye, S. Wang, H. Nie, R. Liu, and T. Wen, "Performance of Ni/ScSZ cermet anode modified by coating with Gd0. 2Ce0. 8O2 for a SOFC," *Materials research bulletin,* vol. 42, pp. 1705-1714, 2007.
[9] K. C. Wincewicz and J. S. Cooper, "Taxonomies of SOFC material and manufacturing alternatives," *Journal of power sources,* vol. 140, pp. 280-296, 2005.
[10] A. Arabacı and M. F. Öksüzömer, "Preparation and characterization of 10 mol% Gd doped CeO2 (GDC) electrolyte for SOFC applications," *Ceramics International,* vol. 38, pp. 6509-6515, 2012.
[11] M. Srivastava, K. Kumar, N. Jaiswal, N. K. Singh, D. Kumar, and O. Parkash, "Enhanced ionic conductivity of co-doped ceria solid solutions and applications in IT-SOFCs," *Ceramics International,* vol. 40, pp. 10901-10906, 2014.
[12] M. Mogensen, N. M. Sammes, and G. A. Tompsett, "Physical, chemical and electrochemical properties of pure and doped ceria," *Solid State Ionics,* vol. 129, pp. 63-94, 2000.
[13] C. Tian and S.-W. Chan, "Ionic conductivities, sintering temperatures and microstructures of bulk ceramic CeO2 doped with Y2O3," *Solid state ionics,* vol. 134, pp. 89-102, 2000.
[14] K. Sato, K. Suzuki, K. Yashiro, T. Kawada, H. Yugami, T. Hashida, A. Atkinson, and J. Mizusaki, "Effect of Y2O3 addition on the conductivity and elastic modulus of (CeO2) 1− x (YO1. 5) x," *Solid State Ionics,* vol. 180, pp. 1220-1225, 2009.
[15] H. Hayashi, R. Sagawa, H. Inaba, and K. Kawamura, "Molecular dynamics calculations on ceria-based solid electrolytes with different radius dopants," *Solid State Ionics,* vol. 131, pp. 281-290, 2000.
[16] D. Kashyap, P. Patro, R. Lenka, T. Mahata, and P. Sinha, "Effects of Gd and Sr co-doping in CeO2 for electrolyte application in solid oxide fuel cell (SOFC)," *Ceramics International,* vol. 40, pp. 11869-11875, 2014.
[17] S. Zha, C. Xia, and G. Meng, "Effect of Gd (Sm) doping on properties of ceria electrolyte for solid oxide fuel cells," *Journal of Power Sources,* vol. 115, pp. 44-48, 2003.
[18] M. Dudek, "Ceramic oxide electrolytes based on CeO2—preparation, properties and possibility of application to electrochemical devices," *Journal of the European ceramic society,* vol. 28, pp. 965-971, 2008.
[19] D. Fogg, J. Abrantes, and D. Perez-Coll, "The Effect of Cobalt Oxide Sintering Aid on Electronic Transport in Ce0. 80Gd0. 20O2-δ Electrolyte, Electrochem," ed: Acta, 2003.
[20] P. Ong, Y. Tan, Y. Taufiq-Yap, and Z. Zainal, "Improved sinterability and conductivity enhancement of 10-mol% calcium-doped ceria using different fuel-aided combustion reactions and its structural characterisation," *Materials Science and Engineering: B,* vol. 185, pp. 26-36, 2014.
[21] M. Dudek, "Ceramic electrolytes in the CeO2-Gd2O3-SrO system—preparation, properties and application for solid oxide fuel cells," *Int. J. Electrochem. Sci,* vol. 7, pp. 2874-2889, 2012.
[22] M. Dudek, W. Bogusz, Ł. Zych, and B. Trybalska, "Electrical and mechanical properties of CeO2-based electrolytes in the CeO2–Sm2O3–M2O3 (M= La, Y) system," *Solid State Ionics,* vol. 179, pp. 164-167, 2008.
[23] X. Guan, H. Zhou, Y. Wang, and J. Zhang, "Preparation and properties of Gd3+ and Y3+ co-doped ceria-based electrolytes for intermediate temperature solid oxide fuel cells," *Journal of Alloys and compounds,* vol. 464, pp. 310-316, 2008.
[24] S. Ramesh, V. P. Kumar, P. Kistaiah, and C. V. Reddy, "Preparation, characterization and thermo electrical properties of co-doped Ce0. 8− xSm0. 2CaxO2− δ materials," *Solid State Ionics,* vol. 181, pp. 86-91, 2010.
[25] S. Dikmen, "Effect of co-doping with Sm3+, Bi3+, La3+, and Nd3+ on the electrochemical properties of hydrothermally prepared gadolinium-doped ceria ceramics," *Journal of alloys and compounds,* vol. 491, pp. 106-112, 2010.
[26] H. T. Handal and V. Thangadurai, "Evaluation of chemical stability, thermal expansion coefficient, and electrical properties of solid state and wet-chemical synthesized Y and Mn-codoped CeO2 for solid oxide fuel cells," *Journal of power sources,* vol. 243, pp. 458-471, 2013.
[27] L. A. Eressa and P. B. Rao, "Structural and Electrical Properties of Ytterbium and Samarium Co-doped Ceria as a Solid Electrolyte for Intermediate-Temperature Solid Oxide Fuel Cell," in *Proceeding of the Third International Research Symposium*, 2019.
[28] A. Arabacı, T. G. Altınçekiç, M. Der, and M. A. F. Öksüzömer, "Preparation and properties of ceramic electrolytes in the Nd and Gd Co-doped ceria systems prepared by polyol method," *Journal of Alloys and Compounds,* vol. 792, pp. 1141-1149, 2019.
[29] G. Accardo, D. Frattini, H. Ham, J. Han, and S. Yoon, "Improved microstructure and sintering temperature of bismuth nano-doped GDC powders synthesized by direct sol-gel combustion," *Ceramics International,* vol. 44, pp. 3800-3809, 2018.
[30] C. Howard, B. Hunter, and D. Swinkels, "Rietica IUCR," *Powder Diffr.,* vol. 22, p. 21, 1997.
[31] X. Guan, H. Zhou, Z. Liu, Y. Wang, and J. Zhang, "High performance Gd3+ and Y3+ co-doped ceria-based electrolytes for intermediate temperature solid oxide fuel cells," *Materials Research Bulletin,* vol. 43, pp. 1046-1054, 2008.
[32] X. Sha, Z. Lü, X. Huang, J. Miao, Z. Ding, X. Xin, and W. Su, "Study on La and Y co-doped ceria-based electrolyte materials," *Journal of Alloys and Compounds,* vol. 428, pp. 59-64, 2007.
[33] D. J. Kim, "Lattice parameters, ionic conductivities, and solubility limits in fluorite ‐ structure MO2 oxide [M= Hf4+, Zr4+, Ce4+, Th4+, U4+] solid solutions," *Journal of the American Ceramic Society,* vol. 72, pp. 1415-1421, 1989.
[34] R. D. Shannon, "Revised effective ionic radii and systematic studies of interatomic distances in halides and chalcogenides," *Acta crystallographica section A: crystal physics, diffraction, theoretical and general crystallography,* vol. 32, pp. 751-767, 1976.
[35] M. F. Öksüzömer, G. Dönmez, V. Sariboğa, and T. G. Altinçekiç, "Microstructure and ionic conductivity properties of gadolinia doped ceria (GdxCe1− xO2− x/2) electrolytes for intermediate temperature SOFCs prepared by the polyol method," *Ceramics International,* vol. 39, pp. 7305-7315, 2013.
[36] A. Arabaci, "Effect of Sm and Gd dopants on structural characteristics and ionic conductivity of ceria," *Ceramics International,* vol. 41, pp. 5836-5842, 2015.
[37] K. Moreno, G. Mendoza-Suárez, A. Fuentes, J. García-Barriocanal, C. León, and J. Santamaria, "Cooperative oxygen ion dynamics in $Gd_2Ti_{2-y}Zr_yO_7$," *Physical review B,* vol. 71, p. 132301, 2005.
[38] M. Dudek and M. Mosiałek, "Utility of Ce0. 8M0. 2O1. 9, Ce8M0. 15Y0. 05O1. 9, M= Gd, Sm powders synthesized by aerosol decomposition method in solid oxide fuel cell technology," *Electrochimica Acta,* vol. 104, pp. 339-347, 2013.

Network Level Attacks and Countermeasures

Trust Tshepo Mapoka[#1], Keneilwe Zuva[*2], C. Katlego[#3]

[#]*First-Third Department of Computer Science, First-Third University of Botswana*
P/Bag 0022 Gaborone Botswana
[1]mapokat@ub.ac.bw
[3]zuvak@ub.ac.bw

***Abstract*— The Morris worm, the first unmanned worm developed by a Cornell Student, which appeared on the United States Advance Research Project Agency (ARPANET) in 1988 has paved a way for the subsequent years. With the use of networked computers having grown over the years, it has proven that network attacks will continue to get more advanced. It is without question that security is the cornerstone and the most desired feature for any network system in an era where new attacks are booming and disrupting network systems. This paper explores and gives insight of the various network level attacks and how they can be counter measured. It goes as far as appreciating the different tools at disposal for performing and identifying such attacks. We explored sniffing the network using macof, performing Denial of Service (DoS) attack using hping3 and Distributed Denial of Service(DDoS) attacks using High Orbit Ion Cannon (HOIC) as well as securing the network from attacks using Anti Distributed Denial of Service Guardian. The experimental results overstate that indeed there is a dire needfor securing networksystems.**

***Keywords*— Attacks, Countermeasures, Machine, Man in the middle, Networks, Packets, System**

I. INTRODUCTION

This Network attacks are fraudulent activities committed against digital assets in a corporate network. These are launched I n order to alter, delete, or steal personal data. Attackers on networks frequentlyaim for network perimeters to get access to systems of different institutions
Network attacks primarily fall into two categories, being, passive and active. A passive attack is whereby a malevolent third party infiltrates the network without authorization, observes it, and obtains sensitive data without any alteration.On the other hand, an active attack is wherebythere is modification, encoding, or corruption of data after an unauthorized access to the system.

Attackers use various attack strategies to compromise the security of a network, potentially causing disruption, damage, and loss to organizations and individuals. Therefore, it is important for security professionals to have an understanding of these attack strategies, because such an understanding is essential for protecting thenetwork from various attacks. Some of the various techniques are, Media Access Control(MAC) flooding, Address Resolution Protocol(ARP) poisoning, Address Resolution Protocol(ARP) spoofing, Denial of Service and Distributed Denial of Service attacks, and session hijacking. These allow attackers to capture data packets containing sensitive information such as passwords, account information, router configuration, Domain Name System(DNS) traffic, email traffic, web traffic, chat sessions, and passwords. Previous work [1] discusses network security attacks and defenses considering the use of firewalls as one of the defense mechanisms. However most of the firewalls are not designed to detect and prevent DOS attacks. Also firewalls can be a drawback as they affect the network speed. Work[2] analyses web attacks and mitigation techniques. It suggest the use of security tools as one of the mitigation tools. However the paper is too general when addressing the tools , it does not go into detail to call out the tools or even break down how security tools are used. In work[3] there's a demonstration of securing hospital networks using wireshark, which is in line with the proposed method of this paper. Most of research papers discuss the general network attacks and mitigation techniques, and do not go further to show how the techniques work. Thus, there is need for more research which breaks down the mitigation techniques , showing users how to use the techniques such as security tools. This paper serves the purpose of sensitizing on the commonly known network attacks, and explores how different security tools can be used to launch an attack, detect it and protect against it.

TABLE 1
SUMMARY OF RELATED WORK

Authors	Discussions	Findings	Limitations
SAXENA, P., & TIWARI, V	network security attacks and defenses	firewall stops unauthorized network traffic across an unsecured network or a private network.	most of the firewalls are not designed to detect and prevent DOS attacks. Also if the firewall is not configured correctly it can allow unauthorized access into thesystem.
Sharif, M. H. U	Analysis of web attacks and mitigation techniques.	Security tools can be used to mitigate web attacks.	The paper does not go into detail on what the security tools that can be used are.
Maity, R., & Chakraborty, R	A progressive	Data packets can be	The topic onlyfocuses

	apporach towards securing hospital networks from packet sniffing using wireshark	monitored through a network by packet sniffing and on the other hand, web attacks can also be generated.	on the working mechanism of wireshark only when capturing packets, it does not show how those packets were launched in the start.

II. Categories of Networks Attacks

An easy way to comply with the conference paper formatting requirements is to use this document as a template and simplytype your text into it.

A. *Passive Attack*

A passive attack is where the hacker gains unauthorized access to the system, and just observes and obtains information, while at it, the attacker does not tamper with the information. The main focus here is to gain information.

B. *Active Attack*

In an active attack, the hacker's main aim is to gain unauthorized access in order to disrupt the system resources by making alterations to existing data or even make changes to the system itself

III. Network Attack Techniques and Tools Used

A. *Packet Sniffing*

The Packet sniffing attack is one whereby there is an interception of data, being the network traffic. The network traffic is detected, observed and captured using packet sniffing tools.A packet sniffer, also known as a packet analyser, is made up of two parts. The first part is a network adapter that allows the sniffer to connect to the existing network. The second, is the software behind the sniffing that gives administrators a way to look at and analyse the data coming through their network. [4] This attack aims at intercepting any network traffic and finding loop holes to exploit in any data traffic. Examples of such an attack include among others, Media Access Control (MAC) flooding and Address Resolution Protocol (ARP) poisoning.

The tool used for sniffing is Wireshark, it is used along with arpspoof for the Address Resolution Protocol (ARP) poisoning attack and the macof tool in a machine terminal.

1) MEDIA ACCESS CONTROL (MAC) FLOODING

When an attacker tries to send manyinvalid Media Access Control addresses to the Media Access Control (MAC) table, this is known as Media Access Control (MAC) flooding. The invalid Media Access Control (MAC) addresses are flooded into the source table. When the Media Access Control (MAC) table's

designated limit is reached, the legitimate Media Access Control (MAC) addresses begin to be removed. One of the eliminates the previous address as new addresses are added to it. Malicious attacker will then be able to steal sensitive data from the user's computer because of this. It will also allow the attacker to obtain any communication data sent and received. A successful Media Access Control (MAC) flooding attack results from this.

What the attacker does is to open the Wireshark application in parrot security, and opens the primary network interface, then leaves Wireshark running and navigates to the Mate terminal.Wireshark is a network protocol analyzer, or an application that captures packets from a network connection, such as from a personal computer to a home office or the internet [5].

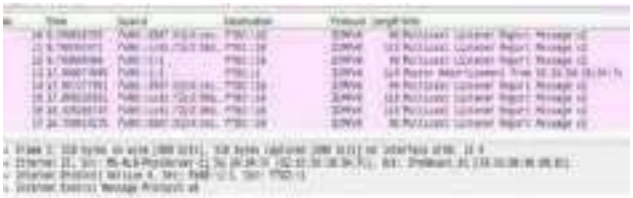

Fig.1. Wireshark before attack

In the terminal, the macof command is typed in as shown in Fig.2. , it specifies the interface and number of packets to be sent is typed in. It then floods the table with random

Media Access Control (MAC) table's properties is that it

Fig.2. macof command execution

Meanwhile, in Wireshark different ipv4 packets from random Internet Protocol addresses are captured. When expanded at the "Ethernet II" node, information about the source and destination of the Media Access Control(MAC) addresses is displayed.

Fig.3. IPv4 packet captured in Wireshark

Fig.3 shows a successful Media Access Control (MAC) flooding attack results from using the macof command together with the wireshark application.

2) ADDRESS RESOLUTION PROTOCOL (ARP)POISONING

Address Resolution Protocol (ARP) poisoning poisoning is a Man in the Middle (MitM) attack that allows attackers to intercept network device communication [6]. The network is scanned for the Internet Protocol (IP) addresses of at least two devices, such as workstations and routers. To send out faked Address Resolution Protocol answers, the attacker uses arspoof. The attacker's Media Access Control (MAC) address is advertised as the correct address for both router and workstation Internet Protocol (IP) addresses in the falsified answers. Both the router and the workstation are fooled into connecting to the attacker's machine rather than each other. The Address Resolution Protocol(ARP) cache on both devices is updated. Thus, a successful Address Resolution Protocol(ARP) poisoning.

The arspoof command in Mate terminal is used along with Wireshark.

The attacker types in the arspoof command which specifies the network interface and specifies target Internet Protocol(IP) address of the target system and the gateway. A few packets are then sent,and the attacker stops sending the Address Resolution Protocol(ARP) packets. When the same step is repeated, the host system informs the target system that it is the access point.

Fig.4. arpspoof command execution

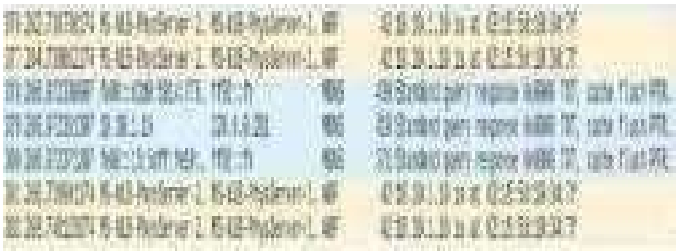

Fig.5. captured Address Resolution Protocol(ARP) packets

Fig.6. duplicate use of the Internet Protocol(IP) address of the target system.

B. Denial of Service

This attack technique is one in which the hacker's aim is to make the system resources inaccessible to the intended users, bydisrupting the services or shutting down the target system [7]. Just as the name implies, it denies the user from using services in the system. The hacker floods the system with invalid services in order to overload the resources. Examples include, Ping of Death(PoD), User Datagram Protocol(UDP) flooding and Distributed Denial Of Service (DDoS) attack.

1) PING OF DEATH ATTACK

In this attack, the hacker attempts to crash or freeze the target system by sending out large sized packets just by using a ping command. When performing the attack, evidence of the attack can be seen under performance tab in the task manager of a Windows computer.

What the attacker does is to type in the ping command, specifically the hping3 command in the terminal which specifies data size,

destination sets the synchronization flag, and sends a substantial number of packets

Fig.7. hping3 command execution

This command launches a Ping Of Death (PoD) attack on the system.

Fig.8. System performance before attack

Fig.9. System performance after launching attack

2) USER DATAGRAM PROTOCOL (UDP) FLOOD ATTACK

With this attack, the hacker sends User Datagram Protocol (UDP) packets, large ones, to a remote host on random ports of a target server [8]. The purpose of the attack is to overload

the internet pipes, making the services to be inaccessible to the intended users.

For this attack to be executed, the attacker has to ensure that the Network Basic Input/Output System (NetBIOS) port 139 is open. This is a transport layer that allows Windows computers to communicate on the same network [9].

Fig.10. NetBIOS port 139 is open

Fig.11.

The hping3 command as in Fig.11. is then run which specifies the User Datagram Protocol(UDP) mode, destination port and to send a substantial number of packets .

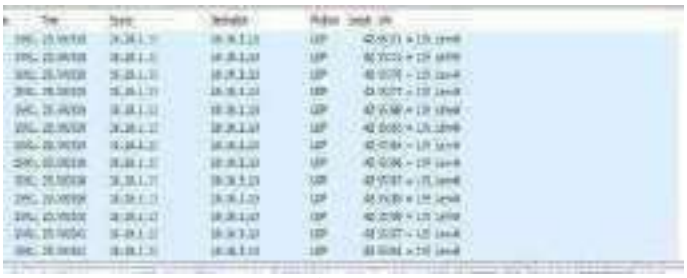

Fig.12.

In Fig.12. there is a huge number of User Datagram Protocol(UDP) packets coming from the SOURCE Internet Protocol(IP) address via

Port 139. This shows a successful User Datagram Protocol (UDP) attack on the system.

3) DISTRIBUTED DENIAL OF SERVICE ATTACK

This attack uses many compromised computers or machines known as a Botnet to attack and flood a single target.Just as the Denial of Service Attack, its aim is to deny system access to the intended users.

To experiment this attack, the High Orbit Ion Cannon application tool was used. HOIC (High Orbit Ion Cannon) is a network stress and Denial of Service/Distributed Denial of Service attack application. It offers a high speed multi-threaded Hyper Text Transfer Protocol(HTTP) Flood; a built-in scripting system allows the deployment of "boosters," which are scripts designed to thwart DDoS countermeasures and increase DoS output [10]. It is used along with Wireshark.

Wireshark is launched and left running on the parrot security .

Fig.13. Wireshark before attack launch

In the other machine, the HOIC tool is opened and set up as needed, setting the target URL to be that of the target Internet Protocol(IP) address in this case being the parrot security.The power bar is then set to high and the "GenericBoost.hoic" is added under the Booster section. The threads are set to 20 and thereafter the "FIRE TEH LAZER!" button ishit to initiate the attack.

Fig.14. HOIC configuration

Fig.15. After configuration

Once the FIRE THE LAZER button is hit, the status changes from readyto engaging as seen in Fig.16. below.

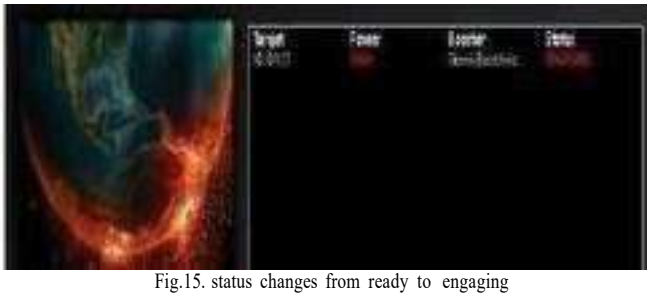

Fig.15. status changes from ready to engaging

Back in Wireshark of the parrot security machine, the volume of packets captured is shown as the attack is launched.

Fig.16. huge number of packets captured

This shows a successful Distributed Denial of Service(DDoS) attack on the system, as the many packets captured will freeze the system.

C. Session Hijacking

No SESSION HIJACKING

Bypassing the authentication process, session hijacking allows an attacker to take control of

an active session. It entails stealing or guessing a victim's legitimate session Identity, which is used by the server to identify authenticated users, and then utilizing it to connect to the server. The server responds to the attacker's queries as if it were conversing with an authenticated user, and the attacker is then free to do whatever they want with the system. The right knowledge must be possessed to hijack an active session between two target machines.

For experimental purpose,Zed Attack Proxy (Zed Attack Proxy(ZAP))

Tool is used. It is a penetration testing tool for finding vulnerabilities in web applications. It is

designed to be used by people with a wide range of securityexperience, and as such is ideal for

developers and functional testers who are new to penetration testing.

Proxysettings are configured in the victim's machine. This is done under settings in a web browser

under the computer proxy setting. The settings are configured and saved.

Fig.17. configured settings.

In the Zed Attack Proxy(ZAP) tool, the local proxies are configured to match those in settings.

Fig.18. local proxies

In the same browser where proxy settings are configured, an address is run, this will give a warning message that it is unsafe to open. There is a proceed link, when the user clicks it, it sends a Hyper Text Transfer Protocol(HTTP) response in the break tab in the Zed Attack Proxy(ZAP).

Fig.19. warning message

The user must then modify the visited address in all the captured GET requests with another web address. Once submitted ,a Hyper Text Transfer Protocol(HTTP) response appear, the Submit tab is clicked on and then step to next request or response icon on the toolbar.

Fig.20. address modification

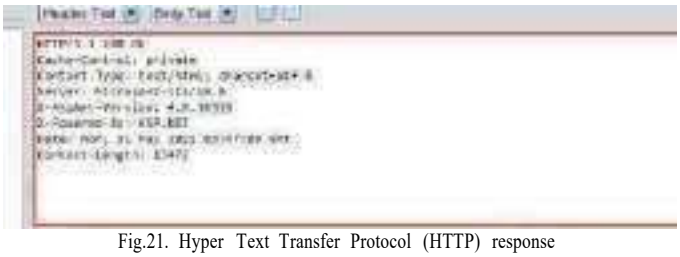

Fig.21. Hyper Text Transfer Protocol (HTTP) response

This must be done several times before getting the desired results. The desired results in this case being the victim's browser displaying the new web address that was modified into in the previous steps.

Fig.22. new web address

IV. DETECTING AND PROTECTING AGAINST NETWORK ATTACKSDETECTING AND PROTECTING AGAINST NETWORK ATTACKS

A. PACKET SNIFFING

Sniffer technologies that enable real-time monitoring and analysis of data packets travelling through computer networks are used in network sniffing. Various techniques can be used to detect these network sniffers, including, Ping Method, Domain Name System(DNS) Method, and Address Resolution Protocol(ARP) Method . For the experiment , The Address Resolution Protocol(ARP) Method was explored.

To detect ARP poisoning the tool used is the Cain and Abel tool. The tool is first configured in order to configure the Ethernet card.

Fig.23. configuration dialogue

The Media Access Control(MAC) address Scanner Window appears, here the range of the IP addresses is configured and “all tests” box is checked. Cain and Abel then scans for Media Access Control(MAC) addresses and lists all those found.

Fig.24. Media Access Control(MAC) address Scanner Window

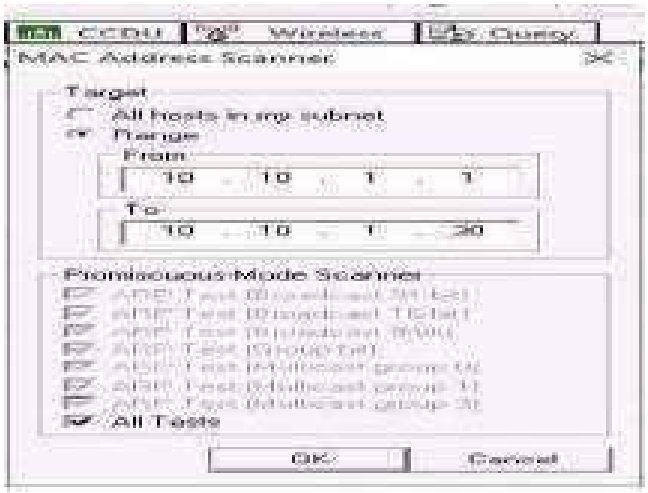

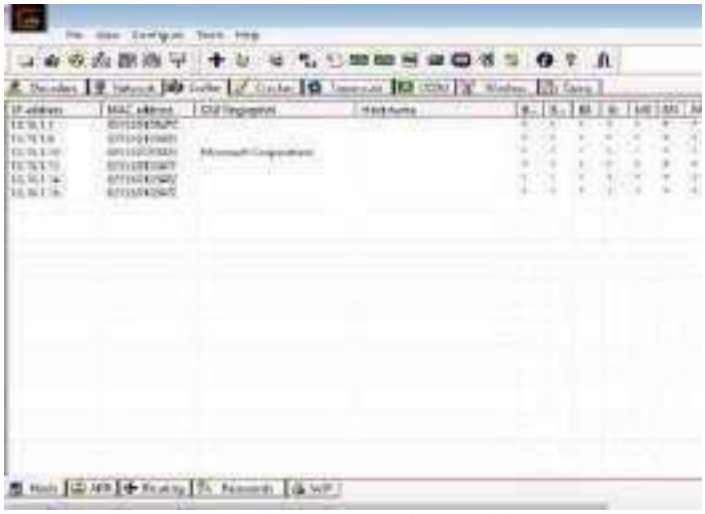

Fig.25. Scanned Media Access Control(MAC) addresses

Next, the user adds Internet Protocol(IP)s to listen to traffic from, this is done in the “New Address Resolution Protocol(ARP) Poison Routing “window. Two addresses are selected to monitor traffic between them, also known as poisoning ,between the first and second target.

Fig.26. New ARP Poison Routing window.

In the Parrot security MATE terminal, the attacker pings the target machine with several packets to be specified in the command. The command is left running.

Fig.27. hping3 command execution

Back in Wireshark, Protocols preferences to detect Address Resolution Protocol(ARP) requests stormsas well the duplicate Internet Protocol(IP) addresses are set. The traffic between thetwo machines is then captured.

Fig.28. protocol preferences

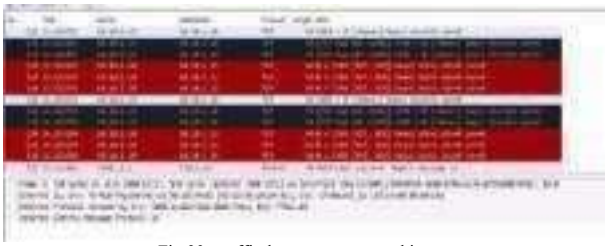

Fig.29. traffic between two machines

In theCain and Abel tool, the poisoning can be viewed.

Fig.30. Display poisoning

Expert information is also shown, among it, is one that indicates duplicate Internet Protocol(IP) addresses that have been detected. It is also shown in Wireshark. This way Address Resolution Protocol(ARP) poisoning has been detected

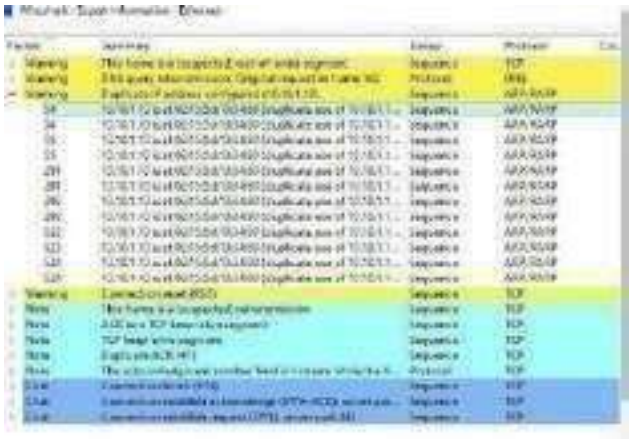

Fig.31. expert information

HOW TO PROTECT SYSTEM FROM SNIFFING ATTACKS

Organizations can protect their systems by using end to end encryption to protect confidential information found in their systems. This will reduce the vulnerability of threats and attacks. Another way is to restrict any physical access to the network media. This will lower chances of packet sniffers being installed into the system. It is also important that network identification broadcasts are turned off to protect the network from being discovered with sniffing tools.

B.DENIAL OF SERVICE

Attacks such as Denial of Service(DoS) and Distributed Denial of Service(DDoS) are common. The volume of traffic is one issue in separating

fake from authentic traffic. To assure protection from a Denial of Service(DoS) or Distributed Denial of Service(DDoS) assault, scanning each data packet is impossible. An attack is defined as an abnormal and visible variation in network traffic statistics and characteristics by all detection systems currently in use. These methods entail categorizing deviations using statistical analysis to categorize malicious and genuine traffic.

One of the tools that can be used to detect such attacks is the Anti Distributed Denial of Service(DDoS) Guardian. When this tool is launched it displays the incoming and outgoing traffic.

Fig.32. incoming and outgoing traffic

When a Distributed Denial of Service attack is launched, in the Anti Distributed Denial of Service(DDoS) Guardian tool, substantial number of packets coming from the host machine are shown.

Fig.33. packets from host machine

When any of the sessions is clicked, the traffic details are displayed. Internet Protocol(IP) sessions can also be blocked.

Fig.34. contents of each session and more functionalities

HOW TO PROTECT SYSTEM FROM DENIAL OF SERVICE ATTACKS

The use of strong encryption mechanism for broadband networks to prevent eavesdropping can counter measure these nature of attacks. Organizations can also block all inbound packets that originate from service ports to block traffic from any reflection servers. Software and protocols of the system have to be up to date at all times, as well as making it a habit to scan all the machines thoroughly for any anomalous behaviour can come in veryhandy.

C.SESSSION HIJACKING

It is important that the required knowledge and skills are possessed to detect session hijacking attacks and protect organization's system against them. There are many tools available that can help detect session hijacking attacks such as packet sniffers, Intrusion Detection Systems, and Security Information and Event Management technologies.

The tool used for experimenting the detection of session hijacking is the Wireshark tool. It

captures live network from the Ethernet.

In the windows machine, the user launches Wireshark and

clicks on the primary network interface to start capturing the traffic and leaves Wireshark running.

Fig.35. Wireshark before any Address Resolution Protocol(ARP) packetsarecaptured

In the Parrot Security machine MATE terminal, a session hijacking attack on the target machine using "bettercap" is launched. In the terminal a command which specifies theinterface to bind to an Ethernet port is run. Then the commands, "net.probe on, net.recon on, and net.sniff on "are run and bettercap starts sniffing the traffic on different machines.

Fig.36. launch session hijacking attack

- bettercap -iface eth0. –i: specifies the interface to bind to the Ethernet port.
- net.probe on - sends different types of probe packets to each Internet Protocol(IP) in the current subnet for the net.recon module to detect them.
- net.recon on - This module is responsible for periodically reading the system Address Resolution Protocol(ARP) tableto detect newhosts on thenetwork.
- net.sniff on - This module is responsible for performing sniffing on thenetwork.
- Back in the Wireshark, huge volume of Address Resolution Protocol(ARP) packets is captured.
- Fig.37. Address Resolution Protocol(ARP) packets is captured.

Something to note is that Bettercap sends

numerous
Address Resolution Protocol(ARP) broadcast requests to the hosts (or potentially active hosts). A high number of Address Resolution Protocol(ARP) requests suggests that the attacker's system is appearing as a client for all the Internet Protocol(IP) addresses within the subnet, because of this that that each of the packets from the victim's node will first visit thehost machine after which, the gateway.

HOW TO PROTECT SYSTEM FROM SESSION HIJACKING

Session Hijacking can be counter measured by using string or a long random number as a session Identity, this makes it complex for attackers to guess it. The use of Secure Shell (SSH) to create a secure communication channel can also be helpful to organizations. It is one of the network protocols which provide the users a secure way to access the remotely situated system or remote computer. This Secure Shell provides the strong way of authentication and more strong way of encryption between two systems in an insecure network also, which help the user to keep the users away from the session hijacking kind of attacks [11]. Moreover, it is advisable to generate session Identifications after a successful login and accept only session identifications generated bythe server.

CONCLUSION

Without the best counter measures and network security mechanisms, network systems are at a very high risk of attacks. It is important that organizations put in place measures that can protect their network systems. One of the measures that can play a great role, is that of carrying out vulnerability assessments of network systems frequently. Employing the counter measures discussed in this paper and many others that other researchers have explored may not be enough. Although Penetration testing can be really risky, in addition to all counter measured, organizations should consider it also.

REFERENCES

[l] SAXENA, P., & TIWARI, V. Network Security Attacks and Defence.

[1] S. Zhang, C. Zhu, J. K. O. Sin, and P. K. T. Mok, "Anovel ultrathin
elevated channel low-temperature poly-Si TFT," *IEEE Electron Device Lett.*, vol. 20, pp. 569–571, Nov. 1999.

[2]
Sharif, M. H. U. Web Attacks Analysis and Mitigation Techniques.
Maity, R., & Chakraborty, R. (2022). *A PROGRESSIVE APPORACH TOWARDS SECURING HOSPITAL NETWORKS FROM PACKET SNIFFING USING WIRESHARK* (No. 7561). EasyChair.
What is Packet Sniffing? Definition and Details. (n.d.). Paessler. https://www.paessler.com/itexplained/packet-sniffing
What Is Wireshark and How to Use It | Cybersecurity | CompTIA. (n.d.). Default. https://www.comptia.org/content/articles/what-is-wireshark-and-how-to-use-it
Gravier, O., Avital, N., S.L., Lynch, B., Lynch, B., Hasson, E., Lynch, B., Hasson, E., & Lynch, B. (2020, May 6). *What is ARP Spoofing | ARP Cache Poisoning Attack Explained | Imperva*. Learning Centerhttps://www.imperva.com/learn/application-security/arp-spoofing/
What is a denial of service attack (DoS) ? (n.d.). Palo Alto Networks. https://www.paloaltonetworks.com/cyberpedia/what-is-a-denial-of-service-attack-dos
R. (n.d.). *UDP Flood Attack*. Radware. https://www.radware.com/security/ddos-knowledge-center/ddospedia/udp-flood/
Petters, J. (n.d.). *What is an SMB Port + Ports 445 and 139 Explained*. Varonis. https://www.varonis.com/blog/smb-port#:%7E:text=Port%20139%3A%20SMB%20originally%20ran,to%20work%20over%20the%20internet.
Ohri, V. A. P. B. A. (2011, December 18). *Occupy the Internet*. DECISION STATS. https://decisionstats.com/2011/12/18/occupy-the-internet/
Baitha, A. K., & Vinod, S. (2018). Session hijacking and prevention technique. *International Journal of Engineering & Technology*, *7*(2.6), 193-198.

Pd-coated porous silicon porous silicon for hydrogen storage

Saloua MERAZGA[1] , Hanane KERRAR[2], Amina Larabi[3], BRIKAFAF[4] Nouredine GABOUZE[5]
Centre de Recherche en Technologie des Semi-conducteurs
pour l'Energétique 2 bd frantz
fanon alger, b.p. 140 alger – 7 merveille, algerie
[1]merazgasal@yahoo.fr

Abstract— **Hydrogen is widely regarded as the most promising alternative to fossil fuels. Depending on needs, the hydrogen sector of tomorrow will therefore not be that of yesterday. In the future, it will make it possible to produce heat, but also electricity thanks to the fuel cell. For this, a lot of research is devoted to this subject and our work falls within this framework which is the storage of hydrogen by electrochemistry. First, we prepared layers of porous silicon (PS) by electrochemical anodization and also we deposited on these layers a deposit of palladium which was used as a catalyst to increase the storage capacity thanks to its catalytic properties and hydrogen absorption. These deposits are made by two methods: thermal evaporation and electroless. The electrode materials obtained (PS and Pd / PS) were characterized by different characterization techniques: SEM microscopy, FTIR spectrometry, contact angle, cyclic voltammetry (CV). The SEM images confirm the formation of layers formed by clusters of Pd nanoparticles obtained by electroless; and a thin layer of Pd of the order of 30 nm deposited by thermal evaporation. The cyclic voltammetry carried out shows that the coverage rate of hydrogen (adsorption) with a catalyst metal is greater than that of porous silicon alone.**

Keywords— **porous silicon, palladium, hydrogen storage ,capacity**

I. INTRODUCTION

Hydrogen storage is a key enabling technology for the advancement of hydrogen and fuel cell technologies in applications including stationary power, portable power, and transportation. Actually, hydrogen may be stored by different techniques such as within compressed tanks, in liquefied form, and as solid state hydrides. Solid state materials considered as a good candidate capable of storing hydrogen at high gravimetric and volumetric densities [1]. The investigation of hydrogen adsorption on porous materials for mobile application has become a big challenge, due to these interesting properties such as the porous structure and specific surface area, which play a crucial role for the physisorption phenomenon of H2 molecules [2].The carbon materials produced are nanostructured with high surface areas, interesting porosities and pore size to possess appropriate characteristics for hydrogen storage [3].

Silicon nanostructures have already been used extensively as electrode with a discharge capacity of 232 mAh/g [4] .while, a hydrogen discharge capacity of 86mAh/g have been obtained by using a nanoporous silicon (PS) layers attributed to their large specific surface area [5]. Due to both its catalytic and hydrogen absorbing properties, Palladium is considered to be single material with strong affinity to hydrogen [6]. Therefore, the use of metal catalyst such as palladium to enhance the hydrogen storage capacity have been widely studied, specially, nano-sized Pd materials which have excellent hydrogen storage capacity compared to the bulk Pd[7]. For that, different structures and sizes Pd nanoparticles have been tested for potential applications for hydrogen storage and hydrogen sensing [8]. S. Couillaud and al reveals the deposition of Pd nanoparticles (Around 10nm) on the binary compound Mg0.65Sc0.35 using the Supercritical Fluid Chemical Deposition (SFCD) method could achieve a hight hydrogen uptake capacityof 3.3 wt.% [9].

Palladium-decorated graphène exhibits a high hydrogen storage capacity by about 437% in comparison to pure graphène [7]. While, thehighest hydrogen storage capacityof 546.1 mAh/g was obtained by using a Pd-coated porous silicon/graphene oxide electrode [4]

.

II. EXPERIMENTAL

To study the growth of palladium on the surface of porous silicon, scanning electron microscopy was used. In taking SEM images, two types of electrons were used: secondary electrons and backscattered electrons. The image of secondary electrons is essentially in topographic contrast and has a higher resolution. However, the images of backscattered electronshave both compositional (the brightness of these electrons..

III. RESULTS AND DISCUSSION

A. SECONDARY IONS MASS SPECTROMETRY ANALYSIS

This technique allowed us to quantify the concentration of hydrogen adsorbed in the porous layer. Measuring signals versus time gives us concentration versus depth profiles using the appropriate SIMS standards.

Figure (III.18) shows the SIMS profiles of a porous silicon layer before and after the insertion , which show the increase in the concentration of hydrogen by 3.5x1020 atom / cm3 at 6.8x1021atom / cm3, which confirms the absorption and storage of H + ions in the PS anode. In addition, it is observed that hydrogen penetrates deeper into the porous Si at 2um after diffusion. These absorbed hydrogen ions may have

ISSN: 1737-9334

bound or remained free on the pores of the porous layer; for this, FTIR measurements must be made in order to confirm thenature of these bonds.

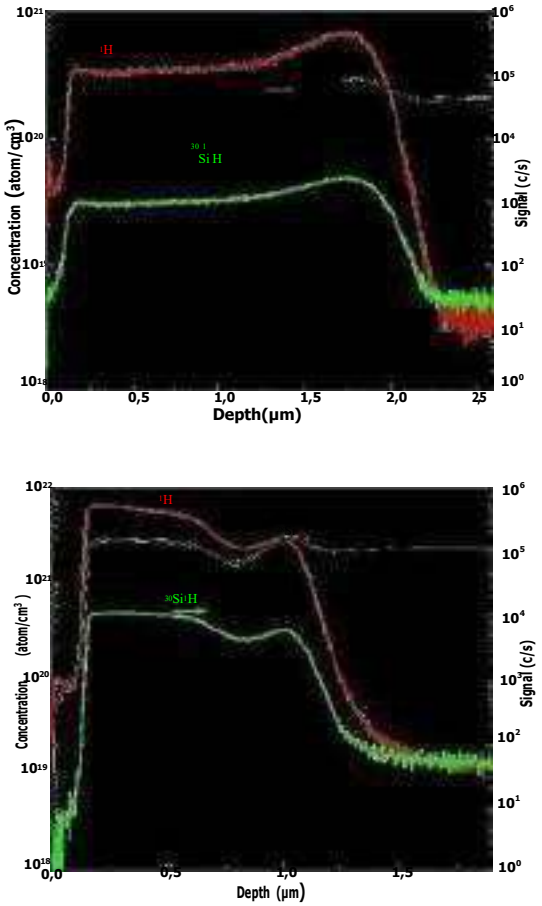

Fig. 1 SIMS profile of a Porous Si sample (: a) before hydrogenation, a) after hydrogenation

b-Mechanism of insertion and desinsertion of hydrogen in SiP:

1) Since the hydrogen absorption into the metal is closely related to the adsorption behavior of the electrolytically deposited intermediate H, involved in the stages of the hydrogen evolution reaction, then a generalized scheme of the overall process could be as shown as follows:

2) Si-H + H3O+ + e- Si + H2 + H2O

3) Si + 2H3O+ + e- Si-Hads + ½ H2 + 2H2O

4)

5) Diagram shows proton discharge reaction and H chemisorption (adsorption)

6)

7) Si-Hads + H3O+ + e- Si + H2 +H2O

8) Si-Hads + Si-H 2

9) Diagram of thereaction ofhydrogen desorption

B. cyclic voltammetry

the cyclic voltammetry of two layers of porous silicon, one without deposition and the other with deposition of a 30 nm layer deposited by thermal evaporation. Voltamograms show that the rate of hydrogen coverage (adsorption) with a catalyst metal is greater than that of porous silicon alone, this highlights the role of Pd metal in improving the hydrogen retention capacity .

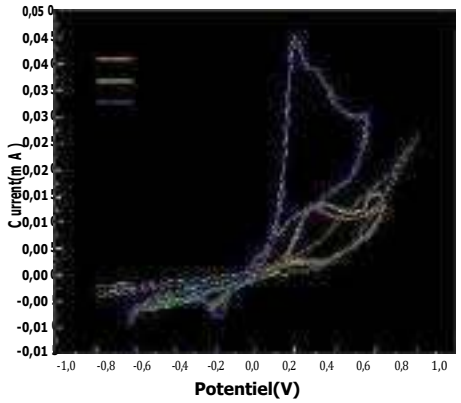

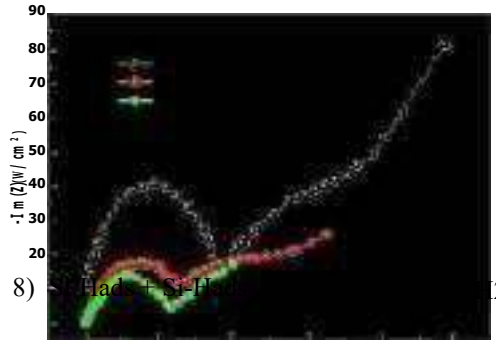

IV. CONCLUSIONS

In this work, we presented the different results obtained, using the different characterization techniques: morphological and physicochemical and structural, which play a very important role in particular on the electrochemical properties and the storage of hydrogen in porous silicon with a specific surface varies on the order of 700 m2/m3 for porosities ranging from approximately 60 to 70%. The SEM images confirm the formation of a 570 nm layer formed by clusters of Pd nanoparticles obtained by auto-catalysis; and a thin layer of Pd (30 nm) deposited by thermal evaporation. The electrochemical measurement (cyclic voltammetry) of porous silicon with a deposition of palladium catalyst (Pd/SiP) gave muchmore favorable results compared to that of porous silicon alone.Finally, we can conclude that palladium is a promising metal in the future of renewable technologies which will lead to several advancements in the physical,

chemical, nuclear and especially in the world of electronics.

ACKNOWLEDGMENT

The authors gratefully acknowledge the financial support from the Directorate General for Scientific Research and Technological Development (DGRSDT-Algeria)..

REFERENCES

[1] [1]Suresh K. Konda and Aicheng Chen. Palladium based nanomaterials for enhanced hydrogen spillover and storage. Materials 2016,19(2):100-108

[2] Rafal Roszak, Lucyna Firlej, Szczepan Roszak, Peter Pfeifer, Bogdan Kuchta. Hydrogen storage by adsorption in porous materials: Is it possible?. Colloids and Surfaces A: Physicochemical and Engineering Aspects .Volume 496, 5 May 2016, Pages 69-76

[3] http://dx.doi.org/doi:10.1016/j.colsurfa.2015.10.046

[4] [J.Andrews.S.M.Rezaei NiyaR.Ojha. Electrochemical hydrogen storage in porous carbons with acidic electrolytes: Uncovering the potential.Current Opinion in Electrochemistry Volume 31, February 2022, 100850 https://doi.org/10.1016/j.coelec.2021.100850

[5] Honarpazhouh Y, Astaraei FR, Naderi HR, Tavakoli O. Electrochemical hydrogen storage in Pd-coated porous silicon/graphene oxide. Int J Hydrogen Energy 2016;41(28):1217582

[6] S. Merazga, A.Cheriet, K.M'hammedi, A.Mefoued, N.Gabouze .investigation of porous silicon thin films for electrochemical hydrogen storage. International Journal of Hydrogen Energy. Vol 4 4, 2019. 9994 -10002.

https://doi.org/10.1016/j.ijhydene.2019.03.017

,

[7] Aram L. Bugaev, Oleg A. Usoltsev, Alexander A. Guda,Kirill A. Lomachenko Ilia A. Pankin,Yuri V. Rusalev,Hermann Emerich,Elena Groppo, Riccardo Pellegrini,

[8] Alexander V. Soldatov, Jeroen A. van Bokhoven,and Carlo Lamberti(2018)Palladium Carbide and Hydride Formation in the Bulk and at the Surface of Palladium Nanoparticles. J. Phys. Chem. C122: 12029−12037

[9] Lingling Du,a Dongliang Feng,a Xiaxia Xing,a Yang Fu,a Luis F. Fonseca b and Dachi Yang (2019)Palladium/cobalt nanowires with improved hydrogen sensing stability at ultra-low temperatures.J.Nanoscale 11: 21074−21080

[10] Samuel Couillaud , Marina Kirikova , Warda Zaïdi , Jean-Pierre Bonnet , Samuel Marre ,Cyril Aymonier , Junxian Zhang , Fermin Cuevas , Michel Latroche , Luc Aymard , Jean-Louis Bobet(2013) Supercritical fluid chemical deposition of Pd nanoparticles on magnesium–scandium alloy for hydrogen storage .Journal of Alloys and Compounds574: 6–12

[11] Brian D. Adams, Robert M. Asmussen, Cassandra K. Ostrom, and Aicheng Chen (2014) Synthesis and Comparative Study of Nanoporous Palladium-Based Bimetallic Catalysts for Formic Acid Oxidation.| J. Phys. Chem 118: 29903−29910

[12] Fatemeh Bakhshi, Nafiseh Farhadian.Improvement of hydrogen storage capacity on the palladium-decorated N-doped graphene sheets as a novel adsorbent: A hybrid MD-GCMC simulation Study. i n t e r n a t i o n a l journal o f hydrogen energy 4 4 (2 0 1 9) 1 3 6 5 5 1 3 6 6 5

PV system performance Assessment in an unbalanced distribution network using MATLAB andOpenDSS

Ben Achour Souheyla[#1], Bendjeghaba Omar[*2]

[#] *LREEI, Universtity of Boumerdes*
Boumerdes, Algeria
[1]so.benachour@univ-boumerdes.dz
[*] LREEI, Universityof Boumerdes
Boumerdes, Algeria
[2]o.bendjeghaba@univ-boumerdes.dz

***Abstract*— The aim of this paper is to present a simulation of distribution systems adding PV generation using MATLAB and OpenDSS, the study was applied on a three-phased unbalanced distribution network, Using the IEEE 13 node distribution feederas a test bed, The irradiance, and load values for each time step are managed on MATLAB and sent to OpenDSS for the calculation of three phase power flow. The simulation allows to analyze the power flows of the feeder without PV generation and further with the DGs, Results indicate that integrating DGs not only reduces the total power losses in the distributed system but improves the voltage profile as well.**

***Keywords*— PV generation, time-series steady-state power flow, optimization, OpenDS*S*.**

I. INTRODUCTION

The continuous grow of electricity demand is saturating the capacity of distribution networks in many regions, this situation can be alleviated by connecting distributedgenerators (DGs) in form of firm generation or intermittentrenewable energy sources like wind and solar farms. It isknown that DGs in a distribution network can compensatethe demand of energy from transmission network, improvethe voltage profile in the feeders, increase the reliability andreduce losses, the addition of DG systems causes changes inthe distribution grid that create a number of technicalchallenges. A true description of grid behaviour alsorequires advanced studies and trustworthy algorithms due tothe complexity of the modeling of these new systems, It ispossible to determine and quantify grid parameters due tosophisticated systems with graphical interactions that haveevolved from simple voltage drop calculators of balancedloads.

In the first section, a time-series simulation will be run through matlab/OpenDSS co-simulation to visualize the active and reactive powers without integrating DGs, and in the second section, a PV system was integrated to the network, as well as its performances were analysed. This paper assesses the impact of PV system on power losses and voltages in three phased unbalanced network.

II. OPENDSS SIMULATION PLATFORM

A. OpenDSS software

OpenDSS (The Open Distribution System Simulator) is a comprehensive simulation software developed by the American Electric Power Research Institute for distribution systems.

The OpenDSS is a simulator specifically designed to represent electric power distribution circuits. OpenDSS is designed to support most types of power distribution planning analysis associated with the interconnection of distributed generation (DG) to utility systems. It also supports many other types of frequency-domain circuit simulations commonly performed on utility electric power distribution systems. It represents unbalanced conditions, stochastic processes, and other aspects of electrical power distribution systems and equipment in far greater detail than many other tools, including commercial products. Through COM and scripting interfaces, other programs can drive OpenDSS in highly customized simulations, Monte Carlo analysis, etc. Users can define their own models through dynamic linking, scripting, or automation. [3]

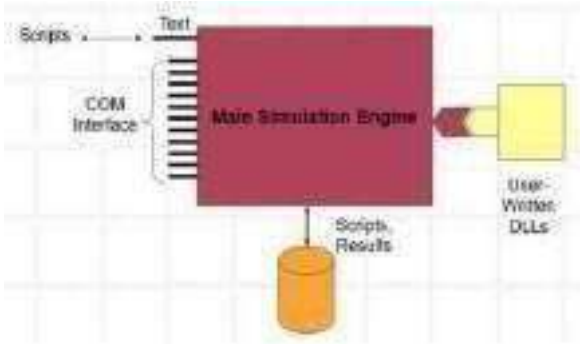

Fig. 1. OpenDSS structure. [4]

B. OpenDSS PVSystem Element Model

Figure 2 shows a schematic diagram of the photovoltaic system model implemented in the OpenDSS software. The present version of the model combines the generator photovoltaic and the inverter to perform simulations with a time interval greater than or equal to 1 second. Thus, it can be assumed that the inverter is able to find the maximum power point (MP) of the panel quickly, simplifying the component modeling individual, photovoltaic panel and inverter. This approach should be suitable for most studies related to interconnection with the distribution network [5].

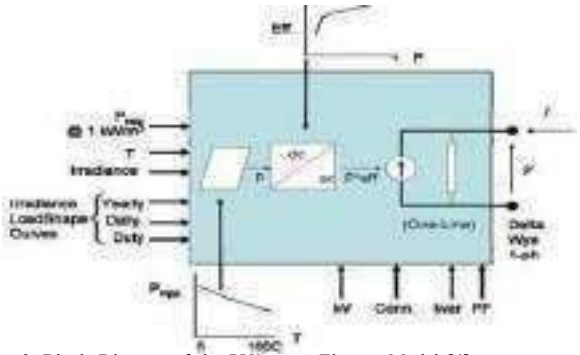

Fig. 2. Block Diagram of the PVSystem Element Model [4].

The photovoltaic system is an energy conversion element. Basically, the model has an active power injected at the interconnection point *P*, which is a function of irradiation, temperature, converter efficiency, network voltage and the Panel's nominal power at the point of maximum power (Pmp). A Pmp applied at the required temperature (25°C), and an irradiation of 1, 0*PP*/*P*2, the power value at the panel outputin an instant ⁉0, is calculated as follow [7]:

$$P(t0) = Pmp(1kW/m^2).irrad(pu)(t0).irrad(base).Pmp(pu,T(t0)) \quad (1)$$

P: Panel output power

Pmp(1Kw/m) : Rated power at the point of maximum power

Irrad(pu)(t0) : Irradiance value in pu at the moment $t0$

Irrad(base) : Maximum irradiance value on the selected day

Pmp(pu,T(t0)) : Pmp correction factor as a function of temperature at the time $t0$

The active power supplied by the photovoltaic system is presented in Equation 2:

$$P_{active}(t) = P(t).eff(P_{active}(t)) \quad (2)$$

eff(Pactive (t)) : Inverter efficiency for a given output power

Reactive power is specified separately from the active power and may be specified as either fixed kvar values or a fixed power factor value. If the PF property is specified, the model holds a constant output power factor until the PF property is changed (default mode). If the kvar property is specified, the inverter is assumed to hold that value despite the present value of the panel power. The actual kvar output is dropped if the rated kVA of the inverter is exceeded [5].

C. MODELING FRAMEWORK

As it is shown in Fig. 1 the data of irradiance, temperature and load power were set and managed using MATLAB And OpenDSS was employed to calculate the three-phase power flow. The output is the set of solutions calculated for the samples of load demand and weather conditions that can be analysed and employed to calculate further indicators of reliability and performance

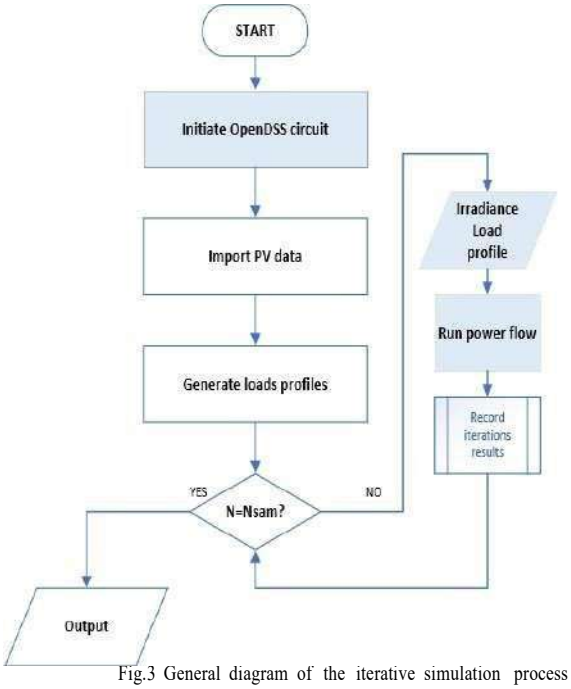

Fig.3 General diagram of the iterative simulation process

III. CASE STUDY

IEEE13 Bus Node Feeder is used for analysis. Fig.4 gives a one-line diagram of the IEEE Node Test Feeder. This feeder is very small and yet displays some very interesting characteristics. It actually displays an approximate model of the small radial feeder for the most common feature of distribution system [7].

The testeIEEE13 bus network features unbalanced three-phase overhead and underground lines, single-phase, two-phase and three-phase branches, two three-phase distribution transformers, localized loads and one distributed load, two shunt capacitor banks and a regulator connected in star.

For this work, which will be simulated through OpenDSS derived trough MATLAB, the powers and voltages behaviours through the insertion of PV system will be discussed, for this, the system has been analysed before the insertion of distributed generation for comparison purposes.

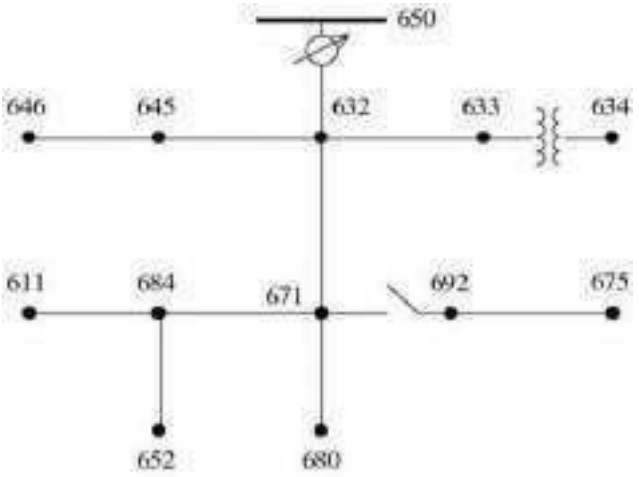

Fig.4. One-Line Diagram of IEEE 13 Node Test Feeder.

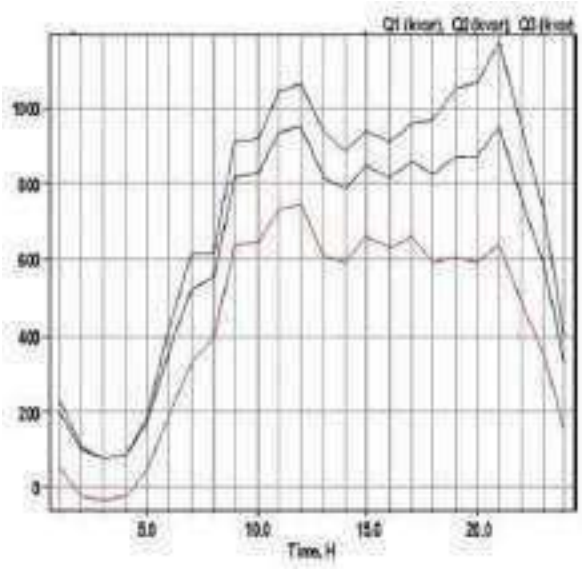

Fig.6. Reactive power provided by the substation.

IV. SIMULATION RESULTS

A. Dailysimulation for IEEE13 node test feeder with no PV

In this simulation, only the substation supplies power to the loads. The electrical power supplied by the substation is shown in Figures.

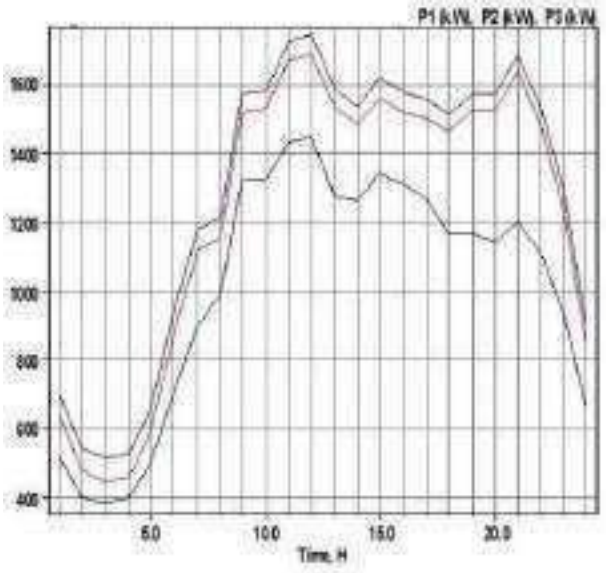

Fig.5. active power provided by the substation.

- Voltages without PV generation

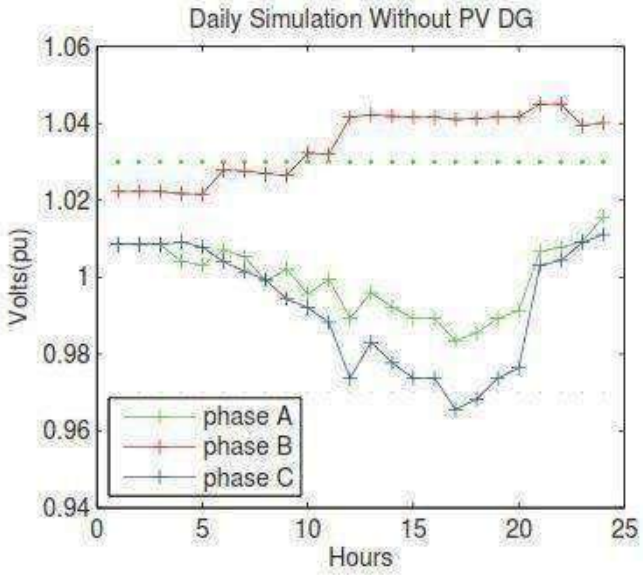

Fig.7. 24-hour voltage variation at bus 680

B. Dailysimulation for IEEE13 node test feeder with PVinsertion

IEEE 13 Node Test Feeder is characterized by being short, relatively highly loaded, with a total of 9 unbalanced loads,a PV system is integrated to bus number 680 in order to assess the performance of the network with the presence of GD, The irradiance, and load values for each time step are managed on MATLAB and sent to OpenDSS for the calculation of the power flow, PV generator unit was given a power rating of 1500 KW.

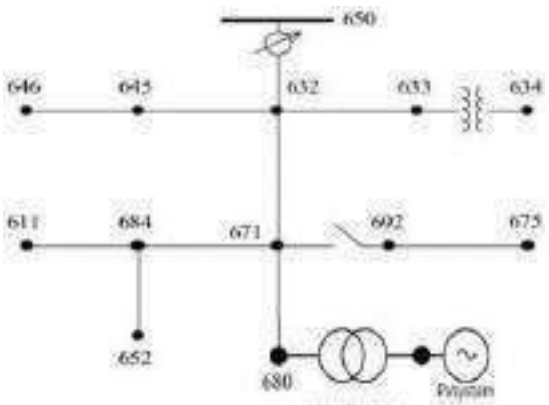

Fig.8. one-line diagram of the testeIEEE13 bus feeder with the presence of the PV system

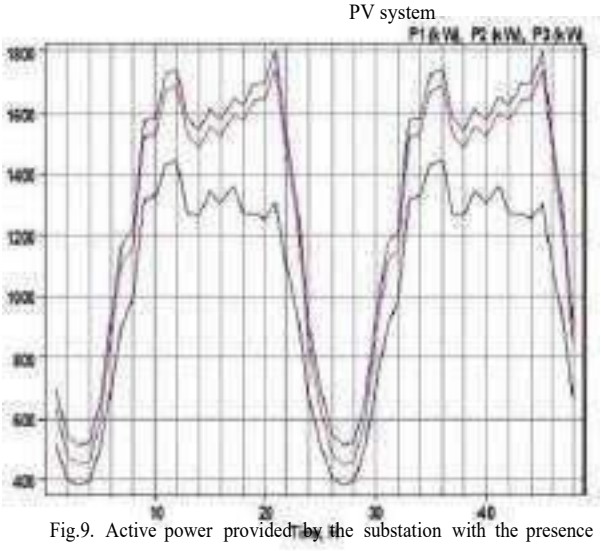

Fig.9. Active power provided by the substation with the presence of thePVsystem

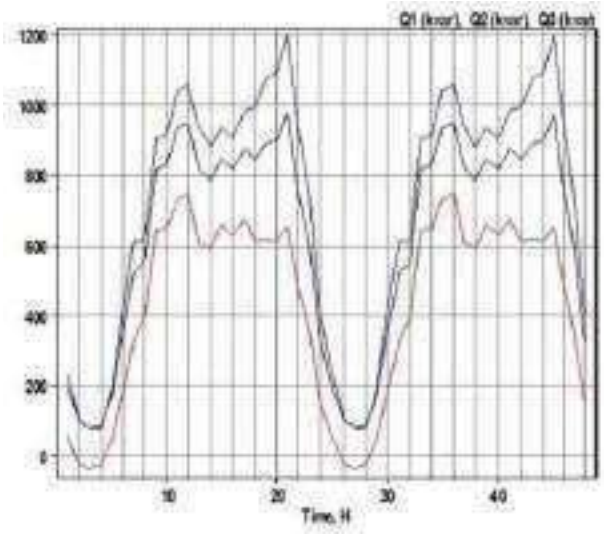

Fig.10.Reactive power provided by the substation with the presence of the PVsystem

It can be seen that the active power supplied by the substationafter integrating PV system is lower than the active power before PV system insertion, on the times at which there is irradiation. The reactive power has not changed, as the PVsystem has a factor of unitarypower throughout the day.

- Voltages with PV generation

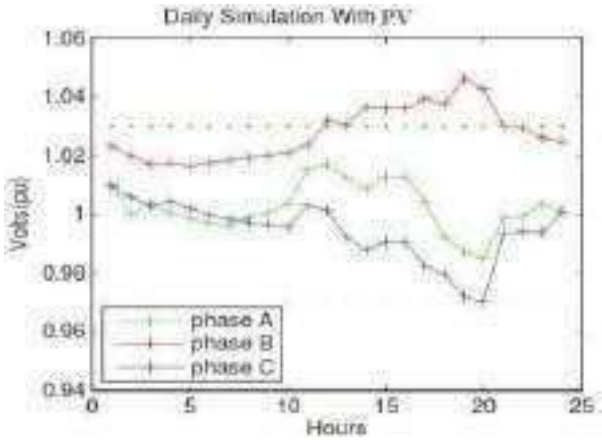

Fig.11. 24-hour voltage variation at point of insertion bus 680.

when comparing the voltages in the presence of PV system with the voltages before the PV system insertion, presented in fig.6, it can be seen that the voltages remain unbalanced dueto the fact that the PVsystem provides balanced three-phase power, that is, identical in each phase.<>The voltages hasbeen improved, as a PV system is connected.

V. CONCLUSION

The main purpose of this work is to analyse Time-series behaviour of distribution network When low-renewable PV (photovoltaic) system are integrated, this study discusses the impact of DG on the distribution network through the OpenDSS simulation platform which been driven by MATLAB. The results from the time-series analysis of the IEEE13 feeder show that grid-connected PV system can effectively reduce peak load and improve voltage profile. but the proposed case study could be extended by integrating wind generators and then performing time-series analysis.

REFERENCES

[1] C. Jan-ngurn and K. Bhumkittipich, "Analysis of Power Grid System with Solar Power Sources and Energy Storage System Integrations using OpenDSS," 2020 59th Annual Conference of the Society of Instrument and Control Engineers of Japan (SICE),2020

[2] Castillo, Tuesman D., and Maarouf Saad. "Optimal location and size for various renewable distributed generators in distribution networks." 2017 IEEE PES Innovative Smart Grid Technologies Conference-Latin America (ISGT Latin America). IEEE, 2017.

[3] Sain, Christopher G. "An OpenDSS implementation of a generic municipal microgrid for co-simulation." (2019).

[4] Electric Power Research Institute, Inc.2021, Reference Guide:The Open Distribution System Simulator(OpenDSS), Roger C. Dugan,Davis Montenegro

[5] Liang, Cheng, et al. "Analysis of access location and capacity of distributed generation based on OpenDSS." 2018 China International Conference on Electricity Distribution (CICED). IEEE, 2018.

[6] Radatz, P. R. "Modelos avançados de análise de redes elétricas inteligentes utilizando o software OpenDSS." São Paulo (2015).

[7] Ribeiro, Luiz Carlos, et al. "Voltage control simulations in distribution systems with high penetration of PVs using the OpenDSS." 2018 Simposio Brasileiro de Sistemas Eletricos (SBSE). IEEE, 2018.

Etude de la dégradation thermique d'un composite biocompatible en utilisant l'ATG

Rayenne Latoui[*1], Djallel Bouzid[*2], Afif Belhani[*3]

[*] *Laboratoire de génie des procédés pour le développement durable et les produits de santé, Ecole nationale polytechnique de Constantine, Algérie*

[1] *rayenne.latoui@doctorant1.enp-constantine.dz*

[2]bouziddjallel@yahoo.fr

[3]afif.belhani@gmail.com

***Résumé*— Les composites lors de leur présence dans le milieu buccal sont en face de plusieurs facteurs qui stimulent leur dégradation et leur vieillissement. Danc ce travail, il est question d'étudier l'impact de ces facteurs sur la cinétique de dégradation du composite. Les échantillons ont été explorés par analyse thermogravimétrique (ATG) et la cinétique de dégradation a été étudiée. Le modèle optimisé a permis de montrer que l'énergie d'activation globale est influencée par la vitesse de chauffe ainsi qu'elle diffère selon le type du milieu de vieillissement. Cette énergie a tendance à augmenter après extraction des monomères non polymérisés.**

Keywords—composite biocompatible, dégradation thermique, énergie d'activation, photopolymérisation, ATG

I. INTRODUCTION

La photopolymérisation des composites dentaires mène à des conversions limitées des monomères. Les monomères non polymérisés affectent la biocompatibilité du matériau et présentent des dangers pour la santé humaine. L'étude de la dégradation de ces composites et la libération des monomères dans la salive se fait In-Vitro afin d'essayer de simuler le comportement du composite dans le milieu buccal en utilisant un milieu artificiel similaire [1].

II. PARTIE EXPERIMENTALE

A. Matériels

Le composite utilisé est un composite dentaire de la marque NT Premium Enamel B2.

Le tableau 1 représente la composition de la salive artificielle

Composés	C(mM)	V(ml)	Provenance
Acide Citrique	0.002	6	SIGMA-ALDRICH (Spain)
Na_2HPO_4	2.4	100	
KH_2PO_4	2.5	100	
K_2CO_3	1.5	100	AnalaR NORMAPUR (Made in EC-EMB)
$CaCl_2$	1.5	100	
$MgCl_2$	0.15	100	
NaCl	1	100	BIOCHEM (France)

HCL de Honey-well (Germany) pour ajuster le pH, éthanol de Sigma-aldrich (Germany), eau distillée (H2O) préparer au laboratoire par un système de distillation.

B. Préparation des specimens

Des spécimens cylindriques de 5mm de diamètre et 2mm d'épaisseur du composite commercial sont préparés à l'aide d'un moule préfabriqué en téflon et polymérisés pendant 40s à l'aide d'une lampe dentaire LED "eighteeth". Les spécimens polymérisés sont ensuite rincés avec de l'éthanol puis sont plongés dans 1ml du milieu de vieillissement [2] dans une vial de 2ml. A la suite, les vials sont incubées dans l'étuve à la température 37°C qui correspond à la température du corps humain pendant 7 jours.

C. Technique d'analyse

L'analyse thermogravimétrique ATG, est une méthode d'analyse thermique qui mesure la vitesse et la quantité de la perte en masse des échantillons en fonction de la température et le temps sous une variation de vitesse constante appelée vitesse de chauffe. Cette analyse permet de connaitre l'état de la stabilité thermique des échantillons [3]. Les échantillons du composite sont soumis à l'analyse sous trois vitesses de chauffe 5, 10, 20 °C/min, allant de la température ambiante 25°C jusqu'à 600°C [2].

D. Modélisation de la cinétique de dégradation

L'équation cinétique de la dégradation est équivalente à celle de la cinétique chimique : $d\alpha/dt = k.f(\alpha)$

Tel que: $f(\alpha)$ est le modèle cinétique,

k est la constante de vitesse obtenue par la loi d'Arrhenius :

$k = A.\exp(-Ea/RT)$

α représente le taux de masse que l'échantillon a perdu durant la thermogravimétrie : $\alpha = (W_i - W_t)/W_i$, avec Wi est la masse initiale, Wt est la masse finale.

La méthode utilisée pour calculer les paramètres cinétiques est appelée la méthode du "Model Fitting", c'est une approche qui consiste au développement de l'équation de sestak-Beggren : $f(\alpha)=c(1-\alpha)^n\alpha^m$. L'injection de cette équation dans l'équation de la cinétique de dégradation nous donne après plusieursmanipulations l'équation suivante :

ln (dα/dt / (1 − α) $^{n}\alpha^{m}$) = ln cA –(Ea/R) * (1/T), cette équation est une droite dont les constantes n et m sont des inconnues. *Un programme MATLAB est établi afin d'optimiser le coefficient de corrélation (r) de la droite présente dans l'équation pour trouver n et m qui donne le coefficient le plus proche de 1[4].*

III. Résultats

A. Analyse thermogravimétrique ATG

Cette analyse est réalisée sur deux échantillons qui ont subi différentes conditions de vieillissement mais qui ont présenté le plus de libération de monomère. Ces échantillons sont CPE37-7 (solution éthanol/eau 75%) et CP0337-7 (Salive artificielle à pH=3.5) incubées pendant 7 jrs à 37°C. Un échantillon non dégradé) est lui aussi analysé par ATG.

Le diagramme de la perte de masse de l'échantillon CPE37-7 en fonction de la température pour les trois vitesses de chauffe est illustré dans la figure 1. Ce diagramme contient trois zones de dégradation.

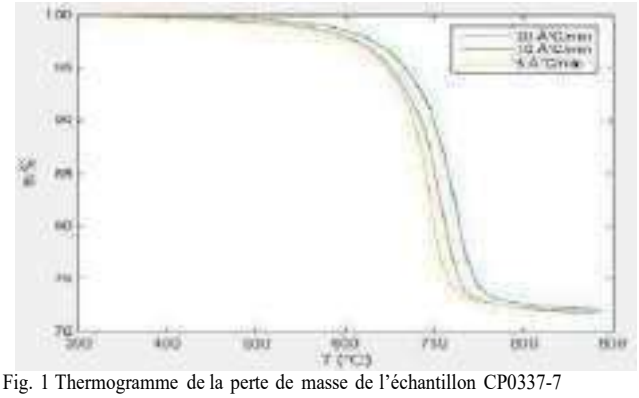

Fig. 1 Thermogramme de la perte de masse de l'échantillon CP0337-7

B. Modélisation de la cinétique de dégradation

L'exécution du programme MATLAB avec les données des analyses ATG, donne les constantes du modèle cinétique ainsi que l'énergie d'activation. La figure 2 illustre la régression des données de dégradation par le modèle cinétique établie de l'échantillon CP0337-7 pour les différentes vitesses de chauffe.

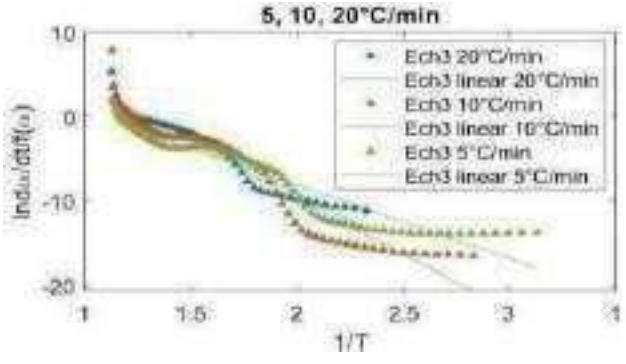

Fig. 2 L'établissement du modèle cinétique pour l'échantillon CP0337-7

Le tableau 1 résume les résultats trouvés pour chaque échantillon sous les trois vitesses de chauffe.

On observe que le coefficient de corrélation est élevé. Ce qui révèle que le modèle cinétique est validé pour les valeurs n et m trouvés.

TABLEAU I
RESULTATS DU CALCUL DES COEFFFFICIENTS N ET M QUI DEFINISSENT LE MODELE CINETIQUE LINEAIRE

Echantillons	Vitesse de chauffe	n	m	r	Ea(kj)
CP0000-0	20	-0.8591	1.7406	0.9776	113.02
	10	-5.5048	1.1683	0.9579	119.60
	5	1.7167	2.307	0.9628	65.38
CP0337-7	20	-5.7361	2.0127	0.9748	106.43
	10	-20.481	1.9014	0.9607	109.43
	5	-12.199	1.8213	0.9557	71.65
CPE37-7	20	-49.944	1.2103	0.9523	221.92
	10	-29.38	1.8548	0.9584	111.33
	5	-19.220	2.0572	0.9524	85.03

IV. Discussion

Pour les énergies d'activation, Il est clair que pour les vitesses de chauffes élevée (10 et 20°C/min), les valeurs de l'énergie d'activation se rapproches. Cela est le résultat du fait de la grande vitesse de chauffe qui empêche les échantillons de prendre le temps nécessaire pour se dégrader afin de révéler l'histoire du matériau. Donc pour des vitesses de chauffes très grande, l'énergie d'activation est influencée par la vitesse de chauffe et non pas par l'histoire du vieillissement de l'échantillon, ce qui explique les valeurs proches des énergies d'activation des grandes vitesses.

Pour cette raison, l'énergie d'activation et les coefficients n et m retenus pour la modélisation de la cinétique de dégradation sont ceux de la vitesse de chauffe de 5°C/min.

Le modèle cinétique de dégradation dans la salive :

$$\ln (d\alpha/dt / (1-\alpha)^{-12,1993}\alpha^{1,8213)} = 9.0936 - 8616.771*(1/T)$$

V. Conclusion

La cinétique de dégradation peut être déterminée par une méthode de modélisation qui permet l'obtention du triplet cinétique. Le modèle optimisé a permis de montrer que l'énergie d'activation globale est influencée par la vitesse de chauffe ainsi qu'elle diffère selon le type du milieu de vieillissement.

References

[1] Inas Mohammed and Zahraa Nazar Alwahab. A comparison of the effect of artificial saliva with different ph values on surface roughness of veneering ceramic to metal and zirconia substructure (in vitro study). 2018.

[2] Dimitris S Achilias, Maria M Karabela, and Irini D Sideridou. Thermal degradation of light-cured dimethacrylate resins: Part i. isoconversional kinetic analysis. Thermochimica Acta, 472(1-2) :74–83, 2008.

[3] M. Benhamada, D. Bouzid, O. Saouli, and O. Boyron. The effects of hydrothermal aging characterized by sec on the degradation kinetic of polycarbonate calculated through tga.
[4] Malika BENHAMADA. Etude de la migration du Bisphénol A des matériaux plastiques alimentaires. PhD thesis, Constantine 3, 2015.

Dihydrogen Storage in Novel $(C_nGe_n)_2$ Nanostructures: Theoretical Study at Density Functional Theory (DFT) Level

Djamila Sellam[##], Moumena Elkebich[#], Yassamina Arbia [#] and Meziane Brahimi [#1]

[#]*Laboratoire de Physico Chimie Théorique et Chimie Informatique (LPCTCI), Université des Sciences et de la Technologie Houari Boumediene (USTHB). BP N° 32 Al alia, 16111, Alger. Algérie.*

[##] *Laboratoire de Chimie Appliqué et Génie Chimique, Université MM Tizi Ouzou, Algérie*

[1]mez_brahimi@yahoo.fr;

Abstract.

The major issue of the substitution of fossil energies is, by far, the storage of solid-state hydrogen-molecular under standard conditions of pressure and temperature (P, T). The solid-state of Dihydrogen can only be obtained at very low temperatures with more than 1.5 million atmospheres. These conditions, draconian are harmful to the economic and safe use of hydrogen, even if several researches speak about solid hydrogen which is in fact only hydrogen adsorbed or absorbed on metallic surfaces or other. The objective of this research is to find new nanostructures with cages form that are able to confine a larger number of hydrogen molecules, under standard conditions of (P, T), which probably would allow as suggesting the geometry of the unit cell of solid hydrogen under standard conditions of (P, T). For this purpose, we use the density functional theory (DFT) method with the B3LYP and ωB97XD functional with the 6-31+G* basis. The calculations of energies formation, IR spectra, the shape of the Molecular Orbitals Frontiers (MOF) and the Energy Gap will be done at theoretical level.

Keywords: New cage structure $(C_nGe_n)2$, DFT, Dihydrogen Solid-State, Hydrogen-Molecule Storage.

Introduction

Fossil energy has received growing interest during the last ten decades because of its advantageous characteristics. Unfortunately, fossil energy is very polluting and non-renewable [1]. The oil crisis of 1973 has considerably directed the search for new alternatives to fossil energy. Thus, Dihydrogen has become a strategic energy issue, it is, today, a credible alternative to fossil fuels such as oil or gas. For the same quantity, Dihydrogen has a higher thermodynamic density than conventional fossil fuels [2] (one kg of hydrogen contains as much energy as about 3 kg of oil), but the energy cost of hydrogen is estimated to be 2.9 times that of hydrocarbons, without taking into account the polluting effect of the latter [3]. However, it presents several challenges to its massive use, among which we can note (i) high energy consumption in its extraction and processing, (ii) difficulty to store, (iii) unstable and easily flammable. These three major constraints make this fuel dangerous and difficult to exploit. The ultimate goal is to use green, non-polluting Dihydrogen from solar energy as an ideal solution [1, 2]. In the meantime, the best solution would be solid Dihydrogen [4], which is obtained at a temperature of 120K and a pressure of about 1.5 million atmospheres. It becomes the only alternative to its exploitation and uses at a large scale [5]. The storage in the solid form of Dihydrogen is possible through two different processes, adsorption [6] and absorption [7]. In both cases, to say that hydrogen is in solid form is a misnomer. In reality, the hydrogen molecules in the gaseous state are absorbed or adsorbed by a material that is in solid form.

In this work, we propose another alternative to the storage of Dihydrogen inside new nanostructures (in cage form) formed from an assembly of carbon and germanium atoms. The study was done using the density functional theory (DFT) level with the B3LYP [8], and ωB97XD [9] functionals that uses a version of Grimme's D2 dispersion model and the 6-31G* basis.

Theoretical Methodology

The software package used to performed calculations was Gaussian 09 [10]. Geometry optimizations and property calculations on $\mathbf{(C_nGe_n)_2}$ (n = 6, 7, and 8) and $\mathbf{(C_nGe_n)_2@mH_2}$ (m = 2, and 3) structures were carried out with B3LYP non-local

hybrid functional [**8**], which is reported to be quite reliable in describing Potential Energy Surface (**PES**) of similar structures [**11**]. Symmetry constraint was not imposed during the geometry optimization. All stationary points were confirmed through calculations on the involved cage structure using DFT/B3LYP and ωB97XD [**9**] with 6-31+G* basis sets with all normal mode of vibration are real.

The highest occupied molecular orbital (HOMO) and lowest unoccupied molecular orbital (LUMO) are the principal orbital taking part in chemical stability and chemical reaction. HOMO and LUMO energies represent the ability to give and receive an electron, respectively. They are directly related to the electron affinity (EA) and the ionization potential (IP) [**12**]. The difference between LUMO and HOMO energies is a gap energy $\Delta E = |E_{LUMO} - E_{HOMO}|$. Atomic Polarizability Tensor (APT) is interpreted as sum of the charge tensor and charge flux tensor, leading to charge-charge flux model [**13**].

On the other hand, the formation energy E_F [**14**] of $(C_6Ge_6)_2$ cage structures was also calculated as defined in the following equation:

$$E_F = E_T - n_{Ge} \cdot E_{Ge} - n_C \cdot E_C \qquad (1)$$

where: E_T is the total energy of cages molecules. n_{Ge}, and n_C are the numbers of Ge, and C atoms, respectively. E_{Ge}, and E_C are the energies, determined at the same level of theory, of an isolated Ge, and C atom, respectively. In all cases, we considered the Zero-Point Energy Correction (ZPEC) [**15**].

Results and discussion

Structural studies

Many authors have synthesized and studied theoretically new molecular structures and nanostructure able to adsorb or absorb one or more hydrogen molecules [**16**]. In this context, we propose new molecules with cage form which are formed by the combination of carbon and germanium atoms (see Figure **1**) where calculation of the formation energies, using the relation (1) leads to strong negative values for the species $(C_nGe_n)_2$ (n = 6, 7 and 8). The values are equal, respectively, for $(C_6Ge_6)_2$ to - 3413kcal/mol, at the level B3LYP/6-31+G*, we find the same order of magnitude with the functional ωB97XD/6-31+G* which takes into account the dispersion energies as defined by S. Grimme [**9**]. The $(C_6Ge_6)_2$ species is formed by 30 bonds (12 CC, 12 CGe, and 6 GeGe bonds), if these latter are identical, the average energy per bond would be around -114kcal/mol. This is lower than that in H_2 (-104 kcal/mol). This new structure would be stable and could be synthesized experimentally.

The optimization of the geometries, without constraints on symmetries, leads to normal modes of vibration which are all real. The stable molecular geometries are given in Figure **1**. The structure of $(C_8Ge_8)_2$ is slightly flattened.

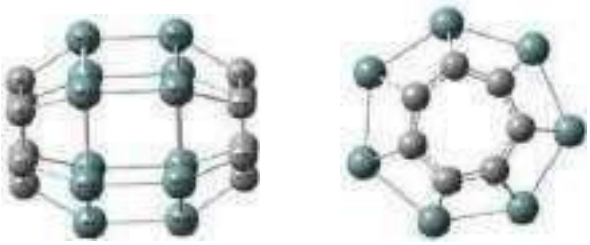

(a) : $(C_6Ge_6)_2$ **(b) : $(C_7Ge_7)_2$**

$E_{elc+ZPEC}$ = -25261.186535 - 29471.336059 u.a

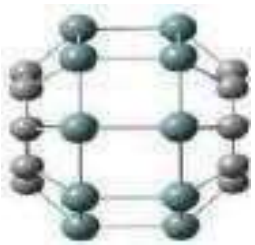

(c) : $(C_8Ge_8)_2$

$E_{elc+ZPEC}$ = -33681.525418 u.a

Figure 1: Optimized geometry of $(C_nGe_n)_2$ (n = 6, 7 et 8) species with sum of electronic energies and Zero point energy Correction (ZPEC) [**15**]

Both of cage structures have zero dipole moments, with all C and Ge atoms hybridized in sp^3 with the respective carbon and germaniumatoms are in the same plane as if they were hybridized in sp^2. This aspect, of hybridization of the C and Ge atom, is discussed by Elkebich et al [**17**].

These new structures, with form of cage, can confine Dihydrogen at room pressure and temperature. Indeed, the complete geometry optimization (without symmetry constraints) of the $(C_nGe_n)_2@mH_2$ species

with (n = 6, 7, 8 and m = 2, 3), lead to optimal geometries with all the normal modes of vibration being real. The geometry of the $(C_6Ge_6)_2@mH_2$ species (m = 2 and 3) are showing in Figure 2. The energy dispersion decreases with increasing of the confined hydrogen molecules number. The difference between $(C_6Ge_6)_2@2H_2$ (- 43.77kcal/mol) and $(C_6Ge_6)_2$ (- 35.02kcal/mol) is equal to - 8.75kcal/mol. The same tendency is observed for the tree confined molecules in the $(C_6Ge_6)_2@3H_2$ species.

The species $(C_nGe_n)_2@mH_2$ (n = 7, 8 and m = 2 and 3) lead to the same results.

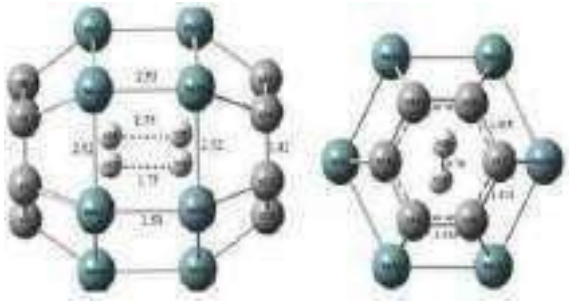

$(C_6Ge_6)_2@2H_2$

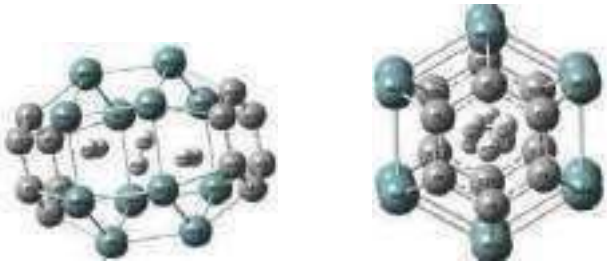

(a) **(b)**

$(C_6Ge_6)_2@3H_2$

Figure 2: optimized species $(C_6Ge_6)_2@mH_2$ (m = 2 et 3) with **(a) =** profile view**; (b):** axial view.

The H_2 molecule is not active in IR. In the $(C_6Ge_6)_2@2H_2$ complex, hydrogen becomes active in IR like in germanium and carbon nanotubes [18]. The characteristic frequencies of the IR spectrum of this complex (see Figure 3) are reported in table 1 with the corresponding intensities. The most intense frequencies correspond to the symmetrical displacement in the same direction of the four hydrogens.

Table 1: IR-vector and characteristic frequencies

IR Vector Displacement	Wave number in cm^{-1}	IR intensity
	459	118
	851	116
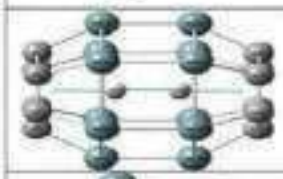	1467	2.8
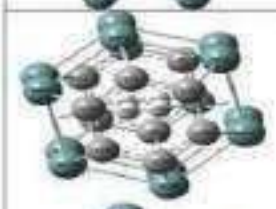	3810	31.5
	3912	0.004

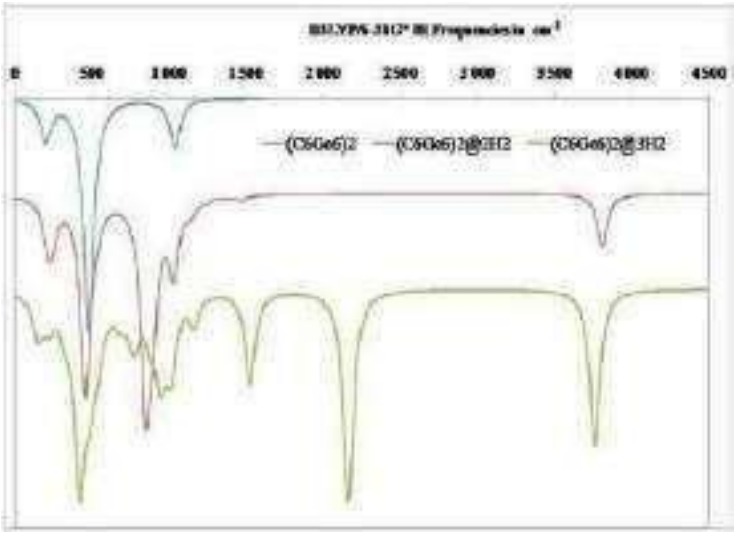

Figure 3: IR spectral of **$(C_6Ge_6)_2$@mH_2** (m = 0(**blue**), 2 (**red**), 3(**green**)), obtained at B3LYP/6-31+G* level. For more clarity, the area under the peaks is multiplied by 10.

The frequency at 480 ($0H_2$), 459($2H_2$) and 453($3H_2$) cm^{-1} appears for all species. This frequency varies in the opposite direction of the increasing number of confined hydrogen molecules. The number of frequencies involving the hydrogen molecules increases as the number of these molecules increases. A normal mode of vibration characteristic of the presence of $_a2H_3$ (antisymmetric elongation of the two bonds H-H, $_{H\text{-}H}$) appears at 3810 cm^{-1}. For the species $(C_6Ge_6)_2@_3H_2$, two other normal modes of vibration, correspond respectively to the symmetrical elongation of the two extreme hydrogen molecules at 2163 cm^{-1} and an antisymmetrical at 1528 cm^{-1}. The examination of the shape of the IR spectra of figure 3 indicates if the cage is occupied by one, two, or more molecules of hydrogen.

The confined hydrogen becomes active in IR because of the APT charges [13] that appear in the **$(C_6Ge_6)_2$@mH_2** complex (see Figure 4) and because of the interlocking Van der Waals radii of the different atoms of the complex (see Figure 5).

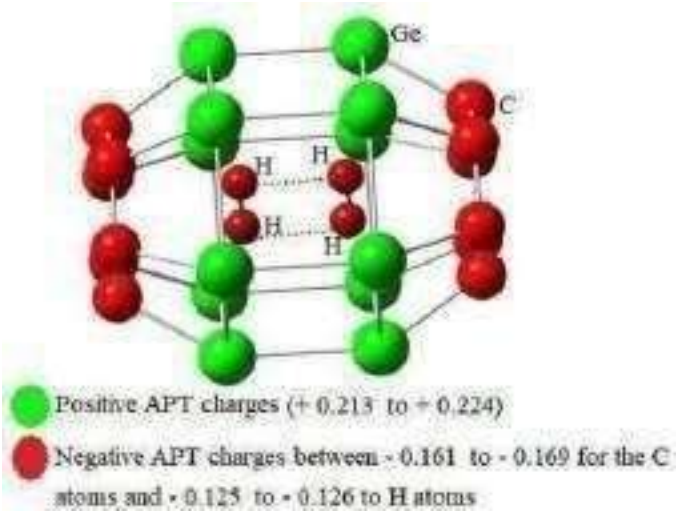

Figure 4: APT Charges of **$(C_6Ge_6)_2$@2H_2.**

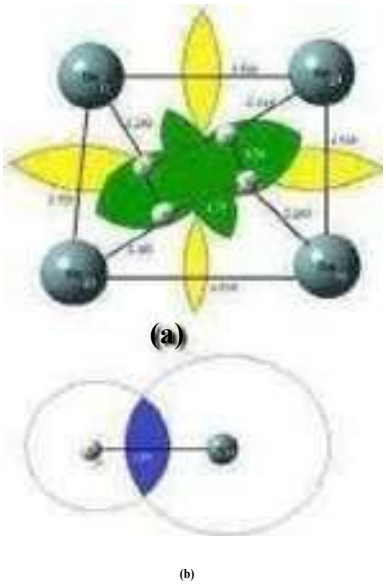

Figure 5: Van der Waals overlap, **(a)** in yellow between the germanium atoms, and green between the hydrogen atoms ; **(b)** between the germanium atom 19, and the hydrogen atom 25. The Van der Waals radii of different atoms are:

$R^{H}_{VdW} = 1.20$ Å; $R^{C}_{VdW} = 1.70$ Å; $R^{Ge}_{VdW} = 2.11$ Å.

The $2H_2$ complex confined in **$(C_6Ge_6)_2$** is located in the middle of the cage. It is centred compared to the benzene and with an angle of 25 degrees between the two planes carrying respectively the atoms of germanium (8, 11, 24, and 21) and hydrogen (25, 26, 27, and 28) (see Figure 6. When we optimize this one, in the isolated state, at the same level of theory, it does not correspond to a minimum of energy. The two hydrogen molecules move away from each other.

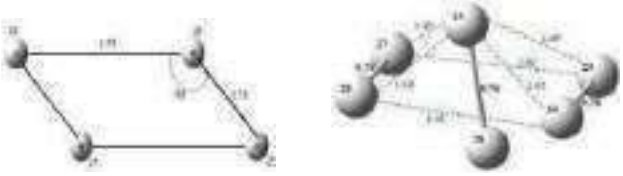

(a) **(b)**

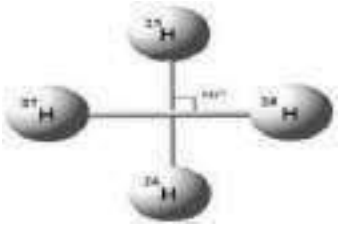

(c)

Figure 6: (a) $2H_2$ geometry complex in **$(C_6Ge_6)_2@2H_2$**, and **$3H_2$** in**$(C_6Ge_6)_2@3H_2$. (b)** profile view were the atom number (27, 28, 29 et 30) are in the same plane, and **(c)** front view were the atom number (25 et 26) are in the plane which is perpendicular to the first one.

When a third hydrogen molecule is introduced into $(C_6Ge_6)_2$, these are placed as shown in figure 2. The $3H_2$ complex, formed inside the cage, is given in Figure 6 (b and c).

The molecule H_{25}-H_{26} with a distance of 0.76 Å is located in a plane that is perpendicular to the one that carries the two molecules H_{27}-H_{28} and H_{29}-H_{30}. The whole forms a bipyramidal geometry with an asymmetric square base, the distances (25, 27) and (25, 29) (1.49 Å) are different from (25, 29) and (25, 30) (1.62 Å).

When we optimize the $3H_2$ complex in the isolated state, it dislocates, showing that its stability is due to the confinement in the new proposed cage structures. We observe the same conclusions when the size of the cages increases. On the other hand, the number of confined Dihydrogen molecules increases with the size of the cages. The **$(C_6Ge_6)_2$** cage can contain $3H_2$, **$(C_7Ge_7)_2$** can easily contain $4H_2$, and **$(C_8Ge_8)_2$** can contain up to $6H_2$.

Molecular Orbital Frontiers (MOF).

If we look closely the Molecular Orbitals Frontiers (MOF) which are plotted in Figure 7, we note that for all cages, with a pair number of C and Ge atoms, the HOMO is essentially localized on the bonds while the LUMO is localized on the atoms. For the structure **$(C_7Ge_7)_2$**, with an odd number of C and Ge atoms, we have the opposite.

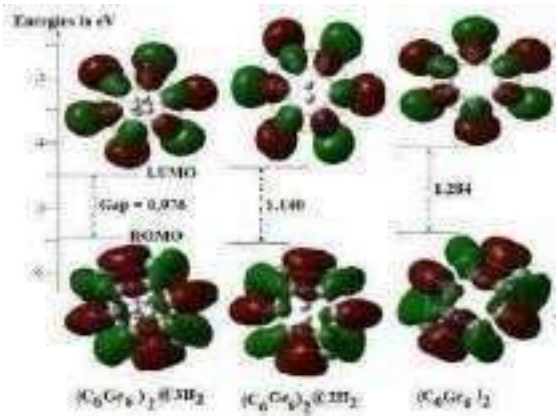

Figure 7: MOF and Gap energies of **$(C_6Ge_6)_2$.**

The different forms of the MOFs of **$(C_6Ge_6)_2@mH_2$** species (m =0, 2, 3) are plotted in Figure 7. The form of the MOFs, with the mH_2 molecules confined, remains the same as for the empty cages. The only change is the volume of the OMFs which become more noticeable that do not involve the confined hydrogen molecules. We obtain the same tendency for the species **$(C_7Ge_7)_2@mH_2$** and **$(C_8Ge_8)_2@mH_2$**.

Conclusion.

The present theoretical study, conducted at the level of density functional theory with the B3LYP and ωB97xp functionals using the 6-31+G* basis, allows us to argue that the species **$(C_nGe_n)_2$** with n = 6, 7, and 8 are, on the one hand, stable and therefore likely to exist or to be synthesized. On the other hand, they are potential candidates for the storage of dihydrogen under standard conditions of pressure and temperature. The mH_2 complexes (m = 2, 3) confined inside **$(C_nGe_n)_2$** are stable and can be highlighted by IR spectroscopy with different characteristic frequencies (see Table 1 and Figure 3). The $2H_2$ complex adopts a planar geometry (see Figure 6a) whereas $3H_2$ adopts a bipyramidal geometry with a square base where two molecules the two (extreme) molecules are in the same plane and the third is between the first two in a plane perpendicular to the first one (see Figure 6b and 6c). This last geometrical arrangement (bipyramid with square base) of the three molecules of hydrogen constitutes, in our opinion, the unit cell of solid hydrogen at standard pressure and temperature. The IR spectrum also allows us to know if one or more hydrogen molecules are

confined in the new structures that we propose (see Table 1 and Figure 3).

References.

[1] Veziroglu T N. International Journal of Hydrogen Energy **1987**; 12:99 INSPEC Compendex.

[2] M. Momirlan, T N. Veziroglu / Renewable and ustainable Energy Reviews 6 (2002) 141–179.

[3] Peter P. Edwards, Friedrich Hensel, 1997 Nature, 388 621-621, https://doi.org/10.1038/41645

[4] Grez J. Hydrogen energy systems. In: Yurum Y, editor. Production and utilization of hydrogen and future aspects. NATO ASI Series, Serie E: Applied Sciences—Vol.295;83.

[5] Muhammad Sad Salman, Nigel Rambhujun, chulaluck Pratthana, Qiwen Lai, Prabal sapkota, Kondo-François Aguey-Zinsou, Nano Tools ans Devices for Enhanced Renewable Energy, Micro and Nano Technologies, 2021, pages 263-287, https://doi.org/10.1016/B978-0-12-821709-2.00020-7.

[6]a- Jain, V., Kandasubramanian, B. Functionalized graphene materials for hydrogen storage. *J. Mater. Sci.* **55**, 1865–1903 (2020). https://doi.org/10.1007/s10853-019-04150-y

b- L. J. Bannenberg, M. Heere, H. Benzidi, J. Montero, E. M. Dematteis et al., 2020 Int. J. Hydrogen Energy, 45(58): 33687-33730. https://doi.org/10.1016/j.ijhydene.2020.08.119

c- D. P. Broom, C. J. Webb, K. E. Hurst, P. A. Parilla, T. Gennett et al. 2016 *Appl. Phys. A* **122**, 151. https://doi.org/10.1007/s00339-016-9651-4

[7] a- Jutao Hu, Jinjing Zhang, Haiyan Xiao, Lei Xie, Huahai Shen et al. 2020 *Inorg. Chem.*, 59, 14, 9774–9782. https://doi.org/10.1021/acs.inorgchem.0c00989

b- Zhao Ding, Hao Li, Leon Shaw, 2020 Chemical Engineering Journal, 385, 123856. https://doi.org/10.1016/j.cej.2019.123856

c- Swaraj D. Lewis, Purushothama Chippar, 2020 Energy, 194: 116942, https://doi.org/10.1016/j.energy.2020.116942

*[8]*a- A. D. Becke (1988). "Density-functional exchange-energy approximation with correct asymptotic behavior". Phys. Rev. A. **38** (6): 3098–3100. *doi:10.1103/PhysRevA.38.3098*

b- K. Kim; K. D. Jordan (1994). "Comparison of Density Functional and MP2 Calculations on the Water Monomer and Dimer". J. Phys. Chem. **98** (40): 10089–10094. *doi:10.1021/j100091a024*

c- P. J. Stephens; F. J. Devlin; C. F. Chabalowski; M. J. Frisch (1994). "Ab Initio Calculation of Vibrational Absorption and Circular Dichroism Spectra Using Density Functional Force Fields". J. Phys. Chem. **98** (45): 11623–11627. *doi:10.1021/j100096a001*

d- *C. J. Cramer (2004).* "Essentials of Computational Chemistry: Theories and Models, 2nd Edition | Wiley". *Wiley.com*. Retrieved 2021-06-24.

[9] T. Yanai, D. P. Tew, N. C. Handy, A new hybrid exchange-correlation functional using the Coulomb-attenuated method (CAM-B3LYP). Chem. Phys. Lett. 393 (2004) 51-57. https://doi.org/10.1016/j.cplett.2004.06.011

[10] Gaussian 09, Revision A.02, M. J. Frisch, G. W. Trucks, H. B. Schlegel, G. E. Scuseria, M. A. Robb, J. R. Cheeseman, G. Scalmani, V. Barone, G. A. Petersson, H. Nakatsuji, X. Li, M. Caricato, A. Marenich, J. Bloino, B. G. Janesko, R. Gomperts, B. Mennucci, H. P. Hratchian, J. V. Ortiz, A. F. Izmaylov, J. L. Sonnenberg, D. Williams-Young, F. Ding, F. Lipparini, F. Egidi, J. Goings, B. Peng, A. Petrone, T. Henderson, D. Ranasinghe, V. G. Zakrzewski, J. Gao, N. Rega, G. Zheng, W. Liang, M. Hada, M. Ehara, K. Toyota, R. Fukuda, J. Hasegawa, M. Ishida, T. Nakajima, Y. Honda, O. Kitao, H. Nakai, T. Vreven, K. Throssell, J. A. Montgomery, Jr., J. E. Peralta, F. Ogliaro, M. Bearpark, J. J. Heyd, E. Brothers, K. N. Kudin, V. N. Staroverov, T. Keith, R. Kobayashi, J. Normand, K. Raghavachari, A. Rendell, J. C. Burant, S. S. Iyengar, J. Tomasi, M. Cossi, J. M. Millam, M. Klene, C. Adamo, R. Cammi, J. W. Ochterski, R. L. Martin, K. Morokuma, O. Farkas, J. B. Foresman, and D. J. Fox, Gaussian, Inc., Wallingford CT, 2016.

[11] Chattaraj P K, Sarkar U et Roy D R 2006 *Chem.* **Rev.106 2065.**

[12] Zeyrek C T, Unver H, Arpacı Ö T, Polat K, İskeleli N O et Yildiz M 2015*J. Mol. Struct.* **108**122.

[13] Yadav RA, Rashmi Singh, Mayuri Srivstava, 215 Pharmaceutica Analytica Acta, 6:9; 2-16. DOI: 10.4172/2153-2435.1000419

[14] Kassaee M Z et Aref Rad H 2010*Comput. Mater. Sci.* **48**144.

[15] Kin-Yiu Wong and Jiali Gao, 2009 J. Chem. Theory. Comput. 2008 Sep 9; 4(9): 1409–1422. https://doi.org/10.1021/ct800109s

[16] a- kaiji Ucida, Naoki Kishimoto, Shin-ichiro Noro, Hiroaki Iguch, Shinya Takaishi, 2021 Dalton Transaction, 50: 12630-12634.

https://doi.org/10.1039/D1DT01404H
b- Romit Chakraborty, Kurtis M. Carsch, David E. Jaramillo, Yuto Yabuuchi, Hiroyasu Furukawa, Jeffrey R. Long, Martin Head-Gordon. 2022, J. Phys. Chem. Lett. 2022, 13, 44, 10471–10478.
https://doi.org/10.1021/acs.jpclett.2c02844
c- Ke Wang, Wei Chen, Lu Li, 2022, Renewable Energy 187: 1118-1129.
https://doi.org/10.1016/j.renene.2022.01.119
d- Kangkan Sarmah, Shahnaz S. rohman, Siddhartha K. Purkayastha, Amlan J. Kalita, Ankur K. Guha, 2022, Phys. Chem. Chem.. Phys. Advance Article.
https://doi.org/10.1039/D2CP04443A
e- G. Siviero, V. Bello, G. Mattei, P. Mazzoli, G. Battaglin, R. Checchetto et al. 2009, International Journal of Hydrogen Energy, 34 :4817-48-26.
https://doi.org/10.1016/j.ijhydene.2009.03.059

[17] M. Elkebich, S. Zaater, S. Abtouche, M. Brahimi, 2020, Bull. Mater. Sci. 43: 160.
https://doi.org/10.1007/s12034-020-02131-5

[18] a- Djitli W., Abdelatif M. L., Belmiloud Y., Abdeldjebar H., Brahimi M., Tangour B., 2018 Superlattices and Microstructures, 122: 596-607.
https://doi.org/10.1016/j.spmi.2018.06.040
b- W. F. Gtari, B. Tangour, A Theoretical Study of the Dihydrogen Molecule Confined Inside Carbon Nanotubes International Journal of Quantum Chemistry 2013, 113, 2397–2404.
https://doi.org/10.1002/qua.24474

On the advantages of MOS-PHEMT in comparison to PHEMT

Hamida Djelti[#1], Fayza Bousalah[*2], Yamina Belhadef[*3], Mounir Khelladi[*4]

[#]*STIC laboratory, Department of Telecommunication, University Abou Bekr Belkaid of Tlemcen*
Faculty of Technology, University of Tlemcen, BP 230 Tlemcen, Algeria
[1]hamida.djelti@univ-tlemcen.dz

[*] *Department of Telecommunication, Faculty of Technology, University Abou Bekr Belkaid of Tlemcen*
[2]bousalah.fayza@gmail.com
[3]belhadef@yahoo.fr
[4]mo.khelladi@gmail.com

***Abstract*— In this paper, we study, by means of numerical simulation the DC and the RF performance of both Pseudomorphic High Electron Mobility Transistor and Metal–Oxide–Semiconductor Pseudomorphic High Electron Mobility Transistor in the context of the out-put characteristics and the cut-off frequency.**

The devices grown on a GaAs substrates with a gate length of 1 μm and a gate periphery of 100 μm exhibits a maximum DC drain current density of 140 mA/mm (PHEMT) and of 170 mA/mm (MOS-PHEMT) at Vgs = 6 V. The DC performance is comparable to state-of-the art AlGaAs/GaAs PHEMT and TiO_2/AlGaAs/GaAs MOS-PHEMT. The use of high-*k* dielectrics on the electrical characteristics of the MOS-PHEMT has been examined. Compared with the PHEMT transistor of a similar geometry, MOS-PHEMT presents a large maximal gate voltage, a higher breakdown voltage, and alsoa high cut-off frequency.

***Keywords*— PHEMT, MOS-PHEMT, TiO2, AlGaAs/GaAs**

I. INTRODUCTION

GaAs-based high-electron mobility transistors (HEMTs) and pseudomorphic HEMT (PHEMTs) are rapidly replacing conventional MESFET technology in many applications such as military, commercial and wireless communications applications requiring low noise figures and high gain, particularly at microwave and millimeter-wave frequencies [1-4]. One critical issue limiting the RF power performance is the device degradation, primarily caused by high gate leakage current [5-7].

In order to inhibit the gate leakage issue, increase the power handling capabilities, and improve the breakdown voltages, a metal-oxide-semiconductor (MOS) structure has been widely investigated. In addition, the MOS-PHEMT not only has the advantages of the MOS structure such as lower gate leakage current [8] and higher breakdown voltage but also has the high-density, high-mobility 2DEG channel due to the wide bandgap of the oxide (or dielectric) and the high conduction band offset at oxide/semiconductor interface [9]. The dielectric was also used to cover the bare surface between the MOS-PHEMT contacts. Various dielectric materials were tried for gate insulator, such as SiO [10, 11], SiNx [12], Al_2O_3 [13,14], HfO$_2$ [15,16,17], ZrO$_2$ [18], and La_2O_3 [19-21]. Also, titanium dioxide (TiO_2) is one of the commonly applied high-k insulators in the semiconductor industry. Until now, there have been many reports on the DC and RF performances of PHEMTs applications [22-24]. However, there have been few reports on the TiO_2/$Al_{0.2}Ga_{0.8}As$/$In_{0.15}Ga_{0.85}As$ MOS-PHEMT.

In the previous work, AlGaAs/InGaAs/GaAs MOS-PHEMTs with Al_2O_3 as a gate dielectric oxide showed larger gate swing voltage, lower gate leakage current, higher breakdown voltage, higher drain current density, and maximum extrinsic transconductance compared to conventional AlGaAs/InGaAs PHEMTs [8]. We propose a comparisons between $Al_{0.2}Ga_{0.8}As$/$In_{0.15}Ga_{0.85}As$ PHEMT and TiO_2/$Al_{0.2}Ga_{0.8}As$/$In_{0.15}Ga_{0.85}As$ MOS-PHEMT, we address the relative merits of each technology.

The following section shows the devices structures of this work. Section III and IV show the simulation results and conclusion.

II. DEVICES STRUCTURES

The PHEMT and MOS-PHEMTs DC and AC characteristics were analysed and simulated using a Drift-Diffusion transport model of industry standard software ATLAS from SILVACO [25], along with the devices dimensions and material of various layers used is presented in Fig. 1.

The proposed structure of the MOSHEMT has been simulated on an ATLAS TCAD device simulator and the simulated results show a significant change in drain current, shift in threshold voltage.

The structures are fabricated and reported by Kai-Yuen Lam and al [4], the gate length of both simulated MOS-PHEMT and PHEMT is 1 µm, the structure consists of GaAs substrate, an i-GaAs buffer layer with a thickness of 100 nm, followed by a 250 nm layer of *i*-$Al_{0.2}Ga_{0.8}As$, and a 60 nm layer of GaAs. A 10 nm layer of $Al_{0.2}Ga_{0.8}As$ with a Si doping density of 4.5×10^{17} cm^{-3} and a 2 nm *i*-$Al_{0.2}Ga_{0.8}As$ spacer layer were then grown on the buffer layer, followed bya 14 nm *i*-$In_{0.15}Ga_{0.85}As$ channel layer, a 2 nm *i*-$Al_{0.2}Ga_{0.8}As$ spacer layer, a 18 nm $Al_{0.2}Ga_{0.8}As$ donor layer with a Si doping density of $\times 10$ cm , a 70 nm $Al_{0.2}Ga_{0.8}As$ Schottky layer with a Si doping densityof 1×10 cm , and a 60 nm GaAs cap layer

with a Si doping density of 5×10^{18} cm^{-3}. The electron sheet density was 2.1×10^{12} cm^{-2} at room temperature. For MOS-PHEMT, the oxide (TiO_2) thickness is 30 nm. The gate-source and the gate-drain spacingare 2 µm.

(a)

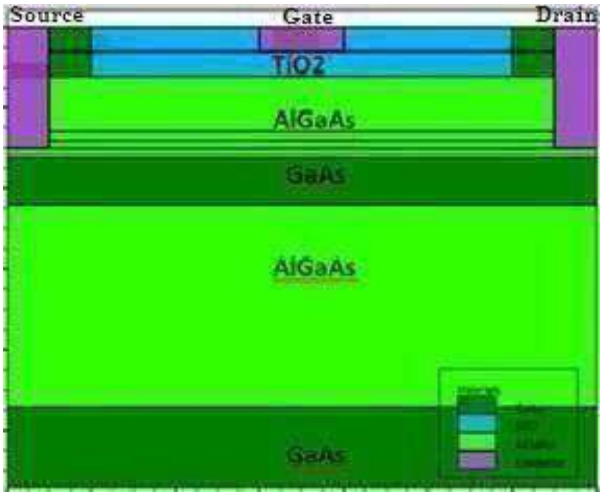

(b)

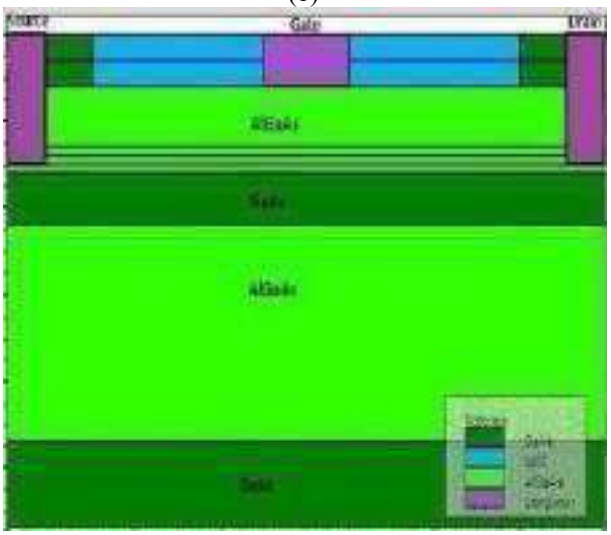

Fig. 1 Cross section simulated of (a) $TiO_2/Al_{0.2}$ $Ga_{0.8}As/In_{0.15}Ga_{0.85}As$ MOS-PHEMT and (b) $Al_{0.2}$ $Ga_{0.8}As/In_{0.15}Ga_{0.85}As$ PHEMT.

III. Results and Analysis

Fig. 2 compares the simulated I-V characteristics of the both MOS-PHEMT (solid line) and PHEMT (dotted line). Clearly, good pinch-off and saturation current characteristics are obtained. Due to the higher energy barriers between the metal gate and the Schottky layer, the MOS-PHEMT can be operated at higher gate-to source voltage and drain-to-source voltage than those of the conventional Schottky gate PHEMT, which can enhance the current driving capability. So the drain current density of the PHEMT is smaller than that of the MOS-PHEMT at the same bias Vgs due to the decrease of the carrier concentration within the AlGaAs 2DEG channel. The peak drain current for MOS-PHEMT and PHEMT were 170 mA/mm and 140 mA/mm respectively.

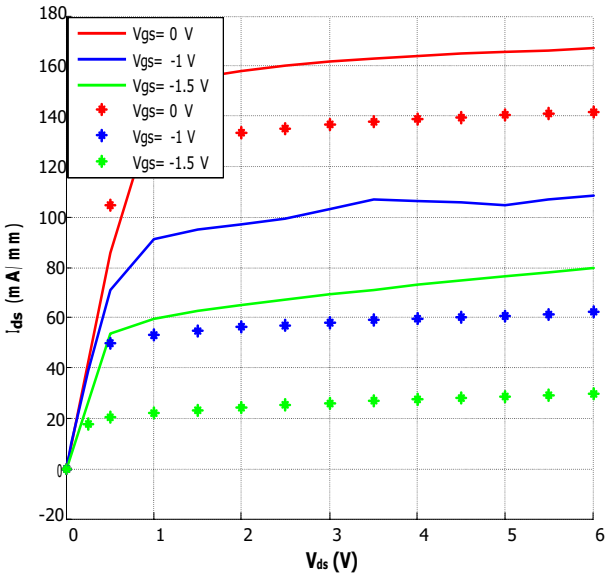

Fig. 2 Simulated I-V characteristics of MOS-PHEMT (solid line) and PHEMT (dotted line).

The technological parameters play an important role in optimizing and improving the electrical performance of such structure. In this perspective, we are interested in studying the influence of titanium dioxide (TiO_2) thickness on the drain current (Ids). Fig. 3 shows a comparison between the simulated drain current for two dielectric thicknesses (20 and 30 nm), gate-source voltage is set to 0 V. This figure shows that the MOS-PHEMT structure for a 20 nm titanium dioxide thickness allows a wide gate polarization compared to that of 10 nm. This can be explained by the increase of the barrier height at the gate interface.

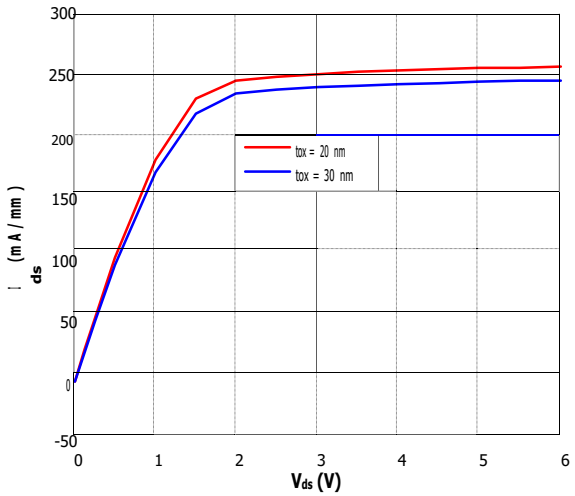

Fig. 3 Effect of oxide thickness in MOS-PHEMT for Vgs = 0 V.

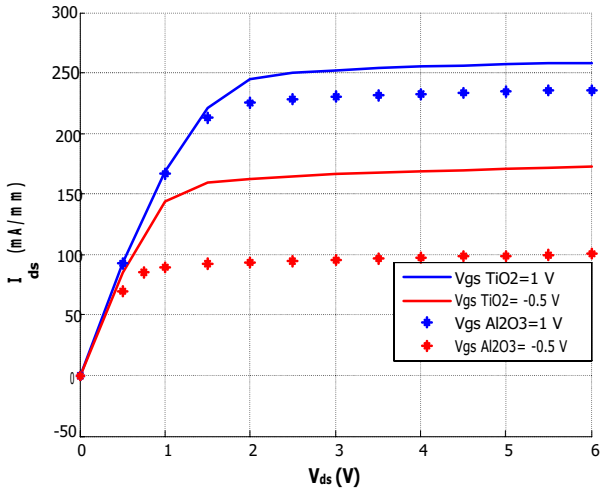

Fig. 4 Network of the output characteristics in MOS-PHEMT with stacking of TiO_2 and Al_2O_3

In order to compare the static performances of MOS-PHEMT with TiO_2 and Al_2O_3, we have plotted in Fig. 4 the source drain current for Vgs = 1 V and -0.5 V, as shown in Fig. 4, it is found that for the same gate polarization point the current is maximum with the stack of titanium dioxide (TiO2). In fact, TiO_2 has better static performance in terms of power. Fig. 5 show the variation of the current gain H21 as a function of the frequency on a logarithmic scale at the room temperature. From Figure 5, the cut-off frequency value for MOS-PHEMT and PHEMT is, respectively, 10 GHz and 9 GHz, for Vds = 2 Vand Vgs = 0 V at room temperature.

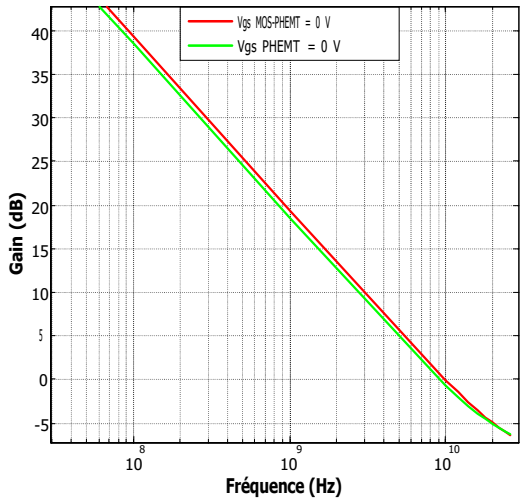

Fig. 5 Comparison of the cut-off frequency at Vgs = 0 V and Vds = 2 V for PHEMT and MOS-PHEMT.

Fig. 6 illustrate the distribution contour of the electric field in the PHEMT (Fig. 6-a) and MOS-PHEMT (Fig. 6-b). The polarizations of the components are done by a gate voltage Vgs = 0 V, the applied drain voltage is Vds = 2V. An increase in the electric field can be noticed below the gate near the drain contact. For example, the maximum value of the electric field in the PHEMT is $8.42.10^5$ V/cm, whereas for the MOS-PHEMT it is of the order of $4.54.10^5$ V/cm. Indeed, this electric field decreases very rapidly when we goes from the channel to the bottom of the substrate.

(a)

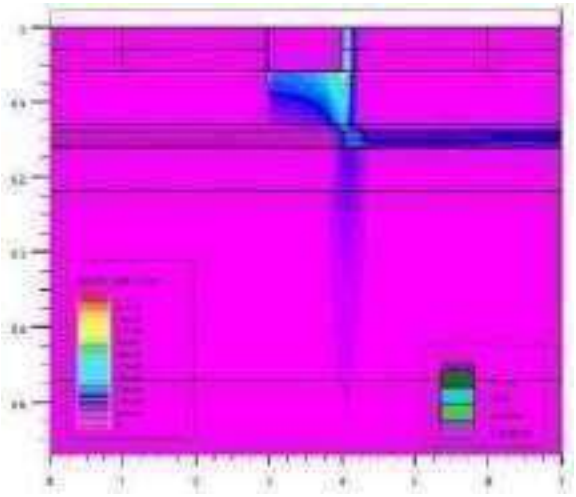

(b)

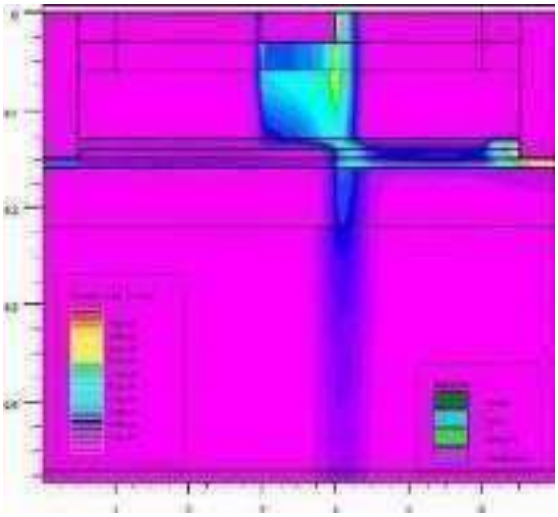

Fig.6 Distribution of the electric field for Vgs = 0 V, Vds = 2 V in: PHEMT (a) and MOS-PHEMT (b).

IV. Conclusions

In this work, we presented the results of the static and dynamic parameterization of the PHEMT and MOS-PHEMT transistors. Taking into account the technological parameters in our simulations, we obtained results comparable to the experimental results published in the literature. In particular, we studied the electrical and the frequency performances of the PHEMT and MOS-PHEMT transistors. The distribution of the electrical quantities such as the electric field of these transistors has also been discussed. As compared to the conventional AlGaAs/InGaAs PHEMT, the MOS-PHEMT

ISSN: 1737-9334

technology with the stack of titanium dioxide (TiO_2) makes it possible to present a better resistance in tension and therefore in power. Also, it has been demonstrated that the use of TiO_2, instead of Al_2O_3, as a gate dielectric increases on-state current above 25 mA/mm. In other words, good DC and RF characteristics are obtained at room temperature by precisely using TiO_2 as gate insulator.

The proposed MOS-PHEMT exhibit promising applications to millimeter-wave integrated circuit designs.

REFERENCES

[1] J. C . Bea n, ― *M ater ials an d Techn o lo gies in Hig h-Sp e ed Semico nd u ctor Devices*‖, S. M. Sze, Editor, John Wiley & Sons, New York, 1990.

[2] Lee, H.L.; Moon, S.M.; Dong, H.J.; Lee, M.Q.; Yu, J.W. K-band 0/180_ Balanced Phase Shifter with DC-Offset Cancellation‖, *Electron. Lett*. 2013,49,1234–1235.

[3] Lin , Y .S., Wu , J .F., Hsia, W. F., Wa n g, P.C .; Chun g, Y.H ., ― D esig n of Electronically Switchable Single-to-BalancedBandpass Low-Noise Amplifier‖, *IET Microw. Antennas Propag*. 2013, 7, 510–517.

[4] Kai-Yuen Lam, Jung-Sheng Huang, Yong-Jie Zou, Kuan-Wei Lee, and Y eon g-H er Wa n g, ― R edu ced Su bthr es h old Chara ct eristics an d Flick er Noise of an AlGaAs/InGaAs PHEMT Using Liquid Phase Deposited TiO2 as a Gate Dielectric‖, *Materials,* 9, 861; doi:10.3390/ma9110861, 2016.

[5] K. K. Chu, *et al*., "9.4 W/mm power density AlGaN-GaN HEMTs on free-standing GaN substrates*," IEEE Electron Device Lett*., vol. 25, no. 9,pp. 596–598,Sep. 2004.

[6] V. Adivarahan, J. Yang, A. Koudymov, G. Simin, and M. Asif Khan, ―Stable C W operation of field -plat ed GaN- AlGaN MOSH FE Ts at 1 9 W/mm,‖ *IEEE Electron Device Lett.,* vol. 26, no. 8, pp. 535–537, Aug. 2005.

[7] Konepachith Ouduangvilai1, Hoon-Ki Lee1, Vallivedu Janardhanam1, P. R. S hek ar Red d y, C hel -J on g C h oi, an d K yu -H wa n S hi m, ―St u d y of Gate Leakage Current on AlGaN/GaN MOSHEMTswith Atomic Layer Deposited Al2O3 Gate Oxide‖, *Journal of semiconductor technology and science*, Vol.19, No.6, December, 2019.

[8] Sarbani Basu, Pramod K. Singh, Po-Wen Sze, and Yeong-Her Wang, ―Al Ga As/In Ga As metal-oxid e-s emicondu ctor pseu do morp hic high - electron-mobility transistor with low temperatureliquid phase deposited Al_2O_3 gate insulator‖, *Journal of Applied Physics* ,104, 054116, 2008.

[9] Y eon g-H er Wa n g an d Ku an - W ei Lee, ― Liqui d Pha s e Oxidatio n o n InGaP and Its Applications‖, *Advances in Solid State Circuits Technologies*, Book edited by: Paul K. Chu, 2010.

[10] P. Kor d oš, et al, ― Hi gh-p o wer Si O2/ AlG aN/ G aN metal-o xide-semiconductor heterostructure fieldeffect transistors,‖ *Appl. Phys. Lett*., vol. 87, No.14, p. 143501-1–143501-3, Sep., 2005.

[11] F. Husna, M. Lachab, M. Sultana, V. Adivarahan, Q. Fareed, andA. Khan, "High-Temperature Performance of AlGaN/GaN MOSHEMT With SiO2 Gate Insulator Fabricated on Si (111) Substrate," *IEEE Transactions on Electron Devices,* vol. 59, pp.2424-2429, 2012.

[12] C h oi, W.; S eok , O .; Ryu , H.; C ha , H . Y .; Seo, K. S. – H i g h-V olt a ge a nd Low-Leakage-Current Gate Recessed Normally-Off GaN MIS-HEMTs with Dual Gate Insulator Employing PEALD-SiNx/RF-Sputtered- HfO2‖. *IEEE Electron. Device Lett.*, 35, 175–177, 2014.

[13] Z. H . Liu, et a l, ― H ig h mi cr owave- n oise per for man ce of AlG aN/ GA N MISHEMTs on silicon with Al2O3 Gate insulator grown by ALD,‖ *IEEE Electron Device Lett., vol. 31, No. 2, pp. 96–98, Feb., 2010*.

[14] Han-Yin Liu ; Wei-Chou Hsu ; Bo-Yi Chou ; Ching-Sung Lee ; Wen-C hin g Su n ; Su n g- Y en Wei ; Shen g- Min, ― T emp er atur e- dep endent electrical performance of AlGaN/GaN MOS-HEMT with ultrasonic spray pyrolysis deposited Al2O3‖, *IEEE 11th International Conference on Power Electronics and Drive Systems*, 2015.

[15] Kef en g H an an d Lin Zhu, ― G aN MO S H É M T emp loyin g H fO_2 as a gate dielectric with partially etched barrier‖, *Semiconductor Science and Technology*, Volume 32, No 9, 2017.

[16] H an, Kef eng; Zhu, Lin, ― GaN MO SH E M T emplo yin g H fO_2 as a gate dielectric with partially etched barrier‖, *Semiconductor Science and Technology*, vol. 32, Issue 9, 2017.

[17] B. Lee, C. Kirkpatrick, Y.-H. Choi, X. Yang, Y. Wang, X. Yang, A. Huang, and V. Misra, "Impact of ALD gate dielectrics (SiO2, HfO2, and SiO2/HAH) on device electrical characteristics and reliability of AlGaN/GaN MOSHFET devices," *ECS Transactions*, vol. 41, pp. 445-450,2011.

[18] Chih-Chun Hu, Chu-An Chiu, Chien-Hua Yu, Jian-Xuan Xu, Tsu-Yi Wu, Po- W en S ze, C h an g-Lu en Wu , Y eong-H er Wa ng, ― Li qu id -pha s e-deposited high dielectric zirconium oxide for metaloxide-semiconductor high electron mobility transistors‖, *Vacuum* 118, pp.142-146,2015.

[19] Feng Qian, Li Qian, Xing Tao,Wang Qiang, Zhang Jin-Cheng, and Hao Yu e, ― P erfor man ce of La2 O 3/In A lN / GaN metal oxide s emi con ductor highelectron mobility transistors*", Chin. Phys. B*, Vol. 21, No. 6, 2012

[20] H. C. Chiu, C. W. Lin, C. H. Chen, C. W. Yang, C. K. Lin, J. S. Fu, L. B. Chang, R. M. Lin, and K. P. Hsu eh, ― Lo w h ysteresis dispersion La2O3 AlGaN/GaN MOS-HEMTs,‖ *Electrochem*. Soc., vol. 157, no. 2, pp. H160–H64, 2010. DOI: 10.1149/1.3264622

[21] H.-Y. Liu *et al.*, ― C o mp ar ati ve stu dies on Al GaN/ G aN MO S -HEMTswith stacked La2O3/Al2O3 dielectric structures,‖ *ECS J. Solid StateSci. Technol.*, vol. 3, no. 8, pp. N115–N119, 2014.

[22] M. A. Kha n, et al., ― Al GaN/ GaN Met al-O xid e-S emi c on du ctor Heterostructure Field-Effect Transistors on SiC Substrates‖, *Appl. Phys. Lett.*77, pp. 1339, 2000.

[23] D. V. Gulyaev, K.S. Zhuravlev, A. K. Bakarov, A. I. Toropov, ―P hoto lu min es cence of AlGa As/ In Ga As/GaAsp hemth eterostructures with donor-acceptor doping of barriers*", 24th International Crimean Conference Microwave & Telecommunication Technology*, 2014.

[24] Ma Lin, FengShiwei, Zhang Yamin, Deng Bing, and Yue Yuan, ―E valu ation of the drain– source voltage effect on AlGa As/In Ga As PHEMTs thermal resistance by the structure function method‖, *Journal of Semiconductors*, vol. 35, No. 9, 2014.

[25] Atlas user's manual device simulation software, 2010.

Evaluation of the DC performance of the multiple quantum-wells AlGaAs/GaAs VCSEL

Hamida Djelti[#1], Mounir Khelladi[*2], Fayza Bousalah[*3], Yamina Belhadef[*4]

[#]*STIC laboratory, Department of Telecommunication, University Abou Bekr Belkaid of Tlemcen*
Faculty of Technology, University of Tlemcen, BP 230 Tlemcen, Algeria
[1]hamida.djelti@univ-tlemcen.dz

[*] *Department of Telecommunication, Faculty of Technology, University Abou Bekr Belkaid of Tlemcen*
[2]mo.khelladi@gmail.com
[3]bousalah.fayza@gmail.com
[4]belhadef@yahoo.fr

***Abstract*— This paper presents the static performances of the Vertical-Cavity Surface-Emitting Lasers (VCSELs) emitting in the third optical window (1,55 m wavelength). We will focus on the thermal effect on the static characteristics on the p-GaAs/AlGaAs quantum wells based VCSELs. Due to their small footprint and low power consumption VCSELs are promising sources for photonic integrated circuits, optical sensing and data communication and sensing that emit at 850–1550 nm wavelength. In this work, device simulated consist of the InGaAsP quaternary material is used as the active region which is sandwiched between the GaAs/AlGaAs distributed Bragg mirror at the top of the structure and the GaAs/AlAs distributed Bragg mirror at the bottom of the structure. In this way, the threshold voltage decrement of 5 % and decrement the optical power by almost 5%, the maximum of the temperature is 317 K underthe applied anode voltage equal to 3 V.**

***Keywords*— VCSEL, AlGaAs, InGaAsP, AlAs, MQW**

I. INTRODUCTION

Historically, Vertical-Cavity Surface-Emitting Lasers (VCSELs), as its name implies, emits vertically, normal to the plane of the device, owing to cavity mirrors grown within the epitaxial material itself. Was pioneered by Kenichi Iga and al. at the Tokyo Institute of Technology**.** Starting in the late 1970‘s with an electrically pumped laser operating at 77 K emitting 1.2 pm wavelength [1]. The first GaAs based VCSELs operating in continuous wave (CW) mode at room temperature were demonstrated at the end of the 1980s [2] and InP-based devices at the beginning of the 1990s [3]. The room temperature pulsed operation has been achieved in 1984 [4], and continuous-wave (CW) at room temperature operation in 1988 [5]. One years later, they also demonstrated the first room temperature CW GaAs VCSEL emitting at 850 nm [6]. 980-nm VCSEL with GaAs/AlGaAs distributed Bragg reflectors (DBRs) and selective oxide configuration has demonstrated a very low threshold current of 8.5 μA [7]. The 1300-nm InGaAsP VCSEL with n-type InGaAsP/InP mirror and SiO2/Si mirror on the p side demonstrates a threshold current of 500 mA under pulsed operation at room temperature [8]. Fabrication of 1550-nm InP QW VCSEL using n-type InGaAsP/InP DBRs on n-InP substrate has demonstrated 1-mW CW output power at room temperature [9]. Alternatively, using GaN and its material systems as the active layer can realize green to UV emitting lasers. Reports on the reliability performance of GaN-based LEDs and facet emitting lasers indicate that blue or shorter wavelength emission can also be realized in VCSELs [10]. It is possible to fabricate monolithic growth VCSELs using AlGaN/GaN DBRs, Continuous wave operation of GaN/InGaN micro disk lasers at 300K [11] and electrical injection of GaN-based VCSELs at 77K [12] have also been demonstrated.

Vertical-cavity surface-emitting lasers (VCSELs) are key optical sources in optical communications. The dominant source deployed in local area networks (LAN) using multimode optical fibers at 850 nm [13, 14, 15, 16, 17, 18, 19]. The advantages of VCSELs include wafer-scale testing, low-cost packaging, and ease of fabrication into arrays [20].

850-nm VCSEL was first commercialized driven by applications such as Ethernet, Infini Band and Fiber Channel. On the other hand, from metro and access networks, long-wavelength VCSELs operating at 1300-nm and 1550-nm are developed due to the low absorption loss and dispersion distortion in optic fibers. In comparison to short wavelength VCSELs, the progress of high-speed long-wavelength VCSELs was slow due to inherent material issues of the InP-based system. These challenges include intrinsic poor thermal conductivity as well as difficulties in finding good DBR candidates with appropriaterefractive indices difference.

The different growth and emission characteristics of VCSELs, compared to edge-emitting lasers, give advantages when it comes to testing the samples during the fabrication steps. Tens of thousands of VCSELs can also be processed in parallel on a wafer.

VCSELs are also promising sources for photonic integrated circuits due to their small footprint and low power consumption. Also, VCSELs are commonly used for a wide variety of applications in the consumer electronics market. These applications range from laser mice to three-dimensional (3D) sensing and imaging, including various 3D movement detections, such as gesture recognition or face recognition.

Novel VCSEL types will include meta structures, exhibiting additional unique properties, of largest importance for next-generation data communication, sensing, photonic integrated circuits, atomic clocks, laser cooling, interferometers, light detection andranging (LIDARs) [21, 22, 23, 24, 25, 26].
In this work, we address the problem to study the thermal effect on the static performance of VCSEL cavity laser with six quantum well $In_{0.76}Ga_{0.24}As_{0.82}P_{0.18}$. Also, we examine the DBR mirror effect on the P-V characteristics ofthis device.
The following section shows the both physical and numerical model of the VCSEL cavity laser devices. Section IV and V show the simulation results and conclusion.

II. Physical and Numerical Model of the VCSEL

The electrical and optical phenomena play a tremendous role in the semiconductor lasers such as the VCSEL structure.
The external electrical and optical characteristics of the VCSEL cavity are strongly linked of the internal electrical and optical properties of the semiconductors materials used in the fabrication of the device. Significant role, for calculation of the corresponding properties quantum mechanics should be applied. This is the fact for QW-regions, and thus we will consider quantum mechanics effects.
To predict the electrical and optical performance of the VCSEL diode, it is very important to take into account interaction of optical, electrical, and thermal phenomena that occur during the VCSEL operation.
The equations governing the electrical and optical operation of the VCSEL diode are Poisson [27], continuity [28], and Helmholtz equations [29].
Poisson's equation relates the electrostatic potential (?) to the space charge density(𝔼

$$div(\varepsilon\nabla\psi) - -\rho \quad (1)$$

Whereε is the local permittivity.

The continuity equations for electrons and holes are defined byequations (2) and (3) as follows:

$$\frac{dn}{\partial t} = G_n \quad R_n \mid \frac{1}{q}\nabla.\vec{J_n} \quad (2)$$

$$\frac{dp}{\partial t} = G_p - R_p + \frac{1}{q}\nabla.\vec{J_p} \quad (3)$$

Where n and p are the electron and hole concentration, Jn and Jp are the electron and hole current densities, Gn and Gp are the generation rates for electrons and holes, Rn and Rp are the recombination rates for electrons and holes, and q is the magnitude of the charge on an electron.
The transverse optical field profile Ek(x,y) is determined by solving a two-dimensional Helmholtz, expressed as follows:

$$\nabla^2 E(r,z,\varphi) + \frac{\omega^2}{c^2}\varepsilon(r,z,\varphi,\omega)E(r,z,\varphi) = 0 \quad (4)$$

Where ω is frequency, ε(r, z, ϕ, ω) is the complex dielectric permittivity, E(r, z, ϕ) is the optical electric field, and c is the speed oflight in vacuum.
The heat flow equation has the form:

$$C\frac{\partial T_L}{\partial t} = \nabla(\kappa\nabla T_L) + H \quad (5)$$

Where C is the heat capacitance per unit volume, κ is the thermal conductivity, H is the heat generation and T_L is the local lattice temperature.
Theheat capacitance can be expressed as $C = \rho Cp$, where Cp is the specific heat and ρ is the densityof the material.

III. VCSEL cavity structure

The VCSEL Direct-Current (DC) characteristics were analysed and simulated using a Drift-Diffusion transport model (Poisson and continuity equations) are solved self-consistently with the Helmholtz Equation, Lattice Heat Flow Equation of industry standard software Atlas from Silvaco [27], along with the devices dimensions and material of various layers used is presented in Fig. 1. This structure consists of GaAs substrate. The active region consists of six quantum wells $In_{0.76}Ga_{0.24}As_{0.82}P_{0.18}$ and seven barrier $In_{0.48}Ga_{0.25}As_{0.82}P_{0.18}$ with a thickness of 5,5 nm and 8 nm, respectively [29]. The top DBR mirror is 30 layers of $GaAs/Al_{0.33}Ga_{0.67}As$ and the bottom mirror has 28 layers of GaAs/AlAs.

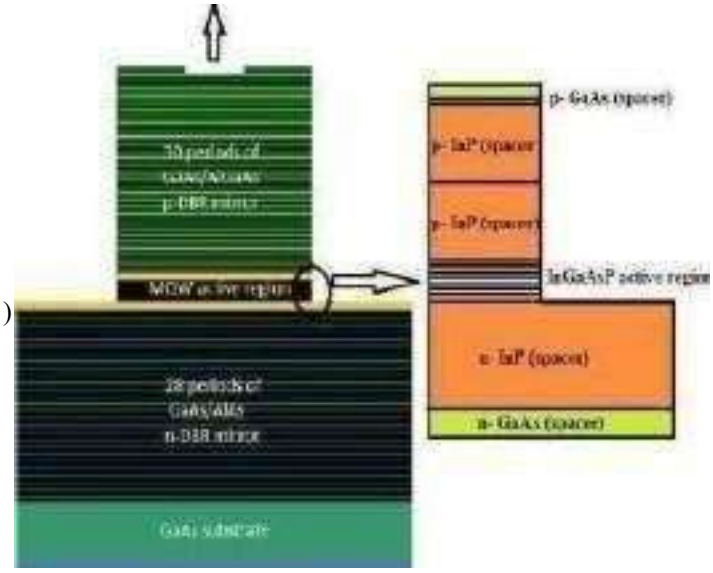

Fig. 1 Schematic structure of the MQW VCSEL cavity structure.

Fig.2 shows the diagram of the energy bands of the simulated structure of the VCSEL cavityaround the active layer.
As shown in Fig.2, the diagram of the energy bands seems very correct because we observe six periods which designate six quantum wells, this quantum wells created by the association of the two layers, is indeed present at the interface between both materials (from $In_{0.76}Ga_{0.24}As_{0.82}P_{0.18}$ and from $In_{0.48}Ga_{0.52}As_{0.82}P_{0.18}$.

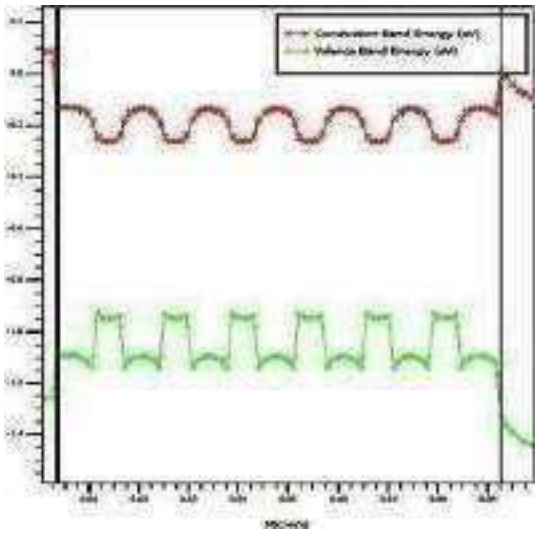

Fig.2 Diagram of the energy bands of p-GaAs/AlGaAs VCSEL cavity laser.

IV. Results and Discussions

Fig.3 shows the total power emitted versus the anode voltage for VCSEL cavity laser multiple quantum well $In_{0.76}Ga_{0.24}As_{0.82}P_{0.18}$. The anode voltage was swept from 0 V to 3 V. As shown in Fig.3, beyond the threshold in terms of anode voltage ($V_{threshold}$ = 1.18 V) and injection current ($I_{threshold}$ = 1.25 mA), the two curves for thermal and non thermal model are straight lines. In fact, it is observed that the light emitted varies linearly with the current and the bias voltage from the threshold value, the value at which the number of carriers is sufficient to emit the stimulated photons. It can be seen that the maximum value of the power with thermal effect decrease by about 5% compared to the power without thermal effect.

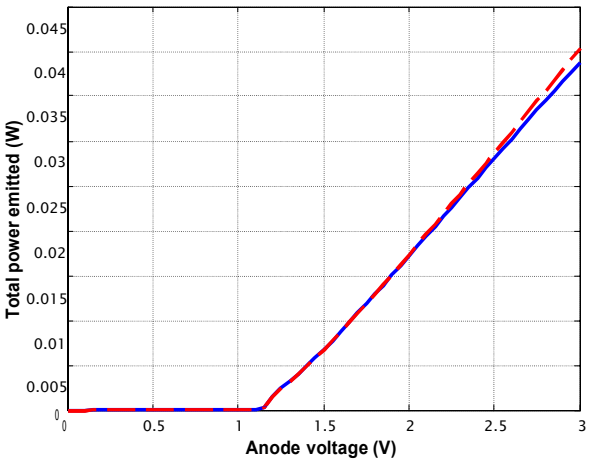

Fig. 3 Thermal (blue) and non thermal (red) P-V Characteristics of the VCSEL MQW $In_{0.76}Ga_{0.24}As_{0.82}P_{0.18}$.

Fig.4 shows I-V characteristics, current versus anode voltage. As Fig.4 presents, we can clearly see the anode current increases from the polarization of the anode voltage, threshold voltage anode is approximately 1 V. Indeed, beyond the threshold, this curve is a straight line, this can be explain by the confinement in the active region of the photons generated by recombination of the carriers injected into the quantum wells.

It can be seen that the maximum value of the current with thermal effect decrease by about 5% compared to the current without thermal effect for anode voltage equal to 3 V.

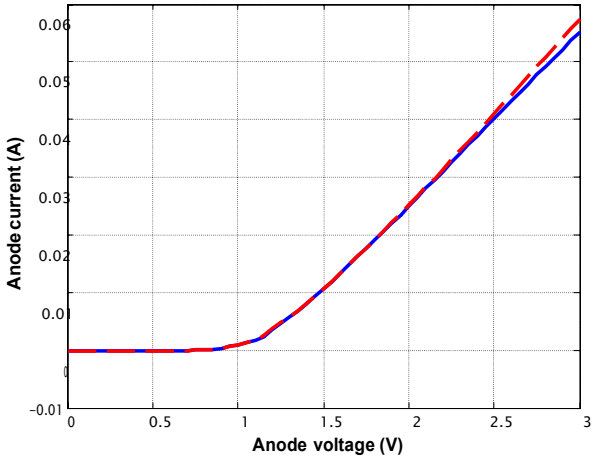

Fig. 4 Thermal (blue) and non-thermal (red) I-V Characteristics of the VCSEL MQW $In_{0.76}Ga_{0.24}As_{0.82}P_{0.18}$.

Fig. 5 shows the evolution of the global device temperature in the VCSEL cavity laser versus the anode voltage. This figure shows that the increase in temperature is proportional to the increase in the polarization of the anode. The maximum temperature which corresponds to the hot spot is almost 317 K for anode voltage of 3 V.

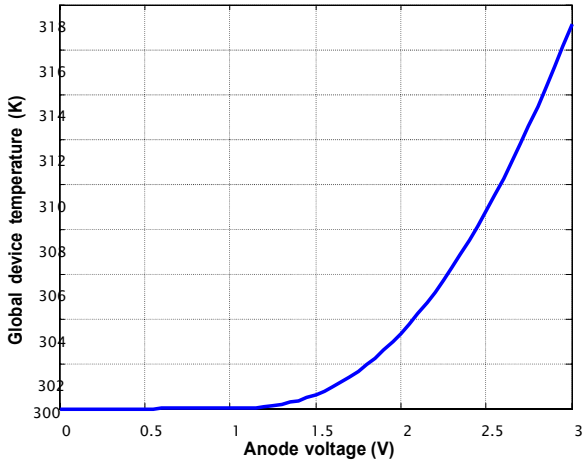

Fig. 5 Global device temperature versus anode voltage of the VCSEL MQW $In_{0.76}Ga_{0.24}As_{0.82}P_{0.18}$.

In order to investigate the effect of the periods number of DBR top and DBR bottom in VCSEL cavity, Fig. 6 shows the P-V characteristics for 32 and 35 periods of GaAs/AlGaAs top distributed-Bragg reflectors (DBR). From Fig.6, the total power emitted increase with decreasing the number of p-GaAs/AlGaAs pairs. It is noted that to achieve the lasing condition in a VCSEL structure for reasonable current

densities, mirrors reflectivity must be at least equal to 99.5 %, for our simulated VCSEL structure mirrors reflectivity of the top and bottom DBR mirrors is about 99.84% and 99.80% , respectively. Therefore, reflectors with extremely high reflectivity are needed to support low threshold and high-output-power VCSELs. Bottom Distributed Bragg reflectors (DBRs) have been widely used as high-reflectivity mirrors in VCSELs. DBRs are stacks of materials with different refractive indices, and the bandwidth of a DBR is determined by the relation Δn/n, where n is the refractive index and Δn is the index difference. AlAs and GaAs are ideal bottom DBR materials for GaAs-based VCSELs. The Δn of these materials is approximately 0.4. Also, it should be noted that to improve the characteristics of the Bragg mirrors their reflective powers and the spectral width "stop-band" it is necessary to choose the difference of index as high as possible.

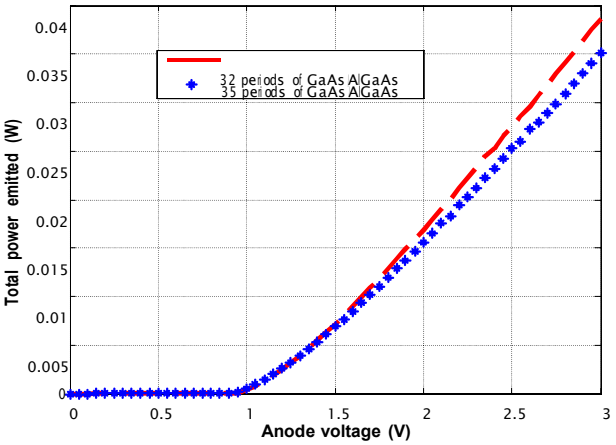

Fig. 6 Effect of the DBR mirror on the P-V characteristics of the VCSEL MQW $In_{0.76}Ga_{0.24}As_{0.82}P_{0.18.}$

In Fig. 7 and Fig. 8, the contour and the variation of the electric field in the active region of the VCSEL diode (barrier layers and quantum wells) for an anode bias voltage of 3 V are illustrated, respectively. It is noted in particular that the peak of the electric field is in the active region and more precisely in wells four and five, it practicallyreaches 68 10^4 V/cm.

The VCSEL multiple quantum-wells laser cavity has the advantage of having a large inversion zone, and therefore of gain. The model gain depends to the carrier and photon number.

Fig. 9 and Fig. 10 shows the light intensity contour and the evolution of the local optical gain in the active region (barriers and quantum wells) of the VCSEL cavity laser, respectively. It is clearly noted that the optical gain is maximum in the first quantum well then begins to decrease linearly throughout the active region. However, the optical gain tends to decrease at high photon densities.

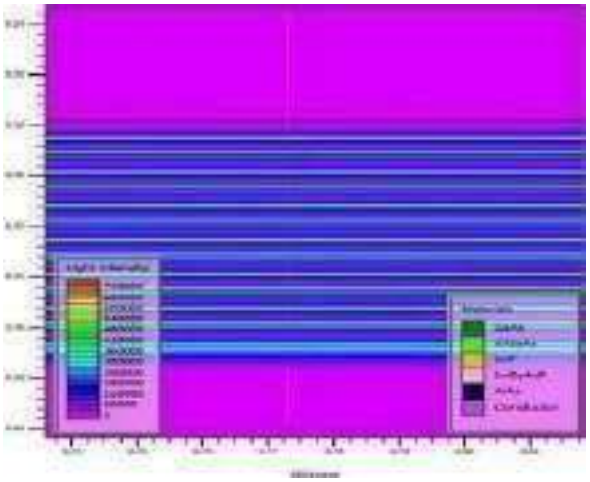

Fig. 7 Electric field contour in the VCSEL MQW $In_{0.76}Ga_{0.24}As_{0.82}P_{0.18.}$ cavity laser.

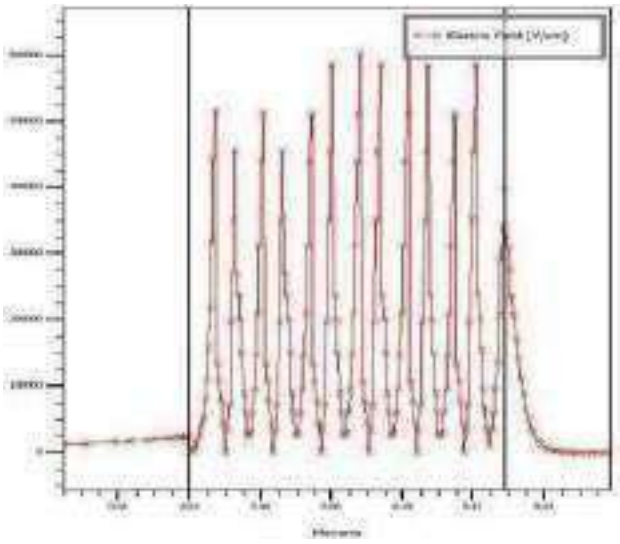

Fig.8 Variation of the electric field in the active region of the VCSEL MQW $In_{0.76}Ga_{0.24}As_{0.82}P_{0.18.}$

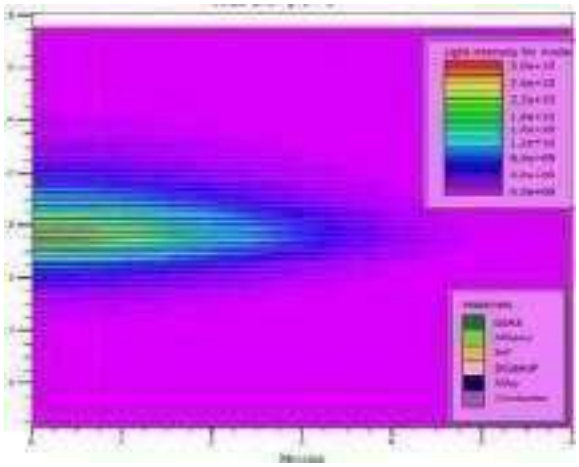

Fig. 9 Light intensity contour in the VCSEL MQW $In_{0.76}Ga_{0.24}As_{0.82}P_{0.18.}$

ISSN: 1737-9334

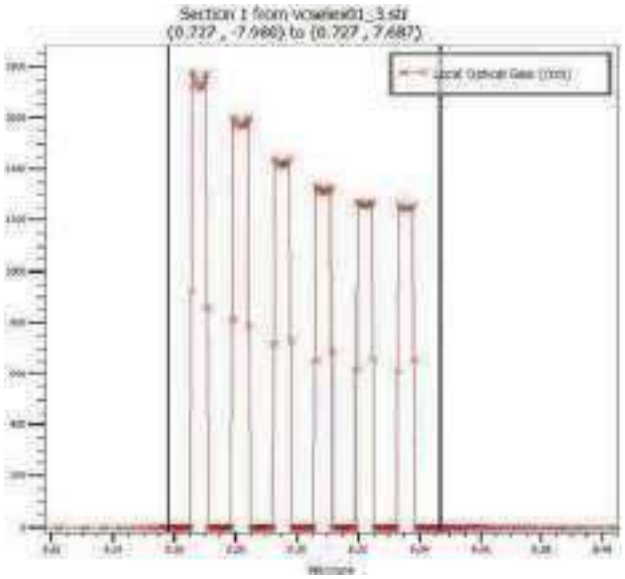

Fig. 10 Local optical gain in the active region of the VCSEL MQW $In_{0.76}Ga_{0.24}As_{0.82}P_{0.18}$.

V. CONCLUSIONS

In this work, the DC performances of the p-GaAs/AlGaAs quantum wells based VCSEL cavity emitting in the third optical window (1550-nm) are introduced. We take into account interaction of optical, electrical, and thermal phenomena in the numerical model using commercial, numerically-based simulation software (silvaco). Clearly, due to the thermal effect, simulated structure decreases the optical power about 5% and decreases the current almost 5% at anode voltage of 3 V in comparison with isothermal numerical model. Also, the global device temperature at anode voltage of 3 V is 317 K. it can be clearly seen that p-GaAs/AlGaAs quantum wells $In_{0.76}Ga_{0.24}As_{0.82}P_{0.18}$ based VCSEL dissipates less heat.

REFERENCES

[1] Jack L. Jewell, J. P Harbison, A. Scherer, Y. H. Lee, and L. T. Florez, "Vertical-Cavity Surface-Emitting Lasers: Design, Growth, Fabrication, Characterization ", *IEEE Journal of Quantum Electronics*. Vol. 27. No. 5. June 1991

[2] Lee YH, Tell B, Brown-Goebeler KF, Leibenguth RE, Mattera VD. Deep-red continuous wavetop-surface-emitting vertical-cavity AlGaAssuperlattice lasers. *IEEE Photon. Technol. Lett*. 1991; 3: 108-10911.

[3] Baba T, Yogo Y, Koyama F, Iga K. Near room temperature continuous-wave lasing characteristic of GaInAsP/InP surface emitting laser. Electron.Lett.,vol, 29, pp. 913-914, 1993.

[4] K. Iga, S. Ishikawa, S. Ohkouchi, and T. Nishimura, –Room temperature pulsed oscillation of GaAlAs/GaAs surface-emitting injection laser,‖ *Appl. Phys. Lett.*, vol. 45, pp. 348–350, 1984.

[5] F. Koyama, S. Kinoshita, and K. Iga, –Room-temperature continuous wave lasing characteristics of GaAs vertical cavity surface-emitting lasers,‖ *Appl. Phys. Lett.*, vol. 55, pp. 221–222, 1989.

[6] F. Koyama, S. Kinoshita, and K. Iga, _Room temperature continuous wave lasing characteristics of GaAs vertical cavity surface emitting laser,‖ *Appl. Phys. Lett.*, Vol. 55, no. 3, pp. 221–222, 1989.

[7] G. M. Yang, M. MacDougal, and P. D. Dupkus, ―Ultralow threshold current verticalcavity surface emitting laser obtained with selective oxidation,‖ *Electron. Lett.*,Vol. 31, pp. 886–888, 1995.

[8] P. Salet, F. Gaborit, Ph. Pagnod-Rossiaux, A. Plais, E. Derouin, J, Pasquier, and J. Jacquet, ―Room temperature pulsed operating of 1.3 µm vertical cavity lasers including bottom InGaAsP/InP multilayer braggmirrors,‖ *Electron. Lett.*, Vol. 33,no. 24, pp. 2048–2049, 1997.

[9] J. Boucart, C. Starck, F. Gaborit, A. Plais, N. Bouche, E. Derouin, L. Goldstein, C. Fortin, D. Carpentier, P. Salet, F. Brillouet, and J. Jacquet, ―1 mW CW-RT Monolithic VCSEL at 1.55 µm,‖ *IEEE Photon. Technol. Lett.*, Vol. 11, no. 5,pp. 629–631, 1999.

[10] S. Nakamura, M. Senoh, S. Nagahama, N. Iwasa, T. Yamada, T. Matsushita, H. Kiyoku, Y. Sugimoto, T. Kozaki, H. Umemoto, M. Sano, and K. Chocho, –High power, long lifetime InGaN/GaN//AlGaN based laser diodes grown on pure GaNsubstrates,‖ *Jpn. J. Appl. Phys.*, Vol. 37, pp. L309–L312, 1998.

[11] A. C. Tamboli, E. D. Haberer, R. Sharma, K. H. Lee, S. Nakamura, and E. L. Hu, "Roomtemperaturecontinuous-wave lasing in GaN/InGaNmicrodisks," *Nat. Photonics* 1, 61-64 (2007).

[12] T. C. Lu, C. C. Kao, H. C. Kuo, G. S. Huang, S. C. Wang, "CW lasing of current injection blue GaN-based vertical cavity surface emitting laser," *Appl. Phys. Lett.* 92, 141102(2008).

[13] K. Iga, "Surface-emitting laser-its birth and generation of newoptoelectronics field," *IEEE J. Sel. Top. Qu*

[14] *antum Electron.,*vol. 6, no. 6,pp. 1201-1215, 2000.

[15] F. Koyama, "Recent Advances of VCSEL Photonics," *IEEE J. LightwaveTechnol.,* vol. 24, no. 12, pp. 4502-4513, 2006.

[16] C. J. Chang-Hasnain, "Tunable Vcsel," *IEEE J. Sel. Top. QuantumElectron.,*vol. 6, no. 6, pp. 978-987, 2000.

[17] J. S. Harris, "Tunable long-wavelength vertical-cavity lasers: the engine ofnext generation opticla networks," IEEE J. Sel. Top. Quantum Electron.,vol. 6, no. 6, pp. 1145-1160, 2000.

[18] M.-C. Amann and W. Hofmann, "InP-Based Long-Wavelength VCSELsand VCSEL Arrays," IEEE J. Sel. Top. Quantum Electron., vol. 15, no. 3,pp. 861-868,2009.

[19] E. Kapon and A. Sirbu, "Long-wavelength VCSELs: Power-efficientanswer," *Nat. Photon.,* vol. 3, pp. 27-29, 2009.

[20] R. S. Geels and L. A. Coldren, "Submilliamp threshold vertical-cavity laser diodes," *Appl. Phys. Lett.,* vol. 57, no. 16, pp. 1605-1607, 1990.

[21] P. Qiao, K. T. Cook , K. Li and C. J. Chang-Hasnain, , ― Wavelength-Swept VCSELs,‖*IEEE Journal of Selected Topics in Quantum Electronics.*, vol. 23, no. 6, 2017.

[22] A. Liu, P. Wolf, J. A. Lott, D. Bimberg, "Vertical-cavity surface-emitting lasers for data communication and sensing" Photonics Research*.,* vol. 7, no. 2, pp. 121-136, 2019.

[23] H. Liu, G. Gredat, G. Baili, F. Gutty, F. Goldfarb, I. Sagnes, and F. Bretenaker, –Noise investigation of a dual-frequency VECSEL for application to cesium clocks,‖ J. Lightwave Technol. 36(18), 3882–3891,2018.

[24] X. Liu, E. Ivanov, V. I. Yudin, J. Kitching, and E. A. Donley, ― Low-drift coherent population trapping clock based on laser-cooled atoms and high coherence excitation fields,‖ Phys. Rev. A 8(5), 054001, 2017.

[25] O. Carraz, F. Lienhart, R. Charrière, M. Cadoret, N. Zahzam, Y. Bidel, and A. Bresson, ― Compact and robust laser system for onboard atom interferometry,‖ Appl. Phys. B: Lasers Opt. 97(2), 405–411, 2009.

[26] A. R. Nehrir, K. S. Repasky, and J. L. Carlsten, ― Eye-safe diode-laser based micropulse differential absorption lidar (DIAL) for water vapor profiling in the lower troposphere,‖ J. Atmos. Oceanic Technol. 28 (2), 131–147,2011.

[27] Chih-Hsien Cheng, Wei-Chi Lo, Borching Su, Chao-Hsin Wu, Gong-Ru Lin, Review of VCSELs for Complex Data-Format Transmission Beyond 100-Gbit/s‖, *IEEE Photonics Journal*, vol. 13, Issue: 5, October 2021.

[28] Atlas user's manual device simulation software, 2010.

[29] Selberherr, S. ―*Analysis and Simulation of Semiconductor Devices*". Wien, New York: Springer-Verlag, 1984.

[30] Rahim faez, Azam Marjani and saeid Marjani, ― Design and simulation of a high power signal mode 1550 nm InGaAsP VCSEL‖, *IEICE Electronics Express,*vol.8, No.13, pp. 1096-1101, 2011.

V_2O_5/NiO composite: Electrode for Li-ion batteries

Ayouz Katia[#1], Ayat Maha[#2], Boudefar Fatima[#3], Yaddaden Chafiaa[#4], Lasmi Kahina[#5], Berouaken Malika[#6], Merazga Salwa[#7], Cheraga Hocine[#8], Gabouze Noureddine[#9].

[#]*NASO-SE, Nano structuration de Silicium et oxydes métalliques pour le stockage d'énergie, Centre de recherche en technologie des semi-conducteurs pour l'énergétique (CRTSE). 02, BD FRANTZ FANON ALGER, B.P. 140 ALGER – 7 MERVEILLES, TÉL. &FAX. : 2130(0)21 43.35.1.*

[1]searchkat12@gmail.com
[2]ayat_maha@CRTSE.dz
[3]boudeffar.fatima@CRTSE.dz
[4]yaddadenechafiaa@CRTSE.dz
[5] lasmikahina@CRTSE.dz
[6] BerouakenMalika@CRTSE.dz
[9]gabouzenoureddine@CRTSE.dz

***Abstract*— In this work, we have synthetized NiO-V_2O_5 composite, by chemical method. The synthetized simples were characterized by Attenuated Total Reflectance (ATR), X-ray diffraction, and Scanning electron microscopy (MEB). The electrochemical performances as cathode electrode based on active material synthetized (NiO-V_2O_5 composite) were studied by cyclic voltammetry (CV), in voltage range of [0.1 – 3] V at a scan rate 0.1 mVs^{-1}, the galvanostatic charge/discharge (CDG) for 100 cycles was also measured.**

***Keywords*—** Vanadium- Nickel oxide, Composite, Li-ion batteries.

I. INTRODUCTION

Lithium-ion batteries (LIBs) have been extensively studied in recent years as one of the most important energy storage devices [1-3]. Transition metal oxides have attracted more interest than commercial graphite as the electrode in lithium ion batteries because of their high theoretical capacity and abundant supply of raw materials in nature [4-6]. Recently, much research has been conducted on a variety of V_2O_5-based composite electrodes such as M^{2+}-V_2O_5 (M: Ni, Mn, Co, Cu, Ag) [7–9] and MO-V_2O_5 (M: Ni, Ti) for their high capacity, and the electrochemical insertion process of lithium ions.

V_2O_5, and NiO, has been extensively studied and applied in different kinds of battery systems, such as Li-ion [10, 11], Na-ion [12-19] and Li-S batteries [20], due to their high catalytic activity, fast ionic diffusivity and large adsorbent ability. In this work, the V_2O_5-NiO composite was successfully fabricated via a chemical method, and then utilized as a cathode material electrode for the Li-ions batteries.

II. EXPERIMENTAL

➢ The NiO-V_2O_5 composite was chemically synthesized using Nickel II Acetate ($C_4H_6O_4Ni_4H_2O$) "Sigma-Aldrich" (98%), and Vanadium Oxide, V_2O_5 "Sigma-Aldrich" (99 %), the process is illustrated in Figure 1.

➢ For the preparation of the working electrode, a mixture of NiO-V_2O_5 composite, poly-vinylidene fluoride (PVDF), and carbon black, were mixed in a weight ratio of 80:15:5 with 1-methy1-2-pyrrolidone (NMP) to make a slurry. The resulting mixture was stirred thoroughly to have a viscous texture and pasted uniformly onto aluminum foil to serve as the cathode.

Different steps of the preparation and composition of the cell is shown in the figure 2.

➢ The electrochemical performance of the as-prepared electrode was evaluated using a home-made lithium-ion batteries based on our previous works [21], which contained a lithium metal anode, a glass-fiber (Whatman GF/C) separator, and an as-prepared active material. The electrolyte for this battery was made up of 1M LiPF6 in ethylene carbonate (EC) /dimethyl carbonate (DC) (1:1 in volume) Sigma-Aldrich, 99.95%) as salt.

The batteries were assembled in an argon-filled glovebox (JACOMEX, $H_2O \leq 1$ ppm, $O_2 \leq 1$ ppm). Cyclic voltammetry (CV) experiments of these batteries were carried out with a potentiostat/galvanostat (VMP3) controlled with EC-Lab software, at a scan rate of 0.1 mV s^{-1} from [0.1 – 3] V (vs. Li/Li^+).

ISSN: 1737-9334

Nickel Acetate (II) + EtOH

+

V2O5 Powder

Precipitate

Annealed

Final active material (Powder)

Figure 1: The experimental synthesis of the NiO-V O composite.

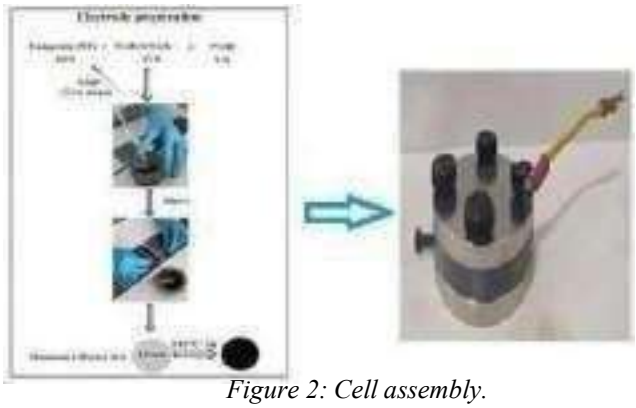

Figure 2: Cell assembly.

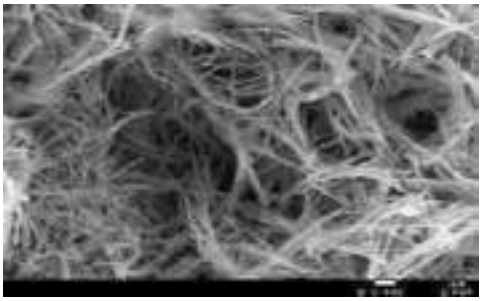

Figure 3: SEM pictures of as prepared NiO-V O

3. Results and discussion

➢ The morphology of synthesized NiO-V_2O_5 composite material was studied by field emission scanning electron microscope JOEL JSM7_7610F PLUS. Figure 3 show nanobelts forms with different diameters.

➢ The crystallinity and phase purity of the synthesized sample was analyzed by X-ray powder diffraction using a monochromatic CuKα radiation (λ = 1.5406 Å) within the 2θ range of 10–80° at a step of 0.02° as shown in Figure 4. All the peaks in the diffraction pattern match well with both of an orthorhombic phase of V_2O_5 (JCPDS # 41-1426), and peaks of NiO *(JCPDS # 47—1049).*

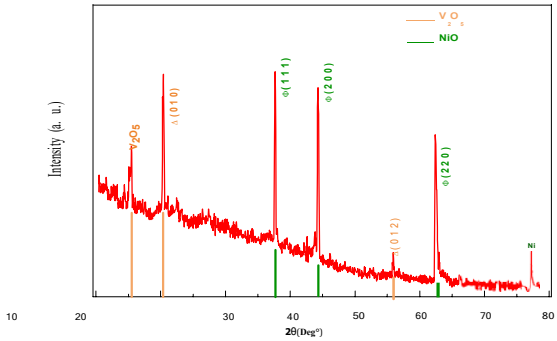

Figure 4: Characterization of composite material: XRD pattern.

➢ **Electrodes preparation and batteries measurements**:

The half-cells with metallic Li as the anode electrode in the presence of 1M $LiPF_6$ were assembled to examine the electrochemical properties of synthesized material as cathode and metallic Li as anode. Both galvanostatic and potentiostatic methods were used to investigate the Li-insertion property of the electrode materials.

nanostructures.

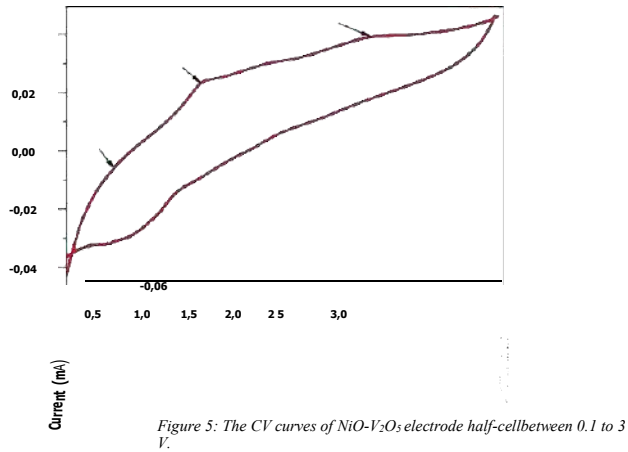

Figure 5: The CV curves of NiO-V_2O_5 electrode half-cellbetween 0.1 to 3 V.

➢ Figure 5, shows the CV traces of half-cell for the first cycle, the curves indicates the presence of three pairs of redox peaks centred at 0.5, +1 and +2.2 V. In addition, the reduction process, we observe in the potential region from 0 to 0.8V a large peak at 0.57 V which, according to several authors, correspondsto theinitial reduction ofNiO to metallic Ni.

➢ The galvanostatic charge–discharge of the Li-ion batteries with NiO-V_2O_5 was plotted within the potential window of 0.1 to 3 V versus Li at room temperature. Figure 6, showed a reversible capacity of 344 mAh g^{-1} after 50 cycles.

➢ The morphology of NiO/V_2O_5 nanocomposite after 50 cycles has been investigated bySEM. Figure 7 shows that the morphology of the NiO/V_2O_5 electrode is preserved after 50 cycles. However, one can observe after cycling the presence of artefacts and granular structures which could be due to the deposit of electrolyte LiPF6 formed on the surface.

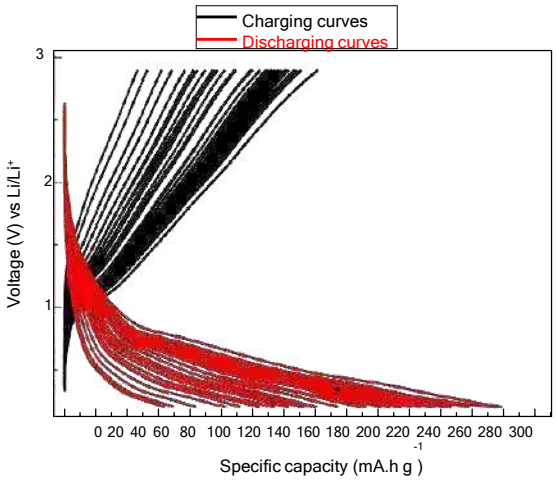

Figure 6: Discharge-charge curves of NiO-V_2O_5 composite electrode vs Li.

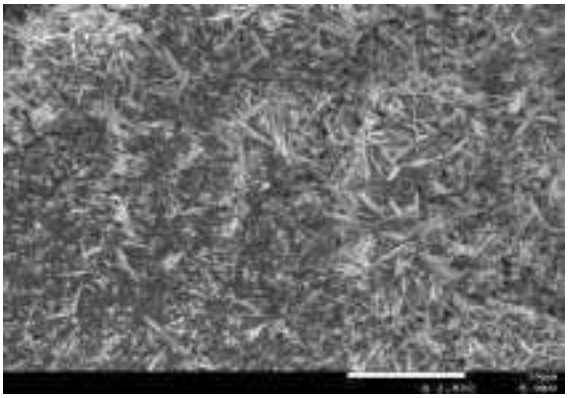

Figure 7: SEM pictures of as prepared NiO-V_2O_5 electrode after 50 cycles.

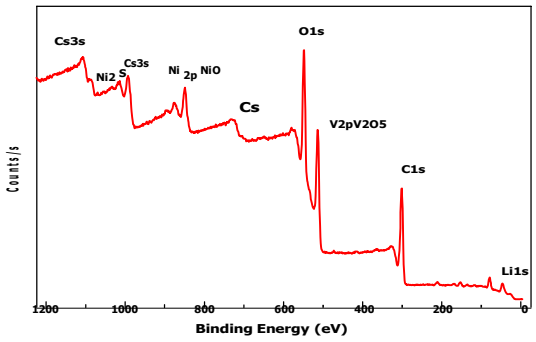

Figure 8: Survey spectrum XPS spectra of the NiO-V_2O_5 electrode after 50 cycles.

➢ To further investigate the chemical states and surface chemical compositions of the composite electrode NiO-V_2O_5 after charge- discharge measurements, XPS analysis was performed as shown in Figure 8. From the full-wide (0–1200 eV) scanned survey spectrum, it is obvious that the presence of Ni, O, V, C and Li in the NiO-V_2O_5 nanocomposite after the insertion/disinsertion process, we have also developed for another paper the decomposed peaks of Ni 2p XPS spectrum, assigned to the Ni $2p_{1/2}$ at 877 eV and its satellite, while the peaks at 850.2 eV are ascribed to Ni $2p_{3/2}$ and its satellite, respectively.

II. Conclusions

In this work, the NiO-V_2O_5 composite nanobelts was successfully fabricated via chemical method, and then applied as cathode electrode for the Li-ion battery. The battery elaborated with this electrode delivers a reversible capacity of 344 mAh g^{-1} after 50 cycles.

Other results have been investigated in order to study the behavior of the composite material as a cathode for 100 cycles and more, with a better specific capacity but also longer discharge times. Finally, the elaborated composite could be a potential candidate as cathode material for Li ion batteries.

Acknowledgment

The work described in this paper was supported by the National Research Fund (DGRSDT/MESRS) from Algeria.

References

[1] Xing, J., Bliznakov, S., Bonville, L. et al. A Review of Nonaqueous Electrolytes, Binders, and Separators for Lithium-Ion Batteries. Electrochem. Energy Rev. 5, 14 (2022). https://doi.org/10.1007/s41918-022-00131-z.

[2] Bashir T, Ismail SA, Song Y, Irfan RM, Yang S, Zhou S, Zhao J, Gao L. A review of the energy storage aspects of chemical elements for lithium-ion based batteries. Energy Mater 2021;1:100019. http://dx.doi.org/10.20517/energymater.2021.20.

[3] Dai, F., Cai, M. Best practices in lithium battery cell preparation and evaluation. Commun Mater 3, 64 (2022). https://doi.org/10.1038/s43246-022-00286-8.
[4] Pender, J. P., Jha, G., Youn, D. H., Ziegler, J. M., Andoni, I., Choi, E. J., … Mullins, C. B. (2020). Electrode Degradation in Lithium-Ion Batteries. ACS Nano. doi:10.1021/acsnano.9b04365.
[5] H. Lee, Y.-J. Kim, D.J. Lee, J. Song, Y.M. Lee, H.-T. Kim, J.-K. Park, Directly grown Co3O4 nanowire arrays on Ni-foam: structural effects of carbon-free and binder-free cathodes for lithium-oxygen batteries, J. Mater. Chem. A. 2 (2014) 11891.
[6] Y. Cui, Z. Wen, Y. Liu, A free-standing-type design for cathodes of rechargeable LiO2 batteries, Energy Environ. Sci. 4 (2011) 4727.
[7] Xing Liang, Guohua Gao, Yindan Liu, Zeyuan Ge, Pengliang Leng, Guangming Wu, Carbon nanotubes/vanadium oxide composites as cathode materials for lithium-ion batteries, J Sol-Gel Sci Techno. DOI 10.1007/s10971-016-4293-8
[8] Wang S, Li S, Sun Y, Feng X, Chen C, Three-dimensional porous V2O5 cathode with ultra-high rate capability. Energy Environ Sci 4(8):2854–2857 (2011)
[9] Pandey GP, Liu T, Brown E, Yang Y, Li Y, Sun XS, Fang Y, Li J , Mesoporous hybrids of reduced graphene oxide and vanadium pentoxide for enhanced performance in lithium-ion batteries and electrochemical capacitors. ACS Appl Mater Interfaces 8(14):9200–9210 (2016).
[10] V. Aravindan, P. Sennu, Y.-S. Lee and S. Madhavi, The Journal of Physical Chemistry Letters, 2017, 8, 4031-4037.
[11] Y. L. Cheah, R. von Hagen, V. Aravindan, R. Fiz, S. Mathur and S. Madhavi, Nano Energy, 2012.
[12] S. Natarajan, K. Subramanyan and V. Aravindan, Small, 2019, 15, 1904484.
[13] C. Vaalma, D. Buchholz, M. Weil and S. Passerini, Nature Reviews Materials, 2018,3, 18013.
[14] H. Zhang, I. Hasa and S. Passerini, Advanced Energy Materials, 2018, 8,1702582.
[15] J. Kim, H. Kim and K. Kang, Advanced Energy Materials, 2018, 8, 1702646.
[16] L. Li, Y. Zheng, S. Zhang, J. Yang, Z. Shao and Z. Guo, Energy & Environmental Science, 2018, 11, 2310-2340.
[17] K. Chayambuka, G. Mulder, D. L. Danilov and P. H. L. Notten, Advanced Energy Materials, 2018, 8, 1800079.
[18] K. Subramanyan and V. Aravindan, Chem, 2019, 5, 3096-3126.
[19] Z. Le, F. Liu, P. Nie, X. Li, X. Liu, Z. Bian, G. Chen, H. B. Wu and Y. Lu, ACS Nano, 2017, 11, 2952-2960.
[20] Liu, M., Li, Q., Qin, X., Liang, G., Han, W., Zhou, D., … Kang, F. (2017). Suppressing Self-Discharge and Shuttle Effect of Lithium-Sulfur Batteries with V2O5-Decorated Carbon Nanofiber Interlayer. Small, 13(12), 1602539. doi:10.1002/smll.201602539.
[21] Yaddaden, C, Berouaken, M., Ayouz, K. et al. Study and Characterization of the Porous Silicon Membrane Anode for LITHIUM-Ion Batteries. Silicon (2022). https://doi.org/10.1007/s12633-022-01885-3

Hydrothermal Synthesis of $TiO_2/Li_4Ti_5O_{12}$ nano powderasLithiumIonBatteryelectrode

Saloua MERAZGA[#1], Fatima BOUDEFFAR[#2], BADIS RAHAL*[3]Malika BEROUKEN[#4], Katia Ayouz[#5], Mebarki Moured[#6] Belkhettabilyes[#7], Nouredine GABOUZE[#8]

[#] *Centre de Recherche en Technologie des Semi-conducteurs pour l'Energétique 2 bd frantz fanon alger, b.p. 140 alger – 7 merveille, algerie*

[1]merazgasal@yahoo.fr

[2]boudeffar.fatima@CRTSE.dz

[4]BerouakenMalika@CRTSE.dz

[5] cheboutkatia@CRTSE.dz

[6]Mebarki.Mourad@crtse.dz

[7]Belkhettab@CRTSE.dz

[8]gabouzenoureddine@crtse.dz

*2Centre de recherche nucléaire d'Alger (CRNA), Alger, Algérie

***Abstract*— The effect of Thermal annealing temperature used in the hydrothermal Li4Ti5O12 nano-particles synthesis and the morphological, structural and electrochemical properties has been studied. Lithium titanate (Li4Ti5O12)The nanoparticles are successfully hydrothermal synthesize and annealed at different temperatures: 600°C, 800°C and 900°C after calcination at 500°C for 5 hour . The structural and morphological characterizations of the synthesized powders were performed by scanning electron microscopy (SEM), Fourier- transform infrared (FT-IR) spectroscopy and X-ray diffraction (XRD). Nevertheless, the study of the electrochemical performances of the elaborated electrode materials was carried out by: cyclic voltammetry (CV) and galvanostatique charge/discharge (CDG).The particle size increase with the annealing temperature due to the agglomeration of the nanoparticles. The prepared electrode by the powder annealed at 800 °C has a good specific capacity of about 173 mAh/g and a good cyclic stability.**

***Keywords*— Include at least 5 keywords or phrases**

I. INTRODUCTION

Rechargeable lithium-ion batteries (LIBs) are gradually emerging because of the depletion of traditional fuels and are of interest to researchers worldwide. Due to their high power density, high efficiency and long cycle life, lithium-ion batteries are becoming the power source of choice for electronic products. As a promising anode material, spinel lithium titanate Li4Ti5O12 (LTO) has been explored intensively, and its excellent safety, zero-stain during charge/discharge processes, great structural stability are attractive properties.

The aim of this work is to synthesize and characterize the nanopowders of titanium dioxide (TiO2) and lithium titanate (Li4Ti5O12) by the hydrothermal method and to use them as cathode in a lithium-ion battery.

II. SYNTHESIS OFLI4TI5O12 POWDER

A. The syntheses were carried out systematically in the presence of a source of titanium (Ti), titanuim tetrabutyl (TBT) and lithium (Li) which is lithium hydroxide (LiOH; H2O) and ethanol as solvent. The reaction was carried out at 180°C for 24 h in a cylinder-shaped autoclave with an internal volume of 250 ml. A precipitate (white powder) is obtained by centrifugation at 1200rpm after 20min, the powder is recovered and dried in an oven at a temperature of 80°C overnight. After the synthesis of the powders, thermal annealings are carried out at different temperatures 600°C; 800° C. and 900° C. for 2 h in a calcining oven (Nabertherm, CRTSE).

Fabrication of electrode for electrochemical measurements

The electrochemical measurements were conducted in threeelectrode setup at room-air temperature in 1 M LiClO4 electrolyte. The working electrode was prepared by making suspension of electro-active materials (LTO) (80%) with carbon black (10%) and polyvinylidene difluoride (PVDF) as a binder (10%) in Nmethyl- 2- Pyrrolidone (NMP) solvent. The prepared homogeneous slurry pasted on Al (1 cm2) followed by drying at 80 °C for 24 h to remove the organic solvent. The loaded weights of active electrode materials were approximately 3 mg, as determined using a microbalance with an accuracy of 0.001 mg.

III. RESULTS AND DISCUSSION

ISSN: 1737-9334

1) SEM observations of the synthesized powders were carried out using a JEOL7610F+ type scanning electron microscope (at CRTSE, El-Harrach, and Algiers).

2) Figure 3.1 shows the SEM images of powders synthesized by hydrothermal route and annealed at different temperatures (500°C, 800°C and 900°C) reveal the formation of nanometric powders with a particle size which increases according to the increase annealing temperature; where it is of the order of 40nm at Tr=500°C, 70nm at T=800°C and finally 100nm for T=900°C. This increase is due to the agglomeration of the nanoparticles with the annealing temperature.

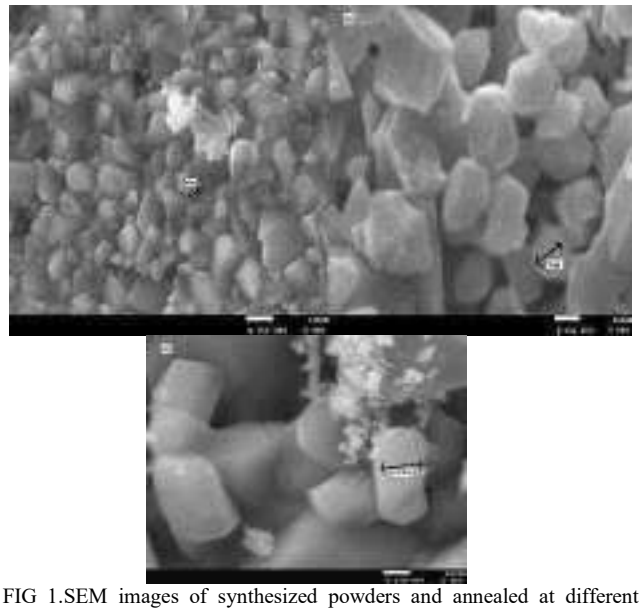

FIG 1.SEM images of synthesized powders and annealed at different temperatures (600°C (a), 800°C (b) and 900°C (c)

X-ray diffraction (XRD), makes it possible to determine in the case of materials crystals, the nature of the phases present as well as the planes (hkl) of these phases which diffracting. The structural analysis of the powders was carried out via the diffraction of a radiation Monochromatic X produced by a copper anode (wavelength of the line Kα=1.54060Å) an XPert MPD type diffractometer (at the CRNA research center, Algiers).The XRD spectrum of commercial TiO2 powder indicates the presence of diffraction peaks at 2θ = 25.3°, 37.7°,48°,53.8° and 55° which correspond respectively to the reticular planes (101), (004), (200), (105) and (211) of the anatase phase of titanium oxide and other phases secondary; the Rutile phase of titanium oxide, identified by the diffraction peaks at 2θ =27.4°, 54.3° and 69°, which correspond to the reticular planes (110), (211) and (301), respectively. Analysis of this spectrum reveals that the anatase structure represents almost 90% of the material and the rest is the Rutile phase of TiO2. The XRD spectrum of the powder annealed at 500°C indicates the presence of a new phase main Li2TiO3 and other secondary phases: titanium oxide (TiO) and LiTi2O4.The main diffraction peaks at 2θ = 18.4°, 36.01° 43.7°, 57.6° and 63.2°, which correspondrespectively to planes (002), (-131), (202), (006) and (312) of the Li2TiO3 phase. Other peaksof diffraction 2θ = 18.2°, 35.3° and 66.6° correspond respectively to the planes (111), (311)and (442) of the LiTi2O4 phase.The third TiO phase was identified by the diffraction peaks at 2θ = 37.8°, 44.8° and 65.2°which correspond respectively to the planes (111) (200) and (220) of the latter. he XRD spectrum of the powder annealed at 800°C which reveals the appearance of anew LTO phase (Li4Ti5O12) which represents almost 50% of this composite with the three polymorphs of TiO2: Anatase, Rutile and Brookite.The diffraction peaks at 2θ =18.3°, 35.5°, 43.2° and 62.8° correspond respectively to the planes (111) (311) (400) and (440) of the main Li4Ti5O12(LTO) phase.The Rutile phase was identified by the diffraction peaks at 27.5°, 36.1°, 41.3, 56.6 and 69.03 of the planes (110), (101), (111), (220) and (301), respectively.Other peaks appear at 2θ = 48°, 53.8° and 70.3° which are attributed to the diffraction of the planes (200), (105) and (220), respectively of the anatase phase and at 2θ = 25.3°, 54.1° and 63° which correspond to the diffraction of the (120), (320) and (160) planes of the brookite phase.The XRD spectrum of the powder annealed at 900°C indicates the presence of two main phases: Li4Ti5O12 and Rutile TiO2 (Figure 3.9). These two phases were identified by peaks characteristics of the LTO phase and the rutile phase TiO2 as we mentioned them in the paragraph above.

We notice on the diffractogram of T=500°C that the peaks are a little wide by compared to the diffractograms of the powders annealed at 800°C and at 900°C. This shrinkage of peaks is due to the enlargement of the grains of the powders after the agglomeration of the particles induced by the increase in temperature, this result was confirmed by the SEM images .The TiO2 and Li2TiO3 phases which appear at 500°C react to give spinel LTO according to the following equation: $3\ TiO_2 + 2\ Li_2TiO_3 \rightarrow Li_4Ti_5O_{12}$

This confirms the appearance of the LTO phase at 800°C and at 900°C (Mahmoud, Amarilla, Saadoune, 2015). The Annealing at 900°C induces complete conversion of the anatase phase to rutile. This shows that the rutile phase of TiO2 is well crystallized at this temperature with the presence of the LTO phase (Li4Ti5O12) to form a TiO2/LTO composite.

ISSN: 1737-9334

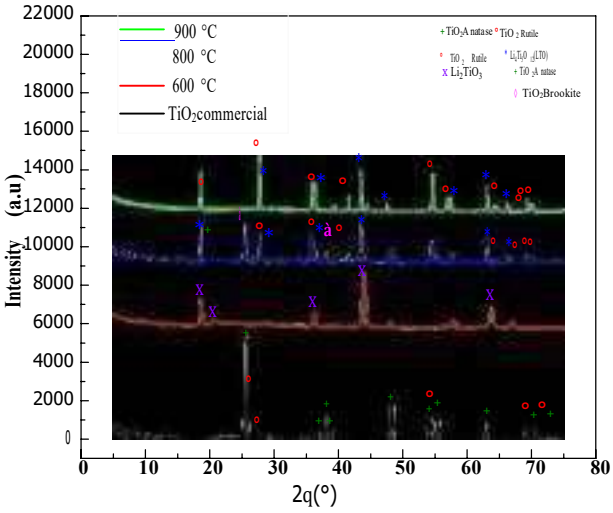

FIG 2.X-ray diffraction patterns of synthesized powders heated at the indicated temperatures for2h.

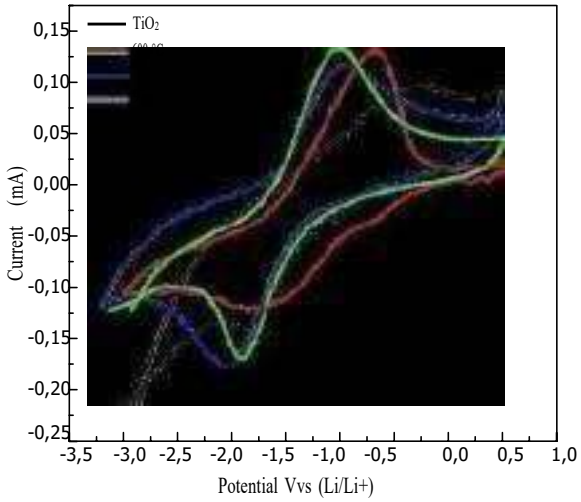

FIG 3.Cyclic voltammograms of synthesized powders heated at the indicated temperatures

Cyclic voltammetry allows us to determine the potential necessary to the intercalation/deintercalation of lithium ions in the active material. In our work, the cyclic voltammetry curves are recorded in a range from potential ranging from -3.2V to 0.5V with a sweep speed of the order of 5 mV/s. Figure 3. represents the cyclic voltammetry of different prepared electrodes. The commercial TiO2 voltammogram clearly shows the cathodic current peaks and anodic for a reversible reaction. The cathodic peak is centered around -1.8 V due to

the insertion of lithium ions (Li+) in the TiO2, while the anodic peak, located at potential

-0.2V is due to the de-insertion of lithium ions (Li+). Nevertheless, the cyclic voltamogram of the annealed powder at T=500°C shows two peaks localized oxidation at -2V and -0.4V (disinsertion of Li+) in the anode side and at -0.2 V and -1.8 V (The insertion of Li+) in the cathodic side in the active material which is in this case a composite of three phases (Li2TiO3, TiO and LiTi2O4). The cyclic voltammograms of powders annealed at T=800°C and T=900°C are similar, where we notice the presence of a single anodic peak for both curves, located at -1V, and in the cathodic side there is a shift of the peaks, for T=800°C the peak is located at -2V and for T=900°C the peak is at -1.9V. This is due to the presence of similar phases in the two samples: Li4Ti5O12 spinel and TiO2 rutile. In addition, we can note the increase in the intensity of the current with the increase the annealing temperature due to the appearance of the Li4Ti5O12 spinel phase for the powders annealed at 800°C and 900°C, which are responsible for a greater insertion of Li+ ions in more than (3*Li*+) therefore the increase in the number of lithium ions inserted into the cathode thus increasing the intensity of the cathodic current.

Galvanostatic charge-discharge (GCD) measurements were performed in the range of potential [-3.2V, 0.5V] for 50 cycles. Figure 3.12 represents the variation of the Capacity experimental specificity of the electrode prepared by the powder annealed at 800°Cas a function ofnumber of cycles.

Figure 4 represents the variation of the experimental specific capacity as a function of the number of cycles of powders annealed at different temperatures (500°C, 800°C and 900°C) and commercial TiO2. We observe that the specific capacity increases according to the annealing temperature which promotes the formation of the Li4Ti5O12 spinel phase which is capable of store 3 ions of Li+ for each intercalation, generating a higher capacity compared to in the other phases (Li2TiO3, TiO2 and LiTi2O), it is around 160 mA.h/g for the powder annealed at 900°C. The Li2TiO3, TiO2 and LiTi2O phases are formed at 500°C and give a specific capacity of the order of 40.6 mA.h/g

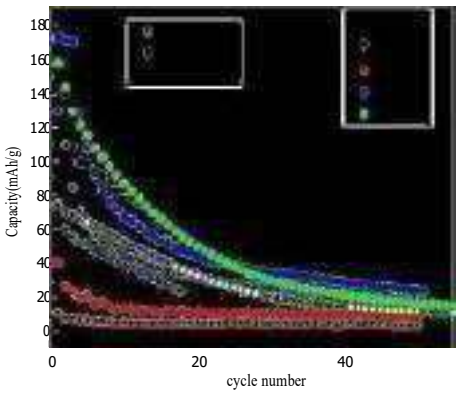

FIG.4. Evolution of discharge capacity vs. cycle number for the samples heated at the indicated temperatures

IV. CONCLUSIONS

SEM images reveal the formation of nanoscale powders with a particle size increasing with the augmentation of the annealing temperature; it is of the order of 40nm at Tr=500°C, 70nm at T=800°C and finally 100nm for T=900°C, This increase is due to the agglomeration of the nanoparticles with the annealing temperature. X-ray diffraction studies have demonstrated that high purity of Li4Ti5O12 spinel was successfully synthesized using the hydrothermal method afte optimization of the thermal treatment conditions. The FTIR spectrum exhibits all the vibration modes characteristic of the bonds present in the TiO2 powder, the Ti-O bonds appear around 532 cm-1, 677 cm-1 and 842 cm-1 (deformation mode) . Finally, the annealed sample at T=800°C for the short time of 2 h shows the best electrochemical performances. With a specific capacity of 173 mA h/g, and a reversible capacity of 40mA h/g with no capacity fading after 50 cycles, this LTO-spinel can be considered a promising anode material to be used in Li-ion batteries in which cycle life and safetyrepresent the primaryconcerns

ACKNOWLEDGMENT

The authors gratefully acknowledge the financial support from the Directorate General for Scientific Research and Technological Development (DGRSDT-Algeria).

REFERENCES

[1] S Ju, S. H., & Kang, Y. C. (2010). Effects of drying control chemical additive on properties of Li4Ti5O12 negative powders prepared by spray pyrolysis. Journal of Power Sources, 195(13), 4327-4331.

[2] 2. Kim, C. S., Moom, B. K., Park, J. H., Choi, B. C., & Seo, H. J. (2003). Solvothermal synthesis of nanocrystalline TiO2 in toluene with surfactant. Journal of Crowth, 257(3-4), 309- 315.

[3] Kim, D. H., Park, H. S., Sun-Jae, K., & Lee, K. S. (2006).). Synthesis of novel TiO 2 by mechanical alloying and heat treatment-derived nanocomposite of TiO 2 and NiTiO 3. Catalysis Letters, 106(1-2), 29-
33. Lazzari, O. (2006). The lithium-ion accumulators in Japan; Les accumulateurs lithium-ion au Japon. Japon.

[4] LEDRA, M., MC, A., KERROUR, F., & Constantine, U. (2014). Etude des propriétés électroniques et photoniques des couches minces à base d'oxydes nanostructurés. Lee, D., Lee, H., Jun, C., & Chang, C.
H. (2007). A variable selection procedure for X-ray diffraction phase analysis. Appl.Spectrosc, 61, 1398-1403.

[5] Levallois, C. (2006). Étude et réalisation de lasers à cavité verticale mono et multi-longueurs d'onde émettant à 1, 55 µm. Doctoral dissertation ,INSA de Rennes. Liu, P. (2016). Vanadium-oxide-based electrode materials for Li-ion batteries. University of Queensland.

[6] Liu, Y., & Yang, Y. (2016). Recent Progress of TiO 2 -Based Anodes for Li Ion Batteries. Journal of Nanomaterials. Lkhagvajav, S., Tsogbadrakh, N., Enkhbayar, E., Galsan, S., & Altantsog, P. (2019).

[7][7]

Economies d'énergie réalisées par un mur Trombe en mode de fonctionnement hiver

Ameni Mokni[1], Marwa Ammar[2],Nahed Soussi[3], Hatem Mhiri[4]
1 mokniameni@gmail.com
2 ammarmriwa@gmail.com

Résumé :

La flambée des prix de l'énergie nous incite à valoriser toute source d'énergie disponible et gratuite. Cet article est une contribution à l'amélioration de l'intégration des systèmes solaires passifs dans les bâtiments. Il consiste en une évaluation des économies réalisées par une pièce munie d'mur Trombe dans la région de Monastir-Tunisie. La simulation a été faite sous des conditions climatiques réelles. Les résultats numériques combinés aux prédictions basées sur l'analyse thermique sont utilisés pour évaluer les différents coefficients d'échange de chaleur, la thermo-circulation dans l'espace, et la quantité totale de chaleur capturée pendant les heures d'ensoleillement. Il a été montré que le mur Trombe peut couvrir jusqu'à 52% des besoins en chauffage de la pièce lors d'une journée du mois de janvier. Ce qui permettra des économies financières allant à 1.37Tnd/jour et évitera 1.35kg de CO_2/jour pour un volume à chauffer égal à 27m^3.

Mots clés :Habitat, rayonnement solaire, chauffage passif, mur trombe, économie d'énergie.

1. Introduction

Le monde actuel continue à produire plus, de se développer et voit sa population sans cesse augmenter. Les ressources, diminuent sans pouvoir se régénérer et sont rapidement exploitées. Le résidentiel et le tertiaire sont à eux seuls responsables d'approximativement 40% de la consommation énergétique. Dans un tel contexte, il faut concilier activité économique, qualité de vie et d'environnement dans un même ensemble ; autrement dit un concept de développement durable.

Le secteur du bâtiment représente 20 à 40 % de la consommation totale d'énergie, dont 33 à 55 % pour le maintien d'un environnement intérieur confortable (chauffage, ventilation et climatisation : HVAC) [1-5]. La réduction de la consommation d'énergie du chauffage, de la ventilation et de la climatisation dans le secteur du bâtiment a donc fait l'objet d'une attention particulière. Une façon constructive de contribuer à la maîtrise de la consommation d'énergie est de concevoir des bâtiments avec une enveloppe parfaitement optimisée, cela assurera une meilleure répartition des charges de chauffage et de refroidissement etpermettra une meilleure consommation d'énergie solaire. Pour atteindre ce résultat, l'utilisation d'un système passif est suggérée. L'objectif est de réduire au maximum les besoins de chauffage des bâtiments et cela peut atteindre 87% selon Akafet al. [6].

Un des moyens les plus efficace pour atteindre cet objectif est le mur Trombe. Ce qui distingue le mur Trombe des autres, c'est sa structure simple et sa facilité d'utilisation. Il améliore l'environnement intérieur sans consommer d'énergie fossile et avec un coût d'exploitation nul [7].Le système de mur Trombe est un concept solaire passif à gain indirect qui a été créé et breveté par Edward Morse, et qui a été intégré à l'enveloppe dubâtiment par Felix Trombe et Jacques Michel dans les années 1960 [8]. Le but était d'assurer le chauffage et la ventilation des locaux en tirant parti du rayonnement solaire.Au fil des décennies, le mur Trombe a été créé pour servir de système de chauffage solaire efficace et fiable. Le mur Trombe est constitué d'un mur thermique solide ainsi que d'une enveloppe transparente en verre entre lesquels se trouve un conduit d'air. Grâce à son exploitation efficace de l'énergie solaire, le mur Trombe a fait l'objet de nombreuses études et expériences, principalement en ce qui concerne le chauffage et la ventilation des locaux.Ce système a fait l'objet de diverses investigations afin de définir les mécanismes qui régissent le transfert de chaleur et d'étudier leur impact sur l'efficacité du mur Trombe.La conduction dans le mur, le rayonnement solaire à travers le vitrage, la réflexion, la transmission [7-9] et la convection dans la lame d'air [10-13]. (Considérée comme une convection naturelle dans un canal avec un rapport de forme élevé) sont les phénomènes identifiés.Les recherches sur le mur Trombe montrent qu'il s'agit d'une technologie efficace pour l'économie d'énergie. Il a également été prouvé qu'elle a un impact considérable sur l'amélioration du confort, quel que soit le climat du lieu.Les études numériques permettent de modifier les paramètres physiques (conductivité de la paroi, épaisseur de la paroi, rapport de forme...), c'est pourquoi elles sont plus courantes dans les recherches sur l'optimisation dela conception.

ISSN: 1737-9334

2. Bilan thermique d'un bâtiment muni d'un mur Trombe

Situation géographique et conditions climatiques du lieu

La Tunisie est dotée d'un gisement solaire assez important qui atteint les dans certaines régions. Cette étude concernera la ville de Monastir dont les coordonnées géographiques sont données par le tableau 1.

Table 1:Système de coordonnées géographiques

Location	Latitude	Longitude	Elevation *(m)*
Monastir	35.76°N	10.8°E	16

Le climat de Monastir est méditerranéen, avec des hivers doux et relativement pluvieux et des étés chauds et ensoleillésÀ Monastir, les précipitations totalisent 375 millimètres par an : elles sont donc assez faibles.E r moyenne on compte 2810 heures de soleil par an.(Figure1)

Les mois le plus défavorable climatiquement est janvier, durant lequel on enregistre les températures les plus basses, la durée d'ensoleillement la plus courte et les jours d'ensoleillement les moinsimportant.

Dans toute la partie qui suit les conditions climatiques du mois de janvier seront les données adoptées pour les simulations numériques.La figure 2 illustre l'évolution de la température ambiante et du rayonnement solaire pour une durée de 12 heures d'un jour standard.

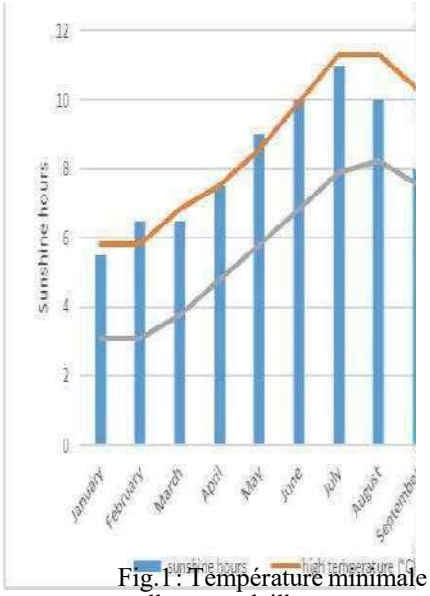

Fig.1 : Température minimale et maximale mensuelle et ensoleillement moyen à Monastir

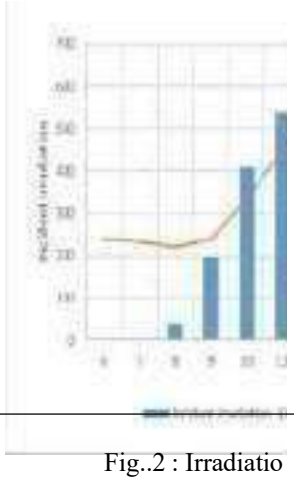

Fig..2 : Irradiatio solaire incidente e t température extérieure durant une journée type du mois de janvier

Analyse thermi ue

Tout d'abord, nous définissons le système à étudier par ses limites dans l'espace et ensuite nous établissons l'inventaire des différents flux de chaleur qui influence l fonctionnement du système.

.

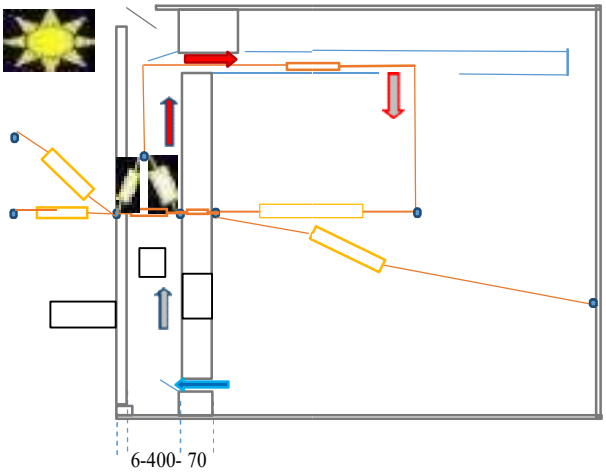

Fig.3: Schematic of est cell of TheTrombe Wall

La pièce test considérée estorientée vers le sud, elle correspond à un v lume à chauffer de 27 m^3 soit 3*3*3 m^3.Le côté exposé au sud a été réalisé avec un verre transparent d'une épaisseur de 6 mm et un panneau de bois de 70 mm d'épaisseur, la lame d'air est de 400 mm. La pièce est isolée intérieurement.

Flux de chaleur reçu à travers les composantes du mur trombe

Les gains totaux obtenus par un mur Trombe Qtot, sont l'addition des transferts de chaleur collectés à travers la surface vitrée, Qsol, et à

ISSN: 1737-9334

travers le mur massif, Qtrans, L'équation (1) illustre ces gains.

$$Q_{Tot} = Q_{sol} + Q_{trans}(1)$$

Le mur de stockage absorbe une partie du rayonnement solaire incident et se réchauffe sous l'effet de serre. Il stocke et transmet une partie de l'énergie captée par conduction à l'intérieur de la pièce

Une autre partie de l'énergie captée est transmise vers la pièce par convection naturelle dans la lame d'air ventilée.Selon la nature du vitrage, lerayonnement solaire qui atteint la surface extérieure du vitrage est réfléchi, transmis et absorbé dans des proportions différentes. Le flux de chaleur au niveau du vitrage est donné par :

$$q_{out} = h_{cout}(T_{amb} - T_g) + h_{rout}(T_{sky} - T_g) + q_{absg}(2)$$

Avec la température du ciel $T_{sky} = 0.0552\,T_{amb}^{1.5}$

Les coefficient d'échange convectif et radiatif sont donnés par :

$$h_{cout} = 5.7 + 3.8V_{wind}(3)$$

$$h_{rout} = \sigma\epsilon_g(T_{sky}^2 + T_g^2)(T_{sky} + T_g)(4)$$

La fraction du flux solaire transmise à travers le vitrage sera à son tour transmise par convection et rayonnement vers l'air intérieur et le mur. Les équationsrégissant ces transferts sont :

$$q_g = h_{g,f}(T_g - T_f) + h_{rw,g}(T_g - T_w)(5)$$

Les coefficients de transfert sont estimés par :

$$h_{g,f} = \frac{Nu_f}{}(6)$$

$$h_{rw,g} = \sigma \frac{1}{(\frac{1}{sg} + \frac{1}{sw} - 1)}(T_g^2 + T_w^2)(T_g + T_w)(7)$$

Flux transmis à travers l'air danscanal

En raison des forces gravitationnelles, un flux d'air ascendant se produit ; nous définissons la températuremoyenne de l'air dans l'espace comme :

$$Tf = \frac{(T_{tv}+T_{bv})}{2}(8)$$

L'énergie transmise à la pièce testée par l'évent supérieur est donnée par :

$$q_{conv} = \frac{\dot{m}C_{pf}(T_{tv}-T_{bv})}{A_w}(9)$$

Le débit massique d'air est proportionnel à la différence de température entre les évents. Il se calcule comme suit:

$$\dot{m} = \rho_f S C_d \sqrt{2gH_v\beta\Delta T}(10)$$

Flux transmis à travers le mur

Les transferts convectif et radiatif entre la surface intérieure du mur et l'espace intérieur de la pièce à chauffer

$$q_{in} = h_{c,in}(T_{w2} - T_{in}) + h_{r,in}(T_{w2} - T_{sur})(11)$$

Les corrélations utilisées pour le calcul du nombre de Nusselt pour des applications du bâtiment sont données par Dascalaki et al. [14].Le bilan établi permettra de calculer les différents flux de chaleur transmis vers l'intérieure de la cellule test et de les comparer aux besoins de chauffage de cette pièce et d'en déduire les économies qui en découlent.

3. Analyse thermique

Températures moyennes des différentescomposantes du mur

L'évolution des températures moyennes du vitrage, la lame d'air et le mur stockant au cours des heures d'ensoleillement sont reportées sur la figure 4.Lescalculs indiquent que la température moyenne de la surface extérieure du mur est supérieure à celle de la lame d'air, qui a en permanence une valeur plus élevée que celle du vitrage. Par conséquent, la convection naturelle du côté du mur est plus importante que celle du côté du vitrage. Le phénomène qui en résulte est celui d'un écoulement dans un canal vertical chauffé de manière asymétrique [46]. La température plus élevée de la paroi provoque un flux d'air ascendant près de la paroi, ce qui est un avantage dans le cas de la paroi Trombe.

Flux de chaleur transmis à l'intérieur de lapièce

La méthodologie adoptée permet de déterminer les gains totaux obtenus pour un mur Trombe exposé à un rayonnement solaire variable durant une journée du mois de Janvier. Les gains cumulés pendant les heures d'ensoleillement d'une journée correspondent à la somme des flux de chaleur transmis par thermo-circulation et de la chaleur transmise par conduction puis par convection à l'intérieur de la surface interne du mur.La valeur maximale de la chaleur transmise a été obtenue pendant la période de fort ensoleillement (12h-13h).Le flux thermique total transmis pour cette journée de la saison de chauffage atteint 7.5kWh soit une valeur de 897W/m2 du mur de Trombe. Cela représente 52% des besoins journaliers de chauffage de cette pièce. Pendant les heures d'ensoleillement intense, il y a un léger avantage pour les transferts par thermocirculation à travers l'évent supérieur. Le maximum est enregistré vers midi, avec des valeurs décroissantes vers la fin de la journée. Les transferts d'énergie par la paroi commencent un peu plus tard que la thermocirculation et demeurent assez importants même en dehors des périodes d'ensoleillement. Les transferts par thermocirculationsont plus importants durant les dernières heures du matin, lorsque l'ensoleillement est plus intense. Le transfert de chaleur par la paroi reste important en fin de journée et même après les

heures d'ensoleillement, ceci souligne l'importance du critère de stockage de la paroi qui permet de continuer à bénéficier de l'ensoleillement reçu durant les premières heures de la soirée. (Figure.5).

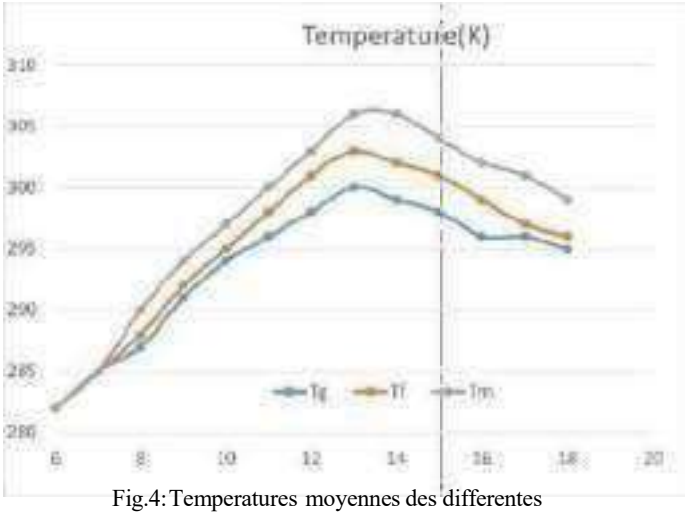

Fig.4: Temperatures moyennes des differentes composantes du mur Trombe

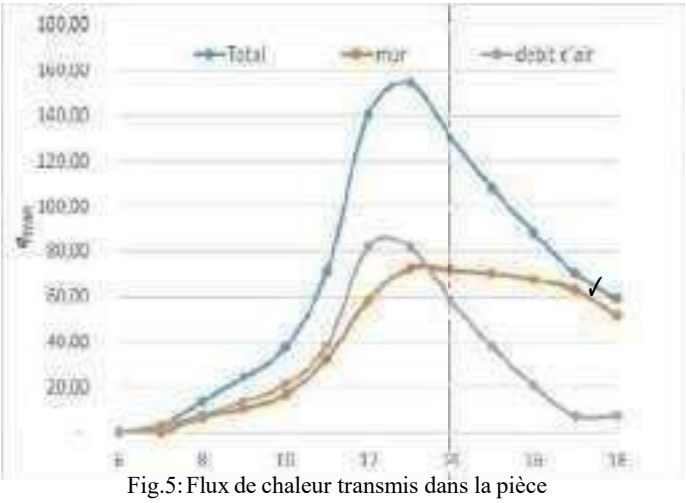

Fig.5: Flux de chaleur transmis dans la pièce

5. Économies réalisées et émissions évitées

Le niveau de satisfaction des besoins en chauffage sera toujours atteintquel que soit la journée de la saison froide puisque nous avons considéré pour le calcul des besoins la valeur de température minimale enregistrée au cours du mois de Janvier, qui est le mois le plus défavorable de l'année.Les gains solaires réalisés pendant la période de chauffage permettront de réaliser des économies et d'éviter les émissions nocives ; les valeurs correspondantes sont indiquées dans le tableau 2.

Table 2**:** Économies réalisées et emissions évitées

Satisfaction besoin de chauffage	Economies (Tnd/jour)	EmissionsCO2 évitées(kg CO2)
50%	0.62-1.37	1.35

6. Conclusion

Les murs Trombe se sont avérés être une solution énergétique passi e adaptée aux crises environnementales et énergétiques actuelles. Cette étude a fourni une analyse énergétique complète et une estimation de l'échange thermique d'une chambre à mur Trombe dans des circonstances les plus défavorables de l'annéeà la ville deMonastir. Il a été montré que :

- ✓ La fraction du rayonnement solaire transmise à travers le vitrage est faible par rapport aux pertes vers l'extérieur.
- ✓ Les échanges radiatifs sont prédominants par rapport aux ec anges convectifs.
- ✓ Les analyses développées ont permis de quantifier la partie de l'échange thermique

se produisant par thermo circulation à travers le mur de Trombe et celle qui est due à la conduction. Le principal résultat est que la thermo circulation est fortement liée aux heures d'ensoleillement et à l'intensité du rayonnement. Quant à la conduction, on pe t remarquer que le mur emmagasine une certaine quantité de chaleur pend nt les heures d'ensoleillement et la dissipe pendant les premièresheures de la nuit.

Le mur Trombe peut couvrirjusqu'à 52% des besoins en chauffage de la pièce.

Les contraintes sociales, culturelles, et surtout esthétiques, qui découragent les individus d'utiliser les murs Trombe devraient être prises en compte pour les différents pays, surtout qu'aujourd'hui l'économie d'énergie devient une obligation etnon un choix.

Nomenclature

a	Diffusivitéthermique(m^2/s)	λ	
Cd	Coefficient de decharge 0.57	μ	
Cp	Chaleur specifique(J/kgK)	ρ	
g	Acceleration de pesenteur(m/s^2)	σ	
Gr	NombredeGrashof	τ	
h	Coefficient ddetransfert onvective (W/m^2K)	ν	
H	Hauteur(m)	***Subscripts***	
I	Rayonnementsolaire (W/m^2)	amb	
m	Debit massique(kg/s)	b	
Nu	Nombre de Nusselt	conv	
Pr	Nombre de Prandtl	e	
q	Flux de chaleur(W)	f	
Ra	Nombre de Rayleigh	g	
S	Surface(m^2)	in	
T	Temperature(K)	rad	
v	(m/s)	sky	

ISSN: 1737-9334

Greekletters

α Absorptivité
β Coefficient d' expansion thermique(K^{-1})
ε Emissivité

Références

[1] Tian Z, Si B, Shi X, Fang Z. An application of Bayesian Network approach for selecting energy-efficient HVAC systems. J Build Eng 2019; 25:100796. https:// doi.org/10.1016/j.jobe.2019.100796.

[2] Kim D-B, Kim DD, Kim T. Energy performance assessment of HVAC commissioning using long-term monitoring data: a case study of the newly built office building in South Korea. Energy Build 2019;204:109465. https://doi.org/ 10.1016/j.enbuild.2019.109465.

[3] Toub M, Reddy CR, Razmara M, Shahbakhti M, Robinett Rd, Aniba G. Model-based predictive control for optimal MicroCSP operation integrated with building HVAC systems. Energy Convers Manag2019;199:111924.

[4] Wang W, Yuan M, Li YZ, Li C. Numerical investigation on the impact of an on-top sunspace passive heating approach for typical rural buildings in northern China. Sol Energy2019;186:300–10.

[5] Kim B, Yamaguchi Y, Kimura S, Ko Y, Ikeda K, Shimoda Y. Urban building energy modeling considering the heterogeneity of HVAC system stock: a case study on Japanese office building stock. EnergyBuild 2019; 199:547–61

[6] Akaf HR, Kohansal ME, Moshari S, Gholami J. A novel decision-making method for the prioritization of passive heating systems use; case study: Tehran. J Build Eng 2019.

[7] Hu Z, He W, Ji J, Zhang S. A review on the application of Trombe wall system in buildings. Renew Sustain Energy Rev 2017;70:976–87.

[8] E. Krüger, E. Suzuki, A. Matoski, Evaluation of a Trombe wall system in a subtropical location, Energy Build. 66 (2013) 364–372. doi:10.1016/j.enbuild.2013.07.035.

[9] S.A.M. Burek, A. Habeb, Airflow and thermal efficiency characteristics in solar chimneys and Trombe Walls, Energy Build. 39 (2) (2007) 128-135.

[10] J.R. Bodoia, J.F. Osterle, The development of free convection between heated vertical plates, ASME J. Heat Transf. 84 (1) (1962) 40-43.

[11] T. Aihara, Effects of inlet boundary-conditions on numerical solutions of free convection between vertical parallel plates, Rep. Inst. High-Speed Mech., Tohoku University28 (1973) 1–27.

[12] H. Akbari et T.R. Borgers, Free convective laminar flow within the Trombe wall channel, Sol. Energy22 (2) (1979) 165-174.

[13] W. Aung, L.S. Fletcher, V. Sernas, Developing laminar free convection between vertical flat plates with asymmetric heating, Int. J. Heat Mass Transf. 15 (11) (1972) 2293-2308.

[14] E. Dascalaki, M. Santamouris, C.A. Balaras, D.N. Natural convection heat transfer coefficients from vertical and horizontal surfaces for building applications. *Energy and Buildings*, Volume 20, 243-249, 1994.

ISSN: 1737-9334

Etude des propriétés électroniques des matériaux organiques type thiophène(C_4H_4S).

Maya Hanane Rezoug [#1], Ghaouti Bassou [*2], Abdelkader Nouri [#3]

[#] *Laboratoire de Développement des Energies Renouvelables et leurs Applications dans les zones Sahariennes (LDERAS), Faculté des sciences exactes, Université Tahri Mahammed, B.P 417 route Kenadsa Bachar, Algérie.*

[1]mayahanane22@gmail.com

[3] nouri.abdelkader@univ-bechar.dz

[*] *Laboratoire de Microscopie, Microanalyse et Sciences des Matériaux (L2MSM) Faculté des sciences exactes, Université Djilali Liabès.22000 .Sidi-Bel-Abbès*

bassoug@yahoo.com

***Résumé*— Dans cette étude nous visons à optimiser la conversion photovoltaïque des matériaux organiques à base de thiophène (C_4H_4S) en utilisant la théorie de la fonctionnelle de la densité (DFT).**

Les résultats de la simulation des polymères conjugués à base de thiophènes démontrent que le niveau énergétique de l'orbitale moléculaire occupée de plus haute énergie (HOMO) et de l'orbitale moléculaire inoccupée de plus basse énergie (LUMO) et qui autorisent la bande interdite (Gap) sont facilement accessible.

Nous avons utilisé le programme GAUSSIAN 09-D pour effectuer des calculs en utilisant la base B3LYP/6-31G(d,p) pour trouver les conformations stables optimales. L'application GaussView 06 a été utilisée pour visualiser les molécules une fois la géométrie optimisée.

***Mots clés*— Optimisation, matériaux organiques, thiophène, DFT, HOMO, LUMO, Gap.**

Introduction

Les cellules photovoltaïques organiques à base de dérivées de thiophène présentent plusieurs avantages par rapport aux matériaux à base de silicium tels que leurs coûts de fabrication relativement faible, un traitement facile, une grande flexibilité et possibilité de recyclage. Comme toutes les cellules solaires organiques, le seul inconvénient de ce type de cellules est leurs rendement relativement faible par rapport aux cellules solaires à base de silicium **[1].**Selon les grands spécialistes du photovoltaïque, cette technologie cachent beaucoup de potentialités et elle sera à l'avenir le premier concurrent de la technologie de silicium.

Dans la présente étude, le calcul par la Théorie Fonctionnelle de la Densité (DFT) a été effectué pour une chaine de molécules conjuguées à base de méthylthiophène. Dans la présente étude, le calcul par la Théorie Fonctionnelle de la Densité (DFT) a été effectué pour une chaine de molécules conjuguées à base de méthylthiophène.

Dans un premier temps, nous avons effectué des calculs d'optimisation utilisant la fonctionnelle B3LYP dans le but d'obtenir les structures géométriques les plus stables.

Le choix de cette base selon Lii et al. **[2]** est motivé par le fait qu'elle donnent des structures stables (base énergie). Les calculs ont été réalisés en utilisant le programme GAUSSIAN 09-D [3].

La visualisation des molécules après optimisation de la géométrie est obtenue par le programme GaussView 06 [4].

Tous les calculs des propriétés électroniques ont été réalisés en utilisant la théorie de fonctionnelle de la densité (DFT) [5-6] combinée avec le jeu de base 6-31G. La stabilité des structures obtenues a été vérifiée et confirmés par un calcul de fréquence.

La tension maximale de circuit ouvert Voc de la cellule solaire organique est liée à la différence entre HOMO du l'électro-donneur et de LUMO de électro- accepteur. Les valeurs de V_{OC} peuvent être calculées à partir de la formule empirique suivante [7]:

$$Voc = |EHOMO(Donneur)| - |ELUMO(Accepteur| - 0,3 \quad (Eq\ 1)$$

I. STRUCTURE

La structure géométrique des molécules π-conjugués a un impact important sur leurs structures électroniques qui influence les caractéristiques du transport de charge ainsi que celles des spectres d'absorption et d'émission [8]. Les structures optimisées des composés étudiés sont illustrées dans la figure 1. Toutes les géométries des molécules ont été calculées avec la fonction hybride B3LYP combiné avec la base 6-31G.

ISSN: 1737-9334

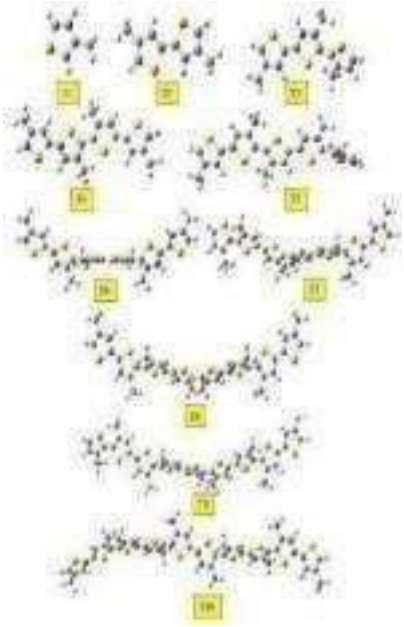

Fig. 1 Structures des molécules étudiées optimisées par la B3LYP/6-31G.

La présence du système d'électrons π, ou d'électrons délocalisés sur l'ensemble du squelette de la molécule confère aux systèmes conjugués des propriétés originales par rapport aux systèmes saturés [9].

- L'existence de la conjugaison permet la propagation des influences électriques le long du squelette carboné ; en particulier la déformabilité du nuage électronique π est particulièrement aisée ce qui conduit à une polarisabilité importante.
- Les matériaux conjugués absorbent fortement les rayonnements dansle visible et proche UV.

II. PROPRIETES ELECTRONIQUES

A. Niveaux Energétiques HOMOet LUMO

Il est très important d'analyser les orbitales occupées de plus haute énergie (HOMO) et les orbitale cristallines inoccupées de plus basse énergie (LUMO) pour ces composés, car ces derniers fournissent une indication qualitative rationnelle des propriétés d'excitation et de la capacité de transport des électrons et trous. D'autre part, la connaissance des niveaux énergétiques HOMO et LUMO des composés donneurs et accepteurs, permet de prévoir si le transfert de charge effective entre le donneur et l'accepteur sera possible. La surface d'iso-densités des orbitales frontières HOMO et LUMO des molécules étudiées sont présentées respectivement dans les figures 2 et 3. La figure 2 montre que les orbitales HOMO présentent un caractère liant par rapport aux liaisons (C=C) caractère anti-liant par rapport aux liaisons (C-C). La même figure montre aussi l'absence de lobes HOMO pour les atomes de soufre. Les orbitales HOMO sont concentrés principalement dans les liaisons (C=C). Les orbitales LUMO (Figure 3) présentent un caractère anti-liant par rapport aux doubles liaisons, et liant par rapport aux liaisons (C-C).

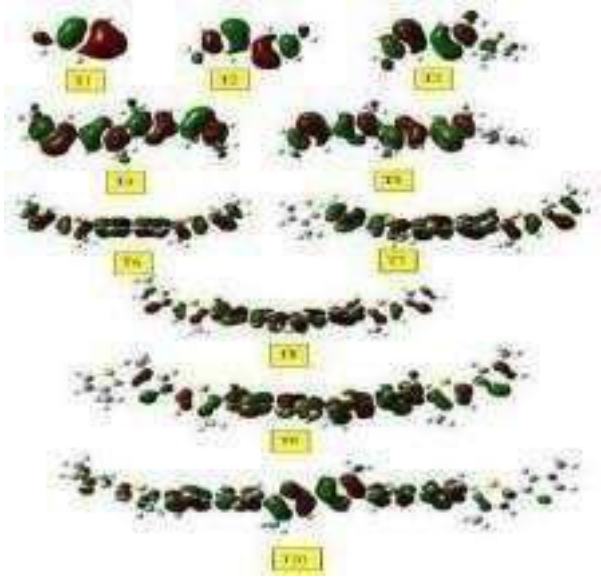

Fig. 1 Surface d'iso-densités des orbitales frontières HOMO des molécules étudiées optimisées par la B3LYP/6-31G.

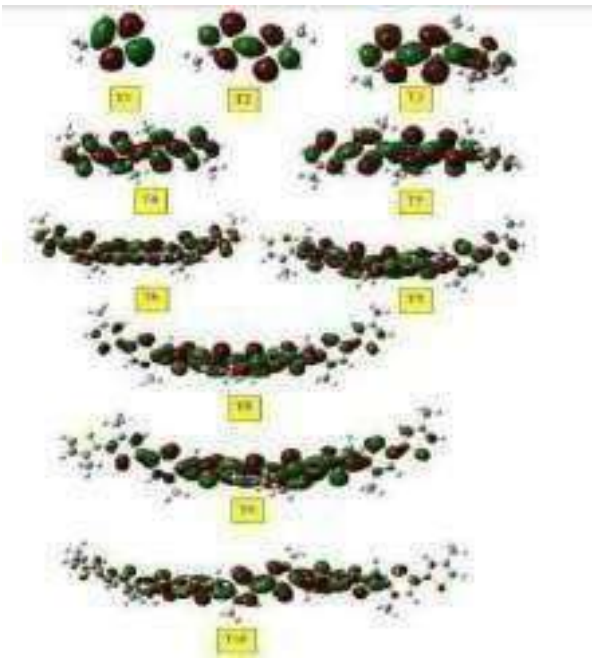

Fig. 3 Surface d'iso-densités des orbitales frontières LUMO des molécules étudiées optimisées par la B3LYP/6-31G.

Les valeurs des énergies HOMO, LUMO sont illustrées dansla figure 4 et 5.

La valeur d'énergie HOMO devient quasi-constante à partir deT5 avec une valeur moyenne de -5,14 eV.

ISSN: 1737-9334

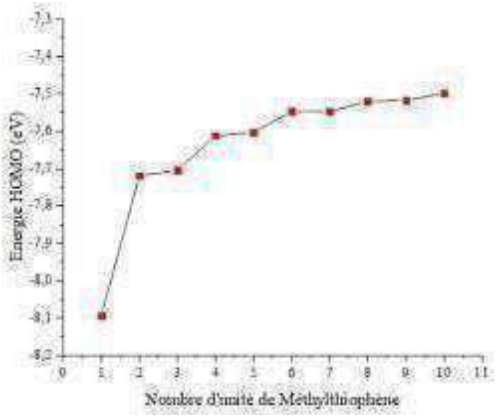

Fig. 4 La variation de l'énergie HOMO en fonction de nombre d'unité de méthylthiophène.

La figure 5 montre une diminution d'une manière proportionnelle de l'énergie en fonction de l'augmentation de nombre d'unité. Les valeurs des énergies LUMO changent légèrement à partir de l'ajout de la cinquième unité.

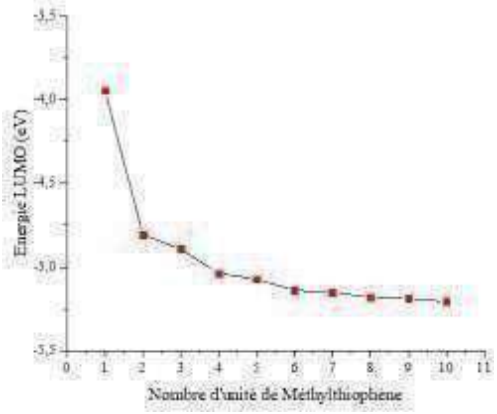

Fig. 5 La variation de l'énergie LUMO en fonction de nombre d'unité de méthylthiophène.

B. Energie de Gap

Dans la science des matériaux, la structure de bande est devenue un paramètre très important puisque l'énergie de Gap est l'un des principaux facteurs pour le contrôle des propriétés physiques des cellules solaires. Dans les molécules conjuguées, l'énergie de Gap est gouvernée par leurs structures chimiques. Leur valeur peut être définie par la différence entre la plus base énergie de la bande de conduction équivalente à E_{LUMO} pour les composés organiques et la plus haute énergie dans la bande de valence équivalenteà E_{HOMO}.

$$E_{Gap} = E_{LUMO} - E_{HOMO} \quad (Eq2)$$

Les valeurs des énergies de Gap des molécules étudiées sont illustrées dansla figure 6.

La figure 6 montre une diminution de l'énergie de gap E_{Gap} avec le nombre d'unité de méthylthiophène. Donc il est possible de contrôler la barrière énergétique entre le niveau HOMO et LUMO par le contrôle de nombre d'unités de méthylthiophène dans la chaine du polymère .

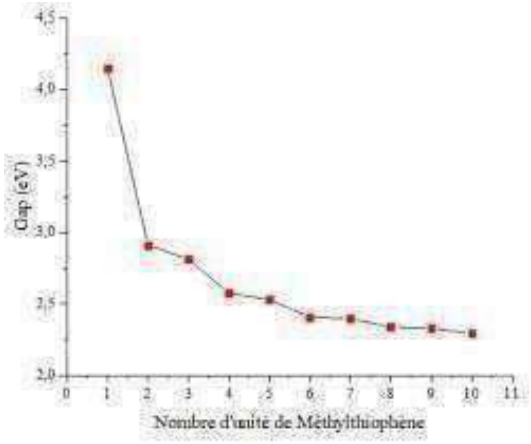

Fig. 6 Énergie de Gap tracée en fonction du nombre d'unité méthylthiophène.

C. Tension de Circuit Ouvert

On peut définir la tension de circuit ouvert V_{OC} comme une tension mesurée lorsqu'aucun courant ne circule dans le dispositif photovoltaïque. Elle dépend du type de cellule solaire, des matériaux de la couche active, et de l'éclairement de la cellule. Les valeurs de V_{OC} sont présentées graphiquement dans la figure 7.

Pour le photovoltaïque organique PVO, la tension de circuit ouvert V_{OC} de la cellule solaire est définie par la différence entre l'énergie HOMO de l'électro-donneur (le méthylthiophène dans notre cas) et l'énergie LUMO de l'électro-accepteur (le C_{60} dans notre cas) [10]. La figure 7 montre clairement une diminution de V_{OC} avec le nombre d'unité de méthylthiophène. Elle montre aussi que la tension de circuit ouvert est quasi constante après l'ajout de sixième unité de méthylthiophène. Le calcul de la tension de circuit ouvert V_{OC} est une étape très importante dans l'étude des matériaux candidats pour les applications liées au photovoltaïque car la connaissance de ce paramètre peut confirmer si le matériau étudié est un mauvais ou un bon candidat. Les matériaux à faible V_{OC} sont des mauvais candidats pour le photovoltaïque.

.

ISSN: 1737-9334

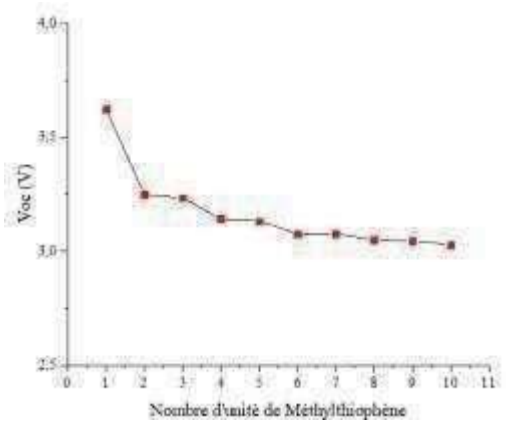

Fig. 7 Tension de circuit ouvert tracée en fonction du nombre d'unité de méthylthiophène.

D. Le Moment Dipolaire

La notion de moment dipolaire en physique et en chimie repose sur l'existence de dipôles électrostatiques. Il s'agit d'une répartition hétéroclite de charges électriques telles que le barycentre des charges positives ne coïncide pas avec celui des charges négatives. Les valeurs] sont présentées graphiquement dans la figure 8.

Le moment dipolaire et très lié à la symétrie de la molécule. Pour une molécule contenant un centre de symétrie, le moment dipolaire est nul, ce qui est le cas de la molécule de C_{60} ainsi que les molécules qui présentent un nombre d'unité paire dont leurs valeurs sont proches de zéro.

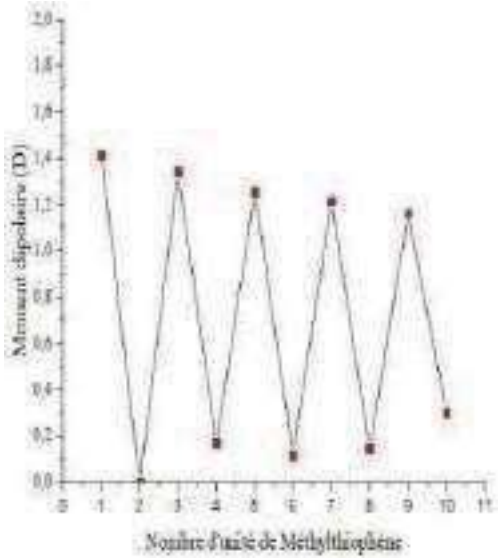

Fig. 8 Moment dipolaire tracé en fonction du nombre d'unité de méthylthiophène.

Le moment dipolaire est paramètre clé dans le processus dans la partie électro-donneur (P) de la cellule solaire. L'existence d'un dipôle permet l'existence d'un champ électromagnétique local responsable de la séparation des paires électron-trou et qui assure cette séparation jusqu' à la jonction P-N de la cellule

III. CONCLUSION

L'optimisation de fullerène C60 et une série poly-méthylthiophène donne des structures stables. L'étude des paramètres électroniques des molécules de méthylthiophène nous permet de savoir la faisabilité d'utilisation ce type de matériaux dans le photovoltaïque organique. Nous avons également montré que le changement de la longueur de la chaine polymérique liée au méthylthiophène a une influence directe sur ses propriétés électroniques.

En jouant sur la chaine polymérique nous pouvons facilement contrôler les propriétés électroniques de ce type de matériaux .Nos résultats prouvent aussi que ce procédé de calculs théoriques peut être utilisé pour prévoir les propriétés électroniques d'autres composés organiques, et concevoir plus loin des futurs matériaux pour l'application aux cellules solaires à base de molécules organique

REFERENCES

[1] P.-L.T. Boudreault, A. Najari, M. Leclerc, Chemistry of Materials, 23 (2011) 456-469.
[2] J.H. Lii, B. Ma, N.L. Allinger, Journal of computational chemistry, 20 (1999) 1593-1603
[3] M. Frisch, G. Trucks, H.B. Schlegel, G.E. Scuseria, M.A. Robb, J.R. Cheeseman, G.Scalmani, V. Barone, B. Mennucci, G. Petersson, Inc., Wallingford CT, 201 (2009).
[4] R. Dennington, T. Keith, J. Millam, (2009).
[5] P. Hohenberg, W. Kohn, Physical review, 136 (1964) B864.
[6] W. Kohn, L.J. Sham, Physical review, 140 (1965) A1133.
[7] .G. Dennler, M.C. Scharber, C.J. Brabec, Advanced materials, 21 (2009) 1323-1338.
[8] H.S. Nalwa, Handbook of Advanced Electronic and Photonic Materials and Devices,Ten-Volume Set, Academic Press, 2000.
[9] A. Maillard, in, École Polytechnique de Montréal, 2012.
[10] G. Chamberlain, P. Cooney, Chemical Physics Letters, 66 (1979) 88-94.

Optimization of Reconfigurable Antenna for Intelligent Cognitive Radio Network

BABA-AHMED Mohammed Zakarya[#1], RABAH Mohammed Amin[*2], TALEB Rahma Djaouda[#3]
BOUSALAH Fayza[#4], DAHO Nabil Mohamed Noreddine[#5]

[#]*First-Third-Fourth-Fifth Department Telecommunication,* [#]*First-Third-Fourth-Fifth University of Abou bekr Belkaid Tlemcen*
[#]*First-Second-Third-Fourth-Fifth Laboratory of Telecommunication Tlemcen, Algeria*
[#]*First- Faculty of Technology, University of Chlef,Algeria*

[1]zaki.babaahmed@gmail.com
[3]rahmadjaouda.taleb@gmail.com
[4]bousalah.fayza@gmail.com

[*]*Second* Algerian Space Agency_ Satellite Development Center.
Oran, Algeria
[2]arabah6@gmail.com

Abstract— **Reconfigurable or so-called intelligent antennas have taken an important place in modern mobile and wireless communications due to their flexibility, low weight, low production costs and integration capabilities for different applications. The current challenge is to preserve the global ecology in order to utilize less material (less antennas) but at the same time an opportunistic use of frequency bands, and to adapt the reconfigurable antenna to the cognitive radio network. This technology allows to adapt to any frequency band and has the main feature to be very flexible without changing hardware.**

Our work is based on optimisation and simulation on CST software of frequency reconfigurable antennas, PIN diode and in multi bands frequency of intelligent cognitive radio networks for several applications.

Keywords— **Reconfigurable antenna; optimization; Intelligent network; PIN diode; Cognitive Radio**

I. INTRODUCTION

Wireless spectrum allocation overload has limited the deployment of wireless communication services and the response of wireless technology to user demand. Approximately 70% of the allocated spectrum is identified by the Federal Communication Commission (FCC) as unused for a reasonable time [1]. For this reason, researchers have proposed a new wireless technology called "cognitive radio" [2].

The concept of cognitive radio (CR) was also proposed by Joseph Mitola in 1998 and subsequently published in an article by in an article by Mitola and Gerald Q. Maguire, Jr. in 1999 [3]. An CR senses the spectrum, determines empty frequency bands, dynamically changes its operating parameters, and then uses the free bands to communicate with other CRs. These capabilities allow the CR to operate in licensed and unlicensed bands. As a result, this allows the CR to use spectrum efficiently, i.e., it fills the holes in the spectrum without needing an additional band to operate. In addition, the unlicensed bands do not correspond to any particular service or user, while the licensed bands are part of the spectrum registered for specific wireless services or applications [4]. The cognitive task includes [5]:

- ✓ The spectrum detection phase detects spectrum holes by estimating interference temperature of the radio environment.
- ✓ The prediction or channel identification task to estimate the channel state information and then predict the channel capacity.
- ✓ Spectrum decision by controlling the transmission power and spectrum management.

With the increase in number of users, functionality, and transmission rates, cognitive radio has led to the need for smart antennas (reconfigurable antennas). A reconfigurable antenna can be defined as a device capable of modifying its operating characteristics (operating frequency, bandwidth, polarization radiation pattern) in a dynamic way after its manufacture. The modification in one of its electrical, optical, physical parameters (mechanical modification) or the integration of controllable materials (ferrites, liquid crystals or graphene which is used in satellite applications [6]) allows to modify the characteristics of the antenna, even during the operation of the antenna in real time. These changes allow the antenna to adapt to the changing environment and to the constraints of the communication systems. Reconfigurable patch antennas are very attractive and represent the best choice for wireless applications due to their many advantages such as simplicity, light weight, compatibility and ease of manufacture and integration. Reconfigurable antennas are classified as polarization reconfigurable antenna, frequency reconfigurable antenna, pattern reconfigurable antenna and the combination of the previous. Frequency reconfigurable antennas are described as antennas that can dynamically change or adjust their operating frequency. An antenna with a reconfigurable pattern can change its characteristics between omnidirectional and directional radiation patterns. The

polarization reconfigurable can switch from left circular to right circular, vertical and horizontal polarization [7].

The UHF bands offer less signal penetration through obstacles than the HF bands, but they allow to reach readings with higher speed and their information exchange rate is important [8], but for this band the size and number of antennas can be a major limitation for some applications, so reconfigurabilityoffer the solution to solve this problem [9].

In this paper, our challenge is to satisfy secondary users (cognitive radio) related to the medical field with reconfigurable and flexible antennas in different frequency bands with a varied use of the radio spectrum for medical applications. For that, we will study the frequency reconfiguration by the diode method; the rectangular slot patch antenna operating at a frequencyof2.5 GHz.

II. ANTENNA DESIGN

The antenna design was done using the electromagnetic simulation software CST Studio Suite v.2019. The antenna was optimized toradiate in the 1-10 GHz band.

The rectangular slot patch antenna operating at a frequency of 2.5 GHz, consists of a patch with dimensions (length: Lp = 28.56 mm and width: Wp = 36.85 mm), printed on thetop layer of a FR4 substrate with relative permittivity ε_r = 4.3, thickness: h = 1.6 mm, length Ls = 54.75 mm and width: Ws = 46.45 mm. A feed line of length Lf = 16.59 mm and width Wf = 3.11 mm is used to feed the antenna as shown in Figure 1.

At a length of 20.69 mm of the patch, a slot of 1 mm length was created on the whole width of the patch in order to insert in it one or more metal tabs of dimensions 1 x 0.5 mm². Note that the dimensions and the position of a slot have a great influence on the resonant frequency of a radiating structure that we want to reach. A ground plane of dimension 54.75 x 46.45 mm² is printed on the back face of the substrate.

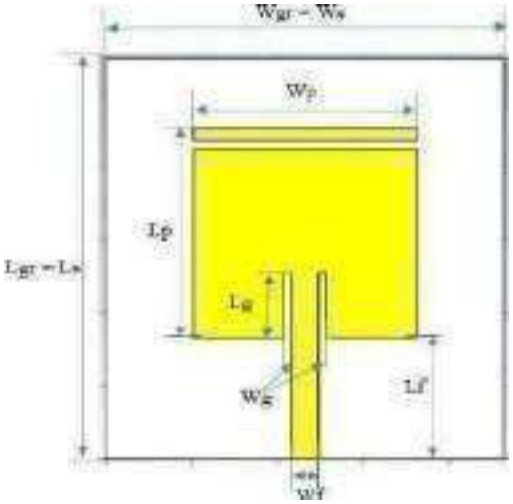

Fig. 1 Geometry of antenna

III. SIMULATION AND RESULTS

To study the frequency reconfiguration by the diode method on our antenna, we placed five diodes in the slots as shown in Figure 2.

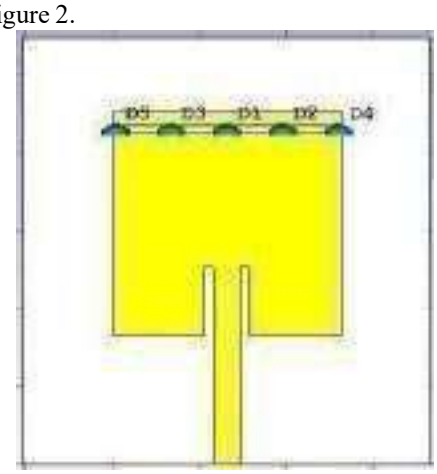

Fig. 2 Reconfigurable antenna with 5 diodes

The use of five diodes and the comparison is done as follows:

- **First comparison:** One diode ON and four diodes OFF with one diode OFF and four others ON (1-ON & 4-OFF vs. 1-OFF & 4-ON).
- **Second comparison:** Two diodes ON and the other three OFF with two diodes OFF and the other three diodes ON (2-ON & 3-OFF versus 2-OFF & 3-ON).
- **Last comparison:** Five diodes ON with five others OFF (5-ON vs 5-OFF).

A. First comparison

Figure 3 shows the curves of the reflection coefficients S11 of the first comparison.

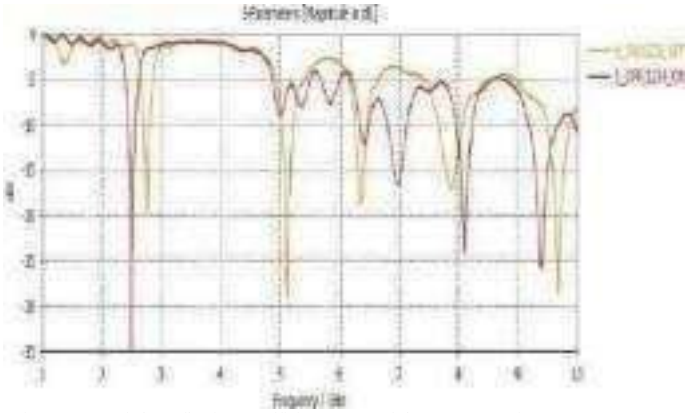

Fig.3 curves of the reflection coefficients S11 of the 1st comparison

Figure 4 corresponds to the 4-OFF & 1-ON state and contains respectively in (a): the VSWR; (b): the gain versus frequency, (c): the 2D radiation pattern; (d): the 3D radiation pattern at f= 2.75 GHz during the 1st comparison

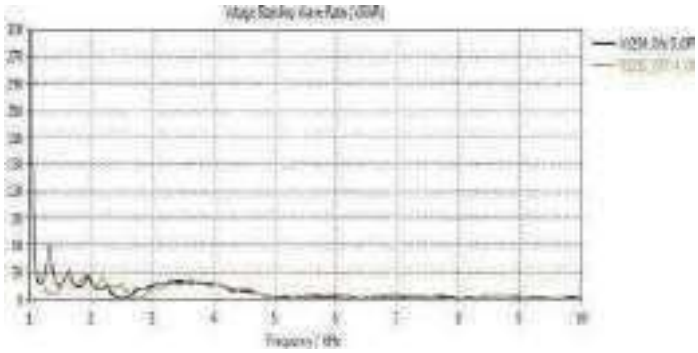

(a)

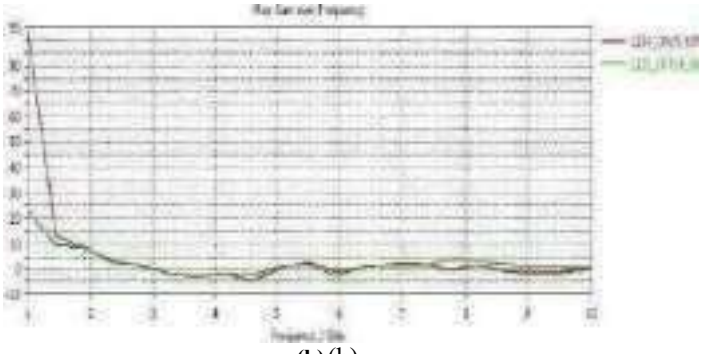

(b) (b)

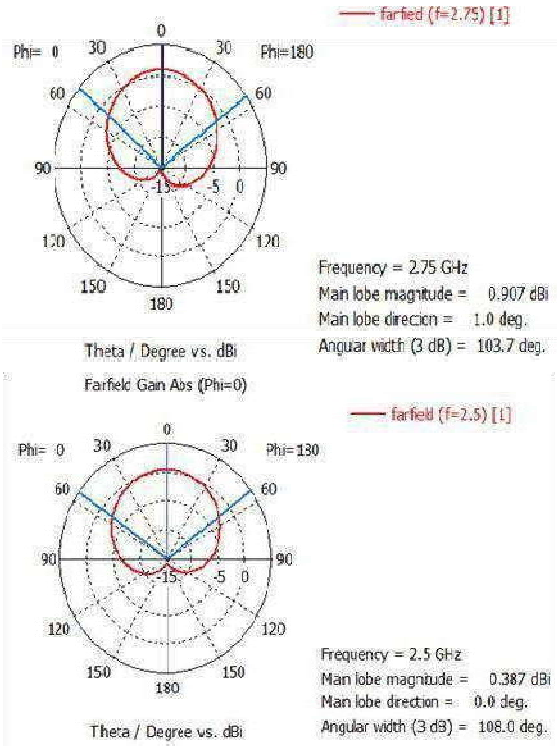

(c) (c)

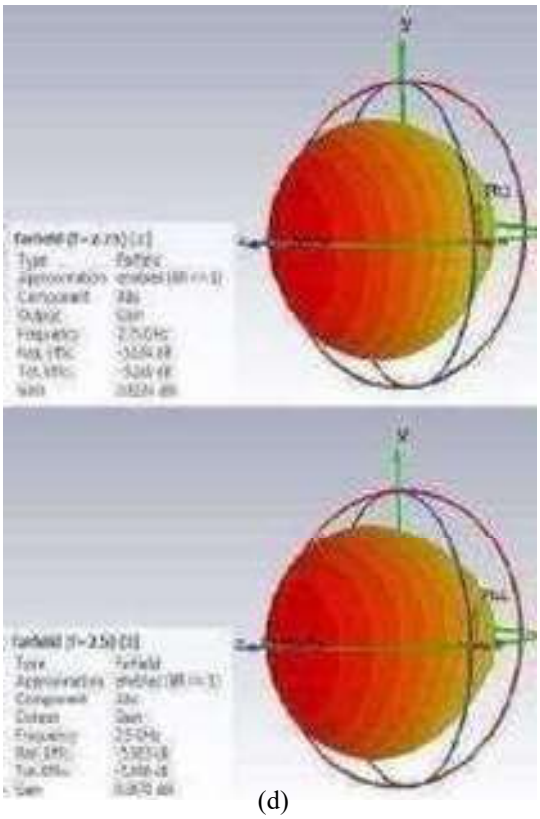

(d)

Fig. 4 The VSWR; (b): the gain versus frequency ;(c): the 2D radiation pattern; (d): the 3D radiation pattern at f = 2.5 and 2.75 GHz in the 1st comparison

In this first comparison, we see that almost the same resonance frequencies are present in both situations with a veryslight shift for the frequencyat 2.5 GHz, translated into 2.75 GHz. The S11 parameters obtained, corresponding to these frequencies are very good, thus offering a good frequency reconfiguration. These resonant frequencies allow the antenna to operate in ISM, WBAN, WLAN and UWB applicationsrespectively.

The antenna has an omnidirectional radiation pattern with a numerical aperture of five degrees difference between the two situations compared, but with a gain of 2.48 dBi, which is higher when the diodes are in the 4-ON & 1-OFF state.

B. Second comparison

Figure 5 shows the curves of the reflection coefficients S11 of the second comparison.

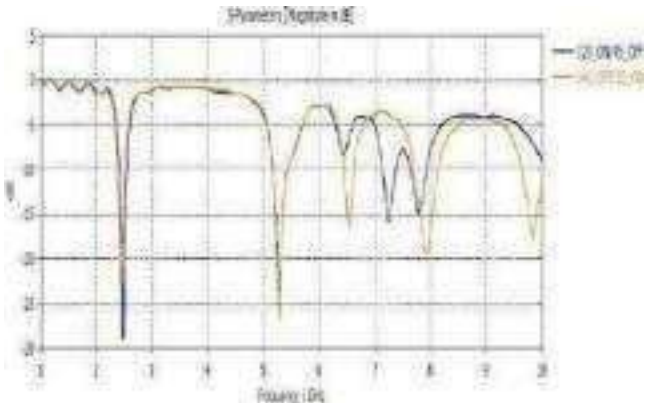

Fig. 5 Curves of the reflection coefficients of the 2nd comparison

Figure 6 contains respectively in (a): the VSWR; (b): the gain versus frequency, (c): the 2D radiation pattern; (d): the 3D radiation pattern at f = 2.45 GHz during the second comparison.

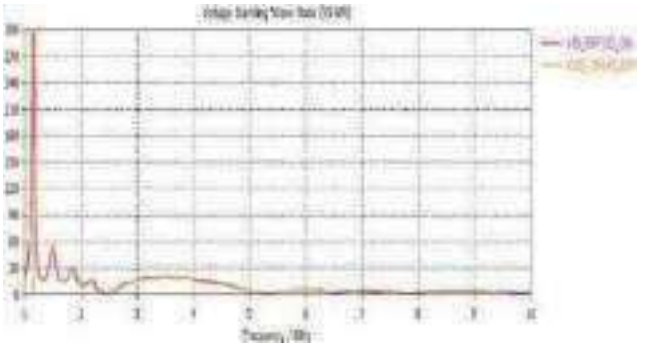

(a)

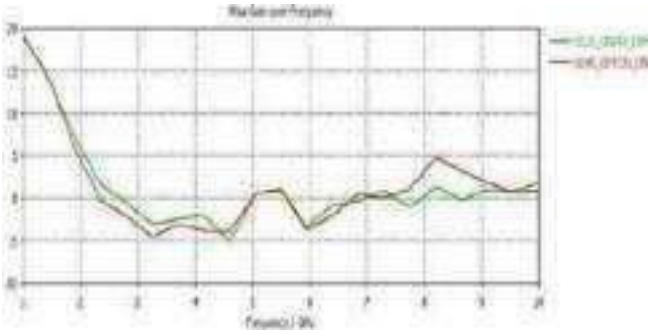

(b)

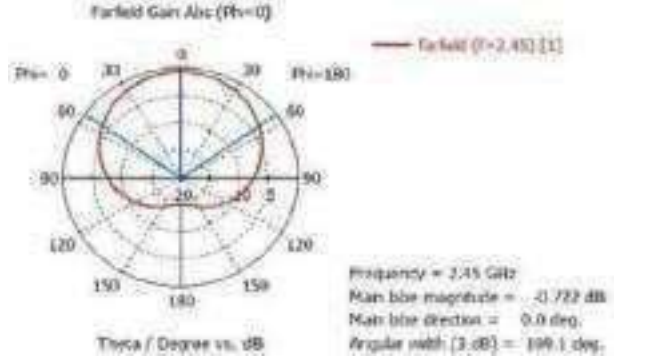

(c)

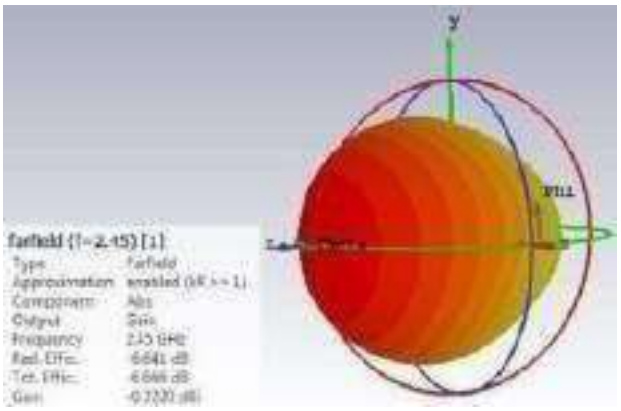

(d)

Fig. 6 (a): the VSWR; (b): the gain versus frequency
: the 2D radiation pattern; (d): the 3D radiation pattern at f = 2.45 GHz

The second comparison shows that both states allow the antenna to resonate at almost the same frequencies with a higher frequency reconfiguration when using three diodes in the OFF state and the other two in the ON state. In fact the antenna has five resonant frequencies (f = 2.44; 5.27; 6.53; 7.93 and 9.82 GHz) operating in ISM, WBAN, WLAN and UWB applications respectively.

The antenna has an omnidirectional radiation pattern with an apertureangle of109 degrees and a gain of0.66 dBi.

C. Third comparison

The figure below presents the curves of the reflection coefficients S11 of the 3rd comparison.

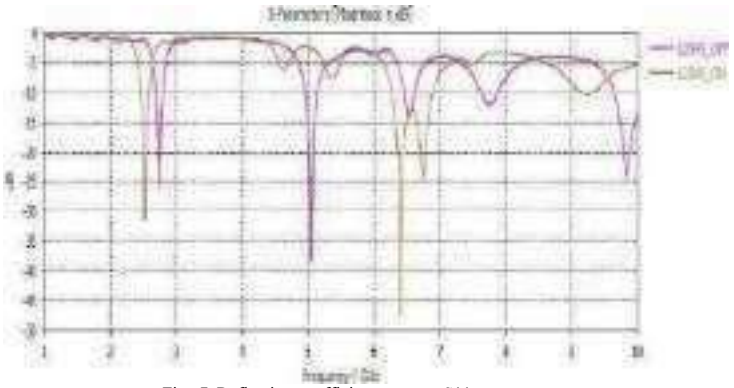

Fig. 7 Reflection coefficient curves S11

Figure 8 includes respectively in (a): the VSWR; (b): the gain versus frequency, (c): the 2D radiation pattern; (d): the 3D radiation pattern at f = 2.52 and 2.73 GHz, for the third comparison

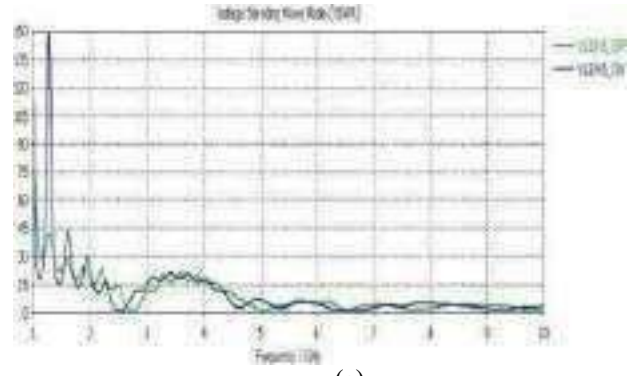

(a)

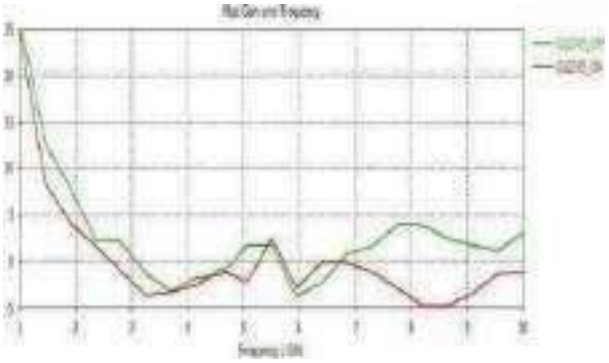

(b)

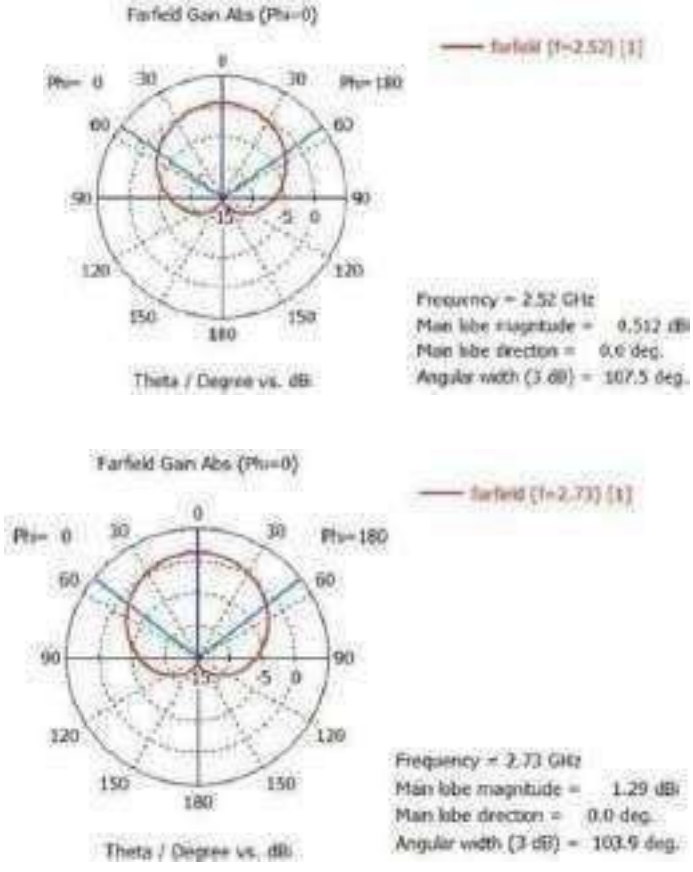

(C)

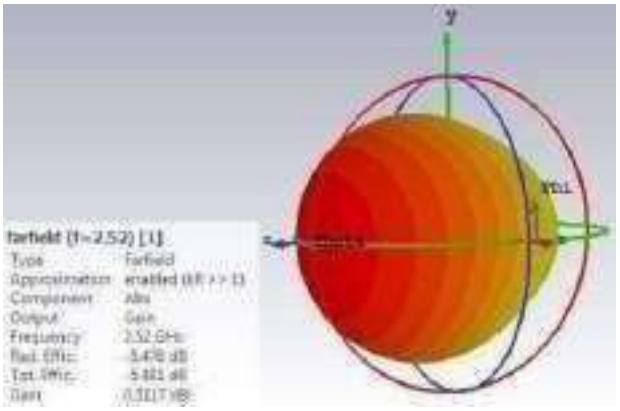

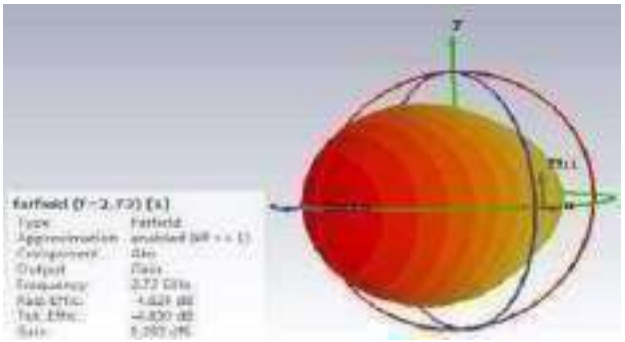

Fig. 8 (a): VSWR; (b): gain versus frequency; (c): 2D radiation pattern; (d): 3D radiation pattern at f = 2.52 and 2.73 GHz in the 3rd comparison

For the latter comparison, more resonant frequencies are obtained when the five diodes are turned off with five frequencies: f = 2.73 GHz (ISM bands), f = 5.04 GHz (Wi-Fi application), f = 6.53; f = 7.75 and f = 9.82 GHz (ultra-wide bands). This can be explained by the fact that the presence of the electrical components (R.L.C) of the five lit diodes, can interfere on the antenna.

IV. CONCLUSION

In this paper, we have used PIN diodes inserted in unit slots as a frequency reconfiguration method. The reconfigurable antenna can thus switch between several frequency bands based on the states of the PIN diodes (ON / OFF).

We have seen that when using five diodes at the same time in different states (3-ON/2-OFF and 3-OFF/2-ON), the frequency reconfiguration results are very good, it can be said that the state of the diodes used and their number can have some influence on the feed current distribution and thus on the resonance of the antenna.

ACKNOWLEDGMENT

This work was carried out at the LTT laboratory in collaboration with the satellite space agency of Oran, we hope to make the realization and the measurements of this type of reconfigurable antenna in our next work with new materials much more ecological and with performances higher.

REFERENCES

[1] Benkler Y. Open wireless vs. licensed spectrum: Evidence from market adoption. Harv. JL & Tech.. 2012; *26, p.69.*

[2] Alnahwi, F. M., Abdulhameed, A. A., Swadi, H. L., & Abdullah, A. S. (2020). A planar integrated UWB/reconfigurable antenna with continuous and wide frequency tuning range for interweave cognitive radio applications. *Iranian Journal of Science and Technology, Transactions of Electrical Engineering*, *44*(2), 729-739.

[3] J. Mitola, and G. Maguire, « Cognitive radio: Making software radios more personal ». August 1999. IEEE Personal Communications, pp. 13-18.

[4] Darabkh, K. A., Amro, O. M., Salameh, H. B., & Al-Zubi, R. T. (2019). A–Z overview of the in-band full-duplex cognitive radio networks. *Computer Communications*, *145*, 66-95.

[5] Nguyen, N. T., Le, T. T., Nguyen, H. N., Voznak, M., & Zdralek, J. (2019, December). Cognitive Radio Architecture for WBAN in e-Health Applications: An Overview. In *2019 6th NAFOSTED Conference on Information and Computer Science (NICS)* (pp. 546-551). IEEE.

[6] Paracha KN, Butt AD, Alghamdi AS, Babale SA, Soh PJ. Liquid metal antennas: Materials, fabrication and applications. Sensors. 2019 Dec 28;20(1):177.

[7] Rabah, M. A., & Bekhti, M. (2019). Dual Graphene Patch Antenna For Ka Band Satellite Applications. *International Journal of Aviation, Aeronautics, and Aerospace*, *6*(4), 6.

[8] Baba-Ahmed, M. Z., Fekar, M. R. E., Seladji-Hassaine, N., & Marouf, F. Z. (2016). Analysis of Patch and Printed Antennas integrated into UHF RFID Passive Tags. *International Journal of Microwave and Optical Technology*, *11*(6), 460-468.

[9] Nejadi, M. R. (2016). A Novel Compact Frequency Reconfigurable Antenna for VHF/UHF/L-Band Airborne Applications. *The Modares Journal of Electrical Engineering*, *16*(2), 20-23.

Studyof ZnO and NiO Effects on the Optical and Photocatalytic Properties of TiO_2 Thin Films

Hacene Serrar[#1], Yassine Bouachiba[*2], Adel Taabouche[Δ3], Abderrahmane Bouabellou[Δ4]

[#] *Research Center in Industrial Technologies CRTI B.P. Box 64, Cheraga16014 Algiers, Algeria*
[1]h.serrar@crti.dz, [1]serrarhacene@gmail.com
[*]*Department of Materials Science Engineering, National Polytechnic School of Constantine, Nouvelle Ville Universitaire Ali Mendjeli, Algeria*
[2]ybouachiba@gmail.com
[Δ]*Thin Filmsand Interfaces Laboratory, University of Constantine1, 25000 Constantine, Algeria*
[3] adelphm@gmail.com
[4] a_bouabellou@yahoo.fr

***Abstract*— In this work we have studied thin films based on metal oxides: TiO2 / ZnO and TiO_2 / NiO. TiO_2 / ZnO and TiO2 / NiO films are successfully prepared by the Sol-gel dip coating method. The layers obtained are characterized by several techniques such as; Raman techniques, m-lines and Uv-visible. Raman spectra show that the TiO2 thin films are characterized by the vibration modes of the Anatase phase. ZnO and NiO induce the reduction of the Raman intensity of TiO2 vibration modes. The Waveguiding results show that the introduction of ZnO and NiO into pure TiO2 causes a decreasing refractive index profile. In the same way, the UV-visible analysis shows an increase in the optical band gap due to the Burstein-Moss effect. MB degradation results show that TiO2 thin films are the best photocatalytic materials. TiO2: ZnO and TiO2: NiO (T7Z and T7N) are less active as photocatalytic materials, due to the screen effect and the effect of TiO2 optical gap widening.**

Keywords: **Titanium Dioxide, Zinc Oxide, Nickel Oxide, Waveguiding, Photocatalysis, Sol Gel**

I. INTRODUCTION

Titanium dioxide (TiO_2) is an important inorganic functional material with good physical properties, which make it suitable for thin film applications. Because TiO_2 has high dielectric constant ε, TiO_2 films have often been used in microelectronic devices, e.g. in capacitors or as a gate dielectric in metal-dielectric-semiconductor devices [1,2].TiO_2 thin films are also often used as various optical coatings for its good transmittance in the visible region, high refractive index and chemical stability [3,4]. Phototocalalysis is the famous application of TiO_2. Mixing of TiO_2 with other metals oxide (based TiO_2 compounds) is a known way to ameliorate its efficiency. A variety of techniques have been used for the preparation of TiO_2 films including chemical vapor deposition [5], sputtering [6], electron-beam evaporation (EBE) [7], Sol–gel [8]. Sol–gel technique has been used for making optical coatings about 50 years ago and in the last decade attracted more attention due to the intensive development of Sol–gel technology.

Indeed, titanium dioxide is preferred as a photocatalyst because of its chemical and biologically inertness, its resistance to corrosion and chemicals, its hydrophobicity, its non-toxicity and its cost-effectiveness. In addition, it is more stable than other photocatalysis under ambient conditions and can be reused [8,9]. In addition, the favorable energy band gap facilitates the extended applications of TiO_2 in the fields of photocatalysis, photovoltaic, batteries, cosmetics, paints, paper and biomedical sciences. But the major drawback of wide TiO_2 band gap is that it prevents the practical application of titanium dioxide to visible light. to solve this problem several strategies such as surface sensitization, modification of the forbidden band by the creation of oxygen vacancies and the doping of photocatalytic metals and non-metals and also the association with other metallic oxide in the form nanocomposites have been discovered for the synthesis of TiO_2 sensitive to visible light [10-11].

This papers consists in the elaboration and the characterization of dip-coated Sol-gel TiO_2, TiO_2:ZnO and TiO_2:NiO thin films for the object to study the Waveguiding regime and evaluating the photocatalytic degradation of organic components.

II. EXPERIMENTAL PROCEDURE

A. Chemicals

Titanium-isopropoxide (TIPT) ((Ti(C4H9O)4, ≥97%) (Alfa Aesar), and Zinc Acetate dihydrate (Zn(CH3COO)2. 2H2O ≥99%) as precursors, isopropanol(≥99.8%) and methanol(99.7%) as solvent, Acetic acid(≥99%) as catalyst and diethanolamine (CH2(OH).CH2)2NH(≥99%) as chelating agent; were

purchased from Sigma Aldrich -except TiPT from Alfa Aesar -and used without anyfurther purification.

B. *Thin Films Preparation*

TiO_2 solution is prepared by mixing Tianium-isopropoxide (TiPT), Isopropanol and Acetic acid using magnetic stirrer. The obtained mixture is stirred for 30 min. Then, Methanol is added to the mixture and stirred for 2 hours. The obtained solution has a transparent yellow color. ZnO solution is prepared by mixing Isopropanol and Zinc Acetate powder during 2 hours using magnetic stirrer. Then, DEA (Diethanolamine) is added and the mixture is kept under stirring for 2 hours. The solutions used in the deposition of TiO_2: ZnO compounds thin films are prepared by mixing TiO_2 and ZnO solutions with 7 % molar portions and stirring the mixture during 2 hours. NiO solution is prepared by mixing Isopropanol and Nickel Acetate powder during 2 hours using magnetic stirrer. Then, DEA (Diethanolamine) is added and the mixture is kept under stirring for 2 hours. The solutions used in the deposition of TiO2: NiO compounds thin films are prepared by mixing TiO2 and NiO solutions with 7% molar portions and stirring the mixture during 2 hours.

The samples obtained TiO_2, TiO_2 doped with 7% ZnO, TiO_2 doped with 7% NiO are denoted T, TZ7 and TN7 in therest of the manuscript.

C. *CHARACTERIZATION OF PREPARED THIN FILMS*

The Raman spectroscopic studies were carried out using Jobin Yvon HR800 (514 nm Ar+ ion laser, equipped with a power of 0.5 mW and 100 objective lens). The surface morphology of thin films was characterized using ZEISS Gemini SEM 300 Scanning Electronic Microscopy (SEM). The optical transmittance and band gap were monitored by Shimadzu-3101PC Uv-Vis Scanning spectrophotometer (UV-VIS) in the wavelength range 190–890 nm. Optical characterization of the sample has been carried out using m-lines spectroscopy (Metricon 2010/M prism coupler). The refractive indices and the film thickness were determined from the measured effective indices. All characterizations were recorded at room temperature.

III. RESULTATS AND DISCUSSIONS

A. *µ-Raman Analysis*

The Raman spectra in the range 50–900 cm^{-1} of our thin films grown on glass substrates by Sol-gel; Dip coatingtechnique, are shown in Fig. 1.

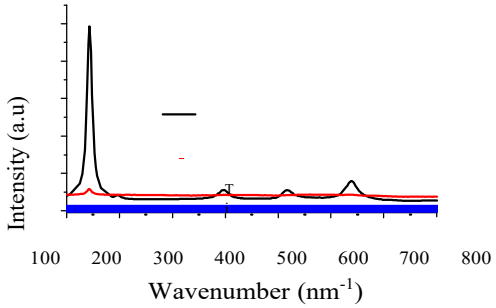

Fig.1. Raman spectra of TiO2 thin films and its compounds: (a) T, (b) TZ7,(c) TN7.

Raman spectrum for pure titanium oxide thin films (Fig.1(a)) shows the symmetric vibrational modes of crystalline tetragonal Anatase phase identified at 143.75cm^{-1} (Eg), 196.71cm^{-1} (Eg), 395.02 cm-1(B1g) , 518.16 cm^{-1}(B1g) and 637.93 cm^{-1} (Eg). The intense band at about 143.75 cm^{-1} is due to O-Ti-O bending vibrations [8]. The other peaks, also, correspond to the Raman active phonon modes of Anatase phase of TiO_2. This Raman spectrum obtained for pure TiO_2 thin films is in good agreement with previous studies for the Anatase phase [9].

The addition of 7% ZnO to TiO_2, induces a considerable decrease in the Raman intensity of the vibrational modes of TiO_2 as can be seen in the main vibrational mode of TiO_2 (Fig.1 (b)). This signifies a degradation ofthe crystalline structure ofTiO_2.

Regarding sample TN7; (Fig. 1 (c)) shows a decrease in fundamental mode intensity greater than that of TZ7 and the disappearance of other vibrational modes; this spectrum indicates that the structure of this sample becomes almost amorphous.

B. *Uv-Visible Analysis*

1. *Transmittance*

Fig.2. shows the transmittance spectra in UV-Vis range of T, TZ7 and TN7 thin films.

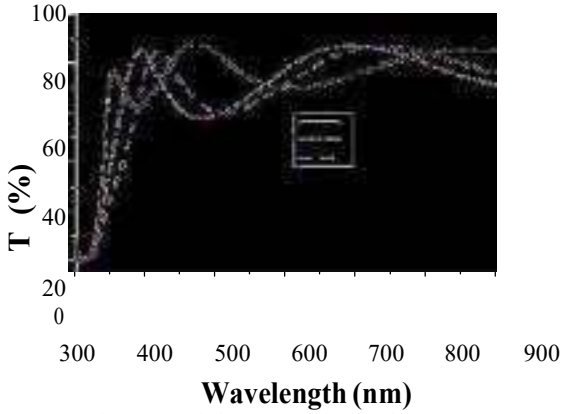

Fig.2. Transmission spectra of (a) T, (b) TZ7, (c) TN7.

The boundary of the fundamental absorption region of the oxide compound samples shifts to shorter wavelengths, which indicates the increase in the optical band gap. We note that the shift with TZ7 is larger than that with TN7.

2. *Optical Band Gap (Eg)*

The behavior in the fundamental absorption region has been confirmed by calculation of the optical band gap using Taucrelation [15]:

$$\alpha h\nu = B(h\nu - Eg)^{n} \quad (1)$$

In this formula, B is a constant and n is a coefficient that depends on the type of transition between the valence band and the conduction band. The values of *n* are 1/2 for an allowed direct transition and 2 for an allowed indirect transition. For TiO_2, n = 2.

Byplotting $(\alpha h\upsilon)^{1/2}$ as a function of the energy$h\upsilon$ (Fig.6), the curve must therefore have a linear part and the extrapolation of this portion of the line for $\alpha = 0$ gives the optical gap value of the material.

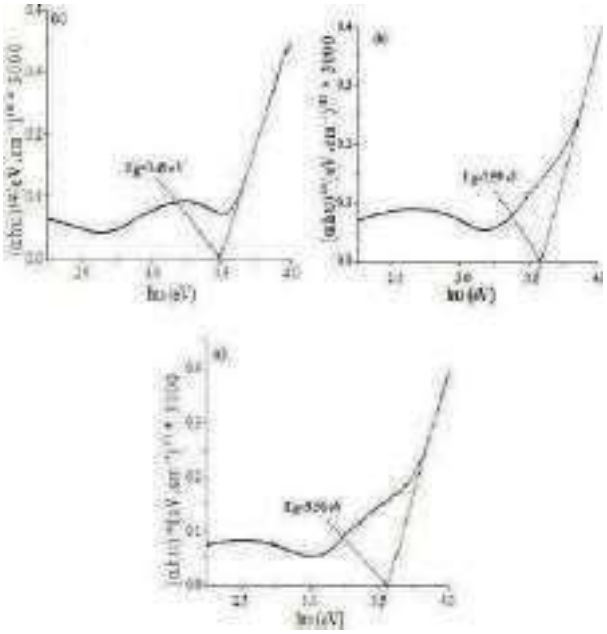

Fig. 3. $(\alpha h\upsilon)^{1/2}$vs photon energy of TiO_2 thin films and its compounds:(A) T, (B) TZ7, (C) TN7,

The obtained optical gap values are summarized in Table 1.

TABLE. 1. *OPTICAL BAND GAP VALUES OF OBTAINED THIN FILMS*

SAMPLE	T	TZ7	TN7
Eg(eV)	3.47	3.65	3.57

Clearly, ZnO in duces the incr easing of the optical band gap. In the nanohomojonction TiO_2 (type n):ZnO (type n), the electrons migrate from ZnO conduction band into TiO2 conduction band [16]. Thereby, this behavior can be explained by the Burstein-Moss effect [17], this effect occurs when the electrons carriers' concentration exceeds the conduction band. This pushes Fermi level higher in energy inside the conduction band. In this case an electron from the top of the valance band can only be exited into conduction band above the Fermi level (which now lies in conduction band) since all the states below the Fermi level are occupied states, thus we observe an increase in the apparent band gap. Concerning the sample TN7 we observe a widening of the optical band gap compared to that of T (pure TiO_2). This can also be explained by the Burstein-Moss effect [18], since NiO has a band alignment with TiO_2 similar to ZnO [19]. However, the electron migration from the NiO conduction band to the TiO_2 conduction band is less than ZnO due to the p-type of NiO. So the electron carrier concentration in this case is less than that in the TZ case. This results in lower optical band energy [20].

C. *Waveguiding Analysis*

Fig.4 shows the optical guided modes of TiO_2 thin films and its compounds. All samples are single guided and accept only TE0 and TM0 modes. The optogeometric parametersarelisted in Table 2.

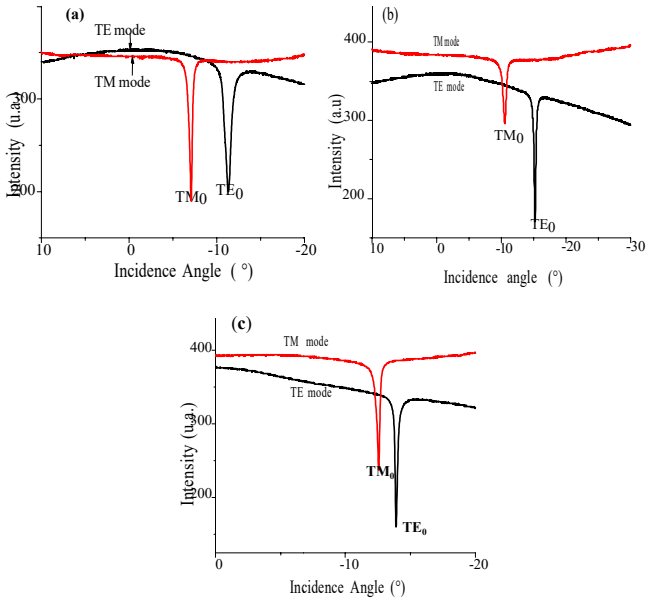

Fig. 4. Optical guided modes (TE0 and TM0) of TiO2 thin films and its compounds: (A) T, (B) TZ7, (C) TN7.

TABLE. 2. THE OPTOGEOMETRIC PARAMETERS OF OBTAINED SAMPLES

Samples	Thickness (±0.1 nm)	n (TE_0) ($\pm10^{-4}$)	n (TM_0) ($\pm10^{-4}$)	Refractive index ($\pm10^{-4}$)
T	194.5	1.8731	1.7297	2.1102
TZ7	193.5	1.8175	1.6844	2.0524
TN7	198.8	1.7763	1.6584	1.9999

According to this table Table.1, the influence of ZnO on the refractive index is remarkable where we can see a decreasing profile in the refractive index. The value of the refractive index of pure TiO2 (T) is typical for a thin film produced by Sol-gel method. The value of the refractive index of ZnO in its bulk state or elaborated by the physical methods is approximately in the range 1.9-2 [10]. When ZnO is deposited by Sol-gel method, the value of the refractive index is decreased. Ghodsi et al. [11] have reported values of the refractive index (using ellipsometric spectroscopy) around 1.58-1.62 in their ZnO thin films produced bythe Sol-gel method at a concentration of 0.12 mol/l. In another work, Znaidi et al. [12] reported a values around 1.78-1.79 (using m-lines technique) for ZnO thin films elaborated by the Sol-gel method at a concentration of 0.75 mol/l. In this work, we believe that the low values of ZnO refractive index deposited by Sol-gel technique explain the decreasing profile of the refractive index in our compounds oxide. In our work, it should be noted that the optical guided modes are not excited in pure ZnO thin films produced by Sol-gel method at a concentration of 0.3 mol/l. Probably; this can be explained by the low refractive index of ZnO thin films which is veryclose to that of glass substrate. Under these conditions, the Waveguiding is so difficult.

Fig.4 shows the optical guided modes of TiO_2 thin films and its compounds with NiO. All samples are single guided and accept only TE0 and TM0 modes. The optogeometric parametersare listed in Table 2.

A decreasing profile in the refractive index is also observed due to the alloys effect. The value of the refractive index of NiO in its bulk state or elaborated bythe physical methods is approximately in the range 2.4 [13]. However, Benramache et al. [14], presented a lower values (in the range 1.6 - 2.1) in their NiO thin films prepared by Sol-gel technique. This explains the decreasing profile in the refractive index. However, the decreasing rate of refractive index in the TiO_2: NiO compounds is important compared to that of the TiO_2: ZnO compounds under the effect of the larger optical gap widening in NiO (Eg = 3.5 eV).) compared to that of ZnO (3.2 eV).

The optical guided modes of NiO thin films are also not detected, probably due to the low value of the refractive index of NiO thin films which is very close to that of glass substrate.

D. Photocatalytic Measurements

In this section, the photocatalytic measurements are performed using the samples T, TZ7and TN7. Fig.8. presents the absorbance of MB in visible region for different times of UV illumination using TiO_2 (T), TZ7 and TN7 as photocatalyst material. MB is characterized by two absorption bands localized at: 615.6 and 652.2 nm. The absorbance of MB shows a great diminution during UV illumination indicating the dissociation of MB into H2O and CO2. According to Fig .5. There is no improvement in photocatalytic activity using TZ7 and TN7 samples as photocatalyst materials, since after 8 hours of UV irradiation the absorbance is not decreased as the case of pure TiO_2 thin films..

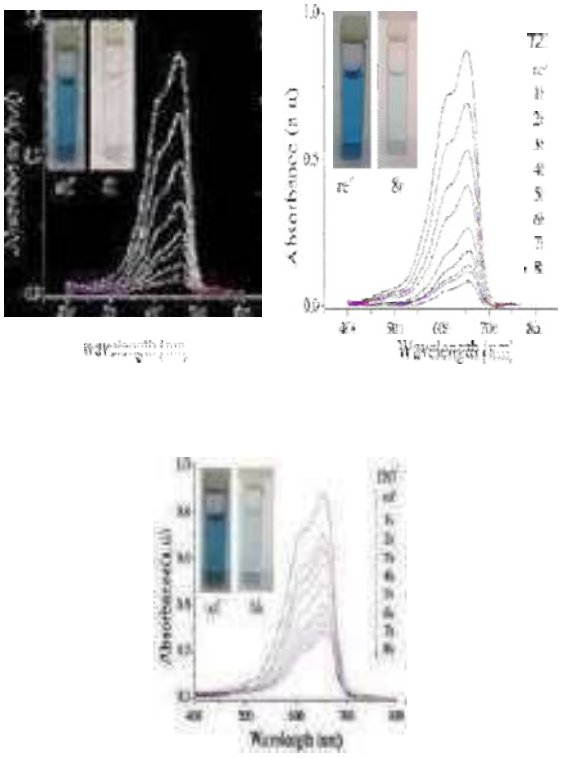

Fig.5. Absorbance of MB in visible region for different times of UV illumination for each sample (T, TZ7 and TN7)

This evolution is confirmed by plotting the degradation rate (%) vs UV irradiation timeas depicted in figures 6 and 7.

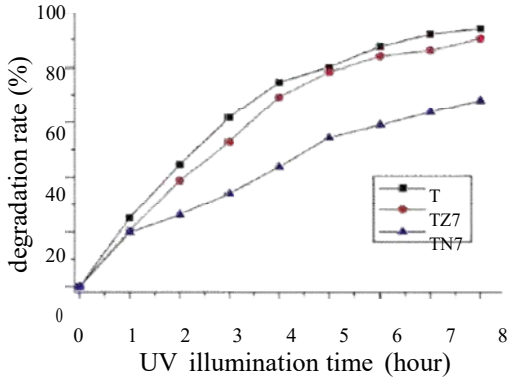

Fig.6. Degradation rate vs UV irradiation time of the samples T, TZ7 and TN7.

According to Fig.6, TiO_2 thin films are more efficient than the compound oxide sample (TZ7). In the previous works, using TiO_2 compounds oxides such as TiO_2: ZnO is an efficient way to ameliorate the degradation rate of TiO_2 thin films [21]. In TiO_2: ZnO diagram band alignment, the electrons migrate from ZnO conduction band into TiO_2 conduction band, whereas the holes drift from TiO_2 valence band into ZnO valence band. In this way, the recombination rate in TiO_2 is decreased and as a consequence the degradation rate will be ameliorated.In

our work, the degradation rate is not enhanced in the sample TZ7, due probably to screen effect of ZnO in this range of alloys (7 % .mol).

Concerning TN7 sample, the degradation rate value; after UV illumination time equals to 8 hours is 67% less efficient than pure TiO_2 thin films. However, the nanohétérojonction TiO2:NiO has the same band diagram alignment as nanohomojonction TiO2:ZnO. The remarkable none enhancement in the degradation rate may be assigned to p-type of NiO as well as screen effect as mentioned above. Qi et al. [21], have reported the same fact in theirs Sol-gel TiO2 and TiO2:NiO thin films.

The kinetic reaction can be expressed by the following relation [22]:

$$\ln(C0/C(t))=Kt \quad (2)$$

Where C(t) is concentration after dissociation, Co is initial concentration and K is the kinetic constant.

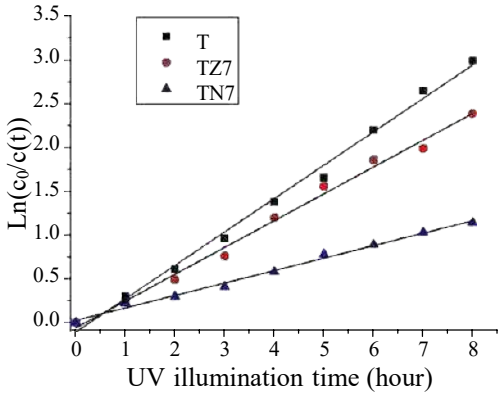

Fig.7. Kinetic reaction vs UV irradiation time of the samples T, TZ7 and TN7.

The evolution of the kinetic reaction is represented in Fig.7. The values of K are 0.00633, 0.005 and 0.0023 min^{-1} for T, TZ7 and TN7samples respectively. These values of K are typical for a photocatalytic measurements performed by thin films photocatalyst. However, these values are higher when nananoparticules are used as photocatalyst materials due to their high specific surface [23].

IV. CONCLUSION

TiO_2 thin films and its compounds; TZ7 and TN7 have been successfully prepared by Sol-gel dip-coating method. Raman, m-lines and UV-visible techniques have been used for the characterization of the samples. Raman spectra show that TiO_2 thin films are characterized by the vibrational modes of Anatase phase. ZnO and NiO induce the decrease in Raman intensity of TiO_2 vibrational modes, indicating the influence of ZnO and NiO on the inelastic scattering of light. UV-visible analysis display that the introducing of ZnO and NiO in pure TiO_2 thin films the shift of the fundamental absorption region into the shorter wavelengths indicating the increase of the optical band gap. Thisincreasing can be explained by Burstein-Moss effect

Waveguiding measurements show single guided modes in both polarizations (TE0 and TM0) in all samples from which refractive index and thickness are calculated. A decreasing profile in the refractive index has been observedwhen ZnO and NiO are introduced in pure TiO_2 thin films. The photocatalytic activity is evaluated by the degradation of MB. Obtained results show that TiO_2 thin films are the best photocatalytic materials. TiO_2:ZnO andTiO_2:NiO (TZ7 and TN7) are less active as photocatalytic materials, due to the screen effect.

REFERENCES

[1] REFERENCES
[1] T. Fuyuki, H. Matsunami, Jpn. J. Appl. Phys. 25 (1986) 1288.
[2] P.A. Bertrand, P.D. Fleischauer, Thin Solid Films 103 (1983) 167.
[3] H.K. Pulker, Thin film science and technology, Coatings on Glass,vol. 6, Elsevier,Amsterdam, 1984.
[4] B.E. Yoldas, T.W. O'keefe, Appl. Opt. 18 (1979) 3133.
[5] H.Y. Ha, S.W. Nam, T.H. Lim, I.H. Oh, S.A. Hong, J. Membr.Sci. 111 (1996) 81.
[6] H. Tang, K. Prasad, R. Sanjine's, F. Le'vy, Sens. Actuators B 26(1995) 71.
[7] D. Bhattacharyya, N.K. Sahoo, S. Thakur, N.C. Das, Thin SolidFilms 360 (2000) 96.
[8] K. Kato, A. Tsuzuki, H. Taoda, Y. Torii, T. Kato, Y. Butsugan, J.Mater. Sci. 30 (1995) 837.
[9] C.Jeffery Brinker. SOL-GEL SCIENCE. Tokio Toronto: academic press ,inc, 1990, 462p.
[10] Robert, D. Shannon, Ruth C. Shannon, OMedenbach, Reinhard, X. Fischer. J. Phys. Chem. Ref. Data. 31 (2002).
[11] F.E. Ghodsi, H. Absalan. Acta physica polonica A. 118 (2010).
[12]L. Znaidia, T. Touam, D. Vrela, N. Souded, S. Ben Yahia, O. Brinza, A. Fischer, A. Boudrioua. Acta physica polonica A 121 (2012).
[13]V. Gowthami1, M. Meenakshi, P. Perumal, R. Sivakumar, C. Sanjeeviraja. International Journal of Chem Tech Research. 6 (2014)5196.
[14]PieroMazzolini. Functional Properties Control of Doped TiO2 for Transparent Electrodes and Photoanodes. POLITECNICO DI MILANO.2015.157p.
[15]P. Ravindran. Bandgap engineering. [enlignie]. India: Department of Physics, Central University of Tamil Nadu, 2013, 96p.< folk.uio.no/ravi/cutn/semiphy/21.Borstein-Moss.pdf> .11/06/18.
[16]N. M. Ulmane, A. Kuzmin, I. Steins, J. Grabis, I. Sildos, M. Pärs.Journal of Physics: Conference Series 93 (2007) 012039.
[17]V. Gowthami, M. Meenakshi, P. Perumal, R. Sivakumar, C. Sanjeeviraja. International Journal of ChemTech Research.6 (2014) 5196.
[18] Said Benramache, Mansour Aouassa. Journal of Chemistry and Materials Research. 5 (2016) 119.
[19] Md. TamezUddin. Metal oxide hetero structures for efficient photocatalysts. Universit´e Sciences et Technologies - Bordeaux I, 2013. English. <NNT : 2013BOR14859>. <tel-00879226>
[20] Je-Luen Li, G.-M. Rignanese, Steven G. Louie. Physical review B ,(2005) 193102.
[21]S.Chen, W. Zhao, Liu Wei, S. Zhang, Applied Surface Science 255 (2008) 2478.
[22]X. Qi, G. Su, G. Bo, L. Cao, W. Liu. Surface & Coatings Technology.2015.
[23] D. Ahirwar, M. Bano, I. Khan1 ,M.Ud-Din Sheikh, M. Thomas, F. Khan1.Journal of Materials Science: Materials inElectronics.(2018).2008

Elaboration et caractérisation de couches minces de TiO_2

Nasr-Eddine HAMDADOU[a], Ibrahim ODEH[b]

[a] Laboratoire de Micro et de Nanophysique (LaMiN), Ecole Nationale Polytechnique d'Oran Maurice AUDIN, BP 1523 E Mnaouer Oran, ALGERIE.

nasreddine.hamdadou@enp-oran.dz

[b] Laboratoire des Couches Minces, Département de Physique, Faculté des Sciences, Université de Yarmouk, Irbid, JORDANIE.

iodeh@yu.edu.jo

***Résumé*— Des couches minces de dioxyde de titane TiO_2 ont été élaborées en deux étapes. La première consistait à déposer des couches minces de titane Ti par la technique de pulvérisation DC assistée par un faisceau d'ions Ar^+. En seconde étape les couches de Ti ont été oxydées thermiquement à des températures variant de 250°C à 550°C pendant 02 heures. L'analyse par la diffraction des rayons X a révélé qu'avant l'oxydation les couches sont polycristallines formées de grains de Ti de structure hexagonale. Après oxydation la structure des couches minces varie de la phase β-TiO_2 monoclinique à la phase anatase tétragonale, lorsque la température d'oxydation varie de 250°C à 550°C. L'épaisseur des couches minces de TiO_2, mesurée par la profilométrie, était de 230 nm. La visualisation et l'analyse de la surface des couches par la microscopie à force atomique (AFM) a permis de montrer que la rugosité augmente lorsque la température d'oxydation est augmentée. Les mesures de spectrophotométrie dans le domaine UV-Visible ont montré que la transmittance optique des couches se situe dans l'intervalle 85-95%. Les valeurs des énergies de la bande interdite étaient de 3.43 eV et 3.61 eV pour les couches obtenues à des températures d'oxydation de 250°C et 550°C, respectivement.**

***Mots clés*— Couche mince / TiO_2 / DRX / AFM / spectrophotométrie.**

I. INTRODUCTION

Les oxydes transparents conducteurs présentent plusieurs propriétés électroniques et optiques intéressantes pour les différentes applications. Le dioxyde de titane TiO_2 est un semiconducteur à bande interdite large, avec des propriétés intéressantes, il est transparent avec un indice de réfraction important (à λ = 550 nm, n = 2.54 pour l'anatase or 2.75 pour le rutile), il est très étudié comme matériau optique [1, 2] destiné à plusieurs applications, telles que les cellules photovoltaïques à colorant sensible, les capteurs de gaz, les guide d'ondes, les dispositifs électrochromiques [3-5].

Le composé TiO_2 est allotropique, il cristallise dans quatre phases : anatase (tétragonale), rutile (téragonale), brookite (orthorhombique) and β-TiO_2 (monoclinique) [6]. Anatase est la phase préférée pour les applications optoélectroniques, ce qui justifie les efforts de recherche investis dans l'étude de cette phase.

Les couches minces de TiO_2 ont été élaborées par plusieurs techniques, telles que la pulvérisation [7], l'évaporation par canon à électrons [8, 9], le dépôt par pulse laser [10], le dépôt par voie chimique (CVD) [11], le procédé sol-gel [12]. Cependant, il a été constaté que les couches minces obtenues ne sont pas toujours stables chimiquement avec les propriétés requises pour les applications. En effet la continuité des travaux sur les couches minces de TiO_2 semble nécessaire.

Le but du présent travail est l'élaboration de couches de TiO_2 par la technique de pulvérisation RF assistée par un faisceau d'ions. La caractérisation des différents échantillons a été établie à l'aide de la diffraction des rayons X (DRX), la profilométrie, la microscopie à force atomique (AFM) et la spectrophotométrie UV-Visible.

II. LES TECHNIQUES EXPÉRIMENTALES

A. *Elaboration des couches minces de TiO_2*

Les substrats utilisés étaient en verre de dimensions (25×8×1) mm^3, ils ont été nettoyés avec de l'acétone pour éliminer toute trace de graisse, puis par l'alcool et rincés à l'eau distillée. Les couches minces de Ti d'épaisseur de 80 nm ont été déposées, à l'aide de la technique de pulvérisation DC magnétron assistée par un faisceau d'ions Ar^+ (IBAD). Le dispositif utilisé était de marque Edwards, UK comportant une cible de titane dehaute pureté.

Les couches de Ti obtenues ont été traitées thermiquement à des températures de 250°C, 350°C, 450°C et 550°C, pendant 2 heures, avec un four programmable de marque MAGHMA THERM type.

B. *Caractérisation des couches minces de TiO_2*

ISSN: 1737-9334

La structure des couches minces a été analysée par un diffractomètre BRUKER D8 en utilisant un rayonnement Cu Kα1 (λ = 1.5406 Å). Les diffractogrammes ont été enregistrés de 10° à 90° avec un pas de 0,01°. La largeur à mi-hauteur (FWHM) des pics de diffraction a été donnée directement par les logiciels X'Pert. L'épaisseur a été évaluée par le profilomètre de type BRUKER Dektak XT. Les images AFM ont été acquises à l'aide d'un système Flex-Axiom Nanosurf. L'imagerie a été réalisée en mode contraste de phase et les dimensions des images étaient de 500 nm x 500 nm et 1000 nm x 1000 nm. Les mesures optiques ont été effectuées dans la gamme de longueurs d'onde de 190 à 1100 nm, à l'aide d'un spectrophotomètre 210 SPECORD Plus UV-Visible.

III. Resultats et discussion

A. L'analyse DRX

La structure des couches minces élaborées a été analysée par diffraction des rayons X (DRX), figures 1 et 2. Les couches sans traitement thermique cristallisaient dans la structure hexagonale Ti, figure 1. Les pics sont indexés à l'aide de la fiche ICDD N° 44-1294. Le pic à 47.606° est attribué au SiO_2 du substrat de verre en référence à la fiche ICDD N°04-0379.

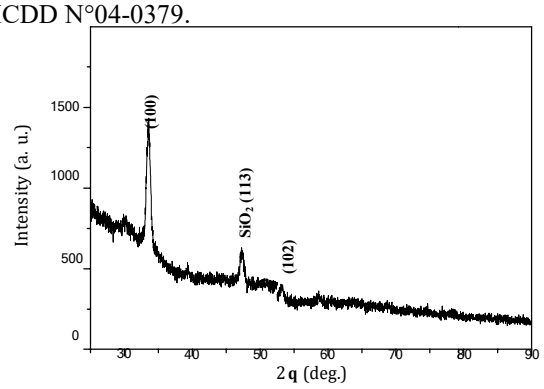

Fig. 1 Diffractogramme DRX d'une couche mince de Ti élaborée par la technique IBAD

La figure 2 montre les diagrammes DRX des couches minces après traitements thermiques à 250°C, 350°C, 450°C et 550°C pendant 2 heures.

Les relations utilisées pour déduire les paramètres de réseaux hexagonal, monoclinique et tétragonal sont respectivement [13].

$$\frac{1}{d_{hkl}^2} = \frac{4}{3}\left(\frac{h^2 + hk + k^2}{a^2}\right) + \frac{l^2}{c^2} \quad (1)$$

$$\frac{1}{d_{hkl}^2} = \frac{h^2}{a^2 \sin^2\beta} + \frac{k^2}{b^2} + \frac{l^2}{c^2 \sin^2\beta} - \frac{2hl\cos\beta}{ac\sin^2\beta} \quad (2)$$

$$\frac{1}{d_{hkl}^2} = \frac{h^2 + k^2}{a^2} + \frac{l^2}{c^2} \quad (3)$$

Avec a, b, c et β sont les paramètres de réseau et d_{hkl} la distance interéticulaire de la famille de plans (hkl).

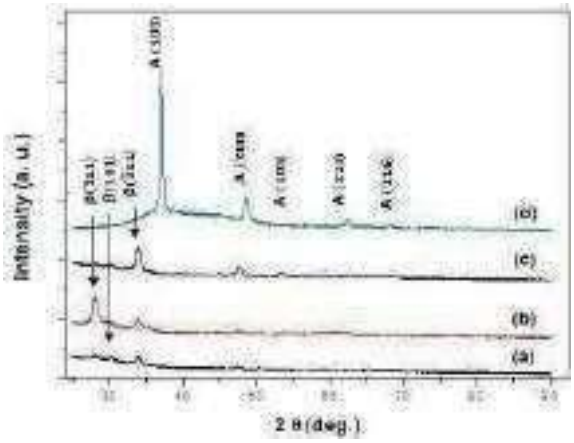

Fig. 2 Diffractogrammes DRX des couches minces obtenues après traitements thermiques à 250°C (a), 350° (b), 450°C (c) et 550°C (d).

La taillemoyenne de grain a été calculée à l'aide de la relation de Scherer [14].

$$D = K\frac{\lambda}{\beta\cos\theta} \quad (4)$$

Avec $K = 0.9$, λ =1.5406 Å et β est la largeur à mi-hauteur réelle (FWHM) du pic de diffraction. La valeur de a été β calculée par la relation de Warren formula [15]:

$$\beta^2 = B^2 - b^2 \quad (5)$$

Avec B la largeur à mi-hauteur observée du pic et b la largeur instrumental, égale à $0.09°$ dansnotre cas.

La structure cristalline et les paramètres de réseau relatifs aux différents diffractogrammes sont portés sur le tableau I. La taille moyenne de grain variait de 20 à 29 nm.

TABLEAU I
La structure et les paramètres cristallins des différentes couches minces élaborées.

Température de traitement thermique	**Structure et paramètres de réseau**

Avant	Hexagonale : a = 2.990 Å c = 4.515 Å
250°C	Monoclinique : a = 12.163 Å b = 3.735 Å, c = 6.513 Å, β = 107.29°
350°C	Monoclinique+Tétragonal
450°C	//
550°C	Tétragonale (Anatase) : a = b = 3.741 Å, c = 9.582 Å

Une transition de phase entre la structure β-TiO_2 monoclinique et la structure anatase tétragonale est observée, lorsque la température de recuit est augmentée de 250°C à 550°C, et la taille des grains n'est pas affectée par l'augmentation de la température de traitement thermique. La présence des deux structures aux températures intermédiaires 350°C et 450°C confirme cette transition. La transformation de la structure de monoclinique à tétragonale sous l'effet de la température, signifie une transition vers une structure plus ordonnée. Ainsi, la cristallinité semble s'améliorer avec la température, ceci s'explique par le fait que lors d'un traitement à haute température, les atomes acquièrent une capacité suffisamment élevée à s'organiser dans un arrangement plus cristallin [16,17].

B. La visualisation AFM

Des images de surfaces des couches minces de TiO_2 ont été prises à des zones de balayage de 500 nm et 1000 nm, figure 3. Les valeurs des paramètres de rugosité comme la hauteur moyenne arithmétique Sa, la hauteur quadratique moyenne Sq, la hauteur maximale Sz, la hauteur de pic maximale Sp et la profondeur de vallée maximale Sv sont reportées dans le tableau II.

La rugosité de surface de la couche traitée à 550°C (4.48 nm rms) a légèrement augmenté par rapport à celle des autres couches.

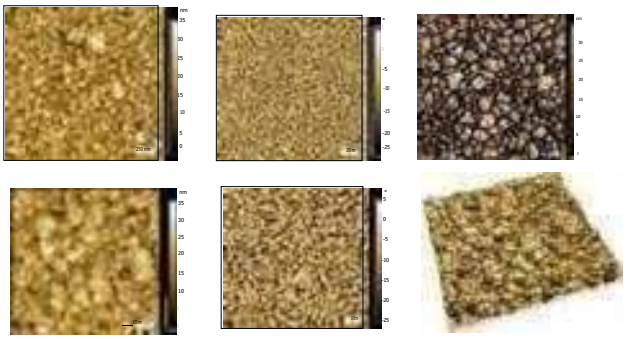

Fig. 3 Images AFM de couches minces de TiO_2 obtenues après traitement thermique à 550 °C pendant 2 h.

TABLEAU III
Les paramètres de rugosité et de grain de couches minces de TiO_2 obtenues après traitements thermiques de 250°C et 550°C.

Température / Paramètres de rugosité et de grain	250 °C	550 °C
Sa (Hauteur moyenne) (nm)	2.38	3.58
Sq (Hauteur quadratique) (nm)	3.01	4.48
Sz (Hauteur maximale) (nm)	22.20	36.00
Sp (Pic maximal) (nm)	11.20	17.60
Sv (Vallée maximale) (nm)	11.10	18.40
Taille moyenne de grain (nm)	29.96	28.80
Nombremoyen de grain voisins	5.84	5.83

Les valeurs de la taille moyenne de grain obtenues confirment celle fournies par la DRX. Chaque grain est entouré en moyenne de 6 grains voisins.

C. Les mesures de spectrophotométrie

La transmittance optique, figure 4, le coefficient d'absorption optique, figure 5 et la bande interdite optique, figure 6, des couches minces d'oxyde de titane oxydés ont présenté des caractéristiques diélectriques typiques de transmission élevée de 85 à 90 % dans la gamme de longueurs d'onde de [300 à 800 nm], et un large écart d'énergie en accord avec les données obtenues par les travaux antérieurs [7-12].

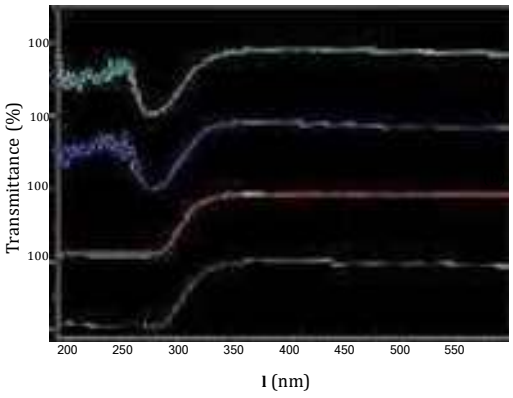

Fig. 4 Spectres de transmittance des couches minces obtenues après traitements thermiques à 250°C (a), 350° (b), 450°C (c) et 550°C (d).

Les résultats du calcul du coefficient d'absorption, pour les différents échantillons, sont présentés dans la figure 5. A partir des spectres de transmission et de l'épaisseur déterminée

par le profilomètre – 230 nm, nous avons calculé les coefficients d'absorption en utilisant la relation suivante [18] :

$$\alpha = \frac{1}{e} \ln\left(\frac{100}{T(\%)}\right) \quad (6)$$

Avec e l'épaisseur de la couche et T sa transmittance.

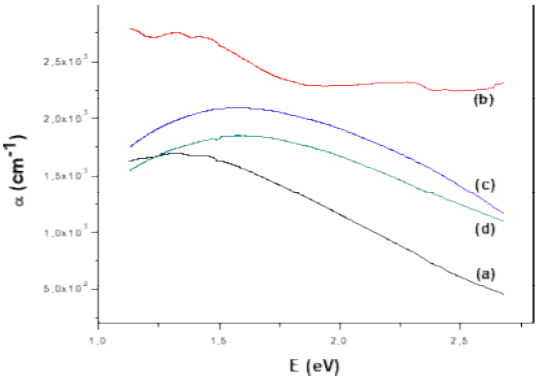

Fig. 5 Le coefficient d'absorption optique en fonction de l'énergie du photon incident des couches minces obtenues après traitements thermiques à 250°C (a), 350°(b), 450°C (c) et 550°C (d).

Dans la région de basse énergie du photon incident (1–2.75 eV), on observe une diminution du coefficient d'absorption. En tenant compte de la température de recuit, nous avons constaté que le coefficient d'absorption optique augmente lorsque la température passe de 250 °C à 350 °C, puis diminue pour les températures 450 °C et 550 °C.
L'énergie de la bande interdite optique des couches minces de TiO_2 traitées thermiquement à 250°C et 550°C a été calculée à partir des spectres des coefficients d'absorption en utilisant la formule Tauc [19].

$$(\alpha h\nu) = A(h\nu - E_g)^n \quad (7)$$

Avec α est le coefficient d'absorption, $h\nu$ est l'énergie du photon, A est une constante, E_g est la bande interdite optique et n est un nombre égal à 2 et 1/2 pour les transitions indirectes et directes autorisées, respectivement. Sachant que TiO_2 est un matériau à gap indirect [20,21], les valeurs de la bande interdite optique sont obtenues en extrapolant la partie linéaire des courbes $(\alpha h\nu)^{1/2}$ à $\alpha = 0$, comme le montre la fig.9.

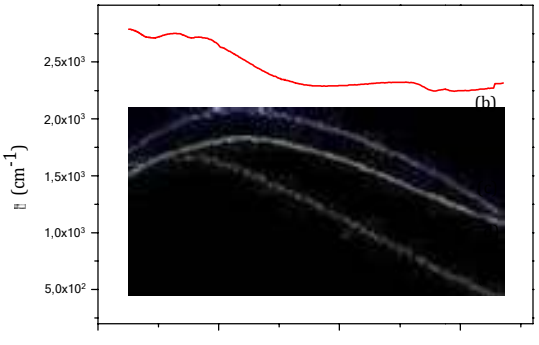

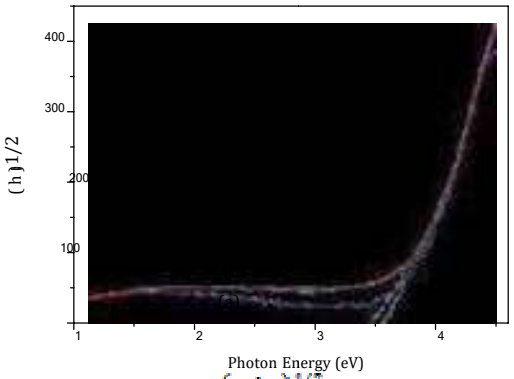

Fig. 6 Représentation de f $(\alpha h\nu)^{1/2}$ en fonction de l'énergie du photon incident des couches minces obtenues après traitements thermiques à 250°C (a) and 550°C (b).

Les résultats des analyses optiques ont été interprétés à la lumière des propriétés cristallines, déduites de la caractérisation structurale des différents échantillons. Les couches minces de TiO_2 avec des structures monocliniques β-TiO_2 et anatase tétragonale, obtenues par traitements thermiques à 250 °C et 550 °C pendant 2 h, respectivement, ont montré une meilleure transmittance, figure 4, et une faible absorption, figure 5, comparées à celles de couches minces de TiO_2 à deux phases, résultant de traitements thermiques à 350 °C et 450 °C pendant 2 h, ce qui conduit à la conclusion évidente, à savoir que l'absorption optique diminue, lorsque l'ordre cristallin est amélioré.
Les valeurs de la bande interdite optique indirecte sont de 3.43 eV et 3.61 eV pour les couches minces recuites à 250°C et 550°C, respectivement. Certes, la valeur la plus citée pour la phase anatase est de 2.23 eV [17], mais certains travaux ont obtenu des valeurs comparables auxnôtres [20,21].

IV. Conclusions

Dans ce travail, nous avons préparé des couches minces de TiO_2, par l'élaboration de couches de titane pulvérisé à l'aide d'un dépôt assisté par faisceau d'ions (IBAD). Les couches obtenues ont été oxydées thermiquement à des températures de
250°C, 350°C, 450°C et 550°C pendant 2 heures.

Les diagrammes DRX ont montré que la phase de la couche était modifiée du type monoclinique au type tétragonal en augmentant la température de traitement de 250°C à 550°C. Les paramètres de la rugosité déduits de l'analyse AFM ont sensiblement augmenté en raison de l'oxydation thermique à des températures plus élevées. Les mesures optiques indiquent que les couches présentent une haute transmittance sur la gamme visible et une large
bande interdite optique dans la gamme 3.43-3.61eV.

REFERENCES

[1] L. Martinu, D. Poitras, *J. Vac. Sci. Technol.* A 18 p 2619 (2000).
[2] Z. Wang, U. Helmersson, P. O. Kall *Thin Solid Films* 405 pp 50-54 (2002).
[3] B. O'Regan, M. Grätzel, *Nature* 353 p 737 (1991).
[4] T.J. Saveninije, J.M. Warman, A. Goosens, *Chem. Phys. Lett.* 287 p148 (1998).
[5] G. Montesperelli, A. Pumo, *Sens. Actuators* B 24–25 p 705 (1995).
[6] M. Borlaf, M. T. Colomer, R. Moreno, A. L. Ortiz, *Journal of the European ceramic society* 34 pp 4457-4462 (2014).
[7] H. Tang, K. Prasad, R. Sanjines, P.E. Schmid, F. Levy, J. Appl. Phys. 75 p2042 (1994).
[8] T. Guang-Lei, H. Hong-Bo, S. Jian-Da S, *Chin.Phys. Lett.* 22 pp 1787-1789 (2005).
[9] S. H. Oh, D. J. Kim, S. H. Hahn, *Mater. Lett* 57 pp 4151-4155 (2003).
[10] J. H. Kim, S. Lee, H. S. Im, *Appl. Surf. Sci.*151 p 6 (1996).
[11] S. A. Campbell, H. S. Kim, D. C. Gilmer, B. He, T. Ma, W. L. Gladfelter, *IBM J. Res. Dev.*43 p 383 (1999).
[12] Z. Wang, U. Helmersson, P. O. Käll, *Thin Solid Films* 405 pp 50-54 (2002).
[13] E. F. Kaeble**;** *Handbook of X-rays*, Ed. : Mac Graw Hill, 1981.
[14] P. Sherrer; *Götinger Nachrichten*, 2 p 98 (1981).
[15] B. E. Warren; *J. Appl. Phys.*, 12 p 3750 (1941).
[16] H. R. Fallah, M. Ghasemi, A. Hassanzadeh, *Physica E* 39 p 69 (2007).
[17] A. F. Khan, M. Mehmood, S. K. Durrani, M. L. Ali, N. A. Rahim, *Mater. Sci. in Semic. Process.* 29 pp 161-169 (2015).
[18] E. D. Palik, *Handbook of optical constants of* solids, Ed.: Academic Press, San Diego, 1998.
[19] J.Tauc, *Amorphous and Liquid Semiconductors*, Ed.: Plenum Press, NewYork, 1974.
[20] Z. Wang, U. Helmersson, P.O. Kall; *Thin Solid Films* 405 p 50 (2002).
[21] S. Sen, S. Mahanty, S. Roy, O. Heintz, S. Bourgeois, D. Chaumontet; *Thin Solid Films* 474 pp 245-249 (2005).

A new formalism that combines advantages of FMEA and Markov graphs for reliability analysis of the self-excited induction generator

Yahia Naoui[1]

[1]Faculty of Technology , University Yahia Faresof Medea,26000,Algeria

yahia.naoui@gmail.com

Abstract— **Reliability as a very important operational safety parameter, it represents a major challenge for ensuring optimal competitiveness for energy generators. Indeed, reliability is involved throughout the product or system life cycle. Although numerous reliability modeling and analysis approaches have been discussed in literature, all of them are dedicated to exclusively study single part or an aspect of the reliability. In fact, some of them are quantitative and others are qualitative, some are static while others are dynamic, some are inductive, but others are deductive, some are predictable and others by contrast are experimental...etc.In this paper, we proposes a new formalism that takes advantage from the combination of two complementary approaches. FMEA , which is a qualitative approach and Markov graphs that is a quantitative approach. Our new formalism is used for the reliability assessment of a self-excited generator vacuum or loaded. Mathematical models for the vacuum self-excited induction generator and load have been designed for the evaluation. These models are simulated under the MATLAB software to determine the parameters that affect the voltage supplied by the generator. Subsequently, the obtained results applying the two combined approaches allowed us determine the installation components failure probability and highlight the failure average rate and the main failure causes.**

Keywords— **Asynchronous generator (AG), Failure mode and Effects Analysis(FMEA),Markov Graphs Modeling, Reliability analysis ,Self-excited induction generator.**

I. INTRODUCTION

The need for electric energy is never ending. For instance, this need remain increasing in the industrialized countries where electricity consumption is expected to double every ten years during a normal growth periods [1].Along with the growth in demand for electric power, electric utilities are becoming more and more stressed notably for distant sites. In fact, the transportation of energy to such sites costs too much since existing transmission and distribution systems are facing their operating constraints with growing load. Under such circumstances, projects of autonomous electrical installations based on diesel, wind or solar to produce energy for isolated locations are indispensable.

However, meeting the energy needs on isolated sites is a crucial task, since distributed generation entails using many isolated generators, situated at numerous strategic points throughout cities and towns, so that each provides power to a certain number of consumers [2]. Therefore, these generators should have better performance parameters from a technical and economic point of view as well.

There are several generic types of generator available as possible candidates for use as a wind or hydro turbine generator but perhaps the most common type of electric generator used throughout the industry is asynchronous machines. Asynchronous machines also known as an "Induction Generators", which are electromechanical conversion tools, are considered the most used in power stations. Albeit originally asynchronous machines were exclusively used in engines, nowadays with the advent of power electronics these machines are increasingly being used as generators in different power plants based on wind, nuclear and diesel [3].These machines are commonly used as generator due to advantages such as simplicity, availability, robustness and more importantly their lowcost [4].

However, the only weakness of the asynchronous machine is that besides active energy essential for their normal operation, these machines need the reactive energy for their excitation during start-up. But, since these machines cannot produce their own reactive energy, they consume this energy from the network for connected sites. For isolated sites, they consume the reactive energy from the capacitor bank connected in parallel to the stator winding [5-6].Considered as an interesting solution for isolated sites, asynchronous machines have widely interest electrical engineering researchers to conduct surveys on their technical comportment to increase the efficiency and reliability of electromechanical conversion and to improve the qualityof energysupplied [7].

Thus, reliability as a very important operational safety parameter represents a major challenge for ensuring optimal competitiveness for energy generators. Indeed, reliability is involved throughout the product or system life cycle (design, manufacture, operation). Albeit several reliability modelling and analysis approaches have been discussed in literature. They are all dedicated to study a part or an aspect of the reliability [8]. In fact, some of them are quantitative and others are qualitative, some are static while others are dynamic, some are inductive, but others are deductive, some are predictable and others by contrast are experimental...etc.

Hence, the Lack of the study and the modelling of the reliability in an integral and a dynamic way for complex systems such as self- excited induction generators remains to be filled and has its place in academic research.

ISSN: 1737-9334

In this context, the present work proposes a new formalism that takes advantage from the combination of two complementary approaches. FMEA which is a qualitative approach and Markov graphics that is a quantitative approach .Our new formalism is used for the reliability assessment of a self-excited generator vacuum or loaded. For this combination, we analyze the operating criteria and evaluate the generator failure probability that provide energyfor both isolated and connect sites.

II. P DEVICE MODELING

The dynamicregime of the Self-excited induction generator is determined by the mutual influence of the physical processes that take place in the diesel actuator, the generators and the loads [9-10].This is why the mathematical model of this regime takes into consideration the description of the autonomous subsystems (diesel actuator, asynchronous machine, the capacitor bank and load) and their characteristic relations as presented on Fig. 1.

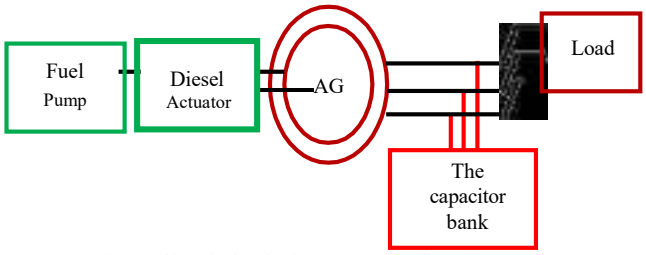

Fig. 1 Self-Excited Induction Generator Bloc Diagram

A. Diesel actuator mathematical model

The rotational speed variation of the diesel actuator is determined by the following equation:

$$\frac{dw_d}{dt} = \frac{1}{j}(C_i - C_r - C_{em} - C_m) \quad (1)$$

Where w_d is the rotational speed pulsation of the axis of the diesel actuator, Ci is the indicated torque of the diesel actuator, Cm is the couple of mechanical losses in diesel, Cr is load torque of the asynchronous generator, Cem is the Electromagnetic torque of the asynchronous generator, j is total inertia moment.

The link between the diesel actuator and the fuel pump is determined by the form shown in equation.(2) :

$$w_h = U_w . w_d \quad (2)$$

Where W_h is the rotational speed of the fuel pump, U_w is the crankshaft gear ratio of diesel to the axis of the fuel pump.

1) Mathematical model of the self-excited induction generator

It is necessary to perform a conversion of the machine variables so as to get those of the primitive machine. This conversion implies the transformation of the original generator coils to an electrically and magnetically equivalent coil set in d and q axes. This transformation is a particular case of the park transformation [11-12-13].

$$\begin{aligned} -u_{sd} &= \frac{d\Psi_{sd}}{dt} + r_s . i_{sd} \\ -u_{sq} &= \frac{d\Psi_{sq}}{dt} + r_s . i_{sq} \\ 0 &= \frac{d\Psi_{rd}}{dt} + r_r . i_{rd} - w_r . \Psi_{rq} \\ 0 &= \frac{d\Psi_{rq}}{dt} + r_r . i_{rq} - w_r . \Psi_{rd} \end{aligned} \quad (3)$$

Where Ψsd , Ψsq , Ψrd , Ψrq are the d-q stator and rotor flux, isd , isq , ird , irq are the d- q stator and rotor currents, usd , usq are the d-q stator voltages ,rs , rr are the stator and rotor phase resistances, wr is the rotational speed of therotor Self-excited induction generator.

The hanging fluxes are related to the generator currents as follows:

$$\begin{aligned} \Psi_{sd} &= L_s . i_{sd} + L_m . i_{rd} \\ \Psi_{sq} &= L_s . i_{sq} + L_m . i_{rq} \\ \Psi_{rd} &= L_r . i_{rd} + L_m . i_{sd} \\ \Psi_{rd} &= L_r . i_{rq} + L_m . i_{sq} \end{aligned} \quad (4)$$

Where Ls , Lr are the proper inductances of stator and rotor windings, Lm is the magnetizing inductance.

2) Mathematical model of the excitation circuit

The stator windings of the induction machine are connected to a star capacitive bank connected in parallel, the diphase stator voltages and currents are linked by the following expression:

$$\begin{aligned} \frac{du_{sd}}{dt} &= \frac{1}{C} . i_{sd} \\ \frac{du_{sq}}{dt} &= \frac{1}{C} . i_{sq} \end{aligned} \quad (5)$$

Where C is the excitation capacitors

The electromagnetic torque of the asynchronous generator is given by:

$$C_{em} = \frac{3}{2} P . L_m (i_{rd} . i_{sq} - i_{rq} . i_{sd}) \quad (6)$$

The empty generator is driven by a diesel actuator and the necessary condition to create a voltage between its edges is the existence of a remaining field. In order to increase this relatively low voltage amplitude to its nominal value, enough reactive power by the capacitor bank magnetization should be supplied to the generator [14] shown in fig .1.

B. Conditions of self-start up of the empty generator

The self-start up of the generators occurs when the two following conditions are satisfied:
Total active power =0
Totalreactivepower =0
What meansthat theimpedance equivalent to a stator phase of the machine is:

$$Z_G = a + jb$$

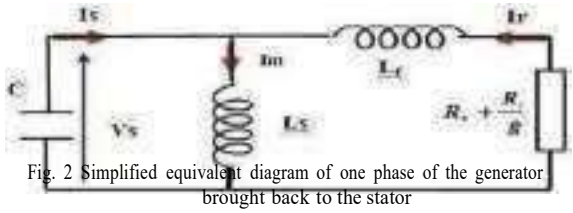

Fig. 2 Simplified equivalent diagram of one phase of the generator brought back to the stator

The diagram of fig. 2. is equivalent to a generator producing on ZC impedance (as shown on fig. 3).

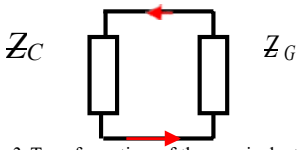

Fig.3 Transformation of the equivalent diagram

Wehave:

$$\left(1 + \frac{Z_C}{Z_G}\right).V = 0 \quad (7)$$

Where:

$$Z_C = j.C.\omega \quad (8)$$

Thus:

$$\frac{R_r + L_f.\omega}{R_s^2 + (L_s.\omega)^2} = C.\omega \quad (9)$$

Where Zc is the impedance of the condenser, ZG is the equivalent impedance of the generator, Lf is the Inductance of total losses, g is the slip of the generator, ω is the rotational speed of the stator of self-excited induction generator.

The self-start-up of the generator cannot occur unless its produced apparent power corresponds to its absorbed one. For thereactive power part, the following equation should be satisfied (for g = 0).

$$\frac{1}{L_s.\omega} - C.\omega = 0 \quad (10)$$

This condition shows that the minimal value leading up to the self-start-up is function of the cyclic stator inductance as well as the rotor pulsation and the sliding thereof [15]. The asynchronous generator does not receive any reactive energy except the one coming from the excitation capacitors [16].

C. Simulation result

To simulate the self-priming vacuum should be resolved voltage equation system taking into account the voltage across the capacitor, the equation system will be written:

$$\begin{aligned} -u_{sd} &= L_s.\frac{di_{sd}}{dt} + L_m.\frac{di_{rd}}{dt} + r_s.i_{sd} \\ -u_{sq} &= L_s.\frac{di_{sq}}{dt} + L_m.\frac{di_{rq}}{dt} + r_s.i_{sq} \\ 0 &= L_r.\frac{di_{rd}}{dt} + L_m.\frac{di_{sd}}{dt} + r_r.i_{rd} - w_r.(L_r.i_{rq} + L_m.i_{sq}) \\ 0 &= L_r.\frac{di_{rq}}{dt} + L_m.\frac{di_{sq}}{dt} + r_r.i_{rq} - w_r.(L_r.i_{rd} - L_m.i_{sd}) \end{aligned} \quad (11)$$

Formed into equation of state: $X = A.Y$ Using the matrixnotation, the eq. (11) can be expressed in the form:

$$[X'] = [A].[Y]$$

$$\begin{aligned} L_s.X'_1 + L_m.X'_3 &= -r_s.X_1 - X_5 \\ L_r.X'_2 + L_m.X'_3 &= -r_s.X_2 - w_r.(L_r.X_4 + L_m.X_2) \\ L_r.X'_3 + L_m.X'_1 &= -r_s.X_4 - w_r.(L_r.X_3 + L_m.X_1) \\ X'_5 &= \frac{1}{C}.X_1 \\ X'_6 &= \frac{1}{C}.X_2 \end{aligned} \quad (12)$$

Where:

$$[X] = \begin{bmatrix} X_1 \\ X_2 \\ X_3 \\ X_4 \\ X_5 \\ X_6 \end{bmatrix} = \begin{bmatrix} i_{sd} \\ i_{sq} \\ i_{rd} \\ i_{rq} \\ u_{sd} \\ u_{sq} \end{bmatrix}; [L] = \begin{bmatrix} L_s & 0 & L_m & 0 & 0 & 0 \\ 0 & L_s & 0 & L_m & 0 & 0 \\ L_m & 0 & L_r & 0 & 0 & 0 \\ 0 & L_m & 0 & L_r & 0 & 0 \\ 0 & 0 & 0 & 0 & 1 & 0 \\ 0 & 0 & 0 & 0 & 0 & 1 \end{bmatrix}$$

[L]: inductance matrix

$$[Y] = \begin{bmatrix} -r_s.X_1 - X_5 \\ -r_s.X_2 - X_6 \\ -r_s.X_3 - w_r.(L_r.X_4 + L_m.X_2) \\ -r_s.X_4 - w_r.(L_r.X_3 + L_m.X_1) \\ \frac{1}{C}.X_1 \\ \frac{1}{C}.X_2 \end{bmatrix}$$

Where: $[A] = [L]^{-1}$

Finally for simulation, simply insert the models of the AAG, diesel actuator and the capacitor bank and implanting under the Matlab/ Simulink environment.
The parameters of the asynchronous generators used for the simulation studies are listed below.
Rated power=2.2Kw, rated stator voltage=220V, frequency= 50Hz,rated speed=955 tr/min, number of poles=2,moment of inertia=0.005 Kg.m2,stator resistance=3.38 Ω/ph , rotor resistance=3.88 Ω/ph.

The simulation block diagram is shown in Fig.4.

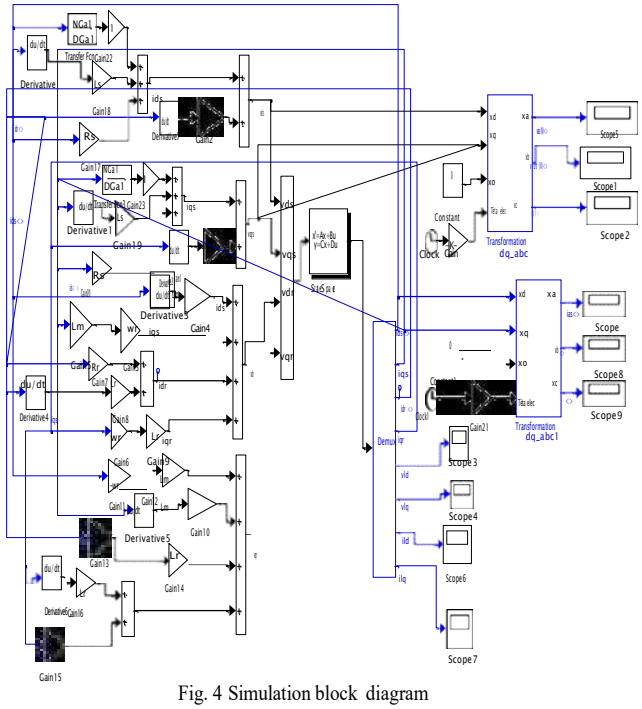

Fig. 4 Simulation block diagram

The simulation model allowed us to obtain theresults of self-priming vacuum.

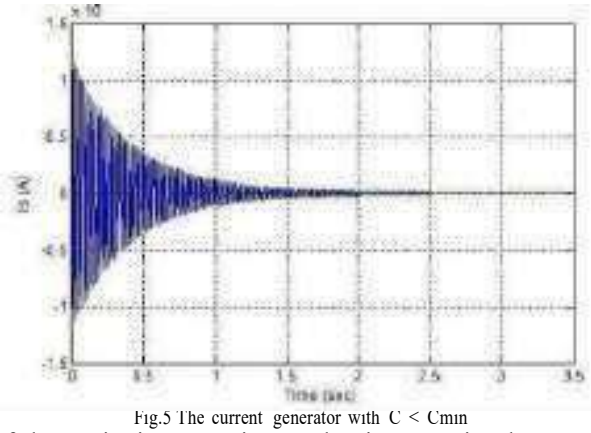

Fig.5 The current generator with C < Cmin

If the excitation capacitors value is C<Cmin, the current of generator (Fig.5) lowers to be cancelled, so the self-priming isnot possible.

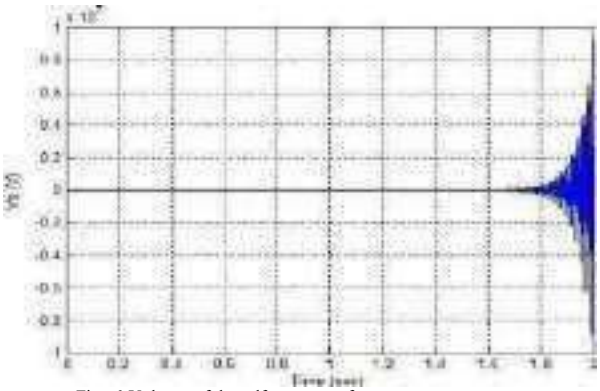

Fig. 6 Voltage of the self start-up of an empty generator

It can be noticed on the figure (6) that the induced tension increases indefinitely, in an exponential way, due to the non saturation ofthe magnetic circuit ofthe machine.

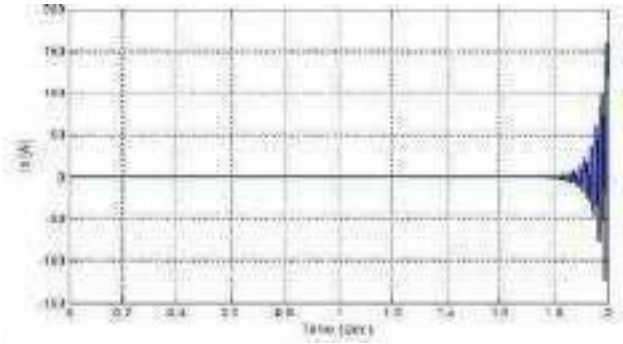

Fig. 7 Stator induced current of the empty generator

In fig.7 the induced stator current reaches, in few seconds, a value that exceeds by several times the nominal value, what is veryfar from thereality.

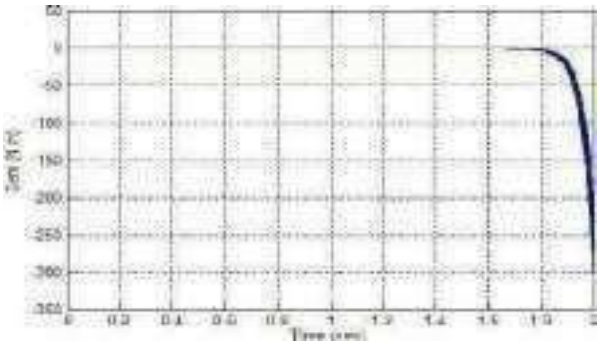

Fig. 8 Electromagnetic torque of the empty generator

In fig.8 when the generator starts itself, its electromagnetic torque rises indefinitely which will increase theactive power.

D. Consideration of the magnetic saturation phenomenon

In saturation regime, the fluxes and the currents are no longer proportional. The magnetizing characteristic is composed in addition to the linear part, of a part of bend

and another called of saturation. This last one will limit the generator magnitudes [17-18].

$$Lm = \left| \frac{\Psi m}{im} \right| \quad (13)$$

Ψm is the modulus of the generator magnetizing flux, imis the modulus of the generator magnetizing current vector.

Expression of the magnetizing current based on stator current androtor is given by:

$$i_m = \sqrt{(i_{sd} + i_{rd})^2 + (i_{sq} + i_{sq})^2} \quad (14)$$

To take account of the saturation magnetic circuit of the machine, it is necessary to model the magnetizing curve Fig. 9.

Several spline interpolation functions are used [19], however, there is no function that covers all points of the curve, and modelling remains approximate with minimal error.

For our raised magnetic characteristic, we adopt the approximation of the iron magnetizing curve fig.9, by the LANGEVIN function[20-21].

$$L(x) = coth(x) - \frac{x}{} \quad (15)$$

The calculation of the asynchronous machine main magnetic circuit saturation is performed using the LANGEVIN function as an approximation of the iron magnetization curve.

$$L_m = \frac{1}{a i_m}\left[\coth\left(\frac{i_m}{b}\right) - \frac{b}{i_m}\right] \quad (16)$$

Which value is obtained bythe magnetizing graph of the generator free regime test shown in fig. 9.

a, b: Coefficient calculating the approximation obtainedbythe magnetizing curve ,fig.9.

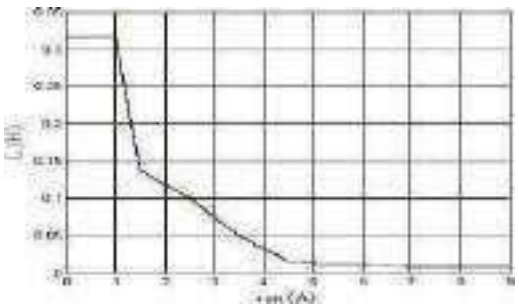

Fig. 9 Variation of the magnetizing inductance Lm according to Im

By resolving the equation system (12), and taking in consideration the eq. (16), the saturation of the machine, with a self-start-up voltage, will be obtained as presented on fig.10.

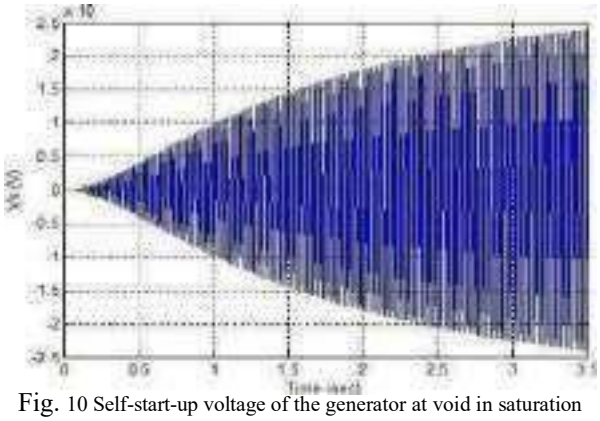

Fig. 10 Self-start-up voltage of the generator at void in saturation regime

In this part, the value of the excitation capacitors is 420 µf while the rotational speed is considered fixed is equal to 100 rd / s.

Fig.10 shows the evolution of the stator voltage in vacuum operation of the asynchronous generator. At start-up, the generated voltage increases exponentially,then due to the generator magnetic saturation, it converges to a fixed value.

III. MATHEMATICAL MODEL OF THE SELF-EXCITED INDUCTION GENERATOR SUPPLYING AN R-L LOAD

This model is obtained by adding to the equations system (5) the following load equations:

$$\begin{cases} \frac{du_{sd}}{dt} = \frac{1}{C}\left(-\frac{u_{sd}}{R} - i_{ld}\right) \\ \frac{du_{sq}}{dt} = \frac{1}{C}\left(-\frac{u_{sq}}{R} - i_{lq}\right) \\ \frac{di_{ld}}{dt} = \frac{1}{L}.u_{sd} \\ \frac{di_{lq}}{dt} = \frac{1}{L}.u_{sq} \end{cases} \quad (17)$$

The equation system (17) solution provides the results of simulation with a variable load speed

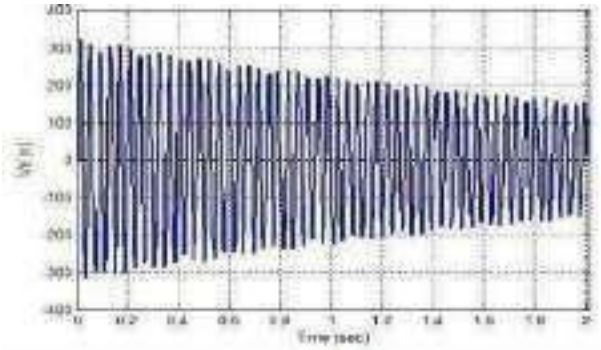

Fig. 11 Evolution of voltage when the generator is loaded (for C=300 µF)

It can be noticed on fig. 11 that, when a load is applied, the voltage decreases with a light variation of frequency which is due to the decrease of the speed.

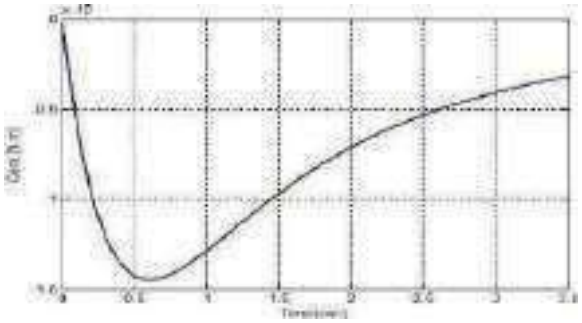

Fig.12 .Electromagnetic Torque of the loaded Generator under loading

In fig. 12 the electromagnetic torque passes from a steady stateto another steadystate defined bythe load.

IV. Model Validation

The simulation results of the Self-excited induction generator functioning are validated by comparing them with experimental ones obtained for transient regime parameters in natural testing of asynchronous machine. These tests are performed on MA-20M series electric devices.

The three-phase asynchronous machine AM72-4M type is used as an asynchronous generator. The table bellow shows the comparison between the simulation and experimental parameters of a loaded Self-excited induction generator running process .The parameters of the load R= 250 Ω and L= 500 mH.

TABLE I. The comparison between simul ation and experimental parameters

The exciter condenser	Experimental		Simulation	
C (µf)	U (v)	Imax (A)	U (V)	Imax (A)
100	0	0.45	0	0.4
300	4.0	2.8	09.0	2.95
470	36.6	3.9	33.0	3.6
680	91.0	3.6	96.0	3.3

Mathematical models for the self-excited empty and loaded Asynchronous Generator have been developed within the scope of this study. Thus, theoretical and experimental functional studies could be performed in addition to evaluating the influence of the regime on the transient regime quality.

There are three parameters that affect the tension delivered by the Self-excited induction generator, which are:

- The value of the excitation capacity
- The rotation speed
- The load

To perform a system reliability analysis all these three parametersshould be considered.

V. Reliability analysis of the system

The mathematical model of the self-excited induction generator established previously is used for the qualitative and quantitative analysis of the reliability of this system to determine the different technological solutions allowing a better continuity of the production of the electric energy and this, whatever the peaks of daily consumptions that affect energy production and to highlight the average failure rate, the main cause of failure and failure detection techniques in isolated sites.

The first step of a reliability analysis consists of making a deep study of the system. A common approach is to perform a " Failure Mode and Effects Analysis " (FMEA). It allows studying the impact of the devices failures on the system. It is about an inductive analysis method retailing systematically all the system components [22-23].

A. Failure Modes and Effects Analysis on the Self-excited induction generator

Failure mode and effect analysis (FMEA) is a powerful reliability engineering methodology that provides a means of comparing and assessing the system configuration [24]. This methodology evaluates systems component by component and identifies their failure modes and their effects on system function and other system components. Its major aim is to detect all the possible potential problems in a complex system and their occurrence probabilities.

To perform a Failure Modes and Effects Analysis (FMEA), the system should be broken down to simple sub-systems. Each component comportment can be determined via data collection process, and consequently, all the failure modes effects of each system components can be concluded using the system physical and functional structure (Tab.2) [25-26-27].

TABLE 2.Failure Modes and Effects Analysis of the Self excited induction generator

Component	Failure mode	Failure Consequences	Failure Causes
Asynchronous Generator	Overcharge of the generator and its actuator	System destabilization and the generating lose excitation	The starting and the commutation of the mechanism with Diesel Actuator
The capacitor bank	The non apparition of an exit voltage on the generator terminals	Lack of the reactive energy for the generator magnetization	Failure in the source of the reactive energy of the AAG excitation system
Diesel Actuator and Fuel Pump	Variation of the generator voltage of exit	Variation of the residual field in the generator's stator	Change of the rotation speed of the actuator motor
Load	-Decrease in the Output voltage	-Variation of the generator's excitation current	Connection of a load to the generator terminals

Considering this FMEA analysis, failure effects exist in the Self-excited induction generator sub-systems and may

lead to failure propagation. The main components mounted in series inside the system (the diesel actuator, asynchronous generator, the capacitor bank) are highly influenced by their internal environments. The variation of the rotational speed of the motor of the actuator for example, can cause a failure of the voltage delivered by the generator. This can conclude to the identification of dependencies between the Self-excited induction generator components.

TABLE 3.DATA USED TO CALCULATE THE EXPECTED FAILURE COSTS GENERATEDIN A2 MWSELF-EXCITED INDUCTION GENERATOR SYSTEM

Component	Number of failures	Downtime/ h	Failure rate	Annual Reliability
Asynchronous Generator	107	219	4.10^{-6}	0.96
Diesel Actuator	59	154	10^{-6}	0.95
The capacitor bank	43	69	10^{-6}	0.93
Load	21	23	6.10^{-6}	0.95
Total	203	465	3.10^{-6}	0.94

The most important findings from the values in this table are the asynchronous generator has a 107 number of failures per year and the mean downtime are219 hours a year. The most critical components are the asynchronous generator and thediesel actuator.

The qualitative study of the reliability by the FMEA method allows us to determine the various failures which influence the functioning of the system and that the critical element in the energy installation is the asynchronous generator.

B. Failuresin asynchronous generator

According to a study of more than 1,200 generators, installed in isolated electric power generation systems, on a wide variety of manufacturers [28-29], Table 4 gives the distribution of faults over the components of the asynchronous generator. This distribution is for generatorsrated above 2MW.

TABLE4. FAILURE MODES AND EFFECTS ANALYSIS OF THE ASYNCHRONOUS GENERATOR

Component	Failure mode	Failure Consequences	Failure Causes
Rotor Failure	Rotor insulation	Short circuit of the windings	warming
Stator Failure	Stator winding	-Defects betweenturns -Defaults between coils	Degradation at manufacture
Bearings	-Holes in bearing rings	Disturbances in the machine	Rotation problem within the machine
Collector rings	The degradation ofinsulation	The voltage spikes generated can cause voltage flashovers between the rings	Thermal cycling

TABLE 5. FAILURE OCCURRENCES AND PERCENTAGE OF FAILURES IN THE ASYNCHRONOUS GENERATOR

Component	Percentage of failures	Failure occurrences
Bearings	59%	182
Stator	16%	48
Stator wedge	12%	44
Rotor	5%	14
Rotor Leads	4%	12
Collector Rings	4%	12

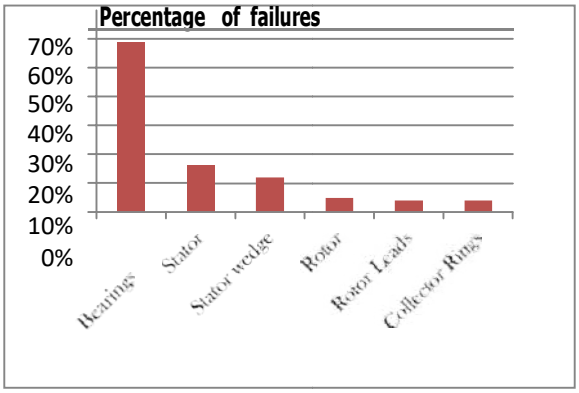

Fig. 13 Percentage of failures per component

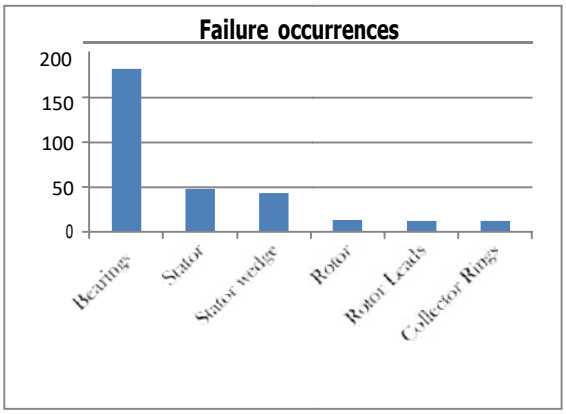

Fig.14 .Failure occurrences per component

The study identifies the bearings and the stator as a major problem point, figure13 and 14 shows the distribution of failures amongst the sub-components in asynchronous generator.

C. Reliability modeling of the self-excited induction generator using the Markov graphs method

Different techniques are available according to the architecture of the studied system, the concerned undesirable events, and the criteria to be evaluated and the hypotheses taken into account in the model [8].The estimated reliability analysis determines the failure rate of each equipment component in the real use conditions.

Thus, reliability databases are consulted. They allow the reliability calculation of a circuit including several components. Many models have already been developed to address this issue. Markov graphs, [30-31-32]. is the one of the most commonly used models.

Markov graphs method or (Markov process) allows the analysis of reliability of repairable systems for which failure rates and repair components are held constant, so it can be applied to our system[33-34].

It considers the system as a set of components which can be in a finished number by states of functioning or of breakdown, we shall build a graph nodes of which will correspond to the various system states, and the arrows indicate the directions of transitions (breakdown and repair) between system states. For a system in components, if every constituent (component) has two states (functioning or breakdown), the maximum number of states is 2n. The calculation of the reliability is realized from various states of the system.

The fundamental interest of the Markov process is its graphical aspect which allows implement without really needing to know about it, in depth, all the theoretical aspects [35-36-37].

Our installation contains four components, every component has two states (functioning or breakdown), and the maximum number of states is 24.

The description of the components states of the installation is represented in following table.

TABLE 6.THE DESCRIPTION OF THE STATES OF THE COMPONENTS OF THE INSTALLATION

Component	Percentage of failures	Failure occurrences
Bearings	59%	182
Stator	16%	48
Stator wedge	12%	44
Rotor	5%	14
Rotor Leads	4%	12
Collector Rings	4%	12

The construction of Markov state diagram concerning the system is made in two stages:

- Identification of the various states which the system can occupy during its operation, there are four named A, B, C and D.
- Construction of Markov graphs according to the identified states by the representation of each of state by a circle, (Operating state / Failure State) and representation of the transitions between states by arrows.

Every transition symbolizes the way the system jumps of a state towards another one. Of the state of perfect functioning E (A B C D), we can jump towards E1 ($\overline{A}$B C D) or by E2 (A $\overline{B}$ C D) failure of A or B, of the state E2 we can go or towards the state of breakdown E3 by failure of C or to return to the state E1 by repair of B.

The analysis of the installation through the Markov process is represented on the fig. 15.

The system states may be represented diagrammatically as:

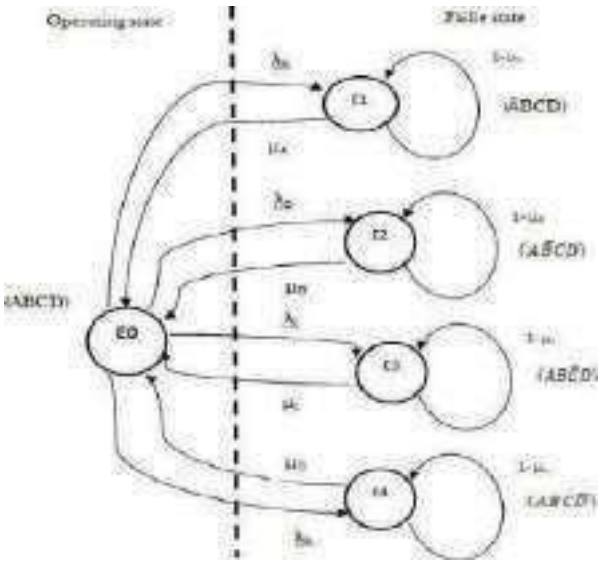

Fig. 15 Markov state diagram of Installation

λi is the failure rate of the component and **μ**i is the repair rate of the component. One to notice that the graph represents, in a synthetic way, all the paths (ways) (sequences of events) which the system can borrow from its initial state during its evolution in time [38].

This graph thus contains paths (ways) allowing the system to pass by the state of breakdown (Ei) then to return in a state of functioning (E). Thus it describes the behaviour of a system which can be underway at the given moment by having been one or several times out of order previously.

Thus it is typically about a model of reliability R(t). The reliability of the system at time (t) is the probability that the system is in states (E1), (E2),(E3) or (E4):

$$R(t) = [P_1(t) + P_2(t) + P_3(t) + P_4(t)] \quad (18)$$

Pi (t) is the probability that the system is in functioning state at time (t) to be ever having broken down previously, that is the probability to have stayed in good working order on all the duration [0, t].Because Markov graphs is homogeneous thus the rate of transition is constant what makes leads (drives) to the consideration of a transition (and the only one) between (t) and (t+dt).At the moment

(t+dt), the system is in the state Ei:

If it was there and if it does not leave it:

$$P_i(t)\left(1 - \sum_{\substack{j=1 \\ j \neq i}}^{n} a_{ij}\, dt\right) \quad (19)$$

(27)

Where α_{ij} is the transition Rate of Ei towards Ej.
If it was not in Ei but the transition with place enters (t) and (t+dt) from
Ej :

$$\sum_{j=1,\ j\neq i} P_i(t)\, a_{ij}\, dt \qquad (20)$$

The general shape:

$$P(t+dt) = P_i(t)\left[1 - \sum_{j=1,\ j\neq i} a_{ij}\, dt\right] + \sum_{j=1,\ j\neq i} P_i(t)\, a_{ij}\, dt \qquad (21)$$

The governing equations:
The full time-dependent equations (including repair transitions) are:

$$\begin{aligned} P_0(t+dt) &= [1-(\lambda_A dt + \lambda_B dt + \lambda_C dt + \lambda_D dt)].P_i(t) + \mu_A dt P_1(t) + \mu_B dt P_2(t) + \mu_C dt P_3(t) + \mu_D dt P_4(t) \\ P_1(t+dt) &= [1-\mu_A dt].P_1(t) + \lambda_A dt.P_0(t) \\ P_2(t+dt) &= [1-\mu_B dt].P_2(t) + \lambda_B dt.P_0(t) \\ P_3(t+dt) &= [1-\mu_C dt].P_3(t) + \lambda_C dt.P_0(t) \\ P_4(t+dt) &= [1-\mu_D dt].P_4(t) + \lambda_D dt.P_0(t) \end{aligned} \qquad (22)$$

$$\frac{P(t+dt)-P_i dt}{dt} = \frac{d}{dt}P_i(t) = P_i'(t) \qquad (23)$$

The equations were:

$$\begin{aligned} P_0' &= -(\lambda_A+\lambda_B+\lambda_C+\lambda_D).P_0(t) + \mu_A P_1(t) + \mu_B P_2(t) + \mu_C P_3(t) + \mu_D P_4(t) \\ P_1'(t) &= \lambda_A.P_0(t) - \mu_A.P_1(t) \\ P_2'(t) &= \lambda_B.P_0(t) - \mu_B.P_2(t) \\ P_3'(t) &= \lambda_C.P_0(t) - \mu_C.P_3(t) \\ P_4'(t) &= \lambda_D.P_0(t) - \mu_D.P_4(t) \end{aligned} \qquad (24)$$

Using the matrix notation, these equations can be expressed in the form:

$$\begin{bmatrix} P_0'(t). & P_1'(t). & P_2'(t). & P_3'(t). & P_4'(t) \end{bmatrix} = \begin{bmatrix} P_0(t). & P_1(t). & P_2(t). & P_3(t). & P_4(t) \end{bmatrix}. \begin{bmatrix} -(\lambda_A+\lambda_B+\lambda_C+\lambda_D) & \lambda_A & \lambda_B & \lambda_C & \lambda_D \\ \mu_A & -\mu_A & 0 & 0 & 0 \\ \mu_B & 0 & -\mu_B & 0 & 0 \\ \mu_C & 0 & 0 & -\mu_C & 0 \\ \mu_D & 0 & 0 & 0 & -\mu_D \end{bmatrix} \qquad (25)$$

Indicating by P (t) the probability vector and by Λ
The transition matrix, we obtain:

$$P'(t) = \frac{d}{dt}P(t) = P(t).\Lambda \qquad (26)$$

$$P_c'(t) = \frac{d}{dt}P_c(t) = P_c(t).\Lambda_{cc}$$

Where:

Pc(t) : Vector of probabilities of non-defaulting states

Λ_{cc}: Transition matrix between non- failing states

$$\frac{P(t+dt) - P_i dt}{dt} = -P_i(t)\sum_{j=1,\ j\neq i} a_{ij} + \sum_{j=1,\ j\neq i} P_j(t)\, a_{ij} = \frac{dP_i(t)}{dt} \qquad (28)$$

Where:

$$a_{ii} = \sum_{j=1}^{n} a_{ij} \qquad (29)$$

We have :

$$\frac{dP_i(t)}{dt} = \sum_{j=1,\ j\neq i}^{n} P_j(t)\, a_{ij} \qquad (30)$$

And we find:

$$P_c(t|P(0)) = P_c(0).e^{-\Lambda_{cc}t} \qquad (31)$$

So the system's comportment is determined by:
The transition matrix Λ
The initial probability vector P(0)
The reliability of the system is given by:

$$R(t) = P_c(0).e^{-\Lambda_{cc}t}.1_E^T \qquad (32)$$

Where 1_E^T is the summation column vector.

We can have the solution of equation (32) by:
Truncated series, numerical integration or the Laplace transform .The method of solution adopted here is that using Laplace Transforms.
The equation solution P(t) by Laplace Transforms:

$$L[f(t)] = f(s) = \int_0^{\infty} e^{-st} f(t)dt \Rightarrow L\left[\frac{df(t)}{dt}\right] = sf(s) - f(0) \qquad (33)$$

Where:

$$L\left[\frac{dP(t)}{dt}\right] = L[P(t).\Lambda] \qquad (34)$$

$$s\tilde{P}(s) - P(0) = \tilde{P}(s).\Lambda \Rightarrow \tilde{P}(s) = P(0).(sI-\Lambda)^{-1} \qquad (35)$$

Where I is the identity matrix
Now the Laplace Transform of equation (32) is given by

$$L[R(t)] = \tilde{R}(s) = \int_0^{\infty} e^{-st}.R(t)dt \qquad (36)$$

Where

$$\tilde{R}(s) = P(0).(sI-\Lambda_R)^{-1}.1_R^T \qquad (37)$$

Where:

$$\Lambda_R = \begin{bmatrix} -(\lambda_A+\lambda_B+\lambda_C+\lambda_D) & \lambda_A & \lambda_B & \lambda_C & \lambda_D \\ 0 & -\mu_A & 0 & 0 & 0 \\ 0 & 0 & -\mu_B & 0 & 0 \\ 0 & 0 & 0 & -\mu_C & 0 \\ 0 & 0 & 0 & 0 & -\mu_D \end{bmatrix}$$

The reliability matrix was:

$$R(s) = [1 \quad 0 \quad 00 \quad 0].(sI - \Lambda_R)^{-1}. \begin{matrix} 1 \\ F_1 1 \\ I1I \\ [1] \end{matrix} \quad (38)$$

The reliability R (t) of the system at time t is:

$$R(t) = A.e^{s1t} + B.e^{s2t} + C.e^{s3t} + D.e^{s4t} \quad (39)$$

Where: A, B, C and D are the equating coefficients.

D. Calculation of the reliability system by Markov process

To estimate the probability of the events it is necessary to return to the essays of experiment on the installation and the data collections of reliability of the components [39]: Operational statistics from self-excited induction generator power plants are regularly collected by the control unit inside the installation. Today, most installation are fitted with equipment that makes it possible to collect the data remotely, via modem or internet .The data from the sources that was accessible for this work areassembled byresearch groups.

To calculate the reliability of the installation by Markov process uses the equation (39) which gives the following results:

TABLE 7.CALCULATION OF THE RELIABILITY SYSTEM BY MARKOV PROCESS

	States				
Time (h)	E1 Fuel pump	E2 Diesel Actuator	E3 Capacitor bank	E4 A|G	R(t)
0	1	1	1	1	1
100	0.990049	0.990049	0.999990	0.999000	0,999568
500	0.980198	0.980198	0.999980	0.998000	0,990064
1000	0.970445	0.970445	0.999970	0.997000	0,964121
2000	0.951229	0.951229	0.998990	0.995012	0,882382
3000	0.932393	0.932393	0.998570	0.993024	0,781528
4000	0.913931	0.913931	0.997990	0.991040	0,677045
5000	0.895834	0.895834	0.984220	0.989060	0,577416
6000	0.895000	0.889954	0.972130	0.976450	0.572113
7000	0.889930	0.886599	0.969920	0.965213	0.569876
7500	0.881230	0.883027	0.959330	0.956896	0.562234
8750	0.880005	0.880011	0.939980	0.941278	0.559984

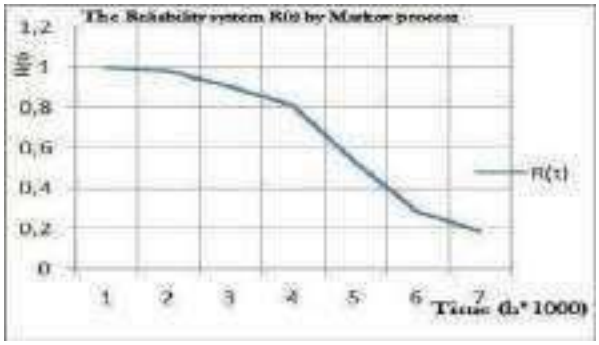

Fig.16 Reliability graph analysis by Markov process

E. Discussion

According to table 3 and 7, the annual reliability results of the asynchronous generator and these of the excitation capacity calculated by the Markov graphical model are relatively close to the data collected by the FMEA method. Hence, satisfactory agreement between the theoretical and experimental results

VI. CONCLUSION

According to afore obtained results, self-excited induction generator can be considered as an effective solution to produce electric energy in both isolated and connected sites. The first test has been done with machine that is operating under vacuum mode taking in consideration the machine saturation conditions to limit the amplitudes of voltages and currents produced. The second test has been affected for machine that is operation under loaded mode.

On the one hand, it is not a matter if the generator works under vacuum mode, but instead, it is most important to set the ideal point of operating under vacuum mode by correctly choose the two principle following values: the excitation capacitor and therotation speed.

On the other hand, the under loaded mode has negatively influence on the machine performance by reducing its speed rotation, which leads to the fall of the voltage and the frequency generated. Therefore, if the load is critical, the generator will completelybe demagnetized.

The established mathematical model of the self-excited induction generator shows that the simulation results are almost similar to those found experimentally .This negligible difference is only due to the experimental survey of the characteristics of the vacuum machine and to the identifying method of its parameters. That definitely has a great influence on the grandeur in transient and permanent regime.

The reliability assessment of the self-excited induction generator in operational phase is usually done according to an analysis based on the structure of the system, the influence of the probabilities of its components failure and the probability of global system failure .For more precious results, two evaluation approaches have been combined in this work.

The first approach consisted of using the FMEA method to observe system comportment and collect failure data, which have helped established statistical analyses, related to the observed failures. Accordingly, reliability levels of the system under the intended conditions of use have been assessed. Failure causes and the most vulnerable component of the installation have been determined as well.

The second approach based on the Markov graph method for a quantitative reliability assessment have produced results relatively close to that produced by the FMEA method

As a conclusion, in this work we have demonstrated that FMEA method is qualified for the qualitative analysis. Indeed, FMEA is suitable to determine the feared elements, undesirable events as well as their causes of occurrence. Also, to determine the impacts of failures on the system .On the other hand, for quantitative analysis, the Markov graph method is preferred in order to control the functional or dysfunctional comportment, offer an important possibility of quantification of the reliability and evaluate the failure probability of the whole system.

REFERENCES

[1] B. Multon ,Y. Thiaux ,H. BenAhmed ,''Consommation d'énergie, ressources énergétiques et place de l'électricité '', Techniques-ingénieur, D3900 v3 , pp.7-17,2011.

[2] A .Benlamoudi, " Etude et simulation d'un système de conversion d'énergie électrique à base d'une machine asynchrone ", Thèse de Magister, Université de Batna ,Algeria ,pp.10-50,1996.

[3] H. Camblong , " Minimisation de l'impact des perturbations d'origine éolienne dans la génération d'électricité par des aérogénérateurs à vitesse variable , " Thèse de doctorat, École Nationale Supérieur d'Arts et Métiers, Centre de Bordeaux, France, 2003.

[4] D. Seyoum , " The dynamic analysis and control of a self-excited induction generator driven by a wind turbine , " Thése de Doctorat , School of Electrical Engineering and Telecommunications,2003.

[5] E.Muljadi, C.P .Butterfield, J.Sallan and M .Sanz, "Investigation of self-excited induction generators for wind turbine applications, "IEEE Trans on Indus Appl., Society Annual Meeting, Phoenix, October 3-7, 1999.

[6] Y.Bendjeddou, " Contribution a l'étude des performances d'un Générateur asynchrone, " Thèse de Magister, Université de BATNA,2013.

[7] F.Poitiers, "Etude et commande de génératrices asynchrones pour l'utilisation de l'énergie éolienne , "Thèse de Doctorat de l'Université de Nantes, France 2003.

[8] B.Yssaad , A.Abene ,''Rational reliability centered maintenance optimization for power distribution systems'', International Journal of Electrical Power & Energy Systems, Vol 73, pp. 350-360,2015.

[9] P.Arques, ''Conception et construction des moteurs alternatifs '' Technosup, Ellipses ,2000.

[10] I. Attoui , ''Contribution au diagnostic de défauts d'une génératrice asynchrone dans une chaine de conversion d'énergie éolienne'' , Faculté des Sciences de l'Ingéniorat ,Thèse de Doctorat , Université de Annaba,2015.

[11] H.Meglouli and Y.Naoui, "Study for a mechanism aided by asynchronous actuator powered by asynchronous diesel generating , " CHAOS,4th chaotic Modilling and simulation international conference,AgiosNikolaos,Crete Greece,2011.

[12] M.Seyoum , F.Rahman and C.Grantham " Terminal voltage control of a wind turbine driven isolated induction generator using stator oriented field control, "Applied Power Electronics Conference and Exposition (APEC'03), Eighteenth Annual IEEE, vol. 2, Miami Beach, 9-13 Fevrier , pp. 846-852,2003.

[13] S. Elkhadiri, L.Elmenzhi, A. Haddi and A. Lyhyaoui '' Control of a Doubly-Fed Induction Generator for Wind Energy by ANN ,'' International Conference on Automation, Control Engineering and Computer Science (ACECS 2017) , Proceedings of Engineering and Technology – PET Vol.21 ,pp.96–101,2017.

[14] J. P .Carone and J. P.Hautier , "Modélisation et commande de la machine asynchrone, "Électrotechnique Édition Technip, pp.100-200,1995.

[15] A. K AI Jabri and A. I .Alolah , " Capacitance requirement for isolated self-excited induction generator , "IEE Proc., B, Vol. 137, No 3, pp. 154-159, May 1990.

[16] C.Grantham, D.Sutanto and B. Mismail, "Steady-state and transient analysis of self-excited induction generators , "IEE Proc. Vol. 136, Pt. B, No. 2, pp. 61-68, March 1989.

[17] L.Shridhar ,C.S Singh Bhim Jha and S.Murthy , "Selection of Capacitors for the Self Regulated Short Shunt Self Excited Induction Generator , "IEEE Transaction of Energy Conversion, Vol. 10, N.1 ,march 1995.

[18] D.Rekioua, "An Approach for the Modeling of an Autonomous Induction Generator Taking Into Account the Saturation Effect , " International Journal of Emerging Electric Power Systems,pp.3-5 ,2005.

[19] Fan. Jianqing and Yao. Qiwei ,"Spline Methods . Nonlinear time series: nonparametric and parametric methods, " Springer. pp. 95-115,2005.

[20] J.H.Vanvleck, " Quelques aspects de la Théorie du Magnétisme ,"Annales de l'I. H. P., tome 10, N° 2 ,pp.57-190,1947.

[21] P.Vas, K.E.Hallenius and J.C.Brown , " The analysis of saturated self-excited asynchronous generator , "IEEE Transaction on energy conversion,Vol.6,N°2 June,1991.

[22] Association Française de Normalisation (AFNOR), CEI 60812:2006, '' Techniques D'analyse de la Fiabilité du Système—Procédure D'analyse des Modes de Défaillance et de Leurs Effets (AMDE) (Reliability Analysis Techniques: Failure Mode and Effect Analysis Procedure FMEA)'', Commission Electrotechnique Internationale (CEI), Geneva,Switzerland, 2006.

[23] L.Betancourt ,S. Birla, J. Gassino,P. Regnier ,"Suitability of Fault Modes and Effects Analysis for Regulatory Assurance of Complex Logic in Digital Instrumentation and Control Systems '' ,Nureg/IA-0254 U.S. Nuclear Regulatory Commission—International Agreement Report; WDC:Washington, DC, USA, 2011.

[24] L.L.C.Chrysler, ''Potential Failure Mode and Effects Analysis (FMEA)'',Automotive Industry Action Group(AIAG): Southfield, MI, USA, 2008.

[25] N.Tazi , E. Châtelet and Y. Bouzidi , ''Using a Hybrid Cost-FMEA Analysis for Wind Turbine Reliability Analysis'', Mdpi journal energies ,Vol .10 ,pp.1-20, 2017.

[26] G.Zwingelstein , " Sureté de fonctionnement des systèmes industriels complexes analyse prévisionnelle et bases de données de fiabilité " , Technique de l'ingénieur, S8251,pp.1-30,2009.

[27] K. Alewine, W. Chen, "A review of electrical winding failures in wind turbine generators " , in 2011 Electrical Insulation Conference (EIC). IEEE, Jun. 2011, pp. 392–397. [Online]. Available: http://ieeexplore.ieee.org/lpdocs/epic03/wrapper.htm?arnumber=5 99618.

[28] C .Egerton,'' Choosing between Failure Modes and Effects Analysis (FMEA) and Fault Tree Analysis (FTA)'',Available online:http://egertonconsulting.com/choosing-between-failure-modes-and-effects-analysisfmea-and-fault-tree-analysis-fta/(accessed on 30 September 2021).

[29] M.Shafiee, F. Dinmohammadi , ''An FMEA-based risk assessment approach for wind turbine systems:A comparative study of onshore and offshore'' , Energies ,vol.7, pp 619–642, 2014.

[30] J. LACROIX , ''Chaînes de Markov '' ,Technique de l'ingénieur, Réf : AF612 v1, 2008.

[31] J.P .Signoret, " Analyse des risques des systèmes dynamiques : approche markovienne , " [SE 4 071] Techniques de l'Ingénieur, base documentaire Sécurité et gestion des risques, pp. 1- 23 ,2005.

[32] R.Schoenig, J.F.Aubry, T.Cambois, and T.Hutinet., " An aggregation method of Markov graphs for the reliability analysis of hybrid systems ",Reliability Engineering & System Safety, 91(2) ,2006,pp.137–148.

[33] M. Bouissou and J.L. Bon, " A new formalism that combines advantages of fault-trees and Markov models: Boolean logic Driven Markov Processes , "Reliability Engineering and System Safety, Volume 82,Issue 2, November ,2003, pp. 149-163.

[34] M. Srinivasa Rao, V. N. A. Naikan ,''A Markov System Dynamics Approach for Repairable Systems Reliability Modeling'' ,International Journal of Reliability, Quality and Safety Engineering, Vol. 23, No. 01,2016.

[35] Anatoly Lisnianski, David Elmakias, David Laredo, Hanoch Ben Haim, ''A multi-state Markov model for a short-term reliability analysis of a power generating unit'' ,Reliability Engineering & System Safety, Volume 98,pp 1-6,February 2012.

[36] F.Grabski, ''Semi-Markov Processes: Applications in System Reliability and Maintenance'', Elsevier,p .270,2014.

[37] N.Privault, ''Understanding Markov Chains Examples and Applications'',Springer,p.351,2013.

[38] B.Sericola ,'' Markov Chains: Theory and Applications '' , Wiley -ISTE, p 416 , 2013.

[39] L.L.1.Mahon , " Diesel Generator Handbook " Butterworth-Heinemann Ltd,pp.45-105, 1992.

Etude de la convection naturelle pour améliorer les performances des murs Trombe

Marwa Ammar[1], Ameni Mokni[2],Nahed Soussi[3],Hatem Mhiri[4]
1 ammarmriwa@gmail.com
2 mokniameni@gmail.com

Résumé :

Les murs Trombe font l'objet d'une attention soutenue en raison de leur capacité potentielle à faire face à la crise environnementale et énergétique. Grâce à la convection naturelle et au stockage de l'énergie dans le mur thermique massif, la charge de chauffage dans un bâtiment est réduite tout au long de la saison hivernale. Cette étude présente une investigation numérique pour l'intégration d'un mur Trombe dans une pièce bien isolée. Les processus de transfert de chaleur et le flux d'air dans un mur de Trombe ont été étudiés mathématiquement et numériquement. On a, dans ce papier étudiéle fonctionnement du mur Trombe sous l'effet du rayonnement solaire et la température ambiante pendant des journées types d'un moi avec les conditions climatiques les plus défavorables. On a utilisé pour ce but le code CFD ANSYS FLUENT 14.0.

Mots clés : Rayonnement solaire, chauffage passif, Mur trombe, températures, flux de chaleur.

1. Introduction

Au cours des dernières décennies, les effets du changement climatique sont devenus une préoccupation essentielle dans les pays développés et en développement, notamment pour le bien des générations futures qui devront supporter le poids de ce changement. Le changement climatique global, principalement causé par les gaz à effet de serre d'origine humaine, entraîne des différences significatives dans les tendances climatiques saisonnières et annuelles.

Le monde entier a subi les conséquences de ce changement climatique.Il est à noter que le changement climatique en général et le réchauffement climatique en particulier est associé de manière significative au taux élevé de consommation d'énergies fossiles.Le secteur du bâtiment représente 20 à 40 % de la consommation totale d'énergie, dont 33 à 55 % pour le maintien d'un environnement intérieur confortable (chauffage, ventilation et climatisation : HVAC) [1-5]. La réduction de la consommation d'énergie du chauffage, de la ventilation et de la climatisation dans le secteur du bâtiment a donc fait l'objet d'une attention particulière.
afin de contribuer à la maîtrise de la consommation d'énergie, des alternatives pour concevoir des bâtiments avec une enveloppe parfaitement optimisée, l'utilisation des systèmes passifs est aussi suggérée. L'objectif est de réduire la demande de chauffage des bâtiments. Parmi ces différentes technologies on peut citer le mur Trombe.
Ce qui distingue le mur Trombe des autres, c'est sa structure simple et sa facilité d'utilisation. Il améliore l'environnement intérieur sans consommer d'énergie fossile et avec un coût d'exploitation nul [6].
Le mur Trombe est un système solaire passif à gain de chaleur indirect, intégré directement à un espace fermé et recouvert d'un vitrage extérieur avec un conduit d'air situé entre les deux [7]. L'énergie captée est émise passivement vers l'air piégé par convection naturelle, ce qui augmente sa température. En raison des effets de flottabilité, l'air chaud piégé, s'écoule vers le haut et réintègre l'espace par l'ouverture supérieure pour la chauffer. Par conséquent, l'air de la pièce dont la température est faible passe dans le canal par l'ouverture inférieure du mur massif pour se chauffer à son tour.

En 1881, Edward Morse a été le pionnier du concept de mur Trombe, qui a été intégré à l'enveloppe dubâtiment par Felix Trombe et Jacques Michel dans les années 1960 [8]. Cette conception a permis d'économiser 60-70% de la charge de chauffage dans le climat méditerranéen et environ 40% dans les climats moins ensoleillés. Ces résultats ont incité de nombreux chercheurs à tenter d'améliorer les performances thermiques du mur de Trombe à des fins de chauffage et de ventilation.

Les études numériques permettent de modifier les paramètres physiques (conductivité de la paroi, épaisseur de la paroi, rapport d'aspect...), c'est pourquoi elles sont plus courantes dans les recherches sur l'optimisation de la conception. Par exemple, Borgers et Akbari [9] se sont intéressés au transfert de chaleur par convection entre des plaques parallèles, et Ormiston et al. [10] ont mis en évidence numériquement la réponse thermique entre le mur de Trombe et une pièce. Bajc et al. [11] ont récemment développé un modèle de transfert de chaleur tridimensionnel d'un mur de Trombe adjacent à une pièce, en examinant différents types de vitrage à l'extérieur du mur et

leurs effets sur l'économie d'énergie. C'est dans ce contexte que s'inscrit notre travail qui a pour objectif d'optimiser les paramètres géométriques d'un mur Trombe intégré dans un bâtiment sous climat méditerranéen

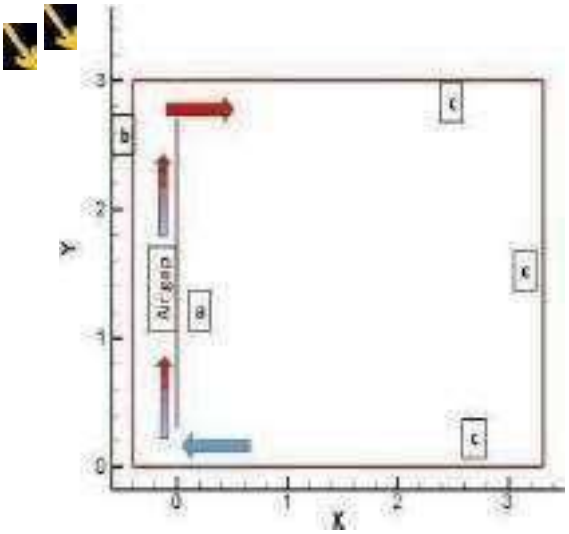

Fig.1: Schématique du Trombe Wall
a : absorbeur : flux :Ø= τφ
b: vitre: échange convectif et radiatif
c: isolation

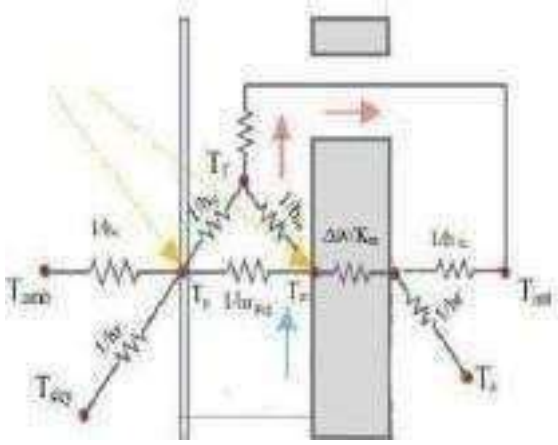

Fig. 2: Diagramme de réseau thermique analogique de la paroi du mur Trombe

2. Simulation numérique

Le schéma du mur Trombe couplé à la pièce est présenté à la Fig.1, qui met en évidence le fonctionnement en mode chauffage. La hauteur du domaine était de 3 m, la base ayant une largeur de 3 m et une longueur de 3 m. Le mur de Trombe,exposé au sud a été réalisé avec un verre transparent d'une épaisseur de 6 mm et un panneau de bois de 70 mm d'épaisseur, la lame d'air est de 400 mm d'épaisseur.

Pour la circulation de l'air dans la pièce adjacente, des bouches d'aération ont été installées au-dessus et en dessous du mur massif. Cela permet à l'air froid de pénétrer par les ouvertures du bas, avec une température d'entrée d'entrée ($T_{f,in}$), l'air chaud s'écoule de l'ouverture supérieure vers l'espace fermé, la température de sortie étant ($T_{f,out}$).Les autres parois de la pièce sont isolées intérieurement.

Hypothèses

Les calculs ont été réalisés sur la base des hypothèses suivantes :

- Les conditions stationnaires sont maintenues dans tout le système
- L'écoulement est laminaire
- Le fluide est incompressible.
- Comme les vitesses en convection naturelle sont faibles, le terme de contrainte visqueuse dans l'équation d'énergie est ignoré.
- La force de flottabilité est modélisée par l'approximation de Boussinesq.
- Les processus de transfert de chaleur sont traités comme unidimensionnels le long du domaine (les gradients thermiques dans la direction verticale sont supposés êtrenuls)
- L'inertie thermique du verre et l'absorption de chaleur de l'air sont négligées.
- La température de l'air à l'entrée du canal est égale à la température initiale de la pièce.

Mise enéquations

Le système d'équations régissant œ problème est donné par :

- Equation de continuité

$$\partial(u_i)/\partial x_i = 0 \quad (1)$$

- Equation demouvement

$$\partial(\rho u_i u_j)/\partial x_i = -\partial P/\partial x_i + \partial[\mu((\partial u_i/\partial x_j) + (\partial u_j/\partial x_i))]/\partial x_j + \partial(-\rho \overline{u_i' u_j'})/\partial x \quad (2)$$

- Equation d'énergie

$$\partial(\rho u_i T)/\partial x_i = \partial((\Gamma + \Gamma_t)\partial T/\partial x_j))/\partial x_j + S_h \quad (3)$$

Les propriétés thermiques de différentscomposants du mur Trombe sont listées dans le tableau 1.

Table 1:Propriétés thermique des composantes du mur Trombe.

Matériaux	Densité (kgm^{-3})	Chaleur spécifique ($Jkg^{-1}k^{-1}$)	Conductivité thermique($Wm^{-1}k^{-1}$)	Emissivité	Absorptivité
Verre	2500	750	1.4	0.89	0.1
Bois	700	2310	0.17	0.88	
Styropore	32	1131	0.03		
Air	1,177	1006	0,023		

3. Résultats et discussion

Afin de déterminer la répartition des températures dans la pièce et d'ajuster l'utilisation des volets des bouches d'aération de manière adéquate, des simulations avec des conditions aux limites réelles ont été étudiées. Le cas d'un jour d'hiver ordinaire à conditions climatiques les plus défavorables ont été simulés en régime permanent.Les 3 cas traités dans cette étude ont été considérés comme des cas stationnaires, à des heures précises de la journée, à savoir,10h (cas1), 12h (cas2) et 13h (cas3). Les rayonnements et les températures ambiantes enregistrées à ces heures de la journée, ont été introduits comme condition aux limites.

Les résultats démontrent que, avec une augmentation de l'intensité du rayonnement solaire, la température de l'absorbeur ainsi que la température de l'arrière de la paroi du mur Trombe augmentent. L'énergie solaire, pénètre dans la couverture en verre, ce qui entraîne son absorption par le mur massif, ce qui se traduit par une élévation de sa température. L'énergie solaire absorbée est transférée à l'air piégé dans le canal par convection naturelle. Par conséquent, un effet de flottabilité se produit, entraînant l'air du bas vers le haut du canal.Comme le montrent les figures 4, 6 et 8, la température de l'absorbeur est plus élevée que celle de l'arrière du mur massif en raison de la perte d'énergie qui a été transférée par conduction l'absorbeur à l'arrière de la paroi.

Les vecteurs de vitesse(Fig.3, Fig.5 et Fig.7.) montrent que l'air froid se déplace de la chambre vers la partie inférieure de l'espace confiné, il migre tout au long du mur massif chaud.
; c'est ici que cet air s'échauffe par convection naturelle. L'air remonte sous l'effet des forces de flottabilitétout au long du mur trombe et il pénètre de nouveau dans la chambre par l'évent supérieur. L'analyse des lignes de courants montrent que l'écoulements s'intensifie en fonction de l'intensité du rayonnement solaire. Une cellule de recirculation est observée dans l'espace confiné quelques soit l'intensité du rayonnement, favorisant d'avantage le réchauffement de l'air.Dans le canal, la vitesse d'écoulement variait de 0,07 à 0,22 m/s près de la partie supérieure du mur massif.

L'existence d'un tourbillon, visible au figures 3,5 et 7, qui, à son tour, forme une circulation d'air. ent, l'air froid se déplace vers la partie e la pièce se dirige vers le fond du se chauffe à nouveau par le mur massif.

L'ar alyse des contours de température (Fig.4, Fig.6 et Fig.8.) montre que la température coté mur est plus importante que celle coté vitre, ce qui favorise la convection naturelle du côté du mur massif. Il en résulte un phénomène d'écoulementasymétrique dans un canal vertical chauffé. Ce qui est considéré comme un avantage dans le cas du mur Trombe.

Durant les premières heures de la matinée ; le rayonnement solaire est minimal ; le système a sa première interaction avec l'énergie solaire. La circulation de l'air de la chambre vers le canal du mur Trombe, et vice versa, débute mais la température demeure quasi constante en raison des faibles transferts qui n'ont pas encore chauffé le mur. (fig.3., fig.4.)

Le transfert par thermo circulationdevient plus intense durant les dernières heures du matin, lorsque le rayonnement solaire atteint son maximum.

L'augmentation du rayonnement solaire favorise les transferts vers l'intérieur, ce qui résulte en une élévation de la température intérieure de la pièce. En effet la température moyenne dans la pièce atteint 301K pour le cas 1 contre 305K pour le cas 2 et 312 K pour le cas 3.

Ces températures élevées assurent le confort thermique à l'intérieur de la chambre. Sauf que les températures dans le canal (vitre-mur massif) sont plus importantes quel que soit l'intensité du rayonnement.

L'analyse de la figure 8 relative au contour de température du cas 3 montre une zone de haute température(320K) close à l'évent supérieur, ceci correspond à une zone de recirculation (fig.7.) ceci nous fait penser à une meilleure configuration pour mieux évacuer cet air de haute température de manière plus efficace vers l'intérieur de la chambre.

La configuration du mur Trombe proposée, prouve une amélioration signifiante du confort thermique durant une journée typehivernale avec des conditions les plus défavorables.

ISSN: 1737-9334

Cas1

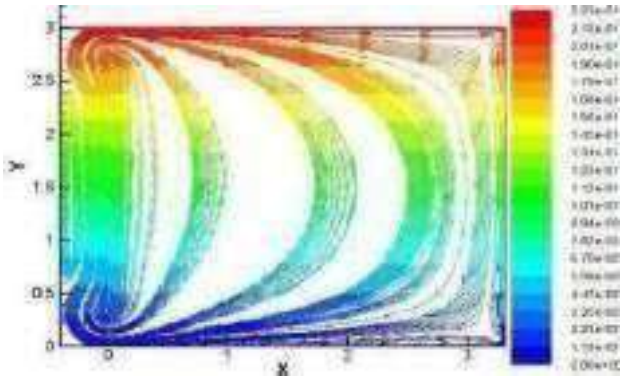

Fig.3: Distribution des contours de vitesse dans le mur Trombe et dans la pièce (I= 362,88W/m² et T_{am}= 294K)

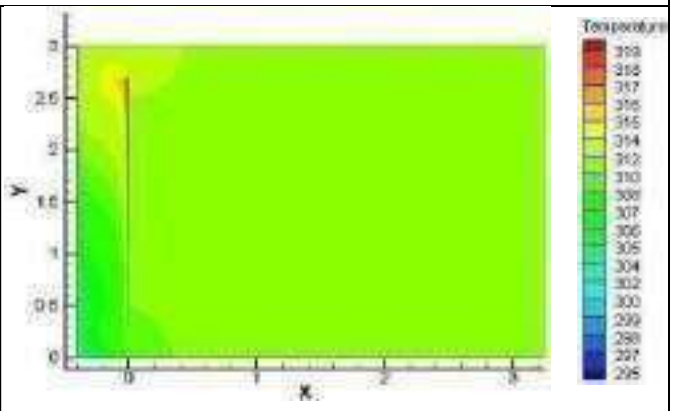

Fig.4: Distribution dedans le mur Trombe et dans la pièce (I=362,88W/m² et T_{am}= 294K)

Cas2

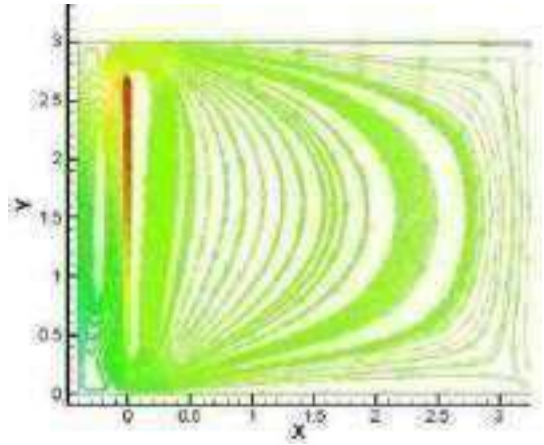

Fig.5 Distribution des contours de vitesse dans le et dans la pièce (I=620,7 W/m² et T_{am}= 296K)

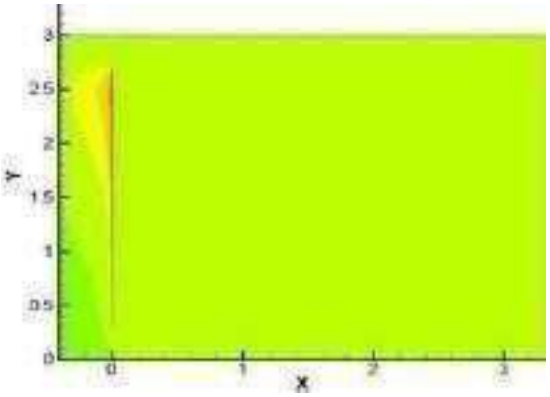

Fig.6: Distribution de dans le mur Trombe et dans la pièce (I=620,7W/m² et T_{am}= 296K)

Cas3

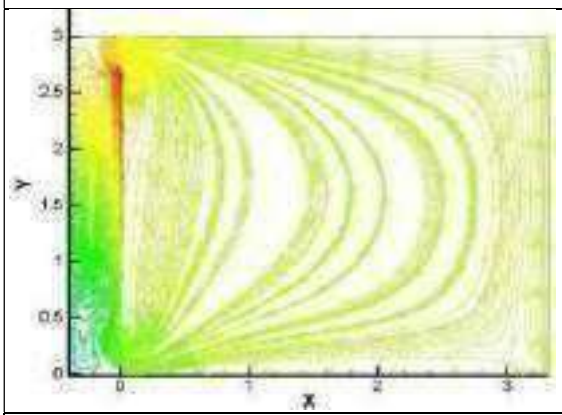

Fig.7: Distribution des contours de vitesse dans le et dans la pièce (I=691,32W/m² et T_{am} =295K)

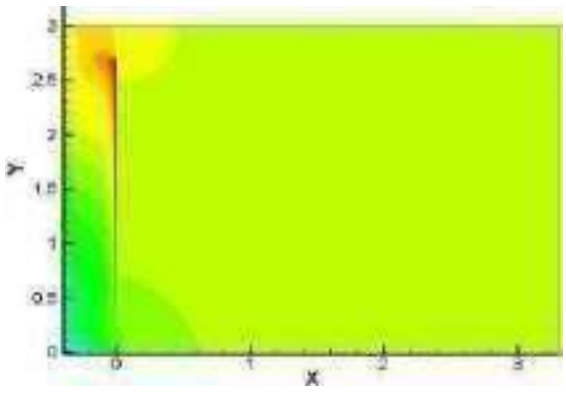

Fig.8: Distribution de dans le mur Trombe et dans la pièce (I=691,32W/m² et T_{am}=295K)

4. Conclusion

Le modèlenumérique développé a pu prédire le transfert de chaleur par convection naturelle à l'intérieur des différents composés du mur trombeen considérant les conditions météorologiques réelles du mois d'hiver avec les conditions les plus défavorables. En outre les simulations numériques ont permis de prédire le schéma de circulation de l'air dans cet espace clos.

Les principales retombées de cette étude sont les suivantes :

- L'augmentation du rayonnement solaire favorise le confort thermique à l'intérieur de la pièce
- Même pendant les heures de faibles ensoleillement et faible température ambiante le mur Trombe assure le chauffage de la pièce.
- Le mur masif est considéré etant l'élément essentiel d'un mur de Trombe en raison de sa capacité à stocker l'energie solaire qui sera par la suite transmise à l'interieur de la pièce
-

Nous tenons à préciser que l'accumulation de chaleur au cours de la journée a été négligée en raison du prolongement considérable des calculs.

Le traitement en régime instationnaire s'avère nécessaires mais, vu qu'il montre un aperçu de l'évolution de la situation, mais, d'autre part, il offre une idée sur les données qui ne pourraient pas être obtenues dans les simulations en régime permanent et qui sont cruciales pour une évaluation précise du système.

Nomenclature

I	Rayonnement solaire (W/m^2)	ε	Emissivité
P	Pression (Pa)	μ	Viscosité cinématique(kg/ms)
q	Flux de chaleur (W)	ρ	Densité(kg/m^3)
S	Surface(m^2)	σ	Constante deStefan Boltzman
T	Temperature(K)	τ	Transmissivité
U,v	Composantes de vitesse (m/s)	ν	Viscosité cinématique (m2/s)

Greekletters

α	Absorptivité
β	Coefficient d' expansion thermique(K^{-1})

Subscripts

amb	Ambiance

Références

[1] Tian Z, Si B, Shi X, Fang Z. An application of Bayesian Network approach for selecting energy-efficient HVAC systems. J Build Eng 2019; 25:100796. https:// doi.org/10.1016/j.jobe.2019.100796.

[2] Kim D-B, Kim DD, Kim T. Energy performance assessment of HVAC commissioning using long-term monitoring data: a case study of the newlybuilt office building in South Korea. Energy Build 2019;204:109465. https://doi.org/ 10.1016/j.enbuild.2019.109465.

[3] Toub M, Reddy CR, Razmara M, Shahbakhti M, Robinett Rd, Aniba G. Model-based predictive control for optimal MicroCSP operation integrated with building HVAC systems. Energy Convers Manag 2019;199:111924.

[4] Wang W, Yuan M, Li YZ, Li C. Numerical investigation on the impact of an on-top sunspace passive heating approach for typical rural buildings in northern China. Sol Energy 2019;186:300–10.

[5] Kim B, Yamaguchi Y, Kimura S, Ko Y, Ikeda K, Shimoda Y. Urban building energymodeling

considering the heterogeneity of HVAC system stock: a case study on Japanese office building stock. Energy Build 2019; 199:547–61
[6] Hu Z, He W, Ji J, Zhang S. A review on the application of Trombe wall system in buildings. Renew Sustain Energy Rev 2017;70:976–87.
[7] W. Smolec, A. Thomas, Theoretical and experimental investigations of heat transfer in a trombe wall, Energy Convers. Manag. 34 (1993) 385–400. doi:10.1016/0196- 8904(93)90089-S.
[8] E. Krüger, E. Suzuki, A. Matoski, Evaluation of a Trombe wall system in a subtropical location, Energy Build. 66 (2013) 364–372. doi:10.1016/j.enbuild.2013.07.035.
[9] T.R. Borgers, H. Akbari, Free convective turbulent flow within the trombe wall channel, Sol. Energy. 33 (1984) 253–264. doi:10.1016/0038-092X(84)90156-7.
[10] S.J. Ormiston, G.D. Raithby, K.G.T. Hollands, Numerical predictions of natural convection in a trombe wall system, Int. J. Heat Mass Transf. 29 (1986) 869–877. doi:10.1016/0017-9310(86)90182-1.
[11] T. Bajc, M.N. Todorović, J. Svorcan, CFD analyses for passive house with Trombe wall and impact to energy demand, Energy Build. 98 (2015) 39–44. doi:10.1016/j.enbuild.2014.11.018.

New Optimized Electrical Architectures of Photovoltaic Generators With Different DC-DC Converter Configuration For Photovoltaic Power System.

Mouhoub Birane[1] , Samah Seba [2], Fatıma Talha[3], Khalil Benmouiza[4], Aicha Degla [5],Sabiha Anas Boussaa[6]

[1, 2, 3,4] *Laboratoire Matériaux, Systèmes Énergétiques, Énergies Renouvelables et Gestion de l'Énergie (LMSEERGE) , l'Université Amar Telidji de Laghouat B.P. 37G. Alger.*

[5] *Centre de Développement des Energies Renouvelables, CDER, 16340, Alger.*

[6]*Division croissance cristalline et procèdes métallurgiques CCPM. Centre De Recherche En Technologie Des Semi-Conducteur Pour L'énergétique CRTSE. 02 frantz fanon, BP 140 ALger 7merveilles, Alger 16200,*

Email : m.birane@lagh-univ.dz

Abstract— **This paper presents energy management study of different topologies in DC / DC converter under Irregular Irradiance of a Photovoltaic Array for evaluation of the efficiency in Photovoltaic system and investigates different photovoltaic array configurations and their effect on the PV array efficiency and the optimization the efficiency of photovoltaic power conversion chain. It provides different improvements on the electrical architecture. In fact, we present a new alternative for improving both the performance of photovoltaic (PV) systems and the efficiency of the energy conversion by using different configuration of power converters while applying the maximum power point tracking (MPPT) for better utilization of the overall system. The MPPT control system in this case can react effectively to atmospheric variations. There are several MPPT and several arrangements of the PV modules inside the array. Among several studied MPPT algorithms for PV panels, the Perturb and Observe (P&O) method is utilized as the simplest and the easiest to be practically implemented. The PV module has been modelled and the MPPT algorithm has been validated by simulation analysis with different arrangements of the PV array were discussed, and a comparison study between the central inverter configuration and the multi- string configuration is conducted. The obtained results are very interesting; it allows the selection of the best PV topology for a given application. We finish with the studies of existing solutions to improve efficiencies and lifetime. We simulated and compared the different conversion configurations in order to find the best one in terms of efficiency and energy produced.**

Keywords— Photovoltaic Generator, Maximum Power Point Tracker MPPT, performance, power, DC-DC Converters. Introduction.

Introduction

Solar energy could be one of the significant sources as an alternative energy for the future. In regard to endless importance of solar energy, it is worth saying that photovoltaic energy is a best prospective solution for energy crisis [1]

The architecture of the power converter is important in a PV system. This structure determines the main characteristics of the photovoltaic installation, as the amount the PV modules need for the PV system and its type of connection. The effect of the partial shadowing or mismatch between PV modules in the energy production will also depends on the type of the architecture. Nevertheless, the price and cost of the PV also depends on the choice of the architecture. [2].

The inverters must guarantee that the PV module(s) is operated at the MPP, which is the operating condition where the most energy is captured. This is accomplished with an MPP tracker (MPPT). It also involves the ripple at the terminals of the PV module(s) being sufficiently small, in order to operate around the MPP without too much fluctuation.

The past technology, was based on centralized inverters that interfaced a large number of PV modules to the grid [3]. The PV modules were divided into series connections (called a string), each generating a sufficiently high voltage to avoid further amplification. These series connections were then connected in parallel, through string diodes, in order to reach high power levels. This centralized inverter includes some severe limitations, such as high-voltage dc cables between the PV modules and the inverter, power losses due to a

centralized MPPT, mismatch losses between the PV modules, losses in the string diodes, and a nonflexible design where the benefits of mass production could not be reached. The grid-connected stage was usually line commutated by means of thyristors, involving many current harmonics and poor power quality[4].

In large PV system (>10 kW) the large number of PV modules are connected to strings, while these strings are connected in parallel via string diodes or string fuses. The PV generator structured like this is then connected to DC input of one of the central inverter. Central inverters are characterized by high efficiency and lowest specific costs. However, the energy yield of the PV plant decreases due to the module mismatching and partial shading conditions [5].Moreover the reliability is limited as whole system is dependent on single power conditioner. In (multi-) string inverter just as with central inverters the PV array is divided into strings. Each of these strings is assigned to their own inverter, called string inverter. Each string operates at its individual (maximum power point) MPP and hence partly minimizes mismatching, reduces losses resulting from shading and avoids losses due to the string diodes and large scale DC-cabling compared to central inverter. The third type, also called AC-modules has individual MPP tracking system for each module and many additional system advantages to the state of the art system [6].

In this paper the perturb and observe MPPT technique is discussed. Moreover, a comparison study between the different PV configurations is carried out by simulation .Further, the effects of partial shading with anwithout bypass diodes are investigated. Then, the performance of state of the art string inverter system is compared with module based MPPT.

IV. CONCLUSIONS

In this paper different topologies of photovoltaic system were discussed, where PV array configuration is significantly affecting the over all system efficiency. This model is used to compare the matching efficiencies of three different topologies for connecting a PV module source to constant voltage (battery)load under different conditions of insulation and temperature. The Perturb and Observe MPPT method was simulated and implemented practically, while the obtained results showed that it can increase the utilization of the overall PV system. The model of the utilized PV panel has been introduced and validated by simulation investigate the effect of PV array configuration on the overall output capability. A comparison study between the central inverter configuration and the Multi-string configuration, for irregular irradiance of the PV panels while applying the MPPT, was conducted. Results showed that the Multi-string inverter configuration could give better utilization of the PV system. It is important to investigate different types of architecture in order to choose the correct PV architecture for each PV installation. This was the motivation behind this work. As future work it is important to compare these simulation results to experimental ones for the different PV arrays architectures.

REFERENCES

[1] Suresh Sagadevano Recent Trends on Nanostructures Based Solar Energy Applications: a Review pages 44-61 materials physics and mechanics(2013)..

[2] Alona, B.A "New Optimized Electrical Architectures of Photovoltaic Generators with High Conversion Efficiency" Doctoral Thesis, University of Toulouse3 Paul Sabatier (UT3PaulSabatier), France 2013.

[3] Chaaban, M. Amer. "adaptive photovoltaic configurations for decreasing the electrical mismatching losses"(2011). architectural engineering -dissertations and student research. paper 10.

[4] M. Meinhardt and G. Cramer, “Past, present and future of grid connected photovoltaic- and hybrid-power-systems,” in Proc. IEEE-PES SummerMeeting, vol. 2, 2000, pp. 1283–1288.

[5] Xiao W, Ozog N, Dunford WG, Topology study of photovoltaic interface for maximum power point tracking, IEEE Transcations on Industrial Electronics, Vol.54, No.3 PP 1696-1704, June 2007.

[6] M. Meinhardt and G. Cramer, “Past, present and future of grid connected photovoltaic- and

hybrid-power-systems," in Proc. IEEE-PES SummerMeeting, vol. 2, 2000, pp. 1283–1288.

[7] Markvart T.: "Solar Electricity", John Wiley & Sons, 1994.

[8] Lorenzo E., Araujo G.L., Cuevas A., Egidio M.A., Miñano J.C., Ziles R.: "Eletricidad Solar Ingenieria De Los Sistemas Fotovoltaicos"; PROGENSA, 1ª edición, 1994.

[9] Pierre Petit; " Optimization of energy transfer in photovoltaic systems". PhD thesis, University of Paul Verlaine, 2011.

[10] Damien Picault; »Reduction of mismatch losses in grid-connected systems using alternative topologies ". PhD thesis, University of Grenoble Polytechnic Institute of Grenoble, 1er October 2010.

[11] G. Sheppard; "Energy Efficiency Technology to Take Solar Market by Storm", February, 2011. Available in: www.isuppli. com.

[12] Dzung N, Lehman B. An adaptive solar photovoltaic array using model-based reconfiguration algorithm. Industrial Electronics, IEEE Transactions on. 2008; 55(7):2644-54.

Étude dynamique d'un cycle frigorifique à absorption-diffusion mono-pression

IkramSaâfi[#1], Ahmed Taieb[#2], Ahmed Bellagi[#3],

U. R. Thermique et Thermodynamique des Procédés Industriels,
Ecole Nationale d'ingénieurs de Monastir (E.N.I.M.),
Avenue Ibn El Jazzar, 5060 Monastir, Tunisie
[1]ikram.saafi@gmail.com
[2]hmed.taieb@gmail.com
[3]a.bellagi@enim.rnu.tn

Abstract— **Dans ce papier une machine frigorifique à absorption-diffusion commerciale de faible capacité a été testé sous différentes conditions opératoires dans le but de maitriser le fonctionnement du réfrigérateur et d'étudier ses performances. Une série de trentaines expériences ont été réalisé qui consiste à faire varier la puissance électrique fournit au générateur de 15W à 63W dans le but d'identifier les conditions optimales de fonctionnement de la machine et d'étudier les différents régimes de fonctionnement. Toutes ces expériences sont toutes effectuées dans un local climatisé à 26°C. Le COP optimal trouvé est de 0.15 pour une production frigorifique de l'ordre de 7W.**

Keywords— **machine frigorifique ; absorption-diffusion ; étude éxpérimentale ; performances.**

I. INTRODUCTION

La machine frigorifique à absorption-diffusion, objet de notre étude, inventé par Platen et Munters en 1928 [1] a été reconnu comme l'une des technologies durables les plus encourageantes pour la production de froid. Le cycle de la machine (**figure 1**) fonctionne à une pression totale constante, et utilise de l'ammoniac comme réfrigérant, de l'eau comme absorbant et de l'hydrogène ou de l'hélium en tant que gaz inerte auxiliaire non absorbable. Ce gaz inerte est nécessaire pour réduire la pression partielle du réfrigérant dans l'évaporateur pour permettre au processus d'évaporation de prendre place dans le dispositif de pression uniforme.

La principale caractéristique de cette machine est qu'elle n'a pas de pièces mobiles, d'où sa bonne fiabilité. La circulation de la solution aqueuse d'ammoniaque est entraînée par une pompe à bulles et celle de gaz circule entre l'absorbeur et l'évaporateur par gravité. Il existe de nombreuses études théoriques et expérimentales sur l'analyse de la performance de cette machine exploité avec différentes sources d'énergie et en utilisant divers mélanges de travail de fluide dans la littérature. Chen et al. [2] a conçu un générateur modifié comprenant un échangeur de chaleur qui réutilise la chaleur rejetée dans le rectifieur pour préchauffer la solution riche de l'absorbeur. La nouvelle configuration du cycle a montré une amélioration significative de la COP de refroidissement, jusqu'à 50% par rapport au cycle original de la même capacité de refroidissement. Srikhirin et al. [3] a effectué une étude expérimentale sur une machine utilisant le mélangeeau-ammoniac et l'hélium comme gaz auxiliaire. Il a également développé un modèle mathématique pourdéterminer les conditions de fonctionnement appropriées pour une performance optimale. Il a observé que les taux de transfert de masse dans l'évaporateur et l'absorbeur ont un effet crucial sur la performance du système [4]. Le COP trouvé dans cette étude varie entre 0,09 à 0,15. Starace et al. [5] a élaboré un modèle thermodynamique du cycle à absorption-diffusion sans aucune hypothèse en ce qui concerne la pureté du réfrigérant sortant du rectifieur. Il a comparé à l'aide de ce modèle les performances de la machine avec celui d'un autre modèlethermodynamique proposé par Zohar et al. [6]. Une plus grande précision a été montré dans la prédiction de l'état réel de la machine. Dans une autre étude, Starace et al. [7] a validé expérimentalement leur modèle à l'aide d'un prototype d'une pompe à bulles couplée à un magnétron domestique pour réduire le transitoire de démarrage du circuit. Afin de valider le modèle, il a varié la puissance thermique fournie à la pompe thermique, il a testé les conditions de fonctionnement de la machine dans chaque élément de la machine.

Dans le présent papier une étude expérimentale est réalisée sur un réfrigérateur commercial de faible puissance, de capacité 25 litres, alimenté par une résistance électrique et qui fonctionne selon le cycle de Platen et Munters. Cette machine met en travail le couple ammoniac/eau comme réfrigérant/absorbant et l'hydrogène, égalisateur de pression, comme gaz inerte.Il est formé principalement d'un générateur, un rectifieur, un condenseur, un évaporateur, un échangeurà gaz, un absorbeur, un réservoir de liquide et un échangeur de solution. Tous ces organes sont construitsen acier.

II. DISPOSITIF EXPERIMENTAL

A. Description ducycle

Lorsque la machine est mise sous tension, la résistance électrique commence à chauffer la solution riche en ammoniac (1), figure 1, avec un apport d'énergie thermique Qg dans la partie inferieure de la pompe à bulles. Cet apport d'énergie est

l'origine de l'évaporation de l'ammoniac, le composé le plus volatil et de faibles quantités d'eau. Lors de cette évaporation, des petites bulles de vapeur se forment et se rassembles pour constituer des grosses bulles occupant la totalité da section du tube. Ayant une densité plus faible que le mélange liquide, ces grosses bulles montent et poussent le liquide entrainant avec elles une quantité de la solution liquide jusqu'à la partie supérieure du générateur (2). Cela se passe dans un tube vertical de faible diamètre. Le liquide pompé est déversé par gravité dans l'espace annulaire du tube coaxial du générateur qui est en contact direct avec la résistance électrique. Ce liquide est alors chauffé d'avantage provoquant ainsi la génération d'une quantité additionnelle de vapeur.

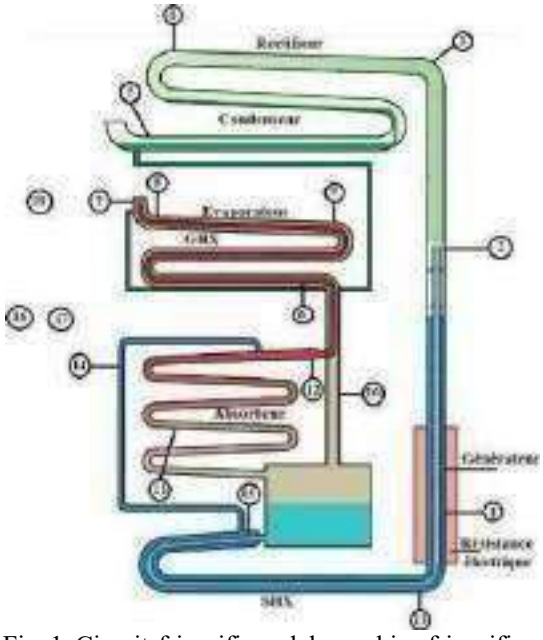

Fig. 1 Circuit frigorifique dela machine frigorifique.

La solution pauvre résultante (13) se dirige sous l'effet de la gravité vers l'absorbeur en passant par un échangeur de solution. La totalité de la vapeur monte vers le condenseur en traversant le rectifieur afin de condenser l'eau qu'elle contient et revient à l'espace annulaire du tube coaxial du générateur pour rejoindre de nouveau la solution pauvre en ammoniac se dirigeant vers l'absorbeur (14). La vapeur d'ammoniac ainsi purifiée (4) se liquéfie dans un condenseur refroidi à l'air ambiant en rejetant une puissance thermique Qc. Le liquide obtenu au point (5) parcourt l'échangeur à gaz, isolé thermiquement, où il est refroidi avant d'accéder à l'évaporateur au point (7). L'échangeur à gaz et l'évaporateur sont constitués de deux tubes coaxiaux : le gaz riche en hydrogène quittant l'absorbeur circule dans le tube central et le mélange binaire composé du gaz inerte froid et du réfrigérant sortant de l'évaporateur dans l'espace annulaire. Le tube ayant le petit diamètre transportant le réfrigérant liquide du condenseur (5) vers l'évaporateur (7) est placé en contact direct avec le tube extérieur du GHX et de l'évaporateur. Le mélange gazeux ammoniac/eau/hydrogène (12) riche en hydrogène. En traversant l'évaporateur, le mélange gazeux ammoniac/eau/hydrogène (9) plus riche en hydrogène est refroidi d'avantage. La pression partielle du système ammoniac/eau dans le flux (8) à l'entrée de l'évaporateur est largement diminuée. L'évaporation de l'ammoniac liquide est complétée dans le GHX et le mélange gazeux (10) riche en ammoniac se dirige vers l'absorbeur.

A l'intérieur de l'absorbeur, la vapeur d'ammoniac dans le flux (10) est absorbée par la solution pauvre ammoniac/eau (14)retournant du générateur. Le mélange gazeux devient ainsi plus léger au point (12) et remonte vers l'évaporateur. La solution liquide devient plus riche en ammoniac et plus froide à la sortie de l'absorbeur (15). Elle repart vers la pompeà bulles à travers l'échangeur de solution. Et le cycle recommence.

ISSN: 1737-9334

B. Appareils de mesures

Pour suivre le fonctionnement du réfrigérateur nous avons commencé par l'équiper par des appareils de mesures adéquates comme présenter sur la figure 2. 18 thermocouples de type K (Chromel / alumel) ont été fixés par des colliers de serrage sur les surfaces externes des tubes à la position souhaité. Ils sont reliés dans l'autre coté à un système d'acquisition de données.

Fig. 1 Dispositif expérimental et différents appareils demesure utilisés.

III. RESULTATS

On a commencé cette étude par l'identification de la puissancemotrice minimale indispensable pour démarrer la machine etassurer la production du froid. En augmentant légèrement àchaque test la puissance motrice et en visualisant l'évolutiondes températures des différents points de la machine, on a pu déterminer la puissance minimale nécessaire pour actionner lamachine, cette puissance est de l'ordre de 22W. Fonctionnement oscillatoire de la machine

On a commencé cette série des essaies à partir de la puissance minimale d'amorçage de la machine 22W. En amplifiant légèrement à chaque essaie la puissance motrice et en visualisant l'évolution des températures des différents points de la machine, on a constate facilement que toutes les températures mesurés sont remarquablement affectées par le fonctionnement oscillatoire du générateur. Dans la figure 3 on constate que l'évolution des températures du générateur et de l'évaporateur (pour les puissances de chauffe 22, 24 et 30W) présentent un régime stationnaire oscillant de même fréquence. La température au niveau du générateur oscille entre 205 et 210°C, celle au niveau de l'évaporateur fluctue entre -12 et - 20°C. Ces trois puissances ne permettent pas d'avoir une température constante dans l'évaporateur.

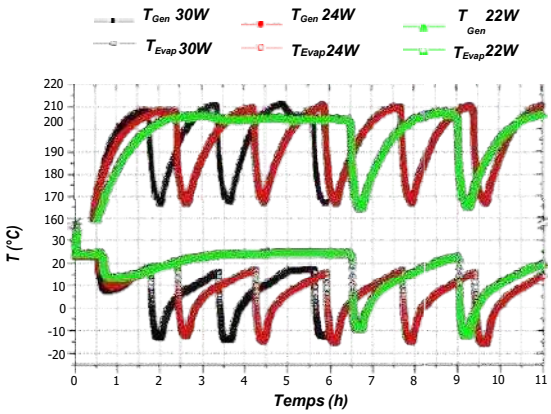

Fig. 3 Evolution des températures du générateur et de l'évaporateur pour les puissances de chauffe : 22, 24 et 30W.

Fonctionnement stable de la machine

Dans cette partie, on a continué la série des essais précédents en augmentant la puissance motrice petit à petit et en visualisant l'évolution des températures des différents points de la machine. Une disparition totale de toutes les oscillations est notée dans les profils des températures mesurées. En particulier, l'évolution des températures du générateur et de l'évaporateur (pour les puissances de chauffe 43, 45, 47, 50, 55, 58 et 63W) sont représentées dans les figures 4 et 5.

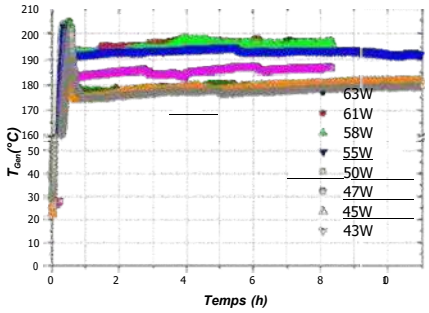

Fig. 4 Evolution des températures du générateur pour les puissances de chauffe : 43, 45, 47, 50, 55, 58, 61 et 63W.

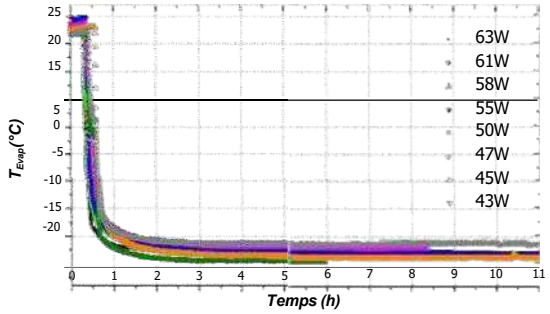

Fig. 5 Evolution des températures de l'évaporateur pour les puissances de chauffe : 43, 45, 47, 50, 55, 58, 61 et 63W.

IV. CARACTERISATION DE LA MACHINE

Pour caractériser les échanges thermiques entre la machine et le milieu extérieur, nous avons retenu la notion du coefficient global d'échange, un pour l'échange cabine-milieu extérieur $(UA)_{ext}$ et l'autre au sein de la cabine entre le contenue de la cabine et l'évaporateur $(UA)_{int}$. Ces coefficients d'échange peuvent être déduits des mesures en régime dynamique ou stationnaire.

Le bilan d'énergie de la cabine s'écrit :

$$\frac{dU_{cab}}{dt} = \dot{Q}_{ext} - \dot{Q}_{int} \quad (1)$$

Où U_{cab} est l'énergie interne de la cabine et $\dot{Q}_{ext}$ et $\dot{Q}_{int}$ respectivement le flux thermique échangé entre la cabine et le milieu extérieur d'un coté, et l'évaporateur et la cabine, de l'autre :

$$\dot{Q}_{ext} = (UA)_{ext}(T_{amb} - T_{cab}) \quad (2)$$

$$\dot{Q}_{int} = (UA)_{int}(\bar{T}_{cab} - \bar{T}_{evap}) \quad (3)$$

Le bilan d'énergie s'écrit alors :

$$\frac{dU_{cab}}{dt} = (UA)_{ext}(T_{amb} - \bar{T}_{cab}) - (UA)_{int}(\bar{T}_{cab} - \bar{T}_{evap}) \quad (4)$$

En utilisant le résultat de l'équation (4), on peut écrire :

$$\frac{dU_{cab}}{dt} = C_{p,cab}\frac{d\bar{T}_{cab}}{dt} = (UA)_{ext}[T_{amb} - \bar{T}_{cab}] - (UA)_{int}[\bar{T}_{cab} - \bar{T}_{evap}] \quad (5)$$

[redacted] moyenne de la cabine, son contenu compris.

En divisant les deux membres par $C_{p,cab}$, la chaleur massique moyenne de la cabine vide, on obtient :

$$\frac{d\bar{T}_{cab}}{dt} = \frac{(UA)_{ext}}{C_{p,cab}}[T_{amb} - \bar{T}_{cab}] - \frac{(UA)_{int}}{C_{p,cab}}[\bar{T}_{cab} - \bar{T}_{evap}] - \frac{(m\,C_p)_{eau}}{C_{p,cab}}\frac{d\bar{T}_{eau}}{dt} \quad (6)$$

[redacted]

$$\frac{d\bar{T}_{cab}}{dt} = \alpha\,[T_{amb} - \bar{T}_{cab}] - \beta\,[\bar{T}_{cab} - \bar{T}_{evap}] - \gamma\frac{d\bar{T}_{eau}}{dt} \quad (7)$$

[redacted]

L'équation (7) devient :

$$\frac{dT_{cab}}{dt} = \alpha[T_{amb} - T_{cab}] - \beta[T_{cab} - \bar{T}_{evap}] \quad (8)$$

En se basant sur les mesures en dynamique des températures T_{amb}, T_{eau} , T_{cab} et $\bar{T}_{evap}$ on a pu résoudre l'équation (9) pour 20 expériences (cabine vide ou avec différents volumes d'eau dans la cabine). Une procédure de régression non linéaire est effectuée en utilisant le logiciel MATIMATICA ® pour déterminer les paramètres α, β et γ du modèle et pour prédire la température de l'eau et de la cabine.

Le modèle de la température de l'eau est de la forme :

$$T(t) = T_0 (1 + a\,t\,e^{-b\,t} + c\,e^{-d\,t} + e\,e^{-f\,t})$$

Où a, b, c ,d, e et f sont des paramètres de lissage identifiés pour chaque température (eau et cabine) et pour chaque expérience (cabine vide ou non).

Les valeurs expérimentales relevées pour la température de la cabine ainsi que du modèle de regression utilisé sont représentés sur la figure 6 pour une cabine vide. On remarque que le modèle de regresion utilisé représente fidèlement les données expérimentales.

Le tableau 1 reprensente aussi les valeurs trouvées des paramètres α, β et γ ainsi que leurs valeurs moyennes pour les expériences réalisées.

La connaissance de la valeur moyenne de **γ** nous permet de déterminer $C_{p,cab}$. Une fois ce dernier paramètre identifié, on peut deduire directement $(UA)_{ext}$ et $(UA)_{int}$ respectivement à partir des valeurs moyennes de α et β.

$$\begin{aligned} C_{p,cab} &= 1{,}91\ \text{kJ/K} \\ (UA)_{ext} &= 0.53\ \text{W/K} \\ (UA)_{int} &= 0.23\ \text{W/K} \end{aligned} \quad (11)$$

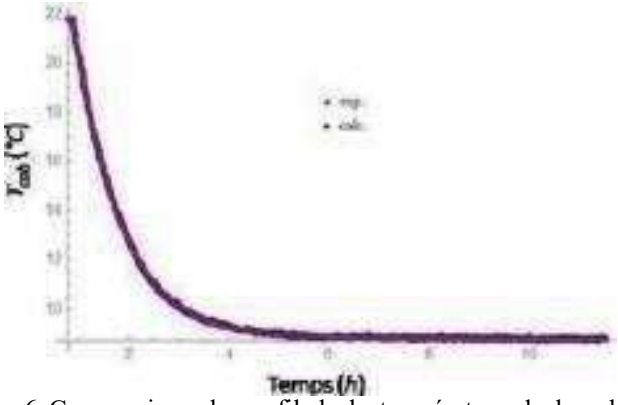

Fig. 6 Comparaison du profil de la température de la cabine (V_{eau} = 0l) avec la modèle de regression trouvé : T_0= 8.40592, a=0.0192634, b= 0.145793, c= -12968, d= 14.3739, e= 1.06511 et f= 1.06511

TABLE I

VALEURS DES PARAMETRES α, β ET γ

n°	α (h^{-1})	β (h^{-1})	γ (kg^{-1})
1	0,954881	0,4022393	0,7888909
2	0,916906	0,3917	0,7888909
3	0,916906	0,3917	0,981186
4	0,903291	0,3847	0,981186
5	1,11416	0,496746	0,955986
6	1,22393	0,568542	0,955986
7	1,22393	0,568542	0,955986
8	1,05858	0,460507	
9	1,05858	0,460507	
10	0,945599	0,442812	
11	0,9099	0,402664	
12	0,945599	0,442812	
13	0,9099	0,402664	
14	1,06664	0,486158	
15	1,06664	0,486158	
16	0,916664	0,355459	
17	0,886484	0,399174	
18	0,983791	0,44676	
19	0,983791	0,44676	
20	0,902639	0,349796	
21	1,0579	0,410276	
22	1,0579	0,410276	
23	1,0579	0,410276	
Moyenne	**1,0027179**	**0,4355317**	**0,9154445**

Etude des performances de la machine

Les performances du réfrigérateur étudié sont représentées dans les figures 7 et 8. Comme présenté précédemment, on remarque qu'une puissance minimale est nécessaire pour le démarrage de la machine frigorifique de l'ordre de 36W. Elle produit une puissance frigorifique de 5W.

Lorsqu'on augmente progressivement la chaleur fournie augénérateur, les débits de la solution pompée et de la vapeur augmentent. L'accroissement du débit de la vapeur et par suite du réfrigérant permet d'avoir une puissance frigorifique de plus en plus grande. Un débit de la solution pompée plus important permet d'absorber une quantité de vapeur plus grande. Ceci explique la croissance de la puissance frigorifique et par suite le coefficient de performance. On rappelle aussi que l'augmentation de la température motrice conduit à une solution pompée plus pauvre en ammoniac. Une solution pompée, à l'entrée de l'absorbeur, de plus en plus pauvre avec un débit de plus en plus croissant conduit à une efficacité de l'absorbeur de plus en plus croissante et une pression partielle duréfrigérant plus basse.

Au delà de 43W, la puissance frigorifique se stabilise et le COP commence à décroitre. Ceci s'explique par fait que l'échange thermique au niveau de l'évaporateur est limité par la température le long de l'évaporateur et aussi par le coefficient d'échange global interne $(UA)_{int}$ entre l'évaporateur et l'intérieur duréfrigérateur.

ISSN: 1737-9334

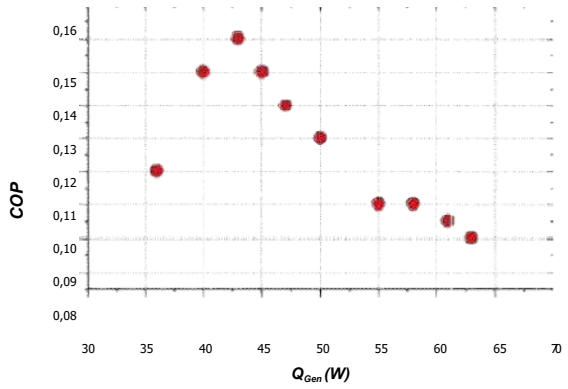

Fig. 7 Variation du *COP* expérimental en fonction de la puissance fournie au générateur.

La quantité d'ammoniac qui peut s'évaporer à l'intérieur de l'évaporateur est alors limitée. La quantité supplémentaire produite par l'augmentation de la puissance ne sera pas évaporée et quittera l'évaporateur à l'état liquide. La puissance frigorifique produite devient constante puisque la quantité d'ammoniac évaporée reste la même. De plus, un chauffage supplémentaire au niveau du générateur n'est pas nécessaire au-delà de ces conditions car il ne fera que réchauffer davantage cette vapeur d'ammoniac qui sera par la suite refroidie dans le rectifieur puis dans le condenseur, ce qui conduit uniquement à une perte de l'énergie et à la diminution du COP.

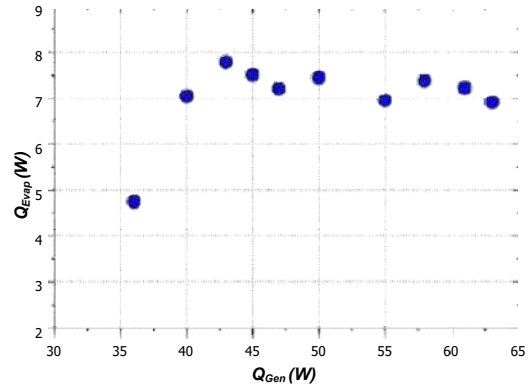

Fig. 8 Variation de la puissance frigorifique en fonction de la puissance fournie au générateur.

V. CONCLUSIONS

Dans ce papier, nous avons procédé à une étude expérimentale d'un réfrigérateur commercial de faible puissance, de capacité 25 litres, alimenté par une résistance électrique. Nous avons étudié les performances de la machine pour diverses conditions opératoires ce qui nous a permis de caractériser complètement cette machine. En régime dynamique, les valeurs de $(UA)_{cab}$ et $(UA)_{evap}$ trouvées sont respectivement de 0.636 0.276 WK^{-1} et WK^{-1}. Ces valeurs nous ont permit d'évaluer la puissance frigorifique 7.5W et le COP de la machine de l'ordre de 0.15.

REFERENCES

[1] B.C. Von Platen, C.G. Munters, Refrigerator, US Patent 1 (1928) 685-764.

[2] J. Chen, KJ. Kim, KE. Herold. Performance enhancement of a diffusion–absorption refrigerator. International Journal of Refrigeration 1996;19:208–18.

[3] P. Srikhirin, S. Aphornratana, Investigation of a diffusion absorption refrigerator, Applied Thermal Engineering 22 (2002) 1181–1193.

[4] L. S. Wilson, A. C. Carlos, A. T. Ednildo, C. S. Jacques, C. M. Evania, Exergoeconomic analysis of a single pressure absorption refrigeration cycle, 20th International Congress of Mechanical Engineering (2009)

[5] A. Zohar, M. Jelinek, A. Levy, I. Borde, The influence of diffusion absorption refrigeration cycle configuration on the performance, Applied Thermal Engineering 27 (2007) 2213–2219.

[6] A. Zohar, M. Jelinek, A. Levy and I. Borde, 'Performance of Diffusion Absorption Refrigeration Cycle With Organic Working Fluids', International Journal of Refrigeration, Vol. 32, N°6, pp. 1241 – 1246, 2009.

[7] N. Ben Ezzine, R. Garma, A. Bellagi, A numerical investigation of a diffusion–absorption refrigeration cycle based on R124–DMAC mixture for solar cooling, Energy 35 (2010) 1874–1883.

10ème Conférence Internationale des Energies Renouvelables CIER-2022
Proceedings of Engineering & Technology-PET-Vol 71

Hygrothermal effect of sheep's wool used as insulation material

Smakdji Nafila*[1], Abderrahmane Khechekhouche[2]
[1]*Laboratory of Applied Energetics and Materials Mohammed Seddik BenYahia University, Jijel Algeria*
[2]*Faculty of Technology University of El Oued Algeria*
[1]nafila_smakdji@yahoo.fr
[2]abder03@hotmail.com

***Abstract*— Currently and since the last century, the whole world has noticed a real climate disruption, due to the increase of greenhouse gases in the atmosphere, especially CO2. The building sector is responsible for 40% of energy consumption. This can be reduced by improving the energy efficiency of existing buildings. One of the most studied improvements is the insulation of external walls, in some cases this measure leads to an increase in airtightness, thus impacting the hygrothermal behavior of the envelope of a building that after the renovation may suffer higher levels of humidity, higher risks of condensation and faster structural degradation related to moisture and mold growth. Our current work is based on solving the problems of condensation in the exterior walls which contributes to the degradation and rotting of building materials. In reality all insulation materials are efficient, and they have an impact on the environment, a bad choice or a bad application increases this impact and makes its use useless. Therefore, a coherent choice as well as the integration of a long-term reflection can improve theinsulation of the walls. according to the principle: for equalperformance, use the material that will have the least possible impact on the environment, our study attempts to provide confirmation by choosing sheep wool, for its availability, its excellent thermophysical and environmental qualities and its low embodied energy compared to other standard insulating materials, where this energy is more important than the primary energy needed for space heating. The calculations were made according to Glaser's method to estimate the hygrometry rate inside the wall. The results obtained encourage us to use this natural material especially for the renovation of buildings already built thanks to the ease of its assembly from the outside.**

***Keywords*— Sheep wool, hygrothermal comfort, insulation materials.**

I. INTRODUCTION

Since the creation of the universe, the atmosphere is the essential gaseous envelope for life on earth to be possible, it ensures an average temperature of 15°C, without it, it would be unbearably cold. The amplification of human activities linked to the growth of the world population, requiring an increased food production as well as the use of fossil energies in the industry in an exclusive way especially in the building sector [1]. Developments that have led to ever-increasing global warming with already real and devastating consequences, notably floods and drought [2]. To overcome this problem man is always concerned with finding adequate solutions to protect his environment. Approximately 50% of the heat exchange between the interior and the exterior takes place through glass, while the remaining 50% is exchanged through the building envelopes, such as walls and roofs [3]. This necessitates excess energy consumption by heating and cooling systems, which account for a significant portion of the energy used in buildings [4]. Given the enormous energy demand of the building sector in the coming decades, the IPCC Agreement's climate targets of 2°C and 1.5°C may not be met unless research continues into replacing fossil fuels with renewable energy [5] and developing energy efficient buildings [6]. This research has received a lot of attention in the last decades in order to stop global warming. Several numerical and experimental studies have been carried out on energy efficiency and building optimization, such as [7] conducted a research on energy saving by insulating buildings with an air gap and with different materials such as polystyrene, rock wool. They found the energy saving by using polystyrene in wall and roof insulation. Aktacir and al
[8] studied the effect of insulation on a simple building located in Adana, Turkey. They showed that increasing the thickness of extruded polystyrene leads to a reduction in cooling energy requirements. Ozel and al. [9] used the finite difference method to determine the optimal position and distribution of insulation on walls. They concluded that exterior wall insulation is the best solution. Al-Sanea and al. [10] showed that the orientation of the walls has a significant effect on the characteristics of heat transfer, while this effect is relatively weaker on the total cost and the optimal thickness of a given insulation. Fezzioui and al. [11] their study consists of the influence of the building envelope on its energy demand during overheating. They introduced elements of improvementof the studied habitat, such as the increase of the thermal inertia, the insulation of the external walls and the roof. Medjelekh et al. [12] evaluated the impact of thermal inertia on the energy consumption of buildings by making a comparison between a house from the colonial era and a contemporary villa. Their results showed that the use of a local material adapted to the climate of the region makes it possible to obtain hygrothermal comfort and thus reduce energy consumption. D.P.P. Meddage et al used lightweight expanded

ISSN: 1737-9334

polystyrene concrete panels in their experimental study to improve the thermal performance of roof slabs in tropical climates. Numerical simulations performed in Design Builder. To propose a holistic life cycle approach to study the economic and environmental feasibility. According to the results, the roof slab with 75 mm EPS insulation was found to be satisfactory with a decrease in life cycle cost, and carbon emissions (kgCO2e) implying that the recommended insulation system is environmentally and economically feasible in tropical climates[13]. Kolokotsa et al [14] found that cool roofs contribute to a 17% decrease in annual cooling energy demand. Cool roofs are designed to reflect more solar radiation compared to a traditional roof. Typically, cool roofs are provided with white or light colors to increase thermal emissivity. [15] This study examines the benefits of incorporating passive techniques into multi-layered clay hollow brick walls to improve their dynamic thermal performance. In addition, it was shown that the total thermal load is reduced by approximately 28% for the improved wall configurations with 100% insulation filled cavities compared to the traditional configurations, which helps to improve the energy efficiency of the building. [16]Thermal optimization of hollow concrete roofing blocks can significantly reduce the huge energy consumption used for building cooling. It is shown in this study that the configuration based on the use of a low emissivity coating and the insertion of an insulating material between the outer surface of the block and the slab could reduce the total 24-hour thermal load by about 93.1% compared to the traditional configuration. The bibliographic research allowed us to classify the studies encountered according to three scales, material scale, component scale and building scale. Our current study concerns the hygrometric behavior at the material scale, where we evoke the transfer of moisture and heat and the values of the intrinsic characteristics of the studied material. where moisture and heat transfer and values of the intrinsic characteristics of sheep's wool are studied. It has been found that sheep's wool can be used as reinforcement for rammed earth construction elements. By adding sheep's wool to the design of the land based building material mix, where their tensile strength, ductility, and impactresistance have been improved. Also this natural fiber is highly hydrophilic, it could improve the environmental sustainability of building components located in three different climates: humid, dry and intermediate [17]. In their study, theyproduced a new boron-doped sheep wool insulation board. This insulation panel has been compared with rock wool and expanded polystyrene, in the acoustic, humidity, ambient and surface temperature tests, they determined that this new insulation panel even with 1 cm in thickness can compete with the rock wool and expanded polystyrene [18].named Cartonlana, is a sheep's wool panel manufactured and studied for the thermal insulation of pitched roofs. Measurements of thermal conductivity, sound absorption coefficient and thermal permeability of a wall were determined, where it was provento be thermally competitive [19].Their study concerns the multilayer reinforcement of clay with sheep wool yarn. It was concluded that the effect of the wool yarns is significant on the thermomechanical behavior of the developed biomaterial, providing high thermal insulation[20].Following a hygrothermal simulation, it was observed that sheep's wool, compared to mineral wool and calcium silicate, offers comparable thermal insulation characteristics revealing better performance in certain applications [21].In their work found that the tensile properties and hardness of the composite determined experimentally confirmed the importance of the sheep wool fiber added in the manufacture of this composite as a reinforcing material to the polyester resin used as matrix material [22].This work confirmed that the production of fiber reinforced concrete reduced the slump values of fresh concrete, thereby improving the concrete's ductility and its flexural tensile strength values [23].In their study, a comparison between the Glaser method and the dynamic simulation methods was made in order to highlight their advantages and disadvantages considering: the different approaches to evaluating not only surface and interstitial condensation, but also of sustainability. They found that when the insulation layer is on the outer side, both methods give similar results, but in the case of interior insulation, the Glaser method [24] is much more conservative than dynamic simulations in evaluating the hygrothermal behavior of the building envelope [25].In order to evaluate the interstitial condensation the EN 15026 method [26] and the Glaser method were used [27] the Glaser method reveals that the risk of condensation was greater during the analysis and observed earlier than during the analysis with the EN 15026 standard.[28] This study presents a comparative analysis of the properties of building insulation materials (thermal, hygroscopic, acoustic, reaction to fire, environmental and cost) and their performance in different climate zones. Therefore the optimization must include the energy, environmental, comfort and economic criteria. The embodied energy of insulation materials is also a critical factor. In insulated buildings, if the reduction in operating energy is higher than the energy used to manufacture the insulation materials, it results in positive net energy balance and decreases the GHG emission [29]. The condensation is defined according to the Glaser approach, which is a practical tool in building design recommended by DIN 4108 and prEN ISO 13788. Several methods have been proposed to study condensation inside building elements, including those described by Krischer et al [30], Luikov [31] and Philip et al [32], and the Glaser method [33], the latter is often used to predict condensation risks and to define quality standards to be met by building elements. The Glaser method is even used in DIN 4108 [34] and prEN ISO 13788 [35] standards to define condensation. It is basedon the following assumptions: the transport of moisture follows Fick's law; heat is transported according to Fourier's law; the process takes place under steady-state conditions; the building components are airtight and the condensed moisture cannot migrate. The material properties are assumed to be constant even under condensation conditions, which occur when the vapor pressure is equal to the maximum allowable vapor pressure (the saturation vapor pressure). Thus, Glaser's

ISSN: 1737-9334

method only considers vapor transport mechanisms and does not consider the effects of liquid transport.

II. Material And Method

A. Embodied Energy

Faced with the threat of global warming, controlling energy consumption is an emergency. The works of the Intergovernmental Panel on Climate Change (IPCC) have led states to initiate policies to reduce greenhouse gas emissions**.** To achieve this, actions must be multiplied at all levels and on three fronts: sobriety, energy efficiency and the use of renewable energies. With 45% of the energy consumed by buildings, this sector also contributes 22% to greenhouse gas emissions [36,37]. This includes the energy used for heating, the production of domestic hot water, electricity consumption and also the share of energy spent for the extraction of raw materials, building materials, their manufacture, their transport and their installation. implemented during the works. This part, called "embodied energy", which must necessarily be taken into account, especially for the choice of materials [38] .

B. Hygrothermal Comfort

Characterizing the temperature and the humidity level of the ambient air inside a room is a frequent measurement when seeking ideal hygrothermal comfort for the health of the inhabitants and the durability of the infrastructures. Specifically, the hygrothermal behavior of a material represents the behavior of a material within an environment in which the temperature and the relative humidity vary [39].

C. Choice Of Insulation Material

Thermal insulation can both reduce energy consumption for heating and air conditioning and increase comfort. But that's not all. Among the materials used in the building, there are differences in environmental impacts, which must be assessed over the entire life cycle; raw material extraction, production, implementation, recycling, etc.). Generally, the energy saved by the action of insulating a building during its life cycle is greater than the embodied energy to manufacture the insulation. But when the building is designed in such a way as to achieve low energy consumption by natural materials, the amount of energy used to make the insulation becomes significant. This highlights further potential for improvement for the environmental impact of renewable based thermal insulation materials by lowering the need for additives [40]

III. Sheep's Wool

A. Description And Characteristics

One of the first animals to be domesticated was the sheep, ten to twelve thousand years ago. They are a supplier of a natural fiber. From shearing (Figure 1) sheep wool has been used for ten thousand years, since prehistoric times, it was already used with other wool for the insulation of yurts in Mongolia. Sheep's wool has gone through the ages and has always founda place of choice among the different types of wool, because it can be used in a variety of ways, it is filleted, woven and knitted and felted. Sheep's wool is now positioned as the main textile fiber for clothing and interior use [41]. (Figure.2). Sheep's wool is an organic product from raw materials of variable nature and quality, it can be used raw or manufactured. The fiber of sheep's wool traps the air that enters its structure because it is hollow. It absorbs 30 to 40% of its weight in water without reducing its insulating power thanks to its capillarity. The fiber is not packed thanks to its impact strength which is due to the creation of a tendril of the strand of wool bit caused by the opening movement of the scales on its surface which are constantly exposed to the various external tensions (figure 3). One of the most important properties of fiber is the tensile property. It depends on both complex fibers arrangements inside the yarn and fabric structure and also on the tensile properties of the fibers. As shown in Fig. 14.1, the tensile properties of wool are quite variable but, usually, at 65% relative humidity and 20°C temperature, the fibers have a tenacity of 140 to 180 MPa, However, when the wool fiber absorbs the moisture, its tensile strength decreases (e.g. Fig. 4). Due to the protein structure, wool is considered the most hygroscopic material among natural fibres. by dissipating a quantity of heat, it absorbs a large quantity of humidity, which binds by a hydrogen bond to the amino acids. Wool fiber can absorb moisture in the form ofvapor (e.g. Fig. 5). Wool has low heat conductivity. Wool fibers do not wrap well in yarns due to their waviness and scales, this makes the wool yarn fuller and able to insert a lot of air. The pith of the wool fiber contains air spaces which reinforce the insulating power of the wool (e.g. Fig.7). Felting is the irreversible shrinkage of sheep's wool fiber. Which has very good felting properties due to its special structure and high degree of crimp. The interlocking of the scales causes the material to shrink. Wool can produce felting even when mixed with other fibers. Felting does not require an adhesive substance for its manufacture. The wool becomes soft at high temperatures. At 130°C, it begins to decompose and carbonizes at 300°C (e.g. Fig. 6) [42].

Fig. 1 Blade sheep hearing demonstration

ISSN: 1737-9334

Figure.2 Different wool types

Figure 3 .Wool purges moisture and releases it

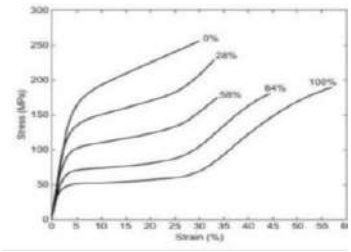

Fig. 4 Stress-strain curves of wool fibres at different relative humidities

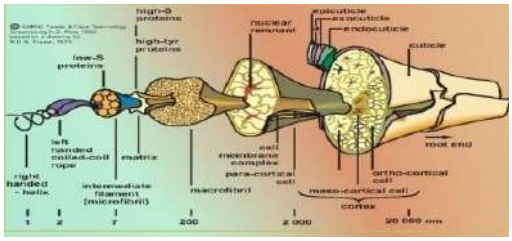

Fig. 5 Components of sheep's wool fiber

Fig. 6 wool is hardly flammable

B. Application Areas

In addition to clothing, wool has been used for blankets, horse rugs, saddle cloths, carpeting, upholstery and insulation (e.g. Fig. 7). Insulation rolls are cut and attached to walls, ceilings and roof slopes. Loose sheep's wool is placed using a carding blower to restore its loft.

C. Insulation

sheep's wool is used for the thermal and acoustic insulation of buildings. This insulation of animal origin for its excellent properties: rigidity and low environmental impact can be used for sustainable architecture [43]The sheep's wool insulation provides comfort in summer and winter. fibers can be blended with polyester or attached to a polypropylene grid [44] Pure sheep's wool has excellent natural insulation properties, it's very strongly hygroscopic, it can absorb and release water up to 33% of its weight (1 kg of wool absorbs up to 330 milliliters of water), in other words, within the limits of this proportion, the fibers are not transformed by a chemical bond with the water which they have encountered, they retain their property of insulation and do not become wet [45]. Combined with the property of thermal insulation, this hygroscopic property makes wool a good climate regulator of the habitat. As a result, the wool practically never molds and forms an anti-mold screen for the areas it covers vis-à-vis the ambient air (e.g. Fig. 8). It is a perfect acoustic insulator with its ability to attenuate and absorb high and low frequency sounds. The complex structure of sheep's wool acts as a wave trap where the soundproofing of a 45 mm panel is 20 dB [46,47] (e.g. Fig. 9). The advantages and disadvantages of sheep's wool are: longevity of wool, low flammability, ecological, very easy to install without treatment against humidity. It has a slight odor, expensive, not suitable for humid areas.

Figure7. Insulation

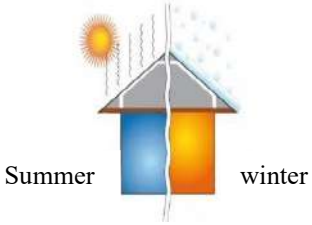

Figure 8.Thermal insulation

Figure 9. 45 mm thick wool

-Condensation

The warmer the air, the higher its vapor content. in a building heated in winter, the quantity of vapor will therefore be greater inside than outside, which generates a natural balance by transporting humidity in the form of water vapor from the inside to the outside. For this transport to take place without

difficulty, the incoming steam must be able to pass through the entire wall unhindered, in other words the wall components are permeable.

-Characteristic quantities

The intrinsic values necessary to characterize building materials are:

-Relative humidity

Relative humidity, or hygrometric degree, commonly denoted "φ", corresponds to the ratio of the partial pressure of the water vapor contained in the air to the saturation vapor pressure at the same temperature. It is a measure of the ratio between the water vapor content of the air and its maximum capacity to contain it under these conditions. This ratio will change if we change the temperature it is calculated by the relation (1)

$$\varphi(\%) = \frac{P_{vap}}{P_{sat}} \times 100 \ldots\ldots\ldots \quad (1)$$

-Phase change;

in the study of the hygrothermal behavior of insulating materials, the phase change of the water contained within these materials will play an interesting role. Indeed, when this phase change occurs, there is then absorption or release of energy in the material.

-Moisture transfer;

the transfer of moisture within the materials was a notion characterized by the movement of each of the phases present (liquid and vapor). The share of each of these mechanisms on the quantity of water fixed depends particularly on the properties of the porosity of the material and the climatic conditions in which it is placed (pressure and temperature).

IV. Simulation Tool

The objective of simulation tools is to optimize the hygrothermal functioning of a wall in order to anticipate condensation phenomena. For the realization of this study, the simulation tool used is the static method of Glaser [24,34].

This simplified method is used to have a quick indication of the risk involved. Glaser's method is the first model used to

analyze the phenomenon of condensation in building materials, it is best known for the graphical exploitations it allows. This theory assumes several simplifying assumptions

such as that moisture moves only in vapor form, that there is no air transport and the transfer of vapor is done only by diffusion, that the materials are non-hygroscopic and the structure is assumed to be dry in the initial state and that there is no interaction between the vapor pressure gradient and the thermal and moisture content gradients. This method is fast and only requires knowledge of the thermal conductivity and water vapor diffusion resistance of the wall materials. It describes the vapor and heat transfers by Fick's and Fourier's laws respectively.

Description Of The Wall

We consider an exterior wall composed of the materials illustrated in table 1. This wall separates two interior and exterior environments, the meteorological data such as temperature, relative humidity and convective exchange coefficient are respectively given below:

-Indoor environment: Ti =20°C , φi = 60% , hi = 9w/m^{2}K .
-Outside environment: Te =-3°C , φe = 85% he = 20 W/m^{2}K.

TABLE 1.
Different Materials Composing The Exterior Wall

Matérials	**e(cm)**	**λ(w/m°C)**	**μ(-)**
1.plaster	1	0.35	8
2.concrete	20	2	80
(**Sh-w**) Sheep wool	5	0.035	1
3.cement	1.5	1.15	15

CALCULATION PROCESS

According to a calculation procedure, it will be useful to draw the temperature and pressure diagrams in order to examine the risks of condensation in the wall, and thus to evaluate the hygrothermal behaviour of the concrete wall.

-Thermal resistance

Ri and Re are respectively the indoor and outdoor air resistances according to DIN4108-3 [48] are calculated as follows:

$$R_i = \frac{1}{h_i} \qquad R_e = \frac{1}{h_e}$$

Suivant la norme DIN6946 [49] le calcul des différentes résistances thermiques se fait par la relation suivante :

$$R_{Material} = \frac{e}{\lambda}$$

According to the equivalent electrical diagram, the total thermal resistance is obtained as follows:

[4]

$$R_t = \sum_{j=1} \mathrm{R_i} + \mathrm{R_j} + R_e \quad \text{et K} = \frac{1}{R_t} \quad (3)$$

K (W/m^2°C) is the surface thermal transmittance

TABLE 1.
Different Properties Materials Composing The Exterior Wall

Materials	**R(m^2°C/W)**	**Rd(m^{2}hmmHg/g)**	**Sd(m)**
plaster	0.0286	0.9	0.08
concrete	0.10	180	16

Sheep wool	1.428	0.555	0.05
cement	0.013	2.53	0.225

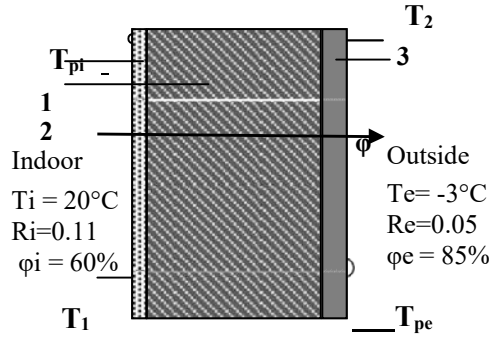

Fig. 10 Exterior wall construction materials

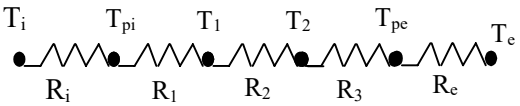

Fig. 11 Equivalent electrical circuit

The total thermal resistance is equal to : $R_t = 0.316\,(m^2.°C/W)$ we deduce the transmission coefficient : K = 3.31 (W/m^2°C), the heat flux is calculated by Fourier's law.

$$\varphi = \frac{S \times \Delta T}{R_t} = K \times S \times \Delta T\ (W)$$

The heat flow density is: $q = \frac{\Delta T}{R_t} = \frac{\varphi}{S}\,(W/m^2)$, $q = 76.41\ (W/m^2)$

Between two interfaces (noted 1 and 2), the heat flux is calculated from the Fourier law :

$$q = q_{int-1} = q_{1-2} = q_{2-3} = q_{3-ext}$$

$$\frac{(T_i - T_e)}{R_t} = \frac{(T_i - T_{pi})}{R_i} = \frac{(T_{pi} - T_1)}{R_1} = \frac{(T_1 - T_2)}{R_2} = \frac{(T_2 - T_{pe})}{R_3} = \frac{(T_{pe} - T_e)}{R_e}$$

This results in the temperatures at the interfaces:

$\boldsymbol{T_2} = T_1 - q \times R_1$), $\boldsymbol{T_3} = T_2 - q \times R_2$, $\boldsymbol{T_{pi}} = T_i - q \times R_i = 11.5\,°C$, $\boldsymbol{T_{pe}} = T_e + q \times R_e = 0.77°C$

-Wall With Insulation (Sheep Wool)

Exterior wall construction materials

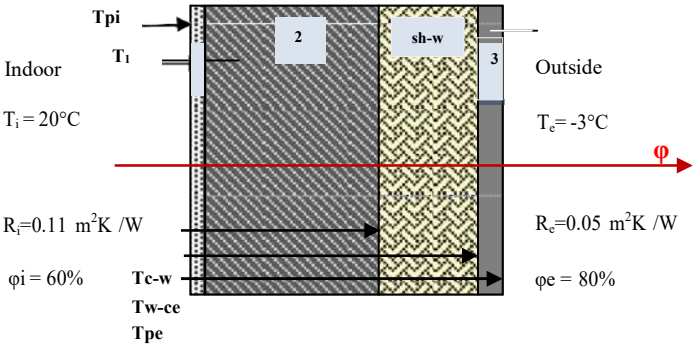

Fig. 12 Temperature at the interfaces of the concrete wall

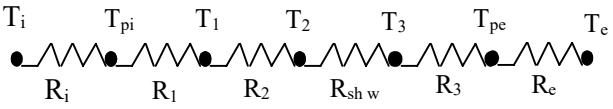

Fig. 13 Equivalent electrical circuit

For a thickness: $e_{sh-w} = 0.5\ cm$ the total thermal resistance is: $R'_t = R_t + R_{sh-w} = 1.73(m^2°C/W)$

We deduce the transmission coefficient: $K' = 0.578\ (W/m^2\,°C)$

The heat flux density is: $q' = \frac{\Delta T}{R'_t} = \frac{\varphi^F}{S}\ (W/m^2)$, $q' = 13.294\ (W/m^2)$

The thermal effect of the insulation is: $\frac{K-K'}{K} = 82.98\%$

-Hygrothermal Behaviour Of The Wall

In order to evaluate the hygrothermal behaviour of the wall, it will be useful to draw the temperature and pressure diagrams in order to examine the risks of condensation. After having carried out the temperature distribution inside the wall, we applied the following calculation procedure:

-Amount Of Water Vapor Diffused

Based on the water vapor diffusion resistance (R_{di}) the amount of diffused water vapor (g) is calculated by applying Fick's law by the following relation:

$$g = \frac{P_{vi} - P_{ve}}{\sum_{i=1}^{n} R_{di}}\ \left[\frac{g}{m^2}.h\right]$$

$$R_{di} = \frac{e}{\pi_i}\ [m^2.h.mmHg/g] \text{ et } \pi_i = \frac{\pi_{air}}{\mu_i}\ [g/m.h.mmHg]$$

P_{vi}, P_{ve} The interior and exterior partial vapor pressures are respectively calculated as follows:

$$P_{vi} = P_{si} \times \varphi_i \quad \text{and} \quad P_{ve} = P_{se} \times \varphi_e$$

P_{si} et P_{se} are respectively the saturated vapor pressure at temperatures T_i and T_e

$$\frac{P_{vi} - P_{ve}}{\sum_{i=1}^{n} R_{di}} = \frac{(P_{vi} - P_{v1})}{R_{d1}} = \frac{(P_{v1} - P_{v2})}{R_{d2}} = \frac{(P_{v2} - P_{vshw})}{R_{vshw}} = \frac{(P_{vshw} - P_{v3})}{R_{d3}} \quad (1)$$

The relations (1) make it possible to calculate the values of partial vapor pressure inside the wall P_{v1} P_{v2} , P_{v3} , P_{vshw} and to draw the corresponding diagram when the wall is insulated and not isolated.

The calculation of saturation vapor pressures is performed using the empirical relationships below and verified online [51].

If $\mathbf{T \geq 273.15}$:

$$P_s = exp\left[\frac{-5800.22}{T} + 1.391 - 0.048640239 \times T + 4.176 \times 10^{-5} \times T^2 - 1.445 \times 10^{-8} \times T^3 + 6.545 \times \ln(T)\right]$$

If **T< 273.15**

$$P_s = exp\left[\frac{-5674.5339}{T} + 6.3 - 0.00967778 \times T + 6.221 \times 10^{-7} \times T^2 + 2.07478 \times 10^{-9} \times T^3 - 9.484 \times 10^{-13} \times T^4 + 4.1635 \times \ln(T)\right]$$

V. Results And Interpretation

The results obtained are presented below for the two cases studied.

According to Fig 14 and 15, the surface temperature of the wall inside the room is lower than the dew point temperature of the indoor air, so we can detect the start of formation of surface condensation where the surrounding indoor air no longer able to hold moisture in gaseous form. Because the internal surface temperature of the wall (Tpi) depends not only on the outside temperature but also on the inside temperature of the room and the thermal resistance of the wall, the latter is significantly reduced by the absence of thermal insulation where the hot interior air comes into contact with cold walls. In Fig.15 we notice that the temperature drops from the inside to the outside, this drop is due to the thermo- physical properties of each layer constituting the wall as well as to the climatic conditions between the inside and outside environment. Fig.16 shows that the curve of the saturation pressure is below that of the partial vapor, this configuration confirms the presence of condensation in the mass and this phenomenon manifests itself inside, of each constituent material of this wall exterior. This is due to the diffusion of vapor in porous materials. It can also be the result of the convection of water vapor transported by the air flow, when there are pressure and temperature differences on either side ofa wall.

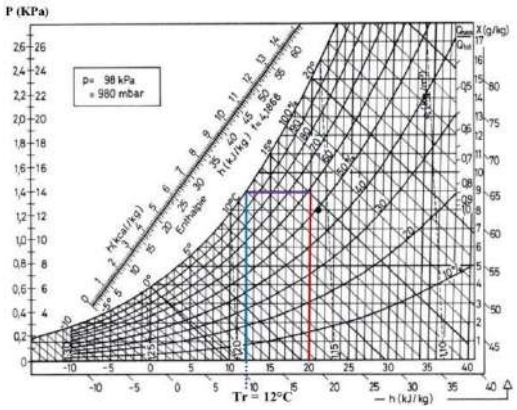

Fig. 14 Designation of dew temperature on the humid air diagram

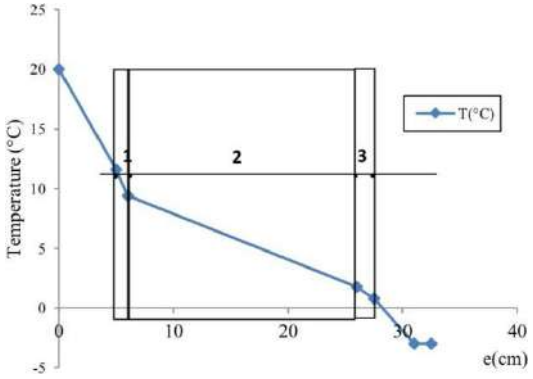

Fig. 15 Temperature profile in the wall without insulation

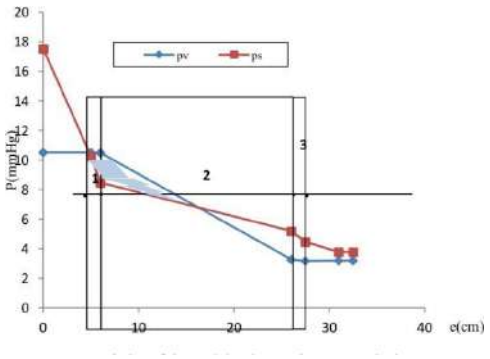

Fig. 16 Evolution of the partial and saturation pressure in the non-insulatedwall

In order to remedy this problem, we have implemented a natural insulating material; sheep's wool within the outer side wall, this insulating material prevented the production of condensation in the mass as shown in Fig. 19. This can be

interpreted by the vapor permeability of sheep's wool from the inside to the outside by preventing the accumulation of water within the wall.. An increase in the temperature of the internal face of the wall clearly indicates the absence of superficial condensation according to Fig 17, as well as a drop in temperature between the interior and the exterior occurs mainly in the thickness insulation. A considerable difference isobtained between this temperature and that of the internal face of the wall insulated by the sheep's wool according to Fig 18.

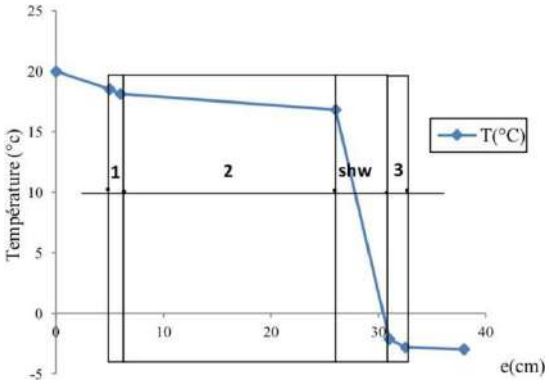

Fig. 17 Temperature profile within the insulated wall

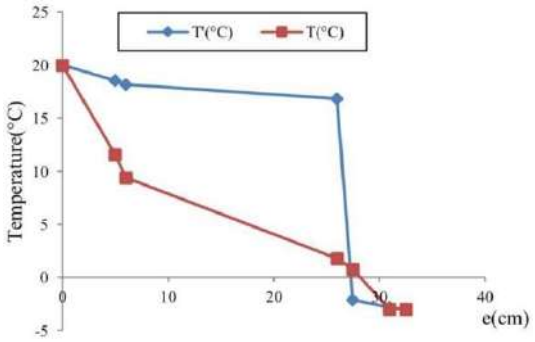

Fig. 18 Temperature profile within the uninsulated (T) and insulated (T') wall

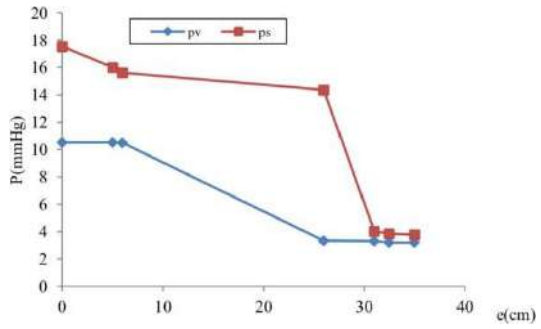

Fig. 19
Profile of the pressure within the insulated wall

According to Fig. 20; By insulating the wall from the inside, we notice that the temperature of the concrete wall is close to the outside temperature, the interior insulation therefore does not make it possible to heat the wall which is subject to a risk of freezing because it is generally more cold and more humid in winter. Indeed, the formation of the gel will take place, thus causing an expansion of the water in the pores of the wall, the latter may undergo a strong mechanical degradation of its structure, which can also reduce its thermal inertia. On the other hand, the greatest temperature variation is observed in sheep wool insulation; this allows rapid heating of the air inside the room. Fig. 21 gives the hygrothermal performance of the wall. At certain points, the partial vapor pressure curve is higher than that of saturated vapor, so there will be condensation in the mass of the wall, reflecting an excess of water vapor near its inner face. There is a large amount of internal condensation in the plaster, the insulation and even in the middle of the concrete, this phenomenon is due to the permeability of sheep's wool and the absence of a vapor barrier. Indeed, and according to Fig. 20 from the inside out, the temperature drop thus causing a drop in the saturation pressure is large in the insulation while the vapor pressure has remained high, and it then exceeds the saturation pressure confirming the existence of internal condensation. Mass condensation exists at the sheep's wool and concrete interface, certainly caused by the different climate between the outdoor environment and the hot and humid indoor environment. Also the vapor diffusion resistance (μ d) of the exterior concrete wall is high compared to the resistance of insulation and plaster.

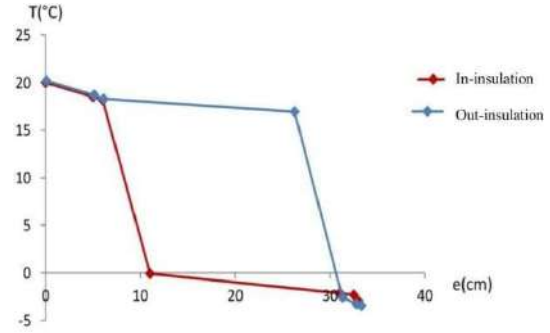

Fig. 20
Temperature profile at the interface of the wall insulated from the inside and the outside

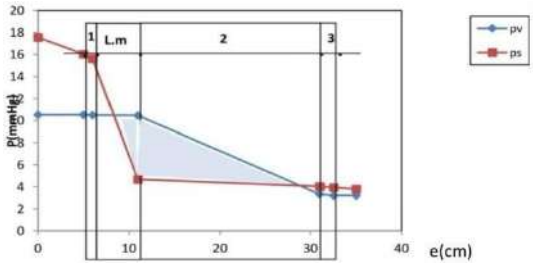

Fig. 21 Evolution of partial vapor pressure and saturation pressure within the wall insulated from the inside

From figure 22 we see that the temperature of the internal face of the wall and those at the terminals of the concrete are proportional to the thickness of the insulation up to the value of 10 cm where they begin to equalize and to stabilize. To this

end, we conclude that a thickness of 10 cm of sheep's wool is sufficient to insulate the wall and avoid the appearance of superficial condensation and in the mass.

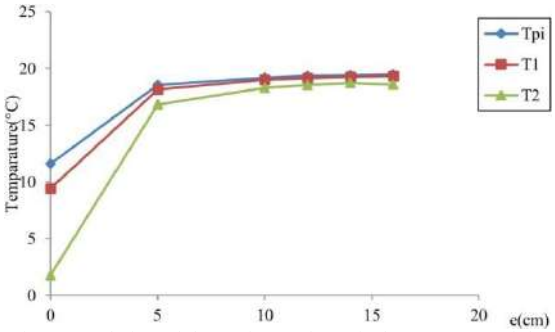

Fig. 22 Evolution of the surface and terminal temperature of the concrete as a function of the thickness of the insulation

VI. CONCLUSIONS

To prevent superficial condensation it is necessary to have an insulation of the external wall so that the temperature of the internal face of this one is higher than the temperature of dew, a ventilation to reduce the relative humidity of the interior air , as well as heating of the inner face of the cold walls. From a thermal point of view, interior insulation and exterior insulation are two equivalent solutions. The interior insulation is a reduction of the interior space and the presence of many thermal bridges which remain to be treated. Interior insulation leaves the wall outside the insulated area, so internal condensation results. To overcome this problem, the implementation of an effective vapor barrier on the interior side is necessary. The implementation of the insulation on the exterior side also prevents the formation of internal condensation as long as the insulation is not given a vapor barrier finish. The external insulation makes it possible to exploit the thermal inertia of the external walls, it limits overheating in summer and protects the wall from hygrothermal stresses resulting from the penetration of rain, the significant variation in daily and seasonal temperature. Sheep wool is a very interesting natural material that remains to be studied for use as an insulating construction material. The rest of our work will be the study of its insulating effect on the acoustics of buildings.

REFERENCES

[1] WRI (2017) Climate Analysis Indicators Tool (CAIT).World Resources Institute http://cait.wri.org.

[2] IPCC, 2014: Climate Change 2014: Synthesis Report. Contribution of Working Groups I, II and III to the Fifth Assessment Report of the Intergovernmental Panel on ClimateChange [Core Writing Team, R.K. Pachauri and L.A. Meyer (eds.)]. IPCC, Geneva, Switzerland, 151 pp.

[3] X. Cao, X. Dai, J. Liu, Building energy-consumption statusworldwide and the state-of-the-art technologies for zero-energy buildings during the past decade, Energy Build. 128 (2016) 198–213.

[4] M. Waite, E. Cohen, H. Torbey, M. Piccirilli, Y. Tian, V. Modi, Global trends in urban electricity demands for cooling and heating, Energy 127 (2017) 786–802.

[5] R. Vakulchuk, I. Overland, D. Scholten, Renewable energyand geopolitics: a review, Renew. Sustain. Energy Rev. 122 (2020).

[6] V.V. Rao, R. Parameshwaran, V.V. Ram, PCM-mortar based construction materials for energy efficient buildings: a review on research trends, Energy Build. 158 (2018) 95–122.

[7] M.S. Mohsen and B.A. Akash, 'Some Prospect of Energy Saving in Building', Energy

Conversion Management, Vol. 42, N°11, pp. 1307 - 1315, 2001.

[8] M.A. Aktacir, O. Büyükalaca and T. Yılmaz, 'A Case Study for Influence of Building Thermal Insulation on Cooling Load and Air-Conditioning System in the Hot and Humid Regions', Applied Energy, Vol. 87, N°2, pp. 599 - 607, 2010.

[9]M. Ozel and K. Pihtili, 'Optimum Location and Distribution of Insulation Layers on Building Walls with Various Orientations', Building and Environment, Vol. 42, N°8, pp. 3051–3059, 2007.

[10] S.A. Al-Sanea, M.F. Zedan and S.A. Al-Ajlan, 'Effect of Electricity Tariff on the Optimum Insulation-Thickness in Building Walls as Determined by a Dynamic Heat-Transfer Model', Applied Energy, Vol. 82, N°4, pp. 313 - 330, 2005.

[11] N. Fezzioui, B. Draoui, M. Benyamine et S. Larbi, 'Influence des Caractéristiques Dynamiques de l'Enveloppe d'un Bâtiment sur le Confort Thermique au Sud Algérien', Revue des Energies Renouvelables, Vol. 11, N°1, pp. 25 - 34, 2008.

[12] D. Medjelakh et S. Abdou, 'Impact de l'Inertie Thermique sur le Confort Hygrothermique et la Consommation Energétique du bâtiment', Revue des Energies Renouvelables, Vol. 11, N°3, pp. 329 - 341, 2008.

[13] D.P.P. Meddage a,, Aaron Chadee , M.T.R. Jayasinghe , Upaka Rathnayake Exploring the applicability of expanded polystyrene (EPS) based concrete panels as roof slab insulation in the tropics Case Studies in Construction Materials 17 (2022) e01361

[14] D. – D. Kolokotsa, G. Giannariakis, K. Gobakis, G. Giannarakis, A. Synnefa, M. Santamouris, Cool roofs and cool pavements application in Acharnes, Greece, Sustain. Cities Soc. 37 (2018) 466–474,

[15] Y. Chihab, M. Garoum and N. Laaroussi, Dynamic thermal performance of multilayer hollow clay walls fille

with insulation materials: Toward energy saving in hot climates, Energy and Built Environment, https://doi.org/10.1016/j.enbenv.2022.08.001

[16] Yassine Chihab , Lahcen Essaleh , Rachid Bouferra , Abdeltif Bouchehma Numerical study for energy performance optimization of hollow concrete blocks for roofing in a hot climate of Morocco Energy Conversion and Management: X 12, (2021), 100113

[17] M.C.M. Parlato , M. Cuomo, S.M.C. Porto a Natural fibers reinforcement for earthen building components: Mechanical performances of a low quality sheep wool ("Valle del Belice" sheep) Construction and Building Materials 326 (2022) 126855

[18] Mustafa Altin , Giray S , amil Yildirim Investigation of usability of boron doped sheep wool as insulation material and comparison with existing insulation materials Construction and Building Materials 331 (2022) 127303

[19] Daniela Bosia, Lorenzo Savio, Francesca Thiebat, AlessiaPatrucco, Stefano Fantucci, Gabriele Piccablotto, Donatella Marino, Sheep wool for sustainable architecture Energy Procedia 78 (2015) 315 – 320.

[20] Aziza Atbir, Moha Cherkaoui, Fatima Zohra El Wardi, Abdelhamid Khabbaz, Improvement of thermomechanical characteristics of multilayer biomaterial of sheep wool and clay, Materials Today: Proceedingshttps://doi.org/10.1016/j.matpr.2022.02.224 2214-7853

[21] A. Korjenic , S. Klarić, A. Hadžić, and S. Korjenic Sheep Wool as a Construction Material for Energy Efficiency Improvement, Energies 8 (6) (2015) 5765–5781.

[22] J. Manivannan, S. Rajesh, K. Mayandi, M.T.H. Sultan, Tensile and hardness properties of sheep wool fiber reinforced polyester composite, Materials Science Forum 969 (2019) 266–270.

[23] Rayed Alyousef , Hisham Alabduljabbar , Hossein Mohammadhosseini , Abdeliazim Mustafa Mohamed , Ayesha Siddika , Fahed Alrshoudi , Abdulaziz Alaskar Utilization of sheep wool as potential fibrous materials in the production of concrete composites Journal of Building Engineering 30 (2020) 101216

[24] ISO13788:2012, Hygrothermal Performance of Building Components and Building Elements. Assessment of moisture transfer by numerical simulation, 2012.

[25] Valeria Cascione, Eleonora Marra, Daniel Zirkelbach, Stefania Liuzzi, Pietro Stefanizzi, Hygrothermal analysis of technical solutions for insulating the opaque building envelope, Energy Procedia 126 (09) (2017) 203–210.

[26] CSN EN 15026, Hygrothermal Performance of Building Components and Building Elements. Assessment of moisture transfer by numerical simulation, 2007.

[27] Kyung-Soo Kim, Hyang-In Chang, Chang-young Park, Dong-Chul Yoo, Chang-Ho Choi, Comparison of total moisture content by internal condensation evaluation method, J. Korean Inst. Archit. Sustain. Environ. Build. Syst. 11 (6) (2017) 558–571.

[28] Dileep Kumar, Morshed Alam, Patrick X.W. Zou, Jay G. Sanjayan,Rizwan Ahmed Memon Comparative analysis of building insulation material properties and performance Renewable and Sustainable Energy Reviews 131 (2020) 110038

[29] Orlik-Ko_zdon B, Steidl T. Experimental and analytical determination of water vapour transmission properties of recyclable insulation material. Construct Build Mater 2018;192:798–807. https://doi.org/10.1016/j.conbuildmat.2018.10.093.

[30] Krischer O, Kast W. Die wissenschaftlichen Grundlagender Trocknungstechnik, Dritte Au&age.Berlin:Springer,1978.

[31] Luikov AV. Systems of di"erential equations of heat and mass transfer in capillary-porous bodies. International Journal of Heat and Mass Transfer 1975;18:1–4.

[32] Philip JR, De Vries DA. Moisture movement in porous materials under temperature gradients. Transactions American Geophysical Union 1957;2:222–32.

[33] Glaser H. Vereinfachte Berechnung der Dampfdi"usion durch geschichtete WRande bei Ausscheidung von Wasser und Eis, KRaltetechnik 1958; 10 (11):358– 64 and (12):386 – 90.

[34] DIN 4108—WRarmeschutz im Hochbau. DIN Deutsches Institut fRur Normung, 1981.

[35] GTR WI 46 and CEN/TC 89 WI29. prEN ISO 13788—Hygrothermal performance of building components and building elements. Internal surface temperature to avoid critical surface humidityand interstitial condensation. Calculation methods. The International Organization for Standardization and European Committee for Standardization, 1999.

[36] IPCC, 2014. Buildings. In: Climate Change 2014: Mitigation of Climate Change. Contribution of Working Group III to the Fifth Assessment Report of the Intergovernmental Panel on Climate Change. Available at:https://www.ipcc.ch/pdf/assessment-report/ar5/wg3/ipcc_wg3_ar5_chapter9. pdf.

[37] Global Alliance for Buildings and Construction and UNEP, 2020. Global Status Report for Buildings and Construction: towards a Zero-Emission, Efficient and Resilient Buildings and Construction Sector, 2020. Nairobi.

Available at: https://globalabc.org/sites/default/files/inline-files/2020 buildings gsr_full report.pdf.
[38] Institution of Civil Engineers, 2015. Embodied energy and carbon. Available at: https://www.ice.org.uk/knowledge-and-resources/briefing-sheet/embodied-energ y-and-carbon.
[39] Y. Kang, S.J. Chang, S. Kim, Hygrothermal behavior evaluation of walls improving heat and moisture performance on gypsum boards by adding porous materials, Energy Build. 165 (2018) 431–439, https://doi.org/10.1016/j. enbuild.2017.12.052.
[40] Stefan Füchsl, Felix Rheude, Hubert R¨oder Life cycle assessment (LCA) of thermal insulation materials: A critical review Cleaner Materials 5 (2022) 100119 www.journals.elsevier.com/cleaner-materials
[41] https://www.dictionnaire-environnement.com/laine_de_mouton_ID1898.html
[42] ICAR- CSWRI, Avikanagar & MANAGE, Hyderabad Sheep Wool & Mutton: Production and Value Addition 2021 éditors :Vino Kadam ; Arvind Soni ; Shahaji Phand ; Arun Kumar
[43] Bosia D, Savio L, Thiebat F, Patrucco A, Fantucci S, Piccablotto G, et al. Sheep wool for sustainable architecture. Energy Procedia 2015;78:315–20.
[44] Dénes O, Florea I, Manea DL. Utilization of sheep wool as a building material. Procedia Manuf 2019;32:236–41.
[45] Zach J, Korjenic A, Petranek V, Hroudova J, Bednar T. Performance evaluation and research of alternative thermal insulations based on sheep wool. Energy Build 2012;49:246– 53
[46] Ballagh KO. Acoustic properties of wall. Appl Acoust 1996;48(2):101–20.
[47] Glé P, Gourdon E, Arnaud L. Acoustical properties of materials made of vegetable particles with several scales of porosity. Appl Acoust 2011;72 (5):249–59.
[48] DIN 4108-3Wärmeschutz und Energie-Einsparung in Gebäuden - "Teil 3: Klimabedingter Feuchteschutz; Anforderungen, Berechnungsverfahren und Hinweise für Planung und Ausführung" 2001-07.
[49] Composants et parois de batiments – Resistance thermique et coefficient de transmission thermique Methode de calcul (Norme EN ISO 6946:2015, version allemande et anglaise)
[50] Le Recknagel, "Manuel pratique du génie climatique - 1ère partie :Données fondamentales", Rechnagel, Sprenger, Hönmann et Schramek, édition PYC.
[51] BBS Slama La méthode Glaser: calcul de la condensation dans les parois www.bbs-slama.com

Novel photocatalyst Hetero-System $BaCr_2O_4/TiO_2$ for the Photo-Reduction of Cr (VI) Under Solar Light Irradiation

H. Lahmar [#1], S. Douafer [#2], M. Benamira [#3] and M. Trari [*4]

[#1,3]*Department of Chemistry,* [#2]*Department of Fundamental Studies of Science and Technology, University of Mohamed Seddik Benyahia, B.P. 98, Ouled Aissa, 18000 Jijel, Algeria*

[1]lahmarhicham18@gmail.com
[2]souaad.douafer@gmail.com
[3]benamira18@gmail.com

[*5]*Laboratory of Storage and Valorization of Renewable Energies, Faculty of Chemistry (USTHB), 16111 Algiers. Algeria*

[4]solarchemistry@gmail.com

Abstract— **The spinel $BaCr_2O_4$ produced by sol-gel process is characterized physically and photo-electrochemically. It is active under the visible region owing to its optical band gap (E_g) equal to 1.47 eV close to the ideal value for the solar conversion. According to Mott Schottky characteristic with a flat band potential (-0.23 V_{SCE}), the chromate is successfully photoreduced on the new hetero-system $BaCr_2O_4/TiO_2$ (P-25)/Cr (VI). The electrons in the conduction band (-1.98 V_{SCE}) of $BaCr_2O_4$ excited by sunlight are injected into CB-TiO_2 (-0.29 V_{SCE}) and subsequently transferred to adsorbed Cr(VI) species. A concentration of Cr (VI, 30 mg/L) is completely converted into less hazardous valence Cr (III) within 120 min under optimal conditions (pH ∼ 4, T= 25 °C, $[C_2H_2O_4] = 10^{-5}$ mol/ L, $BaCr_2O_4/TiO_2$ (1/1) at a dose of 1mg/mL). The oxalic acid used as scavenger in the Cr(VI) solution preclude the photocorrosion of $BaCr_2O_4$ and improve the photoactivity. More interestingly, the reaction between Cr(VI) and $C_2H_2O_4$ does not occur at ambient temperature.**

Keywords— **Spinel $BaCr_2O_4$; $BaCr_2O_4/TiO_2$; sol-gel method ; Chromate ; solar radiation ; photo-reduction.**

I. INTRODUCTION

Over the past century, water, the precious natural element for man and the environment, has been used in a careful and sustainable way. However, freshwater resources are declining due to a significant increase in consumption and technological progress combined with population growth. The time when nature's self-purification capacity is exceeded due to major sources of pollutiontion [1], linked to human activity, mainly produced by agricultural, domestic and industrial discharges. The depollution of these water bodies therefore represents a subject extremely worrying [2].

To limit these risks, polluted water [3] is routed via urban wastewater treatment networks to wastewater treatment plants (WTP) to be decontaminated for human consumption or discharge into the natural environment.

One of the extremely studied, environmentally compatible and proven effective processes for the degradation of a large number of non-biodegradable pollutants using the sun as energetic resource resource is solar heterogeneous photocatalysis [4-6]. This process is based on the photoexcitation of a semiconducting catalyst by solar radiation in order to produce non-selective radical species.

The use of a profitable and economical source like the solar energy lead to photochemical reactions and constitutes a major challenge for autonomous management, with non-presence of an external pollution source and the development sustainable strategy. However, the use of solar energy poses a significant constraint. Indeed, the most commonly used catalysts such are TiO_2 and ZnO [7]. However, the main reason of low yields comes from the limited photosensitivity of these catalysts to UV radiation which represents only 5%, or 50 W^{-2} of the total solar flux received at the surface of the Earth under the most favourable sunlight conditions.

ISSN: 1737-9334

This spectral domain restriction is a major drawback in the development of photo-electrochemical applications under sunlight. Therefore, the use of visible radiation representing 45% of the solar flux would generate significant gains in the photocatalytic performance of catalysts [8]. Intensive research is therefore devoted to development of new innovative catalysts, photosensitive over a wider range, in order to exploit a large number of photons from the visible range [9].

To achieve this objective, our axes of development are oriented toward the hetero-junction of TiO_2 with *p*-type spinels absorbing in the visible region of the solar spectrum. Different methods of physical or chemical synthesis [10] have thus been developed with a view to obtain such catalysts like $BaCr_2O_4$ which is the subject of this work.

The second part is devoted to the presentation of the protocol implemented to define and optimize the conditions of photocatalytic measurements under sunlight for the photoreduction of a model pollutant namely hexavalent chromium under the new $BaCr_2O_4/TiO_2$ hetero-system.

II. EXPERIMENTAL

The starting precursors used for the synthesis of $BaCr_2O_4$ are: $BaCl_2.6H_2O$ (99.5%; Sigma-Aldrich) and $CrCl_3.6H_2O$ (99%, Fluka). In a Pyrex beaker containing absolute ethanol, 3.1 g of $BaCl_2.6H_2O$ and 5.2 g of $CrCl_3.6H_2O$ were dissolved and mixed; propylene oxide was added to the beaker for a long time. A green colored gel was formed and separated by centrifugation and washed with distilled water followed by heat treatment at 900° C. (15°C/min) for 10 h. The $BaCr_2O_4$ powder obtained is black in color and finally ground in a agate mortar. Commercial TiO_2 (P25) was used in this work to formthe hetero-system.

The structural properties are studied from X-Ray Diffraction (XRD). The diffractometer used for this study consists of a copper anticathode ($_{Cu}$= 1.5418 Å). The production of X-rays was created during the impact of electrons, emitted by a heated cathode and accelerated by an electric field, on a metallic anode called an anticathode.

Scanning electron microscope (SEM) was also performed on synthesized $BaCr_2O_4$ to assess the evolution of crystallite morphology and size. The equipment used was SEM type field effect with cold cathode located in our brand laboratory JEOL JSM-6700F, Japan.

The spectrophotometry consists of the detailed analysis of optical spectra over the wavelengths ranging from UV (200 to 400 nm) up to the visible range (400 to 800 nm). The reflectance and absorbance measurements obtained on the photocatalysts from the spectrophotometer make it possible to calculate their optical gap energies. The reflectance and absorbance spectra ~~for wavelengths~~ between 200 and 3000 nm were recorded using a VARIAN Cary 5000 double beam UV-Vis-NIR spectrophotometer equipped with an integrating sphere.

For photoelectrochemical (PEC) characterizations, a Solartron Analytical potentiostat (1287A) with its impedance analyzer (Solartron Analytical, 1260) was used.

In a 200 mL double jacket Pyrex reactor thermostated at 25 ◦C by circulating water, (30 mg/L of chromate) were placed at normal atmospheric pressure; the solution contains the hetero-system ($BaCr_2O_4/TiO_2$) in powder form, stirred with a magnetic bar (300 rpm) under sunlight. Cr(VI) samples were taken periodically for analysis, the precipitate was separated with a mini-centrifuge, a Shimadzu UV1800 double beam UV-visible spectrophotometer a with quartz cell of 1 cm optical path was used to monitor the photoreduction kinetics. The efficiency of the Cr(VI) photo chromate reduction is calculated from the relationship:

$$(\%) = \frac{C_{eq} - C_t}{C_{eq}} 100 \quad (1)$$

C_{eq}:the equilibrium concentration after adsorption in the dark
C_t: the concentration at time (t).

III. RESULTS AND DISCUSSION

A. XRD Characterization

The XRD analysis was performed with a view to confirming the presence of the phase constituting the synthesized $BaCr_2O_4$ catalyst. The X-ray diffractogram is shown in Figure 1.a. The main diffraction lines associated with the Orthorhombic (SG: Pmmn) structure of $BaCr_2O_4$ are indexed according to the reflections of the planes (101), (011), (111), (211), (400), (020), (311) , (220), (002), (021), (102), (121), (411), (221), (012), (112) ,(302) ,(321) ,(420) ,(511), (312), (402), (421), (122), (131), (110), (330), (231), (322), (620), (331), (203), (013), (621), (213), (311), (800), (522), (023), (040), (531), (413), (721) and (820) respectively. The identification of these lines agrees with the standard $BaCr_2O_4$ X-ray pattern from the JCPDS file N° 01-085-1308. Structural analyses were also carried out by XRD on the TiO_2 powder (Fig. 1b). The main diffraction lines are indexed and belong to the TiO_2 reticular planes (100), (103), (044), (112), (200), (105), (211), (204), (116), (220) and (215), according to tetragonal symmetry (Space group: I41/amd) and the JCPDS Card N° 00-071-1166).

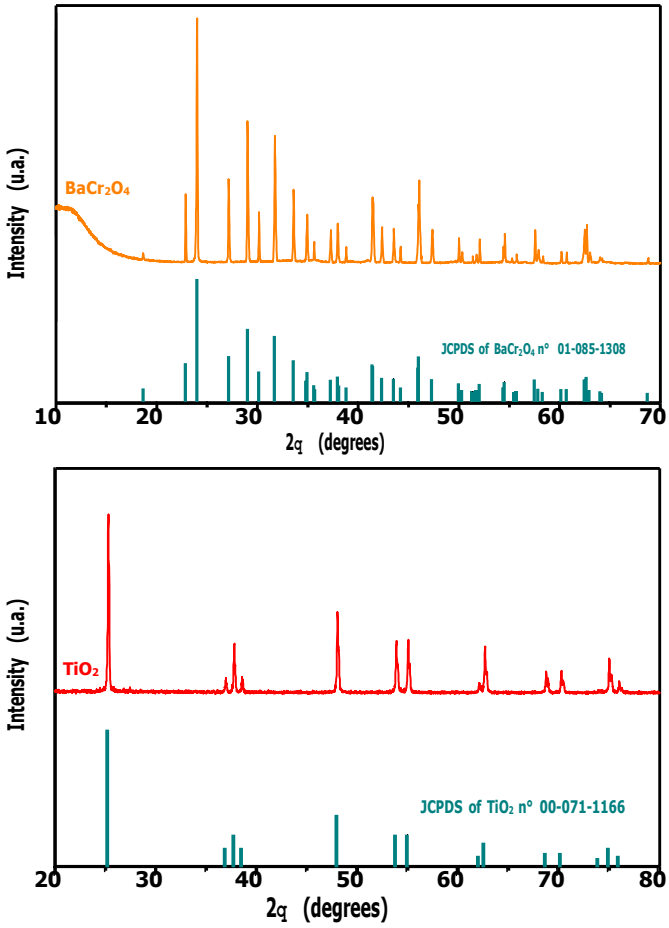

Fig. 1 Powder X-ray diffraction of a) $BaCr_2O_4$ nanoparticles, b) of TiO_2.

B. SEM Analysis

A complementary study is undertaken through characterizations on $BaCr_2O_4$ produced by the sol-gel route from the starting precursors and TiO_2 P 25. The objective is to understand and define the physico-chemical parameters of the catalysts and to anticipate the performance of the catalysts. The SEM images in Figure 4a, b represent nanoscale $BaCr_2O_4$ and TiO_2 powders exhibit a mostly near-spherical crystallite shape with a relatively small and homogeneous size distribution.

a)

ISSN: 1737-9334

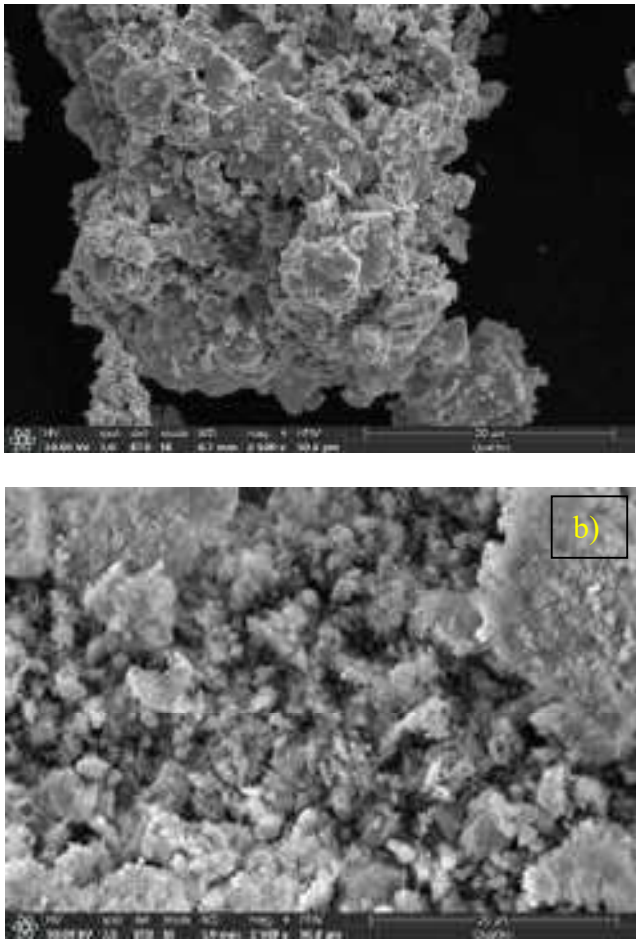

Fig. 2 SEM of a) $BaCr_2O_4$ nanoparticles, b) of TiO_2.

C. Optical Characterization

The Munk-Kubelka equation (2) [11] is used for the determination of the optical gap (E_g):

$$F(R) = \frac{(1 - R)^2}{2R} \quad (2)$$

The diffuse reflectance R {= (I/I) f} of $BaCr_2O_4$ and TiO_2 (Fig. 3.a and 3,b) was obtained from their converted UV-visible absorption spectra. The gap E_g has been determined by extrapolation of the linear part (h)^2 to h = 0 and the transition is directly allowed.

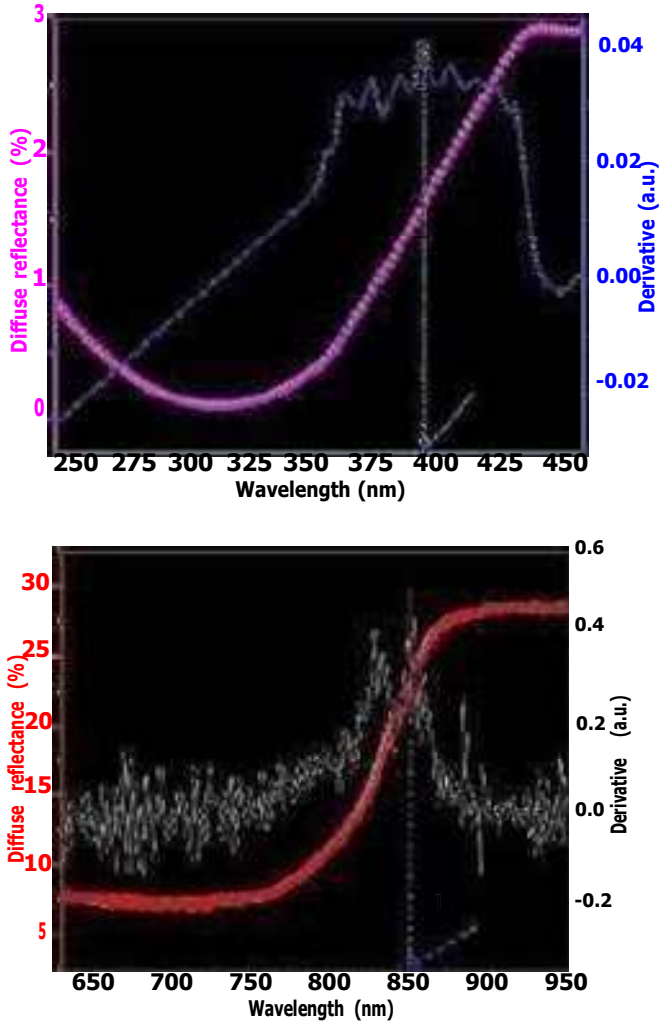

Fig. 3 Diffuse reflectance UV - Vis spectrum of a) TiO_2 b) $BaCr_2O_4$.

D. Electrochemical Characterization

The capacitance data of $BaCr_2O_4$ and TiO_2 follow the Mott-Schottky equation:

$$\frac{1}{C^2} = \frac{2}{\varepsilon \varepsilon_0 N_A} \left(V - V_{fb} - \frac{KT}{e}\right) \quad (3)$$

Where C is the capacitance (F/m2), ε the relative permittivity, ε_o the permittivity of free space and N_A the acceptor density (m^{-3}) are provided from the potential intercept at $C^{-2} = 0$ and the slope of the straight line respectively (Fig. 4.a,b),

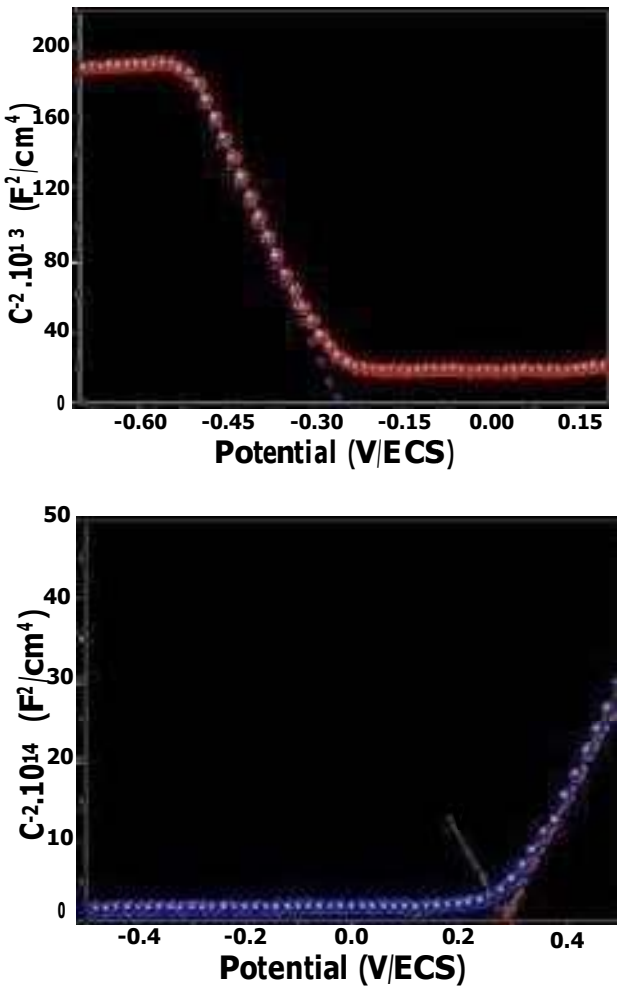

Fig. 4 The Mott Schottky plot at 10 kHz of a) $BaCr_2O_4$ nanoparticles, b) of TiO_2.

IV. PHOTOCATALYSIS

Solar heterogeneous photocatalysis is based on the use of a photosensitive catalyst with natural radiation to accelerate the rate of the chemical reaction [12, 17]. Photocatalysis can be homogeneous when the reaction takes place in a single-phase gaseous or liquid medium, for example in the presence of a liquid catalyst (H_2O_2). It is heterogeneous in a multiphase reaction medium, such as when using a catalyst (TiO_2) in suspension. Heterogeneous solar photocatalysis is the most effective process and has been the subject of numerous studies in recent years [18, 19]. Indeed, this process is capable of degrading a wide range of target pollutants through the production of non-selective radicals [20]. On the other hand, its process is more complex given that in a multiphase medium are involved stages of photoexcitation, transfer of charges and pollutants between the liquid and solid phase.

Heterogeneous photocatalysis consists of naturally or artificially irradiating an intrinsic or extrinsic semiconductor material in our case catalysts ($BaCr_2O_4$ and TiO_2). $BaCr_2O_4/TiO_2$ Fig 5. is photoexcited by photons with energy equal to or greater than the width of the forbidden band (optical gap energy). An electron is then photo-liberated and makes an energy transition from the valence band (BV) to the conduction band (BC). During this transition, electronic vacancies, commonly called holes (h^+), and an electron overload (e^-) are generated [21, 22].

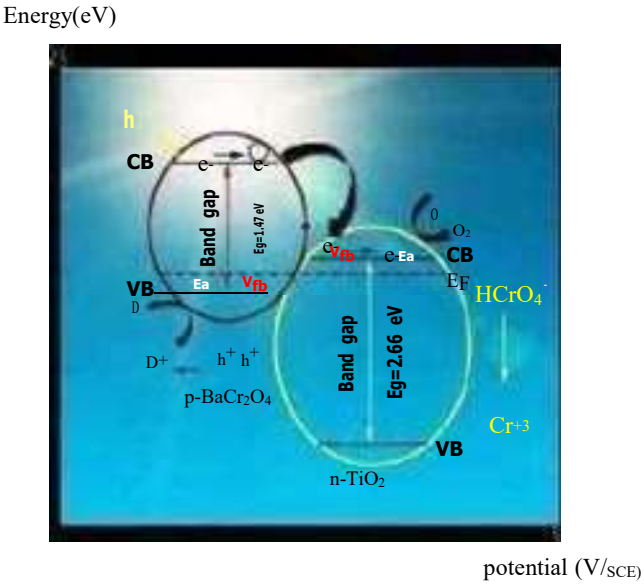

Fig. 5 Schematic diagram of charge transfer between p-type $BaCr_2O_4$ and n-type TiO_2.

The coupling with spinel *p*-$BaCr_2O_4$ E-VB is greater than that of *n*-TiO_2, allowing the transfer of holes to TiO_2-VB. The photocatalytic reaction is therefore described as an oxidation-reduction reaction catalyzed by the hetero-system ($BaCr_2O_4/TiO_2$), on the surface of which the reagents are adsorbed according to the following equations.

$$BaCr_2O_4 + h\nu \rightarrow BaCr_2O_4 (e^-_{CB}, h^+_{VB}) \quad (4)$$

$$BaCr_2O_4 + h\nu \rightarrow CB\text{-}BaCr_2O_4 (e^-) + VB\text{-}BaCr_2O_4 (h^+) \quad (5)$$

$CB\text{-}BaCr_2O_4(e^-) + n\text{-}TiO_2 \rightarrow BaCr_2O_4 + TiO_2(e^-)$ (6)

$TiO_2(3\,e^-) + Cr^{3+} + 7\,H^+ \rightarrow Cr^{3+} + 4\,H_2O + WO_3$ (7)

$TiO_2(2\,e^-) + 2\,H_2O \rightarrow TiO_2 + H_2 + 2\,OH^-$ (8)

$HCrO_4^- + 7\,H_3O^+ + 3\,e^- \rightarrow Cr^{3+} + 11\,H_2O$ (9)

$2\,H_2O + 2\,e^- \rightarrow H_2 + 2\,OH^-$ (10)

$C_2H_2O_4 + \frac{1}{2}\,O_2 + 4\,h^+ \bullet 2\,CO_2 + H_2O + 4\,H^+$ (11)

Cr (VI) forms several species, the relative proportions of which depend on both pH and of the total Cr (VI) concentration. The distribution according to the pH is well explained according to the Potential-pH diagram [22]. Cr (VI) is a strong oxidant in oxidation forms ($HCrO_4^-$, $Cr_2O_7^{2-}$ or CrO_4^{2-}), $HCrO_4^-$ predominates at high Cr (VI) concentrations at pH ~ 4, and turns into $Cr_2O_4^{2-}$ at high pH (> 7).

$$Cr_2O_4^{2-} + H_2O \rightarrow HCrO_4^- + OH^-,\ (pKa = 1.7) \quad (12)$$

In the presence of 1 mg / mL of the hetero-junction (*p*- $BaCr_2O_4$/*n*-TiO_2 (1/1) at (pH 4, T = 25 ° C, $[C_2H_2O_4] = 10^{-5}$ mol / L), the photo-reduction of Cr (VI) in Cr (III) observed is quasi total within 120 min of irradiation (Fig. 6).

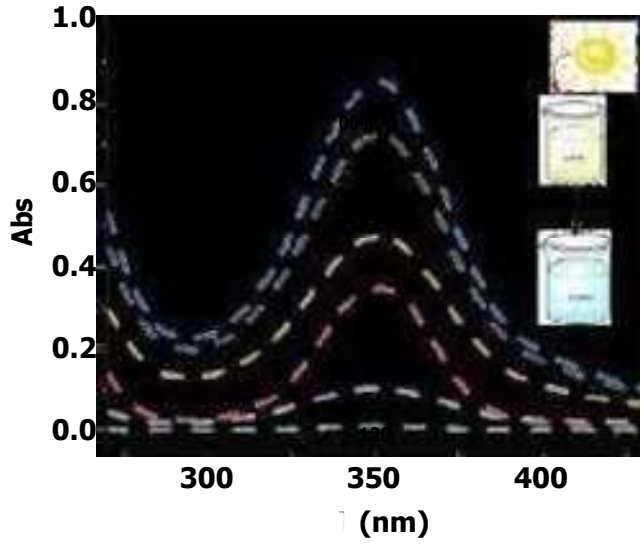

Fig. 6 UV-Vis photo-reduction spectrum of 30 mg/mL of Cr (VI) under $BaCr_2O_4$/TiO2 (1/1).

The Cr(VI) photo-reduction follows a first order kinetic law; the rate constant (K_{app}) is evaluated from the slope Ln (C/C_o) as a function of the solar irradiation time (Fig 7), according to:

$$-\frac{dC}{dt} = k_{app}\,C \quad (13)$$

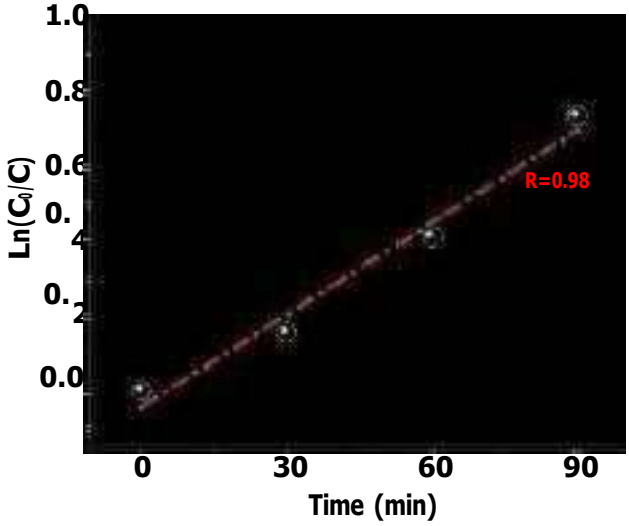

Fig. 7 Kinetics of the Cr (VI) photo-reduction.

This hetero-system has been successfully tested with other experimental conditions for the photocatalytic evolution of hydrogen, and the results will be reported shortly in a future article.

Conclusion

Under mild conditions, hexavalent chromium (30 mg/L) is completely photo-reduced in 120 min at (pH 4) on the new hetero-junction ($BaCr_2O_4/TiO_2$ (1/1)) under sunlight. The spinel $BaCr_2O_4$ was chosen as catalyst because of its chemical stability, narrow band gap (E_g =1.47 eV) and low cost. It was prepared by sol-gel route and its conduction band is more cathodic than Cr(VI). This photocatalyst is active under visible light. The photo-electrochemical characterization of $BaCr_2O_4$ and TiO_2 made it possible to predict the photo-reduction of chromium under solar excitation. Electron injection of $BaCr_2O_4$-CB at less cathodic TiO_2-CB enhanced the Cr(VI) photo-reduction in the presence of ~~a small amount~~ of oxalic acid (10^{-5} M), which promotes the separation charges. The chromate photo-reduction reaction carried out at

room temperature was monitored by spectrophotometry (▪max Cr(VI) = 350 nm). The chromate photoreduction follows pseudo-first order kinetics with an apparent rate constant K_{app} of 0.02 min^{-1}.

Acknowledgment

We thank the financial support of the Thematic Agency for Research in Science and Technology (ATRST) through the national research program (Projets PRFU N° B00L01UN180120230002) and Socio-economic Impact Project N° 06 / Univ Jijel / DGRSDT.

REFERENCES

[1] T.I. Evseeva, S.A. Geras'kin, I.I. Shuktomova, Genotoxicity and toxicity assay of water sampled from a radium production industry storage cell territory by means of Allium-test, J. Environ. Radioact. 68 (2003) 235–248.

[2] Royle, Toxicity of chromic acid in the chromium plating industry (1), Environ. Res. 10 (1975) 39–53.

[3] V. Khandegar, A.K. Saroha, Electrocoagulation for the treatment of textile industry effluent–a review, J. Environ. Manage. 128 (2013)949–963.

[4] F. Mathiason, C. Lidén, Y.S. Hedberg, Chromium released from leather–II: the importance of environmental parameters, Contact Dermatitis. 72 (2015) 275–285.

[5] S. Loyaux-Lawniczak, P. Lecomte, J.-J. Ehrhardt, Behavior of hexavalent chromium in a polluted groundwater: redox processes and immobilization in soils, Environ. Sci. Technol. 35 (2001) 1350–1357.

[6] A. Bielicka, I. Bojanowska, A. Wisniewski, Two Faces of Chromium-Pollutant and Bioelement., Polish J. Environ. Stud. 14 (2005).

[7] D.W. Griffin, C.A. Kellogg, E.A. Shinn, Dust in the wind: long range transport of dust in the atmosphere and its implications for global public and ecosystem health, Glob. Chang. Hum. Heal. 2 (2001) 20–33.

[8] H. Lahmar, M. Benamira, Chromate Reduction on the Novel Hetero-system La 2NiO4/TiO2 under Solar Light, IEEE, 2017.

[9] A.M. Zayed, N. Terry, Chromium in the environment: factors affecting biological remediation, Plant Soil. 249 (2003) 139–156.

[10] N. Doufar, M. Benamira, H. Lahmar, M. Trari, I. Avramova, M.T. Caldes, Structural and photochemical properties of Fe-doped ZrO_2 and their application as photocatalysts with TiO_2 for chromate reduction, Elsevier, 2020. doi:10.1016/j.jphotochem.2019.112105.

[11] H. Lahmar, M. Kebir, N. Nasrallah, M. Trari, Photocatalytic reduction of Cr (VI) on the new hetero-system CuCr2O4/ZnO, Elsevier, 2012.

[12] P.R. Wittbrodt, C.D. Palmer, Reduction of Cr (VI) in the presence of excess soil fulvic acid, Environ. Sci. Technol. 29 (1995) 255–263.

[13] R. Gherbi, N. Nasrallah, A. Amrane, R. Maachi, M. Trari, Photocatalytic reduction of Cr (VI) on the new hetero-system CuAl2O4/TiO2, J. Hazard. Mater. 186 (2011) 1124–1130.

[14] D.A.L. Vignati, J. Dominik, M.L. Beye, M. Pettine, B.J.D. Ferrari, Chromium (VI) is more toxic than chromium (III) to freshwater algae: a paradigm to revise?, Ecotoxicol. Environ. Saf. 73 (2010) 743–749.

[15] S. Bassaid, M. Chaib, S. Omeiri, A. Bouguelia, M. Trari, Photocatalytic reduction of cadmium over CuFeO2 synthesized by sol–gel, J. Photochem. Photobiol. A Chem. 201 (2009) 62–68.

[16] L. Murruni, F. Conde, G. Leyva, M.I. Litter, Photocatalytic reduction of Pb (II) over TiO2: New insights on the effect of different electron donors, Appl. Catal. B Environ. 84 (2008) 563–569.

[17] H. Lahmar, M. Benamira, S. Douafer, L. Messaadia, A. Boudjerda, M. Trari, Photocatalytic degradation of methyl orange on the novel hetero-system La2NiO4/ZnO under solar light, Elsevier, 2020. doi:10.1016/j.cplett.2020.137132.

[18] H. Lahmar, M. Benamira, S. Douafer, F.Z. Akika, M. Hamdi, I. Avramova, M. Trari, Photocatalytic degradation of crystal violet dye on the novel CuCr2O4/SnO2 hetero-system under sunlight, Elsevier, 2020. doi:10.1016/j.ijleo.2020.165042.

[19] M. Benamira, H. Lahmar, L. Messaadia, G. Rekhila, F.-Z. Akika, M. Himrane, M. Trari, Hydrogen production on the new hetero-system Pr2NiO4/SnO2 under visible light irradiation, Int. J. Hydrogen Energy. 45 (2020) 1719–1728.

[20] H. Lahmar, G. Rekhila, M. Trari, Y. Bessekhouad, HCrO4 -reduction on the novel heterosystem La2CuO4/SnO2 under solar light, Wiley Online Library, 2015. doi:10.1002/ep.12058.

[21] R. Laouici, S. Douafer, H. Lahmar, G. Rekhila, M. Trari, M. Benamira, Elaboration and studies of physical and photo-electrochemical properties of La2NiO4 and its use with SnO2 in photo-evolution of hydrogen under visible light irradiation, Optik (Stuttg). 236 (2021) 166654.

[22] K. Telmani, H. Lahmar, M. Benamira, L. Messaadia, M. Trari, Synthesis, optical and photo-electrochemical properties of NiBi2O4 and its photocatalytic activity under solar light irradiation, Elsevier, 2020. doi:10.1016/j.ijleo.2019.163762.J

Modélisation d'un écoulement instationnaire entre deux stations de compression

Benzerhouda Amar[#1], Khelifi Touhami Mohamed salah[#1], Boucetta Rachid[#1], Kessal Mohand[#1]

[#]*Laboratoire de génie physique des hydrocarbures, Université M'hamed Bougara Boumerdès*
Faculté des hydrocarbures Avenue de l'indépendance Boumerdès

[1s]abenzerhouda1@gmail.com

***Résumé*—Ce travail consiste à étudier un écoulement instationnaire isotherme d'un gaz dans une longue conduite entre deux stations de Compression. La modélisation a été faite par la méthode des différences finis explicite. Les équations de continuité et de quantité de mouvement ont été discrétisés afin de solutionner le problème dimensionnel aucours dutemps.**

Les résultats de la pression et du débit massique ont été obtenus et validés par ceux de la littérature pour les mêmes conditions opératoires. Dans cette étude les profils de ces paramètres ont été représentés pour différentes valeurs de temps 500, 1250 et 5000 s le long d'une conduite de 90 km. Deux cas de test ont été validés pour une pression amont de 40 bars et 3.5 bars pour une même pression desortie égale à la pression atmosphérique.

Mots clés — Ecoulement dans les pipelines, Ecoulement non stationnaire, Différences finis, station de compression

1. Introduction

L'écoulement non stationnaire de gaz dans les conduites est un phénomène fréquent dans les installations industrielles conçues pour véhiculer ou exploiter des fluides gazeux. De par leur destination, ces installations peuvent être diverses et leurs applications nombreuses et multiples. Parmi celles qui illustrent le mieux ce phénomène, on peut citer les tuyaux des systèmes d'alimentation d' air comprimé dans les circuits d'asservissement pneumatique, les skids d'alimentation des turbines à gaz ou les moteurs à combustion interne, ainsi que les réseaux de transport et de distribution de gaz. Ces derniers feront l'objet d'une attention particulière dans ce travail. Dans les systèmes précités, le fonctionnement n'est pas uniforme, mais sujet à des perturbations dictées par les conditions d'exploitation. Ce qui signifie que les paramètres du gaz varient dansle temps et en tout point du circuit.

Cet écoulement dit non-stationnaire se produit chaque fois qu'il y a une variation d'un ou plusieurs paramètres à l'entrée ou à la sortie du système. Il est caractérisé par la propagation d'une onde dont l'amplitude et la vitesse dépendent essentiellement des propriétés physiques du fluide ainsi que de la géométrie de l'installation. La durée de ce phénomène, appelé aussi transitoire où non permanent dans certaines situations, peut être grand comme dans le cas d'un gazoduc où la variation des paramètres est petit et le temps d'observation court; elle peut être aussi, rapide quand il s'agit des circuits courts où la variation des paramètres est grande et le temps d'observation court. Les paramètres à observer dans la majorité des cas sont la pression ou la masse volumique, la vitesse d'écoulement ou le débit. L'influence de la température est considérée, seulement dans le cas d'un écoulement adiabatique.

A Nouri [3] a simulé des écoulements transitoires de gaz adiabatiques compressibles dans un long pipeline suite à une défaillance catastrophique. La méthode utilisée est un schéma implicitede différences finies d'ordre élevé.

M.A.Stoner [2] a utilisé la méthode des caractéristiques pour fournir une solution aux équations gouvernantes avec un écoulement instationnaire dans des gazoducs. Ce travail donne de bons résultats comparés aux résultats expérimentaux précédents.

L.M.C. Gato, J.C.C. Henriques [7] ont étudié le comportement dynamique d'un écoulement compressible unidimensionnel en utilisant la méthode Runge-Kutta Galerkin discontinue, avec uneapproximation de troisième ordre dans l'espace et letemps.

Kessal [4] a étudié numériquement un écoulement de fluide compressible isotherme résolu par deux méthodes ; le premier cas est un schéma corrigé par prédicteur pour l'étude de l'écoulement rapide du fluide dans des gazoducs courts et le second est un schéma simple de différences finies utilisé pour l'écoulement lent du fluide.

Alfredo Bermúdeza,b, et al [5] ont utilisé un schéma de volumes finis pour la solution numérique d'un modèle mathématique pour l'écoulement compressible non-adiabatique et non-isotherme d'un gaz réel dans un pipeline.

Atlas V, Akhmetzyanov et Salnikov [6] ont adapté une approche numérique dans leur travail, qui est un traitement des équations aux dérivées partielles non linéaires avec un problème de valeur limite initiale pour les coefficients discontinus décrivant l'instabilité de la pression et la distribution du flux dans le système de transport de gaz. Les méthodes utilisées sont différentes à savoir les volumes finis, les éléments finis et des approximations multi grilles pour des solutions généralisées des équations paraboliques.

Amar shabaik Y, A. Khulief [1] ont évalué plusieurs techniques numériques quant à leur adéquation à la surveillance en temps réel de l'écoulement des fluides dans les pipelines, comme les méthodes de l'espace alternatif et centré ou la méthode prédicteur-correcteur. Leurs résultats seront comparés en fonction de leur vitesse de réponse et de leur temps de stabilisation, qui sont essentiels.

2. EQUATIONS MATHEMATIQUES

L'écoulement non stationnaire du gaz dans les pipelines peut être décrit de manière adéquate par l'approche

unidimensionnelle. Les équations de base sont dérivées des équations de continuité, de quantité de mouvement, d'énergie et de l'équation d'état thermodynamique. Dans la littérature, les études sont adoptées aux cas spécifiques adiabatiques ou isothermes.

Lorsque les transitions sont rapides, on suppose que les changements de pression dans le gaz se produisent instantanément, de sorte qu'il n'y a pas de temps pour le transfert de chaleur entre le gaz dans le pipeline et l'environnement. De même, dans le cas de transitions lentes dues à des fluctuations, on suppose que le gaz dans la canalisation a suffisamment de temps pour atteindre l'équilibre thermique avec son environnement à température constante.

Pour cette étude, nous considérons un écoulement isotherme qui se rapproche d'une application réelle de la dynamique des gaz.

$$\frac{P}{t} + a^2 \frac{Q}{Z} = 0.$$

$$\frac{Q}{t} + A \frac{P}{Z} + \frac{fa^2 Q|Q|}{2AD} + Ag \sin = 0$$

3. METHODES NUMERIQUES

Les méthodes numériques sont plus largement utilisées car, malgré les erreurs qu'elles peuvent générer dans certains cas, leur utilisation est diversifiée et constitue la seule alternative pour traiter des problèmes complexes. En raison de leur principe de résolution et de leurs performances, ces méthodes sont nombreuses et leur mise en œuvre dépend de la complexité des problèmes à traiter. Elles peuvent être simples ou de hauterésolution.

Les équations réelles sont discrétisées par un schéma central de différences finies dansl'espace et une forme directe dans le temps comme suit

Les termes transitoires donnent :

$$\left(\frac{\partial P}{\partial t}\right)_i^{t+\frac{1}{2}} = \frac{P_i^{t+1} - P_i^t}{\Delta t} + O(\Delta t)$$

$$\left(\frac{\partial Q}{\partial t}\right)_i^{t+\frac{1}{2}} = \frac{Q_i^{t+1} - Q_i^t}{\Delta t} + O(\Delta t)$$

Les termes différentiels dansl'espace pour p et q sont discrétisés de la manière suivante :

$$\left(\frac{\partial P}{\partial Z}\right)_i^{t+\frac{1}{2}} = \frac{P_{i+1}^{t+1} - P_i^{t+1}}{\Delta Z} + (1-\theta)\frac{P_{i+1}^t - P_i^t}{\Delta Z} + O(\Delta Z)$$

$$\left(\frac{\partial Q}{\partial Z}\right)_i^{t+\frac{1}{2}} = \frac{Q_{i+1}^{t+1} - Q_{i-1}^{t+1}}{\Delta Z} + (1-\theta)\frac{Q_{i+1}^t - Q_{i-1}^t}{\Delta Z} + O(\Delta Z)$$

Par conséquent, les équations différentielles partielles différentes peuvent être approximées par les équations de différences finies suivantes :

$$P_i^{t+1} + \frac{\theta}{2}(Q_{i+1}^{t+1} - Q_{i-1}^{t+1}) = P_i^t - \frac{1-\theta}{2}(Q_{i+1}^t - Q_{i-1}^t)$$

$$Q_i^{t+1} + \frac{\theta}{2}(P_{i+1}^{t+1} - P_{i-1}^{t+1}) = Q_i^t - \frac{1-\theta}{2}(P_{i+1}^t - P_{i-1}^t) - \Delta_3 Q_i^t |Q_i^t| - \Delta_4 P_i^t$$

$$\Delta_1 = \frac{\Delta t}{A.\Delta Z}$$

$$\Delta_2 = \frac{Z_2}{A.\Delta t}$$

$$\Delta_3 = \frac{f.a.\Delta t}{2.A.D}$$

$$\Delta_4 = \frac{A.g.\sin \Delta t}{a^2}$$

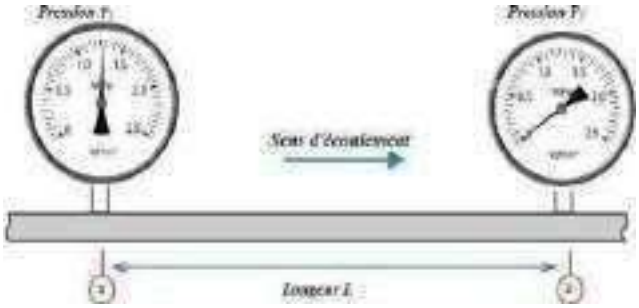

Schéma de l'installation

3. RESULTATS

1. Sensibilité du maillage

Pour la précision de calcul, il est convenable de choisir différents nombres de points le long de la conduite pour tester la variation de nos résultats. A cet effet, nous avons pris 180,190 et 200 points pour 90 km. Sur les figures 1, 2 les distances x sont adimensionnées par la longueur totale de la conduite.

Sur les figures (1) et (2), nous représentons les variations de p et Q en fonction de x+ pour différents Nombre de nœuds N. Nous avons remarqué que les courbes sont totalement superposées pour tous les cas. Cette observation nous permet de conclure que les résultats obtenus ne sont pas sensibles à la variation denombre denœuds.

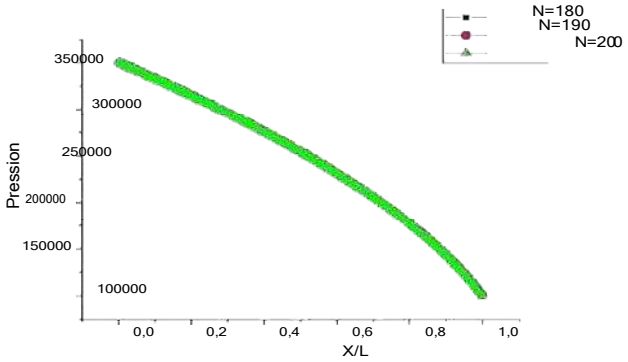

Figure(01) : Profil dela pression pour différents N

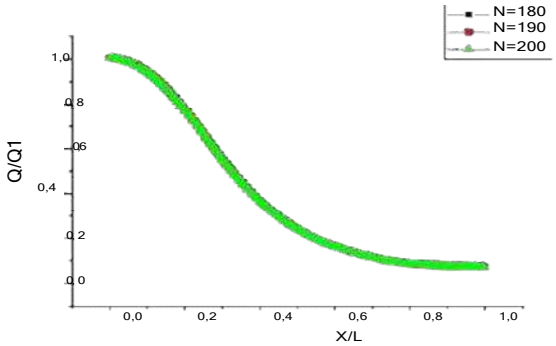

Figure(02) : Profil du débit pour différents N

Nous avons exploité les résultats de la littérature d'Amara shabaik [1] pour valider notre code de calcul. Deux cas ont ét é utilisés pour cette étude. Pour le premier cas et pour une pression amont de 40bars et une pression aval de 1 bar nous avons présenté ci-dessous sur les figures 3 et 4 relatives aux temps réels de 800s et 4000s la variation longitudinale de la pression le long de l'axe x de la conduite

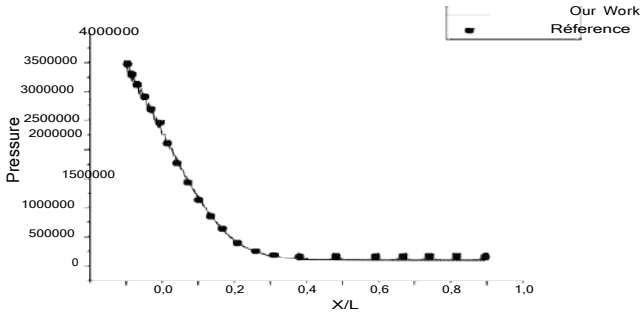

Figure(03) : Profil de la pression pour T=800 S

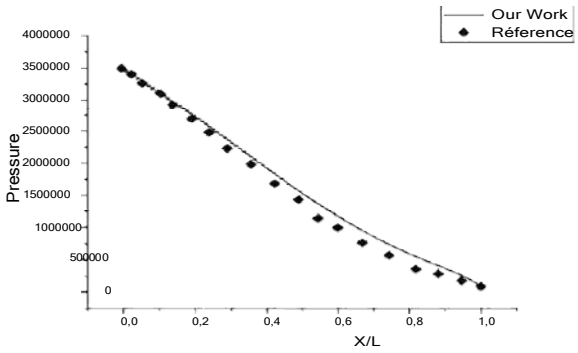

Figure (04) : Profil de la pression pour T=4000 S

Dans le deuxième cas nous représentons les variations de la pression entre l'entrée et la sortie de la conduite les valeurs variant entre 3.5 bar et 1 bar. Les courbes des figures 5, 6 et 7 sont directement comparées avec celles de la référence [1] pour les mêmes conditions aux limites et pour les mêmes temps à savoir 500s, 1250s et 5000s. Une parfaite concordance dansles 03 cas a été bien remarqué.

Nous remarquons une décroissance de P en allant vers la sortie pour tous les cas étudiées ceci est due aux pertes de charge linéaires pour une température constante. Avec l'accroissement du temps la chute de la pression le long de la conduite est de plus en plus ralentit donnant ainsi une courbe concave qui devient une droite puis convexe à la fin puis se stabilise même avec l'élévation dutemps.

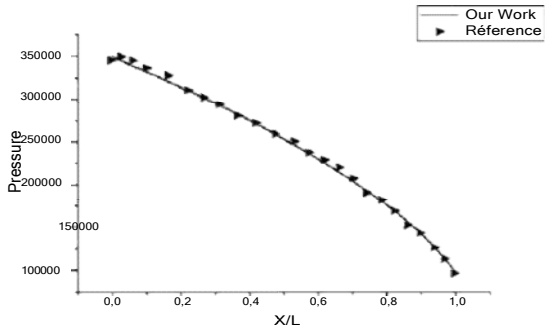

Figure (05) : Profil de la pression pour T=5000 S

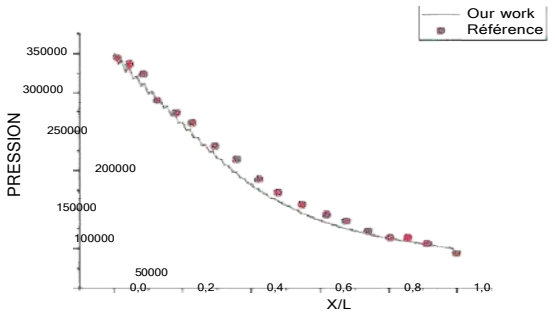

Figure (06) : Profil de la pression pour T=500 S

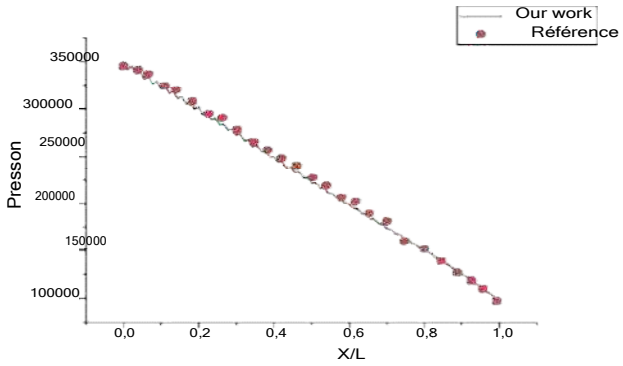

Figure (07) : Profil de la pression pour T=1250 S

Avec les mêmes auteurs nous avons aussi comparé le débit d'écoulement en fonction de x+ pour des temps réels 500 s et 1250s. Pour la première courbe sur la figure 8au temps égal à 500s nous avons noté une certaine déviation par rapport à celle de la référence. Ceci est du certainement à la différence des méthodes utilisées. Mais nous avons observé d'autre part une bonne concordance pour un temps plus poussé 1250s sur la figure 9.

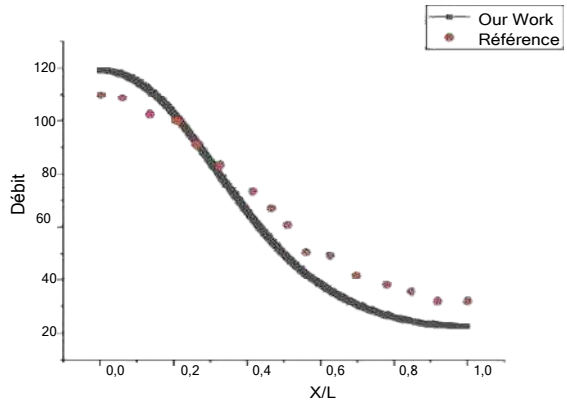

Figure (08) : Profil de débit pour T=500 S

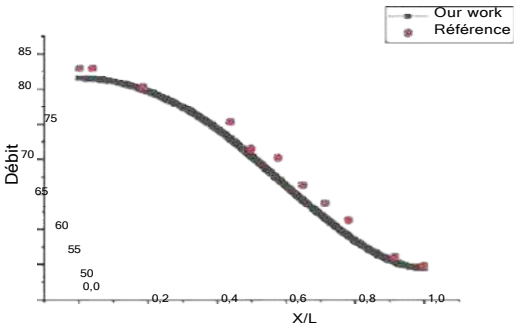

Figure (09) : Profil de débit pour T=1250 S

NOTATION

a : vitesse du son (m/s)
A : section transversale de la conduite (m^2)
L :longueur de la conduite (m)
D : diamètre de la conduite (m)
f: coefficient de frottement

g : accélération de la gravité (/s2)
P :pression du fluide (bar)
Q : débit du fluide (kg/s)
t :temps (s)

P: masse volumique du fluide (kg/m^3)
Ψ :Angle d'inclinaison de la canalisation par rapport à l'horizontale (Deg)
Θ: paramètre constant
Δt :pas de temps (s)
ΔZ : pas spatial le long de l'axe de la conduite (m).
N: nombre denœuds dela conduite.

4. CONCLUSIONS

Dans le cas de l'exploitation des réseaux de conduites de gaz, ce travail a présenté quelques techniques de calcul utiles et simples, sachant que ce type d'écoulement ne nécessite pas uneprogrammation sophistiquée.
Le calcul des écoulements du gaz en régime transitoire utilisée dans cet article, nous a permis de quantifier l'évolution des différents paramètres tels que la pression et le débit le long de la conduite comparés à ceux de la littérature.

La méthode des différences finis est utilisée dans ce travail pour la simulation numérique de cet écoulement transitoire unidimensionnel. Nous avons comparés nos résultats trouvés avec ceux de la littérature. Une bonne concordance de presque tous les résultats sauf pour le débit en fonction de x à 500s ou nous avons remarqué une certaine déviation par rapport à celui d'Amara Shabaik [1].

ISSN: 1737-9334

Nous comptons tester d'autres méthodes numériques dans les prochains travaux pour cette étude. Nous essayons d'étudier aussi le cas de présence des fuites dans la conduite ce qui est énormément utile à l'échelle industriel.

Remerciements

Nous remercions la direction générale de la SONELGAZ. Nous tenons à remercier aussi tous les dirigeants du Congrès International de l'Energie Renouvelable (CIER 2022) d'avoir accepté cette communication et faciliter notre présentation.

References

[1] H. E. Emara-Shabaik1, Y. A. Khulief and I. Hussaini Simulation of transient flow in pipelines for computer-based operations monitoring, International Journal for Numerical Methods in Fluids · January 2004.

[2] M. A. Stoner Analysis and Control of Unsteady Flows in Natural Gas Piping System, ASME, Septembre1969.

[3] A. Nouri-Borujerdi Transient modeling of gas flow in pipelines following catastrophic failure, Mathematical and Computer Modelling 54 (2011) 3037–3045

[4] Mohand Kessal simplified numerical simulation of Transients in gas networks. Institution of Chemical Engineers Trans IChemE, Vol 78, Part A, September 2000.

[5] Alfredo Bermúdeza,b, XiánLópeza,b, M. ElenaVázquez-Cendón Numerical solution of non-isothermal non-adiabatic flow of real gases in pipelines, Journal of Computational Physics 323 (2016) 126–148

[6] Atlas V. Akhmetzyanov_, Anton M. Salnikov Mathematical Models of Unsteady Flow Distribution in Gas Transport Systems, Procedia Computer Science112 (2017) 1160–1167

[7] L.M.C. Gato , J.C.C. Henriques , Dynamic behaviour of high-pressure natural-gas flow in pipelines, International Journal of Heat and Fluid Flow 26 (2005) 817–825

Study of physico-chemical characterizations of nano-crystals of Cerium-doped silicon

Afaf Brik[1], Sabrina Naama[1], Karima Benfadel[1], Faiza Tiour[1], Seif Eddine Friha[1], B. Mahmoudi1

1Research Centre of semi-conductor Technology for Energy, CRTSE-02, Bd.Dr.Frantz FANON, B.P.140 Algiers-7, Merveilles, 16038, Algeria
Tel & Fax: +213 21433511

brikafaf@yahoo.com

naamasabrina@CRTSE.dz

Abstract— **In this work, we report on the electrochemical deposition of Ce-doped silicon rich SiNx:H films (SRSN). Silicon nanocrystals have been produced by thermal annealing of SiNx thin film obtained by low pressure chemical vapor deposition and the cerium was electrodeposited by Chronoamperometry method.**

The morphology, structural and chemical properties of Ce-SRSN were investigated using scanning electron microscopy (SEM), energy dispersive X-ray spectroscopy (EDX) .Optoelectronic behaviors of the nanostructures were studied using micro-Raman and photoluminescence spectroscopies at room temperature.

The results presented in this paper indicate that cerium doped silicon rich silicon nitride is a promising candidate material for silicon-based visible luminescent devices.

Keywords— **Cerium, nanostructure, silicon nitride,electrochemical, photoluminescence (PL).**

I. INTRODUCTION

According To The Findings Of Canham Et Al. Since The Advent Of Porous Silicon With High Photoluminescence (PL) Under Visible Light In 1990, There Has Been Interest In The Luminescence Of Silicon-Based Materials In Optoelectronics [1]. It Would Of Course Be Very Interesting To Make "All-Silicon" Optoelectronics Compatible With Microelectronics Using All-Silicon-Based Devices. However, Due To The Indirect Nature Of Its Band Gap, Solid Crystalline Silicon Is A Weak Light Emitter. Its Nanoscale Size Allows It. Become Stronger The Electronic Structure Of Silicon And Results In The Emission Of Radiation In The Visible Range. Although The Light Intensity Of Silicon Nanocrystals (Ncsi) Increases Significantly Under The Influence Of Quantum Confinement [2], The Intensity Is Still Too Low For Applications Related To Silicon Radiative Emission. Therefore, It Is Necessary To Develop Alternative Methods To Obtain Intense Photon Emission From This Material. Therefore, Silicon-Based Substrates Doped With Light-Emitting Impurities Have Emerged. Rare Earth Ions Are Good Candidates For This Function [3]. Rare Earth Dopants Are Of Particular Interest In Many Host Materials Due To Their High Radiative Recombination Efficiency And Consistent Color Properties At Characteristic Wavelengths In The Visible And Near-Infrared, As They Exhibit High Recombination Efficiency And Consistent Radiance And Color Performance. Once Efficiently Excited, Rare Earth Elements Can Generate Photon Emission In The Infrared (IR) To Ultraviolet (UV) Range. Offers Real Application Possibilities In Various Fields Such As Displays, Lasers, Photovoltaics (PV), Optical Communications [4-6]. The Intended Application Is Rare Earth Elements , Emission At The Wavelength Suitable For The Application Must Be Carefully Selected. As An Alternative, Silicon Nanoclusters [7] Were First Investigated, Which Formed In Silicon-Rich Silicon Nitride Films Deposited By Plasma-Enhanced Chemical Vapor Deposition A Silicon-Rich Silicon System Made Of Oxide Materials Has Also Been Established. Since Oxide-Passivated Silicon Nanostructures Have Been Extensively Studied, Nitride Passivation Offers Several Options Decisive Advantage Over This System. Silicon-Rich Silicon Nitride (SNRS) Is A Promising Material System Because Silicon Nitride Is A Structurally Stable Dielectric Commonly Used In Microelectronics Manufacturing Processes. Compared With Silicon-Rich Silicon Oxide (SRSO), SRSN Has More Encouraging Electrical Properties, Such As B. The Lower Tunnel Barrier Of Sinc That Can Inject Vectors, Making These Films More Suitable For Light-Emitting Device Applications [8]. From The Perspective Of Phosphors, Covalent Nitrides Can Be Considered As The Matrix Of Phosphors, Usually Silicon-Based Nitrides, And Are Of Interest Due To Their Unique And Rigid Crystal Structures. They Have Insulator Or Semiconducting Properties And Are Wide Bandgap, And Can Be Doped With Rare Earth Ions To Provide Sufficient Photoluminescence [9, 10]. In Crystalline Or Amorphous Hosts, Rare Earth Elements Are Usually Doped With Ions In The 2+, 3+ Or 4+ Oxidation State. In Many Host Materials, Rare Earth Ions Coordinated In The 3+ State Have Been Found To Exhibit Strong Luminescence And Narrow Linewidths. Among The

Lanthanides, Ce3+ Has Been Widely Studied For Its Blue, Green And Red Emission Properties. However, The Incorporation Of Large Rare Earth Ions In The Sinx Matrix Is Still Difficult To Achieve Due To The Large Size Variation Of The Elements. The Main Goal Of The Research Discussed In This Paper Is To Advance The Development Of Silicon-Based Light Sources, Especially For Visible Light Emission Applications [11] Or To Improve The Performance Of Solar Cells By Downconversion [12]. There Are Several Processing Techniques For Introducing Rare Earth Ions Into Silicon, Including Spray Hydrolysis, Chemical Vapor Deposition, Sol-Gel Processes, And Melt Infiltration [13–17]. However, Electrochemical Synthesis Has Not Been Widely Used To Deposit Rare Earth Oxide Layers. The Electroplating Process Can Be Complex And Worth Investigating. Generally Speaking, The Redox Potential Of Rare Earth Oxides In Aqueous Solution Is Not Easy To Obtain, And The Synthesis Is Difficult. However, Electrochemical Deposition Offers Several Advantages, Including Its Simplicity, Low Processing Temperature, Driving Force Control, And Various Forms Of Deposition [18,19]. Through This Research, Advances In Materials Science And Engineering Can Provide Important Information To Help Develop Efficient And Cost-Effective Devices Using These Materials.

II. Experiment

As starting material we used 4" CZ grown (100) directional solar grade 4", p-type (boron doped) silicon wafers with a resistivity of 0.5-3 Ωcm. A doped n+ emitter was achieved by diffusion using a liquid POCl3 source at 920 °C. The low frequency PECVD SiNx films were then deposited in an industrial direct plasma pulsed reactor using A mixture of silane and ammonia. During this process, pure silane (SiH4) and ammonia (NH3) are dissociated SRSN deposits. Doping process for europium involves simple electrochemical deposition A technique for high temperature annealing in one step [20]. Electrodeposition was performed by cyclic voltammetry using an Autolab PGSTAT 302N in three-electrode mode at -0.19 V versus an AgCl reference electrode. Two different concentrations of cerium nitrate in water, 0.1M and 0.25M, were tested on SiNx-rich silicon layers. After deposition, the films were rinsed thoroughly with deionized water and air dried to remove chloride salts and unreacted products from the surface. No single characterization technique can provide a clear structural picture of silicon nanocrystals embedded in amorphous silicon nitride. Therefore, it is necessary to combine complementary technologies. The elemental composition and morphology of Ce-doped SiNx were examined by X-ray dispersive spectroscopy (EDS) and scanning electron microscopy (SEM) in JSM-7610FPlus. Raman spectroscopy used to identify the structure of thin films using Renishaw The RM1000 uses a 532 nm laser line as the light source. PL spectra were recorded between 200 and 700 nm using UV light from a xenon lamp as Excitation source from FL3-DFX-iHR320 luminescence spectrometer.

III. Results and Discussion

Figures 1.a and 1.b show planar images of a Ce_2O_3 layer electrodeposited on silicon nitride in a cerium nitrate solution with different concentrations of the two solutions as shown above. The amount of cerium deposited on the silicon nitride was observed to be higher in the 0.25 M cerium nitrate solution than in the 0.1 M solution. EDX analysis (Figures 2.a and 2.b) showed the appearance of peaks corresponding to Ce and the increase in the intensity of the oxygen peaks after the electrodeposition process. This indicates the deposition of oxygen and Ce on the silicon nitride, possibly due to the formation of the Ce2O3 phase. However, it increased significantly as the concentration of Ce ions in the electrodeposition solution increased from 0.1M to 0.25M. This means that the 0.25 M concentration results in higher CeO2 electrodeposition, resulting in thicker layers.

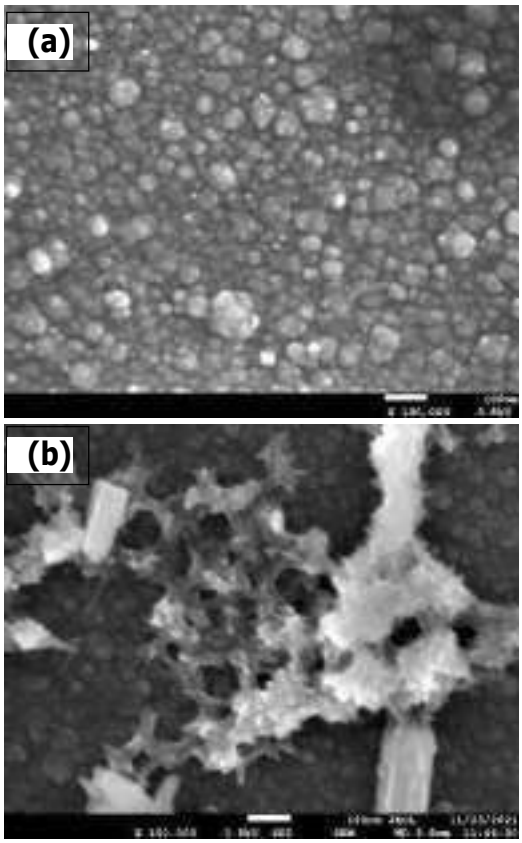

Figure 1: SEM images of a layer of Ce2O3 electrodeposited on silicon nitride in a solution of cerium nitrate in two solutions of different concentrations: (a) 0.1Mand (b) 0.25 M.

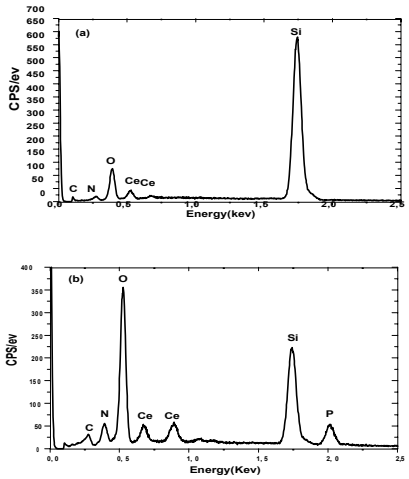

Figure 2: EDX spectra of Ce2O3 electrodeposited on silicon nitride in 0.1 M (a) and 0.25(b) Ce concentration solutions.

Raman spectroscopy is considered a compelling technique for characterizing nanocrystal structures. More information on the microstructure can be found in Raman spectroscopy. Figure 3 shows the Raman scattering spectra of cerium samples in two solutions at concentrations of 0.1 Mand 0.25 M.

CeO2 has a fluorite-like cubic crystal structure with only one allowed Raman mode, T2g. It is based on the symmetric Ce-O-Ce vibration [21, 22]. At high reduction rates, Ce2O3 can be formed, leading to the observation of a band around 158 cm-1 [23,24]. Note that the thin film has previously been assigned the surface mode for the single band observed at 319 cm-1 for CeO2 [25]. This spectrum is consistent with that reported by several authors, and the 465 cm-1 band is assigned to first-order scattering [26,27,28]. Based on the selection rule and using the star ion model to determine the phonon dispersion curve [29], additional second-order features at 935 cm-1 have been assigned to the X- and L-point phonons in the Brillouin zone boundary. Furthermore, the presence of Ce3+ cations in the CeO2 lattice can be demonstrated bytheir Raman electron scattering at 2102 cm-1, which is associated with the 2F5/2 => 2F7/2 transition through the virtual state [30,31,32,33]. Direct transitions can be observed byinfrared spectroscopy[31].

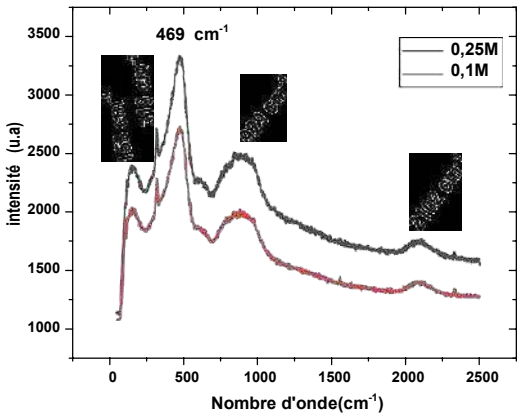

Figure 3: Raman spectrum of a silicon nitride layer of cerium electrodeposited at Pt Potential during 800s from a solution of two concentrations 0.1 ,0.25M

I. Stationary Photoluminescence

Ce^{3+} emission in many materials is well explained. The electronic configuration of the Ce^{3+} ion is 4f1. The ground state of Ce^{3+} consists of doublets 2F5/2 and 2F7/2. The lower excited state has a 5d configuration and is sensitive to the crystal field. Therefore, the emission of Ce3+ corresponds to the transition from the 5d band to the 2F5/2 and 2F7/2 energy levels. The 5d excited state level is sensitive to the crystal field and couples to the vibrations of the lattice, resulting in emission bands rather than emission lines [34]. Of course, the Ce3+ ion has two emission bands due to the nature of the 4f doublet (2F5/2 and 2F7/2). The levels behind are about 2000 cm-1 apart. The absence of the characteristic emission of the 2F5/2 and 2F7/2 doublets in any lattice indicates the presence of a strong crystal field and thus a larger separation of energy levels in the 4f state of Ce^{3+} [34]. The presence of more than one Ce^{3+} excitation band in any lattice is most likely due to the presence of multiple energy levels (up to five) in the 5d state. Ce^{3+} emission is at low wavenumbers when the lowest energy level of the 5d state is abnormally low and the Stokes shift is abnormally high. The nature of the ligands surrounding the cerium also affects the position of the emission band. The more electronegative ligands shift the emission to longer wavelengths due to the reduced energy difference between the ground and 5d states [34]. Since the energy levels of Ce3+ in crystals are strongly influenced by symmetry and crystal field, optical transitions in different lattices transition from ultraviolet to visible light. Increasing the Stokes shift results in a broadening of the emission band. As a result, the emission bands become indistinguishable and appear as a single band [34]. Ce3+ emission can also be broadened by strong electron-phonon coupling or lattice defects in the lattice. Therefore, instead of a doublet, a single band appears [34]. In any host lattice with a high concentration of Ce^{3+} ions, the emission at short wavelengths is reduced in intensity due to self-absorption [34]. At low concentrations, the short-wave emission component predominates. The intensity of the 5d-

ISSN: 1737-9334

2F5/2 component decreases with increasing Ce3+ concentration, indicating the presence of energy migration [34]. Figure 4 shows the photoluminescence emission (a) and excitation (b) spectra of cerium from annealed SiNx films with two concentrations of 0.1M and 0.25M. Record the emission spectrum by setting the excitation wavelength to 275 nm. The emission consists of three bands at 319, 336 and 442 nm, which are characteristic of the 4f → 5d transition of Ce3+ ions [35]. Good correlation with absorption bands observed in diffuse reflectance spectroscopy. Emission at 350 nm, the excitation spectrum of the sample shows a broadband at 276 nm

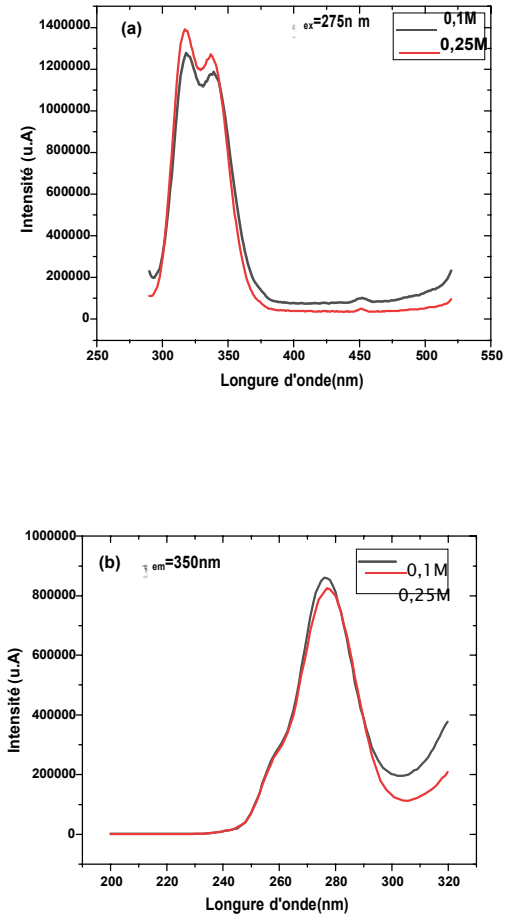

Figure 4: Spectrum (a) emission and (b) excitation of cerium photoluminescence from SiNx films annealed at two different concentrations

II. Conclusion

A new European-style silicon nitride silicon compound is obtained. We have shown that Ce-doped SiNx nanostructures can be fabricated by innovative electrochemical techniques. The synthesis process is simple, reproducible, and inexpensive because expensive equipment is not required. This method is used to dope and optically activate Ce3+ ions in SiNx layers by thermal annealing. The combination of several methods including SEM/EDX, Raman and photoluminescence spectroscopy demonstrated the successful insertion of Ce3+ into the lattice. The valence of cerium has a great influence on luminescence and can be trivalent and/or divalent and/or tetravalent. The number of known nitride phosphors is small, but interest in novel nitrides is rapidly growing among many researchers. Importantly, cerium silicon oxynitride can exist as a second phase in cerium doped silicon nitride.On the other hand, We also noticed that concentration has a significant effect on photoluminescence.

After elaborating the results for thin films of SiNx layers of rare earths, several perspectives are opened to deepen through this very flexible, innovative and application-oriented elaboration: photovoltaics and solar photovoltaic cells. This requiresa series of studies on optoelectronic properties.

Acknowledgment

Acknowledgments We gratefully acknowledge the financial support from Algerian Scientific Research and Technology Development (DGRSDT, MESRS).

References

1. *L.T.Canham Silicon quantum wire Array fabrication by electrochemical and chemical dissolution of wafers. Appl Phys Lett 57:1046 .1990*
2. *T.Y.Kim N.M., Park, K.H.Kim , Sunga GY, Ok YW, Seong TY, Choi CJ Quantum confnement efect of silicon nanocrystals in situ grown in silicon nitride flms. Appl Phys Lett 85:5355.2004.*
3. *Yang J, Zhang H, Wang Z, Huang C, Zou L, Cai P, Zhang Y, Hu S (2013) Hydrothermal synthesis and improved luminescent properties of nanosheet-based rare-earth orthoborates lantern-like assemblies. J Mater Sci 48:225*
4. *Bunzli JCG, Comby S, Chauvin AS, Vandevyver CDB (2007) New opportunities for lanthanide luminescence. Journal of Rareearths 25(3):257–274*
5. *De Bettencourt-Dias A (2007) Lanthanide-based emitting materials in light-emitting diodes. Dalton Trans 22:2229*
6. *Kuriki K, Koike Y, Okamoto Y (2002) Plastic optical fber lasers and amplifiers containing lanthanide complexes. Chem Rev 102(6):2347*
7. *Benyahia B, Tiour F, Guerbous L, Chaoui R, Menous I, Mahmoudi B, Mefoued A, Guenda A, Evolution of Optical and Structural Properties of Silicon Nanocrystals embedded in Silicon Nitride flms with Annealing Temperature. Journal of Nano Research, online: September 2017, 49 (2017) 163. 10.4028/www.scientifc. net/JNanoR.49.163*
8. *Dal Negro L, Yi JH, Kimerling LC, Hamel S, Williamson A, Galli G (2006) Light emission from silicon-rich nitride nanostructures. Appl Phys Lett 88:183103*
9. *Singh M (2016) Recent progress in nitride-based red emitting phosphors. RevAdv Mater Sci 44:134*

10. *Xie R-J, Hirosaki N (2007) Silicon-based oxynitride and nitride phosphors for white LEDs—A review. Sci Technol Adv Mater 8:588*
11. *Trupke T, Green MA, Würfel P (2002) Improving solar cell efciencies by down-conversion of high-energy photons. J Appl Phys 92:1668*
12. *Yu X, Li F, Ye X, Xin X, Xue Z (2000) Synthesis of cerium(IV) oxide ultrafne particles by solid-state reactions. J Am Ceram Soc 83:964*
13. *Ozer N (2001) Optical properties and electrochromic characterization of sol-gel deposited ceria flms. Sol Energy Mater Sol Cells 68:391*
14. *Mikhelashvili V, Eisenstein G, Edelmann F (2001) Characteristics of electron-beam-gun evaporated Er2O3 thin flms as gate dielectrics for silicon. J Appl Phys 90:5447*
15. *Jones L, Kumar D, Singh RK, Holloway PH (1997) Luminescence of pulsed laser deposited Eu doped yttrium oxide flms. Appl Phys Lett 71:404*
16. *Kale SS, Jadhav KR, Patil PS (2005) Characterizations of spraydeposited lanthanum oxide (La2O3) thin films. Mater Lett 59:3007*
17. *Ahmad YH, Mohamed AMA (2014) Electrodeposition of nanostructured nickel-ceramic composite coatings: a review. Int J Electrochem Sci 9:1942*
18. *J-P. Eberhart, (1997) Analyse structurale et chimique des matériaux, ed. Dunod, Paris, chp.58*
19. *V.G.KeramidasandW.B.White,«Ramanspectraofoxideswith the fluorite structure», The Journal of Chemical Physics, vol. 59,no. 3, pp. 1561–1562, (1973).*
20. *V. D. Araujo, W. Avansi, H. B. de Carvalho et al., ―CeO2 ′nanoparticles synthesized by a microwave-assisted hydrothermal method: evolution from nanospheres to nanorods,‖ CrystEngComm, vol. 14, no. 3, pp. 1150–1154, (2012).*
21. *C. Schilling, A. Hofmann, C. Hess, M.V. Ganduglia-Pirovano, Raman Spectra of Polycrystalline CeO2: A Density Functional Theory Study, J. Phys. Chem. C , 121, 20834−20849(2017).*
22. *D. Avisar, T. Livneh, the Raman-Scattering of A-Type Ce2O3, Vib. Spectrosc. 86 ,14−16(2016).*
23. *C. Schilling, A. Hofmann, C. Hess, M.V. Ganduglia-Pirovano, Raman Spectra of Polycrystalline CeO2: A Density Functional Theory Study, J. Phys. Chem. C , 121, 20834−20849(2017).*
24. *D. Avisar, T. Livneh, the Raman-Scattering of A-Type Ce2O3, Vib. Spectrosc. 86 ,14−16(2016).*
25. *Yang J, Zhang H, Wang Z, Huang C, Zou L, Cai P, Zhang Y, Hu S (2013) Hydrothermal synthesis and improved luminescent properties of nanosheet-based rare-earth orthoborates lantern-like assemblies. J Mater Sci 48:225*
26. *V.G.KeramidasandW.B.White,«Ramanspectraofoxideswith the fluorite structure», The Journal of Chemical Physics, vol. 59,no. 3,pp.1561–1562, (1973)*
27. *W. H. Weber, K. C. Hass, and J. R. McBride, «Raman study of CeO2: second-order scattering, lattice dynamics, and particlesize effects», Physical Review B, vol. 48, no. 1, pp. 178–185, (1993).*
28. *S. Dogra, J. Singh, N. D. Sharma et al., «Phase progression via phonon modes in lanthanide dioxides under pressure»,Vibrational Spectroscopy, vol. 70, pp. 193–199, (2014).*
29. *W. Weber, K. Hass, J. McBride, Raman Study of CeO2: Second-Order Scattering, Lattice Dynamics, and Particle-Size Effects, Phys. Rev. B: Condens. Matter Mater. Phys. 48,178−185(1993).*
30. *G. Ferré, L. Burel, M. Aouine, F. Bosselet, S. Ntais, T. Epicier, F.J. Cadete Santos Aires, C. Geantet, A. Gaenzler, F. Maurer, M. Casapu, J.-D. Grunwaldt, S. Loridant, P. Vernoux, Exploiting the dynamic properties of Pt on ceria for low temperature CO oxidation, Appl. Catal. B, submitted.*
31. *V.M. Orera, R.I. Merino and F. Pena, Ce3+ ↔ Ce4+ conversion in ceria-doped zirconia single crystals induced by oxido-reduction treatments, Solid State Ion. 72,224-231(1994).*
32. *S. rban, I. D erd , P. Dolcet, L. Chen, . ller, O. Khalid, H. Camuka, R. Ellinghaus, C. Li, S. Gross, P.J. Klar, B. Smarsly, H. Over, In Situ Study of the Oxygen-Induced Transformation of Pyrochlore Ce2Zr2O7+x to the κ Ce2Zr2O8 Phase, Chem. Mater. 29,9218-9226(2017).*
33. *T. Otake, H. Yugami, H. Naito, K. Kawamura, T. Kawada, J. Mizusaki, Ce3+ concentration in ZrO2-CeO2-Y2O3 system studied by electronic Raman scattering, Solid State Ion. 135,663-667(2000).*
34. *Sankar R., Solid State Science 10, 864-1874 (2008).*
35. *Erwan Leysour de Rohello, «Synthèse et étude des propriétés luminescentes de composés carbodiimides en vue d'application comme luminophores pour diodes blanches», Thèse de doctorat de l'université de rennes 1(2020).*

Ultra-miniature antenna array based on silicone and FR4 for the IOT and 5G applications

Fayza BOUSALAH[#1], Amin RABAH[*2], BABAAHMED Zakarya[*3], Yamina BELHADEF[*4], Hamida DJELTI[*5], Hayat BENOSMAN[*6]

[#1]bousalah.fayza@gmail.com, [2]arabah6@gmail.com, [3]zaki.babaahmed@gmail.com, [4] belhadef_y@yahoo.fr [5]djelti_hamida@yahoo.fr6, [6]benosmanh@yahoo.fr,

[1] dept. nameof Telecommunications, Abou Bekr Belkaid University
[1]Télécommunications Laboratory TTL
[1]BP 230, Chetouane 13000, Tlemcen, Algeria

***Abstract*— Over time, we have integrated computers into various objects of our daily lives. Moreover, with the web, these objects can connect and communicate with each other. Thanks to this emergence of the web, the machines linked to the Internet are designed to execute, then to think, today they learn to perceive, connect and react. In this context we focus our research on the concept of linking objects to the Internet, known today as the "Internet of Things" (IoT).**

Our objective is to design, optimize and miniaturize an array of planar antennas by two methods based on metamaterials and silicon which operates around a resonance of 5.8GHz with high gainfor IoT applications.

IOT and 5G devices embed several elements that will have a positive environmental impact, such as, for example, battery optimization, saving energy for connection to IOT and 5G networks, consumption of digital data collected and stored in Data Centers, preservation the environment, saving electricity, fighting against deforestation, connected solutions for agriculture that consumes less resources, ...

The design of "IOT" and "5G" systems is a facilitator and accelerator of operational excellence. It is therefore surprising that IoT and 5G technology is a huge boon for the clean sustainability sector and, therefore, for the environment.

IoT and 5G technology allows utility companies and other energy providers to extend their services b c nnecting to countless decentralized devices and energy sources like solar panels and microgrids. The result is greater sustainability and reduced energy costs in all socio-economic and other sectors.

Keywords*— *Antenna Vivaldi, Silicon, FR4, Roger, high gain, UWB, network, CST MWS, Matlab, S-parameters.

I. INTRODUCTION

The objective of this work is to design a printed antenna for IoT [1,2,3,4,5] applications under the CST (MWS) environment. We are going to make a study of the first antenna [6,7] based on two types of substrates FR4 and silicon with a single element radiating at the resonance frequency 5.8GHz then we are going to make a comparative study between the two antennas to see the influence of the two substrates. Next, we will design a two-element antenna [8,9] array to increase the gain and radiation of both antennas [10, 11, 12].

II. PLANAR ANTENNA FOR IOT APPLICATIONS

This work consists in realizing a patch antenna at the frequency of 5.8 GHz. The specifications impose the values characterizing the different elements of the antenna [7, 10, 13] :

- Dielectric permittivity of the substrate $cc = 4.3$ (FR4) and cc=11.9 (Silicon).
- Height of the dielectric substrate: $hc = 1.6cc$.
- Desired resonance frequency: $cc = 5.8\ ccc$.

Because it is a licensed band rented for researchers and for medical tests.

- Adaptation to 50 Ohm.
- Powered by microstrip line.
- Thickness of the metallization: $hc = 0.035cc$.

A. Theoretical calculation of the dimensions of the rectangular patch antenna

• We calculate the different parameters of the patch antenna by the following different equations.

• Determiningthe patch length: $cc = \frac{c}{2c_t}\sqrt{\frac{2}{\ \ +1}}$ (1)

• Determining the patch length: $cc = cccc - 2\Delta c = \frac{c}{2c\sqrt{c_{\ \ }}} - 2\Delta c$ (2)

• The effective length: $ccc = c_{cc} = \frac{c}{2c_r\sqrt{e_{ccc}}}$ (3)

• Calculates effective dielectric constants: $c_{ccc} = \ _{\ }+1 + \ -1[(1 + 12\ ^{h})\ ^{21}]$ (4)

•Extension of length $\Delta c = 0.412h\ \frac{(\ \ \ +0.3)(\ +0.264)}{(\ \ \ -0.258)(\ \ +0.813)}$ (5)

• Feed length calculation : $cc = Lf = \frac{c}{2f}$ (6)

• Calculation of substrate length : $cc = cc + c.\ c + cc$ (7)

• Calculate the width of the substrate: $cc = cc + c.\ c$ (8)

• Calculation of the width of the feed line (cc) with Zc=50Ω.

The table I, gives diffrentes dimensions of antenna bytow materials FR4 and silicon.

TABLE I. Dimensions of antenna

	Type of substrat	
Parameters	FR4	Silicon
cp (mm)	15.886	10.18
cccc	3.7601	9.658
cc(*cc*)	12.47	8.321
Δ*c* (mm)	0.7251	0.644
cc (mm)	11.88	7.024
cc (mm)	25.862	25.862
cc (mm)	3.137	1.27
cc (mm)	47.342	42.486
cc (mm)	25.486	19.78

III. DESIGN AND SIMULATION RESULTS OF THE PATCHANTENNA

A. Design of an initial rectangular patch antenna

Figure 1 represents an initial rectangular patch antenna.

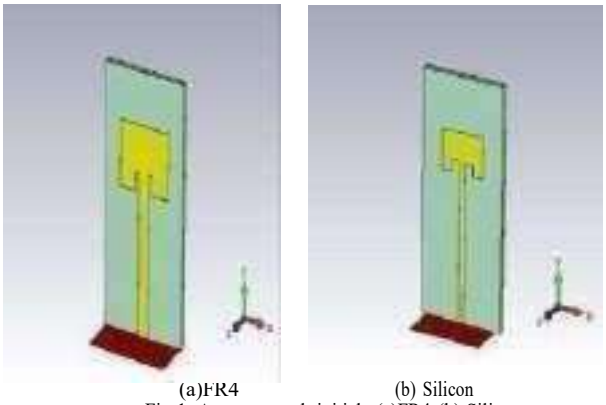

(a)FR4 (b) Silicon
Fig 1. Antenne patch initiale (a)FR4 (b) Silicon.

Figure 2 represents the simulation result of the coefficient S_{11} which is -15.24dB for FR4 and -13.46dB for silicon at the resonance frequency of 5.797 GHz and 5.716 GHz respectively.

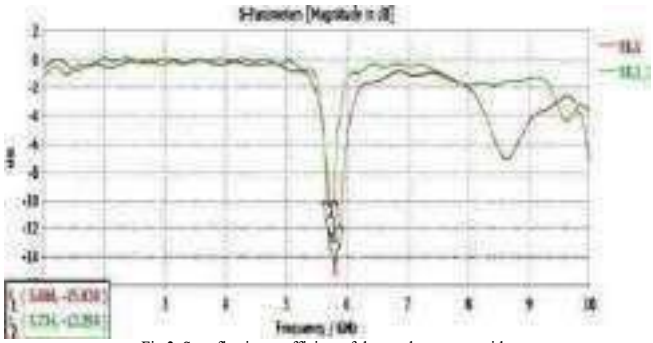

Fig 2. S_{11} reflection coefficient of the patch antenna with notches as a function of frequency (1) FR4 (2) Silicon.

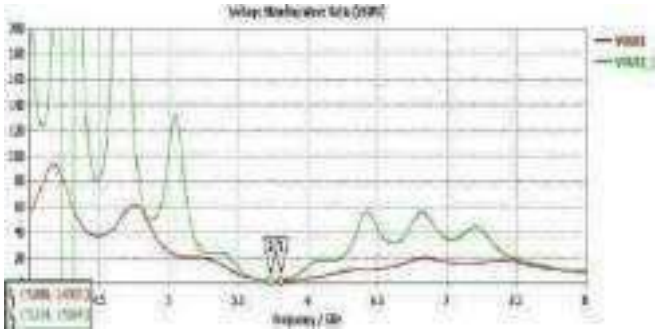

Fig 3. standing wave ratio (1) FR4 (2) Silicon.

Figure 3 shows the standing wave ratio VSWR of the patch antenna with notches.

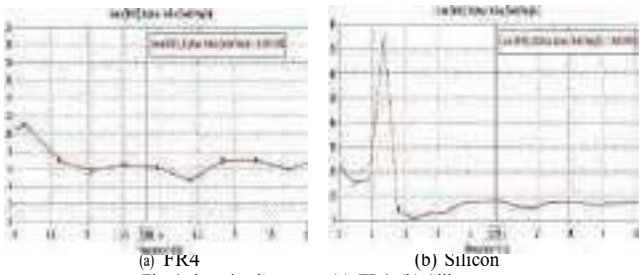

(a) FR4 (b) Silicon
Fig 4. le gain d'antenne (a) FR4 (b) Silicon.

(a) FR4 (b) Silicon
Fig5. Diagramme de rayonnement en 3D.

Figures 5, 6 represent respectively the 3D and polar radiation patterns of the antenna at the5.8GHz resonant frequency.

(a) FR4 (b)Silicon
Fig 6. Diagramme de rayonnement en présentation polaire.

a) Design of the patch antenna with a newstructure

After having made a patch antenna which resonates at 5.8 GHz of rectangular shape known in the literature, we now offer you a new design of the aforementioned antenna [14, 15, 16].

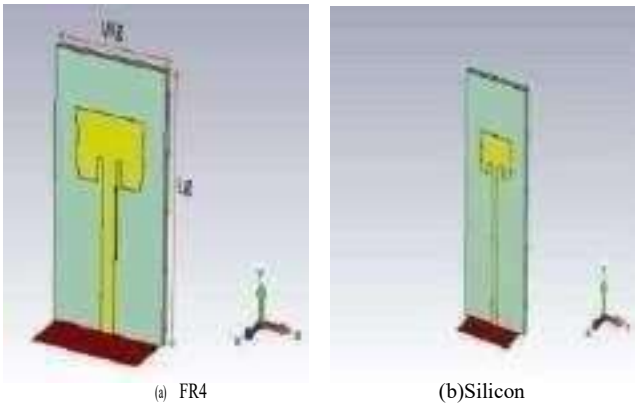

(a) FR4 (b)Silicon

Fig 7. Patch antenna with a new structure (a)FR4 (b)Silicon.

Figure 7 shows the S_{11} coefficient of the antenna resonant at GHz. We notice a maximum bandwidth of 0.173 GHzaround 5.8 GHz for silicone and 0.185 GHz for FR4.

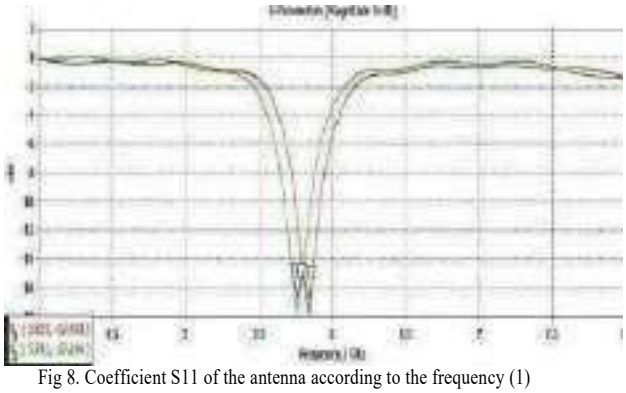

Fig 8. Coefficient S11 of the antenna according to the frequency (1) FR4 (2) silicon.

We noted a VSWR<2 at 5.8GHz between 1 and 2 as shown in Figure 8, which shows a good adaptation of the radiating antenna.

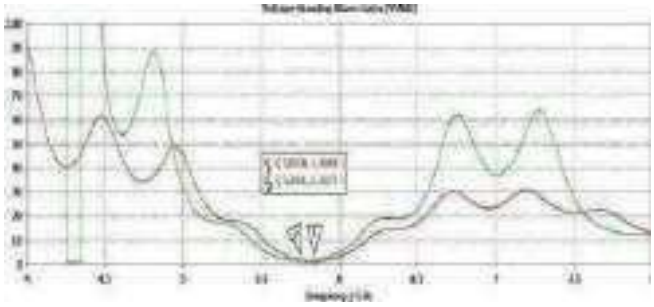

Fig 9. Standing wave ratio for the new structure (1) FR4 (2) Silicon.

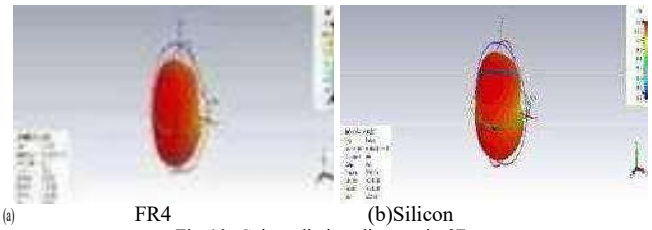

(a) FR4 (b)Silicon

Fig 10. Gain radiation diagram in 3D.

The antenna radiation pattern has an appropriate shape as shown in Figure 10, the gain value is = 5.01 dB for FR4 and

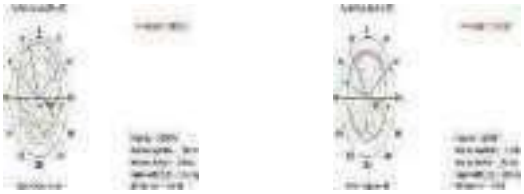

FR4 (b)Silicon

Fig 11. Radiation diagram in polar presentation (a) FR4 (b) Silicon.

Figures 10 and 11 we notice that the radiation is concentrated in the upper part ofthe antenna (between theplane Yand Z).

IV. IMPLEMENTATION OF AN ANTENNA NETWORK FOR THE 5.8GHZ FREQUENCY

To obtain a power divider in the form of a T junction which radiates well, then the following steps must be followed [15,16]:

- The input impedance of the first supply $cc = ccc$.
- The input impedance of the second power supply $cc = 75c$

The input impedance of the third power supply is the same as the first input impedance.

A. Element antenna array

To obtain a power divider in the form of a T junction with good radiation, thefollowing stepsmust be followed [III.4]:

- The input impedance of the first supply $cc = ccc$.
- The input impedance of the second power supply $cc = 75c$

The input impedance of the third power supply has the same value asthe input one.

A. Element antenna array

To facilitate the calculations ofthe length and width of each 4.33 dB for silicon substrate.

supply line we used the program “Microstrip Line Calculator”. This new splitter technique aims to increase the gain, and improve the results of the S_{11} parameter, in order toobtain a good radiation from the 2×1 antenna array.

With L: linelength and W: line width.

The purpose of the 2-element antenna array design is toincrease the gain ofthe antenna.

Calculatedimensions oftheT-junction:

-For thefirst entry:

Thelinewidth W=3.137mm and theline length L=13.996mmFR4)

The line width W=1.27mm and the line length L=9.875mm(Silicon)

-For thesecond entry:

The line width W=1.5mm and the line length L=25mm (FR4)

The line width W=3.137mm and the line length L=12.7mm(Silicon).

-For thethird entry:

The line width W=3.137mm and the line length L=29mm(FR4).

The line width W=1.5mm and the line length L=27.8mm

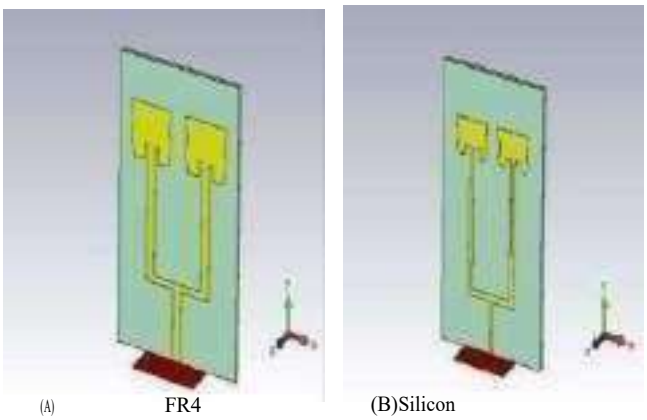

(A) FR4 (B)Silicon

Fig. 12. Structure de jonction de la division reliée avec 2 éléments.

1. TABLE II. 2 Element antenna array dimension.

Parameters	'Wg' (Substrate width and ground plane)		'Lg' (Substrate length and ground plane)		' h' (Height substrat)		'λ ' (Space between 2 élements)	
	FR4	Silicon	FR4	Silicon	FR4	Silicon	FR4	Silicon
Values mm	47.3 95	33 .70 8	62. 73 3	52.359	1.6	1.6	13.966	3.74 75

Figure 13 shows that the adaptation is well done since the reflection coefficient S_{11} is -34.449dB and -25.329dB for FR4 and Silicon respectively at 5.8 GHz

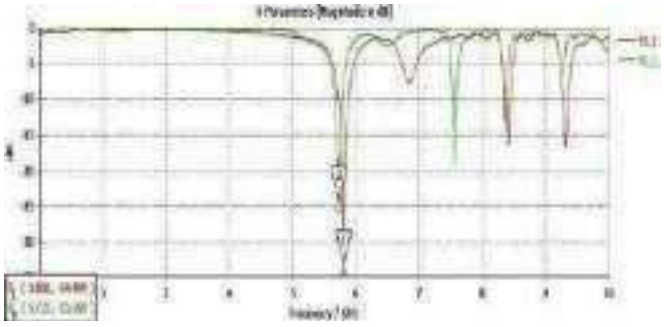

Fig.13. Reflection coefficient (1) FR4 (2) Silicon.

We noted a VSWR <2, equal to 1.038 for FR4 and 1.114 for Silicon which indicates a good adaptation of the antenna compared to the results of a single antenna.

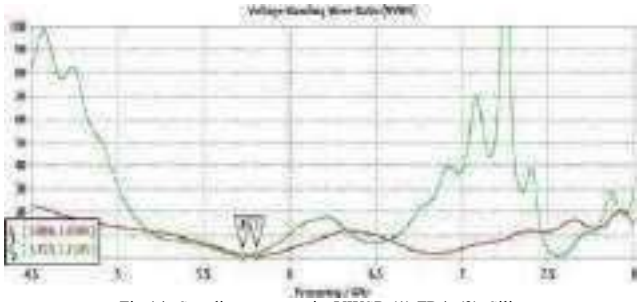

Fig.14. Standing wave ratio VWSR (1) FR4 (2) Silicon.

It is noticed that the gain has increased well compared to a single element antenna meeting the requirement of this design.

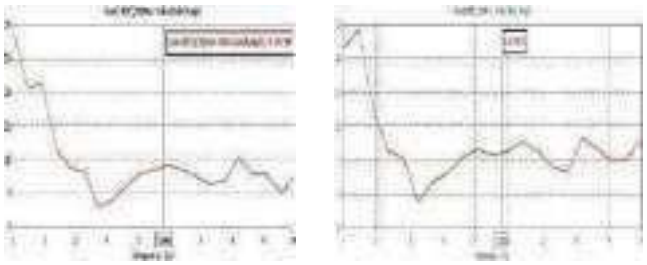

(a) FR4 (b)Silicon

Fig.15. Gain (a) FR4 (b) Silicon.

The antenna radiation pattern has an appropriate shape as shown in figure 16 because the radiation is concentrated at the top of the antenna (Z-plane).

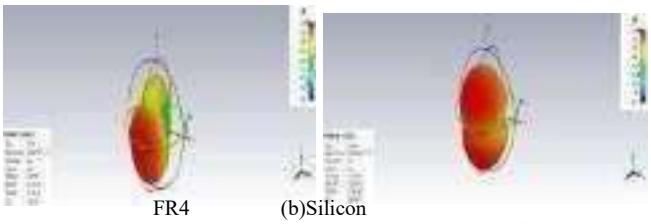

(a) FR4 (b)Silicon

Fig.16. Diagramme de rayonnement en 3d (a) FR4 (b) Silicon.

(a) FR4 (b)Silicon

Fig.17. Diagramme de rayonnement en présentation polaire (a) FR4 (b) Silicon.

From the results infFigure 17, we observe that the radiation pattern of our antenna is directional. But on the E plane, we notice that the main lobe exceeds 3dB unlike the other secondarylobes.

a. TABLE III. comparative results for an antenna with 1 and 2 elements in FR4 and silicone under CST.

PARAMETERS	1 ELEMENT		2 ELEMENTS	
	FR4	SILICON	FR4	SILICON
Frequence (GHz)	5.833	5.779	5.806	5.725
S11 (dB)	-17.437	-16.348	-34.499	-25.329
Gain (dB)	5.006	4.329	8.805	5.940
BP	0.173	0.175	0.174	0.132
VSWR	1.310	1.3593	1.0384	1.1145
EFFICACITE	96.15%	88.48%	99.14%	97.02%

To check the performance of the antennas studied, we made a comparison of the characteristics of the antenna, table III gives thedifferent characteristics oftheproposed ones.

According to theresults obtained in Table III, we find that some characteristics remain relatively constant such as the bandwidth except for the single element antenna.

We can see regarding a single element antenna compared to the 2 one, that the increase in gain remains proportional to the number of elements in the array, which means that the array becomes more directional and the beam of radiation becomes shrinks.

We notice that the antenna based on FR4 has a better adaptation and efficiency and a higher gain than that with silicon and FR4. on the other hand, the use of silicone is intended to miniaturize the dimensions of the antenna and subsequently the antenna array from which the gain decreases. The results obtained remain acceptable and applicable in the field ofIOT [12,13,14,15,16].

V. ANTENNA NETWORK WITH 4 ELEMENTS

The design goal of a 4-element antenna array is to increase the gain of the previouslydesigned rectangular antenna.

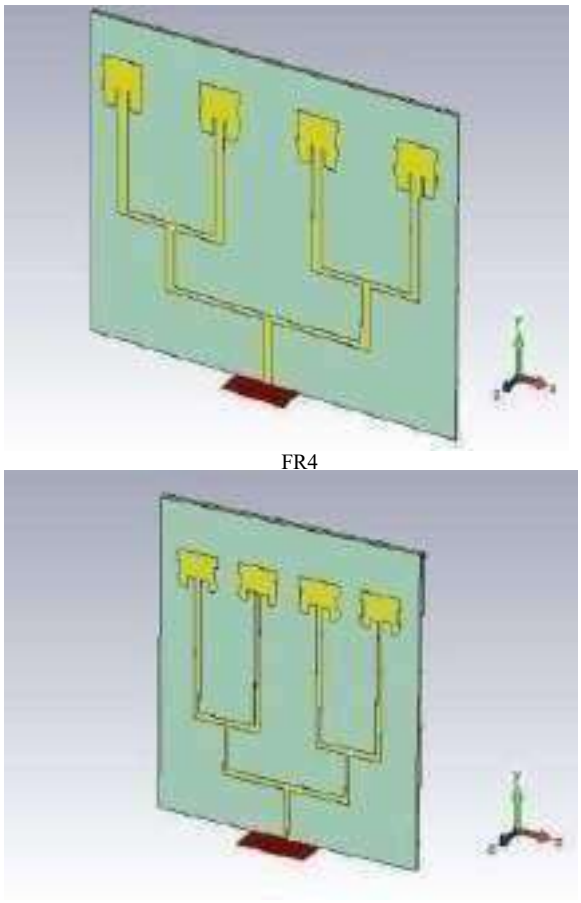

(a) FR4

(b) Silicon

Fig.18. 4-element antenna array.

Table IV summarizes the values of the main parameters used in the design of our proposed antenna array:

TABLE.IV. Dimensions of the 4-element antenna array

Parameters	'Wg' (ength Substrat and ground)		'Lg' (Length Substrat and ground)		' h' (Higth substrat)		'人' (Space bitween 2 elements of patch)	
	FR4	Silicon	FR4	Silicon	FR4	Silicon	FR4	Silicon
Values (mm)	143.49	66.52	78.13	62.23	1.62	1.62	22.45	5.42

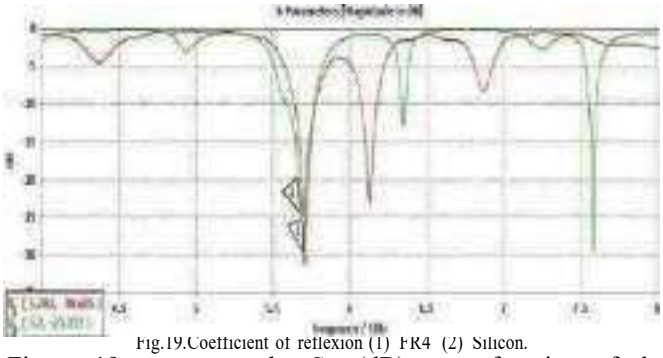

Fig.19.Coefficient of reflexion (1) FR4 (2) Silicon.

Figure 19 represents the S_{11} (dB) as a function of the frequency, this one is -30.685dB and -25.332dB for the FR4 and silicon substrates respectively concerning the first peak, and also for the second peak, we have an S_{11} of -22.76dB at the 6.127GHz frequency for FR4 and -12.7dB for the Silicon, and for the third peak, the S_{11} is -22.62dB for the 6.35GHz and 7.5838GHz frequenciesrespectively.

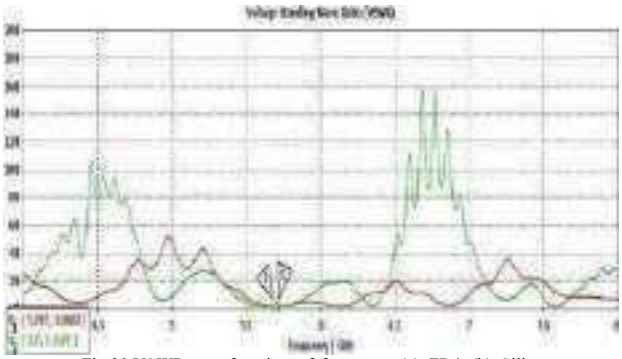

Fig.20.VSWR as a function of frequency (a) FR4 (b) Silicon.

From figure 20 we notice that the VSWR<2, which confirms that our networks are well adapted around the 5.8GHz resonant frequency.

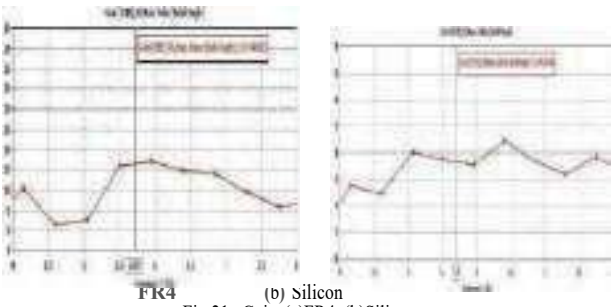

(a) FR4 (b) Silicon

Fig.21. Gain (a)FR4 (b)Silicon.

As for the 2-element array the gain further increased for the 4-element arraymeeting therequirement of this design.

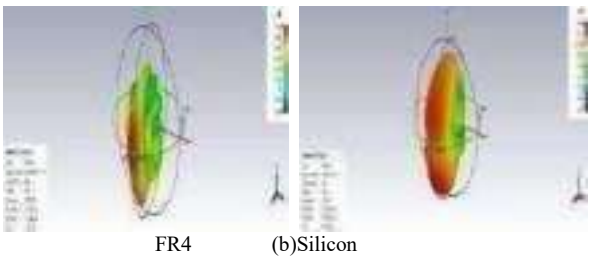

(a) FR4 (b)Silicon

Fig.22. Diagramme de rayonnement du gain en 3d (a)FR4 (b)Silicon.

(a) FR4
(b) Silicon

Fig.23. Radiation diagram in polar presentation (a) FR4 (b) Silicon.

VI. RESULTATS EXPERIMENTAUX

A. Réseau d'antennes (2× 1)

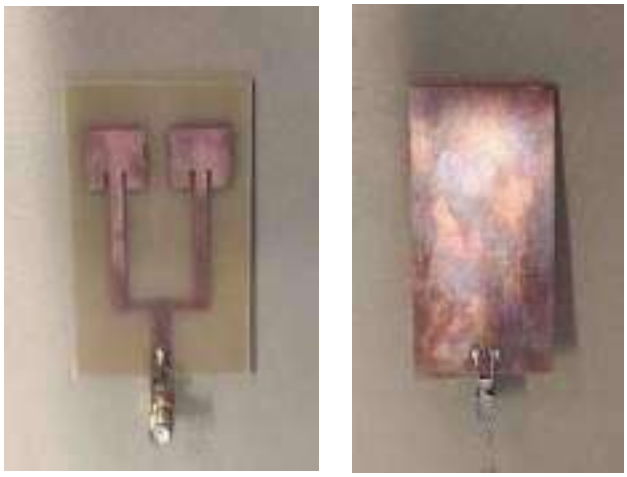

Fig.24. Antenna array (2×1) to be made (upper and lower face).

B. Measurement of reflection coefficient and standing wave ratio

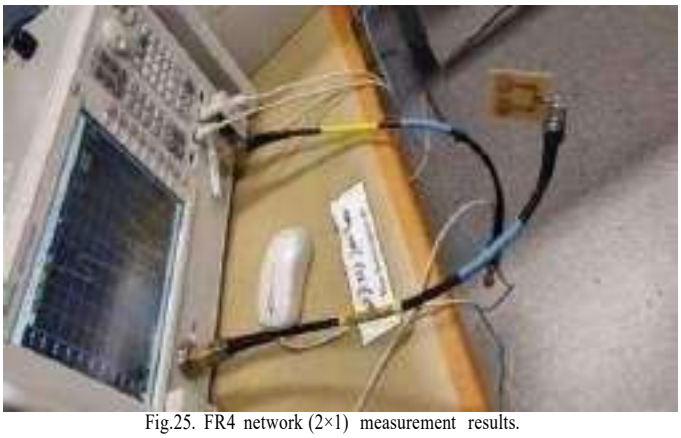

Fig.25. FR4 network (2×1) measurement results.

FR4 network (2×1) measurement results at the Algerian Space Agency-Satellite Development Center, Bir El Djir 31130-Oran-Algeria.

After exporting the analyzer results, we compared them with the electromagnetic simulation results. The simulation / measurement comparison of the antenna array (2×1) is given bythe following figures:

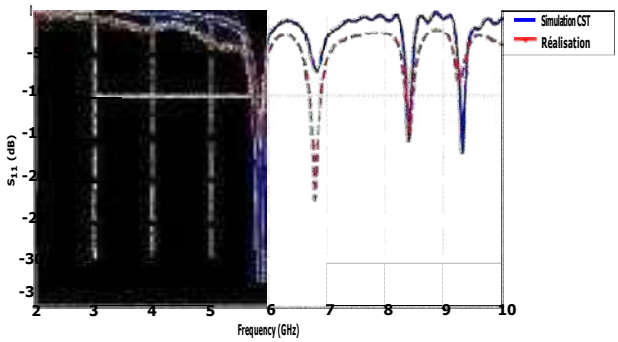

Fig. 26. Comparison of simulated and measured reflection coefficient of antenna arrays (2×1).

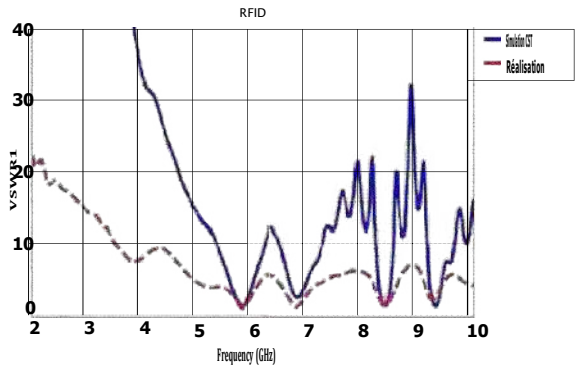

Fig. 27. Comparaison de VSWR simulé et mesuré réseaux d'antenne (2×1).

From figures 26,27 it is to be noted a slight frequencyshift of the bandwidths. For thenetwork, there isa slight lag between simulation and measurement, these differences can be attributed to manufacturing defects and/or measurement uncertainties. Despite these differences, theresults obtained in measurement respect the specifications set in our specifications [16, 17].

The main objective of our work is to find a solution that meets one of the requirements of the IoT which allows to have a higher gain, the solution is the establishment of an antenna network at 2 then to 4 elements from the elementary

the network are interconnected by a T-junction power divider [18, 19, 20]. Consequently, the analysis of the results shows a good adaptation to the 5.8GHz resonant frequency with a remarkable increase in gain. The results show that both 2-element and 4-element arrays have good performance in terms of S_{11}, gain, VSWRand efficiency.

In order to miniaturize our 2×1 and 4×1 antenna array, we used two miniaturization techniques using the first is to use a "partial ground plane", the second is to use a high permittivity substrate which is the "silicon" with a permittivity of 11.9. This technique allowed us to reduce the different dimensions of the planar antenna in order to increase the number of elements of the antenna network.

We conclude that the more we increase the number of elements per array, the more we have good improvements in the characteristics of the planar antenna.

Finally, 5G and IOT systems consume energy and their environmental impact must be taken into account. But the technological advances brought by the IoT can monitor the energy consumed, reduce it and avoid waste in many sectors of activity. In the very near future, it will be inevitable to study whether the positive effects of the Internet of Things on the environment outweigh the negative effects. If so, the deployment of IoT solutions for environmental purposes could continue to be deployed, with the aim of saving even more energy.

REFERENCES

[1] ROXIN, I., BOUCHEREAU A., "Ecosystème de l'Internet des Objets", dans Bouhaï N. et Saleh I., (dir.) "Internet des objets : Evolutions et Innovations ", ISTE Editions Londres, Mai 2017.

[2] THEBAULT P., « La conception à l'ère de l'Internet des Objets : modèles et principes pour le design de produits aux fonctions augmentées par des applications", Thèse soutenue le 31 mai 2013, ParisTech.

[3] CHALLAL Y. , « Sécurité de l'internet des objets :vers une approche cognitive et symétrique », HDR, juin 2012 UTC.

[4] WOOD L., "Today, the Internet, tomorrow—the Internet of Things", ComputerWorld,http://www.computerworld.com/s/article/9221614/Today_the_Internet_tomorrow_the_Internet_of Things, November 2011.

[5] Christophe Baland, Damien Cauquil, Thomas Gayet, Julia Juvigny, Renaud Lifchitz, Nha-Khanh Nguyen. La sécurité de l'Internet des Objets.Digital Security, Livre,2016.

[6] G. Kossiavas, R. Staraj, C. Luxey, A. Papiernik, "Antennes imprimées-Bases et principes", Technique de l'ingénieur, Référence E3310, 05/ 2007.

[7] Constantine A. Balanis, "Antennatheoryanalysis and design", A John Wiley& Sons, INC Publication, Third Edition. Hoboken, New Jersey 2005.

[8] VAUDON Patrick «Les antennes imprimées» – Master Recherche Télécommunications Hautes Fréquences et Optiques IRCOM – Université de Limoges.

[9] Christophe Caloz, Tatsuo Itoh "Electromagnetic Metamaterials: Transmission line theory and microwave applications", JOHN WIlEY&sons, 2006.

[10] T. BOUGOUTIA, « Analyse et conception des antennes microstrip à base de métamatériaux », Thèse de Doctorat Option Micro –Ondes, Université Mohamed Boudiaf-Msila, Mai 2018.

[11] SETHI, Pallavi et SARANGI, Smruti R. Internet of things: architectures, protocols, and applications. Journal of Electrical and Computer Engineering, vol. 2017.

[12] .Fayza BOUSALAH, Hayat .BENOSMAN, Amina SEDJELMACI, "Miniaturization of palanar antennas based on metamaterials for 5G and WIMAX communications applications", "JEEE: Journal o f

[13] Genc and Basyigit et al. Determination and modelling of dielectric properties of the cherry leaves of varying moisture content over 3.30– 7.05 GHz frequency range (2018).

[14] Fayza BOUSALAH, "Design of Miniature Planar Antennas for 5G Systems », Advances in Wireless Communications and Networks, 2021; 7(1):1-8.http://www.sciencepublishinggroup.com/j/awcn: 10.11648/j.awcn.20210701.11, ISSN: 2575-5951 (Print); ISSN: 2575-596X. Published 7 April 2021.

[15] Fayza BOUSALAH, Hayat BENOSMAN, " Design of metamaterial based planar antennas and their applications for 5G », Internationnal conference on advences in communications technology computing and engineering, ICACTCE2021. 24, 26 March 2021.

[16] Hayat BENOSMAN, Fayza BOUSALAH , " Design and Analyzes of Dual Band Microstrip Antenna based on Complementary Split Ring Resonator», Internationnal conference on advences in communications technology computing and engineering, ICACTCE2021. 24, 26 March 2021.

[17] MA Rabah, M Abri, J Tao, "TH VuongSubstrate integrated waveguide design using the two-dimensional finite element method", Prog Electromagn Res M, Vol 35, P21-30 on 2014.

[18] Fatima Zahra Marouf Mohammed Zakarya Baba-Ahmed, Mohammed Riyadh El Mansour Fekar, Nawel Seladji-Hassaine, " ", INTERNATIONAL JOURNAL OF MICROWAVE AND OPTICAL TECHNOLOGY, Vol 11, N°6, P460-468, Banmali S Rawat, 06 Nov 2016.

[19] Fayza Bousalah, Boukli Hacene Nour Eddine, Realisation and Optimization the System of Ridge Waveguide Polarizer by Genetic Algorithms for Telecommunication Satellite Antennas, IJCSNS, Vol 12, Issu 2, P 47, 01 Febryary 2012.

[20] Fayza Bousalah, Boukli Hacene Nour Eddine, Design of Simple and Double Ridge Waveguide T-Coupler for Space Domain, Applied Sciences, Vol 4, Issu 3, P 78-87, 15 Febryary 2019.

Study and design of a new array of wide band and high-gain planar antennas for 5G mobile network

Belhadef Yamina [#1], Bousalah Fayza [#2], Djelti Hamida [#3], Bouacha Abdelhafid[#4]

[#]Department of Telecomunications, Abou-Bekr Belkaïd University-Tlemcen
BP 230, Pôle Chetouane, 13000 Tlemcen- Algerie

[1]belhadef@yahoo.fr

[2]bousalah.fayza@gmail.com

[3]djelti_hamida@yahoo.fr

[4]abdelhafid.bouacha@gmail.com

***Abstract*—5G allows very high throughput, low latency and near-limited connectivity, especially in high frequency. It allows to take a larger volume of data and a larger number of users. Also, for the same volume of data processed, 5G is more efficient, i.e. it consumes less energy. With the new mobile network, it will be possible to transmit 4 times more data without increasing energy consumption. The research work presented in this article is part of the design of a printed antenna array for 5G applications. Initially, the aim of this work consists to study and design a new slot planar antenna structure working in the 28 GHz millimeter frequency band on 5G mobile networks. This structure was then used to design a printed antenna array with two radiating elements and then four radiating elements fed by power dividers. The design is based on the parametric study of the dimensions of the elementary slit antenna and the proposed patch antenna arrays. This work begets in improved performance of the proposed four-element antenna array based on the two-element antenna array in terms of matching, bandwidth and gain. These structures were designed in the CST MWSsimulator on a Roger 5880 type substrate.**

***Keywords*— Printed antenna, Antenna arrays, Power divider, Design, 5G, CSTMWS.**

I. INTRODUCTION

This The fifth generation (5G) of mobile telephony is one of the newest technologies in the wireless communications field. This advance should provide a very great service in terms of speed, diversity and ease. This technology aims to meet all the requirements of customers who aspire to advanced features in mobile phones [1], [2].

The 5G will consume half as much energy as the 4G at its launch, 10 times less by 2025 and 20 times less by 2030. The deployment of 5G could therefore produce long-term energy savings, but also a lower in greenhouse gas (GHG) emissions [3].

In order to meet the current needs of the 5G communication field, increasingly performance antennas are needed [4], [5], [6]. This is in the purpose to meet the increasing demands for antennas providing various functionalities for modern communications equipment. 5G antennas, unlike 4Gantennas, emit a targeted signal and activate on demand. They were also designed to save energy, thanks to the standby mode in the absence of traffic. For this, the designers have elavorated devices at based on printed antenna networks [7], [8], [9].

Printed antennas have very advantageous characteristics in terms of weight, volume, cost, simplicity of manufacture and especially the possibility of implanting them on any type of electronic device. Several researches have studied the characteristics of printed antenna arrays such as resonant frequency, bandwidth, radiation pattern, areal current distribution...etc. The patch antenna array concept is used to improve the gain of the differents elementary antennas and increase the bandwidth. Our main objective in this work is the study, simulation and design of new high gain, very high bandwidth planar antenna networks for fifth generation mobile networks byusing MWS CST software.

II. DESIGN OF THE INITIAL ANTENNA

Figure 1 shows the structure of the initial antenna under CST MICROWAVE STUDIO. This structure is composed of a radiating element of length L and width W, fed by a microstrip line. It is deposited on a dielectric substrate of type Rogers 5880. The ground plane covers the whole back face of the substrate. We introduced notches at the entry of the patch, as shown in Figure 1 :

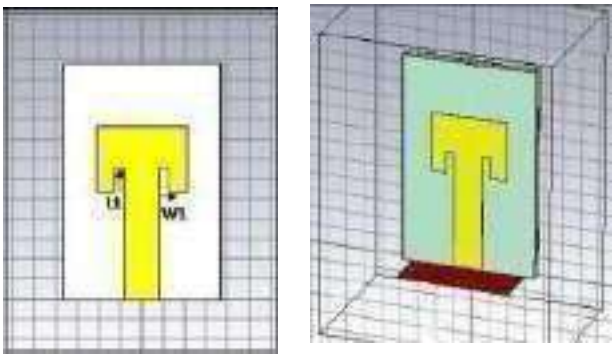

Fig. 1 Geometry of the initial antenna with notches

The dimensions of the initial patch antenna are mentioned in the following table and which are calculated from the theoretical equations of the rectangular patch antenna.[10], [11], [12]

TABLE I
DIMENSIONS OF THE INITIAL RECTANGULAR ANTENNA

	Dimensions (mm)	
	Length	**Width**
Patch	3.462	3.842
Ground plane et substrat	11.696	7.288
Feed line	5.36	1.578
Notches	1.182	0.412

In Figures 2 ((a), (b) and (c)), one represents respectively the return loss, the VSWR standing wave ratio and the gain of the initial antenna.

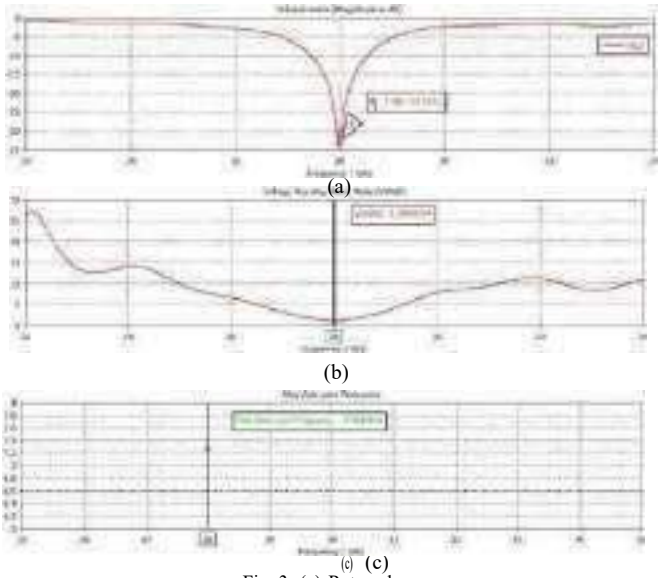

(a)

(b)

(c) (c)

Fig. 3. (a) Return loss
(b) Standing wave ratio
(c) Gain of the initial antenna

We can see that the adaptation is well carried out at the 28GHz resonant frequency with a peak of return loss coefficient equal to -33.51dB. We also measured the standing wave ratio (VSWR), it is equal to 1.04 and the maximum gain of the antenna equal to 7.30 dB. This then translates a perfect adaptation to the chosen frequency.

In figures 3. (a) and (b), one represents respectively the 2D and 3D radiation patterns of the antenna at the 28GHz resonant frequency.

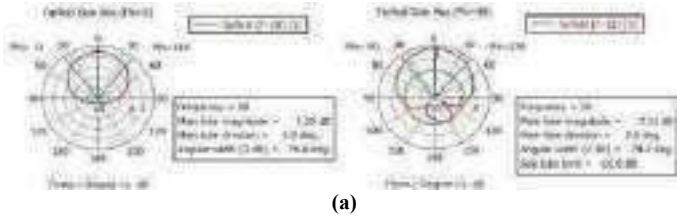

(a)

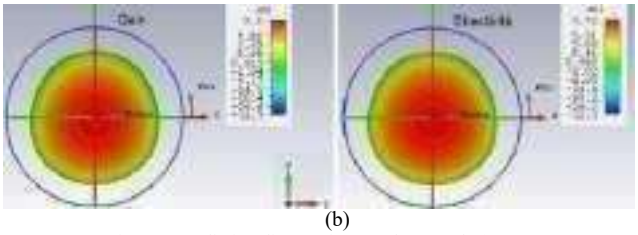

(b)

Fig. 3. (a) radiation diagram in 2D (Plan E and H)
(b) radiation diagram in 3D

From Figure 3, the antenna has a nearly omnidirectional radiation pattern in the two planes E (φ=0°) and H (φ=90°). These plots are verified on the 3D radiation pattern plot. This 3D radiation lobe containing the maximum energy of the radiation, the directivity equal to 7.72dBi and the gain is around 7.3dB.

The efficiency of the radiation is given by the ratio gain on directivity, in our case we obtained an efficiency equal to 94.55%.

III. DESIGN OF A SLOTTED NEW PATCH ANTENNA

We inserted rectangular-shaped slots on the radiating element of the initial patch antenna adapted to the 28GHz resonant frequency. The structure of this antenna on the editor of the CST MICROWAVE STUDIO is given by Figure 4.

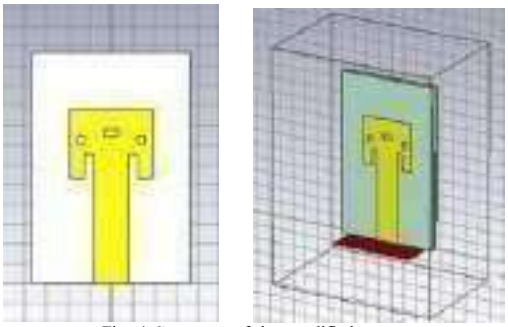

Fig. 4 Geometry of the modified antenna

In Figure 5, one represents the return loss of the antenna modified before the parametric study

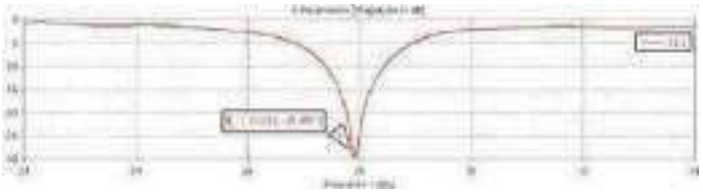

Fig. 5 Return loss

A. Variation of the W1 Width of the Notches

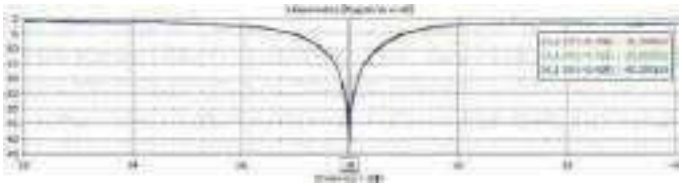

Fig. 6 Variation in the W1 width of the notches of the modified antenna

B. *Variation in the L length of Patch*

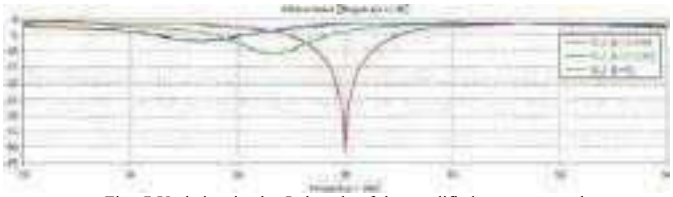

Fig. 7 Variation in the L length of the modified antenna patch

Based on the results found above, we can select the best adaptation of the modified patch antenna.

C. *Results After the Parametric Study of the Proposed Antenna*

In the following figures, one represents respectively the return loss, standing wave ratio, the maximum gain and the input impedance after the parametric study of the proposed antenna.

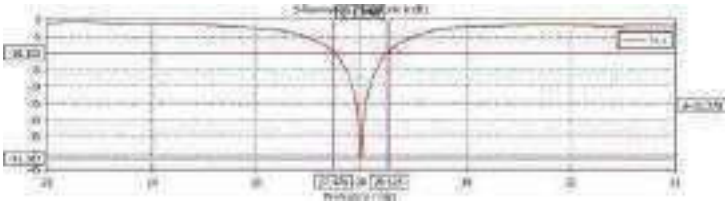

(a)

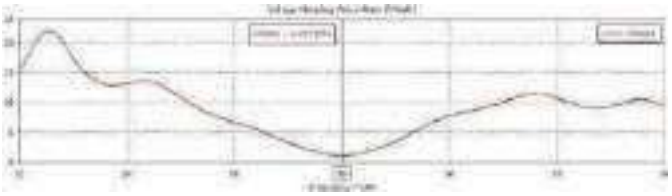

(b)

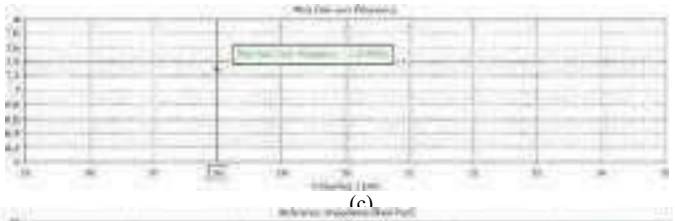

(c)

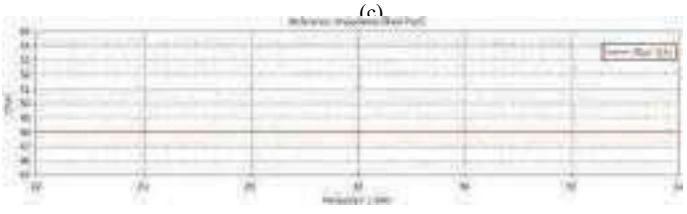

(d)

Fig.8. (a) Return loss
(b) Standing wave ratio
(c) Maximum gain of the antenna
(d) Real part of the input impedance

Figure 8. (a), shows that the adaptation is well carried out since the return loss S11 reaches a level close to -41 dB at the resonant frequency 28 GHz. The bandwidth is equal to 1.048 GHz.

The simulated standing wave ratio curve is shown in figure 8. (b) of value 1.017 which is less than 2, which shows a good impedance adaptation between the radiating element and the feed line.

In Figure 8. (c), the maximum gain equal to 7.31 dB, this explains a good match to the desired frequency. Similarly, the representation of the real part of the input impedance which is around 48 Ω (≈ 50Ω), shows a very good match of the proposed antenna.

Figures 9. ((a) and (b)), represent the 2D and 3D radiation patterns of the modified patch antenna.

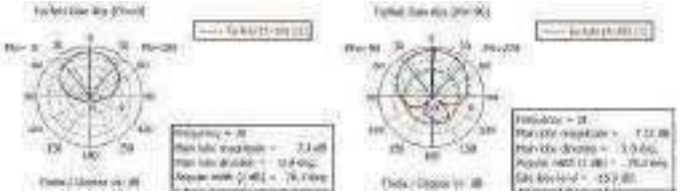

(a)

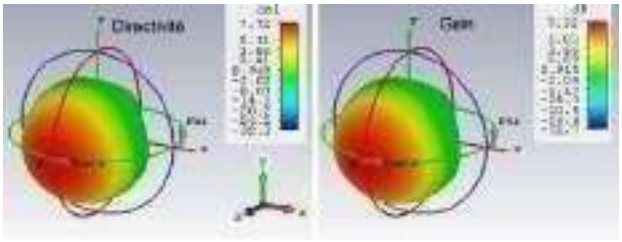

(b)

Fig. 9. (a) Radiation diagram in 2D (E and H plane)
(b) Radiation diagram in 3D

We notice that the antenna has an almost omnidirectional radiation in both planes E and H which are checked on the 3D radiation plot with a maximum gain value that is around 7.32dB and a directivity of 7.72dBi. This implies an efficiency of94.82%.

IV. TWO ELEMENT ANTENNA ARRAY AT THE BASE OF THE MODIFIED ANTENNA

Two-element antenna arraystructure is shown in Figure 10 :

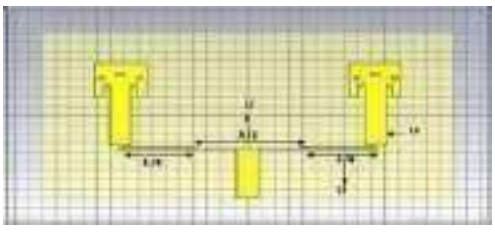

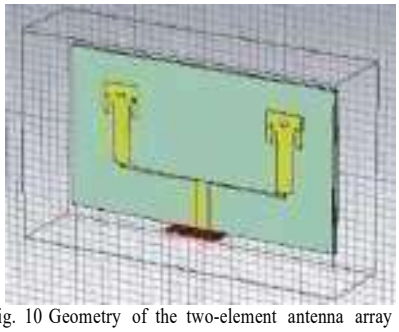

Fig. 10 Geometry of the two-element antenna array

First for a design of a 2-element antenna array, we calculated the length and width of the power divider at junction T as follows:

We use a half-wave line at the input of the main feed line of characteristic impedance calculated bythe following formula :

$$Zc - \frac{120\pi}{\sqrt{\varepsilon_{reff}}\left[\frac{W0}{h}+1.393+0.667\ln\left(\frac{W0}{h}+1.444\right)\right]}$$ half-wave line of

Then, we superimpose a horizontally characteristicimpedance equals to 100 Ω.

Finally, to connect the 100 Ω line with the feed line (50 Ω) of the elementary patch antenna, we use a Zc=70.71Ω impedance quarter wave line.

The quarter wave line impedance is calculated by the following equation:

$$Zc_{\frac{\lambda}{4}} = \sqrt{Z_{in} * Z_{out}}$$

With : Zc: The quarter-wave line characteristic impedance.
Zin : The input impedance.
Zout : The output impedance.

To calculate the width W of the T-junction power divider as a function of the characteristic impedance of the micro ribbon line, we use equation (**[13]** :

$$W - \frac{8e^{A}}{e^{2A}-2} * h$$

$$A - Zc\frac{\sqrt{2(\varepsilon_r+1)}}{120} + \frac{1}{2}\left(\frac{\varepsilon_r-1}{\varepsilon_r+1}\right) * \ln\frac{\pi}{2} + \frac{1}{\varepsilon_r}\ln\frac{\pi}{4}$$

TABLE II
WITH OF THE T-JUNCTION

Characteristic impedance (Ω)	**Width of the T-junction (mm)**
	Theoretical results
50	1.3958
100	0.4146
70.7	0.274

Thereturn loss of the two-element antenna arrayis shown in Figure 11:

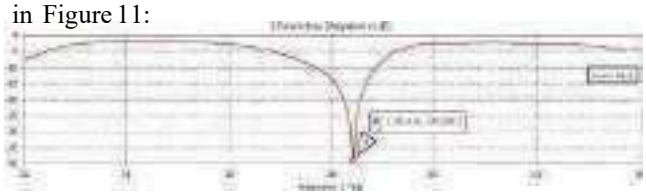

Fig.11 Return loss of the 2-element antenna array

To improve the matching we carried out a parametric study on thedimensions of the proposed two-element antenna array.

A. Variation in the L2 Length of T Junction

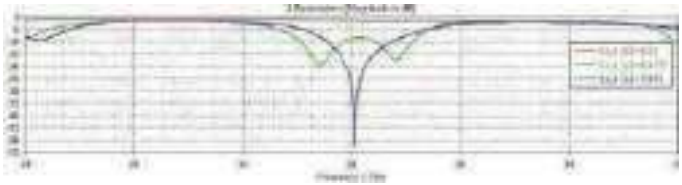

Fig. 12 Variation in the L2 length of T junction

B. Variation in the L3 Length of T Junction

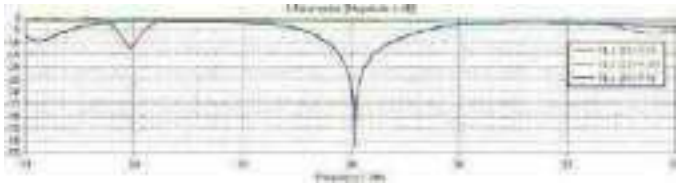

According to the two graphs (12 and 13) above, we notice an improvement of the adaptation which is obtained for L2=7.65mm and L3=5.4mm at the 28 GHz resonant frequency.

C. Results After Parametric Study of a 2-Element Antenna Array

In Figures 14 ((a), (b) and (c)), one represents respectively the return loss, the VSWR standing wave ratio and the real part of the input impedance after the parametric study of a two-element antenna array.

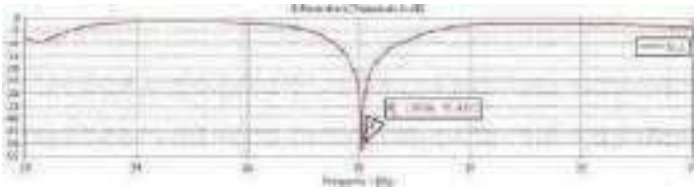

(a)

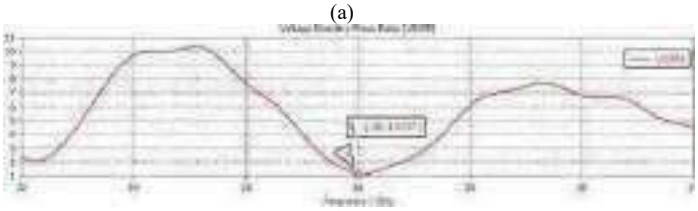

(b)

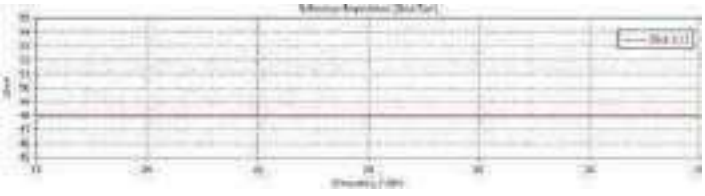

(c)

Fig. 14. (a) Return loss
(b) Standing wave ratio
(c) Real part of the input impedance

It can be seen that the adaptation is carried out at the resonant frequency 28GHz with a return loss of -51.81dB and a bandwidth of 1.27GH. We also measured the standing wave ratio (VSWR), it is equal to 1.07 and the input impedance is around 48 Ω (≈ 50Ω). This then reflects a perfect adaptation to the chosen frequency

(a)

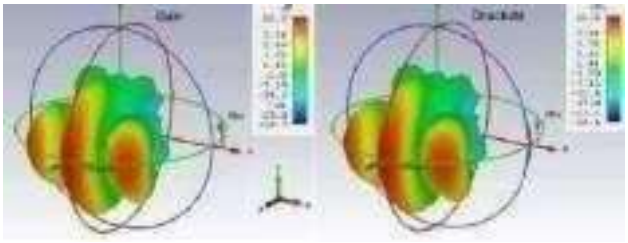

(b)

Fig. 15. (a) 2Dradiation diagram (E-plane and H-plane)
(b) 3Dradiation diagram

The figures above represent the 2D and 3D radiation diagrams of the antenna. We notice that the antenna is almost omnidirectional with a gain value that is around 11.3dB and a directivityof 11.6dBi, so the efficiencyis equal to 97.41%.

V. 4x1 Four-Element Array at the Base of the Two Element Antenna Array

Since the Rogers 5880 substrate gave us a better adaptation, we designed a four-element divider with the same method of the two-element divider calculations. We used a microstrip line of length L5=3λ/2 of characteristic impedance 100Ω, because if we use $\lambda/2$ ou λ, there will be an overlap between theantenna elements.

Figure 16 shows the structure of the four-element antenna array.

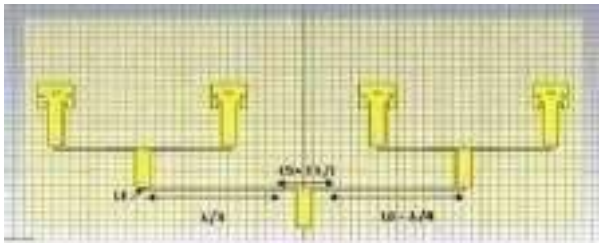

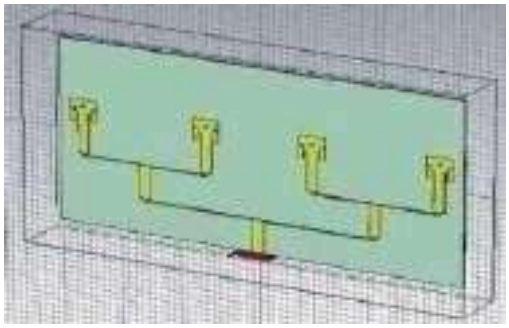

Fig. 16 Geometry of the four-element antenna array

Figure 17 shows the return loss of the four-element antenna array.

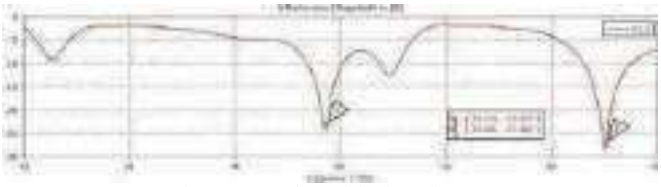

Fig. 17 Return loss of the four-element antenna array

We do not observe any adaptation to the 28GHz resonant frequency. On the other hand, the adaptation is carried out to the resonant frequencies 27.716 GHz and 33.045 GHz, which gives a dual-band operation. So to improve this result, we performed a parametric study on the dimensions of the four-element antenna array.

A. Variation of the Length L5 and L6 of the Power Divider

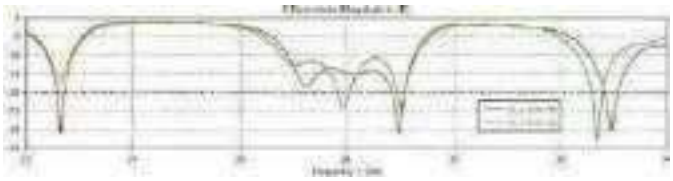

(a)

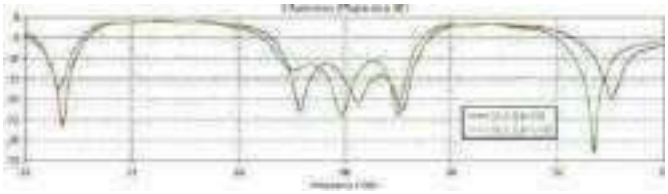

(b)

Fig. 18. (a) Variation of the length L5 of the power divider
(b) Variation of the length L6 of the power divider

From the two graphs above, we notice an improvement of the adaptation which is obtained for L5=5mm and L6=14.6mm at the 28 GHz resonant frequency.

B. Results After Parametric Study of a Four-Element Antenna Array

In Figures 19. ((a), (b), and (c)), one represents respectively the return loss, VSWR standing wave ratio, and gain of the

antenna after the parametric study of the proposed antenna array.

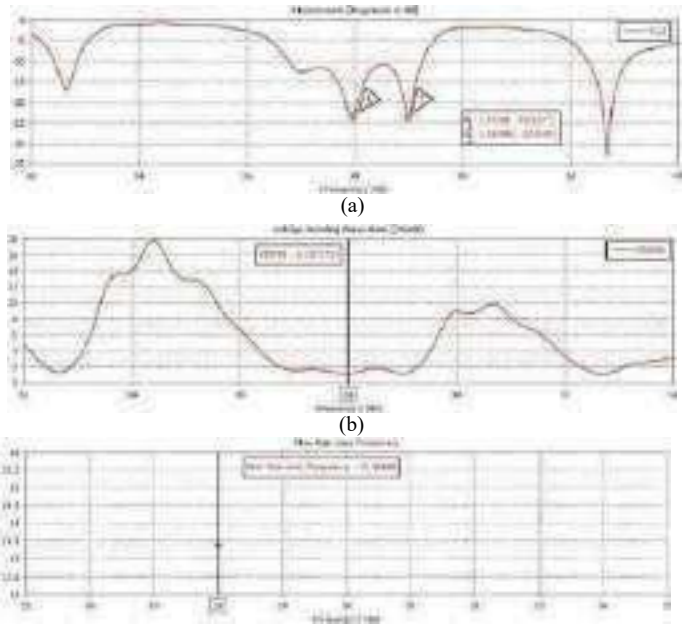

(a)

(b)

(c)

Fig. 19. (a) Return loss.
(b) Standing wave ratio.
(c) Maximum gain of the antenna.

According to the results obtained, we have a favorable adaptation to the 28 GHz resonance frequency with a reflection coefficient S11 equal to -23.54dB. The bandwidth is equal to 2.5GHz, which gives ULB operation of the antenna. The maximum gain is equal to 13.38 dB at the chosen resonance frequency. On the following figures, one represents the 2D and 3D radiation patterns of the four-element antenna arrayat the 28GHz resonant frequency.

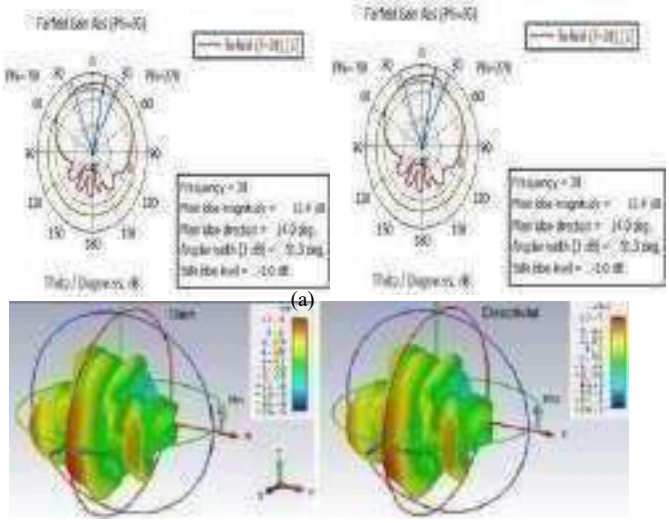

(a)

(b)

Fig. 20. (a) Radiation pattern in 2D (E-plane and H-plane)
(b) Radiation pattern in 3D

We notice that the antenna has a almost omnidirectional radiation in both planes (E and H). The 3D plot gives a good exploration of the radiation pattern. The gain of the antenna is equal to 13.4dB, which gives an efficiency that is around 97.81% (≈98%).

VI. Comparison of the Results Obtained

Table 3 provides a comparison between the proposed new structures with a Rogers 5880 type substrate :

TABLE IIII
Comparison Between the Proposed New Structures width a Rogers 5880Type Substrate

	Modified patch antenna	**2 element array**	**4 element array**
Return loss (dB)	-41	-51.81	-23.54
Gain (dB)	7.32	11.3	13.4
Efficiency(%)	94.82%	97.41%	97.81%
Bandwidth(GHz)	1.048	1.27	2.5

VII. Conclusion

5G must allow a jump in performance in terms of throughput, instantaneity and reliability. The energy efficiency of the 5G network was taken into account at the design phase. 5G will help develop smart grids that will help better control our water and electricity consumption. As an example: adaptation of watering to the level of humidity in the soil, better regulation of collective heating, etc. The 5G will therefore be an essential lever of the ecological transition if its applications are intelligently used.

Through this article, we have designed a rectangular printed antenna feed by a microstrip line with a Rogers 5880 type substrate and which resonates at the 28GHz (5G) resonance frequency. In purpose to improve the performance of the initial antenna which is determined from theoretical calculations of the rectangular patch antenna where we have seen a mismatch at the chosen frequency. We did a parametric study on the patch dimensions and the notches. The positive effect of this study on adaptation is clearly observed using the MWS CST software. After this study, we designed a new slotted antenna structure, then 2-element and 4-element antenna networks powered by T-junction power dividers in order to successively increase the performance of these proposed structures (gain, bandwidth and efficiency). In conclusion, we determined a solution which meet one of the requirements of 5G which is the highest gain and bandwidth, this solution was the networking at four elements that are connected together by a T-junction power divider from the rectangular patch antenna. This new four-element patch antenna array structure is successfully designed.

REFERENCES

[1] W. Roh et al, "Millimeter-Wave Beamforming as an enabling technology for 5G cellular communications: theoretical feasibility and prototype results," IEEE Comm. Magazine, pp. 106-113, Feb.2014.

[2] Mushtaq Talib, Norazizah Binti Mohd Aripin, Noor Shamsiah Othman, Adheed Hasan Sallomi, "Comprehensive Overview on Millimeter Wave Communications for 5G Networks Concentrating on Propagation Models for Different Urban Environments," 3rd International Conference on Mathematics and Applied Science (ICMAS 2022), Journal of Physics: Conference Series, doi:10.1088/1742-6596/2322/1/012095

[3] Michaël Trabbia, "L'impact de la 5G à l'horizon 2030", 2021 Omdia, www.orange.com

[4] Ali Abdulateef Abdulbari, Mustafa Mohammed Jawad, H. O. Hanoosh , Murtaja Ali Saare, Saima Anwar Lashari, Sari Ali Sari, Sarosh Ahmad , Yaser Khalill, Yaqdhan Mahmood Hussain, "Design compact microstrap patch antenna with T-shaped 5G application," Bulletin of Electrical Engineering and Informatics, Vol. 10, No. 4, August 2021, pp. 2072-2078 ISSN: 2302-9285, DOI: 10.11591/eei.v10i4.2935

[5] Bahadır HİÇDURMAZ and Ömer Faruk GÜMÜŞ, "Design and analysis of 28 GHz microstrip patch antenna for different type FR4 claddings," Uludağ University Journal of The Faculty of Engineering, Vol. 24, No. 2, 2019, DOI: 10.17482/uumfd.548410.

[6] Shehab Khan Noor, Nurulazlina Ramli, Norsuzlin Mohd Sahar and Taher Khalifa, "Compact and Wide Bandwidth Microstrip Patch Antenna for 5G Millimeter Wave Technology: Design and Analysis, " CE4CT 2020, Journal of Physics: Conference Series,doi:10.1088/1742-6596/1878/1/012008.

[7] Md Mohiuddin Soliman and Mohammad Lutful Hakim, "Design and simulation of microstrip patch antennas for 5G wireless communication," Department of Electronic and Telecommunications Engineering, October, 2019.

[8] Samarth Agarwal and Prachi, "High Gain Linear 1×4 X-slotted Microstrip Patch Antenna Array for 5G Mobile Technology," Journal of telecommunications and information technology, https://doi.org/10.26636/jtit.2020.137319.

[9] Safpbri Johari, Muhammad Abdul Jalil, Shaifol Ifrad Ibrahim, Mohd Nazry Mohammad and Norhafiza Hassan, "28 GHz Microstrip Patch Antennas for Future 5G," Journal of Engineering and Science Research, pp.01-06, 2018, ISSN: 2289-7127, DOI: 10.26666/rmp.jesr.2018.4.1

[10] C.A. Balanis, "Antenna theory analysis and design," Arizona State UniversityTempe, AZ. 2005.

[11] C.A. BALANIS, "Advanced engineering electromagnetics," John Wiley & Sons, New York, 1989.

[12] G. KUMAR and K.P. RAY, "Broadband microstrip antennas," Artech House, Inc, 2003.

[13] N.L. Chon, "Photonic Antenna for Wireless Local Area Network backhaul Application," Unpublished Master's Thesis, University Technology, Malaysia 2010.

Activités anti oxydante et Antimicrobienne des huilesessentielles et des extraits végétaux de la camomille *(Chamaemelum nobile).*

SANA DALLALI
Laboratoirede Recherches en Systèmes de Production Agricole et de Développement Durable, Ecole,Supérieure d'Agriculture, Mograne, Zaghouan Tunisie,
sanadallali02@gmail.com

RABIAA MOUHBI
Laboratoire des Ressources Sylvo-Pastorales. *Institut Sylvo-Pastoral de Tabarka, Université de Jendouba*
Tabarka, Tunisie
mouhbirabiaa@gmail.com

HOUCINE SELMI
Laboratoire des Ressources Sylvo-Pastorales. *Institut Sylvo-Pastoral de Tabarka, Université de Jendouba*
Tabarka, Tunisie
houcine_selmi@live.fr

HANENE BOURAOUI
Laboratoire des Ressources Sylvo-Pastorales. *Institut Sylvo-Pastoral de Tabarka, Université de Jendouba*
Tabarka, Tunisie
hanenebouraoui@yahoo.fr

***Résumé*— La méthode appliquée pour mesurer l'activité antioxydante est la DPPH, tandis que pour l'activité antimicrobienne est celle de la diffusion en milieu solide. Une analyse statistique a été conduite, à partir des donnés obtenues pour chaque paramètre étudié. Le rendement en huile essentiel était de 11,89%. L'étude de la composition des lipides dans les tiges et dans les fleurs de, *Chamaemelum nobile,* a montré que les rendements en lipides totaux varient significativement entre les organes de la plante .La teneur en lipides la plus élevée est observée au niveau des fleurs (36,4mg/g), par rapport aux tiges (1,02 mg/g). Les résultats ont révélé que les différentes analyses montrent que *Chamaemelum nobile* dispose d'une teneur assez élevée en polyphénols ; en flavonoïde et en tanin.**

L'étude de l'activité antioxydante de l'extrait méthanolique, de différentes organes de *Chamaemelum nobile,* révèle que les fleurs renferment plus de polyphénols et montrent une capacité antioxydante plus importante que celle notée chez la tige. Pour l'activité antibactérienne ; l'huile essentielle du *Chamaemelum nobile,* exerce une activité antibactérienne très importante, sur les souches testées. On peut conclure que l'huile essentielle de cette espèce représente une source naturelle de composés actifs importants, doués d'activités biologiques considérables.

Mots clé—: *Chamaemelum nobile* /Huile essentielle / Rendement / Activité antioxydante / Activité antibactérienne

I. INTRODUCTION

La Tunisie, de par sa situation géographique particulière, bénéficie d'une gamme très variée de Climats, favorisant le développement d'une flore riche et diversifiée. En effet, la Tunisie abrite plus de 2160 espèces végétales, dont plus de 350 sont reconnues comme étant à vertus médicinales (Zaouali, 2005 ; Ben Issa, 2011).

Ces espèces possèdent une valeur importante, non seulement en tant qu'élément de la biodiversité, mais aussi en tant qu'élément de la diversité culturelle, dont leur valorisation demande une parfaite connaissance à mettre en valeur. Plusieurs Plantes Aromatiques et Médicinales (PAM) possèdent des propriétés biologiques très intéressantes et trouvent des applications dans divers domaines, tels que les industries pharmaceutiques et la médicine. Ces plantes représentent une nouvelle source de composés actifs. En effet, les métabolites secondaires font l'objet de nombreuses recherches *in vivo* et *in vitro*, notamment la recherche de nouveau constituant naturel, tel que les composés phénoliques et les huiles essentielles (HAZZIT, 2015). Les Produits Forestiers Non Ligneux (PFNL), en Tunisie, peuvent être exprimés comme étant un produit (bipolaire), vu le double rôle qu'ils jouent, soit dans la vie de la population locale, dont elle tire des revenus non négligeables, pour financier ses dépenses annuelles, ou bien en les utilisant dans des besoins familiaux, soit dans l'économie nationale du pays, comme produit d'exportation, rapportant des devises assez importantes (Chouayet, 2013). Les plantes médicinales peuvent être des espèces cultivées, mais dans la plupart des cas, sont des espèces spontanées, d'où la nécessité de l'identification précise des plantes employées.

L'identification précise des plantes représente une nécessité concrète, car elle est la base de l'utilisation sécuritaire des produits naturels de santé, à base de ces plantes. Sans une identification botanique appropriée au départ, l'utilisation, sans risque, de produits de qualité, ne peut pas être garantie. Étant donné le nombre considérable de végétaux supérieurs, plus de 250 000 dans le monde, il est nécessaire d'avoir un système de classification, à la fois simple et rationnel. Encore faut-il, au préalable, pouvoir désigner toute espèce végétale, d'une façon claire, précise et identique pour tous (Lamnaouer, 2002).

Les études de Benjilali et Zrira (2008), ont permis de montrer que le secteur des Plantes Aromatiques et Médicinales (PAM) connaît une grande activité de recherche-développement à travers le monde. La camomille est une Plante Aromatique et Médicinale, utilisée dans plusieurs domaines. Cette étude à pour

ISSN: 1737-9334

objectif d'évaluer sa composition chimique, ses activités antioxydante et antibactérienne

II. MATERIEL ET METHODES

A. Materiel végétal

Le matériel végétal est constitué de la partie aérienne de l'espèce «*Chamaemelum nobile».* La collecte des échantillons était entreprise manuellement et de manière aléatoire, le 20 février 2021, les plantes étaient en pleine floraison. Les coordonnées géographiques sont déterminées par GPS

Tableau 1: coordonnées des échantillons

Espèce	Provenance	Altitude	Longitude	Latitude
Chamaemelum nobile	Tabarka	76,7 m	8.7904660	36.9274776

1. Préparation du matériel végétalSéchage

La partie aérienne de l'espèce, ainsi collectée, est mise à sécher sur du papier, à température ambiante, à l'abri de la lumière et de l'humidité. Elle est régulièrement retournée. Une fois sèches, ces parties aériennes sont récupérées dans des sacs propres.

Broyage

Les échantillons de *Chamaemelum nobile* ont été coupés en petits morceaux afin de faciliter leur broyage. Les tiges et fleures sont broyées directement à l'aide d'un broyeur mécanique .Le broyat constitue le matériel végétal final que nous avons utilisé pour la préparation des extraits méthanolique.

Détermination du rendement en huileessentielle

Selon la norme AFNOR (1986), le rendement en huile essentielle (RHE) est défini comme étant le rapport entre la masse d'huile essentielle obtenue après l'extraction (M') et la masse de la matière végétale utilisée (M).

Le rendement est exprimé par la formule suivante :

RHE (%) = M'/M × 100 RHE

RHE : Rendement en huile essentielle en ٪.

M' : Masse d'huile essentielle en gramme.

M : Masse de la matière végétale sèche utilisée en gramme.

Extraction des lipides totaux

L'extraction des lipides totaux a été réalisée par la méthode de Bligh et Dyer (1959).La matière végétale, déjà séchée et finement broyée, a été fixée par l'eau bouillante pour inactiver les phospholipides des tissus (Benson et Strickland, 1960).Un gramme de matière végétale est broyé dans un mortier, en présence de 10 ml de chloroforme et de 5 ml de méthanol. Le mélange est ensuite filtré dans des tubes à essai et est déposé dans une étuve à 60°C.

$$\text{teneur en lipide totaux}\% = \frac{\text{masse del extrait}}{\text{masse de prise d'essais (matière végetale)} \times 100}$$

Dosage descomposées phénoliques

Préparation des extraits bruts méthanolique

L'extraction des composées phénoliques a été effectuée selon la méthode d'Owen et Johns**.** Une prise d'essai de 1g de poudre de chaque partie de la plante est macérée dans 20 ml de méthanol, pour les extraits méthanolique et, 20 ml eau distillée, pour les extraits aqueux. L'extrait a été conservé à 4°C pendant 24 h. Après filtration, les solutions méthanolique et aqueuses sont évaporées à sec sous pression réduite à 45°C. Les résidus secs sont pesés et repris par 3 ml de méthanol (Benhamou et *al.,* 2009).

Calcul des rendements des extraits secs

Le rendement d'extraction est calculé par la formule donnée par Falleh et *al.,* (2008) :

$$R\ (\%) = (M_{ext} / M_{éch}) \times 100$$

Avec **:**

-R% : rendements en %

-M ext : masse de l'extrait après évaporation du solvant en mg

-Méch : masse sèche de l'échantillon en mg.

-

1.5.3 Dosage des phénols totaux

Le dosage de poly phénols totaux a été effectué selon la méthode de singleton et *al.* (1999).Cette méthode consiste en une préparation, dans des tubes à essai, d'un mélange de 500 µl d'extrait avec 5 ml duréactif deFolin-Cieucalteu (diluer à 1/10). Ce mélange a été neutralisé avec 1 ml d'une solution aqueuse de carbonatede sodium (7.5%). L'ensemble est incubé à une température de 30 °C, pendant 1h, puis on effectue une lecture de l'absorbance, à 760 nm, en se référant à un blanc sans extrait et à l'aide d'un spectrophotomètre (Jenway-6300 UV/Visible). La teneur en poly phénols totaux a été déterminée par l'étalon, réalisé avec différentes concentrations d'acide gallique .Les résultats sont exprimés en mg Equivalent d'Acide Gallique par g de matière sèche (mg EAG/g MS), en utilisant l'équation suivante : y = 0,0045x (R^2= 0,990) où «y» est l'absorbance, «x» est l'équivalent d'acide gallique (mg/g MS) et «R^2» est le coefficient de détermination de la courbe d'étalonnage.

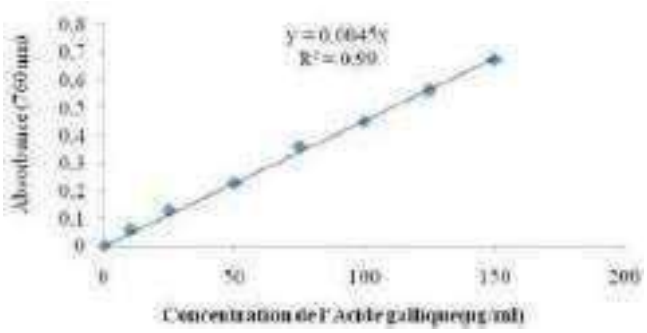

Figure 1: Courbe d'étalonnage de l'acide gallique

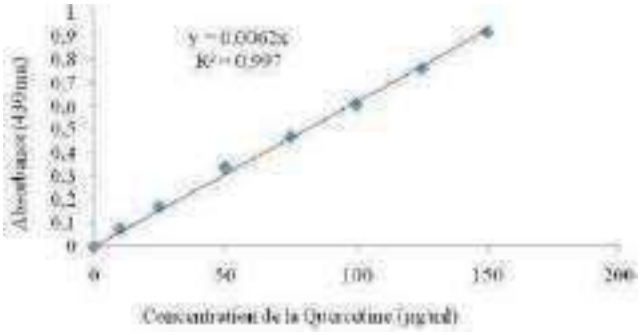

Figure 2: Courbe d'étalonnage de la Quercétine

La teneur en polyphénols totaux a été calculée en utilisant l'expression suivante :

Phénols totaux (ug EAG/g MS)=C*V/M

Avec :

-c : Concentration de l'acide gallique, établie à partir de la courbe d'étalonnage (µg/ml).
-V : Volume de l'extrait méthanolique (ml).
-m: Masse de l'extrait (g).

Dosage de flavonoïdes totaux

Le dosage des flavonoïdes totaux a été effectué selon la méthode du trichlorure d'aluminium, en suivante le protocole de (Yi et *al.* 2007).On prépare, dans des tubes à essai, un mélange d'1 ml de l'extrait, avec 1ml d'une solution méthanolique de chlorure d'aluminium de solution $alcl_3$ (2% dans le méthanol). Ce mélange est à incuber à l'obscurité, pendants 15 min, puis l'absorbance est lue à une densité de 430 nm, contre un blanc, à l'aide d'un spectrophotomètre (Jenway-6300 UV/Visible). Une courbe d'étalonnage, établie par de la Quercétine, est réalisée dans les mêmes conditions opératoires que les échantillons, servira à la quantification des flavonoïdes totaux. La teneur en flavonoïdes est exprimée en milligramme d'Equivalent de Quercétine par g de matière sèche (mg EQ/g MS), en utilisant la courbe d'étalonnage de la Quercétine (y = 0,0062x ; R^2 = 0,997). «Y» est l'absorbance, «x» est l'équivalent de Quercétine (mg/g MS) et «R^2» est le coefficient de détermination de la courbe d'étalonnage :

La teneur en Flavonoïdes totaux a été calculée en utilisant la formule suivante :

Flavonoïdes totaux (µgEQ/g MS) =(c x V) / m

Avec :

-C : Concentration de la Quercétine établie à partir de la courbe d'étalonnage (µg/ml).
-V : Volume de l'extrait méthanolique (ml)
-m: Masse de l'extrait (g).

Tannin condensé

L'évaluation de la teneur totale en tanin condensé a été déterminée en utilisant une méthode décrite par (Sun et *al.*; 1998). On mélange, dans un tube à essai, 50ul de l'échantillon, 3 ml de solution de vanilline (4% dans le méthanol) et 1,5 ml de H_2SO_4 concentrés. Le mélange a été laissé à l'obscurité, pendant 15 min, puis on mesure à l'absorbance 500 nm. La teneur en tanin est déterminée à partir d'une gamme étalon de Catéchine.

Tanincondensé (µg EC/g MS) = (DO*V)/(c*RS)

Avec :

DO : densité optique (nm)
V : volume de 3ml de méthanol pour la solubilisation les résidus secs (ml)
Rs : poids des résidus secs (g)
C : concentration de catéchine

1.6.1 Détermination de la teneur en tanin totaux

L'évaluation de la teneur en tanins totaux a été déterminée selon la méthode décrite par (Kujala et *al.,* 2000). On mélange dans un tube à essai 50ul l'extrait aqueux, dilué avec 0.5 ml de Folin-Cieucalteu (50%), ce mélange est à incuber pendant 2 à 4 min, puis on lui ajoute 1ml de carbonate de sodium (20%) et on l'incube pendant 10 min et on le centrifuge, pendant 10min (1000 T). L'absorbance de surnageant a été mesurée à 730nm.

La teneur en tanin total a été exprimée en équivalent acide tannique

Teneur en Tanin total (mg AT/g MS) = ((DO/a) *V*F) /PE

Avec :
DO : densité optique à 730nm
A : le coefficient déterminé à partir de l'équation de courbe d'étalonnage d'acide tannique
V : volume de l'extrait (20ml)
F : facteur de dilution
PE : poids de la prise d'essai (g)

B. Évaluationdes activités biologiques

1. Évaluation de l'activité antioxydante (DPPH)

Cette méthode est basée sur la mesure de la capacité des antioxydants à piéger le radical 2,2-diphenyl-1-picrylhydrazil (DPPH.), de couleur violette foncée, qui se transforme en coloration jaunâtre (après réduction). Cette décoloration est mesurable par spectrophotométrie (Brand-Williams et *al.,* 1995).
Le DPPH (2,2-diphenyl-1-picrylhydrazil) est généralement le substrat le plus utilisé pour l'évaluation rapide et directe de l'activité antioxydante, en raison de sa stabilité en forme radicale libre et la simplicité de l'analyse. Il absorbe dans le visible à la longueur d'onde de 515 à 520 nm (Bozin et *al.,* 2008 ; Kholkhal et *al.,* 2013).
Dans ce test, le DPPH de couleur violette se réduit en un composé jaune, le diphényl picryl hydrazine, dont l'intensité de la couleur est inversement proportionnelle à la capacité réductrice des antioxydants présents dans le milieu (Sanchez Moreno, 2002).
En effet, 1ml de chaque solution méthanolique des extraits à différentes concentrations (1, 3, 10, 100 µg /ml) sont ajoutés à 1ml de la solution méthanolique du DPPH (2,4 mg/100 ml). Parallèlement, un contrôle négatif est préparé en mélangeant 1ml de méthanol avec 1ml de la solution méthanolique de DPPH. La lecture de l'absorbance est faite contre un blanc préparé pour chaque concentration à 517 nm après 30 min d'incubation à l'obscurité et à la température ambiante. Le contrôle positif est représenté par une solution d'un antioxydant standard ; l'hydroxy toluène butyle (BHT) dont l'absorbance a été mesurée dans les mêmes conditions que les échantillons et pour chaque concentration, le test est répété 3 fois. Les résultats ont été exprimés en pourcentage d'inhibition (I%)(Bougandoura et Bendimerad, 2012). L'activité anti-radicalaire est estimée selon l'équation suivante :

I%= [(Abs contrôle – Abs test)/ Abs contrôle] x 100

Avec :
I% : pourcentage d'inhibition
Abs contrôle : densités optique du contrôle
Abs test : densité optique d'extrait

2. Évaluation de l'activité antibactérienne

L'activité antibactérienne d'huile essentielle de la camomille romaine a été testé contre certaines souches bactériennes, disponibles au laboratoire de microbiologie du l'Institut Sylvo -Pastoral de Tabarka. Ces souches sont composées de deux bactéries à Gram positif et deux à Gram négatif, comme montre le tableau 5.

Tableau2: Classification des souches bactériennes utilisées

Bactérie à Gram positif	Bactérie à Gram négatif
Listeria monocytogenes	*Escherichia Coli ATCC 25922*
Bacillus subtilis ATCC 6633	*Salmonella enterica* (denrée alimentaire)

Méthodologie des tests antibactériens

Préparationdu milieu de culture

On prépare, dans un premier temps, un milieu de culture, qui est constituée par 3,25g de NB, mélangé à 50ml d'eau distillée. En second temps, on prépare le milieu gélosé, pour 1L d'eau distillée on ajoute 15g d'Agar-Agar et 13g de NB. Une fois les milieux sont bien agités, ils sont autoclavés à 121°C, pendant 20minutes. Les pré-cultures des souches sont composées de 20 ml de NB (Nutrim Broth) liquide et de 100 µl de la souche bactérienne, le mélange est incubé à 37°C, durant une nuitée, dans un bain marie.

Préparation des boites de pétries

À l'intérieur de l'hôte, on remplit les boites de pétries par le milieu gélosé (90 cm de diamètre), à raison de 20 ml/boite, support qui permet la culture des bactéries.

Ensemencement

Dans chaque boite de pétrie on verse, à l'aide de micropipette, 100µL de souche bactérienne, puis on étale dans tous les sens, de sorte à couvrir toute la surface de la boite gélosée, à l'aide d'une raclette d'ensemencement.

Méthode de puits

Cette méthode a été décrite par (Güven et a*l.* 2006). Elle est basée sur la technique de diffusion en milieu solide. Après le séchage des boites, pendant 2 heures à température ambiante, la gélose est perforée à l'aide de la partie supérieure d'une pipette Pasteur, à raison de 3 puits par boite. Les cavités, ainsi formées, sont remplies comme suit :
La première cavité par 70µL de l'antibiotique (Gentamicine 80) : contrôle (+).
La deuxième cavité par 70µL de DMSO : contrôle (-).
La troisième cavité par 70µL de dose bien déterminée de l'HE de la camomilleromaine
Finalement, on doit bien enfermer les boites de pétries par le Para film.

Incubation des boites de pétries dans le réfrigérateur puis dans l'étuve

Les boites de pétri, ainsi préparées, sont incubées à +4°C, pendant 3 à 4h, pour permettre la diffusion des huiles essentielles présentes dans les puits. En dernier lieu, les boites seront incubées à l'étuve à 37°C pendant 48h. Après 48 heures d'incubation, on mesure, à l'aide d'une règle graduée, le diamètre d'inhibition des bactéries auteur des disques. Le diamètre (mm) de la zone entourant le disque est proportionnel à la sensibilité du germe étudié.

C. Détermination des teneurs en MS ;MO, Carbone et MM

1. Détermination des teneurs en Matière organique et en Matière minérale

Par référence à (AOAC. ;1995) ; la teneur en matière minérale a été déterminée après incinération complète, à 550 °C, des échantillons dans un four à moufle (durant 4 à 5 heures), jusqu'à la calcination totale. Après calcination totale : les creusets seront refroidis dans un dessiccateur, puis pesés. La perte du poids observé correspond à la MO et le résidu constitue les cendres totales.

MO%=100-%MM

et

MM%=(P1-P2)*100/PE

Avec :

P0 : poids du creuset vide en g
PE : prise à l'essai en g
P1 : Poids de l'échantillon avec creuset en g

2. Détermination teneur en carbone

La teneur en carbone est déterminée par la formule suivante :

C% =%MO/1.724

3. Détermination de la teneur en Matière Sèche

Par référence (AOAC.1995) ; on pèse 5 g d'échantillon de la plante (appelé masse fraîche), chauffés dans uneétuve de séchage, à une température de 105 ° C, pour permettre à l'humidité résiduelle (généralement de l'eau) de s'évaporer. On obtient la teneur en matière sèche du mélange.

MS% = (P0-P1) *100

Avec **:**

MS : matière sèche
P0 : poids du l'échantillon frais
P1 : poids de l'échantillon sec.

D. Analyses statestiques

Les analyses statistiques des données ont été effectuées à l'aide du Logiciel SAS (Statistics Analysis System) version 9.1. Toutes les analyses sont faites, au moins, en trois répétitions et les résultats ont été exprimés en moyenne±écart-type. Une analyse de la variance (ANOVA), suivie par le test multirange de Duncan a été appliquée pour comparer les moyennes, au seuil de probabilité de 5%. L'utilisation des méthodes décrites ci-dessus a conduit aux résultats qui vont être exposés dans le chapitre suivant.

III. RESULTATS ET DISCUSSION

A. Teneur en lipides totaux

Les résultats de la teneur en lipides totaux des organes tige et fleurs du *Chamaemelum nobile* sont présentés dans la figure 1. D'après ces résultats ; on constate qu'il y a une variation au niveau des teneurs en lipide totaux entre les deux organes de la plante. En effet, les fleurs sont plus riches en lipide (36,4mg/g de matière sèche) que la tige (1,02 mg/g de matière sèche).

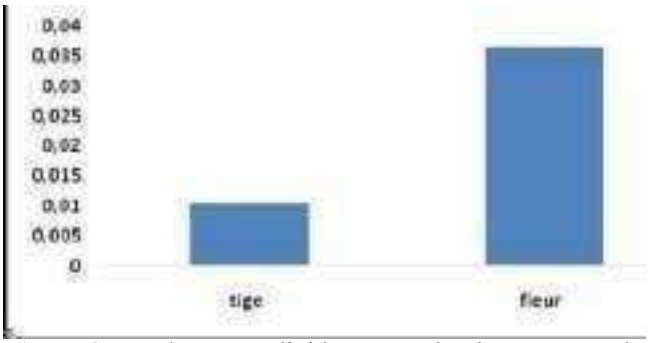

Figure 3: Rendement en lipides totaux des deux organes du *Chamaemelum nobile*

Les variations de la teneur en lipides totaux observées pourraient être dues à l'hétérogénéité de l'échantillon, de point de vue âge des organes, et/ou à l'effet des facteurs génétiques et des conditions environnementales et édaphiques (Uzun et *al.,* 2002; Ravi et *al.,* 2007). Elles peuvent être dues, également, à une activation des processus de dégradation des lipides, via la stimulation des enzymes lipolytiques. Ainsi, il a été bien établi, par de nombreux auteurs, que la teneur en lipides totaux a été influencée par des facteurs abiotiques et biotiques (Laribi et *al.,* 2011; Trabelsi et *al.,* 2012).

B. Etude des paramétres phytochimiques

1. Rendement enextraits bruts

L'extraction méthanolique a été utilisée, afin d'estimer la capacité d'extraction et de sélectivité des composés phénoliques des fleurs et tiges de *Chamaemelum nobile.* Les résultats ont montré une variabilité significative entre organes.

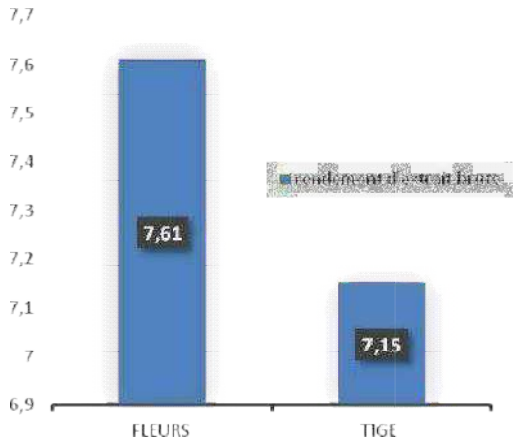

Figure 4: Rendement en extrait brute du *Chamaemelum nobile*

D'après la figure 4, le rendement le plus élevée en extrait méthanolique est observée chez les des fleurs (7,61 %), par rapport à celui observé chez les tiges (7.15%). Le rendement d'extraction et la composition des extraits varient en fonction du solvant et du temps de séchage de l'échantillon (Čanadanović-Brunelui et *al.,* 2008 ; Ghedadba et *al.,* 2014). En outre, la polarité du solvant joue un rôle clé dans l'augmentation de solubilité des composés phénoliques ; plus la polarité du solvant est élevée plus le rendement est plus important. (Naczk and Shahidi, 2003). Le calcul des rendements permet, non seulement, d'apprécier les extraits totaux, issus de chaque espèce, mais également d'envisager la quantité d'organes à prélever en cas de besoin pour une éventuelle étude similaire.

2. Teneurs enphénols totaux

Le choix de quantifier les phénols, parmi les différentes substances phytochimiques, résulte du fait que les phénols ont des activités biologiques très importantes. De même pour les flavonoïdes qui sont considérés comme la classe la plus importante des polyphénols (Meddour et *al.,* 2013). Selon ces résultats, illustrés par le tableau 3, on constate que l'espèce *Chamaemelum nobile* est riche en phénols totaux. Cependant, on note une différence significative entre les deux organes de la plante. En effet, les fleurs du *Chamaemelum nobile* ont la teneur en polyphénols la plus élevé (11,94 mg EAG/g MS), par rapport aux tiges (6,22 mg EAG/g MS).

Tableau 3: teneur en phénol totaux du *Chamaemelum nobile*

Organe	Teneur en phénols totaux
Fleurs	**11,94 ±0,078^{A}**
Tiges	**6,22 ± 0,11^{B}**

Les variations dans la répartition de la teneur en phénols totaux peuvent être, partiellement, dues à des facteurs génotypiques, qui contrôlent l'accumulation de ces composés dans les plantes et aux conditions de croissance des plantes (Hashempour, et *al.,* 2010). Elles seront, également, probablement, dues à de nombreux autres facteurs, notamment les facteurs climatiques et environnementaux (température, altitude, ensoleillement et précipitations), la zone géographique, la sécheresse et les maladies (Ebrahimi et *al.,* 2008; Andarwulan et *al.,* 2010), la période de collecte des échantillons et le stade de croissance et de développement de la plante (Miliauskas et *al.,* 2004).

3. Teneuren flavonoïde totaux

Les teneurs en flavonoïdes totaux des extraits méthanolique des organes du *Chamaemelum nobile,* exprimées en équivalant de Quercitaine/g du matériel végétal sec, sont représentées dans le tableau 4 :

Tableau 4: Teneur en flavonoïdes totaux des organes du *Chamaemelum nobile*

Organe	Teneur en flavonoïde totaux
Fleurs	**32,540 ± 0,969^{A}**
Tiges	**28,306 ± 0,558 ^{B}**

Le tableau 4 montre que la teneur en flavonoïdes totaux varie d'un organe à une autre. La concentration la plus élevé est observée chez les fleurs (32,540 mg EAG/g MS), par rapport à celle observée chez les tiges (28,306 mg EAG/g MS).

Nos résultats montrent que la teneur en flavonoïdes totaux varie significativement ($P<0,05$) d'un organe à un autre, pour la même plante. Les flavonoïdes des végétaux sont, probablement, les composés phénoliques naturels les plus importants. Amjad et Shafighi (2013), ont montré que la zone géographique, les conditions du sol et les pesticides peuvent contribuer aux variations de la teneur en flavonoïdes totaux des plantes.

L'origine génotypique et la botanique de la plante peuvent, également, influencer l'estimation de la teneur en flavonoïdes totaux (Schmidt et al. 2010 ; Tan et al. 2016).

4. Teneurs entanins totaux

D'après le tableau 5 ; les résultats montrent qu'il y a une différence significative entre les organes des extraits méthanolique de la plante. La teneur la plus élevée (80,7954) est enregistrée chez les fleurs de la plante.

Cette teneur élevée pourrait justifier le pouvoir antibactérien élevé, dont dispose notre plante (Bassene et *al.,* 1995).

Tableau 5: teneur en tanins totaux des organes de *Chamaemelum nobile*

Organe	Teneur en tanins totaux
Fleurs	**80,7954 ± 9,4816^{A}**
Tiges	**41,553 ± 6,1346 ^{B}**

5. Teneurs en tanins condensés

Les concentrations en tanins condensés au niveau de notre plante, varient, également en fonction de l'organe. Les résultats oscillent entre 912,29 ± 78.40, ce qui représente un taux de 53%, pour les feuilles et 886,42 ± 132,14, avec un taux de 47%, pour les tiges (Figure 5).

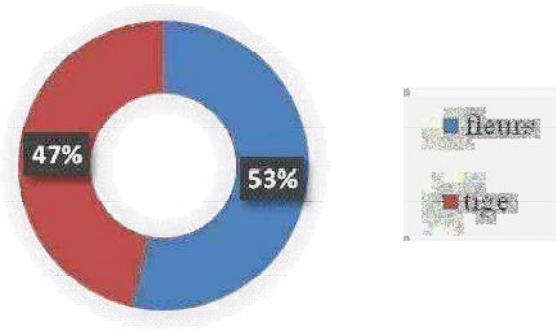

Figure 5: *Teneur en tanins condensés du Chamaemelum nobile*

C. *Pourcentage en MO, MM ,MSet Carbone*

Les résultats de ces teneurs, chez la plante *Chamaemelum nobile,* montrent des différences significatives (figure 6).

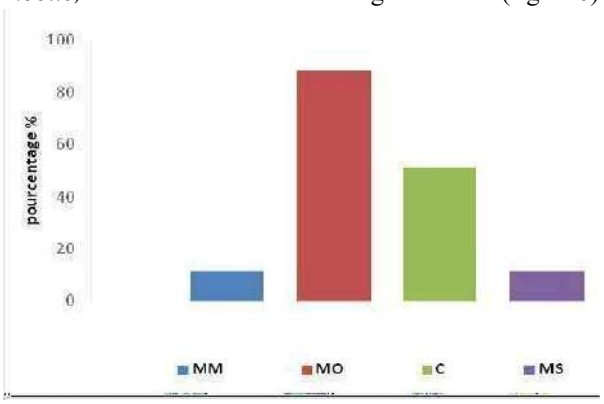

Figure 6: Teneur en matières organique, minérale, sèche et en carbone

D'après la figure 6, on note que la *Chamaemelum nobile* présente une teneur en matière organique de 88,35% et une teneur en carbone de 51,25%, un indicateur important de la richesse de l'échantillon. Selon Drouet et *al*. (2010), le contenu en matière organique de la plante peut être influencé, globalement, par les facteurs climatiques et physiologiques, la végétation, l'âge de la plante et les pratiques culturales. La figure 6 montre que la teneur en matière minérale et en matière sèche est de l'ordre 11,65 %. En effet, le cycle de végétation et le stade de développement influent sur la composition minérale de la plante, non seulement par les variations de la teneur en minéraux, de chaque organe de la plante, mais surtout par les modifications des rapports en poids, de ces organes entre eux (Gueguen L., 1959).

D. *Activités biologiques*

1. *Activité antioxydante*

Le DPPH est un radical libre de couleur violette. Il est réduit en un composé de couleurs jaune en présence des composés anti-radicalaires. L'activité anti-radicalaire du radical DPPH a été évaluée par spectrophotométrie, en suivant la réduction de ce radical, qui s'accompagne par son passage de la couleur violette à la couleur jaune mesurable à 517 nm. Nos résultats sont exprimés en tant que pourcentage de l'activité anti radicalaire.

Tableau6: Evaluation de l'activité antioxydante

Organe	Pouvoir antioxydant
Fleur	**61.5424 ± 1.38847^{A}**
Tige	**50.8977 ± 2.1853^{B}**

Selon les résultats enregistrés, les résultats montrent que les extraits des fleurs sont le plus actifs (61.5424 ± 1.38847) par rapport aux extrait des tiges (50.8977 ± 2.1853).Donc d'après le tableau 6 les résultats nous montre une différence significative entre les deux organes de même plante ; ce qui nous montre aussi que cette activité est directement liée à la présence des phénols et des flavonoïdes dans les plantes étudiées. Et selon les étude Ksouri et al., 2007; Bhoyar et al., 2011 qui ont montré une corrélation significative entre l'activité antioxydante et la teneur en composés phénoliques . Aussi (Bougandour et Bendimerad, 2013) montre que le phénol, flavonoïdes et les tanins réduisent et décolorent le DPPH en raison de leur capacité à céder l'hydrogène.La teneur du polyphénol élevé en fleur du *Chamaemelum nobile* est probablement responsable de l'activité antioxydant élevé par rapport aux tiges. en effet Naffati et al., 2011 a été démontré que les composés phénoliques contribuent directement à l'activité antioxydant .
En effet ; Selon (Zhang et al., 2011), l'activité antioxydant est généralement attribuée aux composés phénoliques et des flavonoïdes des extraits des plantes. Pour cette raison, il y a un intérêt croissant pour la séparation de ces antioxydants végétaux et de les utiliser comme des antioxydants naturels dansles industries agroalimentaires et cosmétiques.

2. *Activité antibactérienne*

C'est l'activité la mieux étudiée par les scientifiques, même s'il est difficile de comparer les résultats publiés, du fait de la grande variabilité des HE (chimiotype) et de l'absence de protocole de normalisation, pour l'évaluation *in vitro* de leur pouvoir bactéricide.
L'évaluation de l'activité antibactérienne de différentes doses, de l'Huile Essentielle d' ***Chamaemelum nobile,*** nous a permis de mettre en évidence l'efficacité de cette huile sur les 4 souches bactériennes testées (*Escherichia coli* (Gram-), *Listeria* (Gram+), *Bacillus* (Gram+), *Salmonella* (Gram-)). En effet, le pouvoir antibactérien a été estimé en termes de diamètre de la zone d'inhibition autour des puits qui contiennent l'huile essentielle, à différentes concentrations.

Tableau 7: Résultats de l'activité antimicrobienne

Bactérie	concentration	Diamètred'inhibition	gentamicine (antibiotique)
salmonella	HE pur	0,87	3,5
	10	1,17	3,3
	50	1,33	3,4
	80	1,8	2,9
	100	2,3	4,1
Escherichia coli	HE pur	0,97	3,37
	10	1,27	3,57
	50	1,6	3,37
	80	1,8	3,67
	100	2,03	5,27
Bacillus	HE pur	0,9	3,5
	10	0,77	3
	50	1,67	4,17
	80	1,43	3,5
	100	2,57	3,83
listeria	HE pur	1,03	2,93
	10	1,47	3,2
	50	1,47	2,57
	80	1,93	3,67
	100	2,17	4,83

Avec :

HE pure : huile essentiel pur
10 : dilution d'extrait 1/10
50 : dilution d'extrait 1/50
80 : dilution d'extrait 1/80
100 : dilution d'extrait 1/100
Concentration : les valeurs sont en mg/ml (Huile Essentielle) et en µg/µl (Antibiotiques).

D'une maniérée générale, l'Huile Essentielle de *Chamaemelum nobile,* testée, a exercé une action antibactérienne très importante, presque égale à celle de gentamicine antibiotique de référence. A travers nos résultats ; on remarque que plus on augmente la concentration, plus l'effet inhibiteur est efficace, contre les quatre souches testées, avec presque inhibition de la moitié du tapis bactérien. La zone d'inhibition augmente largement avec l'augmentation de la concentration des extraits, ce qui a été constatée aussi par (Dordevic et *al.,*2007). L'activité antimicrobienne dépend à la fois de la présence des composés phénoliques et, aussi, de la présence de divers métabolites secondaires, de l'emplacement et du nombre des groupes d'hydroxyles (Falleh et *al.,* 2008).

E. Rendement en huile essentielle et sa composition chimique

1. Rendement en Huile essentielle

Le rendement en Huile Essentielle, obtenu par hydro distillation de 15,36 kg de matière fraiche de *Chamaemelum nobile* collectée à Tabarka, était de l'ordre de 11,89%. Selon plusieurs auteurs, l'origine de récolte de l'espèce, la période de récolte, l'organe de la plante, la durée de séchage et la méthode d'extraction sont des facteurs, parmi d'autres, qui peuvent aussi avoir un impact direct sur les rendements en Huile Essentielle (Russo et *al.,* 1998 ; Tonzibo, 1998 ; Vekiari et *al.,* 2002 ; Karousou et *al.,* 2005 ; Kouamé, 2012).

2. Composition chimique de l'Huile Essentielle

D'après le tableau (8) et le chromatogramme de figure (8) l'huile essentielle de chamaemelum *nobile* est composée majoritairement par beta.-Myrcene (8.64) et les autres composants principaux sont alpha.-Pinene (8.34) et Cyclohexene, 1-methyl-4-(1-methyle thylidene)- (5.25).

Tableau 8: Composition chimique d'huile essentiel de *chamaemelum nobile*

	RT	PIC	*Chamaemelum nobile*
1	7,157	0,8	alpha.-Phellandrene
2	7,446	8,34	.alpha.-Pinene
3	7,703	0,5	Camphene
4	8,949	3,7	Cyclohexene, 4-methylene-1-(1-methylethyl)-
5	8,553	1,15	.beta.-Pinene
6	9,174	8,64	beta.-Myrcene
7	9,537	1,07	3-Carene
8	9,692	0,53	1,3-Cyclohexadiene, 1-methyl-4-(1-methylethyl)-
9	9,928	0,74	Benzene, 1-methyl-4-(1-methylethyl)-
10	10,072	1,61	Tricyclo[2.2.1.02,6]heptane, 1,7,7 -trimethyl-
11	10,644	0,87	1,3,6-Octatriene, 3,7-dimethyl-, Z)-
12	10,939	0,92	1,4-Cyclohexadiene, 1-methyl-4-(1- methylethyl)-
13	11,912	5,25	Cyclohexene, 1-methyl-4-(1-methyle thylidene)-
14	12,163	0,31	Furan, 3-(4-methyl-3-pentenyl)-
15	13,233	0,18	Bicyclo[3.1.1]heptan-3-ol, 6,6-dimethyl-2-methylene-
16	14,035	0,45	Borneol
17	14,426	1,53	3-Cyclohexen-1-ol, 4-methyl-1-(1-methylethyl)-, (R)-
18	14,613	0,32	Thymol
19	14,768	0,3	.beta.-Pinene
20	17,426	0,87	Bicyclo[2.2.1]heptan-2-ol, 1,7,7-t rimethyl-, acetate, (1S-endo)

D'autre étude de (Faucon. ; 2015) et (Franchomme P 2001) a révélé l'existence de plusieurs sesquiterpènes :
L'HE de Camomille est riche en trans-βfarnésène mais doit sa coloration bleue caractéristique à la présence d'une petite quantité de chamazulène qui possède 5 doubles liaisons. Lorsqu'il se dégrade en dihydro-chamazulène, qui ne possède plus que 4 doubles liaisons, l'HE prend alors une coloration verte puis jaunâtre, ce qui indique son vieillissement. (6,7)

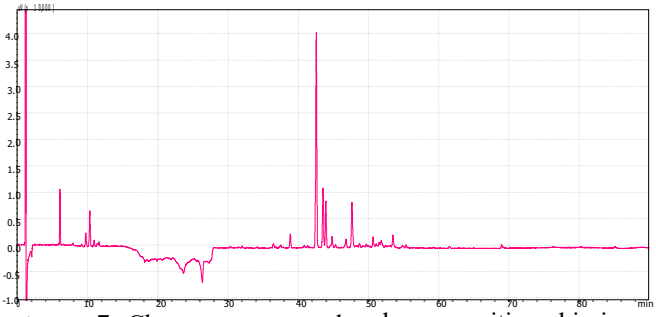

Figure 7: Chromatogramme de la composition chimique d'huile essentiel de *chamaemelum nobile*

Aussi que Bellakhdar, 2006 montre que La camomille romaine contient 0,4 à 1,5% d'huile essentielle contenants 85% d'esters, surtout de l'angélate d'isobutyle, accompagné

des esters des acides méthylacrylique. Elle renferme aussi un alcool (l'anthémole), de la pinocarvone, du pinocarvéol. On y trouve aussi 0,6% de lactone sesquiterpéniques ; des flavonoïdes ; des acides caféique et ses esters glucosés ; des coumarines ; des acides gras, de mucilage et des minéraux.

IV. CONCLUSION

Un grand nombre de Plantes Aromatiques et Médicinales possède des propriétés biologiques très importantes, qui trouvent de nombreuses applications dans divers domaines à savoir en médecine, en pharmacie, en cosmétologie et en agriculture. L'objet de travail a porté sur l'étude phytochimique et les activités biologiques de l'espèce médicinale, *Chamaemelum nobile,* utilisée dans la pharmacopée traditionnelle tunisienne.

Le rendement en huile essentielle de l'espèce a été évalué à 11,89%. Concernant la caractérisation biochimiques des différentes parties de la plante, par les dosages de différentes teneurs en lipide, polyphénols, flavonoïdes et en tannins ainsi que l'effet antioxydant et anti bactérien, les résultats ont montré que les fleurs sont riches en, polyphénols et en flavonoïdes.L'activité antioxydants, évaluée par par le test de DPPH, a révélé que les extraits de *Chamaemelum nobile* présentent des activités anti radicalaires très importantes. Le pouvoir antibactérien de l'huile essentielle est important. En effet, l'analyse effectuée, avec l'huile essentielle, montre que *Chamaemelum nobile* agit sur les deux grams (+ et -) de souche bactérienne, testées.

V. REFERENCES

1. HAZZIT M. B. (2015)., Composition chimique et activité antimicrobienne de l'extrait non volatil et des huiles. (27) ,118-129p.
2. Chouayet W., 2013. Contribution de plantes forestières non ligneuse à la création d'emplois et aux revenus des ménages dans le Kroumirie. Projet de fin d'étude cycle ingénieur l'importance.
3. Lamnaouer D., 2002. Plantes médicinales du Maroc : Usages et toxicité "Résumé" 1-2.
4. Benjilali B., Zrira S., 2008. Plantes aromatiques et médicinales. Atouts du secteur et exigences pour une valorisation durable 16.
5. Agence du Médicament les Cahiers de l'Agence 3- Médicaments à base de plantes, Paris 1998.
6. Leng P., Zhiming Z., Guangtang P., Maojun Z., 2011. Applications and development trends in biopesticides. Afr. J. biotechnol., 10(86), 19864-19873.
7. Porter N., 2001: Essential oil and their production. Corps and Food Research. Number 32.
8. Kaloustian, Jacques, and Francis Hadji-Minaglou. La Connaissance Des Huiles Essentielles Qualitologie Et Aromathérapie ; Entre Science Et Tradition Pour Une Application Médicale Raisonnée. Paris: Springer, 2012.P :13.
9. Desmares C., Laurent A. et Delerme C., 2008. Recommandations relatives aux critères de qualité des huiles essentielles: Contribution pour l'évaluation de la sécurité des produits cosmétiques contenant des huiles essentielles. Agence française de sécurité sanitaire des produits de santé (Afssaps), France.
10. Lahlou, M. (2004). Methods to study the phytochemistry and bioactivity of essential oils. Phytotherapy Research: An International Journal Devoted to Pharmacological and Toxicological Evaluation of Natural Product Derivatives, 18(6), 435-448.
11. Ghedira, K., Goetz, P. et Le Jeune, R., 2009, *Matricaria recutita* L. Camomille allemande, matricaire, Phytothérapie, Vol 7(6) :316-322, DOI: 10.1007/s10298-009-0510-8
12. Zobel A. M. and Brown S. A. (1990). Dermatitis-inducing furanocoumarins on leaf surfaces of eight species of Rutaceous and Umelliferous plants. *Journal of Chemical Ecology* 16, 3:693-700.
13. Sun L., Zhang J., Lu X., Zhang L and Zhang Y. (2011). Evaluation to the antioxidant activity of total flavonoids extract from persimmon (Diospyros kaki L.) leaves. Food Chem Toxicol. 49: 2689-2696.
14. Yi Z.-B., Yu Y., Liang Y.-Z., Zeng B. (2007). In vitro antioxidant and antimicrobial activities of the extract of Pericarpium Citri Reticulatae of a new Citrus cultivar and its main flavonoids, LWT-Food Science and Technology. 4 : 1000-1016.
15. Burt, S.A. (2004). Essential oils: their antibacterial properties and potential applications in foods: International Journal of Food Microbiology. 94: 223-253.
16. Bligh, E.G., Dyer, W.J. (1959). A rapid method of total lipid extraction and purification. Can. J. Biochem. Physiol. 37, 911–917
17. Benson, A.A., Strickland, E.H. (1960). Plant phospholipids III. Identification of diphosphatidylglycerol. Biochem. Biophys. Acta 41, 328–333.
18. Owen P. et Johens T. (1999). Xanthine oxidase inhibitory activity of northeastern North American plant remedies used for gout. Journal of Ethnopharmacology. 64: 149-160
19. Benhammou, N., Atik Bekkara, F., Kadifkova, Panovsk, T., 2009. Antioxidant activity of methanolic extracts and some bioactive compound of Atriplex halimus. C. R. Chimie, 12: 1259–1266.
20. Fallah, S., Suzuki, T., Ktayama, T., 2008. Chemical Constituents from Swietenia macrophylla Bark and Their Antioxidant Activity. Pakistan Journal of Biological Sciences 11(16): 2007-2012.
21. Singleton V. L., Orthofer R., Lamuela-Raventos R. M. (1999). Analysis of total phenols and otheroxidation substrates and antioxidants by means of Folin Ciocalteu reagent. Methods in Enzymology. 299: 152-178.

22. i Z.-B., Yu Y., Liang Y.-Z., Zeng B. (2007). In vitro antioxidant and antimicrobial activities of the extract of Pericarpium Citri Reticulatae of a new Citrus cultivar and its main flavonoids, LWT-Food Science and Technology. 4 : 1000-1016.
23. Sun L., Zhang J., Lu X., Zhang L and Zhang Y. (2011). Evaluation to the antioxydant activity of total flavonoids extract from persimmon (Diospyros kaki L.) leaves. Food Chem Toxicol. 49: 2689-2696.
24. Kujala UM, Jaakkola LH, Koskinen SK, Taimela S, Hurme, M, Nelimarkka O (2000) , Scoring of patellofemoral disorders. Arthroscopy 9(2):159–163
25. Brand-Williams, W., Cuvelier, M.E., Berset, C., 1995. Use of a free radical method to evaluate antioxidant activity. Lebensmitt. Wiss. Technol. 28, 25–30.
26. Bozin B, Mimica-Dukic N et Samojlik I., 2008. Phenolics as antioxidants in garlic (Allium sativum L., Alliaceae).Food Chemistry. 111, pp :925-929.
27. Sanchez-Moreno C., 2002. Review: Methods Used to Evaluate the Free Radical Scavenging Activity in Foods and Biological Systems. Food Science and Technology International, 8(3), pp : 121–137.
28. Bougandoura, N. and Bendimerad N. 2013. Evaluation de l'activité antioxydante des extraits aqueux et méthanolique de Satureja calamintha ssp.Nepeta (L.) Briq. Nature & Technologie 09 : 14 -19
29. Güven K., Yücel E et Cetintaş F.,2006. Antimicrobial Activities of Fruits of Crataegus.and Pyrus. Species, Pharmaceutical Biology44, pp :2,79-83.
30. AOAC. , 1995.official methods of analysis of the association of official analytical chemists.
31. Van Rast, E., Verloo, M., Demeyer, A., Pauwels, J.M., 1999. Manual for the Soil Chemistry and Fertility Laboratory. Ed, 1999.
32. U.S.S.L.S. (United State Salinity Laboratory Staff): Diagnosis and improvement of saline and alkali soils.US Department of Agriculture, Handbook n°60, U. S. Gov. Print. Office, Washington DC, (1954)
33. Olsen S.R. et al., (1954): Estimation of available phosphorous in soils by extraction with sodium bicarbonate. Cir. U.S. Dep. Agr., n° 939, p: 1-19.
34. Uzun, B., Ulger, S., Cagirgan, I.M., 2002. Comparison of determinate and indeterminate types of sesame for oil content and fatty acid composition, Turkish Journal of Agriculture and Forestry 26: 269-274
35. Ravi, R., Prakash, M., Bhat., K.K., 2007. Aroma Characterization of coriander (Coriandrum sativum L.) oil samples. European Food Research and Technology, 225:367-374
36. Laribi, B., Kouki, K., Mougou, A., Marzouk, B., 2011. Essential oil and fatty acid composition of a Tunisian Caraway (Carum Carvi L.) seed ecotype cultivated under water deficit. Advances in Environmental Biology 5 (2), 257-264.
37. Trabelsi, H., O.A. Cherif, F., SakoYhi, P., Villeneuve, J., Renaud, N., Barouh, S., Boukhchina, and P., Mayer. 2012. Total lipid content, fatty acids and 4- desmethylsterols accumulation in developing fruit of Pistacia lentiscus L. growing wild in Tunisia. Food Chem.131: 434–440.
38. Naczk M and Shahidi F. (2003). Phenolics in food and nutraceuticals. Boca Raton, FL: CRC Press. P 576.
39. Miliauskas G., Venskutonis, P.R., Van Beek, T.A., 2004. Screening of radical scavenging activity of some medicinal and aromatic plant extract. Food chemistry, 85, 231-23
40. Amjad, L. and Shafighi, M., 2013. Evaluation of Antioxidant Activity, Phenolic and Flavonoid Content in Punica granatum var. Isfahan Malas Flowers. International Journal of Agriculture and Crop Sciences, 5 (10):1133-1139.
41. Schmidt, S., Zietz, M., Schreiner, M., Rohn, S., Kroh, L.W., Krumbein, A., 2010. Genotypic and climatic influences on the concentration and composition of flavonoids in kale (Brassica oleracea var. sabellica). Food Chemistry 119(4):1293-1299
42. Tan, Li-H., Zhang, D., Wang, G., Yu, B., Zhao, S-P., Wang, J-W., Yao, L., Cao, W-G., 2016. Comparative analyses of flavonoids compositions and antioxidant activities of Hawk tea from six botanical origins. Industrial Crops and Products 80:123–130.
43. Bassene E., Mahamat B., Lo m. C.S,Faye B .; (1995) .Comparaison de l'activité antibactérienne de trios combretaceae :C . Micranthum, Guiera senegalensis ET terminalia avicennioides. Fitoterapia, 66(1), 86-87.
44. Makkar H.P.S. ET Becker K., 1996. Nutrional value and whole and ethanol antinutritional components of extracted moringa oleifera leaves. anim .feed Sci.technol., 63 (1-4):211-228
45. -Gueguen, L. (1959). Etude de la composition minérale de quelques espèces fourragères. Influence du stade de développement et du cycle de végétation.
46. Dordevic S., Petrovic S., Dobric S., Milenkovic M., Vucicevic D., Zizic S. et Kukic J. (2007). Antimicrobial, anti-inflammatory, anti-ulcer and antioxidant activities of Carlina acanthifolia root essential oil .J Ethnopharmacol.
47. Falleh H., Ksouri R., Chaieb K., Karray-Bouraoui N., Trabelsi N., Boulaaba M., Abdelly C., (2008).Phenolic composition of Cynara cardunculus L. organs, and their biological activities. C. R. Biologies.
48. Russo M., Galletti G.C., Bocchini P. & Carnacini A., 1998.- Essential oil chemical composition of wild populations of Italian oregano spice (Origanum vulgare ssp. hirtum (Link): a preliminary evaluation of their use in chemotaxonomy by cluster analysis.

Journal of Agricultural and Food Chemistry, 46: 3741-3746

49. Tonzibo Z.F., 1998.- Contribution à l'étude des huiles essentielles des espèces acclimatées en Côte d'ivoire. Eucalptus citrodora, Ocimum gratissimum et Ocimum basilicum. Thèse de 3eme cycle, chimie organique, Université de Cocody-Abidjan, Côte d'Ivoire, 136 p
50. Vekiari SA, Protopapadakis EE, Papadopoulou P, Papanicolaou D, Panou C. & Vamvakias M., 2002.- Composition and seasonal variation of the essential oil from leaves and peel of a lemon variety. Journal of Agrcultural and Food Chemistry, 5(1): 147-153.
51. Karousou R., Koureas D.N. & Kokkini S., 2005.- Essential oil composition is related to the natural habitats: Coridothymus capitatus and Saturejathymbra in NATURA 2000 sites of Crete. Photochemistry, 66: 2668-2673.
52. Kouamé-Bi K.F.P., 2012.- Valorisation de quatre plantes médicinales Ivoiriennes : étude phytochimique. Thèse de doctorat, chimie organique, Université de Nantes et de l'Université de Cocody-Abidjan. 180 p.
53. Dinon E., Gerstmans, L'Influence du pH sur l'assimilation des éléments nutritifs du sol par les plantes et sur la variété des plantes, Université de Liège, (2008).

Influence du Vitrage sur les Charges de Chauffage et Climatisation pour un Local à usage de Bureau à Tunis

Nahed Soussi[1], Ameni Mokni[2], Marwa Ammar[3], Hatem MHIRI[4]

Laboratoire de thermique et thermodynamique des procédés industrielles
École National d'Ingénieurs de Monastir (Tunisia)
[1]nahed.soussi@yahoo.fr

***Résumé*— La consommation d'énergie dans un immeuble de bureau à Tunis a été analysé dans ce travail. On s'est intéressé à étudier l'effet des propriétés des vitres sur les besoins de chauffage et de climatisation. L'effet de l'épaisseur des vitres, leur couleur ainsi que l'utilisation d'un double ou simple vitrage a été examiné. Les résultats de simulation montrent que le bon choix du type de vitrage permet de minimiser les pertes durant la période hivernale et augmenter les apports par le vitrage en été. La configuration optimale correspond à l'utilisation d'un double vitrage avec des vitres à faible émissivité de 6mm d'épaisseur séparées par de l'argon comme gaz de fenêtre de 13mm d'épaisseur permet diminuer la charge de chauffage de 13.7% et climatisation de 11.2% par rapport à un bâtiment avec des surfaces vitrées avec un simple vitrage transparent de 3mm d'épaisseur.**

***Mots clés*— Économie d'énergie, local de bureau, charge de chauffage, charge de refroidissement, simple vitrage, double vitrage**

I. INTRODUCTION

En raison des crises énergétiques successives, le contrôle et la réduction efficaces de la consommation d'énergie sont devenus une priorité. De nombreuses recherches ont donc été menées pour réduire la consommation d'énergie. Le secteur des bâtiments est l'un des principaux centres d'intérêt de la recherche sur les économies d'énergie en raison de sa part importante dans le mix énergétique mondial. Une variété considérable de recherches sur la conservation de l'énergie dans les bâtiments a été soulevée. La part de la consommation en énergie primaire du secteur bâtiment dans le monde a atteint 52 10^{15}btu en 2010. Ce chiffre n'arrêtera pas de croitre et atteindra approximativement 81.8 10^{15}btu d'ici 2040. Cette évolution ne se fera pas à une même vitesse pour les différents pays du monde, en effet la part des pays de l'Organisation de Coopération et de Développement Economiques (OCDE) qui représentait 54.2% en 2010 se limitera à 39% d'ici 2040. Un saut allant de 23.9 10^{15}btu à 49.8 10^{15}btu de la part des pays non membre de L'OCDE sera enregistré [2]. Cela est expliqué par le développement économique et sociale de ces pays, ce qui implique une quête de la part des citoyens à augmenter leur bien-être social, induisant une augmentation continue de la consommation d'énergie. Une grande partie de cette énergie est consacrée à la climatisation, au chauffage des locaux et de l'eau domestique, les économies d'énergie dans ce domaine sont essentielles [3].

Dans un contexte marqué par un effort croissant de stratégies de développement durable, une grande partie de la recherche se concentre sur les questions liées à l'énergie dans l'environnement bâti. Cependant, la plupart des travaux se sont concentrés sur la conception efficace des nouveaux bâtiments et concernent essentiellement les pays développés [4]–[7]. À cet égard, de nouvelles politiques d'énergie doivent être mises en place, essentiellement pour améliorer l'efficacité énergétique des bâtiments.

Le secteur bâtiment en Tunisie est le premier consommateur d'énergie finale, sa part s'élève à 2976 ktep, soit 37.1% de la consommation totale du pays.

Ce travail sera consacré à l'optimisation énergétique d'un immeuble existant. Le bâtiment, à usage bureautique, est sis à Tunis. Dans une première étape, le bâtiment est simulé et sa consommation d'énergie est déterminée. Ensuite, une étude paramétrique sur l'influence du type du vitrage a été menée.

II. CAS ETUDIE

Dans ce travail, comme mentionné précédemment, le cas d'un bâtiment bureautique est étudié. Tout d'abord, les données climatiques du site sont présentées, les propriétés du bâtiment et les matériaux utilisés dans sa construction ont été extraites.

A. Localisation du bâtiment et Données météorologiques du site

Le bâtiment est localisé à Tunis (tableau I). Les conditions extérieures sont générées à partir des données météorologiques fournies par les fichiers météo au format.epw (EnergyPlus Weather data).

TABLEAU I
LOCALISATION DU BATIMENT

Latitude	36.83
Longitude (°)	10.23
Élévation (m)	4

Le climat tunisien est doux et tempéré. Sur le tableau 2 sont présentées les températures mensuelles moyennes pour la ville de Tunis. Pour assurer le niveau de confort souhaité, le chauffage en hiver et le refroidissement en été sont nécessaires.

TABLEAU II
TEMPERATURE MENSUELLE MOYENNE POUR LA VILLE DE TUNIS

Mois	**Janv.**	**Fév.**	**Mars**	**Avril**	**Mai**	**Juin**
T(°C)	11	12	14	16	21	25
Mois	**Juill.**	**Août**	**Sept.**	**Oct.**	**Nov.**	**Déc.**
T(°C)	27	28	25	22	17	13

ISSN: 1737-9334

B. *Description du bâtiment*

Le bâtiment choisi pour la simulation énergétique est à usage bureautique. Il est reparti sur trois niveaux de hauteur respective 3m. Les trois étages sont identiques. Chaque étage s'étend sur une surface de 25*25 m^2. Le bâtiment comporte au total 24 surfaces vitrées de 20 m^2 chacune. Pour une meilleure analyse des résultats, chaque niveau est divisé, lors des simulations en 5 zones comme illustré sur la figure 1.

(a)

(b)

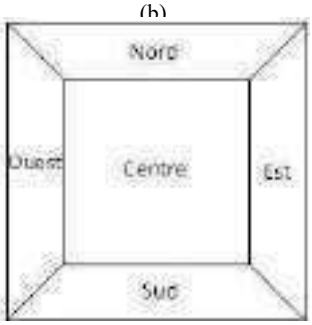

Fig. 1 Description du bâtiment (a) configuration 3D (b) Définition des zones de chaque étage

Le système de conception de base pour les murs intérieurs et extérieurs ont été extraits des spécifications du bâtiment, les propriétés thermo-physiques des matériaux de construction sont présentées sur le tableau 3 [8], [9]. Dans le bâtiment d'origine, les fenêtres sont en simple vitrage transparent de 3mm d'épaisseur. Ces informations sont implémentées dans le logiciel.

III. METHODOLOGIE

Le modèle étant mis en œuvre, ensuite, dans la section d'activité, l'occupation et le calendrier de présence de personnes, ont été implémentés. Dans la rubrique construction, le type et les caractéristiques des matériaux ont été définis et dans la section éclairage, le modèle d'éclairage et le système de chauffage, climatisation et ventilation du bâtiment (HVAC) ont été modélisés.

TABLEAU III
PROPRIETES THERMO-PHYSIQUES DES MATERIAUX DE CONSTRUCTION

	Composition Matériaux	**Conductivité** λ (W/mK)	**Epaisseur** e(cm)
Mur extérieur	Enduit de ciment	0.72	2.5
	Brique B12	0.69	20
	Enduit de ciment	0.72	2
Toit et plafond intermédiaire	Béton coulé	0.38	20
Plancher sur terrain	Dalle de béton	0.38	10

IV. RESULTATS

Les conditions de confort considérées correspondent à une température de consigne de refroidissement de l'ordre de 25°C pendant l'été et de chauffage de 21°C pendant l'hiver.

Les simulations ont été faites pour le bâtiment existant, ensuite des actions de rénovation relatives au vitrage sont considérées. Tout d'abord l'influence de l'épaisseur du vitrage a été étudiée, puis l'impact de la couleur de la vitre et au final un double vitrage a été utilisé avec différentes conception.

A. *Calcul des charges de chauffage et de climatisation du bâtiment*

La charge de chauffage est directement affectée par les déperditions thermiques à travers l'enveloppe du bâtiment. Une forte déperdition thermique implique un besoin de chauffage plus important. La figure 2 présente la répartition des pertes thermiques à travers les vitres, les murs extérieurs et le toit et plafonds pour la conception de chauffage. En minimisant ces pertes, la charge de chauffage diminue ainsi que la consommation énergétique du bâtiment. On constate qu'en première position, les vitres présentent environ 54% des pertes thermiques du bâtiment. Ensuite les murs extérieurs avec des pertes d'environ 39% et finalement le toit et les plafonds intermédiaires avec 7% des pertes totales. En raison des fortes déperditions à travers le vitrage et la simplicité des actions de rénovation pour cet élément, on a consacré ce travail pour évaluer les gains énergétiques associés à chaque modification des surfaces vitrées.

En saison estivale le vitrage est considéré comme un gain solaire et une source d'éclairage naturel. En effet, pour la conception de climatisation, l'apport des vitrages est de l'ordre de 17.65kW.

En se basant sur ces résultats, il a été noté qu'en hiver la première cause des déperditions sont les vitres qui constituent 40% de la surface extérieure du bâtiment. Donc le bon choix du vitrage est important pour optimiser la consommation énergétique d'un bâtiment tout en assurant un confort thermique des occupants.

ISSN: 1737-9334

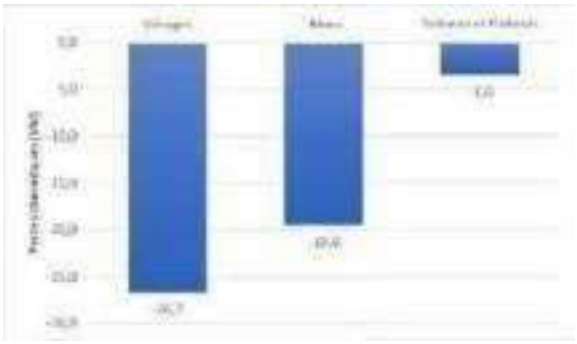

Fig. 2 Répartition de la charge de chauffage par élément de l'enveloppe du bâtiment

Sur le tableau 4, on donne la consommation énergétique totale du bâtiment en une journée type d'été et d'hiver. Les simulations ont été faites pour des conditions de confort de 21°C pour le chauffage et de 25°C pour la climatisation. Dans les sections qui suivent on présente l'effet de certaines caractéristiques de vitrage sur la consommation énergétique du local étudié durant la période hivernale et estivale.

TABLEAU IV
CHARGETOTALE DE CHAUFFAGE ET DE REFROIDISSEMENT

	Charge de chauffage (kW)	Charge de climatisation (kW)
Bâtiment	49.56	207.39

B. Influence de l'épaisseur du vitrage

On analyse dans cette section l'effet de l'épaisseur des vitres sur les charges de chauffage et de climatisation du bâtiment. On compare le cas où l'épaisseur des vitres est égale à 3mm (cas actuel) puis 6mm. Le tableau 5 présente les résultats de simulation pour les épaisseurs considérées.

L'augmentation de l'épaisseur des vitres permet d'enregistrer une amélioration d'une valeur de 0.67% en chauffage et 0.81% dans la charge de climatisation.

TABLEAU V
EFFET DE L'EPAISSEUR DES VITRES SUR LA CHARGE DE CHAUFFAGE ET DE CLIMATISATION

	Charge de chauffage (kW)	Charge de climatisation (kW)
Épaisseur 3 mm	49.56	207.39
Épaisseur 6 mm	49.23	205.71
Amélioration (%)	**0.67**	**0.81**

C. Influence de la couleur du vitrage

On utilise dans cette partie des vitres avec une épaisseur de 6mm (en se basant sur les résultats précédents). On modifie la couleur du simple vitrage étudié. Les résultats des simulations sont présentés sur le tableau 6.

Le tableau 6 indique que les couleurs bleu, bronze, vert et gris n'ont pas d'effet sur la c arge de chauffage contre une diminution de la charge de climatisation qui atteint 10.39 kW pour la couleur grise.

L'utilisation des vitres à faible émissivité (loE) une diminution de la charge de chauffage de 6.85 kW et de climatisation de 6.25 kW ; soit une diminution de la consommation énergétique générale 13.1 kW et une amélioration par rapport au vitrage transparent de 5.2%.

L'utilisation des vitres à faible émissivité (loE) permet d'avoir l'économie en énergie totale la plus élevée. La propriété des vitres à basse émissivité est d'absorber 96% de l'énergie solaire ce qui explique la diminution de la charge de chauffage.

TABLEAU VI
EFFET DE LA COULEUR DES VITRES SUR LA CHARGE TOTALE DE CHAUFFAGE ET DE REFROIDISSEMENT

Couleur	Charge de chauffage (kW)	Charge de climatisation (kW)	Consommation totale (kW)
Transparent	49.23	205.69	254.92
Bleu	49.23	196.44	245.67
Bronze	49.23	196.23	245.46
Vert	49.23	196.28	245.51
Gris	49.23	195.3	244.53
À faible émissivité (loE)	42.38	199.44	241.82

D. Influence du double vitrage

L'effet d'un double vitrage est traité dans cette section, on compare entre le cas simple vitrage, double vitrage et double vitrage avec des vitres faible émissivité (LoE). On garde une épaisseur fixe des vitres (6mm) et de l'air qui sépare les deux vitres (6mm). Les résultats sont groupés sur le tableau 7.

Suite à l'utilisation du double vitrage la consommation totale a diminué. L'utilisation d'un double vitrage avec des vitres à basse émissivité favorise la diminution des charges de chauffage et de climatisation. On note une amélioration d'environ 12% par rapport au cas simple vitrage.

TABLEAU VII
CHARGE DE CHAUFFAGE ET CLIMATISATION POUR SIMPLE ET DOUBLE VITRAGE

	Charge de chauffage (kW)	Charge de climatisation (kW)	Charge Totale (kW)
Simple vitrage	49.23	205.71	254.94
Double vitrage	41.1	192.69	233.79
Double vitrage LoE	38.81	186.15	224.96

E. Influence de l'épaisseur et type de gaz dans le double vitrage

Le gaz de fenêtre peut être de l'air ou de l'argon d'épaisseur de 6mm ou de 13mm. On présente sur le tableau 8 les valeurs et types de gaz de fenêtre.

On constate que plus l'épaisseur de l'air qui sépare les deux vitres est importante, plus la consommation énergétique diminue. L'utilisation de l'argon comme gaz de séparation entre les deux vitres est favorisée pour l'économie d'énergie du bâtiment. En effet, l'utilisation de l'argon comme gaz de fenêtre d'une épaisseur de 13mm permet une amélioration par rapport au cas simple vitrage de 4%.

TABLEAU VIII
EFFET DUGAZ DEFENETRESUR LA CHARGE DECHAUFFAGE ET CLIMATISATION

	Charge de chauffage (kW)	Charge de climatisation (kW)	Consommation totale (kW)
Air 6mm	41,1	186,15	227.25
Air 13mm	35,56	184,71	220.27
Arg 13mm	34,23	184,14	218.37

En regroupant toutes les caractéristiques du vitrage ; soit l'utilisation d'un double vitrage en LoE d'épaisseurs 6mm/13mm Arg, les déperditions thermiques du bâtiment durant période hivernale sont présentées sur la figure 3.

Cette figure montre que, après les actions d'améliorations sur le vitrage, la part des vitres dans les déperditions totales est réduite à 10.3kW.

Fig. 3 Pertes thermiques pour l'Évaluation de charge de chauffage après amélioration vitres

On constate une diminution des déperditions à travers les vitres de 26.7 kW à 10.3 kW et une amélioration globale dans les charges de chauffage et de refroidissement de 11.7% (tableau 9).

TABLEAU IX
CHARGE TOTALE DE CHAUFFAGE ET DE REFROIDISSEMENT APRES AMELIORATION DES VITRES

	Charge de chauffage (kW)	Charge de climatisation (kW)
Bâtiment amélioré	42.78	184.14

V. CONCLUSION

Dans ce travail, l'effet de l'utilisation de différents types de vitrage a été étudié dans le but d'optimiser la consommation énergétique d'un immeuble de bureau localisé à Tunis. L'objectif final est de quantifier l'apport des différentes configurations en terme de réduction de la charge de refroidissement et de chauffage.

Il a été montré qu'en adoptant le double vitrage avec des vitres à faible émissivité et avec une épaisseur de 6mm et de 13 mm pour l'argon comme gaz de fenêtre, jusqu'à 13.7% en charge de chauffage et 11.2% en charge de climatisation peuvent être réduites.

Après avoir optimisé la conception des vitrages, les efforts doivent être dirigés vers les matériaux de construction et l'isolation des murs (61% des déperditions totales) ce qui fait de cette piste d'amélioration un gisement important en terme d'économie d'énergie dans les bâtiments en Tunisie.

REFERENCES

[1] Agence de promotion de l'industrie et de l'innovation, "Les indusries des materiaux de construction, de la ceramique et du verre en Tunisie," 2014. http://www.tunisieindustrie.nat.tn/fr/download/CEPI/mono_imccv.pdf (accessed May 15, 2017).

[2] S. Bilgen, "Structure and environmental impact of global energy consumption," *Renew. Sustain. Energy Rev.*, vol. 38, pp. 890–902, 2014, doi: 10.1016/j.rser.201 .07.004.

[3] G. S. O., "Actual energy consumption in dwellings: the effect of energy performance regulations and occupant behavior," *Amsterdam, NLD: IOS Press*, 2010. https://books.google.tn/books?hl=fr&lr=&id=73obPmrrq0wC&oi=fnd&pg=PP1&dq=Guerra+Santin+O.+Actual+energy+consumption+in+dwellings:+the+effect+of+energy+performance+regulations+and+occupant+behavior&ots=FNAz8NySkZ&sig=dqxXgkT9l16RebeCzCl4LDVaCeY&redir_esc=y (accessed Nov. 15, 2022).

[4] P. J. Rosado and R. Levinson, "Potential benefits of cool walls on residential and commercial buildings across California and the United States: Conserving energy, saving money, and reducing emission of greenhouse gases and air pollutants," *Energy Build.*, vol. 199, pp. 588–607, 2019, doi: 10.1016/j.enbuild.2019.02.028.

[5] A. Tiangket, B. Chullabodhi, K. Eam-O-Pas, and S. Watechagit, *The Energy Saving Calculation for a Residential Sector in Thailand with Top-Down Methodology*, vol. 79. Elsevier B.V., 2015. doi: 10.1016/j.egypro.2015.11.512.

[6] F. Chi, R. Wang, and Y. Wang, "Integration of passive double-heating and double-cooling system into residential buildings (China) for energy saving," *Sol. Energy*, vol. 225, no. August, pp. 1026–1047, 2021, doi: 10.1016/j.solener.2021.08.020.

[7] P. W. Wong, Y. Shimoda, M. Nonaka, M. Inoue, and M. Mizuno, "Semi-transparent PV: Thermal performance, power generation, daylight modelling and energy saving potential in a residential application," *Renew. Energy*, vol. 33, no. 5, pp. 1024–1036, 2008, doi: 10.1016/j.renene.2007.06.016.

[8] N. Daouas, "A study on optimum insulation thickness in walls and energy savings in Tunisian buildings based on analytical calculation of cooling and heating transmission loads," *Appl. Energy*, vol. 88, no. 1, pp. 156–164, 2011, doi 10.1016/j.apenergy.2010.07.030.

[9] F. Abbassi, N. Dimassi, and L. Dehmani, "Energetic study of a Trombe wall system under different Tunisian building configurations," *Energy Build.*, vol. 80, pp. 302–308, 2014, doi: 10.1016/j.enbuild.2014.05.036.

Parametric Study of a Vertical Air-To-Ground Heat Exchanger

Idir Kecili[#*1], Rezki Nebbali[#1]

[#]*Laboratoire d'Energétique, Mécanique et Matériaux (LEMM), Université Mouloud Mammeri Tizi-Ouzou, Algeria*
[1]idir.kecili@ummto.dz

***Abstract*— The cooling of premises, together with increased energy consumption and therefore greenhouse gas emissions, is an important part of global warming. The Canadian/Provencal well can be an interesting alternative. The aim of this work is to characterize a vertical air-to-ground heat exchanger that cools the ambient air before it enters a room.**

The thermal behaviour of a heat exchanger consisting of two concentric tubes through which the hot air, introduced through the air gap, is first cooled by transferring heat to the ground before exiting through the inner tube. The influence of the air flow rate, the diameter and the length of the cylinder is then studied.

***Keywords*— Air flow, Canadian well, cooling, heat exchanger**

I. INTRODUCTION

The growing need for energy is imminent by 2050 [1]. To overcome this deficit and reduce greenhouse gas emissions, other forms of renewable energy are being used. Geothermal energy is used for space cooling. This is a technique traditionally used in our SAHARA region where there are houses in basements (cellars) for natural cooling in summer. It is in this perspective that we want to develop this traditional technique to allow us to use it properly and efficiently in a modern society, it is the Canadian well. The principle of operation consists in supplying a house with fresh air from an exchanger buried at a certain depth in the ground. The warm ambient air is cooled by transferring heat to the ground, which acts as a buffer medium, before being transported to the premises [2]–[5]. In this work, the influence of the diameter and length of the exchanger tubes as well as the flow rate of hot air on the cooling efficiency of the exchanger is investigated. For this purpose, we consider an exchanger consisting of two concentric tubes. The hot air blown through the air gap is cooled by contact with the ground, while the inner tube allows the fresh air obtained to be channelled towards the premises to be cooled.

II. PROBLEM POSITION

It is an air-to-ground heat exchanger buried vertically in the ground. It consists of two coaxial tubes of external diameter D, length L with a fixed air gap of 1cm. The air enters through the air gap to exchange heat with the ground, then it goes up through the inner tube whose wall is adiabatic Fig.1.

Three parameters are studied, namely: The diameter D of the tube, its length L and the air flow rate q. Therefore, the following cases were considered:

- Case 1: External diameters De = 10cm and 20cm, length L= 2m, for an air flowq= 20 g/s.
- Case 2: De = 20cm, L = 2 and 4m, air flow: 20 and 40 g/s.
- Case 3: De= 20cm, L = 4m, air flow: 40 and 80 g/s.

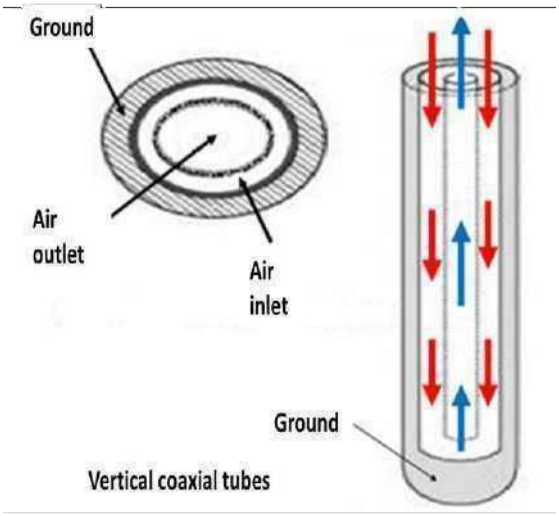

Fig. 1 Descriptive sketch of the air-to-ground heat exchanger

Moreover, for all the cases, the air inlet temperature is fixed at T_{in}=310K (36.85°C) whereas the ground temperature at the initial time is equal to T_g=300K (26.85°C).

III. DISCRETISED DOMAIN AND BOUNDARY CONDITIONS

The discretised domain extends 50cm on each side of the exchanger. Using the "mass flow inlet" condition, a mass flow of air is imposed at the exchanger inlet. At the outlet of the exchanger, the "outflow" condition is used to verify the conservation of the flows between the inlet and the outlet. For the rest of the domain boundaries, the "wall" condition is used to delimit the solid regions from the fluid regions. The study domain consists of a solid zone (soil) and a fluid medium (air). Their thermo-physical parameters are given in the table below.

TABLE I
GROUND AND AIR THERMO-PHYSICAL PARAMETERS

Designation	λ (W/m/K)	C_P (J/Kg/K)	ρ (Kg/m^3)
Ground	2	1300	1200
Air	0.0242	1006	1.2

IV. INTERPRETATION OF RESULTS

A. *Influence of the Diameter D*

The simulations show that the air temperature at the exchanger outlet increases over time for both exchanger diameter configurations Fig. 2. However, the increase of the pipe diameter, which allows the increase of the exchange surface between the exchanger and the ground, favours more the cooling of the air. On the other hand, it can be seen that the operating time of the exchanger is affected. The exchanger can ensure the cooling of 20 g/s of air for a duration of 8 hours when the diameter of the duct is D1=10cm Fig. 3, whereas for a diameter of D2=20cm this time is only 7 hours Fig. 4.

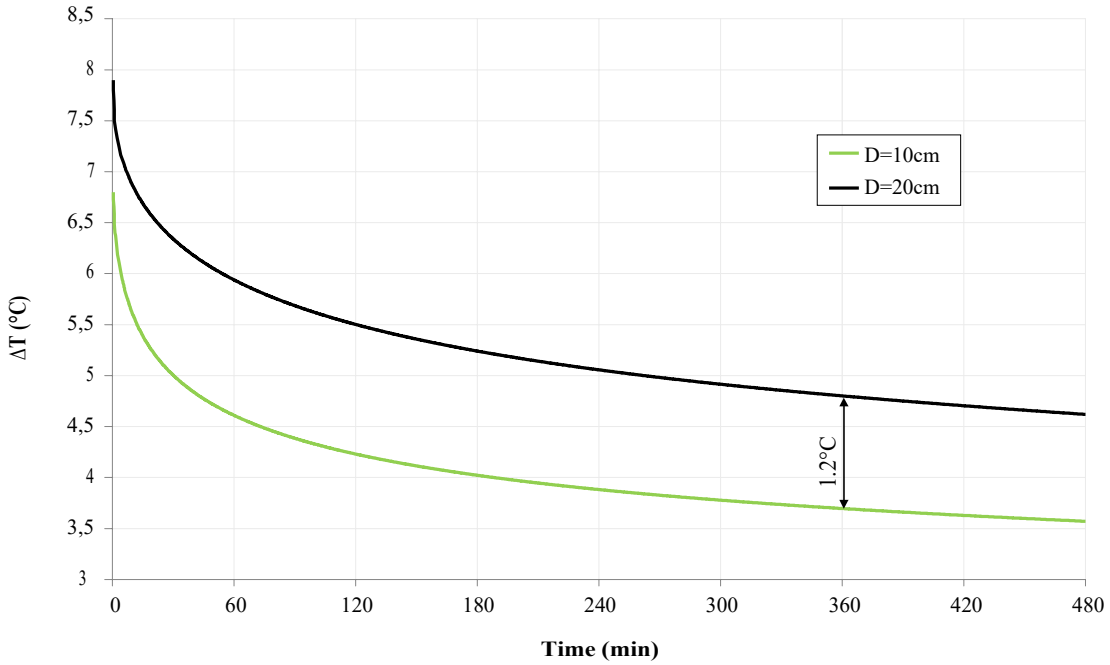

Fig. 2 Influence of the diameter on the cooling of the air ($\Delta T=T_{in}-T_g$) for L=2m q=20g/s

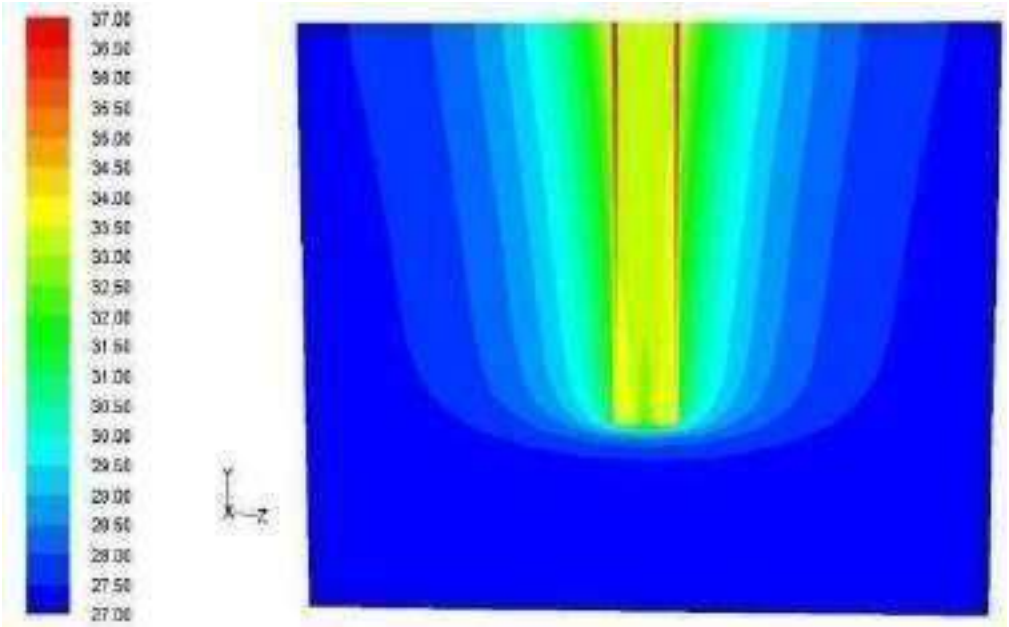

Fig. 3 Temperature field in a vertical plane at time t=8 hours, for D=10cm, L=2m and q=20g/s

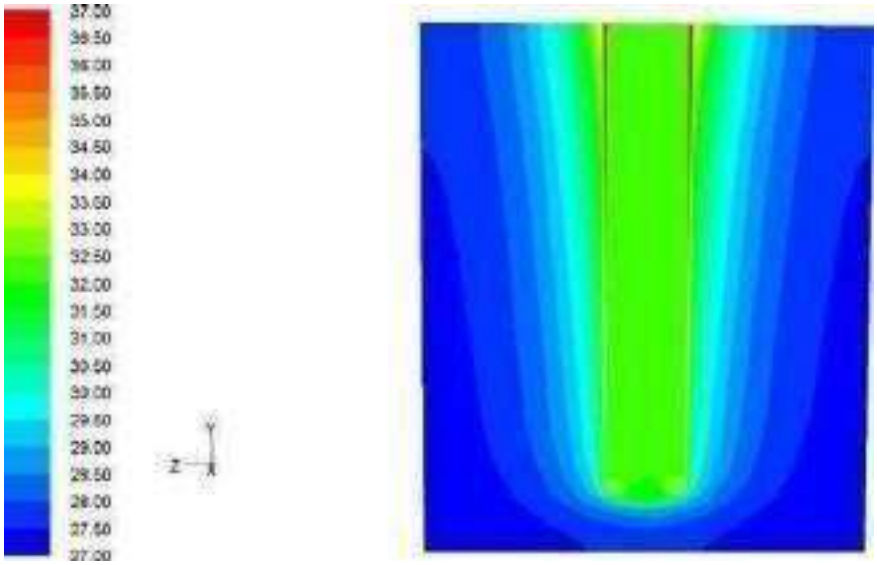

Fig. 4 Temperature field in a vertical plane at time t=7 hours, for D=20cm, L=2m and q=20g/s

B. *Influence of the Length L*

Increasing the length of the heat exchanger will result in better cooling of the air Fig. 5. For an air flow rate q=40g/s, the extension of the exchanger from L=2 to 4m increases the cooling of the air by 1.7°C.

In addition, contrary to the finding on the influence of the diameter, the increase in the length of the duct extends the operating time of the exchanger by one hour Fig. 6-7.

C. *Influence of the Airflowq*

Increasing the air flow rate reduces the cooling effect expected from the ground Fig. 8-9. Indeed, although the convective exchange between the air and the inner wall of the tube is increased, the heat exchanger cannot evacuate the excess heat that the fluid brings to the heat exchanger by doubling its flow rate. Moreover, for the same length L=4m of the tube, the cooling time, which is up to 8 hours with a flow rate q=40g/s Fig. 7, is reduced to only 4 hours for a flow rate (q=80g/s) twice ashigh Fig. 10.

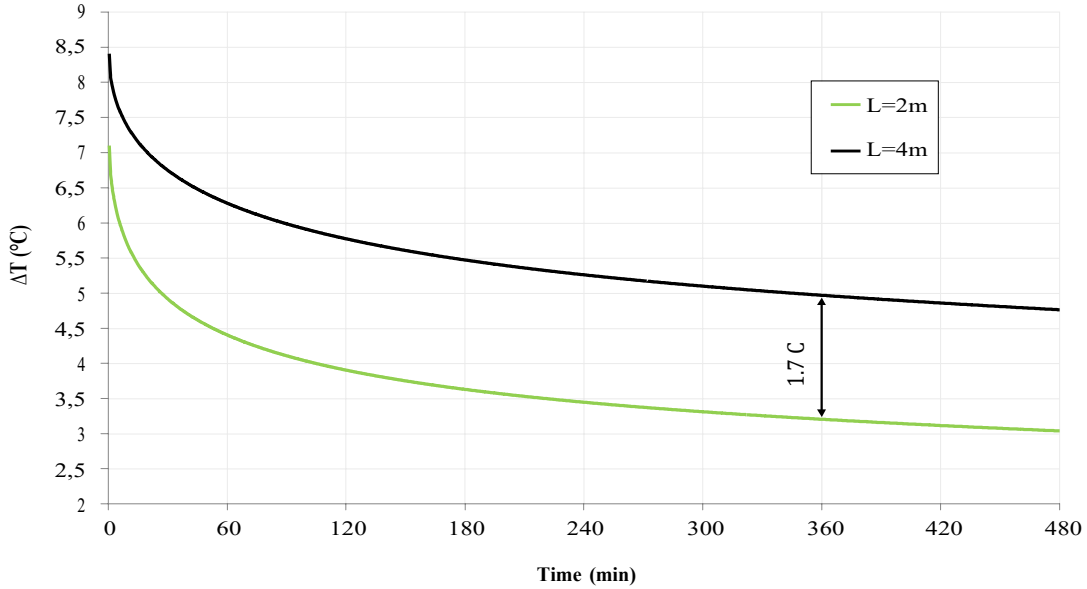

Fig. 5 Influence of the exchanger length on the cooling ($\Delta T=T_{in}-T_g$) of the air, for D=20cm and q=40g/s.

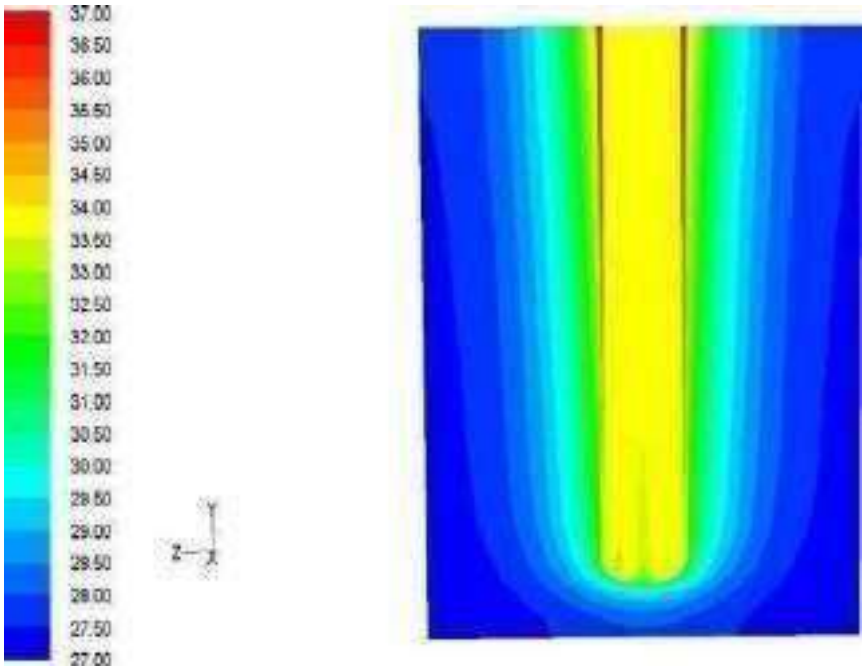

Fig. 6 Temperature field in a vertical plane at time t=6 hours, for D=20cm, q=40g/s and L=2m

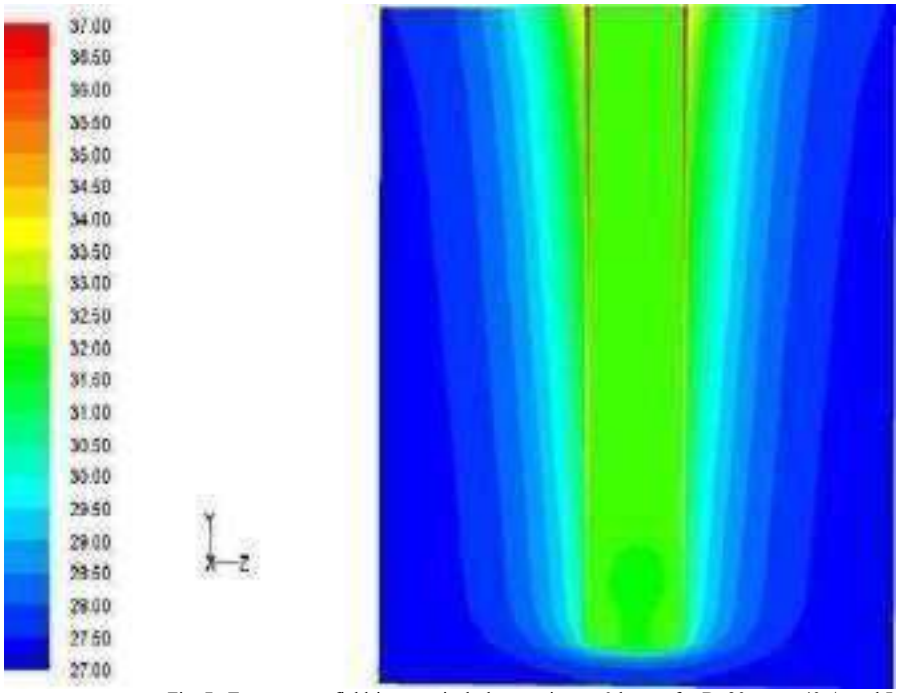

Fig. 7 Temperature field in a vertical plane at time t=6 hours, for D=20cm, q=40g/s and L=4m

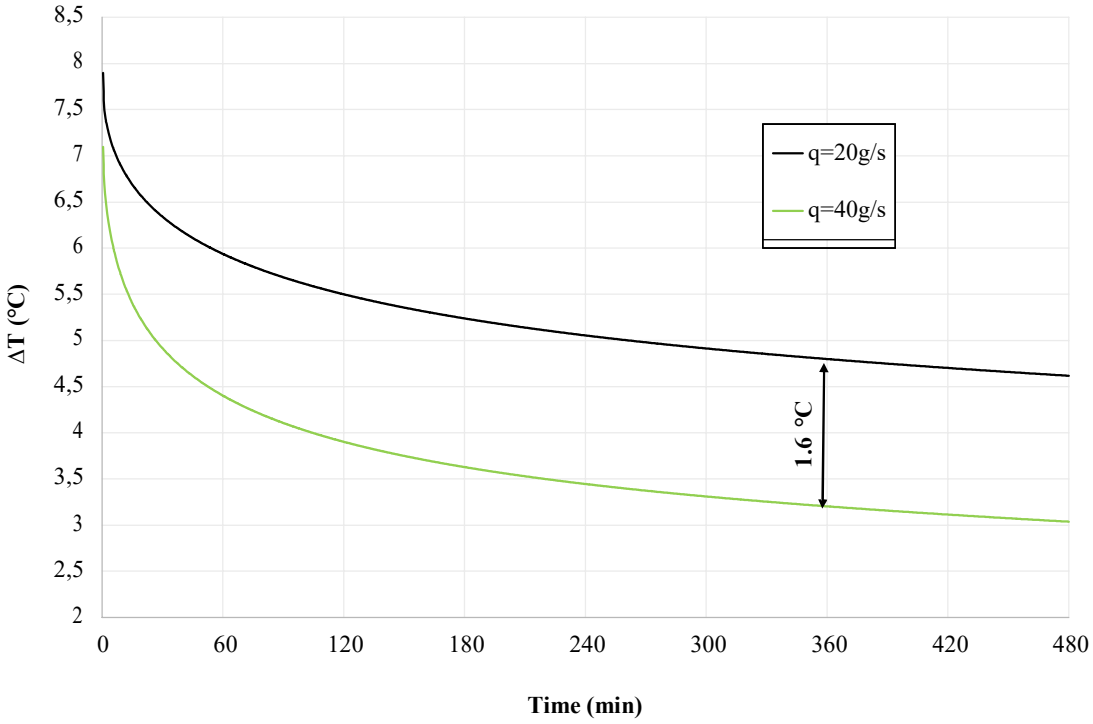

Fig. 8 Influence of the airflow rate on the cooling ($\Delta T=T_{in}-T_g$) of the air, for L=2m and D=20cm.

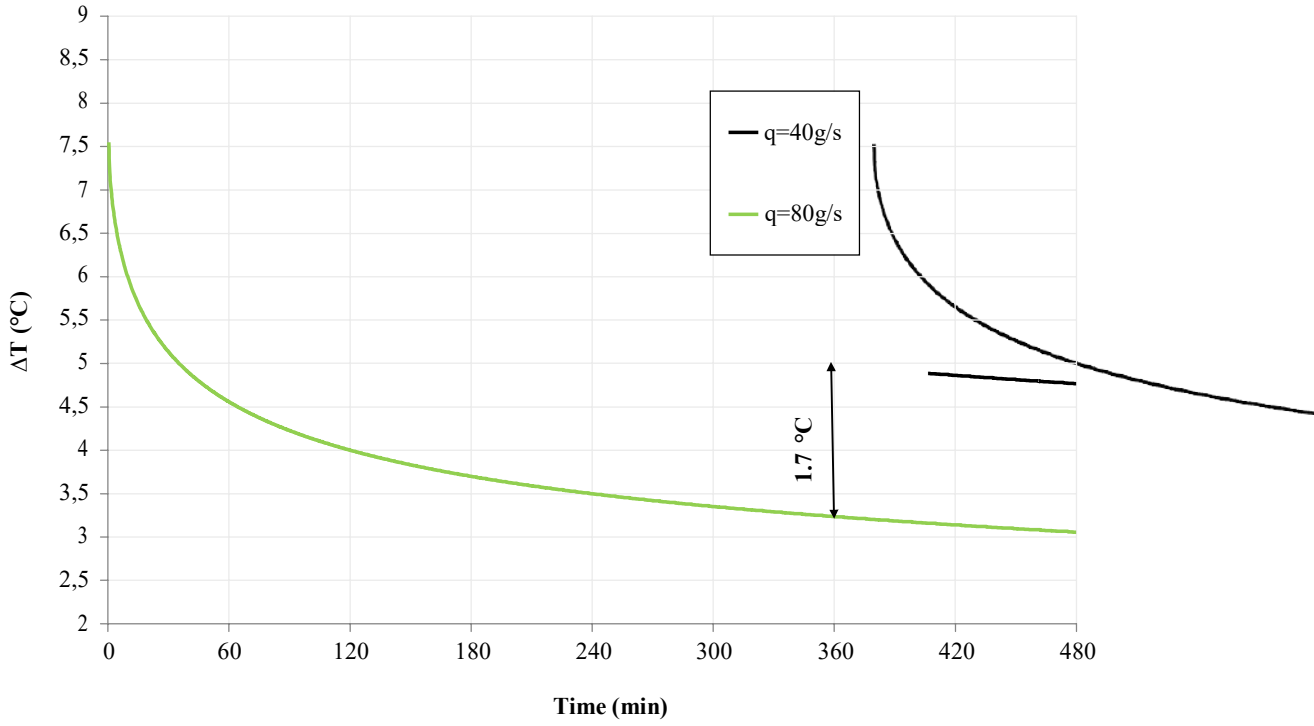

Fig. 9 Influence of the airflow rate on the cooling ($\Delta T=T_{in}-T_g$) of the air, for L=4m and D=20cm.

ISSN: 1737-9334

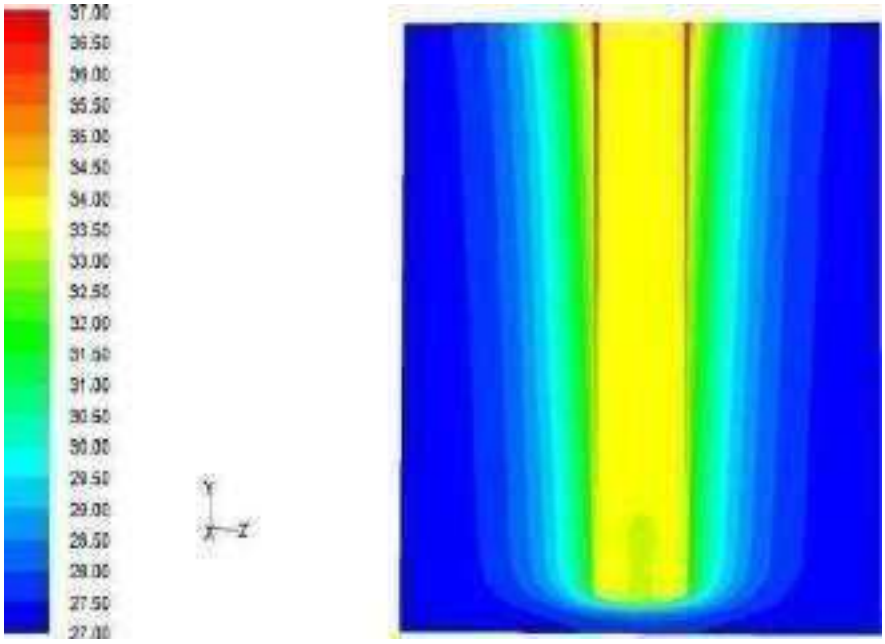

Fig. 10 Temperature field in a vertical plane at time t=4 hours, for D=20cm, L=4m and q=80g/s

V. CONCLUSIONS

The aim of this study was to investigate the influence of certain parameters (air flow rate, diameter, length) on the thermal behaviour of a vertical air-to-ground heat exchanger consisting of two coaxial tubes. The complexity of the equations involved required the use of a commercial numerical simulation tool, in this case Fluent.
The analysis of the results obtained shows that increasing the diameter of the tube increases the air-to-ground heat exchange and therefore improves the cooling of the air at the expense of the operating time of the exchanger.
On the other hand, increasing the length of the tube improves the cooling of the air while prolonging the operating time of the exchanger.
However, increasing the air flow rate reduces the cooling effect of the fluid and the operating time of the exchanger. For this reason, it is advisable, wherever possible, to provide for fairly large tube lengths and diameters. However, the sizing of these exchangers depends on the degree of cooling required for a specific installation.

REFERENCES

[1] B. Mebarki, B. Draoui, S. Abdessemed, A. Keboucha, A. Drici, and A. Sahli, “Etude d’un système de climatisation intégrant un puits canadien dans les zones arides, cas de Béchar,” *Revue des énergies renouvelables*., vol. 15(3), pp. 465–478, 2012.

[2] D. Bartolomeu, “Performance d'un échangeur thermique de type air-sol,” *Technipac.*, vol. 28(3), pp. 27–30, 2005.

[3] P. Hollmuller, “Utilisation des échangeurs air/sol pour le rafraîchissement des bâtiments - Mesures in situ, modélisation analytique, simulation numérique et analyse systémique,” Thèse de doctorat, Faculté des Sciences, section de physique, Université de Genève, 2002.

[4] B. Peuportier, S. Thiers, T. Salomon, R. Mikolasek, Y. Jautard, and A. Trombe, “Dimensionnement du puits climatique, Analyse, modélisation, validation d’un modèle de simulation dynamique pour les puits canadiens ou provençaux,” Région Languedoc-Roussillon, France, PREBAT ADEME 04 04C 000 1. Rapport final.

[5] *Les principes du puits canadien*, Eole, 2014.

10ème Conférence Internationale des Energies Renouvelables CIER-2022
Proceedings of Engineering & Technology-PET-

Grid Assessment Study of the Prospected Tunisia-Italy HVDC Interconnection

Imen KARRAY[1,2], Khadija BEN KILANI[2], Mohamed ELLEUCH[2], Slim TNANI[3],MahranKHALFOUN[2]
[1]The Tunisian Company of Electricity and Gas (STEG), Rades 2040, Ben Arous, Tunisia
[2]Université de Tunis El Manar, ENIT, L.S.E, LR11ES15, BP 37-1002, Tunis le Belvédère, Tunisie,
[3]LIAS/ENSIP, Universityof Poitiers, Poitiers, France

ikarray@steg.com.tn;khadija.kilani@enit.utm.tn;
Mohamed.elleuch@enit.utm.tn; slim.tnani@univ-poitiers.fr;mkhalfoun@steg.com.tn

***Abstract*—In this paper, a grid assessment study is conducted on the prospectedTunisia-Italy High Voltage Direct Current (HVDC) subsea interconnection. Problematic issues of this link emanatefrom system particularities: uneven system inertias, centralized generation assets, and limited AC interconnections. The study assesses how this HVDC link affects the stability of the system in the operational time frame, and whether it assures the power grids support during unplanned contingencies. State of the art HVDC technologies, namely VSC and LCC are compared in terms of their grid support capabilities in voltage/frequenc y. The simulations rely on an industry standard power system simulation software PSS/E and electromagnetic transients program EMTP. The study reveals how the system will behave in the event of disturbances and how it will respond to unplanned disturbances. Besides the scientific outcomes of this work, it may provide a decision support for systemoperators.**

Keywords- Tunisia-Italy HVDC interconnection, Grid support, VSC technology, control strategy.

I. INTRODUCTION

The Tunisian electric power is prospecting tremendous developments of its electric power network. Firstly, an ambitious target of renewable energy integration ratio reaching 35% by the year 2030, has been set. Secondly, the establishment of an interconnection to the European power grid via an HVDC subsea link Tunisia-Italy is prospected. Such interconnection falls in the category of uneven inertia system interconnection. More so, the Tunisian power system features centralized generation and few AC interconnections with adjacent power grids, namelywith Algeria.

Indeed, in order to meet the challenges of integrating a large quantity of renewable energies, the Tunisian electricity and Gas Company(STEG) has undertaken various actions to improve the flexibility of the network through the electrical interconnection in HVDC between Tunisia and Italy, to be operational by the year 2027 [1]. The latter must ensure the pooling of reserves between the two countries, an improvement in the energy mix and participation in system ancillary services. Moreover, integrating huge amounts of variable wind and solar energy in Tunisia's power system needs additional flexible and controllable power sources. The HVDC link with Italy can be a good back up power source. In addition, the converters of HVDC systems offer various control options depending on their technology: Vector Source Converter VSC or Line Commuted Converter LCC.

The HVDC based on LCC and VSC converters offer different system control capabilities: HVDC-LCC is a thyristor based technology, with a transmission capacity reaching up to 12 GW per bipolar system, at a voltage level up to ± 1100 kV. The HVDC-LCC consumes reactive power, requires the presence of AC voltage source for commutations, and the station losses are about 0.7% [2]. In contrast, the HVDC-VSC is an Insular Gate Bipolar Transistor (IGBT) based technology, with a transmission capacity reaching 3GW per bipolar system at a voltage level reaching ± 525kV. The HVDC-VSC doesn't need strong grid, doesn't consume reactive power and so, harmonic filters are not required [3].

This paper presents a grid assessment study on the prospected Tunisia-Italy HVDC subsea interconnection. The study assesses how this link affects the stability of the system in the operational time frame, and whether it can assure the Tunisian power grids support during unplanned contingencies. Firstly, the main European grid code requirements for HVDC are succinctly reviewed. The study considers short-circuit faults, loss of load and loss of generation contingencies. The results are evaluated for voltage and frequency stability, in compliance with grid code requirements.

II. MAIN EUROPEAN GRID CODE REQUIREMENTS FOR HVDC

Electric power networks require a number of functions and services that ought to be continuously provided to assure, their secure and reliable operation. The list of such services is widening and evolving as power quality requirements are becoming more and more constrainable. The main of these services pertain to the following capabilities: loss compensation, frequency control, black start capability, voltage or/reactive power control, oscillation damping, and congestion management. For the High Voltage Direct Current, the European Commission has issued HVDC network code requirements, referenced Commission Regulation (EU) 2016/1447 [4]. According the European Network of Transmission System Operators (ENTSO-E), existing or prospected HVDC interconnections must comply to the established technical codes. Tunisia-Italy HVDC must comply to these requirements, Tunisia being a stakeholder of the bilateral power exchange corridor. The main of these codes are given in the following.

A. *Frequency control*

The frequency support actions are temporized into stages (Fig 1): Inertial support; frequency containment reserve (FCR) provision, which designate the primary Control stage; and frequency restoration reserve activation, which refer to the Secondary Control action. Lastly, the replacement reserve (RR) are activated, corresponding to the tertiary control action. The belgian TSO Elia Grid follow the frequency control services shown in Fig 1.

The support of inertia takes immediate act, while the primary control acts after few seconds (within 30 sec). The activation of secondary reserves starts from 30 sec in order to take the frequency back to its nominal value. The tertiary control starts after 15 minutes. It is almost the same sequence of reserve activation for other ENTSO-E control areas, the variation is in the implementation of threshold values, and activation times [5].

According to [4], the HVDC system should participate in frequency regulation when a fault occurs in AC system by adjusting the active power sent or received as indicated in Fig. 2, respecting the Grid code specified by the TSO as ramp up and ramp down. The HVDC system must be able to respond to frequency deviations in each connected AC network by adjusting the active power transmission as dictated in Fig. 2, for the import mode. This specification shall be subject to notification to the regulatory authority. The modalities of that notification shall be determined in accordance with the applicable national regulatory framework. The quantity ΔP is the change in active power output from the HVDC system, f_n is the target frequency in the AC network where the frequency ancillary service is provided, and Δf is the frequency deviation in the AC network where the frequency ancillaryservice is provided.

B. *Voltage control*

Voltage control is different from frequency control as it is a local quantity that varies for every node of the system. The active power balance affects the frequency while the reactive power balance affects the voltage. Voltage control is ensured by controlling the injection and the absorption of reactive power in the grid and that explains the use of capacitor banks, static VAR compensators and reactors. Controlling voltage locally is important as transmitting reactive power is hard. Therefore, voltage control equipments have to be located at critical locations. The European Union commission regulation on electricity transmission system operation has defined the operational voltage limits for steady-state power system operation [5]. Table 1 shows these limits.

C. *Fault Ride Through*

Fault ride through is an important grid code requirement which mean a system continues to be connected to electrical system during and after a fault within certain limits. Fault ride through requirements for several countries are shown in Fig. 3. The voltage profile of some countries is defined by the type of fault [7]. The Figure represents the lower limit of a voltage- against-time profile at the connection point, expressed by the ratio of its actual value and its reference 1 pu value in per unit before, during and after a fault.

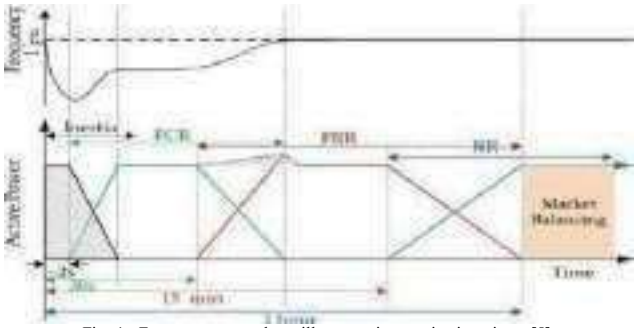

Fig .1. Frequency control ancillary services activation time [5]

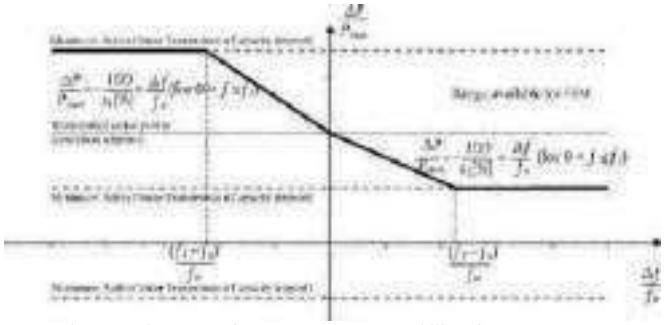

Fig. 2. Active power frequency response capability of an HVDC system

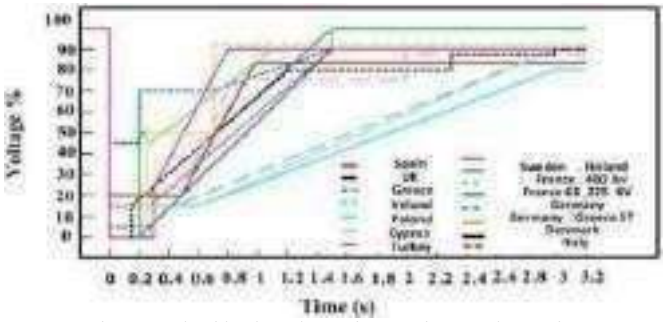

Fig. 3. Fault Ride Through Requirements in several countries

TABLE I. STEADY-STATE OPERATIONAL VOLTAGE RANGE [6]

	CE	Nordic	GB	IE & NI	Baltic
Connection point voltage 110 kV–300 kV					
Voltage range (pu)	0.9–1.118	0.9–1.05	0.9–1.10	0.9–1.118	0.9–1.118
Connection point voltage 300 kV–400 kV					
Voltage range (pu)	0.9–1.05	0.9–1.05	0.9–1.05	0.9–1.05	0.9–1.097

II. HVDC CONVERTER TECHNOLOGY

A. *HVDC LCC TECHNOLOGY*

Line commuted converter known as LCC is a thyristor based technology. The thyristors used in HVDC plants are characterized by large voltage-blocking capabilities. Nonetheless, the direction of power flow depends on the polarity of DC voltage while the direction of the current stays the same. Commutation in this technology depends on the AC line voltage crossing, thus, an HVDC-LCC needs to be connected to a strong grid with a high short circuit power in order to avoid commutation failure. Furthermore, LCC requires a large harmonic filters and therefore, the converter station needs a large ground footprint.

A. HVDC VSC Technology

Voltage source converters (VSC) are self-commutated converters based on insulated gate bipolar transistors IGBT, known for their high degree of flexibility [9]. In the VSC converters, the current is able to be switched on and off at any time independently from the AC voltage, and so, it creates its own AC voltage in case of a blackstart situation. Thus, there is no need for a strong synchronous voltage for the commutation process. The VSC converters operate with high frequency, and they are able to control active and reactive power rapidly and independently. This technology has a little risk in commutation failure unlike LCC technology and faster dynamic response due to higher switching frequency operation, and so the decrease demand in filtering and sosmaller filter size.

The scheme of VSC basic control with vector control strategy is shown in Fig. 4. Each VSC converter controls its reactive power in an independent way of the other converter. The reactive power control depends on the AC voltage control. The transfer of active power can be quickly reversed without changing the control mode and without co verter blocking. The active power flow can be reversed simply by changing the DC current and not like the LCC technology, where we need to change the polarity of the voltages. When needed, the converter can reverse to full power in milliseconds. During the power reversal, the reactive power controller continues its normal operation.

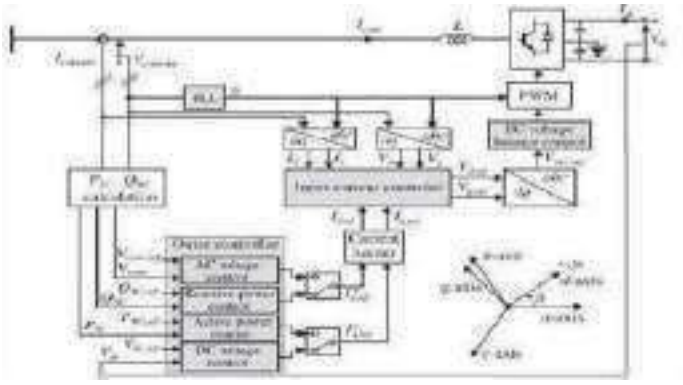

Fig. 4 Topology of HVDC-VSC Technology

.

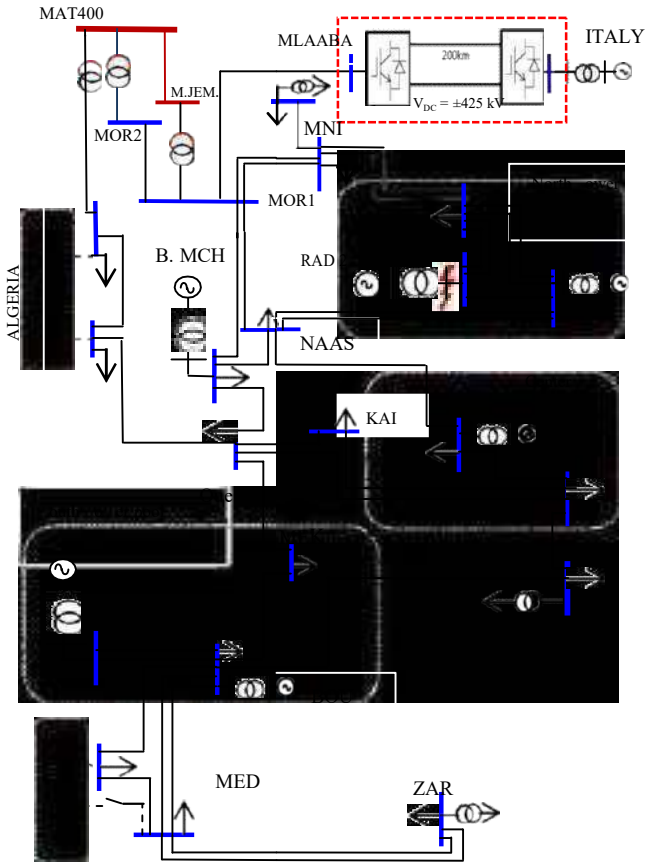

Fig. 5 Equivalent Tunisian transmission power network with its interconnections to Italy and Algeria.

III. STUDY MODEL

Since 2019, Tunisia and Italy have agreed to build a 600 MW Mediterranean power interconnector linking their power grids, via a submarine HVDC cable of length 200 km. The link would make it possible to integrate the two electricity markets, significantly improving the interconnection of the EU system with North Africa. Italy's TERNA and STEG in Tunisia are due to complete the project by2028.

In this study, the system described in Fig. 5 is built based on Power System Simulator for Engineering PSS/E and electromagnetic transients program EMTP. A series of time domain simulations are performed to investigate the controls of both technologies The HVDC interconnection shown in Fig. 5 is described as follows:

- The Tunisian electric network comprises three main power pools with concentrated generators in the North (Rades Power Plant), Sousse Plan Power in the east coast presenting the center power pool, and the southern power plants. An AC interconnection with the neighboring power grid of Algeria is established, with a power import set to 200MW. The AC Algerian and Italian networks are represented byequivalents synchronous generators.

- The HVDC cable link is 200 km long, has a rated power of 600 MW and a DC voltage rating of ±400 kV. In order to evaluate the controls for each technology described in section II, the power flow is assumed from Italy toward Tunisia. The HVDC interconnection uses VSC and LCC technologies.

IV. SIMULATION RESULTS

First, HVDC-LCC and HVDC-VSC control performances are tested for three contingencies: A short-circuit fault of duration 250 ms applied at RADES 2 transformer secondary bus, a loss of load of 250 MW, and a loss of 220 MW generation. These simulations rely on PSS/E software. Next, the VSC converter is used in order to test the ability of this technology in participating in ancillary services. For testing VSC controls, EMTP software is used. In order to evaluate the advanced controls for ancillary services support, the power flow is assumed from Italytoward Tunisia.

A. Synchronous generators active power

Fig 6 shows the active power of the northern machine response for both technologies LCC and VSC when a bolted short-circuit fault of duration 250 ms occurring in the bus of RAD 2. In case of LCC technology, the response exhibits more oscillations than the VSC technology. In VSC, the active power oscillates lightly, reaches 2500MW while for LCC technology the active power oscillates rapidly and reaches 3500MW. After 15 sec, both technologies go back to the stable state. During the fault, each converter controller tries to reduce the effect of the fault on the converter. In case of LCC, in the rectifier controller, the voltage current order limiter (VDCOL) helps to minimize the dc current, but inverter side finds a problem in regaining fast from commutation problem. Fig. 6 shows that HVDC system with VSC technologyis immune to AC fault.

In case of load loss, LCC and VSC have almost the same behaviour (Fig. 7). The northern machine instantly decreases the power generation and reaches 1225MW. After some oscillations, the active power goes back to steady state and decreases the active power by50MW.

In the case of power generation loss, the active power response in Tunisia exhibited almost the same behaviour. The northern RAD power generators instantly increase the power generation and reaches 1575MW. After some oscillations, the active power goes back to steady state and increases the active power by 50 MW. As a power generator is lost, the power lost is compensated bythe remaining machines in service.

B. Grid Frequency

The frequency is an important indicator of active power balance in the grid. In the case a short-circuit of 250 ms at RAD2, the frequency of the HVDC-VSC system demonstrated less oscillations than the frequency in the case of HVDC-LCC system. For the case of HVDC-VSC, the frequency reaches 51.5Hz while for the HVDC-LCC, the frequency reaches 53.5Hz. These simulations confirm that the VSC has better performance than LCC, as LCC require a stronger grid to operate in optimal conditions while VSC doesn't need it. The frequency of VSC returns to its initial value within 15sec while the frequency of LCC returns at 25sec (Fig.8). When the grid lost a generation of 220MW, the frequency of both technologies had the same shape. As the power generation decreases, the frequency decreases and does not return to its initial value, it returns to steady state after almost 19 sec at a frequency of 49.82 Hz (Fig. 9). In case of loss of load, the reverse happens. The frequencyincreases as the active power increases (Fig. 10).

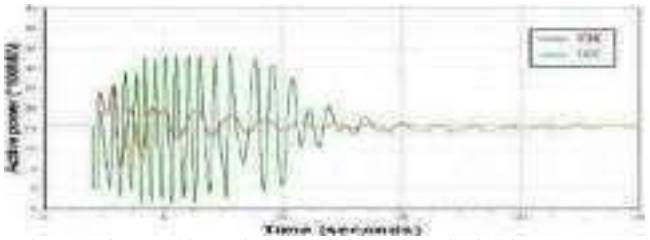

Fig. 6. Northern machine active power during a short-circuit of 250 ms at RAD 2 bus

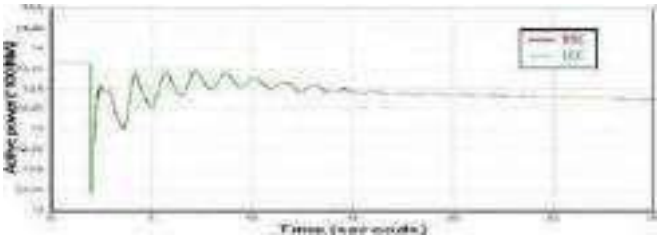

Fig. 7. Active power response of to 250 MW load loss

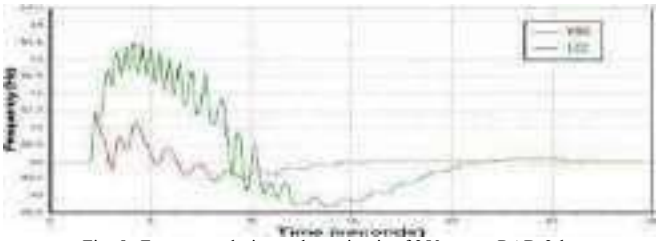

Fig. 8. Frequency during a short-circuit of 250 ms at RAD 2 bus

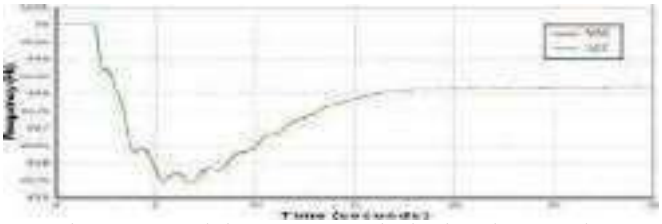

Fig. 9. Frequency during 220MW generation loss in Rades power plant

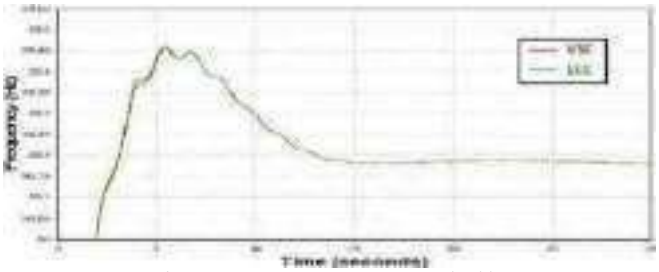

Fig. 10. Frequency response-250MW load loss

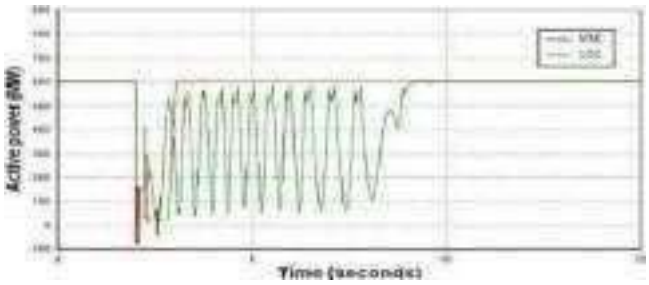

Fig. 11. Transmitted active power from Italy-250ms fault

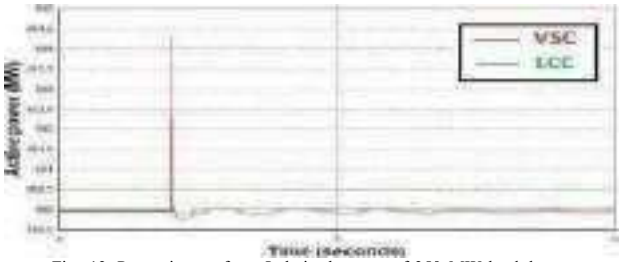

Fig. 12. Power import from Italy in the case of 250 MW load loss

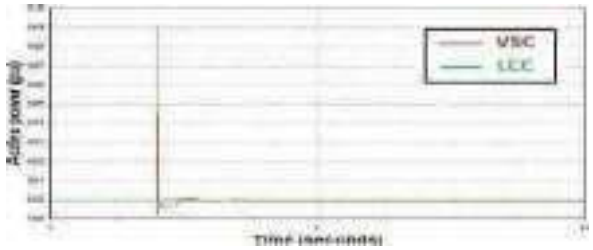

Fig. 13. Power import from Italy in the case of 250 MW load loss

C. Transmitted active power from Italy to Tunisia

In case of 250ms fault, the active power received from Italy returns quickly to its steady state for VSC at t=3sec while for LCC, it presents several oscillations before returning to the steady stated at t=9sec. During the fault, each converter controller tries to reduce the effect of the fault on the converter. In case of LCC, in the rectifier controller, the voltage current order limiter (VDCOL) helps to minimize the dc current, but inverter side finds a problem in regaining fast from commutation problem. Fig. 11 shows that HVDC system with VSC technologyis immune to AC fault.

In case of loss of power generation and load loss, we have almost the same shape for both technologies (Fig. 12/13). The system continues to import power.

D. Ancillary service: frequency control

The rated power of Tunisia-Italy HVDC link is 600 MW. First, an operation with reserve is simulated. In this case, the HVDC power is fixed at 150MW. So, an active power reserve of 75% of rated is preserved based on the request of the system operator. An increase of Tunisian load was simulated in order to evaluate frequency control.

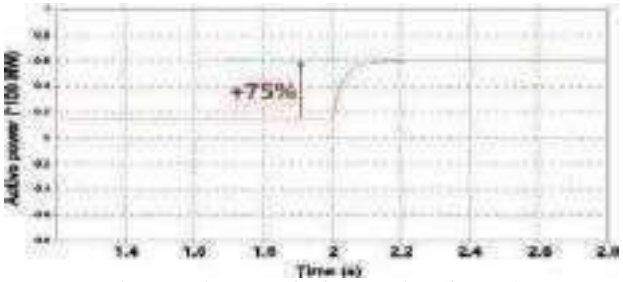

Fig. 14 Active power for frequency drop (f=48.5Hz)

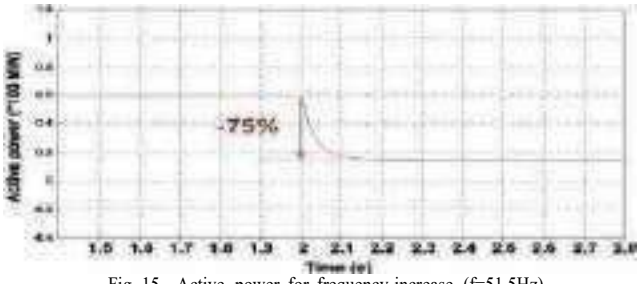

Fig. 15. Active power for frequency increase (f=51.5Hz)

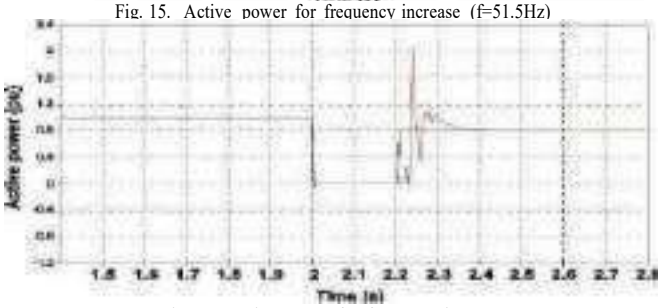

Fig. 16. Active power for frequency increase

As a result, the utility grid undergoes a drop of grid frequency which equals 48,5Hz. In simulation, the frequency droop is chosen equal to 4% (s1=4%) to comply with the Tunisian frequency control requirements.

Finally, the VSC-HVDC converters can participate in the regulation of grid frequency by selecting automatic frequency control. To support the grid, the power delivered by the HVDC increases by 450 MW as a participation in the frequency primary control (Fig. 14). During over-frequencies or under frequencies, the droop functions are activated. The active power share for the HVDC system is calculated based on the defined drooping:

$$\frac{\Delta P}{PPP} = \frac{100}{P1} \times \frac{\Delta f}{fP} = 75$$

Second, the inverse is simulated (Fig. 15). The HVDC power is fixed at 600MW. This time a decrease in Tunisian load is simulated and the frequency reaches 51.5Hz. The downward droop is maintained 4% (s2=4%). In this case, the HVDC decrease the power by450MW from 600 MW to 150 MW.

$$\frac{\Delta P}{PPPP} = \frac{100}{P2} \times \frac{\Delta f}{fP} = 75$$

Frequency control can also be ensured in a local way(Fig. 16). This means that active power can be regulated at one point of

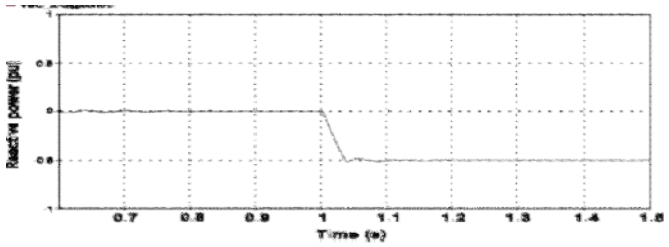

Fig. 17. Reactive power during an increase in the grid voltage

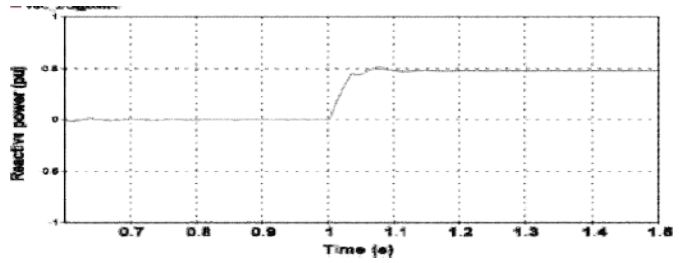

Fig. 18. Reactive power during a drop in the grid voltage

the grid independently of the rest of the grid, following a reference generated by the TSO. In Fig. 16, the TSO order was to import 0.9 pu, stop the importation at t=2s and then import 0.8 pu att=2.2 (The blue curve is reference and the red is the active power response). It is obvious that the VSC response follows the order received from the TSO.

E. Ancillary service: Voltage Control

In order to participate in ancillary services, the HVDC system is required to respond to the decrease and increase in grid voltage by the absorption or injection of reactive power by the converter in the grid. For testing, the main voltage was varied. As the voltage increases, the system responds with a decrease in reactive power (Fig. 17). When the voltage drops, the system responds with a rise in reactive power (Fig. 18).In this section, the EMTP software is used.

VI. CONCLUSION

This paper presented a grid assessment study on the prospected Tunisia-Italy HVDC subsea interconnection. Firstly, the main European grid code requirements for HVDC are succinctly reviewed. Grid support in frequency, voltage and Fault ride through have been investigated. By simulating short-circuit faults, loss of load and loss of generation contingencies. The HVDC-VSC technology has been used. The results were discussed for compliance with grid code requirements, in power import scenario. Compliant responses have been found.

Future works have to deal with more ancillary services that HVDC interconnection should provide to strengthen power system stabilitywith large renewable energyintegration.

ACKNOWLEDGMENT

The authors are grateful to electrical systems laboratory of National Engineering school of Tunis (ENIT), to the Tunisian Company of Electricity and Gas (STEG) and to Erasmus+ Exchange Program KA107.

REFERENCES

[1] RINA to Undertake Tunisia Interconnection Marine Feasibility - RINA.org.15July2021, www.rina.org/en/media/press/2021/07/15/i taly-tunisia-interconnection.

[2] HVDC Classic (LCC) – HVDC | UHVDC, Thyristor. siemens-energy.com Global Website. Retrieved July 10, 2022 from https://www.siemens-energy.com/global/en/offerings/power- transmission/portfolio/high- voltage- direct-current-transmission- solutions/hvdc-classic.html

[3] HVDC PLUS (VSC) - Siemens Energy HVDC | IGBT, MMC. siemens-energy.com Global Website. Retrieved July 10, 2022 from https://www.siemens-energy.com/global/en/offerings/power- transmission/portfolio/high- voltage- direct-current-transmission- solutions/hvdc-plus.html

[4] COMMISSION REGULATION (EU) 2016/1447 of 26 August 2016 establishing a network code on requirements for grid connection of high voltage direct current systems and direct current-connected power park modules. https://eurlex.europa.eu/legalc ntent/EN/TXT/PDF/?uri=CELEX:32016R1 *4* 7&from=EN

[5] Kaushal, Abhimanyu& Van Hertem, Dirk. (2019). An Overview of Ancillary Services and HVDC Systems in European Context. Energies. 12. 3481. 10.3390/en12183481.

[6] Official Journal of the European Union: Commission Regulation(EU) 2017/1485 of 2 August 2017 Establishing a Guideline on Electricity Transmission System Operation. Available online: https://eur-lex.europa.eu/

legal-content/EN/TXT/PDF/?uri=CELEX:32017R1485&from=EN (accessed on 9 September 201).

[7] Aya M. Moheb, Enas A. El-Hay and Attia A. El-Fergany, Dirk. (2022).Comprehensive Review on Fault Ride-Through Requirements of Renewable Hybrid Microgrids.Energies.*15*(18), 6785; https://doi.org/10.3390/en15186785

[8] MIRCEA EREMIA,CHEN-CHING LIU, ABDEL-ATYEDRIS," Advanced Solutionsin Power SystemsHVDC, FACTS, and Artificial Intelligence", IEEE Press Series on power engineering, 2016

[9] Working Group B4.46, "Voltage Source Converter (VSC) HVDC for Power Transmission – Economic Aspects andComparison with other AC and DCTechnologies", CigréISBN: 978-2-85873-184-8, 2012

[10] Siemens Energy,"HVDC PLUS- the decisive step ahead Stabilized power flows improve transmission grid performance", Siemens Energy Global GmbH & Co. KG, 2022.

Caractérisation phytochimique du *Globularia alypum* L. Collecté de Djebel Zaghouan (Tunisie)

SANA DALLALI
Laboratoirede Recherches en Systèmes de Production Agricole et de Développement Durable, Ecole,Supérieure d'Agriculture, Mograne, Zaghouan Tunisie,
sanadallali02@gmail.com

RABIAA MOUHBI
Laboratoire des Ressources Sylvo-Pastorales. *Institut Sylvo-Pastoral de Tabarka, Université de Jendouba*
Tabarka, Tunisie
mouhbirabiaa@gmail.com

HOUCINE SELMI
Laboratoire des Ressources Sylvo-Pastorales. *Institut Sylvo-Pastoral de Tabarka, Université de Jendouba*
Tabarka, Tunisie
houcine_selmi@live.fr

HANENE BOURAOUI
Laboratoire des Ressources Sylvo-Pastorales. *Institut Sylvo-Pastoral de Tabarka, Université de Jendouba*
Tabarka, Tunisie
hanenebouraoui@yahoo.fr

***Résumé*— La méthode appliquée, pour mesurer l'activité antioxydante, est la DPPH, tandis que, l'activité antimicrobienne a été évaluée par la méthode de diffusion en milieu solide. Les résultats obtenus ont montré des teneurs variables et significativement différentes, entre organes et nature d'extrait. En effet, la teneur en lipides, la plus élevée, est obtenue au niveau des feuilles et la teneur la plus faible, au niveau des fleurs, avec des pourcentages respectifs, de l'ordre de 95%et de18,7%.On a noté, aussi, que les extraits méthanoliques des feuilles(80,78mg EAG/g MS) sont dotés d'une teneur assez élevée en polyphénols comparée à celles au niveau des tiges (51,93mg EAG/g MS), des fleurs (35,19 mg EAG/g MS) et des racines(33,48 mg EAG/g MS).Pour les extraits aqueux, les polyphénols existent, aussi, dans tous les organes analysés, mais avec des teneurs plus faibles, comparées à celles enregistrées au niveau des extraits méthanoliques. Elles sont de l'ordre de 27,85 ; 26,19 ; 25,81 et 16,53 mg EAG/g MS respectivement pour les feuilles ; les tiges ; les fleurs et les racines. L'espèce contient aussi des teneurs variables en flavonoïdes, dont la plus remarquable, a été enregistrée au niveau de l'extrait méthanolique des feuilles (60,15 mg CE/g ms), comparée à la teneur de l'extrait aqueux (14,62 mg CE/g ms), dans ces mêmes organes. Grace à cette richesse en composés secondaires, les feuilles du *Globularia alypum* L., disposent d'une capacité antioxydante importante, par rapport aux autres organes testés. L'étude a révélé que l'espèce offre, en plus, a un effet antimicrobien, variable d'une bactérie à une autre.**
.

Mots clé—: activités antimicrobiennes, activités antioxydantes, Globulariaalypum L., polyphénols.

I. INTRODUCTION

Grace à sa situation géographique particulière, la Tunisie dispose d'une gamme bioclimatique très variée, qui la spécifie, en favorisant le développement d'une flore riche et diversifiée, regroupant plus de 2160 espèces végétales, dont plus de 350 sont reconnues comme étant à vertus médicinales (Zaouali 2005 ; Ben Issa 2011).Ces espèces jouissent d'une valeur importante, non seulement en tant qu'élément de la biodiversité floristique, mais aussi en tant qu'élément de la diversité culturelle, dont la mise valeur sollicite une attention particulière. Dans le milieu rural, les risques de dégradation des écosystèmes constituent une menace, de plus en plus, contraignante, dans un contexte où l'emprise humaine ne fait que s'amplifier. En effet, dans ce milieu, les relations entre la population et le milieu naturel, à travers les activités pastorales et les pratiques agricoles et domestiques, sont étroites (Zouaghi et al. 1998).

Les Plantes Aromatiques et Médicinales (PAM), jouent un rôle socioéconomique très important. Traditionnellement, elles sont destinées pour les besoins d'herboristerie, de la pharmacopée et comme aromates alimentaires. Elles sont, aussi, utilisées pour la production d'extraits aromatiques, destinés, essentiellement, à l'industrie de parfumerie et du cosmétique, ainsi que pour la préparation des produits d'hygiène et pour la formulation des arômes (Benjilaliand Zrira 2005). Cependant, cette filière demeure sous-évaluée, en Tunisie, malgré un grand regain de l'intérêt pour les produits naturelles à l'échelle internationale (TAP 2013 ; APIA 2013).De nos jours, entre 20.000 et 25.000 plantes sont utilisées dans la pharmacopée humaine. Signalons, à ce titre, que 75% des médicaments ont une origine végétale, dont 25% contiennent, au moins, une molécule active d'origine végétale(Benayad 2013 ; Neffatiand Sghaier 2014). Les extractions, des différents produits, se réalisent sous différentes formes, dont les plus importantes sont : les tisanes, les gélules, les suspensions intégrales de plantes fraîches, les teintures mères, les macérât glycérinés et les huiles essentielles (Benayad 2013). Les grands types de Plantes Aromatiques et Médicinales, utiles à l'homme, peuvent être définis par référence à leur principal usage. On peut, ainsi, parler: des plantes pour tisanes, des plantes pour boissons hygiéniques et

ISSN: 1737-9334

d'agrément, des plantes à usages cosmétiques, des plantes à usages aromatiques et condimentaires, des plantes à usages alimentaires, des plantes à usages industriels, et des plantes médicinales (Tardivonand St Mohamed 2012.). Parmi ces espèces, on a choisi, pour cette étude, une plante spontanée de la flore Tunisienne. Il s'agit de la globulaire (*Globularia alypum* L.), de la famille des Globulariaceaes. Cette espèce est un sous arbrisseau, rencontré, surtout, dans les endroits secs. Elle est très, souvent, associée au ciste et au romarin. C'est une plante vivace, qui pousse dans les lieux rocailleux et broussailleux secs, de préférence sur du calcaire. En effet, ces buissons poussent, fréquemment, sur de gros rochers, isolés ou sur des falaises. L'espèce est un arbuste rameux, d'environ 60 cm de hauteur (Quezel and Santa 1962 ; Khantouche and Abderabba 2018). Ses feuilles, dites spatulées, sont persistantes, coriaces, ovales, lancéolées, élargies à l'extrémité et atténuées à la base. Ses fleurs, réunies en capitules denses, à bractées ciliées, atteignent près de 2 cm de diamètre et sont disposées le long et au sommet des tiges. Elles sont d'un bleu clair, réunies en capitule globuleux solitaire, situé à l'extrémité des rameaux (Quezeland Santa 1962).La plante joue un rôle important, dans la prévention des maladies chroniques, telles que les pathologies du cœur, le cancer, le diabète, l'hypertension et la maladie d'Alzheimer, en combattant le stress oxydant (Meddour et al. 2013). Plusieurs travaux sont réalisés, sur le genre *Globularia*, où les auteurs avancent la présence des polyphénols totaux, des flavonoïdes et des anthocyanine, dans ces espèces (Chograni et al. 2013). Les feuilles, de *Globularia alypum* L., sont hypoglycémiques : elles augmentent la production du taux de l'insuline et de laxative (Jouad et al. 2002 ; Skim et al. 1999 ; Bellakhdar et al. 1991). Elles sont, en outre, cholagogues, stomacales, purgatives et sudorifiques (Sijelmassi 1993).Dans ce contexte, nous avons jugé nécessaire d'étudier la richesse, de cette espèce, en certains composés secondaires, en relation avec des différentes activités biologiques, au niveau de quatre organes de la plante(feuilles, fleurs, tiges et racines).

II. MATERIEL ET METHODES

A. Site et materiel végétal

Le Matériel végétal a été prélevé sur *Globularia alypum*L.,de Djebel Zaghouan, dans la région de Mograne (Tunisie), au mois de février 2019(tableaux 1 et 2). Les échantillons obtenus, ont concernés des feuilles, des fleurs, des tiges et des racines, collectés séparément. Ils ont été, ensuite, séchés dans un endroit bien aéré, à l'abri de la lumière, pour préserver leur effet aromatique et éviter leur oxydation. Ensuite, ils ont été broyés et conservés, à l'obscurité, dans des flacons en verre.

Tableau 1..

Tableau 1: Caractéristiques géographiques de provenance de *Globularia alypum*L

Provenance	Latitude	Longitude	Altitude	Bioclimat	Pluviometrie
Mograne (DjebelZaghouan)	36°22'45, 14412"N	10°06', 137304"(E)	5 m	Sub-humide	500-650 mm/an

Photo 1: Prise de vue, février 2019

B. Caracterisation édaphique des provonances de Globularia alypum L

Tableau 2: Ressources en sol du gouvernorat de Zaghouan (H.A.R, 2008)

Type de sol	Superficie (ha)	Pourcentage (%)	Fertilité
Sols minéraux bruts	31 617	11,1	Faible
Sols peu évolués d'apport	73 437	25,8	Bonne à moyenne
Rendzines	30 633	10,8	Faible à moyenne
Sols bruns calcaires	72 130	25,4	Moyenne à bonne
Vertisols	11 421	4	Bonne
Sols calcimorphes	47 320	16,6	Moyenne à faible
Sols fersiallitiques	1 562	0,6	Bonne
Sols halomorphes	7 013	2,5	Faible
Sols hydromorphes	3 167	1,1	Faible à moyenne
Sols isohumiques	6 068	2,1	Bonne
Total	**282000**	**100**	

C. Analysesphytochimiques

1. Extraction deslipides totaux

L'extraction des acides gras est faite manuellement, selon la méthode de Bligh et Dyer (1959).

2. Dosage des composés phénoliques

Le dosage des polyphénols totaux a été effectué selon la méthode de Singleton et al. (1999), simplifiée et modifiée par Dewantoet *al.* (2002).

3. Dosage des flavonoïdes totaux

Le dosage des flavonoïdes totaux a été effectué selon la méthode du trichlorure d'aluminium, en suivant le protocole de Yi et *al*.(2007).

D. Evaluationdes activités biologiques

1. Activités antioxydantes (DPPH)

Le protocole expérimental, suivi pour étudier les activités du piégeage du radical libre(DPPH), est celui décrit par Ammar et *al.* (2009). Les résultats sont exprimés en pourcentage d'inhibition (I%) (Meddour et al. 2013 ; Bentabet et al. 2014).

2. Activités antibactériennes

La détermination des activités antibactériennes a été effectuée, uniquementsur les feuilles du *Globulariaalypum*L.,en suivant la méthode des puits,décrite par Guven et *al.* (2006).

E. Analyses statestiques

Les analyses statistiques ont été effectuées à l'aide du Logiciel SAS (StatisticsAnalysis System), version 9.1. Une analyse de la variance (ANOVA), complétée par le test multirange, de Duncan, a été appliquée,afin de comparer les moyennes,à un seuil de signification de 5%.

III. RESULTATS ET DISCUSSION

A. Teneur en lipides totaux

Les résultats de la teneur en lipides totaux des feuilles, tiges, racines et fleurs du*Globulariaalypum*L. sont présentés dans le tableau 3.

Tableau 3: Rendement en lipides totaux (%) des feuilles, des tiges, des racines et des fleurs du *GlobulariaalypumL.*

Organes	Rendement en lipides (%)
Feuilles	$0,95 \pm 0,05^{a}$
Fleurs	$0,18 \pm 0,10^{b}$
Racines	$0,23 \pm 0,09^{b}$
Tiges	$0,32 \pm 0,33^{b}$

D'après ces résultats, on constate qu'il y a une différence significative ($p<0.05$) entre les organes analysés. Les feuilles sont plus riches en lipides, comparées aux autres organes, avec des teneurs de l'ordre de (0,95 %). Viennent, ensuite, par ordre décroissant, les teneurs des tiges (0,32 %), des racines (0,23 %) et des fleurs (0,187 %).

Les variations,dans les rendements,en lipides totaux, pourraient être dues au facteur âge de la plante et/ou à l'effet des facteurs génétiques etaux conditions environnementales et édaphiques (Uzun et al. 2002; Ravi et al. 2007). Elles peuvent être dues, également, à une activation des processus de dégradation des lipides, via la stimulation des enzymes lipolytiques. Ainsi, il a été bien établi, par de nombreux auteurs, que la teneur en lipides totaux est influencée par des facteurs abiotiques et biotiques (Laribi et al.2011; Trabelsi et al. 2012).

Chez la majorité des espèces végétales, les métabolismes primaires (lipides, protéines, glucides…) sont fortement influencés par de nombreux facteurs, notamment par la physiologie de la plante, par le statut minéral du sol, par les propriétés physico-chimiques du sol, par le climat et par la région de culture (Msaâda et al. 2009 ; Ramakrishna et Ravishankar 2011; Dallali et al. 2014). À cela, s'ajoute les conditions opératoires et analytiques, qui peuvent induire des variations, remarquables, de la composition lipidique (Cheikh-Rouhou et al. 2007 ; Dallali et al. 2016).

B. Teneurs en polyphénols totaux

Selon les résultats obtenus, on constate que l'espèce *Globulariaalypum* est riche en polyphénols totaux avec une différence significative ($p<0.05$) entre le type d'extrait et la nature de l'organe testé.

Il s'est avéré que, l'extrait méthalonique,des feuilles,contient la plus forte teneur en polyphénols totaux,affichant une valeur de l'ordre de 80,77 mg EAG/g MS. Suivi de celui des tiges (51,92 mg EAG/g MS) ; des fleurs (35,18 mg EAG/g MS) et des racines (33,48 mg EAG/g MS).

Concernant les teneurs en polyphénols totaux, au niveau des extraits aqueux, on a enregistré des valeurs inférieures à celles des extraits méthanoliques. Les feuilles ont enregistré les teneurs les plus élevées (27,85 mg EAG/g MS), suivies des tiges (26,18 mg EAG/g MS) ; des fleurs (25,81 mg EAG/g MS) et des racines (16,52 mg EAG/g MS).

Il en résulte quel'espèce,*Globulariaalypum*L., accumule plus de composés phénoliques,au niveau de ses feuilles et, à des degrés moindres, aux niveaux de ses tiges et de ses fleurs.La faible teneurest exprimée au niveau des racines.

Cette variation, dans la teneur en polyphénols totaux,en fonction de l'organe,pourrait être due, en partie, à des facteurs génétiques, qui contrôlent l'accumulation de ces composés dans les plantes, ainsi qu'aux conditions de croissance des plantes (Hashempour et al. 2010). Comme elle pourrait êtredue,probablement,à de nombreux autres facteurs,en particulier climatiques et environnementaux (température, altitude, ensoleillement et précipitations). Il s'ajouteaussi l'origine géographique, la sécheresse et les maladies (Ebrahimi et al. 2008; Andarwulan et al. 2010). En outre, d'après Miliauskas et al. (2004), la période de collecte des échantillons et le stade de croissance et du développement de la plante, jouent un rôle important,dans cette variabilité. D'autres études ont

suggéré que les conditions biotiques, à savoir l'espèce, l'organe, les stress abiotiques,les facteurs édaphiques, la luminositéet la salinité, peuvent jouer un rôle important dans la production et dans l'accumulation des composés phénoliques (Andarwulan et al. 2010; Jemâa 2014). Le procédé d'extraction et de quantification, influe, également, sur l'estimation de la teneur totale en polyphénols totaux (Lee et al. 2003).

C. Teneurs en flavonoïdes totaux

Par référence aux résultats, exprimés dans le tableau 4, l'espèce *Globulariaalypum*L., est riche en flavonoïdes totaux, avecune teneur qui varie, significativement($p<0.05$), selon le type d'extrait et selon la nature de l'organe analysé. Les feuilles du*Globulariaalypum*L.,offrent, toujours et pour les deux procédés, la teneur la plus élevée,comparée aux troisautres organes.

Au niveau des extraitsméthanoliques, ces teneurs sont de l'ordre de 60,15 ; 32,08 ; 30,62 et de 22,85 mg EAG/g MS respectivementpour les feuilles ; les fleurs ;les tiges et les racines.

Par contre au niveau des extraits aqueux, les valeurs sont inférieures à celles des extraits méthanoliquesavec 14,62 ; 12,52 ; 12,25 et 8,22 mg EAG/g MS pour les feuilles ;les racines ;les fleurset les tiges.Ces résultats se concordent avec ceux de Chograniet al. (2012),qui ont montré que les feuilles et les fleurs du*Globulariaalypum*L., de la Tunisie, sont riches en polyphénols et en flavonoïdes totaux par procédé méthanolique.

La différence, entre organes, observée, pourrait être due à de nombreux facteurs, notamment, à la période de la collecte des échantillons, au stade phénologique de la plante, aux facteurs édaphiques et à d'autres facteurs environnementaux (température, altitude, ensoleillement…) (Miliauskas et al. 2004 ; AmjadandShafighi 2013). L'origine génétique et la botanique de la plante peuvent, également, influencer la teneur en flavonoïdes totaux (Schmidt et al. 2010; Tan et al. 2016). Les flavonoïdes des végétaux sont, probablement, les composés phénoliques naturels les plus importants.AmjadandShafighi (2013), ontdémontré que la zone géographique, les conditions du sol et les pesticides,peuvent contribuer aux variations de la teneur en flavonoïdes totaux des plantes. Ces composés possèdent un large spectre d'activités chimiques et biologiques, y compris des propriétés anti radicalaires (Agbor et al. 2005 ; Karioti et al. 2010). Ils sont présents dans les légumes, dans les fruits, dans les fleurs et dans les feuilles (Stanković 2011). Ces composés phénoliques, sont généralement, trouvés dans les plantes comestibles et non comestiblesetleurs effets biologiques, multiples, y compris leurs activités antioxydantes, ont été signalés (Kim et al. 2011; Ghasemzadeh et al. 2010).

Tableau 4: Teneurs en Polyphénols totaux(%) et Flavonoïdes totaux, des différents organes du *GlobulariaalypumL.*

	Organes	Extraits Méthanoliques	Extraits aqueux
Polyphénols totaux(%)	Feuilles	80,77± 6,366[a]	27,85 ± 2,667[a]
	Fleurs	35,18± 6,055[b]	25,81 ± 1,22[a]
	Racines	33,48 ± 36,26[b]	16,52 ± 1,966[b]
	Tiges	51,925 ± 23,015[ab]	26,18 ± 4,458[a]
Flavonoïdes totaux	Feuilles	60,15±5,64 [a]	14,62 ± 1,27 [a]
	Fleurs	32,075±16,221 [b]	12,25 ±1.49[b]
	Racines	22,84±5,707[b]	12,52± 1,08[ab]
	Tiges	30,61± 7,43[b]	8,23± 0,21[c]

Les valeurs, dans la même colonne, avec des lettres différentes (a-c), sont significativement différentes à $p < 0.05$.

D. Evaluation des activités biologiques

1. Activitéantioxydante

L'activité antioxydante des extraits des feuilles, des tiges, des fleurs et des racines du ***G****lobulariaalypum*L.a été évaluée,*in vitro,* par le test de DPPH et le résultat a été exprimé en termes de pourcentage de réduction de DPPH (tableau 5).

Tous les extraits ont montré une activité antioxydante, en fonction du solvant et de l'organe.Les extraits méthanoliques et ceux aqueux sont dotés d'un pouvoir antioxydant modéré. Lesfeuillessont les plus actives (72,91 ± 5,17) par rapport aux autres organes.Il n'y a pas de différences significatives, de l'activité antioxydante,entreles fleurs et les racines. Les tigesprésentent, cependant, l'activité antioxydante la plus faible.

Concernant les extraits aqueux, il n'a pas de différences significatives entre les différents organes analysés.

Ces résultats se concordent avec ceux trouvés par (Es-Safi et al. 2005 ; Ghlissi et al. 2016), qui rapportent que les extraits méthanoliques de cette espèceont uneactivité antioxydante.

Il semble que cette activité est directement liée à la présence des polyphénols et des flavonoïdes dans les plantes étudiées. Il a été rapporté que les molécules antioxydantestelles que le phénol, les flavonoïdes et les tanins réduisent et décolorent le DPPH, en raison de leur capacité à céder l'hydrogène (Bougandour and Bendimerad 2013). Les polyphénols, contenus dans les extraits de *Globulariaalypum*L.sont, probablement, responsables de l'activité antioxydante de ces extraits. En effet, il a été démontré que les composés phénoliques contribuent directement à l'activité antioxydante (Naffati et al. 2011). De nombreuses étudesont montré une corrélation

significative, entre l'activité antioxydante et la teneur en composés phénoliques (Ksouri et al. 2007; Bhoyar et al.2011). Cependant, Babbar et al.(2011), ont montré que les composés phénoliques ne sont pas les seules responsables de l'activité antioxydante des plantes. En effet, d'autres constituants, tels que les ascorbates, les hydrates de carbone réducteurs, les tocophérols, les caroténoïdes, les terpènes, les pigments et l'effet de synergie entre eux, pourraient, éventuellement, contribuer à cette activité.L'activité antioxydante, des extraits des plantes, dépend également du type et de la polarité du solvant d'extraction (Ismail et al. 2010). Selon Zhang et al. (2011), l'activité antioxydante est généralement attribuée aux composés phénoliques et aux flavonoïdes des extraits des plantes.

2. Activité antibactérienne

Les résultats de l'activité antimicrobienne d'extrait alcoolique(éthanolique) et d'extrait aqueux sontenregistrés dans le tableau 5

L'extrait éthanoliquedes feuilles du*Globulariaalypum*L. présente une activité antimicrobienne importante,comparée à l'extrait aqueux. En effet, les microorganismes les plus sensibles à l'extrait ethanolique, ne présentent aucune activité antibacterianne chez les quatre bactéries testées(*Escherichia-coli* ;*Bacillus sibtilis* ;*salmonella enteridis* et *Listeria*).

Les investigations deTaghzouti et al.(2016) et de Ghlissi et al.(2016), ont révélé une activité anti-Bacillus subtilise, une activité anti-*Escherichia-coli* et une activité anti-*sallmonellaenteridis.* Cette étude ne présente aucune activité anti-*listeria*. Ceci peut être expliqué par la différence remarquable de la concentration des extraits.

L'activité antimicrobienne, des extraits alcooliques des feuilles du *Globulariaalypum*L.,peut être expliquée par sa richesse en polyphénols. Néanmoins, on note que cet extrait ne présente aucune action d'inhibition sur *listeria.*

Tableau 5: Evaluation des activités biologiques : antioxydante et antimicrobienne

	Extraits	Organes			
		Feuilles	Fleurs	Racines	Tiges
Activitéantioxydant	Méthanolique	72,91 ± 5,17 ^{a}	72,64 ± 8,403^{a}	64,84 ± 4,64^{a}	58,04 ± 3,77^{ab}
	Aqueux	42,06 ±2.80 ^{a}	46,070 ±4,69 ^{a}	61,01± 39,24^{a}	60,18 ± 6,45^{a}
		Microorganismes			
		Escherichia –coli	*Bacillus sibtilis*	*lmonella enterid*	*Listeria*
Activité antimicrobienne	Ethanolique (100 mg/ml)	+	+	+	-
	Aqueux(100 mg/ml)	-	-	-	-

Les valeurs, dans la même colonne, avec des lettres différentes (a-c), sont significativement différentes à $p < 0.05$
(-) absence d'activité antimicrobienne
(+) présence d'activité antimicrobienne

IV. CONCLUSION

Les métabolites secondaires constituent une large gamme de molécules végétales, dont la nature chimique et les teneurs sont extrêmement variables d'une espèce à une autre. En particulier, chez *GlobulariaalypumL.*, les teneurs sont variables selon l'organe et selon la méthode d'extraction. L'étude phytochimiquedes extraits, des différentes parties (feuilles, fleurs, tiges et racines)du*Globulariaalypum*L., a montré une certaine richesse, de la plante,en polyphénols totauxet en flavonoïdes. L'activité antioxydante évaluée,*in vitro,* par le test de DPPH, a révélé que les extraits (méthanoliques et aqueux) du*Globulariaalypum* L., présentent des activités anti-radicalaires, très importantes, surtout au niveau des feuilles. L'activité, des extraits méthanoliques, est plus performante, au niveau de tous les organes de la plante, par rapport aux extraits aqueux.

En ce qui concerne l'activité antibactérienne, *Listeria* n'aété sensible à aucun extrait. Cependant, les extraits ethanoliques des feuilles, concentrés à (100 mg/ml), possèdent une activité anti-*Bacillus*, une activité anti *Escherichia-coli* etune activité anti-*sallmonellaenteridis.* Cependant l'extrait aqueux n'a présenté aucune activité bactérienne, pour les souches testées. A la lumière de ces résultats, nous recommandons la séparation des antioxydants végétaux et leurs utilisations comme antioxydants naturels, dans les industries agroalimentaires et cosmétiques.

V. REFERENCES

Agbor GA, Oben JE, Ngogang JY (2005) Haematinic activity of *Hibiscus cannabinus*, African Journal of Biotechnology. 4 (8): 833-837.

Amjad L, Shafighi M (2013) Evaluation of antioxidant activity, phenolic and flavonoid content in Punicagranatum var. Isfahan Malas flowers. International Journal of Agricultureand Crop Sciences. 5-10: 1133-1139.

Ammar R, Smith AM, Heisler LE, Giaever G, Nislow C (2009) A comparative analysis of DNA barcode microarray feature size. BMC Genomics. 10:471.

Andarwulan N, Batari R, Agustini Sandrasari D,Bolling B,Wijaya H (2010) Flavonoid content and antioxidant activity of vegetables from Indonesia, Food Chemistry, 121(4): 1231-1235, https://doi.org/10.1016/j.foodchem.2010.01.033.

APIA (2013) Etude de l'amélioration de la Qualité et du positionnement des Plantes Aromatiques et Médicinales, Rapport , Agro-services, 180 pp.

Babbar N, Oberoi HS, Uppal DS, Patil RT (2011) Total phenolic content and antioxidant capacity of extracts

obtained from six important fruit residues. Food Research International 44: 391-396.
Bellakhdar J, Claisse R, Fleurentin J, Younos C (1991) Repertory of Standard herbal drugs in the Moroccan pharmacopoea. J.Ethnopharmacol. 35 (2): 123-43.
Benayad N (2013) Évaluation de l'activité insecticide et antibactérienne des plantes aromatiques et médicinales Marocaines. Extraction de métabolites secondaires des champignons endophytiques isolés de plantes Marocaines et activité anticancéreuse. Thèse de doctorat, UNIVERSITÉ MOHAMMED V – AGDAL FACULTÉ DES SCIENCES RABAT, 186 pp.
Benjilali B, Zrira S (2005) Plantes aromatiques et médicinales (Atouts du secteur et exigences pour une valorisation durable). Actes éditions, IAV Hassan II, Rabat. 346 p.
Bentabet N, Boucherit-Otmani Z, Boucherit K (2014) Composition chimique et activité antioxydante d'extraits organiques des racines de *Fredoliaaretioides* de la région de béchar en Algérie. Phytothérapie. 12 : 364-371.
Bhoyar MS, Mishra GP, Naik PK, Srivastava RB (2011). Estimation of antioxidant activity and total phenolics among natural populations of Caper (*Capparisspinosa*) leaves collected from cold arid desert of trans-Himalayas, Australian journal of crop science. 5(7): 912-919.
Bligh EG, Dyer WJ (1959) A rapid method of total lipid extraction and purification. Can. J. Biochem. Physiol., 37: 911-917.
Bougandoura N, Bendimerad N (2013) Évaluation de l'activité antioxydante des extraits aqueux et méthanolique de *Sature jacalaminthas*sp. Nepeta (L.) Briq. Revue « Nature & Technologie » B- Sciences Agronomiques et Biologiques. 9 : 14-19.
CheikhRouhou S,Besbes S, Hentati B, Blecker C,Deroanne C, Attia H(2007). *Nigella sativa* L.: Chemical composition and physicochemical characteristics of lipid fraction, Food Chemistry.101 (2): 673-681.
Chograni H, Riahi L, Zaouali Y, Boussaid M (2012) Polyphenols, flavonoids, antioxidant activity in leaves and flowers of Tunisian *Globulariaalypum* L. (Globulariaceae). Afr J Ecol. 51: 343-347.
Chograni H, Riahi L, Zaouali Y, Boussaid M (2013) Polyphenols, flavonoids, antioxidant activity in leaves and flowers of Tunisian *Globulariaalypum* L. (Globulariaceae). African Journal of Ecology. 51: 343-347.
Dallali S, Lahmayer I, Mokni R, Marichali A, Ouerghemmi S, Ltaief HBH, Sebei H (2014) Phytotoxic effects of volatile oil from Verbena spp. on the germination and radicle growth of wheat, maize, linseed and canary grass and phenolic content of aerial parts. AllelopathyJournal. 34(1): 95.
Dallali S, Montserrat L lovera, Jordi Eras Joli, Sebei Houcine, Ramon Canela-Garayoa (2016) Rapid Gas Chromatographic Determination of Free Fatty Acids in Rosemary (*Rosmarinusofficinalis* L.) Leaves, Analytical Letters, 49:4, 467-
476, DOI: 10.1080/00032719.2015.1072826.
Dewanto V, Wu X, Adom KK, Liu RH (2002) Thermal processing enhances the nutritional value of tomatoes by increasing total antioxidant activity. J. Agric. Food Chem. 50: 3010-3014.
Es-Safi NE , Khlifi S , Kerhoas L, Kollmann A, El Abbouyi A , Ducrot PH (2005) Antioxidant Constituents of the aerial parts of Globulariaalypum growing in Morocco. J.Nat Prod. 68 (8): 1293-1296.
Ghasemzadeh A, Jaafar HZE, Rahmat A, Wahab PEM, AbdHalim MR (2010) Effect of Different Light Intensities on Total Phenolics and Flavonoids Synthesis and Anti-oxidant Activities in Young Ginger Varieties (*Zingiberofficinale Roscoe*), International Journal of Molecular Sciences. 11: 3885-3897; doi:10.3390/ijms11103885.
Ghlissi Z, Kallel R, Silia A, Harrabi B, Atheymen R, Zeghal K, Bougatef A, Sahnoun Z (2016) *Globulariaalypum*methanolic extract improves burn wound healing process and inflammation in rats and possesses antibacterial and antioxidant activities. Biomedicine and pharmacotherapy. 84: 1488-1495.
Hashempour A, Ghazvini RF, Bakhshi D, Ghasemnezhad M, Sharafti M, Ahmadian H (2010) Hort. Environ. Biotechnol. 51(2):1-7.
https://www.webmanagercenter.com/2013/06/24/136608/tunisie-la-filiere-des-plantes-aromatiques-et-medicinales-est-porteuse-selon-une-etude/.
Ismail HI, Chan KW, Mariod AA, Ismail M (2010) Phenolic content and antioxidant activity of cantaloupe (Cucumismelo) methanolic extracts. Food Chemistry. 119: 643-647.
Jouad H, Maghrani M, Eddouks M (2002) Hypoglycaemic effect of *Rubusfructicosis* L. and *Globulariaalypum* L. in normal and streptozotocin-induced diabetic rats. J Ethnopharmacol. 81 (2) : 351-356.
KariotiA, BolognesiL, VincieriFF, BiliaAR (2010) Analysis of the constituents of aqueous preparations of *Stachys recta* by HPLC–DAD and HPLC–ESI-MS, Journal of Pharmaceutical and Biomedical Analysis. 53(1):15-23. https://doi.org/10.1016/j.jpba.2010.03.002.
Khantouche L, Abderabba M (2018) Dosage des poly phénols et étude de l'activité antioxydante et antimicrobienne des différents extraits des feuilles du *Globulariaalypum* L., IOSR Journal of Environmental Science, Toxicology and Food Technology (IOSR-JESTFT). 12(1) I : 68-74
Kim W, Kim HJ, Lee SH, Chang MB, Maeng WJ (2011) Effect of extruded canola seed supplementation on blood metabolites and lactational performance in lactating dairy cows. J. Anim. Sci. Technol. 43 (6): 859-872.
Ksouri R, Megdiche W, Debez A, Falleh H, Grignon C, Abdelly C (2007) Salinity effects on polyphenol content and antioxidant activities in leaves of the halophyte Cakile maritime. Plant. Physiol. Biochem. 45: 244-249. https://doi.org/10.1016/j.plaphy.2007.02.001
Kujala TS, Loponen JM, Kika KD, Pihlaja K (2000): Phenolics and betacyanins in red beetroot (Beta vulgaris) root: distribution and effect of cold storage on the content of total phenolics and three individual compounds. Journal of Agricultural and Food Chemistry. 48: 5338-5342.

Laribi B, Kouki K, Sahli A, Mougou A, Marzouk B (2011) Essential oil and fatty acid composition of a Tunisian caraway (*Carumcarvi* L.) seed ecotype cultivated under water deficit. Advances in Environmental Biology. 257-265.
Lee KW, Kim YJ, Lee HJ, Lee CY (2003) Cocao has more phenolic phytochemicals and a higher antioxidant capacity than teasandred wine. Food chemistry. 51: 7292-7295.
Meddour A, Yahia M, Benkiki N, Ayachi A (2013) Etude de l'activité antioxydante et antibactérienne des extraits d'un ensemble des parties de la fleur du *Capparisspinosa*. L. Science Journal. 14 : 49-60.
Meddour A, Yahia M, Benkiki N, Ayachi A (2013) Étude de l'activité antioxydante et antibactérienne des extraits d'un ensemble des parties de la fleur du *Capparisspinosa* L. Lebanese Science Journal, 14(1) :49-60.
Miliauskas G, Venskutonis PR, Van Beek TA (2004) Screening of radical scavenging activity of some medicinal and aromatic plant extract. Food chemistry. 85: 231-23.
MiliauskasG,VenskutonisPR,van BeekTA(2004) Screening of radical scavenging activity of some medicinal and aromatic plant extracts, Food Chemistry. 85(2): 231-237, https://doi.org/10.1016/j.foodchem.2003.05.007.
Msaâda K, Hosni K, BenTaarit M, Hammami M, Marzouk B (2009) Effects of growing region and maturity stages on oil yield and fatty acid composition of coriander (*Coriandrumsativum* L.) fruit. ScientiaHorticulturae. 120: 525–531.
Neffati M, Sghaier M (2014) Developpement et valorisation des plantes aromatiques et medicinales (pam) au niveau des zones desertiquesde la région MENA (Algérie, Egypte, Jordanie, Maroc et Tunisie), OSS, Projet MENA-DELP, 152 pp.
Neffati M, Sriti J, Hamdaoui G, Kchouk ME, Marzouk B (2011). Salinity impact on fruit yield, essential oil composition and antioxidant activities of *Coriandrumsativum* fruit extracts. Food Chemistry. 124(1) : 221-225.
NejadEbrahimiS,HadianJ,
MirjaliliMH,SonboliA,YousefzadiM (2008) Essential oil composition and antibacterial activity of *Thymus caramanicus* at different phenological stages, Food Chemistry. 110 (4): 927-931.
Quezel et Santa (1962) Nouvelles Flore de l'Algérie et des régions désertiques méridionales, centre National de la recherche scientifique (Ed) 15, quasi Anatole-France- Paris 7e) pp636.
Ramakrishna A, Ravishankar GA (2011) Influence of Abiotic Stress Signals on Secondary Metabolites in Plants. Plant Signaling & Behavior. 6: 1720-1731. http://dx.doi.org/10.4161/psb.6.11.17613.
Ravi R, Prakash M, Bhat KK, (2007) Aroma Characterization of coriander (*Coriandrumsativum* L.) oil samples. European Food Research and Technology. 225, 367-374.
Schmidt GA, Ruedy R, Miller RL, Lacis AA (2010) The attribution of the present-day total greenhouse effect. J. Geophys. Res. 115, doi:10.1029/2010JD014287.
Sijelmassi A (1993) Les plantes médicinales du Maroc, Le Fennec (3ème Edition) (Casablanca) pp285.
Singleton VL, Orthofer R, Lamuela-Raventos RM (1999) Analysis of total phenols and otheroxidation substrates and antioxidants by means of FolinCiocalteu reagent. Methods in Enzymology, 299:152-178.
Skim F, Kaaya A, Jaouhari TJ, Lazrek HB, Jana M, El Amri H (1999) Hypoglycaemic activity of *Globulariaalypum* leaves in rats. Fitoterapia.70: 382-389.
Sun B, Ricardo da Silva J, Spranger I (1998) Critical factors of the vanillin assay for catechins and proanthocyanidins. Journal of Agricultural and Food Chemistry. 46: 4267-4274.
Taghzouti OK, Balouiri M, Ouedrhiri W, Echchahad A, Romane A (2016) In vitro evaluation of the antioxidant and antimicrobial effects of *Globulariaalypum* L. extracts. Journal of Materials and Environmental Science. 7: 1988-1995.
Tan HSG, van den Berg E, Stieger M (2016) The influence of product preparation, familiarity and individual traits on the consumer acceptance of insects as food. Food quality and preference. 52: 222-231.
TAP (2013) Tunisie : La filière des plantes aromatiques et médicinales est porteuse, selon une étude.
Tardivon JC, St Mohamed C (2012) Les plantes aromatiques et médicinales, Livret PAM, 20pp.
Trabelsi H , Dendana F, Sellami A, Cheikhrouhou F, Neji S, Makni F, Ayadi A (2012) Pathogenic free-living amoebae: epidemiology and clinical review Pathol. Biol. 60: 399-405.
UzunB, Ülger S, Çağirgan Mİ (2002) Comparison of determinate and indeterminate types of sesame for oil content and fatty acid composition. Turkish journal of agriculture and forestry. 26(5): 269-274.
Yi ZB, Yu Y, Liang YZ, Zeng B (2007) In vitro antioxidant and antimicrobial activities of the extract of *PericarpiumCitriReticulatae* of a new Citrus cultivar and its main flavonoids, LWTFood Science and Technology. 4: 1000-1016.
Zaouali Y, Messaoud C, Salah AB, Boussaïd M (2005) Oil composition variability among populations in relationship with their ecological areas in Tunisian *Rosmarinusofficinalis* L..FlavourFragr. J., 20: 512-520. doi:10.1002/ffj.1428.
Zhang L, Zhao H, Gan M, Jin Y, Gao X, Chen Q, Guan J, Wang Z (2011) Application of simultaneous saccharification and fermentation (SSF) from viscosity reducing of raw sweet potato for bioethanol production at laboratory, pilot and industrial scales. BioresourTechnol 102(6): 4573-9.

Catalytic activity of graphene covered on copper nickel alloys for hydrogen evolution reaction

Chaima Chaib [1] ,Tarik Bordjiba [2] , Riane Nor El Houda Chiheb[3], Akram Issam Zermane[4]

[1,2,3] 8 Mai 1945 Guelma university, Science and technology faculty, Electrical engineering department, Guelma city, Algeria.

[1]alchaima1@gmail.com ; [2]bordjiba_tarik@yahoo.ca ; [3]rianechiheb@gmail.com ; [4]a.zermane.heliotech@gmail.com

***Abstract*— Water splitting has various advantages such as its ability to generate hydrogen and minimize the amount of pollutants. In this study, we show how to make highly and electro-catalytic graphene for water splitting. The copper-nickel alloys was joined with graphene to form an electrodes. The high electrocatalytic activity was achieved by keeping the nickel and copper contents on the surface at high temperature on the chemical vapor deposition reactor . We found that the Cu/G/Ni/G exhibits an excellent catalytic activity , this catalyst shows a small onset overpotential of – 65 mV,a tatef slope of 54 mVdec-1 Furthermore, the material demonstrated an excellent electrochemical durability in acidic electrolytes .**

***Keywords*— HER, Graphene, renewable energy, CVD,copper nickel alloy.**

I. INTRODUCTION

Most countries' energysystems are based on fossil fuels [1] , which has caused several negative environmental impacts [2] and bring in great threat to human health [3]; for that, researchers and scientists are becoming investigators. Searchingrenewable, newer and greener sources of energy, [4] that have limited impact on the environment and reduce their contribution to global warming [5] hydrogen is the most abundant element in the universe and as a gas can be used in the same way natural gas is used [6]. Hydrogen produces zero carbon emissions when used for energy [7] , also it is proposed as a promising energy carrier,[8] because it can be generated using renewable energy stored, [9] and used on demand either to generate electricity [10]. Splitting of water by electrolysis is the simplest way to produce hydrogen of high purity [11] , at the most economical price [12] . Pt-based materials are considered as the most efficient electrocatalysts [13] , towards hydrogen evolution reaction (HER) of water splitting [14], but the high cost of the Pt may limit its practical application in HER . Thus, it is highly important to explore cost-effective and efficient catalysts for HER. [15] Herein , the most studies have been investigated and selected transition metals as catalysts due to their relatively low cost and demonstrated promising electrocatalytic properties in HER.[16] .

In the past few years, researches have focused on nanocarbon based materials for large-scalemanufacturing and application HER electrocatalysts have shown wide-ranging and fascinating prospects for this field [17]]graphene-based nano-composite [18] materials possess many advantageous properties, such as large surface area[19]; adjustable porosity; high electrical conductivity[20]; versatile morphology [21]; chemical inertness and abundant electrocatalytic active sies[22].

Several studies show that the utilization of carbon based materials as electrocatalyst for hydrogen evolution reaction (HER) with good durability in acidic electrolytes , . Table 1 summerises a Comparative study of HER performance for Carbon and graphene catalysts ,however, the study of hydrogen evolution on graphene @ Copper/ Nickel alloys is limited. The present effort is hence a contribution towards this field .In this work , we synthesized transition-metal composites which is the graphene based on Copper and nickel alloys Cu/C/Ni/G ,Cu/Ni/G and Cu/G/Ni leading to a highly-active HER electrocatalyst with a small onset overpotentialsand a good tafel slops summerised in table 2 .

TABLE I
COMPARATIVE STUDY OF HER PERFORMANCE FOR CARBON AND GRAPHENE CATALYSTS

Electrode	η_0(mV)	η_{10}(mV)	b(mVdec^{1})	J_0 (mAcm^{2})	Ref
Act CNTs	100mV	220	71.3	16 x10^{-3}	23
NCNS	-65	204	81	50	24
MoS_2/RGO	-100	/	41	/	25
CFG	-248.3	/	116.6	47.9	26
NFG	-259	/	121.4	41.2	//
$C_{60}(OH)_8$	-110	/	78	7 x 10^{-7}	27
Mo_xC	/	/	50	1 x10^{-4}	28
ACs	/	450	163.32	/	29

TABLE II
COMPARISON OF HER PERFORMANCE FOR PT, CU/G/NI/G , CU/NI/ G AND CU/G/NI

Electrodes	η0(mV)	η010(mV)	b(mVdec^{1})	J_0 (mAcm^2)
Pt	-46	101	30	1,28
Cu/G/Ni/G	-65	127	54	1.70
Cu/Ni/G	-101	245	65	1,99
Cu/G/Ni	-119	290	105	2,75

η0: onset potential.
η10: overpotential at current densityof 10 mA cm-2 .
b: Tafel slope.
j0: exchange current density

II .EXPERIMENTAL

A. *Synthesis of Cu/G/Ni/G alloy*

Graphene was synthesized on the commercially copper foil from sigma -Aldrich (purity: 99,98% thickness :25 µm) was cut to dimension of 20 mm ×10 mm . the chemical etching of these copper foil was effected by putting the Cu foil into the etching solution which is the acetone (1mol/L) and the application of an ultrasonic wave for 30 minutes than for 15 minutes in the diluted ethanol , followed by rinsing with distilled water for 3 times . The Cu substrates were placed into the CVD furnace (OTF 1200X) and heated up to 1000°c at a heating rate of 20 C min-1 and kept at this temperature for 20 min under AR (250 SCCM) and H_2 (25 SCCM) gas mixture , then C_2H_2 (15 SCCM) was flowed into the quartz tube for 15 min , after graphene deposition , the system rapidly cooling to the room temperature under an Ar (250 SCCM) and H_2 (25 SCCM) ambience. For nickel electrodeposition, nickel (II) sulfate hexahydrate ($NiSO_4.6H_2O$, 99%) and boric acid (H_3BO_3) was purchased from sigma -Aldrich Company. As a cathode, the copper electrode coated with graphene was immersed in 0,1 M nickel sulfate and 0,5 boric acid solution , and Pt was used as a counter electrode. Nickel was deposited on the copper covered by graphene at constant current of 10 mA cm² for 5 min. After the electrodeposition process, the electrode was washed with deionized water for 1 min and dried for 1 h at room temperature. The second layer of Graphene was layered on the deposited nickel on copper covered by the first layer of Graphene , under low vacuum conditions at CVD and used the same above method. The cooling was controlled at a rate of 10 C min-1 .

B. *Synthesis of Cu/Ni/G alloy*

The commercially copper foil from sigma -Aldrich (purity: 99,98% thickness :25 µm) was cut to dimension of 20 mm ×10 mm . the chemical etching of these copper foil was effected by putting the Cu foil into the etching solution which is the acetone (1mol/L) and the application of an ultrasonic wave for 30 minutes than for 15 minutes in the diluted ethanol , followed byrinsing with distilled water for 3 times . For the nickel electrodeposition, nickel (II) sulfate hexahydrate ($NiSO_4.6H_2O$, 99%) and boric acid (H_3BO_3) was purchased from sigma -Aldrich Company. As a cathode, the copper electrode was immersed in 0,1 M nickel sulfate and boric acid solution and Pt was used as a counter electrode. Nickel was deposited on the copper at constant current of 10 mA cm² for 5 min. After the electrodeposition process, the electrode was washed with deionized water for 1 min and dried for 1 h at room temperature. The Nickel on copper (Cu/Ni) substrate were placed into the CVD furnace (OTF 1200X) and heated up to 1000°c at a heating rate of 20 C min-1 and kept at this temperature for 20 min under AR (250 SCCM) and H_2 (25 SCCM) gas mixture , then C_2H_2 (15 SCCM) was flowed into the quartz tube for 15 min , after graphene deposition , the system rapidly cooling to the room temperature under an Ar (250 SCCM) and H_2 (25 SCCM) ambience .

C. *Synthesis of Cu/G/Ni alloy*

Graphene was synthesized on the commercially copper foil from sigma -Aldrich (purity: 99,98% thickness :25 µm) was cut to dimension of 20 mm ×10 mm . the chemical etching of these copper foil was effected by putting the Cu foil into the etching solution which is the acetone (1mol/L) and the application of an ultrasonic wave for 30 minutes than for 15 minutes in the diluted ethanol , followed by rinsing with distilled water for 3 times . (Cu/Ni) substrate were placed into the CVD furnace (OTF 1200X) and heated up to 1000°c at a heating rate of 20 C min-1 and kept at this temperature for 20 min under AR (250 SCCM) and H_2 (25 SCCM) gas mixture , then C_2H_2 (15 SCCM) was flowed into the quartz tube for 15 min , after graphene deposition , the system rapidly cooling to the room temperature under an Ar (250 SCCM) and H_2 (25 SCCM) ambience .

For the nickel electrodeposition, nickel (II) sulfate hexahydrate ($NiSO_4.6H_2O$, 99%) and boric acid (H_3BO_3) was purchased from sigma -Aldrich Company. As a cathode, the copper electrode was immersed in 0,1 M nickel sulfate and 0,5 M boric acid solution and Pt was used as a counter electrode. Nickel was deposited on the copper at constant current of 10 mA cm² for 5 min.

Ⅲ. CHARACTERIZATION

Morphologies, structure and composition of the Cu pre-treated and CVD Cu graphene were investigated by scanning electron microscopy(Variable Pressure-SEM , JEOL (JSM7600F)) apparatus with an accelerating voltage of 4 kV and a working distance of 6.1 mm using secondary electron imaging mode . The Cu surface graphene stretching vibration modes were evaluated using Raman spectrometers with alpha 300 R Confocal Raman Microscope with WITec UHTS 300 spectrometer with a 532 nm laser

IV. ELECTROCHEMICAL TESTS

The HER evaluation was carried out on an SP -300 BIO Logic potentiostat using a three-electrode cell. The electrolyte solution degassed by bubbling high purity N_2 for 1 h before tests, to eliminate dissolved oxygen Pt wire was served as the counter electrode and the reference electrode was a saturated Ag/AgCl electrode. The Cu/C/Ni/G ,Cu/Ni/G,Cu/G/Ni electrodes were used as the working electrodes. All the potentials here are without iR correction and were calibrated with respect to the reversible hydrogen Electrode. The calibration was performed in a high-purity H_2 saturated electrolyte with Pt wires as the working electrode and counter electrode: E (RHE) = E (Ag/AgCl) + 0.263 V. The linear sweep voltammetry (LSV) was measured at a scan rate of 2 mV/s in 0, 5 M H2SO4 electrolyte.

V. RESULT AND DISCUSSION

The scanning electron microscopy (SEM) images of the single-layered graphene deposited on the copper Cu /G obtained through the chemical vapor deposition method CVD are shown in Fig. 1.The SEM images clearly show successful transfer of large-area graphene layers on copper by using CVD . The graphene films obtained via CVD are further characterized by Raman spectra (Fig. 2), which provides information on the graphitization of different samples[26] . Peaks in the Raman spectra are purely generated from graphene without any side products. The tow most intense features are the G peak at ~ 1580 cm-1 and the 2D peak historically named G' at 2700 cm -1 are applied to evaluate the layer numbers [27]. If the G to 2D band ratio is near 0.5, graphene successfully formed a single-layer [28]. If G and 2D band ratio are near1, graphene is double layered. In addition, as the G to 2D band ratio is higher than 1, these graph e n e films formed a multi-layer. In the present work, the stretching of the C-C bond in graphitic materials gives rise to the so-colled G-band Raman feature which is common to all Sp ² carbon system [29] at 1579. cm−1, whereas the carbon material edge about the A1g mode of the sp3 at 1344.5 cm−1[30], which contrasted to the D band. In addition, the secondary vibration scattering of phonons at regional boundaries to the 2D peak is observed at 2739 cm−1 [31].The single layered graphene, prepared CVD and , are observed through Raman spectrometry. The G to 2D band intensity ratio of CVD graphene at ~0.5 without D band generation are a single-layer graphene. Raman mapping on the graphene films shown in Fig are recorded to further confirm the graphene layers. Fig. , the CVD graphene show the single layer. The mapping can analyze the area of the thin film thickness [32]. Moreover, D band, which served as defect structures on graphene layers, are observed in the Raman spectrum CVD graphene .

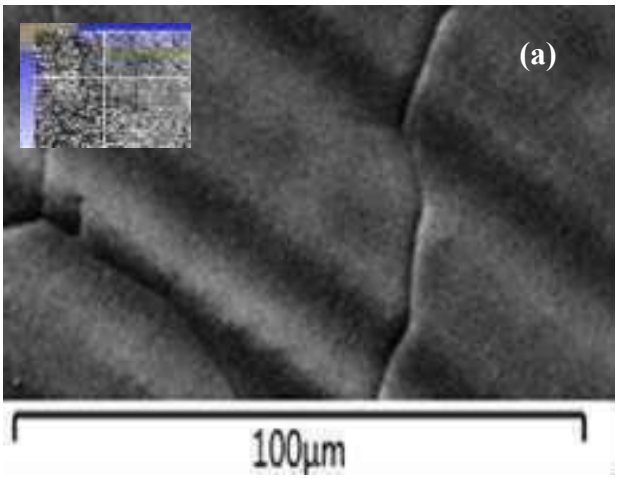

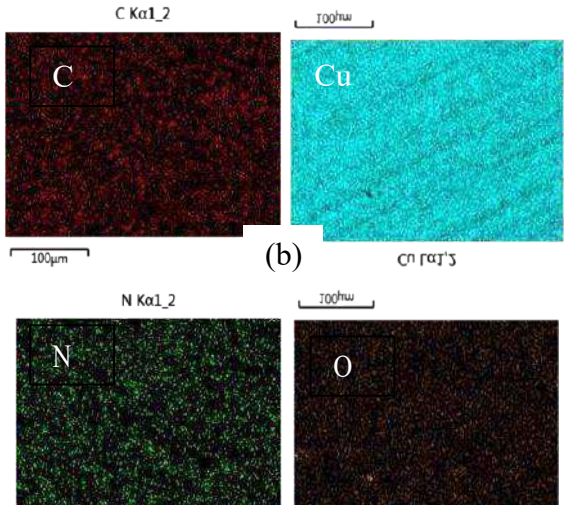

Fig. 1. (a) The SEMimage(b) EELS mappings of Cu/G

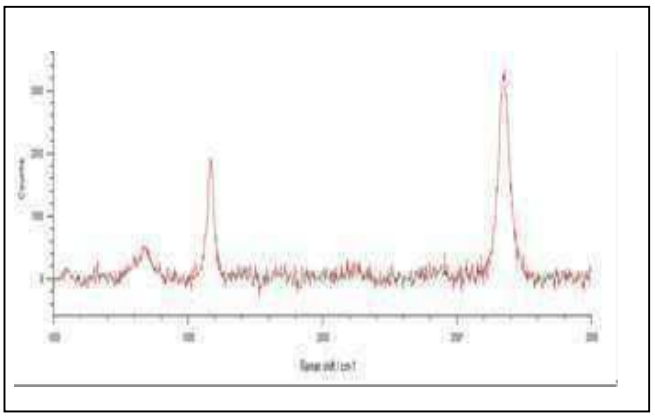

Fig. 2 :Raman spectra

The HER performance of the simples was investigated using a standard three-electrode electrochemical cell including the Cu/C/Ni/G ,Cu/Ni/G and Cu/G/Ni as a working electrodes, a saturated Ag/AgCl electrode as the reference

electrode, and a Pt wire as the counter electrode. The electrolyte (0.5 M H_2SO_4) was degassed by bubbling N_2 for at least 60 min Before electrochemical measurements, Linear sweep voltammograms (LSVs) measurements were performed with a scan rate of 2 mV s^{-1} without iR-correction for the three samples and Pt wire in a range from 0 V to -0.8 V (vs. Ag/AgCl satd KCl) in N_2 saturated aqueous solution of 0.5 M H_2SO_4. . As shown in Fig.3 , the Pt wire is the best catalytic activity with a -46 mV onset potential. Cu/C/Ni/G shows a small onset potential of -65 mV .When , the Cu/Ni/G and the Cu/G/Ni show inferior catalytic activities with onset potential of - 101and -119 mV, respectively. To achive a current density of 10 mA cm^{-2}, an overpotential of 127 mV is needed for Cu/G/Ni/G confirming its superior HER catalytic activity.

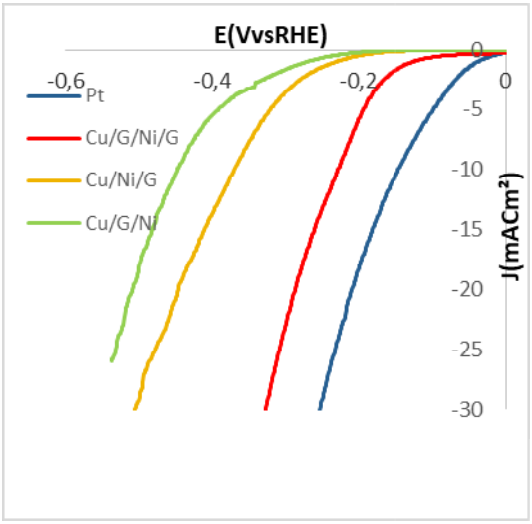

Fig. 3 :LSVs without iR correction of catalysts in 0.5 M H2SO4 at a scan rate of 2 mV s-1 for Pt , Cu/C/Ni/G ,Cu/Ni/G,Cu/G/Ni respectively

Tafel slope is an inherent property of the catalyst that is determined by the rate-limiting step of the HER. [33] Tafel plots are fit into the Tafel equation The Tafel slope is usually utilized to indicate the mechanism of the electrochemical process of HER [34]. Fig. 4 shows the linear regions of the Tafel plot for Pt , Cu/Gac ,Cu/G and Cu and there Tafel slope. By fitting the data with the equation are respectively 68mV dec-1, 70 mV dec-1, 120 mV dec-1 and 144 mV dec-1 Mechanistically, three principal steps can participate in the conversion of 2H+ to H2 commonly referred to as the Volmer (1), the Heyrovsky(2) and the Tafel (3) steps [35]

1- Volmer : H+ + e- -> H ads
2- Heyrovsky : Hads + H+ + e- -> H2
3-Tafel : Hads +Hads -> H2

Combination of steps (1 and 2) or (1 and 3) can lead to the production of molecular H2. Kinetic models of the HER, under a specific set of conditions have shown that if the Volmer step is the therate determining step (rds) a slope of ~120 mV/dec should result, while a rate determining Heyrovsky or Tafel step should produce slopes between 30-40 mV/dec. these values can be used as a guide in identifying HER mechanisms [36]

A durability test for Cu/G and Cu/Gac was performed by cyclic voltammetry (CV) for 1000 cycles with a scan rate of 100 mV s^{-1}. Fig.5 shows the polarization curves before and after the long-term cycling conducted in acidic solutions. Negligible current loss and a slight change in the shape of curves are observed, implying the good corrosion stability of this catalyst.

Figure 4 shows the logarithmic current density as a function of overpotential (Tafel plots) for Pt , Cu/C/Ni/G ,Cu/Ni/G and Cu/G/Ni measured in 1 M H_2SO_4 (2 mV/s scan rate) in the electrochemical cell (inset Figure 3). This is compared for the same measurement conditions. The Cu/G/Ni/G electrode exhibits the best performance(45 $mVdec^{-1}$) after the Pt (30mV dec-1) comparing with Cu/Ni/G and Cu/G/Ni (65 mV dec^{-1} and 105 mV dec^{-1} respectively) which can explain the HER activity is the interactions between active species and electrolyte [17] .

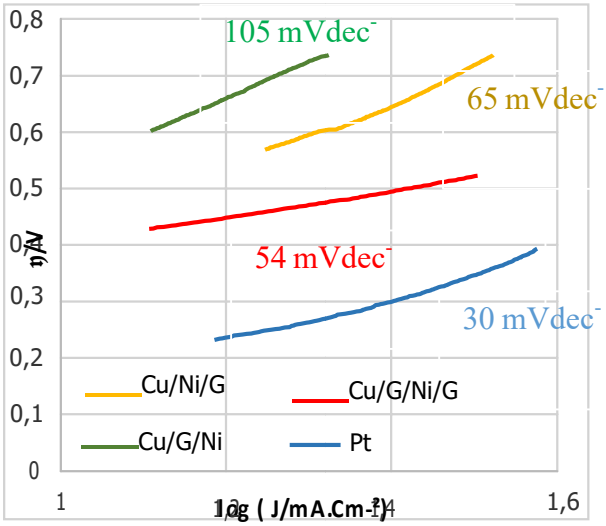

Fig. 4 : The corresponding Tafel plots

VI. CONCLUSIONS

In this paper, we have successfully synthesized and studied an efficient HER electrocatalyst derived from Graphene-based on copper nickel electrocatalyst . this electrocatalyst is synthesized by the chemical vapor deposition method (CVD) , and electrodepsition . we have developed graphene on copper nickel alloys as electrocatalyst with high activity for HER. Our study opens up a promising strategy for developing graphene based materials for renewable energy conversion also it is the first exploration of using graphene based on copper /Nickel alloys as a low-cost and highly-efficient HER electrocatalys This work reveals the new active sites on graphene materials, and provides a new facile strategy for the synthesis of high-performance electrocatalyst . Resulting in

ISSN: 1737-9334

excellent electrocatalytic activity and long-term stability for HER.

REFERENCE

[1] Energies 2019, 12, 964; doi:10.3390/en12060964
[2] Paul A. Adedeji et al 2019 IOP Conf. Ser.: Earth Environ. Sci. 331 012039
[3] Miklos et al . ,2018 sherlala et al.,2018
[4] M.S. Nazir et al. / Science of the Total Environment 683 (2019) 436–444
[5] S.E. Hosseini, M.A. Wahid / Renewable and Sustainable Energy Reviews 57 (2016) 850–866851
[6] J. A. Turner, Science, 2004, 305, 972-974 (b) M. Dresselhaus, I. Thomas, Nature, 2001, 414, 332-337
[7] J. De Vrieze, et al.New BIOTECHNOLOGY 55 (2020) 12–1813
[8] J. Zhuo, T. Wang, G. Zhang, L. Liu, L. Gan and M. Li, Angew. Chem.Int. Ed., 2013, 52, 10867
[9] international journal of hydrogen energy 44 (2019) 5661e56755662
[10] international journal of hydrogen energy 34 (2009) 7368–7378
[11] S. Shiva Kumar, V. Himabindu /Materials Science for Energy Technologies 2 (2019) 442–454443
[12] M. G. Walter, E. L. Warren, J. R. McKone, S. W. Boettcher, Q. Mi, E. A. Santori and N. S. Lewis, Chem. Rev., 2010, 10, 6446
[13] R. Subbaraman, D. Tripkovic, D. Strmcnik, K. C. Chang, M. Uchimura, A. P. Paulikas, V. Stamenkovic and N. M. Markovic, Science, 2011, 334, 1256-1260
[14] H. Yin, S. Zhao, K. Zhao, A. Muqsit, H. Tang, L. Chang
[15] L. Yang, W. Zhou, J. Jia, T. Xiong, K. Zhou, C. Feng, J. Zhou, Z.Tang, S. Chen, Carbon, 2017, 122, 710-717
[16] X. Zou, X. Huang, A. Goswami, R. Silva, B. R. Sathe, E. Mikmeková, T. Asefa, Angew. Chem. Int. Ed., 2014, 126,4461-465
[17] W. Zhou et al. / Nano Energy 28 (2016) 29–43
[18] A.T. LawalBiosensors and Bioelectronics 141 (2019) 1113842
[19] |J. Am. Chem. Soc. 2011, 133, 7296–7299
[20] X. Wang, Q. Li, Penghui Shi, J.Fan, Y. Min, and Q. Xu Small 2019, 1901530
[21] J. Mater. Chem. A journal The Royal Society of Chemistry 2019 DOI: 10.1039/c9ta10667g
[22] Y. Ito, W. Cong, T. Fujita, Z. Tang and M. Chen, Angew. Chem. Int. Ed., 2015, 54, 2131-2136
[23] Chem.commun.,2014,50,9340
[24] Carbon 161 (2020) 665-673
[25] J.Name., 2013,00,1-3
[26] Y.-M. Zhao et al. Microporous and Mesoporous Materials 297 (2020) 110033
[27] C.-P. Han et al. Catalysis Today 335 (2019) 395–401
[28] A. C. Ferrari et al. PhysRevLett.97.187401
[29] A.C. Ferrari, J. Robertson, Phys. Rev. B 64 (2001) 075414
[30] Mildred S. Dresselhaus et al. Nano Lett. 2010, 10, 751–758
[31] Schwan et al J. Appl. Phys., Vol. 80, No. 1, 1 July 1996
[32] L.M. Malard et al. / Physics Reports 473 (2009) 51–87
[33] Maarof et al. Nanoscale Research Letters (2019) 14:143
[34] W.Zhouetal./NanoEnergy28(2016)29–43
[35] Chem. Commun., 2014, 50, 9340
[36] Conway et al. Electrochimica Acta 2002 47
[37] Fletcher in J of solid state electrochemistry 2009 13, 4, 537
[38] W. Zhou et al. / Nano Energy 28 (2016) 29–43

Transportable wind adapter system: Modelling study and experimental investigation

Marwa Ezzine *, 1, Zied Guidara 2, Hiba cherif 3 Jalila Sghaier 3

1- Laboratory of Thermal and Thermodynamics of Industrial Processes (LTTIP), National School of Engineers of Monastir (ENIM), University of Monastir (UM), Avenue Ibn El Jazzar 5019 Monastir, *TUNISIA*

(E-mail: marwaezzine26@gmail.com)

2- Laboratory of Electro-Mechanic Systems (LASEM), NationalSchool of Engineers of Sfax (ENIS), University of Sfax (US),B.P. 1173, Road Soukra km 3.5, 3038 Sfax, TUNISIA

(E-mail: ziedguidara@yahoo.fr)

3- Laboratory of Thermal and Thermodynamics of Industrial Processes (LTTIP), National School of Engineers of Monastir (ENIM), University of Monastir (UM), Avenue Ibn El Jazzar 5019 Monastir, *TUNISIA*

(E-mail: jalila.sghaier@enim.rnu.tn, Hiba.cherif@yahoo.fr)

ABSTRACT – The improvement of Wind system efficiency is a very important research topic and it is considered as one of the most important technology of renewable energy sources. In this research, a new transportable wind adapter system is designed firstly to increase wind energy efficiency. Secondly, the designed transportable adapter system is modeled by the use of ANSYS FLUENT where the used turbulence models are: standard k-ε ,realizable and RNG. Thirdly, an experimental investigation is done in the region of Kairouan – Tunisia under ambient conditions .The obtained results showed a good agreement between experimental investigation and numerical study.

Keywords: Wind Energy, numerical study, experimental investigation.

1. INTRODUCTION

Wind energy is one renewable energy, which can be considered as inexhaustible on the scale of human time. Nowadays the way of production Electricity is very important and wind energy can be a good solution. To increase the domain of its use, a wind power adapter is used [1]. This system is able to focus the wind energy through a diffuser-shaped envelope enclosing a conventional wind turbine with horizontal or vertical axis [2,3]. This makes it possible to extract more wind power, typically 3 to 4 times the power that can be extracted from a conventional wind turbine in the same area of wind turbines [1, 2].

[4-5] developed numerical modeling of INVELOX wind turbine application in low wind speed region.

The present research proposes firstly a new transportable design for the wind energy system. Secondly, a numerical simulation is done using the CFD approach "ANSYS Fluent" .The simulation processing is based on the use of standard turbulence mathematical models standard k –ε, realizable k –ε and RNG k –ε.

Finally, experimental investigations are presented to validate the numerical study and to determine the wind speed performances of the transportable wind adapter system.

2. Design of the system

The proposed system *figure 1* is destined to produce electricity. When designing, these conditions were taking into consideration:

- Easy manufacturing,
- Available manufacturing materials in local market,
- Easyexploitation.

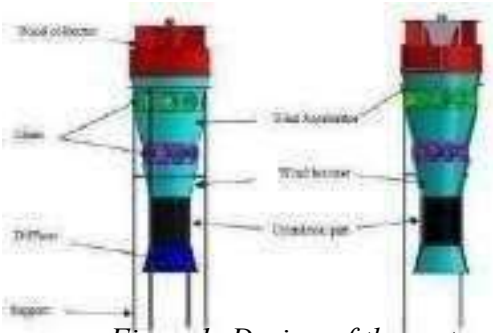

Figure1: Design of the system

Table 1: geometrical parameters of the system.

Parameter	Value	Unit
Diameter of the cones	0.1	m
Length of the system	1.533	m
Diameter of the big canal	0.5	m
Diameter of the cylindrical part	0.25	m

3. Numerical simulation

Inthis study, the objective is as follow:

ISSN: 1737-9334

10ème Conférence Internationale des Energies Renouvelables CIER-2022
Proceedings of Engineering &Technology-PET

- Determine the outlet wind speed at the exit of the tunnel.

This simulation is done by the use of ANSYS Fluent software. Table 2 shows the simulated values by the use of three models : standard k –ε, realizable k –ε and RNG k –ε.

Figure 2 presents the distribution of the air velocity in the wind adapter.The maximum value is obtained in the middle of the cylindrical part, which is equal to 11.5 m/s for an inlet wind speed equalto 5 m/s.

This simulation is done through the use of realizablk-–ε model.

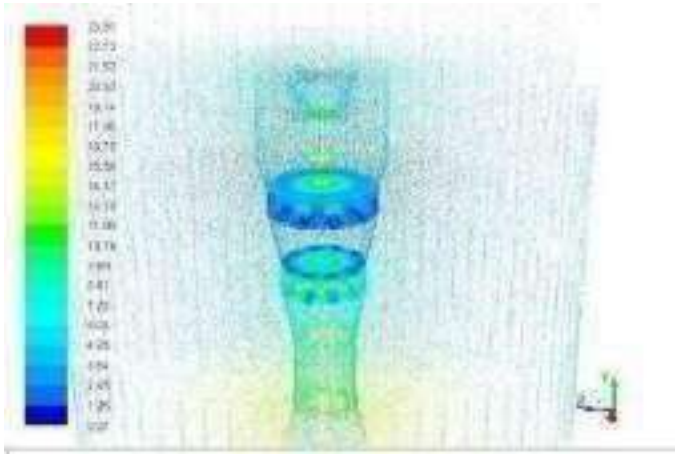

Figure 2: Distribution of the air velocity

4. Experimental investigation

In this study, the main objectives are as follow:

- Measure the inlet wind speed.
- Measure the wind speed at the exit ofthe tunnel.

The wind speed values are recorded bythe WH3081: Wireless Weather Station.

The reported results were obtained, during several days in the region of Kairouan-Tunisia

Figure 3 shows the different assembly step of the system

Figure 3: experimental system.

Table 3 shows the outlet wind speed values in the cylindrical part.

Table 3: Outlet wind speed values

Inlet wind speed	Outlet wind speed
3	7
3.5	7.4
4	7.9
4.5	9.22
5	11.44

5. Conclusions

This paper present a transportable wind adapter system. The main components are a wind collector, the wind accelerator surrounded by small cones, the wind booster and a diffuser. In addition, a simulation and experimental studies were developed. The obtained results are very satisfactoryand validate our numerical results.

6. References

[1]. Clive a. j. fletcher., (2006). Diffuser –augmented wind turbines, Department of Mechanical Engineering, University of Sydney, Australia 175-183.

[2]. *Daryoush Allaei et al,(2014).* INVELOX : *Description of a new concept in wind power and its performance evaluation.* Energy xxx (2014) volume(1-9).

[3] *Daryoush Allaei et al(2015), INVELOX with multiple wind turbine generator systems,* Energy 93 volume(1030-1040).

[4] *Freshteh Sotoudeh et al.,(2019). Field tests and numerical modeling of INVELOX wind turbine application in low wind speed region*. Energy 181 volume (745-759)

[5] *Nallapaneni Manoj Kumar et al.,(2015), Design and Wind Tunnel Testing of Funnel Based Wind Energy Harvesting System.* Procedia Technology 21 volume(33 – 40)

Mise en œuvre en temps réel d'un onduleur dans un système solaire photovoltaïque

Abdelkader El Kebir, Hafida Belhadj, A. Baghdad Bey
Department of Electrical Engineering, University Mustafa Stambouli of Mascara, Algeria
Abdelkaderelkebir7@gmail.com, a.elkbir@univ-mascara.dz
belhadjhafida22@yahoo.com, baghdadbey68a@yahoo.fr

Abstract –**L**'objectif de ce travail est d'étudier et de concevoir un onduleur pour panneau solaire d'une tension d'entrée de 12 VDC et une sortie à onde purement sinusoïdale de 230 VAC à une fréquence de 50 Hz. A deux étages.Le premier étage est un convertisseur (DC/DC) hacheur de type flyback dont les tensions continues d'entrées et de sortie sont respectivement 12V et 324V Commander par TL494 qui nous génère un signal MLI pour la commande des deux transistors utilisés ce qui nous a permis d'avoir une tension de 324V réglable avec une boucle de régulation qui tiens la tension constante quelque soit les influences de la température et l'ensoleillement.**L**e deuxième étage est un convertisseur (DC/AC) en pont de transistor MOSFET, alimenté par hacheur de type flyback à partir de sa tension de sortie (324V). Ce dernier, étant commandé par MLI du microcontrôleur (16F877A fournit un signal alternatif (50Hz, 230V) utilisable dans la vie quotidienne.

Keywords–**. Onduleur, hacheur flyback, transistor MOSFET, MLI, microcontrôleur, transformateur, logiciel de routage TCI, logiciel de simulation PROTEUS, Pico scope**

I. INTRODUCTION

Depuis la generalization de l'utilisation de l'électricité, la consommation énergétique[1 2] n'a cessé d'augmenter, le problème de la conversion et du stockage de l'énergie a conduit à la recherche et au développement de nouvelles sources d'approvisionnement. Cet intérêt s'est accru face à l'épuisement inéluctable des énergies fossiles, à leur impact sur l'environnement et aux déchets qu'ils engendrent. Le but de notre travail est de réalisé un convertisseur a deux etage (DC/DC)est (DC/AC) pour un systeme photovoltaique. [3 4 5 6 7 8 9 10 11 12 13]

II. Convertisseur DC/DC Fly back

La figure 1 montre la structure du convertisseur fly back dont le circuit de commande et le TL494 qui est un circuit de contrôle [14 15] à fréquence fixe et à modulation de largeur d'impulsion, destiné aux alimentations à découpage et aux convertisseurs de tension.

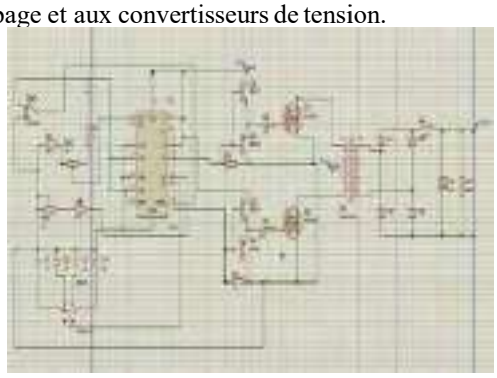

Fig. 1. Schéma de principe de l'hacheur Flyback

A. Présentation du TL 494

Comme le montre le montage de la figure 2, le TL 494 contient un oscillateur ajustable, un modulateur de durée d'impulsion et un amplificateur d'erreur. Il offre également des fonctions supplémentaires telles que la détection des courants excessifs, un régulateur de précision de 5V et une logique de contrôle de sortie

B. Dimensionnement de la commande

La modulation des impulsions de sortie est réalisée par la comparaison du signal en dents de scie créé par l'oscillateur et le signal de contrôle. L'étage de sortie est activé lorsque la tension en dent de scie de la broche 5 est supérieure à la tension du signal de contrôle.
Pour la fréquence de l'oscillateur du TL494, on lui connecte un circuit d'oscillation externe, représenté dans le schéma (figure.2) à travers CT et la résistance RT insérés entre les broches 5 et 6.

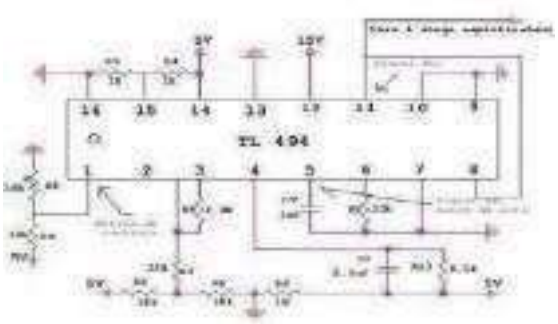

Fig 2. Circuit TL494 de commande MLI.

L'oscillateur est destinéà fonctionner à 50 kHz. Pour cela, on a :

$$f_{OSC} = \frac{1.1}{R_T \cdot C_T} \qquad (1)$$

Avec $C_T = 1nF$ et $R_T = 22\ k\Omega$ (On prend une résistance de 33 kΩ).

C. *Principe de fonctionnement :*

La porteuse est un signal en dents de scie de fréquence 50 kHz (Figure.3) générée par le TL494 au niveau de la broche 5. Ce signal est comparé à la tension de contrôle injectée à la patte 1 du circuit intégré. Le résultat de la comparaison se traduit par la génération d'un signal modulé en largeur d'impulsion sur la broche 11.

978-1-5386-6692-0/18/$31.00 ©2018 IEEE

Pour avoir un rapport cyclique variable du signal de sortie, il suffit de faire varier la valeur de la résistance R_8. **[35]**

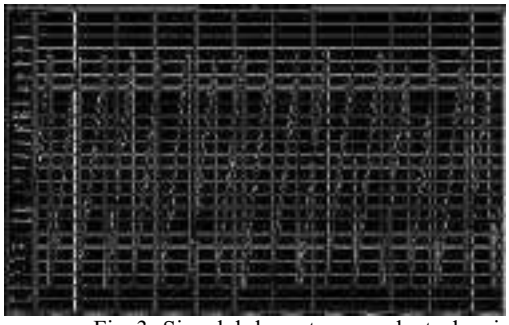

Fig. 3. Signal de la porteuse en dents de scie.

D. Convertisseur DC/DC Fly back

La figure montre la realization a temps real du convertisseur. DC/DC Fly back dans la tension d entrées est. 12Vest la tension de sortie324.2 VDC

Fig.4. Convertisseur DC /DC flyBACK

III. Convertisseur DC/AC

La figure 5 est celle d'un pont complet [3 16 17] dans lequel, on suppose que Q2 et Q3 étaient fermés pendant la première alternance de la tension U, rendant celle-ci égale à +E , et les interrupteurs Q1 et Q4 sont fermés pendant la deuxième alternance, ce qui rend la tension u égale à -E .

Les commandes de (Q2, Q3) et (Q1, Q4) sont complémentaires, mais ne sont pas nécessairement simultanées, elles peuvent êtres décalées.

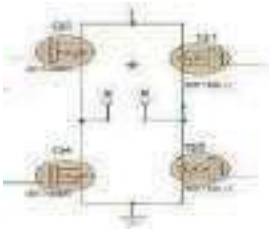

Fig. 5 Convertisseur DC/AC en pont

K. Circuit de commande du convertisseur AC/DC:

L'architecture particulière des microcontrôleurs permet une vitesse de calcul qui n'est pas ralentie par des accès mémoires comme c'est le cas dans les systèmes à plusieurs circuits Notons que le microcontrôleur utilisé dans notre application appartient à la famille PIC16F de MICROCHIP , soit le 16F877A il présente beaucoup d'avantages par rapport à d'autres microcontrôleurs de la même série, le 16F877A

L. Simulation du convertisseur DC/AC

Les résultats de simulation de l'étage convertisseur DC/AC figure est donnée par les graphes des figures ci-dessous :

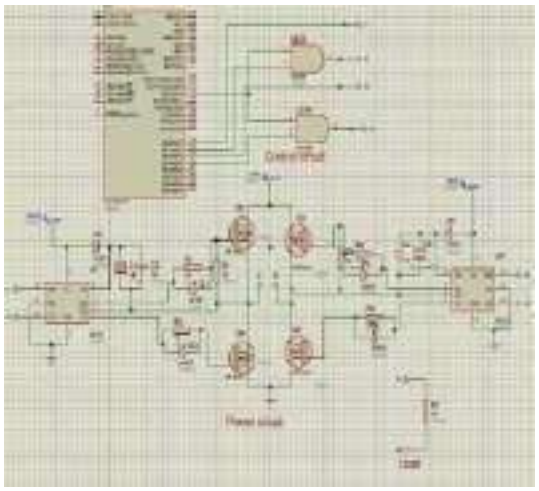

Fig. 6. Schéma complet du convertisseur DC/AC.

M. *Generation du signal complémentaire* ***:***

. Pour génère le signal complémentaire on utilise deux portes ''ET'' câblées comme indiqué par la figure 8. Une entrée de chaque porte est relié a la sortie MLI du PIC, les autres entrée sont relié aux microcontrôleurs pour bascules chaque 10ms entre deux états logiques.

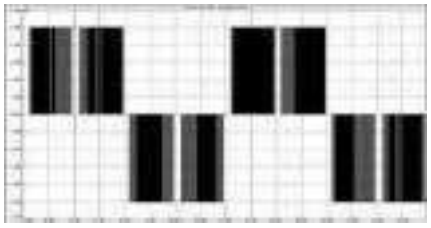

Fig. 7. signaux de commande MLI.

O. Simulation duconvertisseur DC/AC Proteus ISIS

Les résultats de simulation obtenue pour déférente charges (résistive et inductive) montre que la commande en modulation de largeur d'impulsion MLI permet d'aboutir à un signal sinusoïdal.

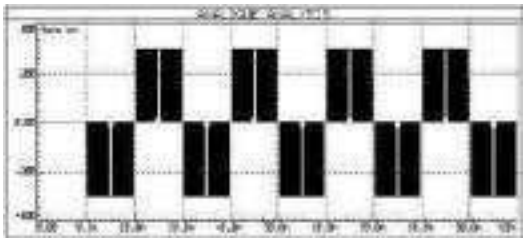

Fg. 8. sortie pour une charge résistive (R= 1KΩ)

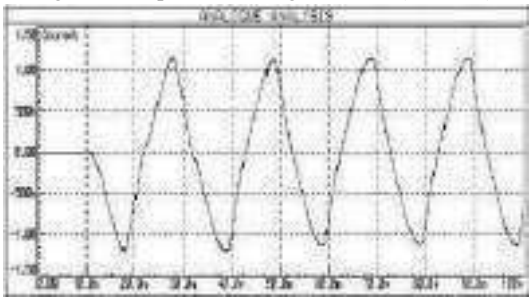

Fg. 9.Courant de charge pour une charge inductive (R=100Ω, L=1H).

P. Réalisation pratique

Dans cet article la nouvelle méthode [3 9 18 19 20 21] à utiliser est d'ajouter à la méthode classique un microcontrôleur PIC16F877. Il a un faible coût et réduit la complexité du circuit pour l'onduleur à pont complet monophasé

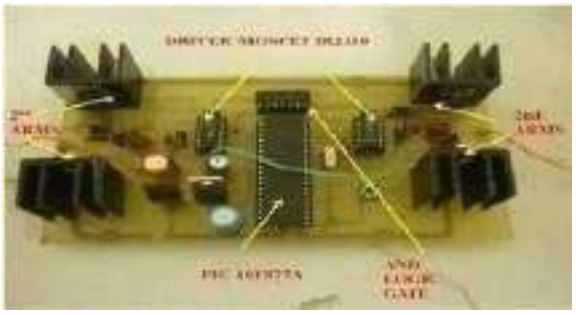

Fig. 10. réalisation pratique du convertisseur DC/AC

R. resultat experimental duconvertisseur DC/AC

La figure10 montre [3 9 18 19 20 21] les deux signaux MLI qui vont commander le convertisseur en pont H

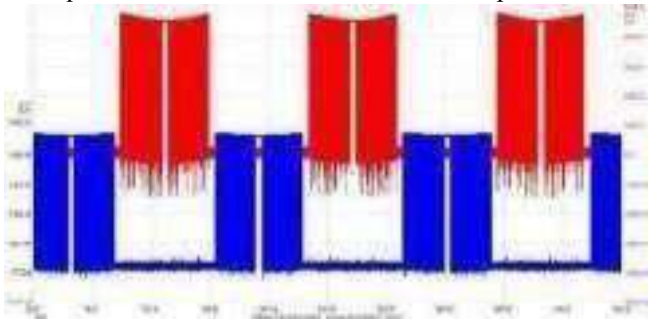

Fig. 11. Signaux MLIdu convertisseur DC/AC.

IV. CONCLUSION

Le travail présenté dans ce mémoire a pour objectif d'étudier et réaliser un ondulaire monophaser pour un systeme photovolatiques convertisseur statique . Ce dernier nous a pris à réaliser deux convertisseurs en même temps. Le premier étage de la conversion c'est un hacheur de type flyback (buck-boost) 12V /324V DC alimenté par un panneau photovoltaïque munis d'un circuit imprime est le TL494 qui nous génère un signal MLI pour la commande des deux transistors utilisés ce qui nous a permis d'avoir une tension de 324V réglable avec une boucle de régulation qui tiens la tension constante quelque soit les influences de la température et l'ensoleillement.

Ce hacheur alimente le deuxième étage qui est un convertisseur DC/AC en pont de transistor MOSFET, chaque bras de l'onduleur est piloté par un driver de puissance de type IR2110 qui transmet la commande MLI du microcontrôleur (16F877A) au MOSFET. Ce dernier fournit un signal quasi sinusoïdal d'une tension de 230 V et d'une fréquence de 50Hz utilisable dans la vie quotidienne.

REFERENCES

[1] fraunhofer"photovoltaics report".Institute for Solar Energysystems, isewith support ofpse conferences & consulting gmbhfreiburg, 19 june 2018.

[2] Andris PiebalgsJanez Potočnik"*Photovoltaic solar energy: development andcurrent research*ISBN 978-92-79-10644-6doi: 10.2768/38305Luxembourg: Office for Official Publications of the European Union, 2009.

[3] **Abdelkader El Kebir, Hafida Belhadj, Karim Negadi** and **A. Baghdad Bey**" design and construction of an inverter for a photovoltaic system". Proc. XXVII International Scientific Conference Electronics - ET2018, September 13 - 15, 2018, Sozopol, Bulgaria

[4] Yasar Birbir ,Kaner Yurtbasi b, Volkan Kanburoglu "Design of a single-phase SPWM inverter application with PIC micro controller". Engineering Science and Technology, an International Journal 22 (2019) 592–599 Available online 13 February2019

[5]A. yahya odeh. A. hamad "Single Phase Inverter Using Microcontroller". Graduation Project An-Najah National University Faculty of Engineering Electrical Engineering Department2010

[6] Abdel-Salam Shaaban, Jean Thomas and Ramadan Mostafa" Design and Implementation of a Single Phase Sinusoidal Pulse Width Modulation Inverter Based Microcontroller for Wind Energy". Conversion Systems Research Journal of Applied Sciences, Engineering and Technology 14(2): 86-94, 2017 ISSN: 2040-7459; e-ISSN: 2040-7467

[7] Mr. Pratik Patel1, Prof. Sweta Shah" Design and development of solar photovoltaic inverter using psim software," *International Journal for Technological Research in Engineering Volume 4, Issue 3, ISSN (Online): 2347 – 4718 November-2016,*

[8]S. Elisa Braco. W. Andreas. Design and simulation of a single-phase inverter with digital PWM.Bachelor Final Thesis. Industrial TechnologiesEngineering.2016.*academicae.unavarra.es/xmlui/bitstream/./TFE_ElisaBraco.*

[9]B. Mutua Joshua. G. Kamucha.Microcontroller based power inverter.Project index: PRJ 015.F17/28234/2009.University of NairobiFaculty of engineeringdepartment of electrical and information engineeringsubmitted on: April, 2014.

[10]S.Mali P, A. B.Patil, P. P.Patil, P.P. Pati"Single Phase Inverter using PIC Controller". *IJARIIE-ISSN (O)-2395-4396Vol-3 Issue-2 2017*

[11] Zhou Hai-feng .Xu Zhi-long.Lin Zhong-hua.Wang Rong-jie .Dong Jing-de .Huang Yuanqing. Simulation" Design of Inverter in Solar Photovoltaic System". 978-1-4244-4412-0/09/$25.00 ©2009.

[12] Guangru Zhang"An Optimal Control Scheme for Single-Phase Grid-Connected Photovoltaic Inverter".JOURNAL OF COMPUTERS, VOL. 9, NO. 2, FEBRUARY 2014

[13] Nishit Kapadia, Amit Patel and Dinesh Kapadia" Simulation and design of low cost single phase solar inverter "International Journal of Emerging Technology and Advanced Engineering Website: www.ijetae.com (ISSN 2250-2459, Volume 2, Issue 1, February2012

[14] TL494 pulse-width-modulation control circuit's **SLVS074H**January 1983Texas Instruments Incorporated M.Joshua Bernard project index: PRJ 015microcontroller based power inverterf17/28234/2009-revised March 2017.

[15] Database of TL494 Switch Mode Pulse Width Modulation Control Circuits, [2010-08-10], http:// www.ti.com

[16] Sundas Hannan, Sohaib Aslam, Muhammad GhayurDesign and real-time implementation of SPWM based inverterConference Paper · February2018DOI: 10.1109/ICEET1.2018.8338637

[17] Nuzhat Noor Sayeed, Ahmed Aaqib Sajjad Hossain and Menhajul Abedin Bhuiyan "Design of a Pure Sine Wave Inverter for PVApplication ".BRAC UNIVERSITY Thesis Supervised Dr. A.B.M Harun – Ur –Rashid

[18] *IR2110 Datasheet*, International Rectifiers. Products; Power; Motor Control & GateDriver ICs; Non-Isolated Gate Driver IC; General Purpose Gate Driver ICs-Industrial IR2110,availablein:http://www.infineon.com/dgdl/ir2110.pdf?fileId=5546d462533600a4015355c80333167e.

[19] Ashok Kumar L, Indragandhi V, Sujith Kumar N Design and implementation of single-phase inverter without transformer for PV applications. IET Renew. Power Gener., 2018, Vol. 12 Iss. 5, pp. 547-554 https://doi.org/10.1049/iet-rpg.2017.0257

[20]C. Dhanamjayulu Sanjeevikumar Padmanaban Jens Bo Holm-NielsenAnd Frede Blaabjerg" Design and Implementation of a Single-Phase15-Level Inverter With Reduced Components for Solar PV Applications"IEEE Access, 9, 581-594.https://doi.org/10.1109/ACCESS.2020.3046477

[21]Chittathuru, D., Padmanaban, S., Holm-Nielsen, J. B., & Blaabjerg, F. (2021) ". Design And Implementation Of A Single-Phase 15-Level Inverter With Reduced Components For Solar PV Applications". IEEE Access, 9, 581-594.[9303355].Https://Doi.Org/10.1109/ACCESS.2020.3046477

Solar Photo-degradation of Methylene Blue dye on the novel Heterojunction $CdMn_2O_4/SnO_2$

S. Douafer[#1], H. Lahmar[#2], R. Laouici[#3], M. Benamira[#4] and M. Trari[*5]

[#1]Department of Fundamental Studies of Science and Technology, [#2,4]Department of Chemistry, [#3]Department of Physics, University of Mohamed Seddik Benyahia, B.P. 98, Ouled Aissa, 18000 Jijel, Algeria

[1]souaad.douafer@gmail.com

[2]lahmarhicham18@gmail.com

[3]rima_ph2019@gmail.com

[4]benamira18@gmail.com

[*4]Laboratory of Storage and Valorization of Renewable Energies, Faculty of Chemistry (USTHB), 16111 Algiers. Algeria

[5]solarchemistry@gmail.com

***Abstract*— In this study the physico-chemical properties of spinel $CdMn_2O_4$ were studied. the photoacatalytic effect of the latter was improved when used in a hetero-system with SnO_2 ($CdMn_2O_4/SnO_2$). Spinel CdMn2O4 is stable against photo-corrosion, it has a direct gap (Eg=1.44 eV), the behavior of CdMn2O4 is p-type compatible with chrono-amperometry. The flat band potential (Vfb = -0.21 VSCE) was determined from the capacitance measurement. At pH=8, the degradation of Methylene Blue (MB) (10 mg/L) is total under $CdMn_2O_4/SnO_2$ under sunlight after 120 min of irradiation.**

***Keywords*— $CdMn_2O_4/SnO_2$; sol-gel method; MB dye; solar radiation; photo-degradatction.**

I. INTRODUCTION

Les colorants sont parmi les polluants les plus dangereux. Ils sont utilisés dans des nombreux secteurs industriels tels que les produits alimentaires, cosmétiques et cliniques, en particulier dans les industries textiles. Les molécules de ces colorants, sont difficilement biodégradables, difficiles à dégrader par les méthodes classiques [1]. L'organisation mondiale de la santé et l'union européenne quand a elles ne fixent pas des lois mais donnent des orientations pour la fixation des orientations maximales admissibles (CMA) [2].

Et parallèlement les chercheures scientifiques sont Busy de trouver des méthodes pour traiter les eaux usées et la réutilisation afin de mobiliser de plus important volumes d'eau et satisfaire ainsi la demande de plus en plus croissante [3].

Les progrès les plus récents dans le traitement de l'eau ont été réalisés dans l'oxydation des composés organiques. Ces méthodes reposent sur la formation d'entités chimiques très réactives qui vont décomposer les molécules, les plus récalcitrantes, en molécules biologiquement dégradables ou en composés minéraux tels que CO_2 et H_2O : ce sont les Procédés d'Oxydation Avancés POAs. Ces procédés reposent sur la formation des radicaux hydroxyles $HO^{\cdot}$ possédant un pouvoir oxydant supérieur à celui des oxydants traditionnels tels que Cl_2, ClO_2 ou O_3. Ces radicaux sont capables de minéraliser partiellement ou en totalité la plupart des composés organiques [4, 6].

Afin de traiter les polluants chimiques dangereux, deux pistes radicalement différentes sont envisageables, soit leur stockage sur des matériaux adsorbants, soit leur minéralisation. Actuellement, le procédé le plus utilisé demeure l'intégration dans la chaîne de traitement, l'adsorption des polluants organiques sur des adsorbants solides, comme par exemple le charbon actif (CA) [7, 9]. Si cette méthode permet d'aboutir à des performances épuratoires satisfaisantes, il n'en demeure pas moins qu'elle présente l'inconvénient de seulement transférer les polluants organiques à une autre phase, i.e. l'adsorbant, accentuant ainsi le coût élevé de sa régénération thermique périodique [10].

ISSN: 1737-9334

Actuellement, les techniques d'oxydation avancées connaissent un fort intérêt. Parmi les polluants majeurs difficiles à éliminer, et pouvant être soumis à des procédés POA, on peut citer: les composés benzéniques et phénoliques, les composés chlorés et polychlorés, les herbicides, les pesticides, les détergents, les tensioactifs et enfin les colorants issus des fabriques de textiles [11, 12]. Dans le souci de contribuer à la lutte contre ce danger, nous avons fixé comme objectif, l'étude de la dégradation photocatalytique du colorant à savoir le Bleu de méthylène.

Le bleu de méthylène trouve son utilisation majeure en toxicologie dans le traitement de la méthémoglobinémie à la dose de 1 à 2 mg/kg par voie intraveineuse [13]. En interagissant avec la méthémoglobine et les systèmes enzymatiques des érythrocytes pour réduire le retour à l'hémoglobine, le bleu de méthylène est un médicament généralement sûr avec des effets hémolytiques liés à la dose. Les personnes présentant un déficit en G-6-PD, ainsi que les patients exposés aux colorants d'aniline et à la dapsone, peuvent présenter des risques particuliers dans le traitement de la méthémoglobinémie.

Dans tous les cas, la photocatalyse hétérogène fait référence à un semi-conducteur photocatalyseur ou à un semi-conducteur photo-sensibilisateur [14]. Cette technique de purification fait appel à une source d'énergie propre comme la lumière. Pour cela le procédé de purification est appelé photocatalyse et le matériau : photocatalyseur. Ce procédé pourrait s'appliquer avec succès en Algérie où la durée d'ensoleillement moyenne est d'environ 2500 heures par an [15]. nearly 40% of the solar resource would generate significant gains in the photocatalytic performance of catalysts [16]. Intensive research is therefore devoted to development of new innovative catalysts, photosensitive over a wider range, in order to exploit a large number of photons from the visible range [17].

Pratiquement, parmi les oxydes semi-conducteurs utilisés, TiO_2 a sous forme d'anatase est unanimement reconnu comme le plus prometteur en raison de son activité, stabilité et faible coût [18, 19]. Seulement, son utilisation sous forme de poudre, notamment du composé commercialement disponible sous le nom de TiO_2-Degussa P25 constitué de 80% d'anatase et 20% de rutile, pose des problèmes d'agglomération de ses particules ultrafines en larges particules, ce qui en engendre une diminution de l'activité photocatalytique [20] ainsi que la nécessité d'utiliser une microfiltration coûteuse en vue de sa séparation des eaux traitées [21].

Pour s'affranchir de tels problèmes, des efforts ont été déployés pour synthétiser des catalyseurs semeiconducteurs qui absorbant dans la région visible ; et ceux ça fait l'objet du choix de $CdMn_2O_4$ dans ce présent travail, $CdMn_2O_4$ est stable chimiquement sur un vaste saut de pH. La photoactivité améliorée est attribuée au transfert d'électrons du sensibilisateur $CdMn_2O_4$-CB, activé, en SnO_2-CB entraînant la dégradation de BM et le conduit à une minéralisation totale en raison de l'importance de durée de vie des porteurs de charge.

II. EXPERIMENTAL

$CdMn_2O_4$ a été préparée par la méthode sol-gel en présence de l'agent de combustion PVP. Plus précisément, dans une procédure de synthèse typique, une quantité de (PVP K30) a été dissoute dans 50 mL d'eau distillée. Des quantités stoechiométriques de $[Cd(NO_3)_2{\cdot}3H_2O]$ et $[Mn(NO_3)_3{\cdot}9H_2O]$ ont également été dissoutes dans la même solution ; un excès d'acide citrique à 5 % a été ajouté. La solution a été chauffée sur une plaque chauffante à 60°C pendant 2h après solubilité complète. La solution a ensuite été évaporée à 85 °C pendant 18 h sous agitation constante. Le gel obtenu a été séché à 180°C puis calciné à 850°C pendant 6h. La poudre obtenue est le spinelle $CdMn_2O_4$. SnO_2 a été préparé comme indiqué dans nos travaux précédents [22].

ISSN: 1737-9334

La diffraction des rayons X permet de connaître la nature et la structure des produits cristallisés du fait que leurs atomes sont arrangés dans un ordre à grande distance selon des plans cristallins spécifiques. Les paramètres de la maille des cristaux formés pourront également être déterminés ainsiqu'une estimation de leurs tailles.

Dans le cadre de nos études, les analyses à la température ambiante ont été effectuées sur un diffractomètre (Bruker D8). Le rayonnement incident est engendré par la raie Kα du cuivre (λ= 1,54051 Å). La divergence du faisceau est d'environ 0,2° alors que son épaisseur est de l'ordre de 1 mm et sa largeur de l'ordre de 10 mm.

Le spectre de réflectance diffuse est enregistré avec un spectrophotomètre UV-VIS (Specord 210 Plus) équipé d'une sphère d'intégration, le PTFE est utilisé en standard.

Les expériences électrochimiques sont conduites à l'air sous température ambiante dans une cellule remplie de la solution de travail (BM10 mg/L). Les potentiels sont donnés par rapport à une électrode de calomel saturée (SCE). Le potentiel a été balayé à une vitesse de 5 mV s-1 et contrôlé par un potentiostat Solartron 1287. Le contact électrique avec le fil de cuivre sur la pastille arrière de nos électrode de travail.

Un réacteur Pyrex de 100 ml de capacité est utilisé dans les conditions ambiantes comme support photo catalytiques. 50 mg de catalyseur est dispersé dans 50 ml d'une solution de BM (10 mg/L). Après avoir maintenir la poudre dans la solution de BM jusqu'à saturation, le réacteur est exposé à l'irradiation solaire. Le suivi des résultats d'analyse ont été réalisés par spectrophotomètre de marque (Shimadzu1800). La concentration a été déterminée en mesurant l'absorbance (densité optique) de la solution de BM et en appliquant la loi de Beer-Lambert, les courbes de cinétique ont été tracées en mesurant la concentration sur des prélèvements de 3 mL de solution, effectués à des temps précis, à l'aide d'une seringue. Le taux de dégradation est calculé à partir de la relation :

$$(\%) = \frac{C_{eq} - C_t}{C_{eq}} 100 \qquad (1)$$

C_{eq}: la concentration d'équilibre après adsorption dans l'obscurité
C_t : la concentration au temps (t).

III. RESULTAS ET DISCUSSION

A. Caractérisation par DRX

$CdMn_2O_4$ (fig. 1a) obtenu après calcination à 950 °C (préparé par voie sol gel) révèle l'existence d'une phase pure et homogène. $CdMn_2O_4$ a également montré les pics caractéristiques qui lié à la carte JCPDS n°. 073-1747.

La figure 1b présente le diagramme DRX de SnO_2, les pics sont bien définis ce qui prouve que la poudre est bien cristallisée. Le traitement par le logiciel HighScore permet l'identification de la structure comme étant une phase SnO_2 en accord avec la carte (JCPDS N° 021-1250.

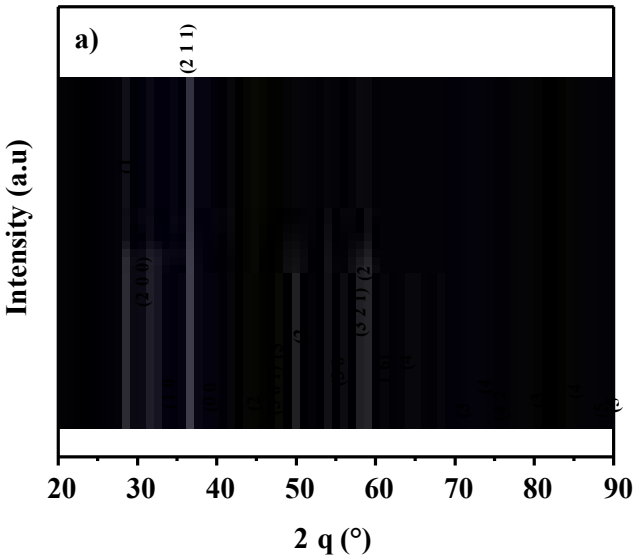

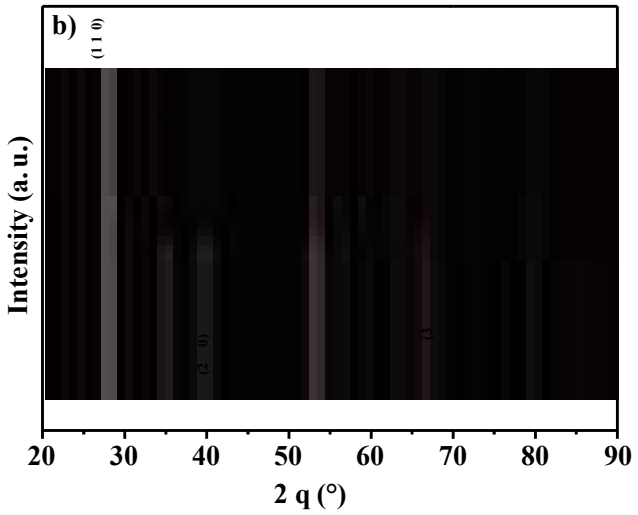

Fig. 1 Diffraction des rayons X des poudres : a) nanoparticules de $CdMn_2O_4$, *b)* de SnO_2.

B. Analyse FTIR

La technique d'analyse infrarouge du spectre électromagnétique réalisée pour ($CdMn_2O_4$, SnO_2) vise à identifier davantage leur caractère de liaison métallique et inorganique. La figure.2a montre les spectres infrarouges (FT-IR) des échantillons de $CdMn_2O_4$ dans la plage de nombres d'onde de 450–4000 cm^{-1}. Le pic à 3440 cm^{-1} est attribué à la vibration d'étirement de l'eau, et le pic à 1390 cm^{-1} est appartenait aux vibrations de flexion des molécules d'eau. Les pics trouvés dans la gamme de 491 cm^{-1} et 625 cm^{-1} sont liés à l'étirement des vibrations Mn–O et Cd–O. La figure 2b est celle de SnO_2.

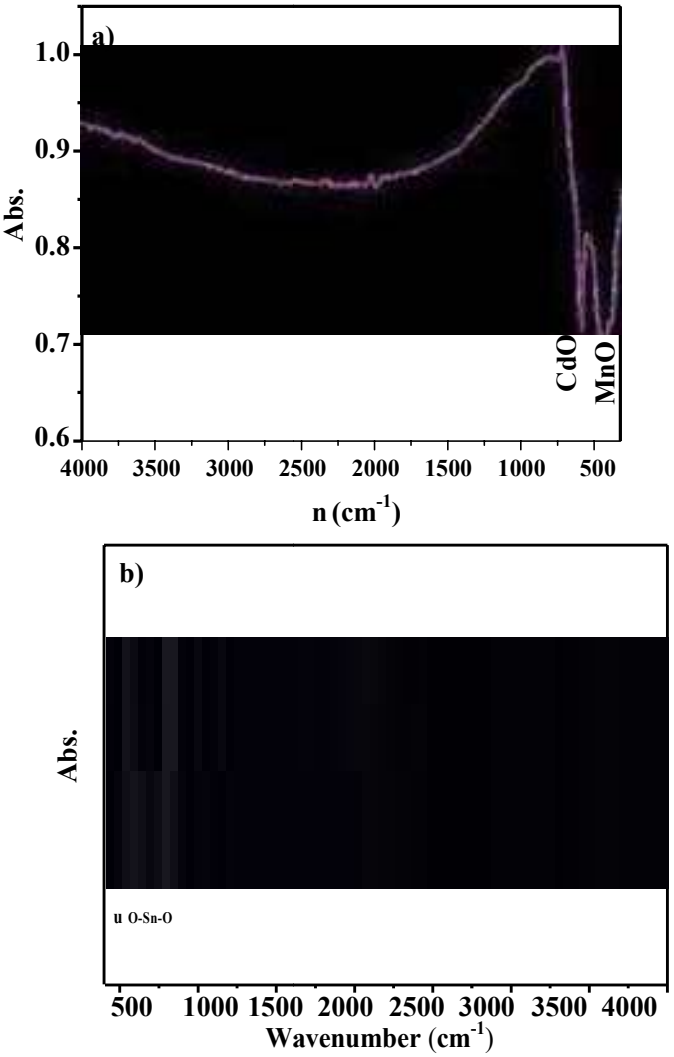

Fig. 2 FTIR de : a) $CdMn_2O_4$, b) SnO_2.

C. Caractérisation optique

L'équation de Munk-Kubelka est utilisée pour la détermination du gap optique (Eg) graphiquement :

$$F(R_\infty) = \frac{(1-R_\infty)^2}{2R_\infty} \qquad (2)$$

La réflectance diffuse R = (I/Io)dif est obtenue à partir du spectre d'absorption UV-visible converti. Eg a été déterminé par l'extrapolation de la partie linéaire de de la courbe, $(h\nu)^2$ en fonction de

l'énergie, pour hn= 0 et la transition est directement permise (Figure 3)

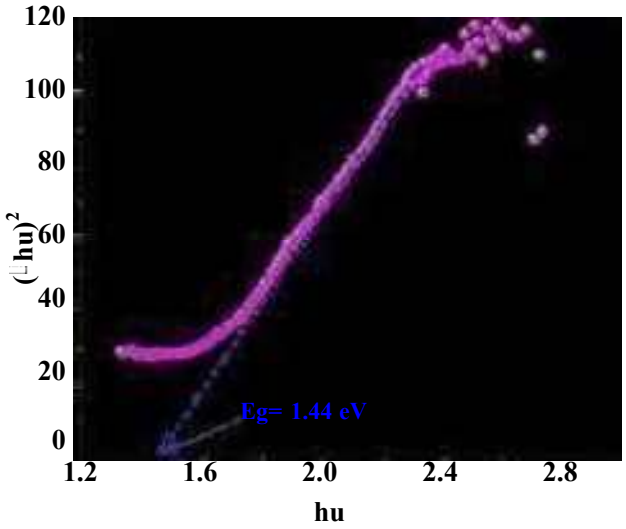

Fig. 3 Transition directe de bande interdite de $CdMn_2O_4$.

D. Caractérisation électrochimique

The La détermination du potentiel de la bande plate (E_{bp}) est obtenue à partir de la relation de Mott-Shottky[23].

$$\frac{1}{C_{sc}^2} = \frac{2}{e \varepsilon \varepsilon_r \varepsilon_0 N_d A^2} \left(V - V_{fb} - \frac{KT}{e}\right) \quad (3)$$

Csc : la capacité de la couche de la charge d'espace (RCS)

ε: Constante diélectrique du semi-conducteur

εo: Permittivité du vide (8.84×10^{-12} F m^{-1})

e : La charge de l'électron

L'utilisation de cette technique consiste à tracer l'inverse de la capacité (C^{-2}) en fonction du potentiel appliqué (E) Fig 4. La courbe obtenue est une droite et le potentiel de la bande plate (E_{bp}: flat band potential) pourra être estimé pour $C^{-2}= 0$.

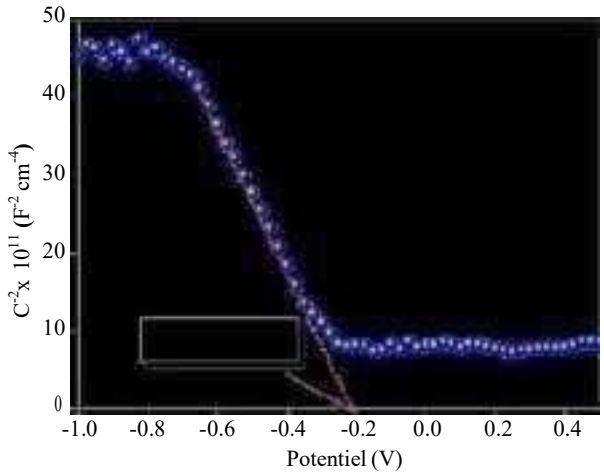

Fig. 4 Tracé de Mott Schottky à 10 kHz de nanoparticules de $CdMn_2O_4$.

IV. PHOTOCATALYSE

Afin d'évaluer l'activité photo catalytique de ce nouveau hétéro-système pour la dégradation du méthylène bleu (MB) en solution aqueuse sous irradiation solaire on a réalisée des tests photo-catalytiques au mois de septembre en plein air dans un réacteur en verre Pyrex double paroi de 200 ml de capacité placé à l'extérieur du bâtiment de notre laboratoire contenant l'échantillon (MB 10 mg /L, 50 ml) et une quantité de 50 mg d'hétéro système 50%wt$CdMn_2O_4$/50%wt SnO_2. Le rayonnement solaire$_2$ incident a été mesuré avec un radiomètre (W/m) dans la gamme de longueur d'onde de 300 à 2400 nm. L'intensité moyenne de la lumière du soleil du demi-jour estimée est de 750 W/m^2. La température quotidienne moyenne était de 31 °C. La suspension du catalyseur est agitée pendant 1 h dans l'obscurité avant l'irradiation pour atteindre l'équilibre dans la solution de MB à pH naturel. Pendant l'irradiation, le photo-réacteur est mis sous agitation magnétique afin d'avoir une suspension homogène pour favoriser l'adsorption à la surface d'hétéro système d'une part, et l'absorption du maximum de la lumière solaire d'autre part. 3 ml du liquide en suspension ont été prélevés et centrifugés. Les mesures des absorbances ont été réalisées à l'aide d'un spectrophotomètre UV-visible (Shimadzu UV 1800) dans la gamme d'énergie photonique de longueur d'onde de 300 à 700 nm.

En effet, $CdMn_2O_4$-CB se situe au-dessous du SnO_2-CB lui-même plus cathodique que le potentiel du couple $O_2/O_2^{\bullet}$ (~ -0,5 V) responsable de la dégradation de MB. La performance photocatalytique est expliquée par la séparation des charges suivie du transfert d'électrons due à la flexion de la bande inter faciale. Les électrons générés à partir de Cd_2MnO_4-CB irradié sont injectés dans SnO_2-CB qui agit comme pont d'électrons et ensuite transférés vers les molécules adsorbées du colorant.

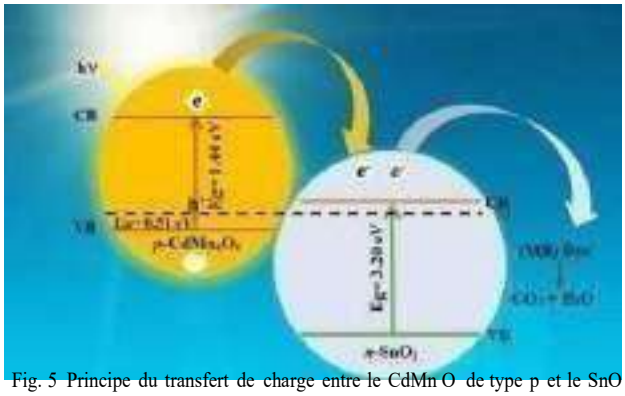

Fig. 5 Principe du transfert de charge entre le $CdMn_2O_4$ de type p et le SnO_2 de type n.

Le potentiel (eVbp= -0.21 V) de Cd_2MnO_4, décrit la position énergétique de VB par rapport au vide :

$$eVbp + Ea + 4{,}75 \qquad (4)$$

Par conséquent, son potentiel CB (VB-Eg) est situé en dessous de niveau du couple $O_2/O_2^{\bullet}$ (~ -0,5 V) qui devrait participer à la dégradation spontanée du MB. SnO_2 est stable dans un domaine de pH (3-13) et le potentiel eV_{bp} (- 0,21 V) est approximativement évalués à partir des courbes de potentiel selon le modèle de Gartner [24].

Le mécanisme réactionnel de la dégradation photo-catalytique du méthyle orange (MB) sous l'etérosysteme $CdMn_2O_4/SnO_2$ indique que les électrons de la bande de conduction (e-) et les trous de la bande de valence (h^+) sont générés lorsque la suspension de ce dernier est irradiée avec une énergie lumineuse plus importante que son énergie de bande interdite. La photo-génération des électrons pourrai réduire le colorant ou réagir avec des électrons accepteurs tels que O_2 adsorbé ou dissous dans l'eau le réduisant en radical super-oxyde anion $O_2^{\bullet}$. Les trous photo générés peuvent oxyder la molécule organique pour former R^+ ou réagir avec OH ou H_2O est former des radicaux OH• qui sont signalés à être responsable de la photo décomposition de substrats organiques comme colorants. Selon ceci, les réactions pertinentes pour la dégradation des colorants peuvent être exprimées comme.

$$CdMn_2O_4 + hv \rightarrow CdMn_2O_4(CBe^- + VBh^+) \qquad (5)$$

$$CdMn_2O_4 + (VBh^+) + H_2O \rightarrow CdMn_2O_4 + H^+ + OH^- \qquad (6)$$

$$CdMn_2O_4 + (VBh^+) + OH^- \rightarrow CdMn_2O_4 + OH^{\bullet} \qquad (7)$$

$$CdMn_2O_4 (^{\bullet}OH) + SnO_2 \rightarrow CdMn_2O_4 + SnO_2(OH^{\bullet}) \qquad (8)$$

$$SnO_2 + (CBe^-) + O_2 \rightarrow SnO_2 + O_2^{\bullet -} \qquad (9)$$

$$O_2^{\bullet -} + H^+ \rightarrow HO_2^{\bullet} \qquad (10)$$

$$2\,H_2O + 2\,e^- \rightarrow H_2 + 2\,OH^- \qquad (11)$$

$$C_2H_2O_4 + 0.5\,O_2 + 4\,h^+ \rightarrow 2CO_2 + H_2O + 4\,H^+ \qquad (12)$$

$$BM + {\bullet}OH \rightarrow \text{Degradation products} \qquad (13)$$

Le radical OH• résultant est un très fort agent oxydant (potentiel redox standard +2,8 V) [29] qui peut oxyder l'orange de méthyle en produits finaux minéraux. Une concentration initiale de 10 mg/L de MB a été utilisée. Le spectre UV-Vis figure (5. a) confirme l'activité de $CdMn_2O_4/SnO_2$. La photolyse est réalisée dans les mêmes conditions en présence d'acide oxalique (OA) 10^{-5} M sans l hetero-systeme utilisée dans cette conversion photo catalytique.

L'activité photocatalytique de $CdMn_2O_4/SnO_2$ est maintenue, les cycles répétés de la dégradation de MB montrant une désactivation significative de l'hétéro-système (figure 6).

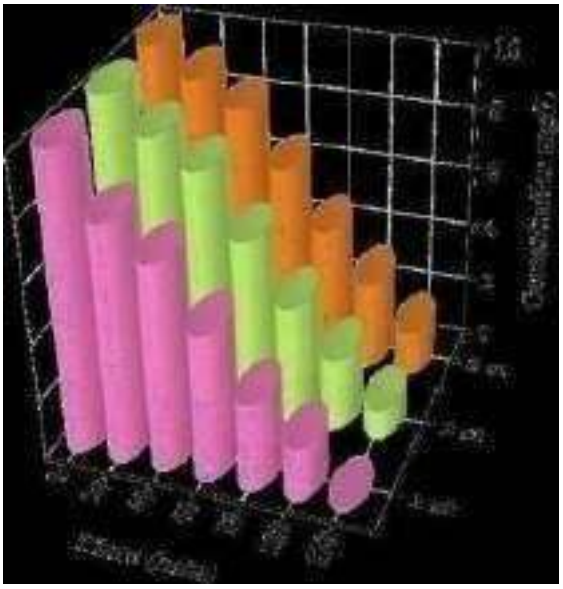

Fig. 6 Cycles répétés de dégradation du MB par 50 % en poids de $CdMn_2O_4$/50 % en poids de SnO_2.

Conclusions

Dans ce travail, une nouvelle hétérojonction $CdMn_2O_4/SnO_2$ a été élaborée pour une application photocatalytique, l'analyse par DRX de montre la formation des deux phases. Le spectre de réflectance diffuse de $CdMn_2O_4$ et SnO_2 présente les valeurs Eg= 1,44 eV pour $CdMn_2O_4$ et Eg= 3,20 eV pour SnO_2 avec une transition optique directe. Plus au moins ces caractéristiques nous a permis de construire le diagramme énergétique de l'héterosysteme en expliquent le phénomène d'injection d'électrons confirmé par l'activité photocatalytique observée sous lumière solaire pour la dégradation totale de 10 mg de MB à pH naturelle et une température de 25°C après 120 min d'irradiation. Le taux observé par l'étude des cycles répétés de dégradation de MB prouve l'efficacité de l'eterosystème 50wt%$CdMn_2O_4$/50wt%SnO_2.

Acknowledgment

We thank the financial support of the Thematic Agency for Research in Science and Technology (ATRST) through the national research program (Projets PRFU N° B00L01UN180120230002) and Socio-economic Impact Project N° 06 / Univ Jijel / DGRSDT.

References

[1] Robinson, T., McMullan, G., Marchant, R., & Nigam, P. (2001). Remediation of dyes in textile effluent: a critical review on current treatment technologies with a proposed alternative. Bioresource technology, 77(3), 247-255.

[2] Bechtold, T., Mussak, R., Mahmud - Ali, A., Ganglberger, E., & Geissler, S. (2006). Extraction of natural dyes for textile dyeing from coloured plant wastes released from the food and beverage industry. Journal of the Science of Food and Agriculture, 86(2), 233-242.

[3] Hessel, C., Allegre, C., Maisseu, M., Charbit, F., & Moulin, P. (2007). Guidelines and legislation for dye house effluents. Journal of environmental management, 83(2), 171-180.

[4] Kårelid, V., Larsson, G., & Björlenius, B. (2017). Pilot-scale removal of pharmaceuticals in municipal wastewater: Comparison of granular and powdered activated carbon treatment at three wastewater treatment plants. Journal of environmental management, 193, 491-502.

[5] Banat, I. M., Nigam, P., Singh, D., & Marchant, R. (1996). Microbial decolorization of textile-dyecontaining effluents: a review. Bioresource technology, 58(3), 217-227.

[6] Forgacs, E., Cserhati, T., & Oros, G. (2004). Removal of synthetic dyes from wastewaters: a review. Environment international, 30(7), 953-971.

[7] Van der Zee, F. P., & Villaverde, S. (2005). Combined anaerobic–aerobic treatment of azo dyes—a short review of bioreactor studies. Water research, 39(8), 1425-1440.

[8] Stolz, A. (2001). Basic and applied aspects in the microbial degradation of azo dyes. Applied microbiology and biotechnology, 56(1-2),69-80.

[9] Rice, R. G. (1996). Applications of ozone for industrial wastewater treatment—a review. Ozone: science & engineering, 18(6), 477-515.

[10] Banerjee, S., Pillai, S. C., Falaras, P., O'shea, K. E., Byrne, J. A., & Dionysiou, D. D. (2014). New insights into the mechanism of visible light photocatalysis. The journal of physical chemistry letters, 5(15), 2543-2554.

[11] Douafer, S., Lahmar, H., Benamira, M., Rekhila, G., & Trari, M. (2018). Physical and photoelectrochemical properties of the spinel LiMn2O4 and its application in photocatalysis. Journal of Physics and Chemistry of Solids, 118, 62-67.

[12] Akika, F. Z., Benamira, M., Lahmar, H., Tibera, A., Chabi, R., Avramova, I., ... & Trari, M. (2018). Structural and optical properties of Cu-substitution of NiAl2O4 and their photocatalytic activity towards Congo red under solar light irradiation. Journal of Photochemistry and Photobiology A: Chemistry, 364, 542-550.

[13] Paul, B., Bhuyan, B., Purkayastha, D. D., Dhar, S. S., & Behera, S. (2015). Facile synthesis of spinel CuCr2O4 nanoparticles and studies of their photocatalytic activity in degradation of some selected organic dyes. Journal of Alloys and Compounds, 648, 629-635.

[14] Pathania, D., Gupta, D., Ala'a, H., Sharma, G., Kumar, A., Naushad, M., ... & Alshehri, S. M. (2016). Photocatalytic degradation of highly toxic dyes using chitosan-g-poly (acrylamide)/ZnS in presence of solar irradiation. Journal of Photochemistry and Photobiology A: Chemistry, 329, 61-68.

[15] Khare, P., Singh, A., Verma, S., Bhati, A., Sonker, A. K., Tripathi, K. M., & Sonkar, S. K. (2017). Sunlight-induced selective photocatalytic degradation of methylene blue in bacterial culture by pollutant soot derived nontoxic graphene nanosheets. ACS Sustainable Chemistry & Engineering, 6(1), 579-589.

[16] Chen, K., Gao, F., Lin, W., Cai, H., Li, G., Dong, X., ... & Lu, X. (2010). Room-temperature multiferroic properties in NiBi2O4. EPL (Europhysics Letters), 89(2), 27004.

[17] Lahmar, H., Benamira, M., Akika, F. Z., & Trari, M. (2017). Reduction of chromium (VI) on the hetero-system CuBi2O4/TiO2 under solar light. Journal of Physics and Chemistry of Solids, 110, 254-259.

[18] Lahmar, H., Kebir, M., Nasrallah, N., & Trari, M. (2012). Photocatalytic reduction of Cr (VI) on the new hetero-system CuCr2O4/ZnO. Journal of Molecular Catalysis A: Chemical, 353, 74-79.

[19] Drits, V., Środoń, J., & Eberl, D. D. (1997). XRD measurement of mean crystallite thickness of illite and illite/smectite: Reappraisal of the Kubler index and the Scherrer equation. Clays and clay minerals, 45(3), 461-475.

[20] S.H. Ben Hariz, H. Lahmar, G. Rekhila, A. Bouhala, M. Trari, M. Benamira, A novel MgCr2O4/WO3 hetero-junction photocatalyst for solar photo reduction of hexavalent chromium Cr (VI), J. Photochem. Photobiol. A Chem. 430 (2022) 113986.

[21] C. Rouquié, Microfiltration de jus de fruits et suspensions à base de fruits: faisabilité et performances d'une filtration par membranes immergées,(2018).

[22] H. Lahmar, G. Rekhila, M. Trari, Y. Bessekhouad, reduction on the novel heterosystem La2CuO4/SnO2 under solar light, Environ. Prog. Sustain. Energy. 34 (2015) 744–750.

[23] Kennedy, J. H., & Frese, K. W. (1978). Flatband Potentials and Donor Densities of Polycrystalline α - Fe2 O 3 Determined from Mott - Schottky Plots. Journal of the Electrochemical Society, 125(5), 723-726.

[24] Bessekhouad, Y., Trari, M., & Doumerc, J. P. (2003). $CuMnO_2$, a novel hydrogen photoevolution catalyst. International journal of hydrogen energy, 28(1), 43-48.

MODELISATION DE LA TURBULENCE DANS UNE CAVITE CYLINDRIQUE APPLICATION AU STOCKAGE DE GNL

Khelifi Touhami Mohamed Salah[#1]

[#]*Laboratoire de génie physique des hydrocarbures, Université M'hamed Bougara Boumerdès*
Faculté des hydrocarbures Avenue de l'indépendance Boumerdès

[1s]s.khelifi@univ-boumerdes.dz

Résumé— Une simulation numérique a été menée pour étudier la convection naturelle dans une cavité cylindrique ayant un rapport d'allongement égal à 1 rempli de GNL est chauffée latéralement par un flux constant et refroidis par évaporation à travers la surface libre. Les équations de vitesse moyennées dans le temps (RANS) sont résolues en deux dimensions couplées avec l'équation d'énergie. La viscosité turbulente estmodélisée par lemodèle K-ε à bas nombre de Reynolds. La méthode de discrétisation est celle des volumes finis avec l'algorithme SIMPLER. Le schéma de la loi de puissance est favorisé dans ce présent travail. La méthode de balayage utilisée est l'algorithme Thomas (TDMA) pour la solution itératif des systèmes d'équations discrétisées. L'équation de pression est obtenue de façon à satisfaire l'équation de continuité. Le maillage non uniforme est employé pour plusieurs mailles afin de s'assurer sur l'unicité de la solution. Les solutions du code de calcul ont été comparées avec succès avec les solutions expérimentales dans une cavité carrée. Nous présentons à cet effet, les champs de vitesse et de température en fonction du nombre de Rayleigh variant entre 10^8 jusqu'à 10^{11}

***Mots clès*— Turbulence, convection naturelle, modèle k-ε, Modélisation**

I. INTRODUCTION

Les écoulements de convection naturelle à l'intérieur des cavités possèdent plusieurs applications dans le génie thermique comme les collecteurs solaires, les refroidissements des équipements électroniques et les isolations dans les habitats et les grands réservoirs de stockage des hydrocarbures. La configuration carrée de la cavité est un bon choix de comparaison afin d'évaluer les performances des techniques numériques et des modèles de turbulence. Plusieurs travaux numériques comme ceux de Peng et Davidson [4] ou ceux de Vasic et Hanjalic [19] ont été confronté avec les résultats expérimentaux d'Ampofo et Karayianis [1].

Des études expérimentales ont été menées pour la convection naturelle dans les réservoirs cryogéniques par plusieurs chercheurs. Khemis et al. [12-13], Boukeffa et al. [15].ont fait des mesures pour l'azote liquide au niveau de laboratoire en utilisant des cryostats pour prédire l'évaporation de ces liquides par la technique Schlieren. Kanazawa et al. [16] ont visualisé le profil d'écoulement convectif dans un réservoir de GNL avec une étude expérimentale.

D'autre part, des études numériques ont été reportées pour la convection naturelle à l'intérieur du réservoir cryogénique. Li et al. [14] ont travaillé sur l'effet du niveau liquide sur le transfert de chaleur dansleréservoir de stockage de l'azote.

Pham et Petit. [7] Ont étudié numériquement en turbulent le phénomène du Rollover dans une cavité carrée contenant du GNL. Bates et Morrison [17] ont aussi examiné le phénomène du Rollover dans un réservoir de stockage. Pour ce phénomène, Hubert et al. [20] ont aussi développé un code numérique pour étudier le comportement dynamique du GNL dans un réservoir de stockage.

Chen et al. [18] ont analysé le changement de température et de pression dans un réservoir de stockage de GNL. Khelifi-Touhami et al. [6] ont simulé numériquement la convection naturelle laminaire dans le réservoir de GNL en montrant que l'évaporation n'est pas uniforme. Pour justifier l'influence de la tension de surface sur l'évaporation Kozhevnikov et Sheremet [9] ensuite Rachedi et al. [10] ont ajouté le terme adimensionnel de Marongoni dans leurs calculs numériques lors de la convection naturelle du GNL. Roh et son [8] ont examiné numériquement la convection naturelle dans un réservoir de stockage du GNL et ont montré que la génération du BOG dépend fortement du contact solide liquide.

Haddar et al. [21] ont proposé d'ajouter un système de refroidissement de cloisons à l'intérieur des réservoirs de GNL afin d'absorber la perte de chaleur dans l'environnement et de réduire ainsi le taux de BOG. Hasan et al. [11] ont démontré que la minimisation du BOG dépend de plusieurs facteurs comme la température ambiante, la pression du réservoir LNG, la composition du GNL etc.

Dans ce travail, on se concentre sur l'observation des champs de vitesse et de température ainsi au contrôle de la viscosité turbulente au cours de l'augmentation du nombre de Rayleigh tout en tenant compte de l'évaporation non uniforme [6] sur la surface libre du liquide.

En premier lieu nous présentons une comparaison de nos résultats avec ceux expérimentaux [1] (Problème Benchmark) afin de valider les calculs actuels en cavité carrée.

Après une série de solutions graphiques sera présentée pour illustrer l'écoulement et le champ de température pour différentes valeurs de Rayleigh pour le cas actuel d'une cavité cylindrique contenant du GNL (Pr = 2,1) et un allongement fixe Al = 1. La simulation numérique en deux dimensions sera limitée au calcul de la mi-partie droite de la cavité vu que l'écoulement est supposée axisymétrique.

II. MODÈLE MATHÉMATIQUE

Le problème considéré est expliqué schématiquement par la figure (1). Le domaine de calcul intérieur en 2 dimensions dans une cavité cylindrique (Al = 1) de diamètre D et d'hauteur H. La base étant considérée adiabatique, le sommet représente la surface libre là où s'effectue l'évaporation. Alors que la paroi latérale est soumise à une densité de flux constante.

Le fait d'augmenter du nombre de Rayleigh Ra plus de 10^8 nous permet d'augmenter les dimensions de la cavité si nous conservons une valeur du flux constant latéralement.
Le GNL est chauffée latéralement ce qui implique une variation de la masse volumique du fluide se traduisant par une montée des masses de liquide plus chaudes le long de la paroi. Ces dernières se refroidissent et viennent tomber au milieu de la cavité. Ce phénomène est illustré par une recirculation permanente du liquide tant que le chauffage persiste.
L'écoulement du fluide est incompressible, visqueux et turbulent, Il est supposé que le fluide satisfait l'approximation de Boussinesq. Les équations qui gouvernent l'écoulement sont l'équation de continuité et les équations de Navier-Stokes moyennées dans le temps en coordonnées cylindriques.
Les tensions de Reynolds sont modélisées par le modèle k-epsilon à bas nombre de Reynolds (FLB) [2]. Les équations sont adimensionnées en introduisant les variables suivants :

$$r = r^*/H,\quad z = z^*/H,\quad u = u^*H/\nu,\quad v = v^*H/\nu,$$

$$p = \frac{p^*}{\rho\nu^2},\quad T = \frac{T^* - T_m^*}{T_i^* - T_0^*},\quad T_m^* = \frac{T_i^* + T_0^*}{2},$$

$$k = \frac{k^*}{u_\tau^2},\quad \varepsilon = \frac{\varepsilon^* H}{u_\tau^3};\quad t = \frac{t^*}{H^2/\nu}$$

Equation de continuité

$$\frac{1}{r}\frac{\partial (r.u)}{\partial r} + \frac{\partial v}{\partial z} = 0$$

Equations de quantité de mouvement

Suivant x :

$$\frac{\partial u}{\partial t} + \frac{1}{r}\frac{\partial (r.u.u)}{\partial r} + \frac{\partial (uv)}{\partial z} = -\frac{\partial p}{\partial r} + \frac{1}{r}\frac{\partial}{\partial r}\left(r(1+\nu_t)\frac{\partial u}{\partial r}\right) + \frac{\partial}{\partial z}\left((1+\nu_t)\frac{\partial u}{\partial z}\right) - (1+\nu_t)\frac{u}{r^2} + S_u$$

Suivant y :

$$\frac{\partial v}{\partial t} + \frac{1}{r}\frac{\partial (r.v.u)}{\partial r} + \frac{\partial (vv)}{\partial z} = -\frac{\partial p}{\partial z} + \frac{1}{r}\frac{\partial}{\partial r}\left(r(1+\nu_t)\frac{\partial v}{\partial r}\right) + \frac{\partial}{\partial z}\left((1+\nu_t)\frac{\partial v}{\partial z}\right) + Gr.T + S_v$$

Equation de l'énergie

$$\frac{\partial T}{\partial t} + \frac{1}{r}\frac{\partial (r.u.T)}{\partial r} + \frac{\partial (vT)}{\partial z} = \frac{1}{r}\frac{\partial}{\partial r}\left(r\left(\frac{1}{Pr} + \frac{\nu_t}{Pr_t}\right)\frac{\partial T}{\partial r}\right) + \frac{\partial}{\partial z}\left(\left(\frac{1}{Pr} + \frac{\nu_t}{Pr_t}\right)\frac{\partial T}{\partial z}\right)$$

Equation de l'énergie cinétique turbulente

$$\frac{\partial k}{\partial t} + \frac{1}{r}\frac{\partial (r.u.k)}{\partial r} + \frac{\partial (vk)}{\partial z} = \frac{1}{r}\frac{\partial}{\partial r}\left(r\left(\nu + \frac{\nu_t}{\sigma_k}\right)\frac{\partial k}{\partial r}\right) + \frac{\partial}{\partial z}\left(\left(\nu + \frac{\nu_t}{\sigma_k}\right)\frac{\partial k}{\partial z}\right) + S_k$$

Equation du taux de dissipation de k

$$\frac{\partial \varepsilon}{\partial t} + \frac{1}{r}\frac{\partial (r.u.\varepsilon)}{\partial r} + \frac{\partial (v\varepsilon)}{\partial z} = \frac{1}{r}\frac{\partial}{\partial r}\left(r\left(\nu + \frac{\nu_t}{\sigma_\varepsilon}\right)\frac{\partial \varepsilon}{\partial r}\right) + \frac{\partial}{\partial z}\left(\left(\nu + \frac{\nu_t}{\sigma_\varepsilon}\right)\frac{\partial \varepsilon}{\partial z}\right) + S_\varepsilon$$

$$S_u = \frac{\partial}{\partial z}\left(\nu_t \frac{\partial u}{\partial z}\right) + \frac{1}{r}\frac{\partial}{\partial r}\left(r.\nu_t \frac{\partial v}{\partial r}\right) - \frac{u}{r^2}$$

$$S_v = \frac{\partial}{\partial z}\left(\nu_t \frac{\partial v}{\partial z}\right) + \frac{1}{r}\frac{\partial}{\partial r}\left(r.\nu_t \frac{\partial u}{\partial z}\right)$$

$$\nu_t = C_\mu f_\mu \frac{k^2}{\varepsilon},\quad S_k = P_k - \varepsilon + D,$$

$$S_\varepsilon = f_1 c_1 P_k - c_3 Gr\left(\frac{\partial T}{\partial z}\right) - f_2 c_2 \frac{\varepsilon}{k} + E$$

$$Gr = \frac{g\beta(T_i^* - T_0^*)H^3}{\nu^2},\quad Ra = Gr.Pr = \frac{g\beta(T_i^* - T_0^*)H^3}{\nu\alpha}$$

$$P_k = \nu_t\left[2\left(\frac{\partial u}{\partial r}\right)^2 + 2\left(\frac{u}{r}\right)^2 + 2\left(\frac{\partial v}{\partial z}\right)^2 + \left(\frac{\partial u}{\partial z} + \frac{\partial v}{\partial r}\right)^2\right],$$

$c_1 = 1{,}44$, $c_2 = 1{,}92$, $c_\mu = 0{,}09$

$$f_\mu = \tanh\left(\frac{y}{14}\right)^3,\quad \sigma_k = 0{,}9,\quad \sigma_\varepsilon = 1,$$

Le modèle FLB permet de donner les coefficients suivants:

$D = 0 \quad E = 0$

$f_1 = 1$

$$f_2 = [1 - 0.22\exp(-[R_T/6]^2)]f_w$$

$$f_\mu = \frac{0.4 f_w}{\sqrt{R_T}} + [1 - \frac{0.4 f_w}{\sqrt{R_T}}][1 - \exp(-\frac{R_y}{42.63})]^3$$

$$f_w = 1 - \exp[-\frac{R_y}{2.3\sqrt{R_y}} + (\frac{R_y}{2.3\sqrt{R_y}} - \frac{R_y}{8.89})(1 - \exp(-\frac{R_y}{20}))^3]$$

Conditions aux limites :
Sur toutes les parois solides

$$u = v = k = 0,\quad \varepsilon = \frac{c_\mu^{3/4} k^{3/2}}{0{,}41.y_1}$$, y_1 est la distance du 1er nœud de la maille à partir de la paroi

Notons que Le modèle FLB impose un gradient de ε nul.Nous l'avons changé pour ce travail vu la stabilité numérique remarquée avec la fonction de paroi.

Sur la paroi verticale : $T = T_i = 1$

Sur la paroi horizontale : $\frac{\partial T}{\partial z} = 0$

Sur l'axe : $u = 0,\quad \frac{\partial v}{\partial r} = \frac{\partial k}{\partial r} = \frac{\partial \varepsilon}{\partial r} = 0$

Sur la surface libre du liquide : $\frac{\partial u}{\partial z} = \frac{\partial T}{\partial z} = \frac{\partial k}{\partial z} = \frac{\partial \varepsilon}{\partial z} = 0,\quad v = 0$

Pham et Petit. [7], Khelifi-Touhami et al. [6], Hubert et al. [20] Kozhevnikov et Sheremet [9], Rachedi et al. [10] ont tous utilisé la loi d'évaporation trouvée par Hashemi et Wesson [3] pour une bonne modélisation de l'évaporation du GNL en surface.

Si $T^*(r^*, t) \geq T^*_{sat}$ alors

$$\dot{m}^*_{ev} = c.\frac{\lambda^*}{L^{*4/3}}(T(r,t) - T^*_{sat})^* \quad \text{avec } c = 0{,}13$$

Si $T^*(r^*, t) < T^*_{sat}$ alors

$$\dot{m}^*_{ev} = 0$$

III. MÉTHODES NUMÉRIQUES

Les équations qui gouvernent l'écoulement ont été résolues par l'approche des volumes finis.

Les équations sont intégrées sur un volume de contrôle élémentaire localisé autour de chaque nœud de la maille. Les positions des nœuds sont calculées par une fonction tangente hyperbolique de telle façon à avoir un raffinement plus dense près des parois. Les composantes de la vitesse sont calculées d'une façon décalée alors que les variables scalaires sont calculées sur les nœuds centraux.
Les termes convectifs des équations sont discrétisés en utilisant le schéma de la loi de puissance. La méthode SIMPLER a été utilisée afin de corriger la pression et les vitesses de façon à satisfaire l'équation de continuité. La méthode de résolution utilisée est la méthode purement implicite décrite dans le livre Versteeg et Malalasekera [5]. Les matrices triangulaires obtenues ont été résolues par l'algorithme Thomas.

IV. RESULTATS

1. Validation du code dans une cavité carrée

Nous avons présenté en premier lieu les résultats de validation de notre code de calcul en cavité carrée vu l'absence complète des résultats expérimentaux en coordonnée cylindriques surtout pour le cas turbulent. Ampofo et karayiannis [1] ont présenté des résultats très intéressant sous forme de données afin de faciliter la validation des modèles numériques. Leurs résultats ont été utilisés dans ce travail nous présentons par exemple la variation du nombre de Nusselt coté chaud et coté froid de la cavité et la variation de l'énergie cinétique turbulente à mi-hauteur de la cavité comparés à ceux de l'expérience. Nous avons obtenu de bons résultats vis-à-vis des résultats numériques de la littérature d'une part et d'autre part avec ceux expérimentaux observés sur les figures ci-dessous. Sur la figure 1 le nombre de Nusselt décroît au fur et à mesure que l'écoulement monte à proximité de la paroi chaude de la alors que sur la figure 2 le nombre de Nusselt croît au fur et à mesure que l'écoulement descend à proximité de la paroi froide. Nous avons noté une légère élévation de nos valeurs pour y compris entre 0.5 et 0.9 mais une valeur maximale de 140 est très voisine de celle obtenu par ces auteurs sur les deux parois.

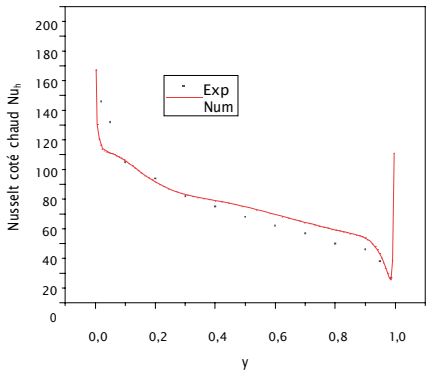

Fig.1 : Variation du nombre de Nusselt près de la paroi chaude

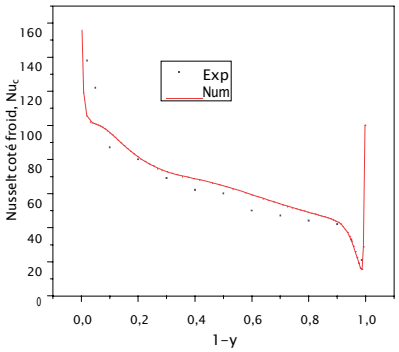

Fig.2 : Variation dunombre de Nusselt près de la paroi froide

Sur la Figure 3 nous avons présenté la variation de l'énergie cinétique turbulente qui a été trouvé très proche de celle expérimentale comparés aux résultats numériques déjà obtenus pour ce cas de figure. Une valeur maximale proche de 4.5 a été obtenue avec une allure de notre courbe presque confondue avec celle de l'expérience. Notons que le modèle k-epsilon standard donne de très fortes valeurs près de la paroice qui dévie carrément des résultats expérimentaux.

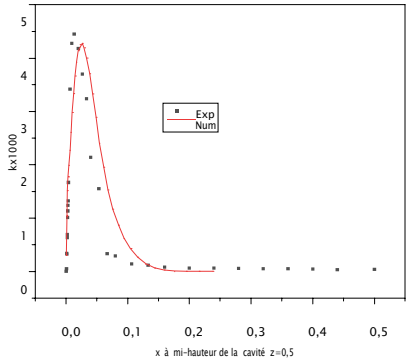

Fig.3 : Variation de l'énergie cinétique dimensionnelle à mi-hauteur dela cavité y=0.5

2. Résultats dans une cavité cylindrique

Il est avantageux d'avoir des résultats numériques concernant la cavité cylindrique et avec des nombres de Rayleigh élevé pour s'approcher le mieux que possible aux résultats pratiques du bac de stockage de GNL.

A. Sensibilité du maillage

Avant toute modélisation il est plus adéquat d'effectuer un test de maillage pour voir la sensibilité des résultats numériques envers le changement du maillage nombre de nœuds et raffinement près des obstacles.

ISSN: 1737-9334

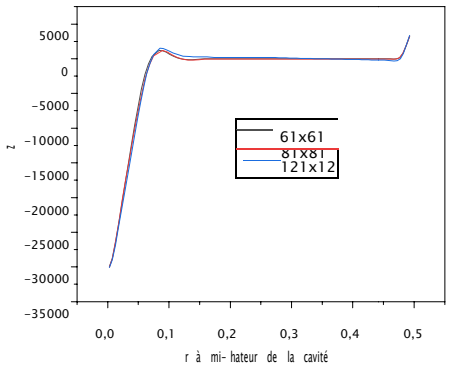

Fig.4 sensibilité du maillage pour $Ra=10^{11}$

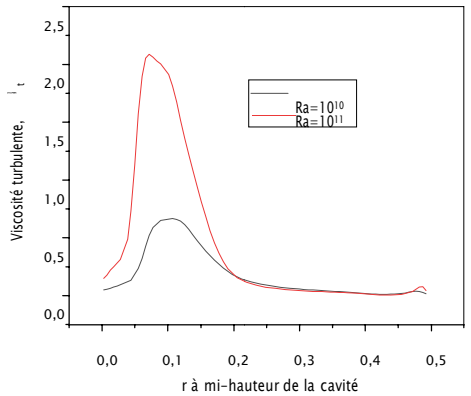

Fig.5b : Variation de la viscosité turbulente à mi-hauteur de la cavité pour $Ra=10^{10}$ et $Ra=10^{11}$

B. Résultats

La cavité choisie possède un allongement Al=1 fixé. Nous contrôlons l'effet du changement du nombre de Rayleigh sur les champs d'écoulement et de température et surtout sur l'intensité de turbulence. Nous débutons par l'exposition de certains résultats de turbulence à savoir la viscosité turbulente à mi-hauteur de la cavité pour différents nombre de Rayleigh (Fig.5)

Les valeurs de la viscosité turbulence commencent à augmenter avec l'augmentation du nombre de Rayleigh. Pour $Ra=10^8$ et $Ra=10^9$ sur la figure 4 les valeurs augmentent sur tout l'axe horizontal (z=0.5) par contre pour $Ra=10^{10}$ et $Ra=10^{11}$ sur la Figure 5 les valeurs augmentent seulement près de l'axe pour x inférieur à 0.2 et se stabilise ailleurs vers l'annulation de cette variable

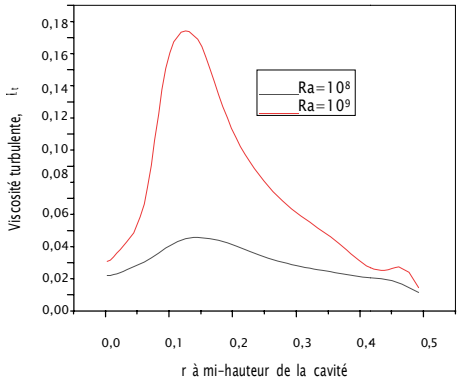

Fig.5a : Variation de la viscosité turbulente à mi-hauteur de la cavité pour $Ra=10^8$ et $Ra=10^9$

Sur les figures 6a et 6b, nous exposons la variation de la vitesse radiale le long de la verticale z en fixant la position radiale en r=0.25 loin de l'axe. Les valeurs de u sont négatives au sommet z=1 et positives en bas z=0 ce qui confirme la direction de la recirculation du fluide. Par ailleurs ses vitesses sont presque nulles entre 0.2 et 0.8 pour les nombres de Rayleigh considérés. Les modules de vitesses sont à peu près le double en passant de $Ra=10^8$ à $Ra=10^9$ ou en passant de $Ra=10^{10}$ à $Ra=10^{11}$ que ce soit au sommet ou sur la base de la cavité.

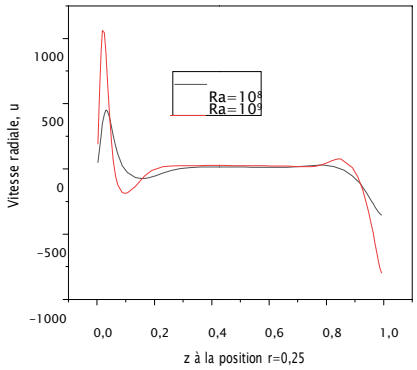

Fig.6a: Variation le long de la verticale de la vitesse radiale à r=0.25

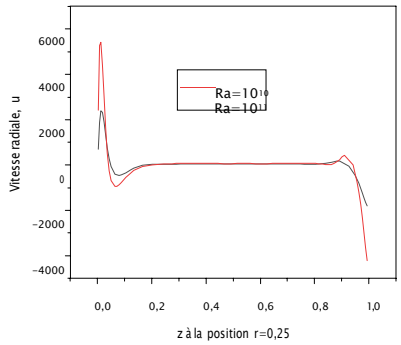

Fig.6a: Variation le long de la verticale de la vitesse radiale à r=0.25

Sur la Figure 7a et 7b, nous avons présenté les variations de la vitesse axiale pour tous les nombres de Rayleigh. Nous avons remarqué que les valeurs de u varient fortement sur l'axe en faisant varier le nombre de Rayleigh par contre cette variation est faible près de la paroi chaude.

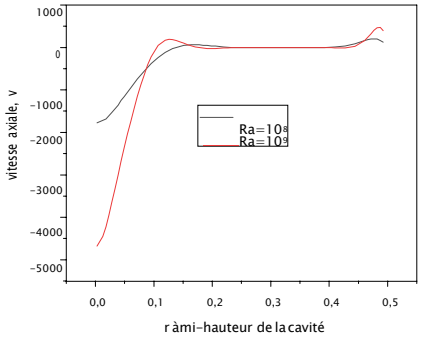

Fig.7a : Variation à mi-hauteur de la cavité de la vitesse axiale pour Ra=10^8 et Ra=10^9

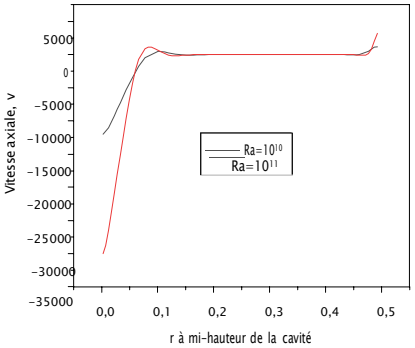

Fig.7b : Variation à mi-hauteur de la cavité de la vitesse axiale pour Ra=10^{10} et Ra=10^{11}

Sur la Figure 7a 7b, nous avons montré les variations de la vitesse axiale à mi-hauteur de la cavité en fonction du nombre de Rayleigh. Le changement de la vitesse axiale au niveau de l'axe est appréciable avec l'augmentation du nombre de Rayleigh par contre le changement de v à proximité de la paroi chaude est moins important. Ceci est dû à la rencontre des débits de GNL au centre de la surface libre qui retombent ensuite vers e bas suite au refroidissement par évaporation.

Pour mieux visualiser ce phénomène, nous avons exposé les champs de vitesse et de température pour tous les nombres de Rayleigh considérés sur les figures 8 et 9.

La température diminue en valeur adimensionnelle suite à l'élévation du nombre de Rayleigh et la stratification des couches et de plus en plus prononcée. Ceci peut être expliqué par le fait que la vitesse est presque nulle aux endroits où la température est constante horizontalement pour le même nombrede Rayleigh.

Par ailleurs la vitesse varie dans le même sens que le nombre de Rayleigh ce qui explique que l'écoulement devient de plus en plus intense en créant une seule recirculation du fluide tant que Ra est inférieur à 10^9. Au-delà de cette valeur le jet commence à se prolonger de la base centrale et frappe la paroi latérale pour Ra=10^{10} et Ra=10^{11} sur la figure 9 et donne naissance à une deuxième petite recirculation qui tourne au sens inverse par rapport à la plus grande et crée un écoulement ascendant vers la surface du liquide.

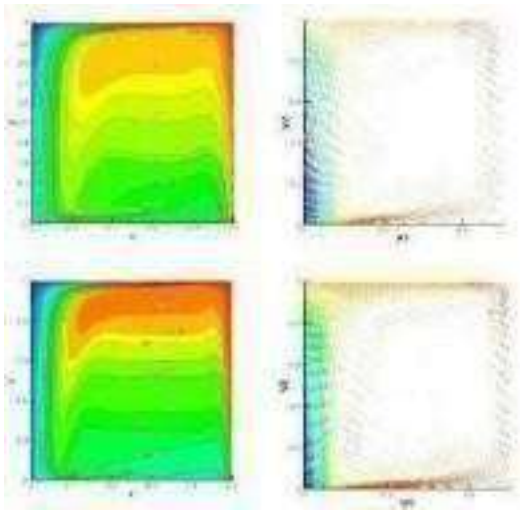

Fig.8 : profiles de vitesse et de température pour Ra=10^8 et Ra=10^9

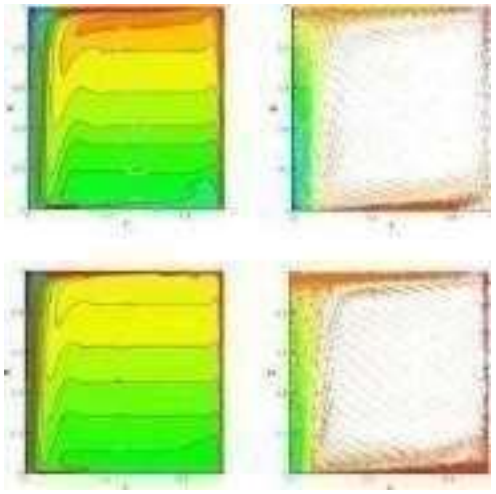

Fig.9 : profiles de vitesse et de température pour $Ra=10^{10}$ et $Ra=10^{11}$

V. CONCLUSIONS

Le modèle k epsilon à bas nombre de Reynolds a été appliqué avec succès dans cette présente étude pour modéliser les écoulements de convection naturelle turbulente à l'intérieur d'une cavité cylindrique. Pour des raisons de validation du code avec les résultats expérimentaux et vu l'indisponibilité de ces résultats en coordonnées cylindriques nous avons utilisé une cavité carrée différentiellement chauffée contenant de l'air en écoulement turbulent. Une concordance de nos résultats pour les valeurs de Nusselt expérimentaux. Une légère augmentation de nos valeurs entre la position x=0.5 et x=0.9 a été remarquée. L'énergie cinétique turbulente k à proximité de la paroi est très proche de celle expérimentale avec une valeur maximale de l'ordre de 4.5. Notons que les résultats numériques obtenus auparavant surtout avec le modèle k-epsilon standard s'éloignent énormément des résultats expérimentaux

Ce modèle de turbulence (modèle FLB) a été utilisé ensuite pour la cavité cylindrique pour des nombres de Rayleigh allant de 10^8 jusqu'à 10^{11} où nous avons contrôlé l'augmentation progressive de la viscosité turbulente avec l'augmentation du nombre de Rayleigh Ra. Des valeurs maximales atteignant 0.04 et 0.17 à mi-hauteur de la cavité pour $Ra=10^8$ et $Ra=10^9$ et des viscosités maximales encore plus élevées 0.7 à 2.2 sont obtenues pour des valeurs de Rayleigh plus élevées. Ceci montre la zone de transition vers la turbulence dans cet endroit de la cavité. Notons que le centre de la base de la cavité renferme les valeurs les plus élevées de la viscosité turbulente vu le choc du jet provenant du sommet.

Nous avons aussi exposé les variations de vitesses radiales au milieu de la partie cylindrique étudiée et les valeurs de la vitesse axiale à mi-hauteur de la cavité ceci montre bien la dépendance du profil de vitesse avec le nombre de Rayleigh.

Nous cherchons dans les prochains travaux à présenter la variation du Nusselt latérale et en surface libre et le profil d'évaporation en fonction du nombre de Rayleigh pour évaluer le taux d'évaporation numériquement afin de s'approcher de celui du bac de stockage de GNL pour les mêmes conditions climatiques.

Remerciements

Nous remercions la direction générale de recherche scientifique (DGRSDT), la direction de la faculté des hydrocarbures et celle du Laboratoire de Génie physique des hydrocarbures de l'université de Boumerdès.
Nous tenons à remercier aussi tous les dirigeants du Congrès International de l'Energie Renouvelable (CIER 2022) d'avoir accepté cette communication et faciliter notre présentation.

Nomenclature

A : diffusivité thermique
Al : rapport d'allongement, H/D
c_1, c_2, c_3 : Coefficients dans l'équation de
c : Coefficient dans l'équation de ε
f_1 : Facteur de correction pour c_1
f_2 : Facteur de correction pour c_2
f_μ : Facteur de correction pour c_μ
g : accélération de pesanteur
H : hauteur de la cavité
k : Énergie cinétique turbulente
Nu : nombre de Nusselt à la paroi chaude
$\overline{Nu}$: Nombre de Nusselt moyen à la paroi chaude
P : pression
P_k : Terme de production de l'énergie cinétique turbulente
Pr : Nombre de Prandtl, ν / a
Ra : nombre de Rayleigh, $g \beta \Delta T H^3 Pr / \nu^2$
t : temps
T : température locale
ΔT : Différence de température caractéristique
u : vitesse horizontale
v : vitesse verticale
D : diamètre de la cavité
r : coordonnée horizontale
z : coordonnée verticale

Symboles grecs

λ : Conductivité thermique du GNL (w / mK)
α : Diffusivité thermique du GNL (m^2 / s)
β : Coefficient d'expansion thermique
ΔT : Échelle de température $\Delta T = \beta . H /$
ε : Taux de dissipation de l'énergie cinétique turbulente
ν : viscosité cinématique moléculaire (m^2 / s)
ν_t : viscosité cinématique turbulente
ρ : Masse volumique
σ_k : Nombre de Prandtl pour k
σ_t : Nombre de Prandtl pour T
σ_ε : Nombre de Prandtl pour ε

References

{1] F.Ampofo, T.G.Karayiannis, Experimental benchmark data for turbulent natural convection in an air filled square cavity, Int. J. heat and Mass Transfer 46 3551-3572, (2003).[

2] B.E. Launder and D.B. Spazlding, The numerical computation of turbulent flows, computer Methods in Applied Mechanics and Engineering, vol. 3,pp. 269-289,(1974).

[3] H.T. Hashemi and H.R. Wesson, Cut LNG storage costs, Hydrocarbon Processing, August 1971, pp. 246-249.

[4] S.H. Peng, L. Davidson, Numerical investigation of turbulent buoyant cavity flow using LES, in: 3rd International Symposium on Turbulence, Int. J. Heat Mass Transfer (2000) 1–8.

[5] VERSTEEG and W. MALALASEKERA, « An introduction to computational fluid dynamics the finite volume method » Edinburgh Gate Harlow Essex CM 2JE England (1995). .

[6] M.S. Khelifi Touhami, A. Benbrik, D. Lemonnier, D. Blay Laminar natural convection flow in a cylindrical cavity application to the storage of LNG.J. Pet. Sci. Eng, 71 (2010), pp. 126-132.

[7] C.T. Pham et J. P. Petit, Simultaneous heat and mass Transfers with or without evaporation in unsteady turbulent Natural convection and application to a liquefied natural gas Storage, 4th International Symposium on stratified flows Grenoble (F), June 29- July 2, 1994.

[8] S. Roh, G. Son. Numerical study of convection in a liquefied natural gas tank, J. Mech. Sci. and Tech 26 (2012) 3133-3140.

[9] Kozhevnikov, D. A. & Sheremet, M. A. 2018. Natural convection with evaporation in a vertical cylindrical cavity under the effect of temperature-dependent surface tension. *Continuum Mechanics and Thermodynamics,* 30**,** 83-94.

[10] K. Rachedi, H. Ragueb, M. Boussaid, Numerical investigation of surface evaporation and thermo capillarity effects on natural convection within a contained fluid in cryogenic tank, J. Pet. Sci. Eng, volume214 (2022), 110533

[11] W.M.F. Hasan, A.M. Zheng. I.A. Karimi, Minimizing boil-off losses in liquefied natural gas transportation, Ind. Eng. Chem. 48 (2009)9571-9580.

[12] O. Khemis, M. Boumaza, M. Ait Ali, M. X. Francois, Experimental and numerical analysis of heat transfers in a cryogenic tank without lateral insulation, Appl. Therm. Eng 23 (2003) 2017-2017.

[13] O. Khemis, R. Bessih, M. Ait Ali, M.X.Francois, Measurement of heat transfers in cryogenic tank with several configurations, Appl. Therm. Eng24 (2004)2233-2241

{14] Y. Li. C. Wang, R. Wang, Study on effect of liquid level on the heat leak into vertical cryogenic vessels, Cryogenics 50 (2010) 367-372

[15] D. Boukeffa, M. Boumaza, M.X. Francois, S. Pellerin, Experimental and numerical analysis of heat losses in a liquid nitrogen cryostat, Appl. Therm. Eng 21 (2001) 967-975

[16] T. Kanazawa, K. Kudo, A. Kurodo M. Tsui, Experimental study on heat and fluid flow in LNG tank heated from the bottom and the sidewalls, Heat Transfer-Asian Res. 33 (2004). 417-330.

[17] S.Bates, D.S. Morrison, Modeling the behavior of stratified liquid natural gas in the storage tanks: a study of the rollover phenomenon, Int. J. Heat Mass Transfer 40 (1997) 1875-1984.

[18] Q.S. Chen, J. Wegryzyn, V. Orasad, Analysis of temperature and pressure changes in liquefied natural gas (LNG) cryogenic tanks, cryogenics 44 (2004) 701-709.

[19] S. Vasic, K. Hanjalic, Turbulent natural convection in a square cavity– –benchmark computations, in: R.A.W.M. Henkes, C.J. Hoogendoorn (Eds.), Turbulent Natural Convection in Enclosures—A Computational and Experimental Benchmark Study, Editions Europeennes Thermique et Industrie, 1993, pp. 133–144.

[20] Hubert, A., Dembele, S., Denissenko, P. & Wen, J. 2019. Predicting Liquefied Natural Gas (LNG) rollovers using Computational Fluid Dynamics. *Journal of Loss Prevention in the Process Industries,* 62**,** 103922.

[21] Haddar, M., Hammami, M. & Baccar, M. 2019. Numerical parametric study of a cooling system for an LNG storage tank. *Oil & Gas Science and Technology–Revue d'IFP Energies nouvelles,* 74**,** 21.

.

Simulation of the SPR multilayer detector sensitivitybased on a heterogeneous Nano-metallic layer intended for the detection of industrial gases

AbdelaliSAOULI[#1], BouchraALICHE[#2], ChouaibSAOULI[*3]

[#]*Microsystems and Instrumentation Laboratories (LMI)*
Mentouri Brothers University of Constantine. Constantine, Algeria
[1]*abdelali.saouli@lec-umc.org*
[2]*bouchra.aliche@doc.umc.edu.dz*
[*]*Department ofchemistry*
[*]*Mentouri Brothers University of Constantine.Constantine, Algeria*
[3]*saouli.chouaib@umc.edu.dz*

Abstract— **The SPR gas sensor is used to detect industrial gases such as hydrogen, in this work we studied the sensitivity of the SPR detector in the homogeneous and heterogeneous Nano-metallic layer by T-Matrix method, this study carried out that SPR effect is present in these heterogeneous structures with linearsensitivity.**

Keywords—**SPRGas sensor, Sensitivity, T-Matrix**

I. INTRODUCTION

The Surface Plasmon Resonance (SPR) effect has become one of the leading techniques in the field of optical sensors [1]. The effect of the surface plasmon (SPR) present in several domains in force during the last years, optics [2,3], solar energy [4], and gas detection [5-8]. As it provides, with its conveniences in real-time detection and monitoring, non-invasiveness [9] Thehigh sensitivity and label-free applications in many-sided fields, including food security [10,11], biomedical diagnosis [10,12]. Each application signifies by a specific structure, either metallic nanostructures continued or discrete [10,11]. The SPR effect is greater in noble metals whose imaginary part ε2 of the dielectric function (ε = ε1 + i × ε2) i .weak.

Therecycling and sensing hydrogen (H_2) gas has received a great deal of attention not only by material science community but also by renewable energy specialists.

In this work we are simulated the sensitivity of the spectral response of SPR multilayer detectors with heterogeneous Nano-metallic layer by T-matrix method.

II. PHYSIC-MATHEMATICAL APPLIED MODELS

The spectral SPR response of the structure based on multilayers of materials is related by the reflectance profile signal R. Thus, in order to obtain a theoretical model of the SPR profile, a matrix is used for multi-beam interference (Fig. 1). For clarification, the following derivation is based on the work of Klein and Furtak [13]:

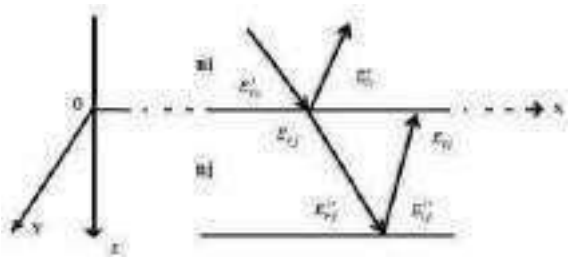

Fig.1. Detailed model of the optical situation analysed. The electric field (E'_{ri}) moves from top to bottom through the mediums characterized by their refractiveindices ni and nj [13].

Therelation between the electric fields is given byequation 1 [13].

$$E'' = \begin{pmatrix} E''_{lj} \\ E''_{rj} \end{pmatrix} = S_{1N} E' = S_{1N} \begin{pmatrix} E'_{li} \\ E'_{ri} \end{pmatrix} \quad (1)$$

Where S_{1N} is the matrix transfer given in equation 2 [14]:

$$S_{1N} = \begin{pmatrix} S_{11} & S_{12} \\ S_{21} & S_{22} \end{pmatrix} \quad (2)$$

The reflectance of the stack is then given by[14]:

$$R = \left| \frac{S_{21}}{S_{11}} \right| \quad (3)$$

This study based on the model of Drude with two critical points (D2CP) whose the metal dielectric function presented bythe equation (45) [15].

$$\varepsilon_{D2CP} = \varepsilon_{\infty} + \frac{\omega_p^2}{-i\omega^2 + i\omega\Gamma_0} + \sum_{i=1}^{2} A_i e^{i\varphi_i} \frac{\Omega_i}{\omega + i\Gamma_i} e^{i\varphi_i} \quad (4)$$

The parameters of the D2CP model for gold obtained in the 400-1000 nm optical range utilised in this study are presented in Table 1, this parameters optimized by A. Vial and T. Laroche [15].

TABLE 1

OPTIMIZED PARAMETERS OF THE D2CP MODEL FOR GOLD AND SILVER OBTAINED IN THE 400-1000 NM OPTICAL RANGE [15].

ε_∞	ω_p (rad.s^{-1})	γ (rad.s^{-1})	A_1
1.0300	1.3064×10^{16}	1.1274×10^{14}	0.86822
Ω_1 (RAD.S^{-1})	**φ_1 (rad)**	**Γ_1 (rad.s^{-1})**	**Γ_2 (rad.s^{-1})**
4.0812×10^{15}	-0.60756	7.3277×10^{14}	6.7371×10^{14}
A_2	**Ω_2 (rad.s^{-1})**	**φ_2 (rad)**	
1.3700	6.4269×10^{15}	-0.087341	

Then, the permittivity of the heterogeneous medium can be described bythe Maxwell–Garnett equation[16,17]:

$$\varepsilon = \varepsilon_{Au} \frac{s^2 + 2\times s_{Au} + 2\times f\times(s^2 - s_{Au})}{s^2 + 2\times s_{Au} - f\times(s^2 - s_{Au})} \quad (5)$$

Where ε is the permittivity of the medium that has been composited with the gold Nano-particle, and f is volume fraction given byequation 6.

$$f = N \times V \quad (3)$$

Where N is the Nano-particle density and V is the Nano-particle volume.

III. RESULTS AND DISCUTION

The SPR response of a biomedical detector structure is based on the detection of change in the SPR wave length as a function of change in the optical properties of the biological medium studied (therefractive index) [18].

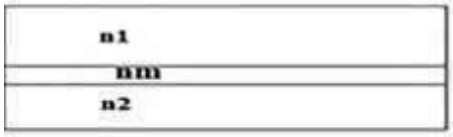

Fig. 2.Three-layer homogeneous structure

In the beginning, we present the recent result of homogenous layer published in [19,20] where the structure (see Fig.2) based on three layers with complex refractive indices n1, n2, nm where nm is the refractive index of the metal. The metals used in this structure is Gold for a fixed angle of incidence Theta = π / 5 (rad) of a plan wave in visible TM mode.

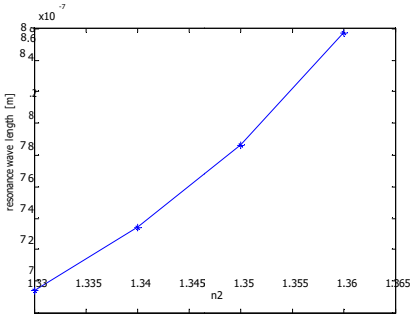

Fig. 3.Resonance wavelength variation for the SPR as a function of n2, n1=2.39, d[Au]=50 [nm]. [19,20]

The sensitivity is shown in figure 2, we notice that the SPR sensitivityis almost linear with S= 5.4333×10^{-6}[m].

In this work we present the same structure dimension with heterogeneous Nano-metallic layer (see Fig.4).

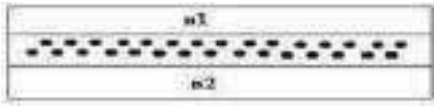

Fig. 4.Heterogeous structure based on three layers

The SPR response based on Gold Nano-metallic is presented in Figures 5. We note that the SPR effect is present in all the reflectance curves with the parametric and geometric conditions presented in the figure (Fig. 5).

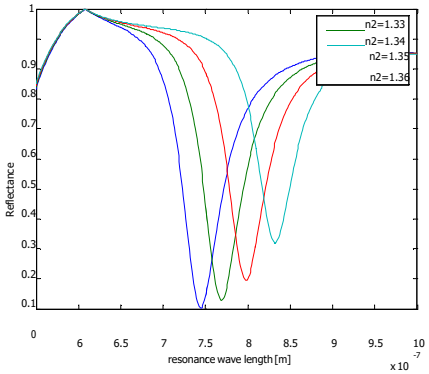

Fig. 5. Variation of the reflectance as a function of the wavelength and different values of n2:n1=2.39, d[Au]=50 [nm], N=800 [µm^3]

The sensitivity of heterogeneous Nano-metallic structure is shown in figures 6, 7 and 8 with nanoparticle density N equal to 400, 600 and 800 [µm^3] respectively. We notice that the SPR sensitivity is almost linear with S equal to 4.7666×10^{-7}[m], 1.1666×10^{-6}[m], and 2.9333×10^{-6}[m] for N equal to 400, 600 and 800 [µm3] respectively.

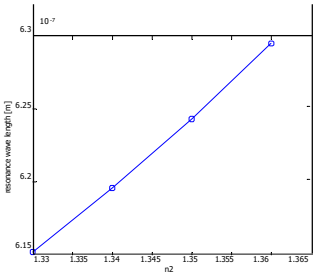

Fig. 6. Resonance wavelength variation for the SPR as a function of n2, n1=2.39, d[Au]=50 [nm], N=400 [µm³]

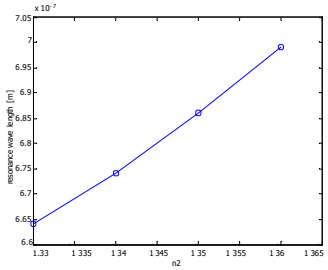

Fig. 7. Resonance wavelength variation for the SPR as a function of n2, n1=2.39, d[Au]=50 [nm], N=600 [µm³]

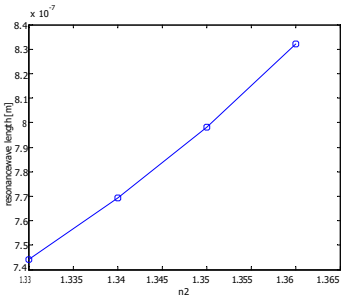

Fig. 8. Resonance wavelength variation for the SPR as a function of n2, n1=2.39, d[Au]=50 [nm], N=800 [µm³]

IV. Conclusions

In this study, we presented the simulation of the response of a heterogeneous Nano-metallic multilayer SPR structure. The work carried out focused on the part of the design of the structure and the response of the latter in the optical band visible in TM mode based on the T-Matrix semi-analytical method and the Matlab software. The results of the simulation that we obtained and the theoretical approach that led to it, show that the SPR effect existed in heterogeneous Nano-metallic multilayer structure and the sensitivity of this later is influenced by the nanoparticle density in Nano-metallic heterogeneous layer used in the structure, and the optical properties and the thicknesses of the layers that make up the structure.

References

[1] Hossain MB, Mehedi IM,"Moznuzzaman M, Abdulrazak LF, Hossain MA. High per-formance refractive index SPR sensor modeling employing graphene tri sheets". Results Phys, vol. 15, p.102719, 2019.

[2] N. G. Khlebtsov, L. A. Dykman, "Optical properties and biomedical applications of plasmonic nanoparticles", Journal of Quantitative Spectroscopy &Radiative Transfer, vol. 111, pp. 1-35, 2010.

[3] A. Elmholdt Christensen, C. Uhrenfeldt, et all, "Interaction between Au nanoparticles and Er3+ ions in a TiO2 matrix: Up-conversion of infrared light", Energy Procedia., vol. 10, pp.111-116, 2011.

[4] Di Qu, Fang Liu, Xujie Pan, et all, "PLASMONIC CORE-SHELL NANOPARTICLE ENHANCED OPTICAL ABSORPTION IN THIN FILM ORGANIC SOLAR CELLS", Photovoltaic Specialists Conference (PVSC), 37th IEEE, pp. 924-928. 2011.

[5] Kreno, L.E., et al, "Metal−Organic Framework Thin Film for Enhanced Localized Surface Plasmon Resonance Gas Sensing", Anal. Chem, vol, 82(19), pp. 8042-8046, 2010.

[6] XIANG, Yuanjiang, ZHU, Jiaqi, WU, "Leiming, et al. Highly sensitive terahertz gas sensor based on surface plasmon resonance with grapheme", IEEE Photonics Journal, vol. 10(1), pp. 1-7, 2017.

[7] BINGHAM, Julia M., ANKER, Jeffrey N., KRENO, Lauren E., et al. "Gas sensing with high-resolution localized surface plasmon resonance spectroscopy", Journal of the American Chemical Society, vol. 132(49), pp. 17358-17359, 2010.

[8] LIEDBERG, Bo, NYLANDER, Claes, et LUNSTRÖM, Ingemar. "Surface plasmon resonance for gas detection and biosensing", Sensors and actuators, vol. 4, pp. 299-304, 1983.

[9] Nico J, Fischer MJ, "Surface plasmon resonance: a general introduction". In: Surface plasmon resonance. Humana Press, pp. 1 -14, 2010.

[10] Y. Liu, J. Kim, "Numerical investigation of finite thickness metal-insulator-metal structure for waveguide-based surface plasmon resonance biosensing", Sensors and Actuators B: Chemical., vol. 148, pp. 23-28, 2010.

[11] Rasooly A, "Surface plasmon resonance analysis of staphylococcal enterotoxin B infood", J Food Prot, vol. 64(1), pp-37-43, 2001.

[12] Chung J, Kim S, Bernhardt R, Pyun JC, "Application of SPR biosensor for medical diagnostics of human hepatitis B virus (hHBV)", Sens Actuators: B, vol. 111, pp. 416-22, 2005.

[13] *Thomas E., Furtak Miles V Klein* , "Optics", wely, 2eme edition, p. 676, 1986.

[14] *J. Singh*, "Optical Properties of Condensed Matter and Applications", Livre, edition Wiley & Sons, 2006, pp. 440.

[15] A. Vial and T. Laroche, "Description of dispersion properties of metals by means of the critical points model and application to the study of resonant structures using the FDTD method", J. Phys. D : Appl. Phys., vol. 40, pp. 7152–7158, 2007.

[16] SARENI, Bruno, KRÄHENBÜHL, Laurent, BEROUAL, Abderrahmane, et al. "Effective dielectric constant of random composite materials". Journal of Applied Physics, 1997, vol. 81, no 5, pp.2375-2383.

[17] SARENI, Bruno, KRÄHENBÜHL, Laurent, BEROUAL, Abderrahmane, et al. "Effective dielectric constant of periodic composite materials". Journal of Applied Physics, vol. 80, no 3, p. 1688-1696,1996.

[18] Richard B. M. Schasfoort, "Handbook of Surface Plasmon Resonance", 2nd Edition, Royal Society of Chemistry, 2017.

[19] SaouliAbdelali, SaouliChouaib, "Simulation of spectral response of SPR multilayers nanostructures detector intended for biomedical application", Materials Today: Proceedings. vol. 31(S1),p. S24, 2020.

[20] SaouliAbdelali, SaouliChouaib, "THE STUDIES OF SPECTRAL SPR MULTILAYERS DETECTOR RESPONSE BASED ON T-MATRIX INTENDED FOR BIOMEDICAL APPLICATION", U.P.B. Sci. Bull., Series C: Electrical Engineering and Computer. Vol.83 (2), pp. 73-79, 2021.

Design of Multiband PIFAs antennas for mobile phone systems

Belhadef Yamina [#1], Bousalah Fayza [#2], Djelti Hamida [#3]

[#]Department of Telecomunications, Abou-Bekr Belkaïd University-Tlemcen
BP 230, Pôle Chetouane, 13000 Tlemcen- Algerie

[1]belhadef@yahoo.fr

[2]bousalah.fayza@gmail.com

[3]djelti_hamida@yahoo.fr

***Abstract*— This paper presents the design of an original Planar Inverted F Antenna (PIFA). The modification of several parameters of the initial structure gives a very good matching of the antenna to the 2.047 and 2.817 GHz resonant frequencies according to the UMTS and WiMax Standards. The insertion of parasitic resonators next to the radiating element of the PIFA antenna leads to multiband antennas. These new antenna configurations are intended for applications in the fields of mobile communications and wireless communications. The design tool is the CST Microwave Studio software which uses the Finite Integration Method (FIT). The simulation results for these types of PIFAs antennas are then presented and discussed.**

***Keywords*— PIFA antenna, Parametric studies, resonator parasites, Multiband antennas, Mobile and wireless communications, CSTMicrowave Studio software, Results.**

I. INTRODUCTION

Currently, the proliferation and diversity of radio-mobile communications standards have created a pressing need for the multi-frequency antennas, allowing in particular ensure compatibility of different standards or to access to multiple services from the same device [1]. Some researchers have proposed compact antennas which make generally call certain geometric structures, and this is how the technology orientates towards new types of antennas which assure functionality for several applications at the same time, called multi-band antennas or broad bands. Among these radiating sources, we cite the PIFAs antennas (Planar Inverted-F Antenna). These antennas are the most used in portable devices for mobile and wireless network applications due to their low manufacturing cost, compactness and the fact that they support working with several frequency bands [2-9]. Some researchers have proposed PIFAs antennas with the insertion of the parasitic resonators techniqueis oriented towards new types of multiband antennas that offer functionality for several applications at the same time.

II. GEOMETRY OF THE PROPOSED ANTENNA

The PIFA antenna is obtained by placing the short circuit (planar, wire or tab type) between the half-wave resonator and the ground plane, at the precise location where the electric field cancels for the fundamental mode.

The proposed PIFA-type original miniature antenna is shown in Figure 1. The metal patch is etched on a Fr-4 dielectric substrate of effective permittivity (ε_r=4) and thickness equal to mm. The radiating element is suspended on a ground planeof size 68 x 46 mm and between these two elements there is the feed wire and a short-circuit plane ofheight 7 mm.

The dimensions of the proposed structure in millimetres are shown in Table 1. The geometry of the PIFA antenna is designed and simulated by CST Microwave Studio (Computer Simulation Technology) software which is based on the finite element method.

.

TABLE I
DIMENSIONS OF THE PROPOSED ANTENNA

Ground plane		Radiating element		Short circuit plane
W	L	W_0	L_0	M
46 mm	68 mm	34 mm	42 mm	25 mm

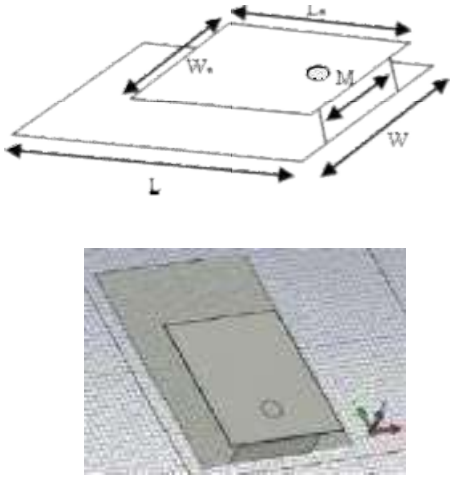

Fig. 1 Geometry of the proposed PIFA antenna and its structure in the CST Microwave Studio editor.

In Figures 2.((a) and (b)), one represents respectively the return loss and input impedance loci of the proposed initial antenna are shown.

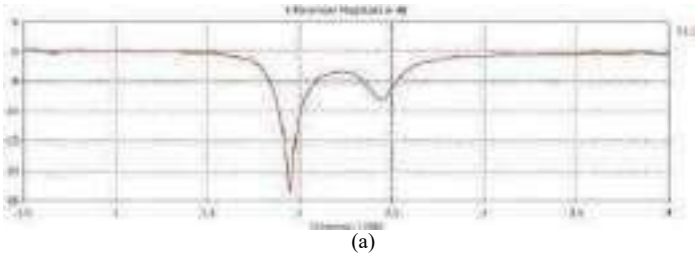

(a)

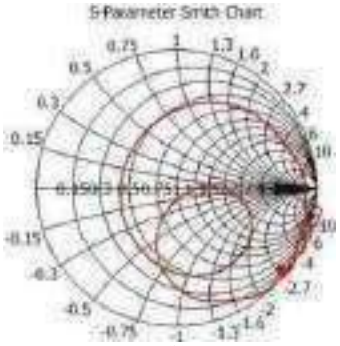

(b)

Fig. 2. (a) Return loss
(b) Input impedance loci

The design of this structure leads to a miniature antenna with a bandwidth of the order of 6.48% which finds its application in the second generation mobile systems and precisely the PCS standard. Figure 2. (a) shows that the antenna is matched to the resonant frequency 1.942 GHz with a return loss level close to -23.54 dB. This is also verified on Smith's abacus. To improve the results found, we varied some antenna parameters to observe the influence of these parameters on antenna adaptation.

III. Parametric Study of the Proposed PIFA Antenna

In the following, we will present some simulations performed by the CST Microwave studio software which show the influence of some parameters on the operating characteristics of the PIFA antenna.

A. Variation of the Width of the Short Circuit Plane M

The first parameter to be varied is the width of the short circuit plane from 10 to 17 mm with a step of 1 mm keeping the dimensions of the other parameters constant in order to be able to deduce its influence on the antenna operation. Figure 3 shows the obtained results.

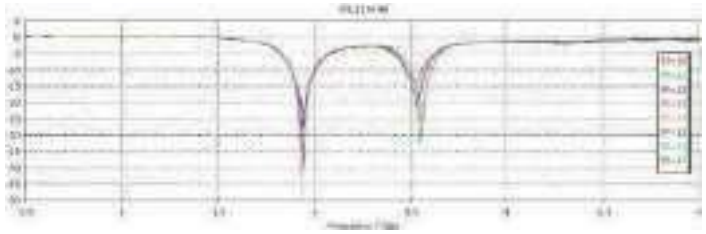

Fig. 3 Influence of the width M of the short-circuit plane on the return loss

From this figure it can be deduced that the more the width of the short-circuit plane M increases, the more the return loss adaptation becomes better and particularly for the first frequency band on the other hand it decreases for the second frequencyband.

B. Variation of the L_0 Length of the Radiating Element

It is also interesting to show the influence of the length of the radiating element. To visualize the effect of the length L_0, we will pose the same initial dimensions where we have fixed the width M to 11 mm. Figure 4 illustrates the improvement of the return loss in adaptation and bandwidth terms

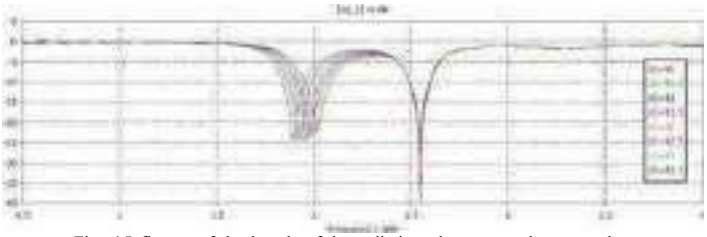

Fig. 4 Influence of the length of the radiating element on the return loss

It can be seen from the figure above that the variation of the length L0 is affected both operation modes, however it has brought a change in the adaptation of -39 dB for a length L0 = 41 mm at -22.9 dB for length L0 = 43.5 mm for second resonant frequency.

C. Variation of the Width W0 of the Radiating Element

We will now focus on the third parameter which is the width of the radiating element W0 (W0 = W1 x 2), such that the elements values M and L0 are placed at 11 and 41 mm respectively. The influence of this parameter is shown in Figure 5.

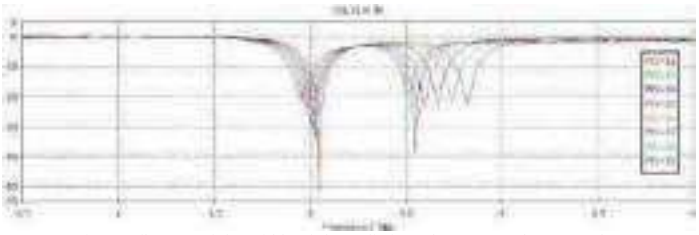

Fig. 5 Influence of the width of the radiating element on the return loss

We well notice that the variation of the width of the radiating element in relation to the resonance frequency affects the improvement of the adaptation level of the designed antenna, such that the most important value of W0 is equal to 24 mm (W0= W1 x 2).

Similarly, the width W (W = w x 2) of the ground plane influence on the operation of the antenna.

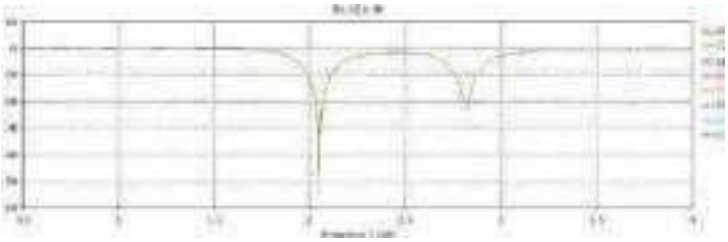

Fig. 6 Influence of the width of the ground plane on the return loss

According to the graphs shown in Figure 6, we notice that the increase in the width of the ground plane generates to a decrease in the adaptation of the proposed antenna.

The dimensions of the optimized final PIFA antenna are shown in Table 2.

TABLE III
DIMENSIONS OF THE OPTIMIZED ANTENNA

Ground plane		**Radiating element**		**Short circuit plane**
W	L	W_0	L_0	M
40 mm	68 mm	24 mm	41 mm	11 mm

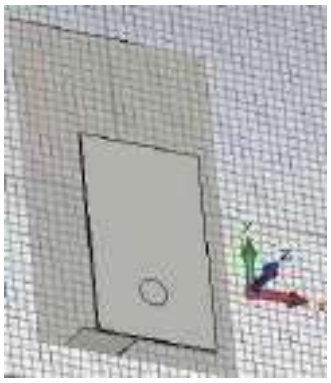

Fig. 7 Geometry of the optimized PIFA Antenna

In figures 8.((a) and (b)), we represent respectively the return loss, the input impedance loci and the 2D polar radiation patterns of the PIFA antenna.

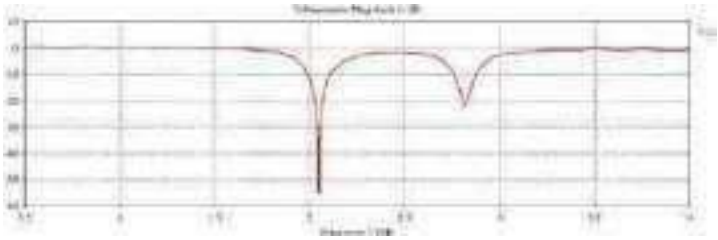

(a)

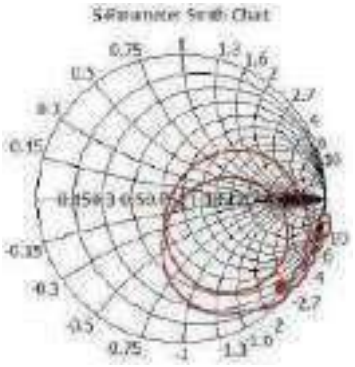

(b)

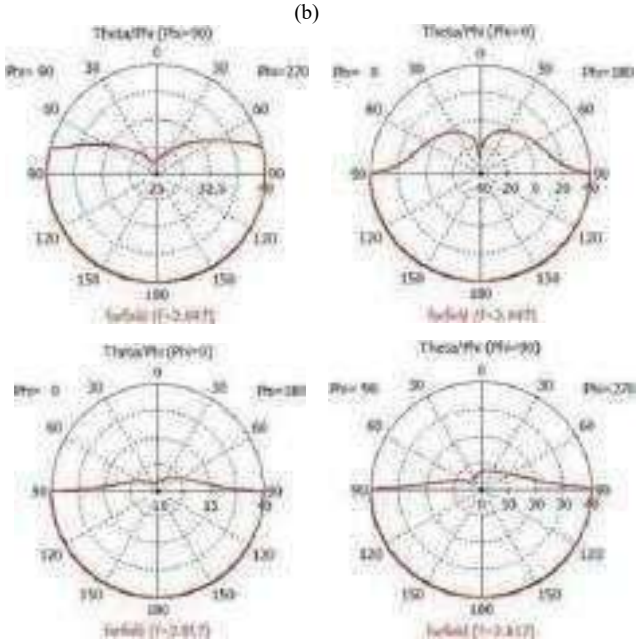

Fig. 8. (a) Return loss
(b) Input impedance loci
(c) Radiation patterns in 2D

The design of the optimized PIFA structure by CST Microwave Studio gives a dual band antenna operating at two 2.047 and 2.817 GHz resonance frequencies. The first reflection coefficient for the first frequency has a peak of less than -55.22 dB and the second for the 2.817 GHz frequency goes down to a value of -22.63 dB. These results reflect a very good adaptation of the antenna. The bandwidth for the two resonant frequencies is around 6.15% and 4.22% respectively.

On Smith's abacus, the positions of the input impedance loci at the two desired frequencies are located almost in the centre of the abacus.

The polar coordinate radiation diagrams in the two planes E (φ=0°) and H(φ=90°) at the two resonance frequencies represented in Figure 8.(c) show that the radiation is almost omnidirectional.

IV. Techniques Used for Multiband Operation

Several techniques are used tohave a multiband operation, we applytwo main techniques ones namely:

- The use of a juxtaposed parasitic resonator excited by electromagnetic coupling.
- Adding a plane-type short-circuit inserted at the end of the radiating element toreduce antenna footprint.

The new PIFA antenna geometries designed by adding the two previous techniques are shown in Figure 9.

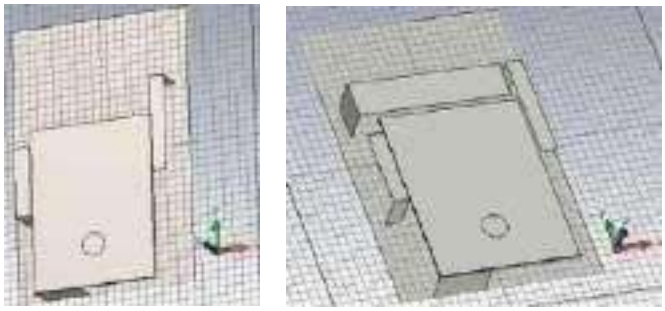

(a) : Quad-band antenna (b) : multiband antenna

Fig.9 New PIFAs antennas and its structures in the CST Microwave Studio editor

TABLE IIIII
Dimensions Of the Quadband and Multiband Antennas

	Parameters (mm)	Quad band antenna	Muliband antenna
Patch	W_0	30.2	30.2
	L_0	40	40
Ground plane	W	44	44
	L	68	68
Left parasitic resonator	W_1	3.5	3.5
	L_1	17	17
	H_1	8	8
Right parasitic resonator	W_2	3.5	3.5
	L_2	23	23
	H_2	8	8
resonator on the middle	W_3	-	8
	L_3	-	33
	H_3	-	8

Figure 10. ((a) and (b)), one represents respectively the return loss and the input impedance loci for the two proposed antennas.

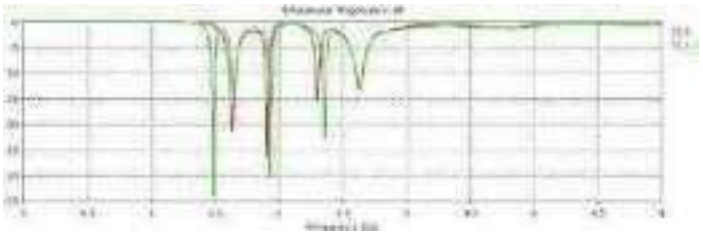

(a)

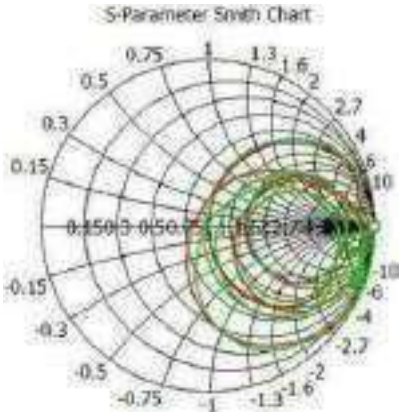

(b)

Fig. 11. (a) Retun loss
(b) Input impedance loci

Table 4 summarizes the results of the two new antennas created by CST Microwave Studio.

TABLE IVV
Electrical Characteristics of the Two Antennas with Parasitic Resonators

	Frequency [GHz]	Returnloss [dB]	Bandwidth (%)
Quadband	1.635	-21.330	3.06
	1.910	-26.514	1.31
	2.305	-15.230	1.10
	2.630	-13.200	1.90
Multiband	1.485	-33.940	1.683
	1.645	-14.150	1.520
	1.930	-30.380	1 .040
	2.355	-22.756	1.061
	2.635	-11.987	2.087

The addition of two L-shaped parasitic resonators close to the main patch in the two sides to the right and left of the structure designed according to Fig. 9 .(a) introduces a quad-band antenna. The latter is well suited to four resonance frequencies cited in Table 4.

The geometry of the multiband antenna is based on the structure of the quad-band antenna in which we have added a third inverted L-shaped parasitic resonator which is characterized by the parameters W_3, L_3 and H_3 which are

indicated by Table 3. The adaptation of the multiband antenna is then perfect and the antenna can be integrated into mobile and wireless systems. For Smith's abacus, the input impedance for both quad-band and multiband antennas is almost at the center of the abacus for each frequency, showing that the reflection is zero.

V. CONCLUSION

First, we studied a PIFA antenna where we modified several parameters of the proposed antenna in order to arrive at a dual-band structure which presents a perfect adaptation to the desired frequency according to the UMTS and WiMax standards. Next, we designed multiband antenna structures by inserting the parasitic resonators next to the radiating element of the optimized antenna. It is a technique used to have multi-band operation. The proposed structures result in multiband antennas operating on distinct frequency bands according to the following different standards : satellite L-band, PCS, WiFi and LTE. The results found show a good adaptation to resonance frequencies.

REFERENCES

[1] R. A. Bhatti, Young Sin Shin, Ngoc-Anh Nguyen and Seong-Ook Park, "Design of a Novel Multiband Planar Inverted-F Antenna for Mobile Terminals," Antenna Technology: Small Antennas and Novel Metamaterials, 2008. iWAT 2008. International Workshop on, 2008, pp.530- 533.

[2] K. L. Virga and Y. Rahmat-Samii, "Low-Profile Enhanced-Bandwidth PIFA Antennas for Wireless Communications Packaging," *IEEE Trans. Microwave Theory Techn.*, vol. 45, no. 10, Oct. 1997, pp. 1879–1888.

[3] Wong, H., C. H. Chan, K. Luk, Q. Xue, K. K. So, and H. W. Lai, "Small Antennas in Wireless Communications," Proceedings of the IEEE, Vol. 100, 2012, pp. 2109–2121.

[4] Bhatti, R. A., Y. Im, and S. Park, "Compact PIFA for Mobile Terminals Supporting Cellular and Non-Cellular Standards," IEEE Transactions on Antennas and Propagation, Vol. 57, 2009, pp. 2534–2540.

[5] R. Gomez-Villanueva, R. Linares-y-Miranda, José A. Tirado-Méndez, and H. Jardon-Aguilar, "Ultra-Wideband Planar Inverted-F Antenna (PIFA) for Mobile Phone Frequencies and Ultra-Wideband Applications," Progress In Electromagnetics Research C, Vol. 43, 2013, pp.109–120.

[6] L.Wakrim, S.Ibnyaich, and M.M.Hassani, "Novel Miniaturized Multiband and Wideband PIFA Antenna for Wireless Applications," 3rd International Conference on automation, Control, Engineering and Computer Science (ACECS'16), Proceedings of Engineering & Technology (PET), 2016.

[7] Xingyu Zhang and Anping Zhao, "Enhanced-Bandwidth PIFA Antenna With a Slot on Ground Plane," PIERS Proceedings, Beijing, China, March 23-27, 2009.

[8] K. Kundu, A. Dubey, A. Dhama and N. Nath Pathak, "Planar Inverted F Antenna, PIFA Array in 5G applications," Journal of Physics: Conference Series, ICCIEA 2021, doi:10.1088/1742-6596/2062/1/012002.

[9] A.T. Nahla, A. A Fadhel and M. A. Faris, "PIFA Antenna Design for 5G Wireless Application," Journal of Xi'an Shiyou University, vol 15, no: 1673-064X., Issue 3, 2019.

Détection de Défaut d'un Système Thermique par RSOM

Nejib Khalfaoui[#1], Mohamed Salah Salhi[#2], Radwen Bahri[*3]
[#]*LR SITI - ENIT*
[1]nejibkhalfoui@gmail.com
[2]msalah.salhi@gmail.com
[*]*MACS- ENIG*
[3]bahriradwen16@gmail.com

Résumé **-**Cet article traite d'une stratégie intelligente utilisant la carte auto-organisatrice récurrente RSOM pour la détection de défaut d'un système thermique. L'idée proposée implique le fonctionnement le plus important de RSOM pour localiser et apprécier l'origine de défaut, telles que la structure topologique de la carte, l'algorithme d'apprentissage en profondeur non supervisé.
La mesure et le traitement du signal issu d'un capteur approprié fixé sur le banc d'expérimentation, s'est fait à un instant précis au Laboratoire d'Automatisme et d'Informatique Industrielle. Une analyse comparative des performances de détection des défauts a été réalisée à l'aide de la carte neuronale RSO et de la méthode d'analyse spectrale.

Mots clés –Système thermique, Carte RSOM du réseau de neurones, Détection intelligente des anomalies, Analyse spectrale.

I. INTRODUCTION

La détection des défauts des processus industriels repose sur le traitement des signaux mesurés pour identifier leurs indicateurs au sein du système. Cependant, la fiabilité de la procédure de diagnostic nécessite des informations suffisantes sur le fonctionnement du système à surveiller. Cette approche implique l'application de capteurs pour mesurer les différentes variables du processus.
Selon les résultats de recherche de source IEEE, il apparaît que l'engagement des techniques intelligentes, pour le diagnostic de défaut, comme le réseau de neurones es rendu efficace pour la surveillance en ligne des systèmes industriels [1] [2] [3].
De même, de nombreuses recherches publiées [4], [5], [6], [7], [8], [9] [10], [11], [12], [13], [14], Introduit des systèmes neuronaux dédiés à la détection de défauts, tels que la carte SOM de Kohonen, qui se présente comme un outil puissant pour les tâches de diagnostic dans divers domaines. Cet outil intelligent est remplacé par le Contextuel-SOM 'CSOM' et le Recurrent-SOM 'RSOM établi par Thomas Voegtlin en 2002 et 2005, pour l'intégration de l'aspect temporel et l'adéquation du classifieur avec la reconnaissance des signaux dynamiques.
Par la suite, le but même de notre article est de développer davantage cette technique pour détecter le défaut du système thermique en surveillant ses performances à l'aide de la carte RSOM.
Par ailleurs, dans ce papier on présente les outils de détection des défauts, le modèle de la carte RSOM, l'algorithme d'apprentissage ainsi les résultats expérimentaux et la détection par la carte RSOM.

II. Outils de détection des anomalies

La détection des défauts des processus industriels se base sur l'analyse des grandeurs mesurées afin d'identifier l'indicateur en vue de signaler la présence d'un défaut au sein du système. Ces grandeurs peuvent être :

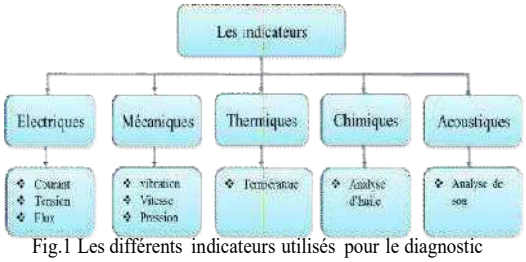

Fig.1 Les différents indicateurs utilisés pour le diagnostic

La grandeur surveillée subit, au cours de fonctionnement du système deux types de variation [8] [14]:

*Des fluctuations autour de sa valeur nominale qui sont dues aux diverses perturbations agissant sur le système considéré.

*Une dérive qui peut être due à un phénomène de dégradation progressive.

Le suivi de cette grandeur permet alors de vérifier qu'elle ne s'écarte pas, de façon significative de sa valeur nominale. Un système de maintenance doit donc être en mesure de réaliser les trois étapes essentielles suivantes :

*La détection d'un défaut à partir de l'analyse des grandeurs mesurées.

*Le diagnostic du défaut.

*La prise de décision pour un retour au fonctionnement normal.

Donc le diagnostic a pour objectifs, rechercher l'origine d'un défaut constaté .Un défaut correspond à une déviation jugée anormale d'une grandeur caractéristique du système.
Les indicateurs utilisés dans notre système sont :

- h : sain
- fs est la fréquence du réseau électrique
- fc est la fréquence de bruit

III. Algorithme d'apprentissage de la carte RSOM

Lorsque les intégrateurs à fuite des sorties d'unités sont placés aux entrées, on obtient un TKM modifié appelé 'Récurrent Self Organizing Map', RSOM, cette variante est

proposée par Varsta et al. en 1997. Le fait de déplacer les intégrateurs à fuite des sorties vers les entrées de chaque unité de la carte apporte un vecteur temporel de différence de fuite donné par la relation suivante [1] [3] [6]:

$$y_i(t)=(1 \; y_i(t \; 0)+ .(x(t) \; w(t)) \quad (1)$$

Dans l'équation α constante comprise entre 0 et 1 désigne le coefficient de fuite qui remplace d dans la TKM. Une unité de RSOM est donc schématisée comme suit :

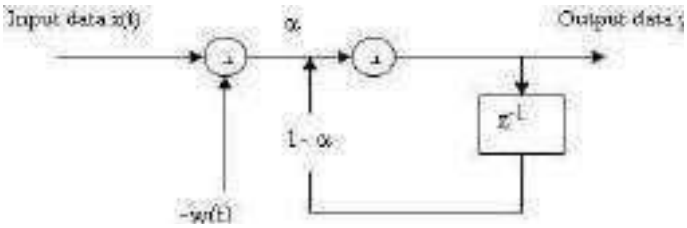

Fig.2 Représentation d'une unité de RSOM qui agit en tant que filtre récurrent

Le neurone ayant réussi la concurrence détermine le centre dune zone de la carte appelée voisinage, zone dont l'étendue varie au cours du temps. Cependant, la phase de mise à jour ou adhésion, change l'emplacement des prototypes de façon à les assembler de l'individu présenté au réseau. Les prototypes sont d'autant plus prés de l'individu en question qu'ils sont voisins sur la carte du neurone gagnant. La pondération permettant de trouver l'impact des transformations de position. L'algorithme de Kohonen est donné par les étapes suivantes [2] [3]:

1. Initialisation des prototypes
2. Sélection d'un individu
3. Détermination du neurone vainqueur pour cet individu ; c'est la phase de compétition.
4. Modification de la totalité des prototypes de la carte : phase d'adaptation et de mise à jour.
5. Reprise à l'étape 2 si la condition d'arrêt est non satisfaits.

IV. Résultats expérimentaux

A- Mesure des signaux

La mesure du signal au niveau du capteur du banc expérimental fournit par la figure 3 et la figure 4 avec des conditions nominales de fonctionnement.

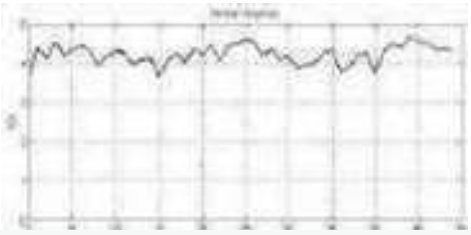

Fig.3 Signal du capteur en l'absence de défaut

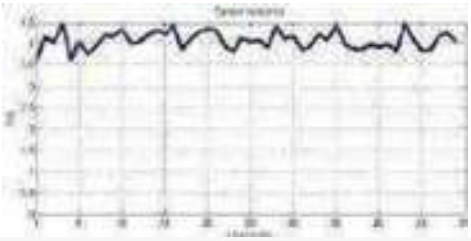

Fig.4 Mesure du signal du capteur en présence de défaut dans le domaine temporel

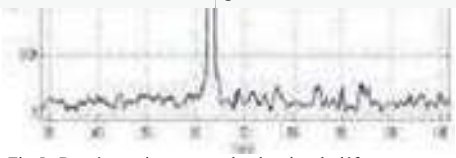

Fig.5 Représentation spectrale du signal défectueux

B- Interprétation

Une analyse spectrale du signal mesuré présentant un défaut est établie par la figure 5 Il montre un pic de défaut encadré par les fréquences : f1=60 hz et f2 =70 hz so fc≈63hz

Cette analyse est généralement subjective et manque de précision par rapport au modèle adopté par RSOM qui prend en considération l'état président.

V. Résultat d'apprentissage

Après acquisition des données des capteurs et traitement en matrice de MFCC du signal issu du capteur, nous avons suivi cette opération par une concaténation en une ligne vectorielle. Ce vecteur mesuré expérimental sera introduit dans la carte RSOM. Ensuite, nous avons appliqué un entraînement non supervisé sur le modèle de reconnaissance RSOM. Le résultat est donné par la topologie suivante (Figure 6) :

Fig.6 Détection du défaut par RSOM résultat

VI. BANC EXPÉRIMENTAL

Le banc expérimental est composé de :
Un capteur de temperaturePT100
Une résistance chauffante contrôlée par hacheur
PLC Programmable logic controller S7-1215c DC-DC-DC:

- 14 digital inputs / 10 digital outputs
- 2 analog inputs ADC 12 bits
- 2 analogoutputs DAC 12 bits

Carte arduino MEGA

- 54 inputs/ digital outputs
- 16 analog inputsADC
- Oscillator*16 Mhz*
- Power supplyUSB 5 V / DC *7 V - 12 V*

Fig.7 Photo du banc expérimental

VII. CONCLUSION

Le capteur nous envoie un signal, qui sera traité par le processeur de l'automate programmable CPL, avant d'être introduit dans la carte RSOM après quelques itérations la topographie dénote l'existence d'un indicateur de défaut représenté par la fréquence fc (liée à la fréquence de bruit).

Les résultats expérimentaux indiquent que la carte RSOM est plus précise qu'une analyse spectrale car la topologie est facile à lire avec un apprentissage de 99%. Il nous offre une évaluation objective basée sur des modèles mathématiques intégrés dans l'algorithme RSOM. Alors que l'analyse spectrale projette des lignes à des fréquences caractéristiques, elle nécessite une évaluation subjective par l'œil. Cependant, l'efficacité de la détection des défauts est fortement liée à la qualité d'apprentissage du système neuronal.

REFERENCES

[1] V. Baier: “Motion perception with recurrent self-organizing maps based models‖, In Proceedings of the IEEE International Joint Conference on Neural Networks (IJCNN‘05), pages 1182–1186, 2005

[2] N. Khalfaoui, M. S Salhi, H Amiri ‘‘ The SOM Tool in Mechanical Fault Detection over an Electric Asynchronous Drive‘‘ IEEE 4th CIET-2016

[3] Heni Ben Amor and Achim Rettinger: “Intelligent Exploration for Genetic Algorithms Using Self-organizing Maps in Evolutionary Computation”, February 4, 2005

[4] M. Amar,l. Gondal, andC. Wilson,"Vibration Spectrum Imaging: A Bearing Fault Classification Approach," IEEE Trans. ind. Electron., vol. no.99, pp. I,ldoi: 10.1109/TIE.2014.2327555. 2014

[5] Khalfaoui, N., & Bahi, T.” Map-Reduce based approach for Anomalies Isolation and Classification of Asynchronous Training by the SOM”. Proceedings of the 4th International Conference on Recent Advances in Electrical Systems (2019).

[6] Neubauer, N.: “Recursive SOMs and Automata”. M.Sc. Thesis, Cognitive Science, University of Osnabruck, 2005

[7] Khalfaoui, N., Salhi, M. S., & Amiri, H. “Aparallel approach for the diagnosis of electrical asynchronous training anomalies”. International Journal of Applied Engineering Research (IJAER), 12(9), 1836-1843. (2017).

[8] J.F. Bangura, N.A. Demerdash, " Effects of Broken Bars/end-Ring Connector and Airgap Eccentricities on Ohmic and Core Losses of Induction Motors in ASD'S Using a Coupled Finite Element-State Space Method", IEEE Transactions on Energy Conversion, Vol. 15, No. 1, March 2000.

[9] Andrzej, M. Trzynadlowsk, and Ritchie, " Comparative Investigation of Diagnostic Media for Induction Motors: A Case of Rotor cage Faults", IEEE Transaction on Industrial Electronics, Vol, 47, No. 5, October 2000.

[10] J. Faiz, I. Ardekanei, H.A. Toliyat, "An Evaluation of Inductances of a Squirrel-Cge Induction Motor Undre Mixed Eccentric Conditions", IEE Transaction on Energy Conversion, Vol. 18, No. 2, June 03.

[11] Mohamed Salah Salhi, Najet Arous, and Noureddine Ellouze Principal temporal extensions of SOM: Overview’’ International Journal of Signal Processing, Image Processing and Pattern Recognition Vol. 2, No. 4, December, 2009.

[12] Kohonen, T.: “The self-organizing map”, Proceedings of the IEEE, 78 (9), 1464-1480, 1990

[13] M.Cottrell, S. Ibbou & P. Letrémy: “SOM-based algorithms for qualitative variables”, Neural Networks, vol, 17, p.1149-1167, 2004.

[14] F. Immovilli, C. Bianchini, M. Cocconcelli, A. Bellini, R. Rubini, "Bearing Fault Model for Induction Motor With Externally Induced Vibration," IEEE Trans. ind. Electron., vo1.60, no. S, pp. 340S-341S, Aug. 2013.

Etude des échanges thermiques dans un échangeur de chaleur à tubes concentriques par simulation

A. Trabelsi [#1], R. Elgaroui[#2], A. KHELIFA[*3], B. ZITANI [#4]

[#1] Laboratoire LENREZA, faculté des sciences et de la technologie et des sciences de la matière, université de Ouargla, route de Ghardaia, 30 000 Ouargla, Algérie

[#1,2,4] *Département de génie des procédés,*
Faculté des sciences et technologies, Université de Ghardaïa
Box 455, Zone Scientifique ‘, Bounoura 47000 Ghardaïa, Algérie
[*3] *Unité de recherche appliquée en énergies renouvelables, URAER,*
Centre de développement desénergies renouvelables, CDER, 47133, Ghardaïa, Algérie
[1] *prof.am4741@gmail.com*
[2] *elgaroui@gmail.com*
[3] *khelifa_karim@hotmail.fr*
[4] *Zitani_Brahim@yahoo.fr*

***Résumé*— L'étude concerne un travail expérimental et numérique sur les échanges thermiques, existant au niveau d'un échangeur à tubes concentriques. Les mesures expérimentales ont été effectuées à l'aide d'un banc d'essai, situé au niveau du laboratoire de génie des procédés 2 à l'université de Ghardaïa. Deux modes de circulation des fluides dans l'échangeur ont été considérés, à savoir : co-courant et contre-courant pour différentes conditions aux limites.**

En revanche, le modèle mathématique de l'écoulement en 3D dans l'échangeur a été résolu numériquement en utilisant un logiciel CFD commercial ANSYS 2019 R1.

Les résultats numériques et expérimentaux obtenus ont été proches. Ce travail a permis de mieux connaître le principe de fonctionnement et le phénomène de l'échange thermique dans les échangeurs. Il a été démontré que le mode contre-courant était le meilleur en terme d'efficacité.

***Mots clés*— Échangeur de chaleur à tubes concentriques ; Simulation numérique ; Écoulement co-courant et contre-courant ; Convection ; Efficacité.**

I. INTRODUCTION

La technique d'échange thermique en utilisant les échangeurs de chaleur comme équipement est extrêmement utilisée dans diverses applications industrielles. Du fait que le principe de fonctionnement d'un échangeur de chaleur est simple et connu, le calcul, le dimensionnement et l'optimisation de ce dernier restent un domaine de recherche actif, et le phénomène physique via les échangeurs de chaleur n'est pas totalement élucidé à ce jour.

Dans l'industrie, les échangeurs thermiques ont acquis une importance économique très grande. Une grande part 90% de l'énergie thermique utilisée dans les procédés industriels transite au moins une fois par un échangeur de chaleur, aussi bien dans les procédés eux-mêmes que dans les systèmes de récupérations de l'énergie thermique de ces procédés [1-2].

Dans de nombreux processus d'ingénierie, les échangeurs de chaleur sont des dispositifs thermiques importants, tels que les centrales électriques et chimiques, les raffineries de pétrole, les turbines à gaz, les chaudières et les turbosoufflantes, etc [3-7].

Ces équipements sont couramment utilisés dans un large éventail d'applications : ils sont présents dans des secteurs extrêmement divers malgré la même fonction de base, qui est de transférer de l'énergie thermique entre deux ou plusieurs fluides à des températures différentes. Ils sont présents aussi bien dans le secteur industriel (chimie, pétrochimie, agroalimentaire, etc.), le secteur résidentiel (chauffage et climatisation), ainsi que le secteur de transport (automobile, marine… etc) [2].

La diversité des domaines d'applications des échangeurs thermiques entraine un foisonnement de formes géométriques (tubulaires, plaques, à ailettes…etc). Les échangeurs de chaleur utilisant les tubes comme constituant principal de la paroi d'échange sont les plus répondus, l'échangeur thermique à double tube concentrique est la forme la plus simple dans cette famille [2].

Mohamed Amine Abdelghani Mokrane et al ont étudiés numériquement le comportement thermique des deux fluides en circulation dans un échangeur de chaleur à tubes concentriques, l'étude de simulation numérique à été réalisée par un code de calcul puissant (fluent) basé sur des

ISSN: 1737-9334

interprétations visuelles qui ont permis de mieux comprendre le phénomène de transfert de chaleur pour différentes configuration d'écoulement [8].

LASKOWSKI a considéré l'échangeur de chaleur comme une « boite noire », son objectif a été d'étudier la façon dont les paramètres d'entrée de l'échangeur de chaleur (températures et débits des deux fluides) affectent celles de sortie de l'échangeur de chaleur (températures et débits des deux fluides) et ainsi essayer d'introduire un nouveau rapport de l'efficacité de transfert de chaleur de l'échangeur à double tube concentrique à contre-courant en fonction des paramètres d'entrée seulement. L'efficacité de transfert de chaleur a été obtenue sous forme d'une fonction de deux paramètres : le rapport des capacités calorifiques des deux fluides et le NUT [9].

N. Boultif a étudié numériquement l'échangeur de chaleur à triple tube concentrique en régime transitoire et permanent et pour différents arrangements de fluides. Un programme de calcul numérique en langage FORTRAN a été réalisé pour déterminer les variations : des températures (fluides et parois), des deux coefficients d'échange globaux, des pertes de charge des trois fluides en fonction du temps, ainsi que les réponses transitoires aux différentes sollicitations sur les températures d'entrées des fluides, Les résultats ont montré que l'échangeur à double enveloppe sous des conditions des diamètres est plus efficace que l'échangeur de chaleur à triple tube concentrique de même longueur [2].

Notre travail est basé sur deux approches, une étude expérimentale en utilisant un banc d'essai d'un échangeur de chaleur coaxial, disponible au niveau du laboratoire de l'université de Ghardaïa pour les travaux pratiques et une étude numérique par le logiciel ANSYS 2019 R1. Le comportement dynamique et thermique des fluides en circulation est présenté dans cette étude afin de comparer les résultats expérimentaux avec ceux numériques.

II. PARTIE EXPERIMENTALE ET METHODOLOGIE

Pour l'étude expérimentale, un banc d'essai d'un échangeur à tubes concentriques a été utilisé. Pour réaliser ce but, nous avons effectué plusieurs essais pour les deux arrangements d'écoulement, co-courant et contre-courant.

A. Fiche technique du dispositif

Le banc d'essai de l'échangeur, telle que présenté sur la figure 1 comporte :

- Structure en acier inoxydable AISI 304, montée sur roues ;
- Échangeur à tubes concentriques, en acier inoxydable AISI 304, surface d'échange de 0.3 □², symbole E1 ;
- Débitmètre à section variable pour l'eau chaude, en verre et en acier inoxydable; plage de 100 à 1000 l/h, symbole FI1 ;
- Débitmètre à section variable pour l'eau froide, en verre et en acier inoxydable ; plage de 100 à 1000 l/h, symbole FI2 ;
- Quatre (4) capteurs de température à résistance avec afficheurs numériques :

- TI1 : température d'entrée eau chaude ;
- TI2 : température de sortie eau chaude ;
- TI3 : température d'entrée eau froide ;
- TI4 : température de sortie eau froide ;

- Tableau électrique (IP 55) avec synoptique de l'installation et disjoncteur à courant de défaut (E.L.C.B) ;
- Bouton d'urgence.

Fig.1 : Dispositif expérimental de l'échangeur thermique eau/eau de type concentrique

III. PARTIE SIMULATION

Cette partie consiste à l'étude numérique à l'aide du logiciel ANSYS 2019 R1, basé sur la méthode des volumes finis.

A. Modélisation numérique

Le modèle physique considéré dans cette étude numérique est similaire à celui utilisé dans la partie expérimentale, illustrée dans la figure 1.

La géométrie a été créée par le logiciel ANSYS Workbench, en se basant sur les dimensions réelles du banc d'essai.

L'échangeur coaxial étudié contient deux tubes concentriques, un tube interne où circule l'eau chaude et un autre tube externe, où circule l'eau froide. La longueur de l'échangeur est de 6,1 m.

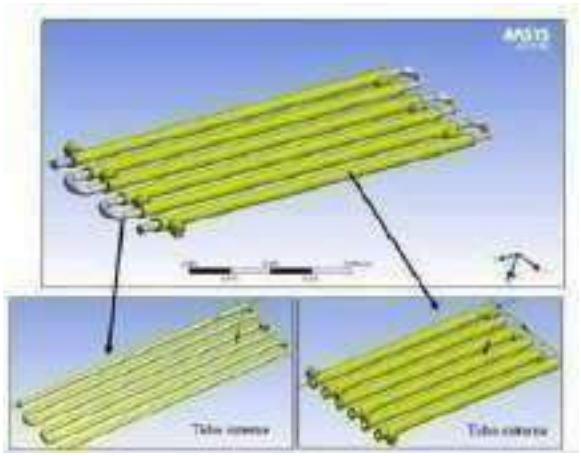

Fig.2 : Modèle de l'échangeur de chaleur simulé en 3D par ANSYS 2019 R1

B. *Résolution numérique*

Le système d'équations, régissant l'écoulement des fluides a été résolu en utilisant la méthode des volumes finis ; le couplage vitesse-pression est réalisé à l'aide du schéma « coupled ». Nous avons optimisé le maillage afin de choisir celui qui convient à notre étude.

Fig.3 : Présentation du maillage choisi sur ANSYS Workbench

C. *Conditionsaux limites utilisées*

Dans cette étude, on a choisi six (06) cas, mesurés au cours de la partie expérimentale, selon le tableau (1). Ces cas représentent les conditions aux limites, obtenues au cours des essais expérimentaux, pour les deux modes de circulation des fluides.

TABLEAU 1
CAS CHOISIS POUR LA SIMULATION NUMÉRIQUE POUR LES CIRCULATIONS À CONTRE-COURANT ET À CO-COURANT

N° des cas	FI1 chaud (l/h)	FI2 froid (l/h)	TI1 (C)	TI3 (C)
Contre-courant				
01	750	350	76,1	31,4
02	600	350	70,9	31,4
03	500	350	71,1	31,4
Co-courant				
04	750	350	73,2	31,4
05	600	350	75,3	31,4
06	500	350	76,7	31,4

D. *Optimisation du maillage*

L'objectif de l'étude de l'optimisation du maillage est donc d'obtenir un maillage convenable, qui contient le minimum des nombres des nœuds, où les résultats de calcul ne changent pas avec le raffinement du maillage.

Pour cela, six maillages ont été générés et testés toute en faisant varier le nombre des nœuds. Ensuite, on a comparé les résultats de la température de sortie de l'eau chaude pour un cas à contre-courant. Le raffinement a été fait près des parois afin de tenir compte de l'effet de la couche limite turbulente. Pour tous les cas, un maillage triangulaire non-structuré (par défaut) loin des parois et un maillage structuré (par *Inflation*) proche des parois ont été conçus.

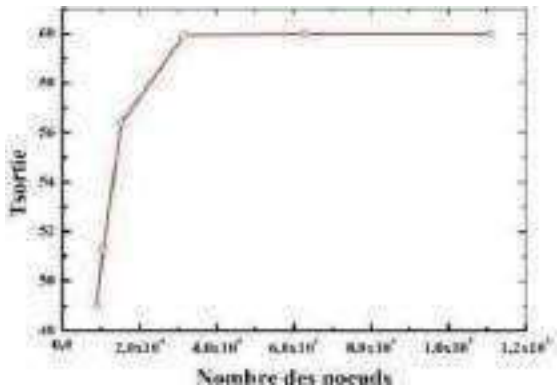

Fig.4 : Etude de l'indépendance de maillage sur la température de sortie

A partir des résultats obtenus, on a constaté que la température de sortie augmente avec l'augmentation des nombres des nœuds de maillage jusqu'à ce que se stabilise pour un maillage de 31459 nœuds (cas n°4).

Par conséquent, le maillage numéro quatre (n°4), qui contient 31459 nœuds a été opté pour toutes les simulations effectuées dans cette étude.

E. *Validation numérique*

Pour valider les résultats numériques obtenus, nous avons comparé la température de sortie de l'eau froide et de l'eau chaude pour chaque cas étudié par rapport aux mesures expérimentales effectuées au laboratoire. Les résultats de la comparaison sont présentés sur le tableau (2) et sur les figures (5) et (6).

ISSN: 1737-9334

N° des cas	TI2 Num	TI2 Exp	Err (%)	TI4 Num	TI4 Exp	Err (%)
01	59.94	62.10	03.48 %	58.82	60.90	03.41 %
02	54.95	56.60	02.91 %	54.01	55.60	02.87 %
03	53.33	54.40	01.97 %	53.19	54.20	01.86 %
04	59.29	61.10	02.97 %	53.45	55.10	02.91 %
05	59.55	60.80	02.06 %	53.81	54.90	01.99 %
06	58.87	59.60	01.23 %	53.27	53.90	01.17 %

A partir de l'analyse de ces résultats, on peut remarquer que les résultats numériques trouvés présentent une bonne concordance avec les résultats expérimentaux. L'erreur relative ne dépasse pas 4 % pour tous les cas étudiés.

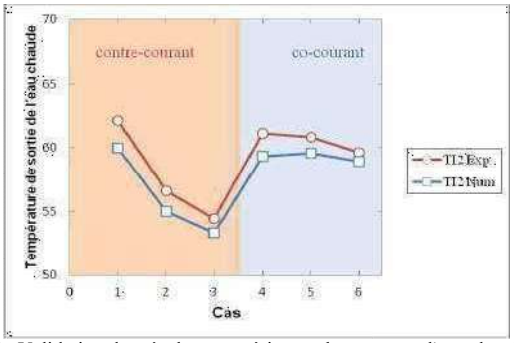

Fig.5 : Validation des résultats numériques obtenus pour l'eau chaude

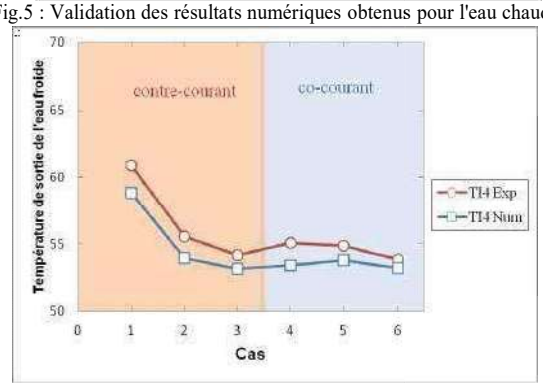

Fig 6 : Validation des résultats numériques obtenus pour l'eau froide

On a constaté que l'erreur augmente avec l'augmentation du débit de l'eau chaude. Aussi, l'erreur pour les cas de la configuration co-courant est faible par rapport au cas contre-courant. En général, les résultats sont en bon accord avec les mesures expérimentales, cela confirme la fiabilité de la simulation.

IV. RESULTATS ET DISCUSSION

A. *Effet des modes de circulation des fluides sur la différence moyenne de température logarithmique*

La variation de la température de sortie pour l'eau chaude (figure 5) et pour l'eau froide (figure 6) en fonction du débit volumique du fluide chaud montre que pour le cas du mode co-courant la variation est presque stable (on remarque une légère augmentation), par contre, dans le mode contre-courant, la température de sortie augmente rapidement avec l'augmentation du débit.

Pour bien illustrer cette remarque, nous avons tracé sur la figure (7) la variation de la température moyenne logarithmique (DTLM), qui exprime la moyenne logarithmique de la fonction ΔT entre l'entrée et la sortie de l'échangeur en fonction du débit volumique de l'eau chaude. Le débit de l'eau froide a été fixé à 350 l/h. A partir de cette figure (7), il est bien clair que la différence logarithmique moyenne de la température augmente avec l'augmentation du débit pour le mode contre-courant. Par contre, dans le mode co-courant, on a observé le cas contraire, cette variation diminue avec l'augmentation du débit.

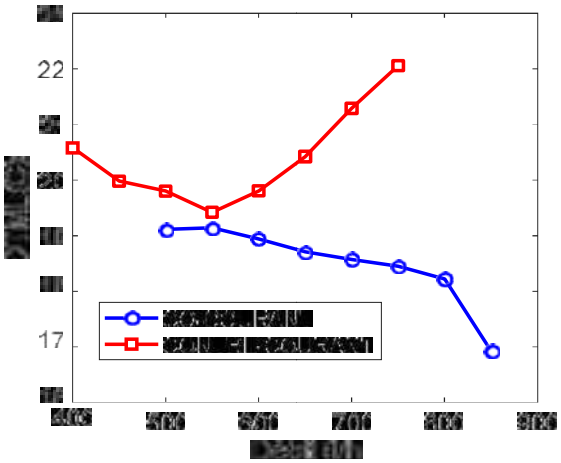

Fig. 7: Variation de la DTLM en fonction du débit volumique de l'eau chaude pour les deux modes

B. *Effet des modes de circulation des fluides sur l'efficacité de l'échangeur*

La figure (8) montre la variation de l'efficacité de l'échangeur pour les deux modes de circulation et pour différents débits volumiques de l'eau chaude. A partir de cette figure, on a constaté que pour les deux modes (co et contre-courant) l'efficacité augmente avec l'augmentation du débit, mais cette augmentation est remarquable pour la circulation en contre-courant. Un débit additionnel de 350 l/h permet d'augmenter l'efficacité jusqu'à 13 %.

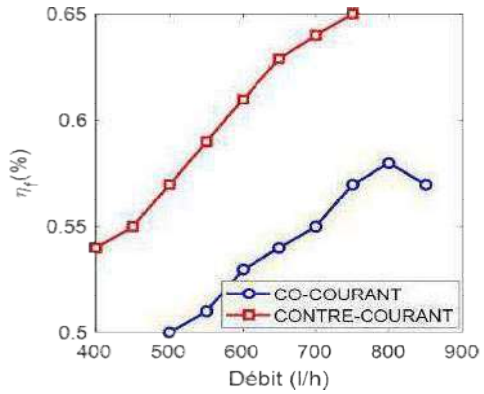

Fig 8 : Variation de l'efficacité en fonction du débit volumique de l'eau chaude pour les deux modes

V. CONCLUSION

Ce travail consiste à l'étude expérimentale et numérique d'un échangeur de chaleur à tubes concentriques. Pour cela, une étude expérimentale a été effectuée au sein du laboratoire en utilisant le banc d'essai de l'échangeur coaxial, eau/eau, Mod.UTC-3/EV (coté E1).

Au cours des essais, deux modes de fonctionnement de l'échangeur ont été étudiés : mode co-courant et mode contre-courant. Les températures de l'entrée et de sortie ont été mesurées pour différents débits volumiques de l'eau chaude, tandis que les débits volumiques de l'eau froide ont été fixés pendant tous les tests.

Dans la deuxième partie de ce travail, nous avons procédé à une étude numérique de l'échangeur. Dans un premier temps, nous avons effectué la configuration géométrique de l'échangeur par le logiciel ANSYS Workbench, en se basant sur les dimensions réelles du banc d'essai utilisé pendant les expériences. La résolution du problème à été effectuée par ANSYS fluent,

D'après les résultats obtenus, nous avons validé nos résultats numériques avec ceux expérimentaux, ce qui nous a donné un excellent accord pour les cas testés. L'erreur maximale de la température de sortie n'a pas dépassé 4%.

L'Analyse des résultats révèle que l'efficacité thermique de l'échangeur augmente avec l'augmentation du débit de l'eau chaude, qui peut aller jusqu'à 13 %.

Aussi, nous avons pu montré à l'échelle du laboratoire que le mode contre-courant est plus performant que le mode co-courant, où la différence de l'efficacité entre les deux modes dépasserait les 8 %.

ACKNOWLEDGMENT

Je remercie le groupe de recherche, qui a contribué à accomplir ce modeste travail.

REFERENCES

[1] A. Bontemps, A. Garrigue, C. Goubier, J. Huetz, C. Marvillet, P. Mercier, R. Vidil, Échangeurs de chaleur-Description des échangeurs. Technique de l'ingénieur (1995) Réf: B2341.

[2] N. Boultif, Etude d'un échangeur de chaleur à triple tube concentrique en régime permanent et transitoire. Thèse de doctorat en science, option génie mécanique, université de Biskra (2017).

[3] Peng, Y., et al., A complete procedure for residual generation and evaluation with application to a heat exchanger, *IEEE Trans. Control Syst. Technol., 5* (1997), 6, pp. 542–555, DOI No. S 1063-6536(97)07775-0.

[4] Persin, S., Tovornik, B., Real-time implementation of fault diagnosis to a heat exchanger, *Control Eng. Practice.,13* (2005), 8, pp. 1061–1069, DOI No. 10.1016/j.conengprac.2004.12.005

[5] Weyer, E., et al., Grey box fault detection of heat exchangers, *Control Eng. Practice., 8* (2000), 2, pp. 121–131, DOI No. 10.1016/S0967-0661(99)00132-X.

[6] Zavala-Rio, A., Santiesteban-Cos, R., Reliable compartmental models for double-pipe heat exchangers: an analytical study, *Appl. Math. Model, 31* (2007), 9, pp. 1739–1752, DOI No. 10.1016/j.apm.2006.06.005.

[7] Zhang, T., et al., Stability analysis of heat exchanger dynamics, *Proceedings* of the American Control Conference, St. Louis, MO, USA, 2009, pp. 3656-3661.

[8] A.Mokrani, A. Moummi, N. Moummi, Simulation de transfert de chaleur dans un échangeur de chaleur coaxial, Premier Séminaire National de Génie Mécanique (SNGM01), (2011).

[9] R. Laskowski, The black box model of a double-tube counter-flow heat exchanger, Heat and Mass 51 (8) (2015) 1111-1119.

Adsorption of an Active Principle Bythe clayand modeling byartificial neural network

DjebbarMustapha*, TheniaAhmed

Laboratory of process engineering and chemistry of solutions (LGPCS), Departmentof processEngineers (ST), University of Mascara , (Algeria),

Laboratory of Quantum Physics Matter and Modeling (LPQ3M), Department of process Engineers (ST), University of Mascara , (Algeria),

B.P. 305, 29000, Mascara, Algeria

Abstract: The adsorption of salicylic acid on natural and treated clay has been studied. Kinetics, and adsorption isotherms were used to identify retention mechanisms. The experiments for determining the kinetics, conducted in a closed reactor with perfect agitation, were examined, including the pH, the mass of adsorbent, and the initial salicylic acid concentration.

The results were modeled using the pseudo-first order and pseudo-second order kinetic equations compared to Artificial Neural Network (ANN) and Mean square error (MSE) values were used to find the best number of neurons. Using the MATLAB R2009a software, we determined the test, the validation and the global regression value.

The experimental results of the global reaction have very large regression coefficients and are perfectly adjustable to the pseudo-second order. After 60 minutes of contact, the adsorption process is determined by intra-particle diffusion. The thermodynamics and the adsorption isotherms are of the spontaneous exothermic type of chemistry-sorption, with retention of the molecules of salicylic acid in monolayers organized on the surface of the adsorbent.

Keywords: Adsorption isotherms, salicylic acid, Artificial Neural Network, science, Kinetics. (3-8 keywords are required.)

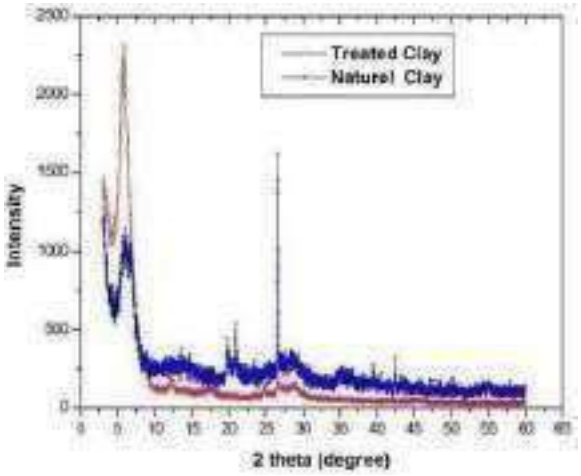

Graphical abstract

***Correspondingauthor:**DjebbarMustapha
E-mail: djebbar_Mustapha@yahoo.fr.

1. Introduction

The drug may produce unintended toxic effects, limiting its therapeutic index with low or insufficient activity and greater toxicity, and it is not guaranteed that it will reach its target. So this is an issue worth studying. A similar trend has been observed in a number of research reports focused on the charging of acid salicylique in clay and zeolites. Clays are commonly used as excipients, shielding, and adsorbent agents in the domain of pharmaceutical production **[1, 2].**

Drug molecules are encapsulated in clay minerals to modify the rate, the time, and to target the site of drug release. Moreover, this strategy can be useful to protect drugs against aging due to chemical and enzymatic degradation. On this basis, a new concept of ‘‘excipient’’ is generated for clay minerals as they are not inert fillers but, instead, can have a functionality allowing targeted release, preventing or reducing side effects, and increasing the product shelf-life.

Salicylic compounds have received a lot of attention because of their important pharmacological actions and side effects: salicylic acid is the forerunner of aspirin (acetyl-salicylic acid) and is an important hydroxybenzoic acid with anti-inflammatory, antiseptic, anti-radical, pain-relieving, analgesic, astringent, anti-rheumatic, antioxidant, and anticarcinogenic properties, **[3]**, but it cannot be used directly on the Clays and clay minerals can be used as vehicles for this salicylic molecule, reducing the effects due to its acidity, even if several limitations occur during salicylic–clays interactions. In fact, salicylic acid has pKa = 2.78 **[4]**; at lower pH, the molecule mainly occurs in the undissociated form, whereas at higher pH it is in the anionic form. Therefore, the adsorption of salicylic acid on clay minerals like smectite is quantitatively limited. Furthermore, salicylic acid is not very soluble in water (water solubility at 20 °C is 0.011 M) **[5]**. Salicylic acid is a strong iron chelator, forming a cationic complex in an acidic aqueous environment **[6]**. To overcome these challenges, a new approach involves combining the active principle with a nanovector, whose size is in the micrometer range and whose role is to encapsulate and effectively transport the active principle to its target. The transport of active principles directly into the target organs requires a precise structure, such as nanometric vectors. In our work, we used clay as a carrier of the Atif principle. It is salicylic acid. Here, the minerals first serve as a carrier, and then as a releaser of the active ingredient. Because of their large specific surface area and high adsorption capacity, kaolinite and zeolites are well suited to acting as drug carriers and releasers **[7].**

2. Salicylic acid Structure

Salicylic acid is an active ingredient used as a drug and as a precursor of acetylsalicylic acid. Aspirin's formula is $VS_7H_6O_3$ and its molar mass is 138.121 g/mol as given bythe “Fig.1”.

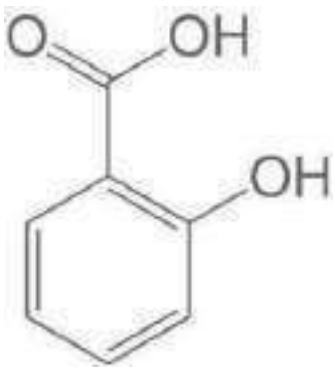

Fig. 1 Structure of salicylic acid

Adsorptionexperiments.

The adsorption experiments were carried out in batches at different initial values of pH, temperature,

and concentration of salicylic acid. The adsorption experiments were performed by introducing a precisely weighed amount of adsorbent into a volume of 100 mL of pure solution of salicylic acid at a concentration of 100 mg/L. The solution of salicylic acid was separated from the adsorbent by centrifugation at 2700 rpmfor 5 min.

The absorbance of the supernatant solution was measured using a 50 UV/visible spectrometer at the wavelength which corresponds to the maximum absorbance of the sample (λ = 270 nm). The concentration of salicylic acid residual in the reaction mixture was calculated using the calibration curve, whose equation is given by:

The adsorption capacity of salicylic acid was calculated using the following formula:

The amount adsorbed was determined by calculating the difference between the final and initial concentrations after correcting for soil blank solutions bythe following equations [8].

$$V = (V - V) \times \frac{V}{(V)}$$

Where Q_e (mg/g) is the quantity adsorbed at equilibrium, C_0 (mg/L) is the initial concentration in salicylic acid, Ce concentration at equilibrium, V is the volume of the solution (mL) and m is the amount of adsorbent in solution (g).

Influence of pH

The influence of the pH of the solution on the adsorption was studied using different pH values from 4 to 12. The experiments were carried out by adding 20 mg of natural and purified clay to 50 mL of salicylic acid solution with a concentration of 0.025 mg/L at a constant temperature (25 °C). The pH of the water system salicylic acid-clay was adjusted to the desired values by the addition of HCl to acidify or NaOH.

Influence of concentration

The influence of the initial concentration of the solution on the adsorption was studied using different concentrations of active principles ranging from (5 to 100 mg/l) were brought into contact with a mass of 20 mg of clay at a temperature of 20°C. The determination of the quantity of the fixed active ingredient, corresponding to the adsorption equilibrium, allowed the establishment of adsorption isotherms for natural and treated clay.

3. Results analysis

Transmission electron microscopy (TEM)

The TEM micrograph of natural and treated clay is shown in Figs. 1 and 2. It shows the laminated clay layers and the average layer thickness of 10 nm. This is a characteristic of the nano clay of natural and treated clay. TEM analysis often requires a small beam size down to 50 nm to determine the chemical composition of claythat is mixed with other minerals.

The difference between treated clay and natural clay was more clearly observed when the clay was examined by TEM. The treated clay has shown that a homogeneous distribution of the layers appears in the form of numerous visible parallel sheets was observed by TEM.

.

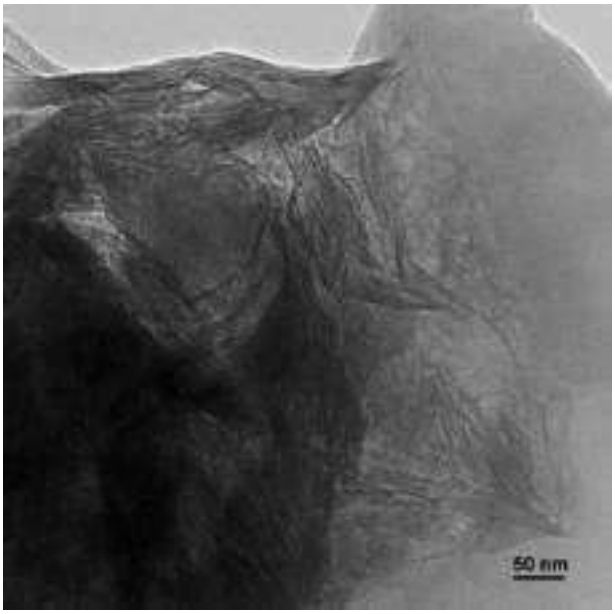

Fig. 2Transmission electron microscopy (TEM) of naturel Clay.

Fig. 3 Transmission electron microscopy (TEM) of treated Clay

3.2 X-ray diffraction

TheThe DRX spectrum in Figure 1 noted the presence of crystalline phases essentially in the form of Clayand quartz:

• An intensification of certain lines located at 2Θ= 6.4 °, Examination of the DRX spectrum of treated clay presented in **Fig4** confirms good purification with:

• Absence of lines characteristic of the quartz at 2Θ = 26.34 °.

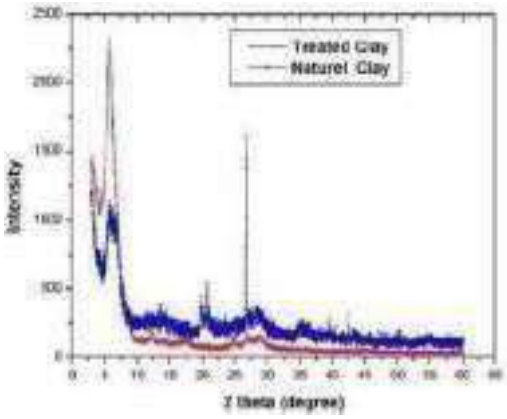

Fig 4: DRX spectra ofNatural, treated clay**.**

4. Adsorptionapplication:

Effect of the initial concentration in salicylic acid.

TheFig 4 represents the evolution curve of the quantity of salicylic acid adsorbed per gram of clay at different initial concentrations (5 to 100 mg/L) of salicylic acid in natural and treated clay. It is noted that the quantity adsorbed at equilibrium increases with the concentration. We also note that the initial adsorption rate increases with the concentration; this is due to the fact that the diffusion of the molecules of salicylic acid on the surface of the adsorbent is accelerated by the increase in the concentration of salicylic acid.

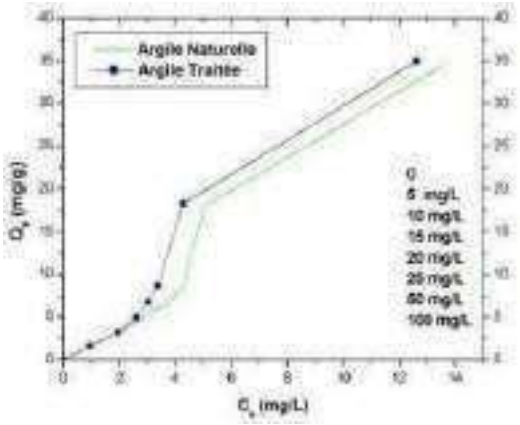

Fig 5: Adsorption isotherm of the active principle of salicylic acid by natural and treated clay.

Effect of pH

The adsorption behavior of salicylic acid on the adsorbent has been studied over a wide pH range of 3–12. Figure 4 shows a slight increase in the adsorbed amount of salicylic acid by the raw clay with the pH of the solution. The pH of natural and treated clay is 9 and 10, respectively. This behavior may be due to the fact that the clay surface is negatively charged, which favors the adsorption of the salicylic acid. On the other hand, for pH values>7, the surface of the clay is positively charged and therefore likely to repel salicylic acid. As the pH decreases, the number of negatively charged sites decreases and the number of positively charged sites increases [8-9].

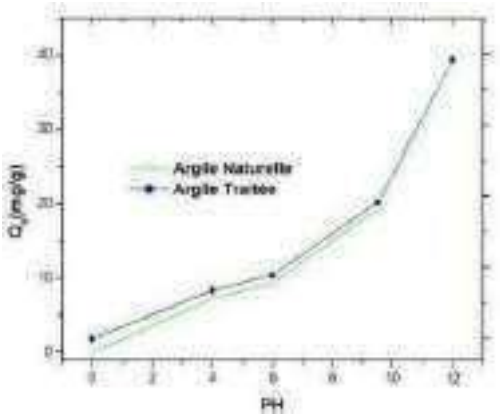

Fig 6: Effect of pH variation on the adsorption of the active principle of salicylic acid by natural and treated clay.

The adsorption reaches its maximum at pH = 12, the quantityadsorbed, and 40 mg/g for the treated clay. We examined the adsorption of the active principle of salicylic acid on a clay matrix of natural and treated clay. The selection of this molecule was motivated on the one hand by its toxicity, particularly to thehuman stomach, and on the other hand by the ease of administration in water.

4. Mechanism of adsorption kinetics

In order to examine the mechanism of adsorption, pseudo-first-order and pseudo-second-order kinetic models were used to test the dynamic experimental data.

Pseudo-first-order model

The pseudo-first-order kinetic model is expressed as follows [21, 22]:

$$VV(V_e - V_t) = VVV_e - V_1 \times V \quad (2)$$

Q_t are, respectively, the quantities of salicylic acid ($mg \bullet g^{-1}$) adsorbed on the clay at time t. k_1 is the speed constant (min^{-1}).

4.2 Pseudo second-order model

The adsorption data were also examined using the pseudo-second-order kinetic model, which is expressed as follows: [16, 17]:

$$\frac{V}{V_t} = \frac{1}{(V^2 V_e^2)} + (V_e) \times V \quad (3)$$

4.3. Kinetic study

The adsorption tests of salicylic acid at different initial concentrations on natural and treated clay were conducted for 60 min. The adsorption of salicylic acid by natural and treated clay occurs rapidly during the first hundred minutes (Figures 2), then evolves slowly and stabilizes after 40 min. Two models have been applied to describe the mechanism of adsorption kinetics: pseudo-first-order and pseudo-second-order. Fig 7 shows that Q_t as a function of time is linear. It is deduced that the adsorption kinetics of salicylic acid on natural and treated clay can be described by pseudo-first-order kinetics. On the other hand, the equilibrium adsorption capacities and the correlation coefficients calculated for the pseudo-second-order show in (Table .3).

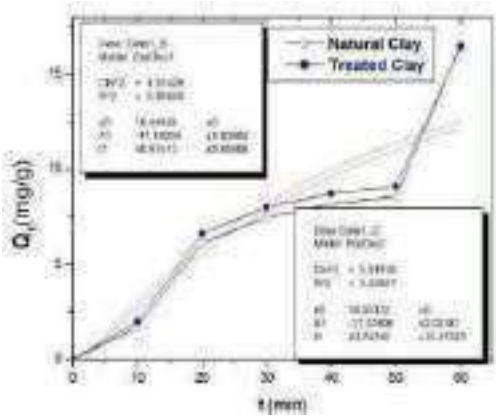

Fig 7: Pseudo-first-order kinetic model of the adsorption of the salicylic acid by the natural and treated clay.

5. Artificial Neural Network

Various factors determine Artificial Neural Network (ANN) topology like number of principle layers, that is, whether it is single layer perceptron or multilayer perceptron, number of nodes in each layer, i.e., number of input parameters, number of neuron in the hidden layer, and number of output parameters and transfer function that is applied.

Optimization of all these factors is one of the essential steps in developing the ANN model. In the present work number of neurons in the hidden layer was optimized to 15, and Mean square error (MSE) values were used to find the best number of neurons. Fig. 8 shows a plot obtained from ANN using MATLAB R2009a software for train, test, validation, and overall regression value. From Fig. 6, it is seen that the regression value obtained for training is 0.99873, for the test, it is 0.99879, for validation, it is 0.99956, and overall it is 0.99893. All the regression values are close to 1, indicating that the ANN model optimized above fits salicylic acid adsorption on Clay better than the Pseudo Second-order.

Table 1 MSE, RMSE, Chi-square error values obtained for ANN model and Pseudo second order kinetic model for salicylic acid adsorption on Clay.

Artificial Neural Network	**Qexperimental (mg g^{-1})**	**16,55**
	Q predicted (mg g^{-1})	16,57
	R^2	0,9989
	MSE	0,203
	$\chi 2$	0,451
Pseudo-Second order model	**Qexperimental (mg g^{-1})**	**16,55**
	Q predicted (mg g^{-1})	16,59
	R^2	0,823
	MSE	0,101
	RMSE	0,318

χ2	0,444

Kinetic model. Table 4 shows error values obtained for the ANN model and Pseudo second-order kinetic model. Mean square error (MSE), Root mean square error, and chi-square error was calculated for the ANN model and Pseudo Kinetic model using equations (4), (5) and (6).

$$MSE = \frac{1}{V}\sum_{i=1}^{n}(V_{predicted} - V_{experimental})^2 \quad (4)$$

$$RMSE = \left(\frac{1}{V}\sum_{i=1}^{n}\{ \quad predicted \quad - V \quad experimental\right)^2 \quad (5)$$

$$= \frac{\sum_{i=1}^{n}(V \quad predicted \quad - V \quad experimental)^2}{V_{predicted}} \quad (6)$$

Q predict represents absorption capacity (mg g-1) obtained from the ANN model, qexp represents absorption capacity (mg g-1) obtained experimentally, and N is the total number of samples studied. It is observed that the error is less for the ANN model compared to the Pseudo Second-order kinetic model. The degree of correlation between experimental and ANN predicted data is shown in Fig. 8.

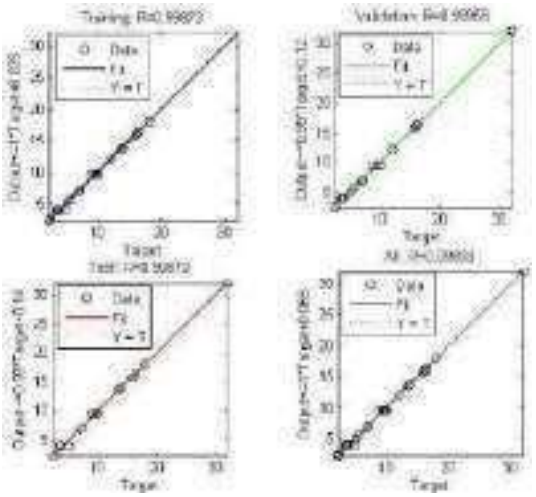

Fig 8 Shows regression plots obtained for training, validation, test and overall fitting of ANN model for salicylic acid adsorption on clay

6. Conclusions

During this study, we used the same Algerian clay taken in its natural state and purified. We have tested clay as an adsorbent of active ingredient salicylic acid. We have shown that the equilibrium is reached after 40 min for the active ingredient salicylic acid and the adsorption isotherm obeys the Langmuir and Freundlich models. Purified clay has a salicylic acid adsorption capacity of 20 mg/g and natural clay has a capacity of 15 mg/g. It was deduced that theadsorption kinetics of active ingredient salicylic acid on the raw clay and the purified clay can be described by pseudo-first-order kinetics and the correlation coefficients R^2 are very close to 1, and the adsorption capacity values calculated (Q_{ecal}) from thepseudo-first-order model-second-order are very close to the values obtained experimentally (Q_{eexp}). The thermodynamic study shows that the adsorption is endothermic in favor of a physisorption for the active ingredient of salicylic acid.

Acknowledgments

The preferred spelling of the word “acknowledgment” in America is without an “e” after the “g.” Try to avoid the stilted expression, “One of us (R.B.G.) thanks ...” Instead, try “R.B.G. thanks ...” Put sponsor acknowledgments in the unnumbered footnoteon the first page.

References

[1] M.T. DroyLefaix, F. Tateo, in F. Bergaya, B.K.G. Theng, G. Lagaly (Eds.) Handbook of Clay Science, Developments in Clay Science, 2006, pp. 743–752.

[2] F.P. Bonina, M.L. Giannossi, L. Medici, C. Puglia, V. Summa, F. Tateo, Appl. ClaySci. 36 (2007) 77–85.

[3] Radtke, J., Linseisen, J., Wolfram, G., 1998. Phenolic acid intake of adults in a Bavarian subgroup of the national food consumption survey. Zeitschrift fur Ernahrungswissenschaft 37, 190–197.

[4] Lajunen, L.H., Portanova, R., Piispanen, J., Tolazzi, M., 1997. Stability constants for alpha-hydroxycarboxylic acid complexes with protons and metal ions and the accompanying enthalpy changes – Part I: aromaticortho-hydroxycarboxylic acids (Technical Report). Pure and Applied Chemistry 69, 329–381

[5] Peña, M.A, Bustamantea, P., Escalera, B., Reíllo, A., Bosque-Sendra, J. M., 2004. Solubility and phase separation of benzocaine and salicylic acid in 1,4-dioxane-water mixtures at several temperatures. Journal of Pharmaceutical and Biomedical Analysis 36, 571–578.

[6] Alvarez-Ros, M.C., Sánchez-Cortés, S., García-Ramos, J.V., 2000. Vibrational study of the salicylate interaction with metallic ions and surfaces. SpectrochimicaActa. Part A56, 2471–2477.

[7] C. Aguzzi, P. Cerezo, C. Viseras, C. Caramella, Appl. ClaySci. 36 (2007) 22.

[8] Huang, Y., Ma, X., Liang, G., Yan, H., 2008. Adsorption of phenol with modified rectonite from aqueous solution. Chemical Engineering Journal 141, 1–8.

[9] S.S. Tahir and NaseemRauf Removal of a cationic dye from aqueous solutions by adsorption onto bentonite clay, Chemosphere 63 (2006) 1842–1848. doi:10.1016/j.chemosphere.2005.10.033

[10] Chih-Huang Weng and Yi-Fong Pan, Adsorption of a cationic dye (methylene blue) onto spent activated clay. Journal of Hazardous Materials; Volume 144, Issues 1–2, 1 June 2007, Pages 355-362. https://doi.org/10.1016/j.jhazmat.2006.09.097.

[11] 24. Li YH, Wang S, Zhang X et al. (2003) Adsorption of fluoride from water by aligned carbon nanotubes. Materials Research Bulletin 38(3): 469–475, https://doi.org/10.1016/S0025-5408(02)01063-2.

[12] Freundlich H (1906) Over the adsorption in solution. Journal of Physical Chemistry 57: 385–471.

[13] Langmuir I (1916) The constitution and fundamental properties of solids and liquids. Part I. Solids. Journal of the American Chemical Society 38(11): 2221–2295, https://doi.org/10.1021/ja02268a002.

[14] Al-Degs Y, Khraisheh MAM, Allen SJ and Ahmad MN (2000) Effect of carbon surface chemistry on the removal of reactive dyes from textile effluent. Water Research 34: 927–935, https://doi.org/10.1016/S0043-1354(99)00200-6.

[15] Namasivayam C, Radhika R and Suba S (2001) Uptake of dyes by a promising locally available agricultural solid waste: coir pith. Waste Management 21(4): 381–387, https://doi.org/10.1016/s0956-053x(00)00081-7.

[16] Al-Degs Y, Khraisheh MAM, Allen SJ and Ahmad MN (2000) Effect of carbon surface chemistry on the removal of reactive dyes from textile effluent. Water Research 34: 927–935, https://doi.org/10.1016/S0043-1354(99)00200-6.

[17] Namasivayam C, Radhika R and Suba S (2001) Uptake of dyes by a promising locally available agricultural solid waste: coir pith. Waste Management 21(4): 381–387, https://doi.org/10.1016/s0956-053x(00)00081-7.
[17-3]

[18] B.Karagozoglua and M.Tasdemira and E.Demirbasb and M.Kobyac ; The adsorption of basic dye (Astrazon Blue FGRL) from aqueous solutions onto sepiolite, fly ash and apricot shell activated carbon: Kinetic and equilibrium studies. Journal of Hazardous Materials, Volume 147, Issues 1–2, 17 August 2007, Pages 297-306, https://doi.org/10.1016/j.jhazmat.2007.01.003

[19] Hameed, B.H., 2007. Equilibrium and kinetics studies of 2,4,6-trichlorophenol ads

[20] orption onto activated clay. Colloids and Surfaces A: Physicochemical and Engineering Aspects 307, 45–52.

[21] Weng C.H. et Y.F. Pan, (2007). Adsorption of a cationic dye (methylene blue) ontospent activated clay. J. Hazard. Mater., 144, 355 362

[22] Gürses A., Ç. Dogar, M. Yalçin, M.Açikyildiz, R. Bayraket S. Karaca (2006). The adsorption kinetics of the cationic dye, methylene blue, onto clay. J. Hazard. Mater., B131, 217 228.

[23] Önal Y., C. Akmil-Basar et Ç. Sarici-Özdemir (2007). Investigation kinetics mechanisms of

[24] adsorption malachite green onto activated carbon. J. Hazard. Mater., 146,194 203. M. Young, The Technical Writer's Handbook. Mill Valley, CA: University Science, 1989.

Simulation of flow and heat transfer inside the Double acting Stirling engine

Houda HACHEM[#1], Ramla GHEITH[*2], Fethi ALOUI[*3]

[#]*Energy Research and Technology Center (CRTEn), BP 95, Hammam-Lif 2050, Tunisia*

[1]houdahachem@yahoo.fr

[*]*University of Monastir, National Engineering School of Monastir (ENIM), LESTE Laboratory Avenue Ibn El Jazzar 5019 Monastir, Tunisia*

[2]ramla2gheith@yahoo.fr

[3] *Université Polytechnique Hauts-de-France (UPHF), LAMIH CNRS UMR 8201, INSA Hauts-de-France, INSA Hauts-de-France, F-59313 Valenciennes, France*

[3]fethi.aloui@uphf.fr

***Abstract*— This research proposes CFD numerical simulation of a double effect Stirling engine. On the basis of the k-SST turbulence model, a very specific Stirling engine configuration with a single-cylinder arrangement is numerically simulated in order to analyse the heat transfers and flows and increase the engine's output power. Discussion and interpretation of the cyclic evolution of pressure, temperature, and velocity are presented. Researchers looked at how the engine load pressure and regenerator porosity affected the mechanical power generated. The findings indicate that there is an optimum porosity for maximizing power.**

***Keywords*— CFD, temperature, pressure, speed, heat exchanger**

I. INTRODUCTION

Numerical simulation has evolved over the previous ten decades into a crucial tool for pre-analyzing industrial systems and installations. The numerical solutions to the differential equations regulating the movement of mass, momentum, and energy are the focus of CFD. The flux and heat transport in a double-acting Stirling engine are studied in this article using CFD.

The performance of the Stirling engine has recently been the subject of numerous research (CFD) [1–7,12]. A compact porous sheet heat exchanger's heat flow and transfer were modelled by Zhigang Li et al. (2015) [4]. According to his findings, a regenerator of this type has a low viscous friction loss of 800 Pa when operated at 1 atm and 2600 rpm. The porous sheet regenerator has outstanding heat transfer properties, and because to its small size, dead volume is significantly reduced. They discovered that the porous sheet regenerator has a total entropy generation rate of 38-51%, which results in less loss and, consequently, more power and thermal efficiency, compared to the standard metal mesh regenerator. The properties of heat transport in a Stirling engine of the -type were researched by José Leon et al. in 2014 [3]. He discovered that at any one time, the temperature distribution across the engine is not uniform.

The impact of regenerator inefficiency, engine piston crank radius, initial charge pressure, and rotational speed on the power dynamics and efficiency of a two-piston double-acting Stirling engine was examined by Wen-Lih Chen et al. (2012) [6] using CFD numerical simulation. Wen-Lih Chen et al. [7] investigated how a mobile regenerator affected the efficiency of a Stirling engine of the kind in 2015. They specified the shape, model, mesh, and physical parameters for this. In the CFD simulation, features like the piston movement of the cold and hot chamber were added.

The geometry of the Whispergen double-acting Stirling engine was taken into consideration for the current study in order to simulate the flow and heat transmission inside the Stirling engine. The findings

show the variations in pressure, temperature, and velocity and how the mechanical power generated is impacted by regenerator porosity and initial charge pressure.

II. CFD MODELING

II.1. Geometry and assumptions

The double acting Stirling engine is composed of four cylinders. Each cylinder consists of the compression space, the expansion space, the cooler, the regenerator, and the heater. In the present CFD simulations, it is assumed that all the mechanical work will be done by one piston; so the heated gas will be passed through the regenerator to the cooled part of the same piston rather than using two pistons as the real geometry, this will allow us to avoid a lot of errors and make the CFD possible and easier. The geometry under study consists of five working spaces, as shown in Fig. 7, the expansion zone in contact with the hot heat exchanger, the hot and cold tube connections, the annular porous regenerator, the regenerator, and cold tube connections, and the compression zone in contact with the cold heat exchanger.

TABLE 1. Initial properties and data for the simulation

Parameters	Values	unit
Engine Piston Number	4	
Piston diameter	4.34	cm
Displacement Volume	64	cm3
Expansion space volume	33.85	cm3
Compression space volume	30.11	cm3
Regenerator volume	22.11	cm3
Phase angle	90	°
Enginespeed	25	Hz
Wire matrix diameter	6E-5	m
Matrix screen width	2.16E-04	m

TABLE 2. Initial working gas proprieties

Parameters	Values	unit
Gas	N_2	--
Molecular weight	28.013	Kg.kmol-1
Dynamic Viscosity	1.76837E-5	Pa.s
Specific Heat	1042	J.kg-1.K-1
Thermal Conductivity	0.0258	W.m-1K-1
Prandtl number	0.713	--

Every region has boundaries and its physics values. boundary conditions are made based on the Engine working process there are three main regions, the first one is the hot chamber domain region which is a fluid type region, composed of HEX and inner volume which is the N_2, the second one is the Regenerator domain which is Porous Media region and finally, the last one is The cold chamber which is the fluid region type, it is composed by inner volume that represents N_2 and the cooler.

As was mentioned before for a complex CFD simulation that requires a moving motion either we use a morphing method or a "Translation method", in our case we used the morphing method, which gives us the possibility to move boundaries without or with deformation, the floating specification means we can modify the volume of our geometry from one axe to another and the total displacement means we can deplace boundaries with their vortices, the idea is to make the two inner volume of the cold and hot chamber the piston as Floating morphing which can simulate the expansion and the compression and the surface between the Piston and the cold and hot chamber as a total displacement morphing programmed by a function, which can simulate the pressure done by the piston when he moves up and down.

Temperature is supposed to be 1100k for the boundaries that are connected to the heat exchanger and 313k for the ones that are connected to the cooler and an adiabatic condition for the ones that have contact with the piston and finally the regenerator has 706.5 K which is a mean temperature.

Every volume is composed of surfaces and every surface has its boundary conditions as summarized in tables 1 and 2.

The k-ω SST turbulence model was used to simulate the turbulent flow inside the Stirling engine.

To resolve the flow field and the temperature distribution inside the Stirling engine, a physics-controlled tetrahedral mesh of 1,428,376 elements has been generated. The mesh quality is shown in Fig. 1.

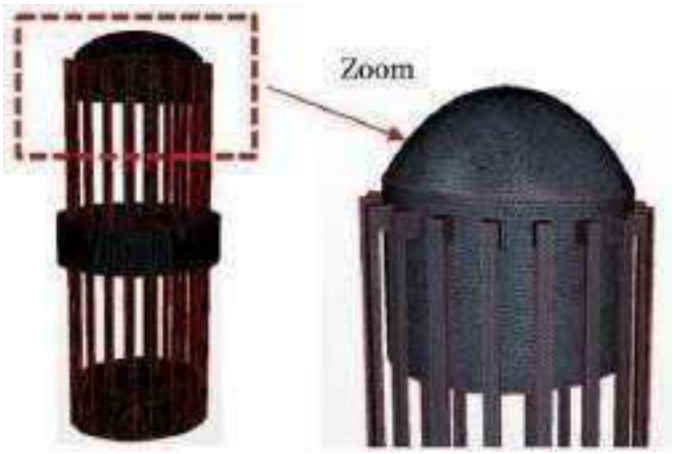

Fig. 1. (a) 3D Geometry and Mesh quality (b) 2D Piston View

III. Results and discussions

Fig 2 (a) represents 2D temperature distribution during the compression-expansion process at a time t. It can be seen that the maximum Temperature in the hot chamber domain (red color) represents a temperature of around 1000 K, the yellow color in the interface between the regenerator and the hot canals shows that the temperature rises on that side from 785k to almost 900 K and in the other hand the interfaces between the regenerator and the cooler show the existence of light blue color which is in the middle between the dark blue color of the cooler temperature and the green color of the regenerator which shows that the regenerator works as a heat exchanger between the two chambers not onlyto prevent thermal shock but also to fasten the heat process of the hot chamber to get hotter and of the cold chamber to get cooler which increase the temperature difference between the compression and the expansion spaces and will end up by rising the engine efficiency.

Fig 2 (b) and Fig 2 (c) represent respectively mean hot end temperature and mean cold end temperature evolutions during a steady state cycle. the maximum temperature difference between cold and hot spaces was observed at the end of the compression phase (180°). As shown in Fig 2 (c), the evolution of mean temperature inside the cold space ng the compr l then increa 80° to 360°). oes a discon ty can be exp or and its ro before reachi . Fig 2 (b), th soidal evolut 0° to 90°,) t 1270° during olution is reproduced during the expansion phase.

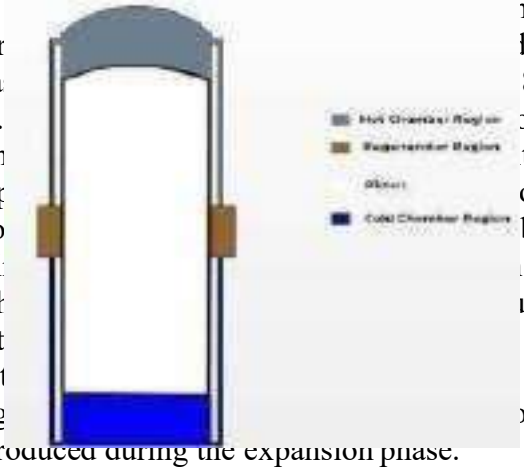

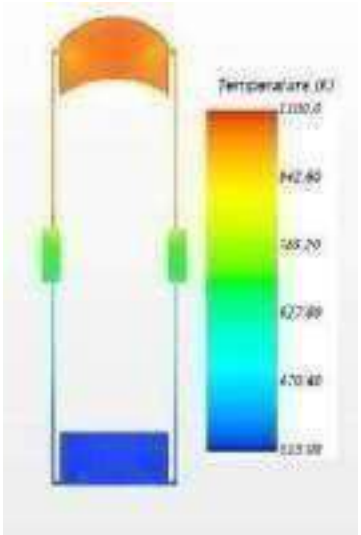

(a)

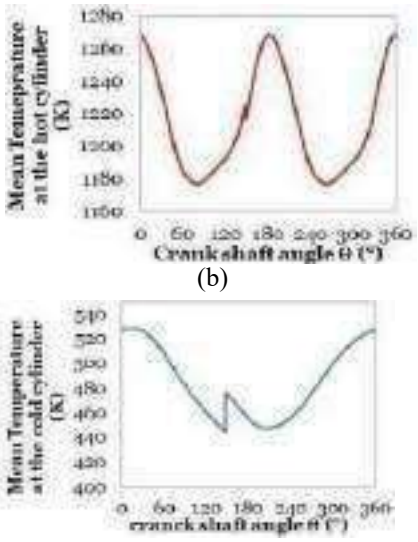

Fig. 2. (a) 2D Temperature distributions and mean temperature evolution (b) at the hot cylinder and (c) at the cold cylinder

Fig. 3 (a) represents the 2D distribution of pressure at an instant t. The cold chamber (represented by the red colour) has the highest pressure, while the hot chamber has the lowest pressure (represented by the blue colour). However, the regenerator's pressure is somewhere between that of the two hot and cold spaces (represented by the colour Yellow). The maximum pressure is not located always in the cold chamber, it is a sinusoidal pressure as seen in Fig. 3 (b) and Fig. 3 (c) , however, the pressure in the regenerator remains as the mean pressure between the hot and cold chamber and it is represented by the green colour.

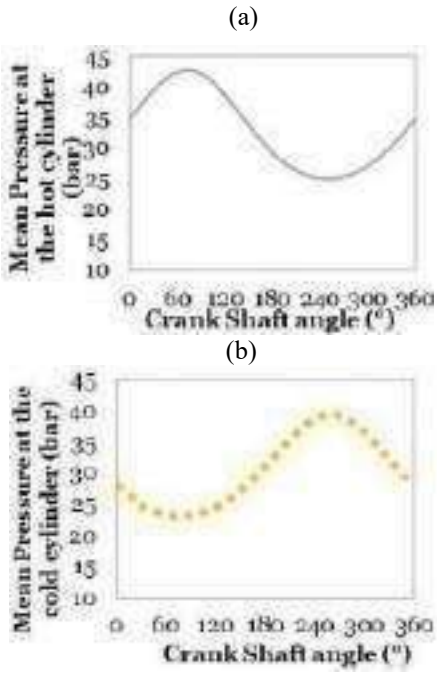

Fig. 3. (a) 2D Pressure distributions and mean pressure evolution (b) at the hot cylinder and (c) at the cold cylinder

Fig. 4 reported the velocity field in m/s. In the heated expansion chamber, there are four (4) recirculating zones formed due to N_2 fluids coming from canals at a high speed. However, in the cooled compression chamber, there are only two recirculating zones this phenomenon can be explained by the location of the connecting channels. These recirculation zones enhance the heat transfer between walls and the working fluid. The regenerator (porous media) slows down the flow. As confirmed in Fig. 4 the speed decreased from 3m/s in the canals part to 1 m/s in the regenerator pores and 0 m/s in another point of the regenerator. The change of surfaces between canals and chambers causes not only causes pressure drop but also turbulence in the fluid flow, which lead to the formation of two turbulent in the compression chamber.

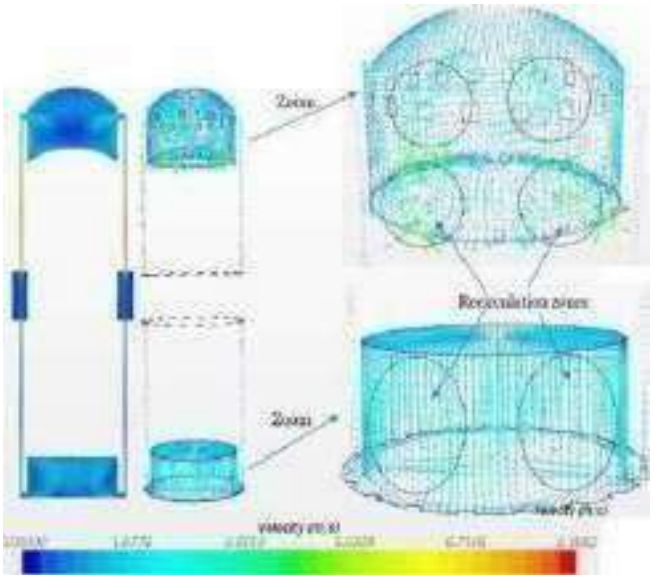

Fig. 4. Velocity distribution (m/s) on the upper heated and bottom cooled cylinders

At the expansion space (Fig. 5), the evolution of speed undergoes a periodic evolution as shown in Fig. 5(a). The maximum speed is observed during the expansion phase between 170° and 350°. The evolution of the temperature is in advance of phase compared to speed. This time lag, about 0.0068s, can be explained by the phenomenon of thermal agitation of the working gas (nitrogen) molecules due to the rise in its temperature which subsequently increases its speed.

The temperature evolution is in advance of phase compared to the pressure evolution (Fig. 5(b)). Response time is the term for this delay about 0.0015s. The increase of working fluid density with pressure and temperature explains (the compressibility effect). The pressure undergoes a sinusoidal periodic evolution that reaches its minimum value at 71.2° and its maximum value at 251.2°.

At the regenerator, the evolution of the mean velocity, temperature, and pressure drop as a function of crank angle was shown in Fig. 6 . This periodic evolution of temperature varies from 340K to 560 K. The maximum temperature of the regenerator is reached when its pressure drop is minimal (at 180°). Pressure drop is strongly related to energy dissipation. The shape of the temperature curve at the regenerator differs from that at the expansion space which demonstrates the non-ideal behaviour of the regenerator. During the expansion phase (between 0° and 180°) the pressure increases and the volume decreases in the hot chamber. Thus, the regenerator stores the heat coming from the fluid circulating from the hot chamber to the cold chamber. During the expansion phase (between 180° and 360°), the regenerator releases this stored heat to the working fluid circulating from the cold room to the hot room. This phenomenon is similar to the behaviours of an electrical capacitor that charges and discharges due to the presence of electrical resistance in the circuit.

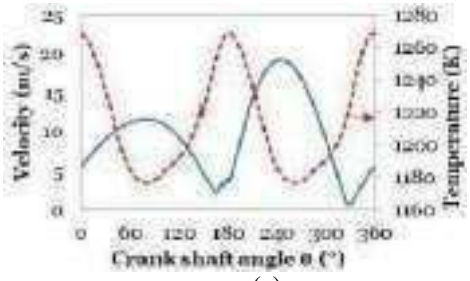

(a)

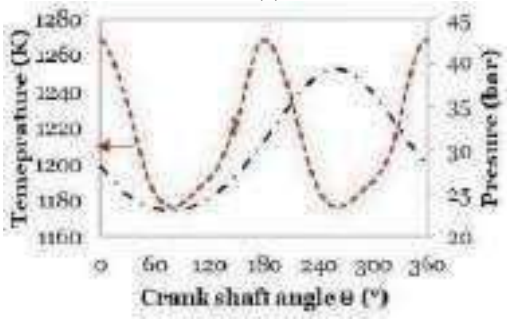

(b)

Fig. 5. (a) Velocity and Temperature, (b)Temperature and Pressure evolutions at the hot space during a cycle

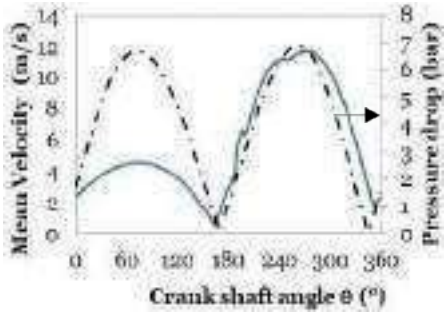

(a)

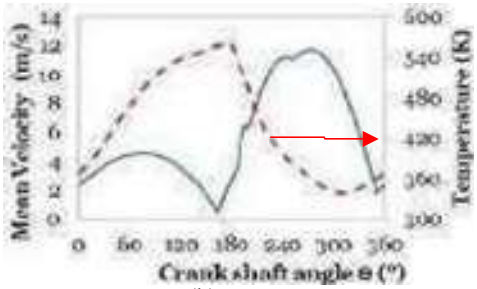

(b)

Fig. 6. (a) Pressure drops and Velocity (b)Velocity and Temperature evolution at the regenerator during a compression/expansion cycle

At the compression space, the evolution of mean temperature, velocity, pressure, and volume versus the crank angle was presented in Fig. 7. The Temperature evolution is in advance of phase compared to the velocity (Fig. 7 (a)). This response time (about 0.0067 s) describes the impact of rising temperature on the velocity and it could be explained by the Molecular agitation due to the elevation of the temperature. The two evolutions of pressure and volume are in phase opposition (Fig. 7 (a)) as reported in major Stirling engine simulations.

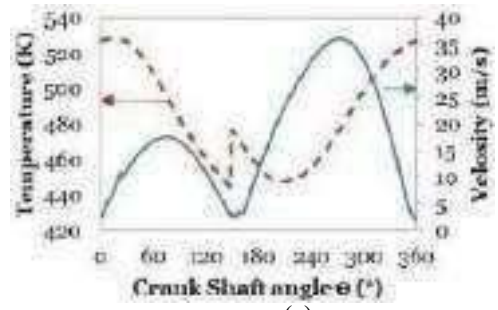

(a)

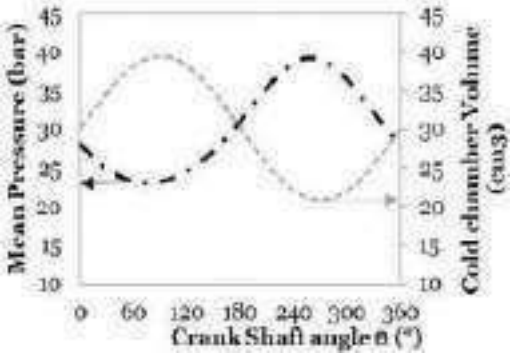

(b)

Fig. 7. (a) Temperature and Velocity (b)Pressure and volume evolution at the cold space during a compression/expansion cycle

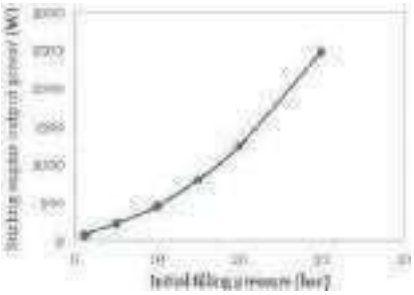

Fig. 8. The output power of the Stirling engine vs. initial filling pressure (when ε=85%, Th=1100k, Tc=313k)

At 1500 rpm, 1100 K, 313K, and 85% respectively of rotation speed, hot end temperature, cold end temperature, and regenerator porosity, It is shown (Fig. 8) that the output power increases with initially charged pressure. At 1 bar as initial charge pressure, the Stirling output power is only 68 W. As the initial pressure is increased to 30 bar the output power was elevated to approximately 2500 W. This result was confirmed by Cheng and Chen [15] using Helium as working gas they found the same behaviour of increasing the initial pressure with the output power and also confirmed by Hachem et al. [10] using N_2 as working gas.

The regenerator was described using the equation related to a porous media based on ERGUN Equation as follows:

$$\frac{\Delta P}{L} = \frac{150\mu V_0}{D_P^2}\frac{(1-\varepsilon)^2}{\varepsilon^3} + \frac{1.75\,\rho_g V_0^2}{D_p}\frac{(1-\varepsilon)}{\varepsilon^3} \quad (1)$$

Thus, the two principal parameters for the Porous Media (regenerator) which are viscous Resistance and inertial Resistance can be introduced as follow:

$$\frac{\Delta p}{L} = R_v * \mu * v_0 + R_i * \rho * {v_0}^2 \quad (2)$$

$$R_i = \frac{(1-\varepsilon)^2 * 150}{\varepsilon^3 Dp^2} \quad (3)$$

$$Rv = \frac{(1-\varepsilon)}{\varepsilon^3 Dp} * 1.75 \quad (4)$$

The Inertial porous resistance and porous viscous resistance are calculated according to ERGUN equation and presented in Table 3.

TABLE 3. Porous Inertial Resistance and Porous viscous Resistance with different porosity

Porosity	Rvz	Riz
0.65	1.8586e+10	7.4344e+04
0.725	8.2688e+09	4.2095e+04
0.85	1.5266e+09	1.4248e+04
0.95	1.2149e+08	3.4019e+03

The regenerator porosity and matrix wire diameter are critical to the Stirling engine performance. High matrix porosity values lead to high regenerator effectiveness but low engine performance. An increase in the matrix heat capacity leads to a reduction in the engine's performance, torque as well as work output. A low-speed engine is more effective with a low porosity regenerator installed as you can see our engine is a 1500 rpm and the optimum porosity is about 77.5% (Fig. 9). In conclusion, the maximum Stirling engine output power is about 1473 W is obtained at 20 bar and 77.5% respectively as initial filling pressure and regenerator porosity. the maximum Stirling engine output power is about 2500 W at 30 bar and 85% respectively as initial filling pressure and regenerator porosity. The obtained numerical results follow closely the trend of Valenti et al. [16] experimental data. Assuming that the conversion coefficient of mechanical to electrical power is about 0.7, thus, the obtained electric efficiency is about Pel=1.473*0.7 = 1.031 kW which is confirmed by the commercial electrical power output ofthe Whispergen unit [10].

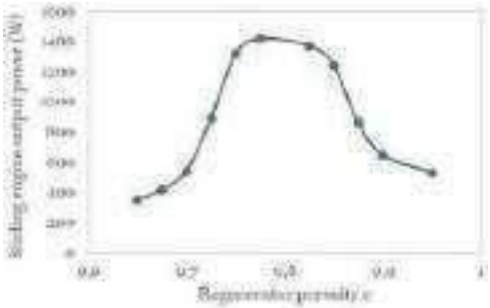

Fig. 9. The output power of the Stirling engine vs. regenerator porosity(when P=20 bars, Th=1100K, Tc=313K)

The present case study covers a numerical study of a micro-cogeneration Stirling unit for automobile future application. The unit is analysed by varying the initial charge pressure of the working fluid (Nitrogen) and varying the regenerator porosity. An optimum regenerator porosity is expected for each Stirling engine working parameters. At P=20bar, N=1500rpm, Th=1100K and Tc= 313 K, the optimum regenerator porosity is about 77.5%.

IV. CONCLUSIONS

A double-effect Stirling engine CFD simulation has been successfully created. The results are subtracted as follows:

-During an engine cycle, the distribution of temperature in the various engine compartments is not constant.

-When compared to the evolution of the pressure, the temperature is out of phase. Response time is the term for this delay.

-The Stirling engine's mechanical power grows with initial charge pressure, and an ideal porosity of the regenerator (equal to 0.775) ensures maximum mechanical power.

ACKNOWLEDGMENT

This work was financially supported by the "PHC Utique 2022" program number 47613ND of the French Ministry of Foreign Affairs and Ministry of higher education, research and innovation and the Tunisian Ministry of higher education and scientific research in the CMCU project number CMCU 22G1102. There is a lot of gratitude for these two supporters.

REFERENCES

[1] Cun-quan Zhang, Cheng Zhong, Theoretical modeling of a gas clearance phase regulation mechanism for a pneumatically-driven split-Stirling-cycle cryocooler, Cryogenics 66, 13-23, (2015).

[2] Cun-quan Zhang, Cheng Zhong, Experimental study of a gas clearance phase regulation mechanism for a pneumaticallydriven split-Stirling-cycle cryocooler, Cryogenics 66, 24-33, (2015).

[3] Jose Leon Salazar, Wen-Lih Chen, A computational fluid dynamics study on the heat transfer characteristics of the working cycle of a β-type Stirling engine, Energy Conversion and Management, 88 , 177 - 188 (2014).

[4] Zhigang L., Yoshihiko H., Yohei K., Dawei T., Analysis of a high-performance model Stirling engine with compact porous-sheets heat exchangers, Energy, 64, 31-43, (2014).

[5] Hachem H., Gheith R., Aloui F., Ben Nasrallah S., A CFD Analysis of the Air Flow through the Stirling Engine's Singularities. 7th international Exergy,Energy and Environment Symposium , (2015).

[6] Wen-Lih Chen, King-Leung Wong, Li-Wen Po. A numerical analysis on the performance of a pressurized twin power piston gamma-type Stirling engine. Energy Conversion and Management. Volume 62, 2012, 84-92.

[7] Wen-Lih Chen, Yu-Ching Yang, Jose Leon Salazar. A CFD parametric study on the performance of a low-temperaturedifferential γ-type Stirling engine. Energy Conversion and Management, Volume 106, 2015, 635-643.

[8] Hachem, H., Gheith, R., & Aloui, F. (2022). Theoretical investigations of Stirling engine performances for different filling gas properties. International Journal of Energy Research.

[9] Hachem, H., Gheith, R., Aloui, F., Nasrallah, S. B., & Dincer, I. (2016). Exergy assessment of heat transfer inside a Beta type Stirling engine. International Journal of Exergy, 20(2), 186-202.

[10] Hachem, H., Gheith, R., Aloui, F., Delprat, S., & Paganelli, S. (2019). Energetic and exergetic investigations of an innovative heat recovery exhaust system using a double acting type Stirling engine based on theoretical analysis. International Journal of Exergy, 28(3), 273-300.

[11] Hachem, H., Gheith, R., Aloui, F., & Nasrallah, S. B. (2018). Technological challenges and optimization efforts of the Stirling machine: A review. Energy conversion and management, 171, 1365-1387.

[12] Hachem, H., Gheith, R., Aloui, F., Nasrallah, S. B., & Wang, M. (2018). A CFD Analysis of the Air Flow Through the Stirling Engine's Singularities. In Exergy for A Better Environment and Improved Sustainability 1 (pp. 271-287). Springer, Cham.

[13] Hachem, H., Gheith, R., Aloui, F., & Nasrallah, S. B. (2015). Numerical characterization of a γ-Stirling engine considering losses and interaction between functioning parameters. Energy conversion and management, 96, 532-543.

[14] Hachem, H., Creyx, M., Gheith, R., Delacourt, E., Morin, C., Aloui, F., & Ben Nasrallah, S. (2015). Comparison based on exergetic analyses of two hot air engines: A Gamma type Stirling engine and an open joule cycle Ericsson engine. entropy, 17(11), 7331-7348.

[15] Cheng, C. H., and Chen, Y. F. (2017). Numerical simulation of thermal and flow fields inside a 1-kW beta-type Stirling engine. Applied Thermal Engineering, 121, 554-561.

[16] Valenti, G., Silva, P., Fergnani, N., Di Marcoberardino, G., Campanari, S., and Macchi, E. (2014). Experimental and numerical study of a micro-cogeneration Stirling engine for residential applications. Energy Procedia, 45, 1235-1244.

ISSN: 1737-9334

Proceedings of Engineering & Technology-PET-Vol 71

Numerical investigation of a nanofluid flow inside a Stirling engine's cooling circuit using the lattice Boltzmann method

Insaf MEHREZ[1,2], Houda HACHEM[3], Ramla GHEITH[1], Fethi ALOUI[2]

[1] *University of Monastir, National Engineering School of Monastir (ENIM), LESTE Laboratory Avenue Ibn El Jazzar 5019 Monastir, Tunisia*

[2] *Université Polytechnique Hauts-de-France (UPHF), LAMIH CNRS UMR 8201, INSA Hauts-de-France, INSA Hauts-de-France, F-59313 Valenciennes, France*

[3] *Energy Research and Technology Center (CRTEn), BP 95, Hammam-Lif 2050, Tunisia*

***Abstract*— An important concept in numerous engineering and commercial applications is nanofluids. It can be used in heat exchangers, generator cooling, nuclear system cooling, and other engineering applications thanks to its broad absorption range, low pressure drop, and good thermal conductivity. This paper discusses a numerical study of laminar forced convection heat transport of nanofluids in a channel of a Stirling engine's cooling circuit. Pure water is employed as the base fluid. Silver (Ag) and Copper (Cu) are designated as nanoparticles. The Maxwell-Garnetts and Brinkman models are used to evaluate the effective thermal conductivity and viscosity of the nanofluid. A thermal Lattice Boltzmann model (LBM) has been proposed for solving the obtained governing differential equations for the considered physical problem. The simulations are performed for different parameters throughout as volume fraction (φ), type of nanofluid and Reynolds number (Re). a new geometry was added to studied the effect of n of laminar forced convection heat transport of nanofluids. Results show that the system's ability to transport heat in this new geometry is significantly improved by the inclusion of lower nanofluids content.**

***Keywords*— Stirling engine, Nanofluid, heat transfer, thermal Lattice Boltzmann model, attached and separated flow**

I. INTRODUCTION

The application of nanofluids is considered to have a high potential for improving heat transfer characteristics and continues to be of great interest in many technological and industrial applications [1] (vapor compression cycles, cooling applications, heat exchangers, automotive cooling, biomedical applications, solar energy and desalination applications). To improve the heat transfer of a nanofluid flow, another method was adopted. It is represented by the addition of an oscillating component to the flow of nanofluid. Indeed, the use of a pulsed flow has the advantage of preventing sedimentation of the nanoparticles in the base fluid; therefore, a good mixture of nanoparticles can be obtained near the wall. The combined effect of attached flow and nanofluids can improve heat transfer and fluid mixing in the channel. The flow and heat transfer of nanofluids in a horizontal tube was first time studied by Rahgoshayet al.[2]. They reported that a further increase in heat transfer is observed with the increasing of the Reynolds number and volume fraction. Other studies [3-4] investigated the heat transfer characteristics of Al2O3-water-based nanofluids under pulsating inlet flow conditions. Results showed that overall heat transfer coefficient of the base fluid flow increases by using nanofluid into the base fluid flow up to 14 %. Heat transfer results also indicated that combination of the nanofluid and the pulsation into the fluid flow can increase significantly the overall heat transfer coefficient up to 23 %. Some researchers [5-11] have proven that the use of nanoparticles under pulsed flow conditions increases the rate of heat transfer compared to the case of constant flow.

All these studies are related to the aspect of forced convection over the rectangular channel, however, little is known about forced convection nanofluid flow and heat transfer in separate and reattached flow. Therefore, this paper deals with a numerical simulation for forced convective flows over a BFS in a channel fully filled by porous medium using different types of nanofluids. The local thermal equilibrium has been assumed for the energy equation including viscous dissipation effects. The problem is solved with Lattice Boltzmann Method (LBM). Effects of Reynolds number, nanofluid volume fraction on the fluid flow and heat transfer were numerically investigated.

II. NUMERICAL SIMULATION

A schematic description of the physical problem considered in this study is shown in Figure 1. A channel is considered with aheight H and length 12H. The boundary conditions for the considered problem in dimensionless form are summarized in Table I.

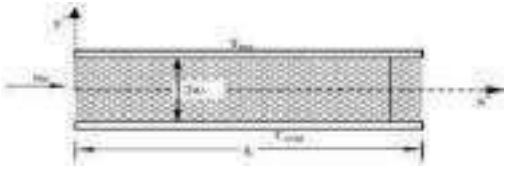

Fig. 1: Geometry with boundary conditions

Table 1: boundary conditions

	Velocity	*Temperature*
South wall	U = 0,V = 0	**Θ=1**
North wall	U = 0,V = 0	**Θ=2**
East wall	U=Uo, V=0	**Θ=1**
West wall	$\frac{\partial U}{\partial X} = 0,\ V = 0$	$\frac{\partial \theta}{\partial X} = 0$

It is worth noting that the following assumptions are considered:

- Viscous dissipation effects are not negligible in the energyequation,
- Nanofluid flowand heat transfer are fullydeveloped.

Thermophysical properties of water and nanofluids at the reference temperature are presented in Table II [12].Fluid flow and heat transfer in the present system are described by mass, momentum, and energy conservation equations. To simulate this physical problem, many researchers employed the thermal Lattice Boltzmann model (LBM).

Table II: Properties of various types of used nanofluids at 25°C

Properties	Water	Ag	Cu
λ (W.m .K)	0.613	429	400
ρ (kg.m^{-3})	997.1	10500	8933
Cp(J/kg.K)	4179	235	385

In this case, the differential form of these equations at macroscopic level, obtained by using the volume averaging technique [15], can be expressed as follows:

Mass conservation equation

$$\frac{\partial U}{\partial X} + \frac{\partial V}{\partial Y} = 0 \quad (1)$$

Momentum conservation equation

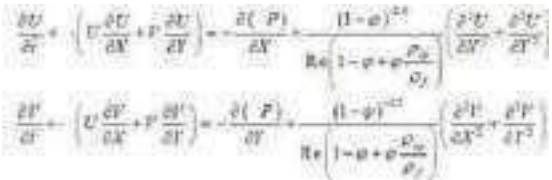

Energyconservation equation

The physical quantities are non-dimensionalised by using the reference variables: $L_{ref} = H,\ U_{ref} = u_0,\ t = \frac{H}{u_0},\ P_{ref} = \rho u_0^2,\ T = Te, St = f\frac{H}{uo}$

The equations are written in dimensionless form and involve the following dimensionless numbers: Reynolds number $\mathrm{Re} = \frac{u_0 H}{\nu_f}$, Prandtl number $\mathrm{Pr}_f = \frac{\nu_f (\rho c_p)_f}{k_f}$. The added nanoparticles to the base fluid change the thermal conductivity, viscosity and other basic characteristic of the base fluid. Thermal diffusivity, density, heat capacitance and thermal expansion of nanofluid [15] can be defined as:

$$\begin{aligned}
&(\rho)_{nf} = (1-\varphi)\rho_f + \varphi\rho_p \\
&\frac{\mu_{nf}}{\mu_f} = \frac{1}{(1-\varphi)^{2.5}} \\
&\frac{\nu_{nf}}{\nu_f} = \frac{\mu_{nf}}{\rho_{nf}} \\
&\frac{k_{nf}}{k_f} = \frac{k_p + 2k_f - 2\varphi(k_f - k_p)}{k_p + 2k_f + \varphi(k_f - k_p)} \\
&(\rho c_p)_{nf} = (1-\varphi)(\rho c_p)_f + \varphi(\rho c_p)_p \\
&\frac{\alpha_{nf}}{\alpha_f} = \frac{k_{nf}}{(\rho c_p)_{nf}}
\end{aligned} \quad (3)$$

Local Nusselt number and time-spatial averaged Nusselt number along the upper wall downstream of the step can be defined as:

$$Nu = \frac{k_{eff}}{k_f}\frac{\partial T}{\partial n}\Big|_{wall}\frac{1}{T_w - T_b(x)}; \quad Nu_m = \frac{1}{L}\int_0^L Nu_x\,dx; \quad T_b(x) = \frac{\int_0^H u\,T\,dy}{\int_0^H u\,dy}$$

III. NUMERICAL METHOD

One of the useful numerical methods that have been used in recent years is the Lattice Boltzmann Method. It was a powerful numerical technique to simulate the heat transfer and fluid flow has been obvious in the last decade, used for simulating the flow field in wide ranges of engineering applications such as natural convection [38], porous media [39], multiphase flow [40] etc. Considering the explicit nature of the lattice Boltzmann method, this method is selected to simulate pulsating flow by Jafari et al. [41]. They concluded that the pulsating flow plays a more powerful role in heat transfer enhancement of thepure fluid in comparison with nanofluid.

Lattice Boltzmann Equation: Flowand thermal fields

The progress of using the LBM as a numerical technique to convectional flows has been obvious in recent years. The basic form of the lattice Boltzmann equation withan external force by introducing BGK approximations can be written as follows for both the flow and the temperature fields [35]:

$$f_i\left(x + c_i\Delta t, t + \Delta t\right) - f_i(x,t) = -\frac{1}{\tau_f}\left[f_i(x,t) - f_i^{eq}(x,t)\right] + \Delta t F_{ei} \quad (2)$$

$$g_i\left(x + c_i\Delta t, t + \Delta t\right) - g_i(x,t) = -\frac{1}{\tau_g}\left[g_i(x,t) - g_i^{eq}(x,t)\right]$$

Where f_i and g_i are particle distribution function (PDF) and internal energy particle distribution function (EPDF), respectively. f_i^{eq} and g_i^{eq} are the equilibrium distribution functions (EDF) for f_i and g_i respectively, and are given as:

$$f_i^{eq} = \omega_i \rho \left[1 + \frac{e_i u}{c_s^2} + \frac{uu : (e_i e_i - c_s^2 I)}{2 c_s^4}\right]$$

$$g_i^{eq} = \omega_i \rho \left[1 + \frac{e_i u}{c_s^2}\right]$$

where Δt is the lattice time step size, τ_e and are the dimensionless collision–relaxation times for the flow and internal energy, respectively. In this study, the two-dimensional nine-bit model (D_2Q_9) is used. The discrete velocities (e_i) are given in model D_2Q_9 by:

$$e_0 = (0, 0),$$

$$e_i = c\left[\cos\left(\frac{(i-1)\pi}{2}\right), \sin\left(\frac{(i-1)\pi}{2}\right)\right], \text{ for } i = 1, 2, 3, 4$$

$$e_i = \sqrt{2}c\left[\cos\left(\frac{(2i-9)\pi}{4}\right), \sin\left(\frac{(2i-9)\pi}{4}\right)\right], \text{ for } i = 5, 6, 7, 8$$

Boundary conditions in the LBM

a. Dynamic Boundaries with LBM

Boundary conditions are very important for the accuracy and stability of LBM simulation. Since the inlet velocity of the flow is specified, the inward distribution functions should be computed at the boundary. In the D_2Q_9 model, the values of the distribution functions pointing out of the domain (Fig.3) at the inlet boundary, the only unknowns are (f_1, f_5, f_8) as well as the fluid density ρ. Following the work of Zou and He [47], the inlet density and the distribution functions can be expressed as follows:

$$\rho_{in} = \frac{f_0 + f_2 + f_4 + 2(f_3 + f_6 + f_7)}{1 - u_{in0}}$$

$$f_1 = f_3 + \frac{2}{3} u_{in0}$$

$$f_5 = f_7 - \frac{1}{2}(f_2 - f_4) + \frac{1}{6} u_{in0} + \frac{1}{2} v_{in0}$$

$$f_8 = f_6 + \frac{1}{2}(f_2 - f_4) + \frac{1}{6} u_{in0} - \frac{1}{2} v_{in0}$$

An extrapolation scheme is used to simulate the outlet flow condition, which can be represented as:

$$f(n, j, 3) = 2f(n-1, j, 3) - f(n-2, j, 3)$$

$$f(n, j, 6) = 2f(n-1, j, 6) - f(n-2, j, 6)$$

$$f(n, j, 7) = 2f(n-1, j, 7) - f(n-2, j, 7)$$

The bounce-back scheme is used to specify the boundary conditions for north, south and stepped wall, the distribution functions pointing to the fluid are equal to those pointing out of the domain. $f_2 = f_4$, $f_5 = f_7$, $f_6 = f_8$

b. Thermal Boundaries with LBM

The left-hand boundary (channel inlet) is kept at a constant temperature(Dirichlet boundary condition) and set to a dimensionless value of 1. Therefore, theresulted equations of the unknown distribution functions on the left boundaryare obtained using the following equation:

$$g_1 = \frac{\tau_e}{\tau_e + \tau_3}(\tau_e + \tau_3 - 2)\, g_3$$

$$g_5 = \frac{\tau_e}{\tau_e + \tau_6}(\tau_e + \tau_6 - 2)\, g_7$$

$$g_8 = \frac{\tau_e}{\tau_e + \tau_6}(\tau_e + \tau_6 - 2)\, g_6$$

with θ_e is the dimensionless temperature in the inlet. The north and south wall are maintained at a constant wall temperature, $2\theta_e$, the unknown distribution functions areobtained using the following equations:

$$g_4 = 2\theta_e(\omega_4 + \omega_2)\, g_2$$

For north wall:

$$g_7 = 2\theta_e(\omega_7 + \omega_5)\, g_5$$

$$g_8 = 2\theta_e(\omega_8 + \omega_6)\, g_6$$

For south wall: $g_{i+2} = T_w(\omega_i + \omega_{i+2})\, g_i, i = 6,5,2.$

For the adiabatic boundary condition, the gradient of the dependent variable normal to the boundaryshould be zero, $\partial\theta/\partial Y=0$. The distribution functions for the right-hand side boundary(channel outlet) as follows:

$$g_i^{n+1}(x, l) = g_i^{n+1}(x, l+1)$$

IV. Results and Discussions

Validation of the model

In order to validate the present numerical code based onthe Lattice Boltzmann Method (LBM), our numerical results were quantitatively compared to the published onesfor several cases. The first one concerned an experimental study dealt with analytical solution (axial velocity) and Haddel et al (Nusselt number).

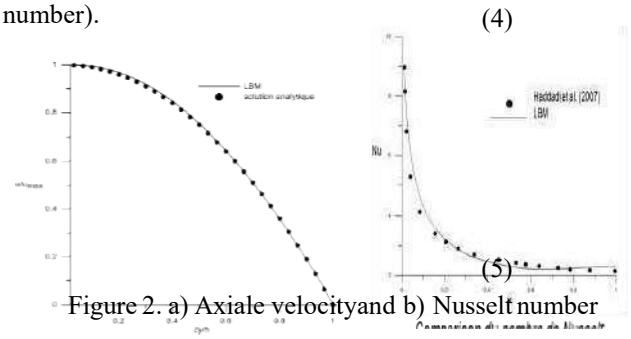

Figure 2. a) Axiale velocityand b) Nusselt number

The Nusselt number and axial velocity for poiseuille flow for Re = 200 are shown in figure 2. The results of LBM model is

in good agreement with the results of Haddadi et al., and the analytical solution.

Rectangular channel

In this section, our attention is focused on the influence of great number of parameters on flow and heat transfer behaviors in a rectangular channel. Some of them are kept constant. All computations are conducted for water (Pr =0.71).

(a)

(b)

(c)

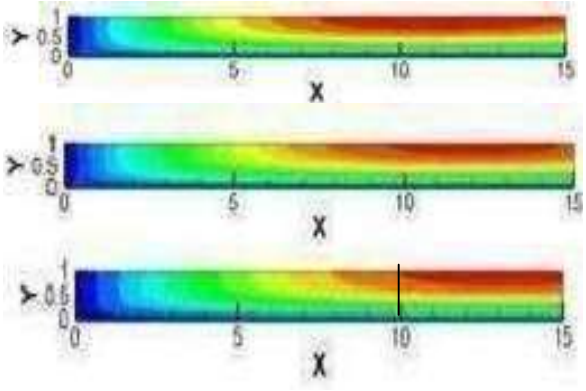

Figure 3: Temperature profile for Re=200 at volume fraction a) 1%, b)2% and c) 4%

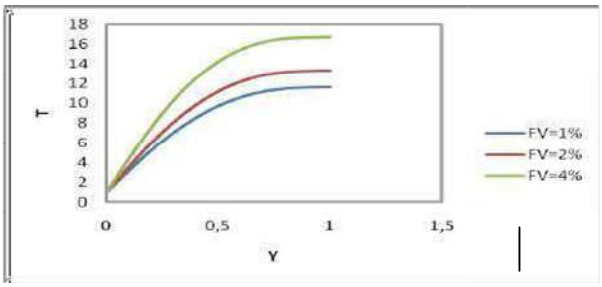

Fig.4: profile of temperature for different volume fraction

The temperature is 15 times greater for a volume fraction of Cu=4% and for a Reynolds number equal to 200.
The temperature is more important when approaching the upper wall for y=10x.

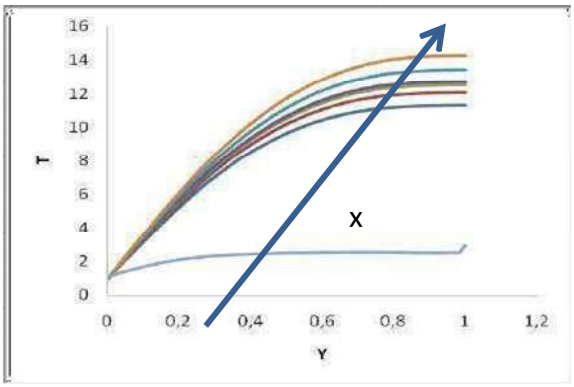

Fig.5: profile of temperature for positions x

Effect of separated and reattached flow

Fig. 6: Geometry of separation and attached flow

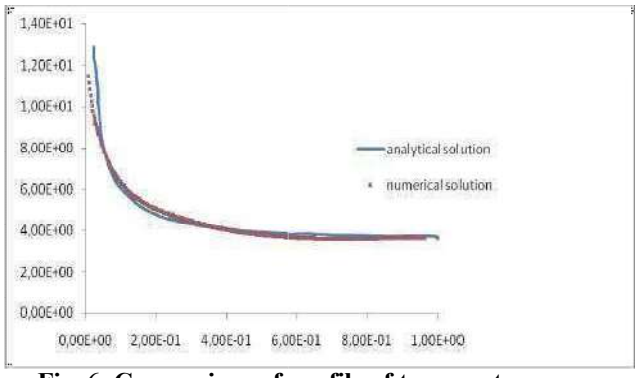

Fig. 6: Comparison of profile of temperature

(a)

(b)

(c)

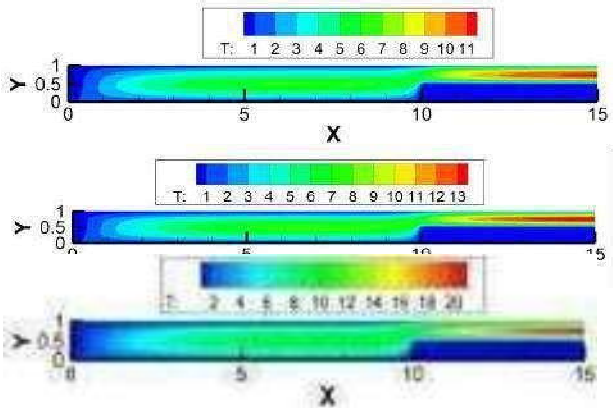

Figure 3: Temperature profile for Re=200 at volume fraction a) 1%, b)2% and c) 4%

V. CONCLUSIONS

The Lattice Boltzmann Method has been used to simulate poiseuil flow and heat transfer of forced convection in a separation and attached flow. The results show that using flow this geometrie, as an active wayto enhance heat transfer is an

important consequence. It caused the movement of maximum heat transfer on the higher wall with lower nanoflow content. The index of performance is about 3 for only 1% of nanofluids.

ACKNOWLEDGMENT

This work was financially supported by the "PHC Utique 2022" program number 47613ND of the French Ministry of Foreign Affairs and Ministry of higher education, research and innovation and the Tunisian Ministry of higher education and scientific research in the CMCU project number CMCU 22G1102. There is a lot of gratitude for these two supporters.

REFERENCES

[1] MohamoudJama, Tejvir Singh, Seifelislam Mahmoud Gamaleldin, MuammerKoc, Ayman Samara, J. Rima Isaifan, and A. MuatazAtieh, J. Nanomaterials 2016, 6717624 (2016).

[2] Rahgoshay, M., Ranjbar, A.A. and Ramiar, A. (2012) 'Laminar pulsating flow of nanofluids in a circular tube with isothermal wall', Int. Commun. Heat Mass Transfer, Vol. 39, No. 3,pp.463–469.

[3] Akdag, U., Akcay, S. and Demiral, D. (2014) 'Heat transfer enhancement with laminar pulsating nanofluid flow in a wavy channel', Int. Commun. Heat Mass Transfer, December, Vol. 59, pp.17–23.

[4] F. IlamiDoshmanziari · A. E. Zohir · H. RamezaniKharvani · D. Jalali-Vahid· M. R. Kadivar, Characteristics of heat transfer and flow of Al2O3/water nanofluid in a spiral-coil tube for turbulent pulsating flow, Heat Mass Transfer (2016) 52:1305–1320P.

[5] P. Naphon , S. Wiriyasart, T. Arisariyawong, Artificial neural network analysis the pulsating Nusselt number and friction factor of TiO2/water nanofluids in the spirally coiled tube with magnetic field,International Journal of Heat and Mass Transfer 118 (2018) 1152–1159

[6][6]

[7] UnalAkdag, Selma Akcay and DoganDemiral, Heat transfer enhancement with nanofluids under laminar pulsating flow in a trapezoidal-corrugated channel, Progress in Computational Fluid Dynamics, Vol. 17, No. 5, 2017

[8][8]

[9] Mohammad Jafari, MousaFarhadi ,KouroshSedighi, Convection heat transfer of SWCNT-nanofluid in a corrugated channel under pulsating velocity profile ,International Communications in Heat and Mass Transfer 67 (2015) 137–146

[10][10]

[11] V.K. Karthikeyan , K. Ramachandran , B.C. Pillai , A. Brusly Solomon, Effect of nanofluids on thermal performance of closed loop pulsating heat pipe, Experimental Thermal and Fluid Science 54 (2014) 171–178

[12] Mohammad AlhuyiNazaria, RoghayehGhasempoura, Mohammad Hossein Ahmadib, GholamrezaHeydarianc, Mohammad BehshadShafiic, Experimental investigation of graphene oxide nanofluid on heat transfer enhancement of pulsating heat pipe, International Communications in Heat and Mass Transfer 91 (2018) 90–94

[13] PaisarnNaphon , Songkran Wiriyasart, Experimental study on laminar pulsating flow and heat transfer of nanofluids in micro-fins tube with magnetic fields,International Journal of Heat and Mass Transfer 118 (2018) 297–303

[14] Qingping Wu, RongjiXu ,Ruixiang Wang , Yanzhong Li, Effect of C60 nanofluid on the thermal performance of a flat-plate pulsating heat pipe ,International Journal of Heat and Mass Transfer 100 (2016) 892–898.

[15] H. Bararnia, S. Soleimani, D.D. Ganji, Lattice Boltzmann simulation of natural convectionaround a horizontal elliptic cylinder inside a square enclosure, Int. Commun.Heat Mass Transfer 38 (2011) 1436–1442.

[16] M. Jafari, M. Farhadi, K. Sedighi, Effect of wavy wall on convection heat transfer ofwater-Al2O3 nanofluid in a lid-driven cavity using lattice Boltzmann method, Int. J.Eng. Trans. A 25 (2012) 168–180.

[17] A.Mohamad, Applied lattice Boltzmann method for transport phenomena,momentum,heat and mass transfer, SurePrinting,, Calgary, 2007.

[18] Q. Zou, X. He, On pressure and velocity boundary conditions for the lattice BoltzmannBGK model, Int. J. Phys. Fluids 6 (1997) 1591-1598.

REFERENCES

[19] Cun-quan Zhang, Cheng Zhong, Theoretical modeling of a gas clearance phase regulation mechanism for a pneumatically-driven split-Stirling-cycle cryocooler, Cryogenics 66, 13-23, (2015).

[20] Cun-quan Zhang, Cheng Zhong, Experimental study of a gas clearance phase regulation mechanism for a pneumaticallydriven split-Stirling-cycle cryocooler, Cryogenics 66, 24-33, (2015).

[21] Jose Leon Salazar, Wen-Lih Chen, A computational fluid dynamics study on the heat transfer characteristics of the working cycle of a β-type Stirling engine, Energy Conversion and Management, 88 , 177-188 (2014).

[22] Zhigang L., Yoshihiko H., Yohei K., Dawei T., Analysis of a high-performance model Stirling engine with compact porous-sheets heat exchangers, Energy, 64, 31-43, (2014).

[23] Hachem H., Gheith R., Aloui F., Ben Nasrallah S., A CFD Analysis of the Air Flow through the Stirling Engine's Singularities. 7th international Exergy,Energy and Environment Symposium , (2015).

[24] Wen-Lih Chen, King-Leung Wong, Li-Wen Po. A numerical analysis on the performance of a pressurized twin power piston gamma-type Stirling engine. Energy Conversion and Management. Volume 62, 2012, 84-92.

[25] Wen-Lih Chen, Yu-Ching Yang, Jose Leon Salazar. A CFD parametric study on the performance of a low-temperaturedifferential γ-type Stirling engine. Energy Conversion and Management, Volume 106, 2015, 635-643.

[26] Hachem, H., Gheith, R., & Aloui, F. (2022). Theoretical investigations of Stirling engine performances for different filling gas properties. International Journal of Energy Research.

[27] Hachem, H., Gheith, R., Aloui, F., Nasrallah, S. B., & Dincer, I. (2016). Exergy assessment of heat transfer inside a Beta type Stirling engine. International Journal of Exergy, 20(2), 186-202.

[28] Hachem, H., Gheith, R., Aloui, F., Delprat, S., & Paganelli, S. (2019). Energetic and exergetic investigations of an innovative heat recovery exhaust system using a double acting type Stirling engine based on theoretical analysis. International Journal of Exergy, 28(3), 273-300.

[29] Hachem, H., Gheith, R., Aloui, F., & Nasrallah, S. B. (2018). Technological challenges and optimization efforts of the Stirling machine: A review. Energy conversion and management, 171, 1365-1387.

[30] Hachem, H., Gheith, R., Aloui, F., Nasrallah, S. B., & Wang, M. (2018). A CFD Analysis of the Air Flow Through the Stirling Engine's Singularities. In Exergy for A Better Environment and Improved Sustainability 1 (pp. 271-287). Springer, Cham.

[31] Hachem, H., Gheith, R., Aloui, F., & Nasrallah, S. B. (2015). Numerical characterization of a γ-Stirling engine considering losses and interaction between functioning parameters. Energy conversion and management, 96, 532-543.

[32] Hachem, H., Creyx, M., Gheith, R., Delacourt, E., Morin, C., Aloui, F., & Ben Nasrallah, S. (2015). Comparison based on exergetic analyses of two hot air engines: A Gamma type Stirling engine and an open joule cycle Ericsson engine. entropy, 17(11), 7331-7348.

[33] Cheng, C. H., and Chen, Y. F. (2017). Numerical simulation of thermal and flow fields inside a 1-kW beta-type Stirling engine. Applied Thermal Engineering, 121, 554-561.

[34] Valenti, G., Silva, P., Fergnani, N., Di Marcoberardino, G., Campanari, S., and Macchi, E. (2014). Experimental and numerical study of a micro-cogeneration Stirling engine for residential applications. Energy Procedia, 45, 1235-1244.

PLL grid synchronization and Dc-link voltage regulation for wind energy conversion system

Boukhili Farhat
ISET, Jendouba, Tunisia
ENSIT University of Tunis, LISIER Laboratory, Tunis, Tunisia
boukhilifarhat@yahoo.fr

Dami Mohammed Ali
ENSIT,
LISIER Laboratory,
Tunis, Tunisia
medalidami@yahoo.fr

Zaafouri Abderrahmen
ENSIT,
LISIER Laboratory,
Tunis, Tunisia
Abderrahmen.zaafouri@isetr.rnu.tn

Bahi Tahar
Badji Mokhtar University
Annaba 23000, Algeria
LASA Laboratory.
tbahi@hotmail.fr

Abstract— nowadays we are witnessing the expansion of the installation of energy conversion systems based on renewable resources thanks to their remarkable advantages. Indeed, they are considered as the indisputable solution for the replacement of production systems based on fossil fuels (coal, oil, etc.). However, it is within this framework that the contribution of the work presented by this paper fits. He presents the study of of the synchronization system to ensure a desired frequency and a DC-link voltage regulation in a variable speed wind energy conversion system in order to investigate the enhanced control and operation of wind power generation systems based on permanent magnet synchronous generator . Since these systems are in the most designed to be connected to the grid through a power converter. In this purpose, it is necessary to regulate the DC-link voltage of the capacitor, placed between the AC/DC and DC/AC converters at a desired value. In this work, the wind conversion system is studied, simulated and discussed in Simulink/Matlab software environment.

Keywords—wind turbine; PMSG; DC-link voltage control; simulation.

I. INTRODUCTION

The need of electric energy is clearly increasing worldwide [1, 2]. Indeed, this energy is necessary to guarantee a comfortable for the humanity and to ensure a respectable economic development. However, because of the undisputed depletion and close to fossil reserves (oil, gas, coal, ...) on the one hand and the pollution on the other hand that is due to their use, the encouragement of exploitation of Renewable energy resources (wind, solar, biomass, ...), emerged to be essential because they have no consequences for humanity and the environment. Among these sources, wind energy is the most promising because it represents an enormous field and their capabilities to operate at variable speed with high energy efficiency [3]. The variable speed operation permits to increase the energy efficiency, to reduce the mechanical efforts and get better the electrical energy's quality produced. It is the development of the electronic variators which makes it possible to control the rotation speed of the wind turbines at everymoment. Wind is a random size, of a veryfluctuating nature [4, 5]. The variations in the resulting power of wind fluctuations are the main disturbance of the wind energy conversion chain.

Currently, the development of renewable energy conversion system required a rectifier voltage regulation by using a DC-link capacitor which plays a very important role in variable-speed wind energy conversion systems. The proposed conversion system is based on a permanent magnet synchronous generator (PMSG), directly driven by a wind turbine and connected to three-phase voltage rectifier [6]. Pulse width modulation (PWM) converter control adopted in the way to obtain a sufficient voltage across the capacitor terminals and reducing the fluctuation caused by wind speed variations [7]. Considering in particular the rectifier output voltage adjustment, the obtained results shows the high performance of adopted regulation.

The following parts paper organized as follows: in section II we present the wind energy conversion system (WECS). In section III we develop the adopted mathematical model. Section IV is reserved for simulation results. In section V we finished by a conclusion.

II. CONVERSION SYSTEM

The structure studied from wind conversion system (WECS) is shows in Fig. 1. It is mainly composed of the wind turbine equipped with a synchronous generator with permanent magnet which delivers an alternating voltage which is rectified by the rectifier controlled in pulse width modulation, of the control loop of this last voltage and of a PI speed controller. The conversion chain is composed by permanent magnet synchronous generator (PMSG) while the rotor is coupled to the wind turbine while the stator is connected to three-phase rectifier supplying a capacitor plugged in at its output when grid voltage is associated phase-locked loop system . The maximum power point tracking (MPTT) [3, 8] provide the permanent magnet synchronous generator speed reference W_{g_ref} which is compared to the generator real speed $W_{g.}$ Moreover, the voltage dc-link and its reference respectively designed by V_{dc_ref} and V_{dc} are as well compared in order to control the converter.

ISSN: 1737-9334

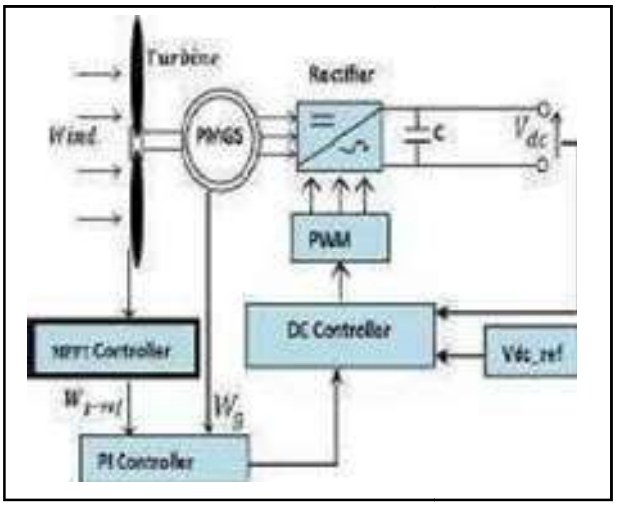

Fig. 1 Wind conversion system

III. MATHMATICAL MODELS

The desired PMSG speed is calculated using the following equation:

$$W_{g-ref} = \frac{V_t}{V_w} \quad (1)$$

The extracted mechanical power (V_V) and the torque produced (V_V) from the wind turbine; are respectively given by the following expressions [5]:

$$V_V = V_V(V, V).V.V.\frac{3}{2}.V_w^3 \quad (2)$$

$$V_V = \frac{V_V}{V_w} \quad (3)$$

Where,

Cp: aerodynamic coefficient;
V: tip speed ratio;
V: air density;
V_V: radius of wind generator;
V_w: ratio wind speed.

Moreover, the PMSG model in the *d-q* synchronously rotating reference frame can be given by[9, 10, 11]:

$$V_{iV} = V_V.i_V + V_g.V.w.i_V + \frac{1}{V}.V \quad (4)$$

$$\frac{V}{V} = -\frac{V}{V_g}.i_V - \frac{V}{V_g}.V.w.i_V - \frac{1}{V_g}.V.w.\phi_V + \frac{1}{V_V}.V_V \quad (5)$$

Where,

V : Pole pairsnumber;
R_a : armature resistance;
L_d , L_q : generator inductance components ;
i_d , i_q : current components;
u_d, u_q : voltage components;
φ_m : permanent magnet flux

The windturbine generator drive can writing with the following equation [12]:

$$V_V - V_{eV} = V.\frac{V\Omega}{VV} + f.\Omega \quad (6)$$

Where;
V_{eV}: is the electromagnetic torque;
J: moment of inertia;
f: is the turbine rotor friction.

IV. PHASE-LOCKED LOOP

The phase-locked loop (PLL) is an error signal feedback system based on the principle of synchronous rotating frame, low-pass filters and voltage-controlled oscillator, which is shown in following Fig 2.

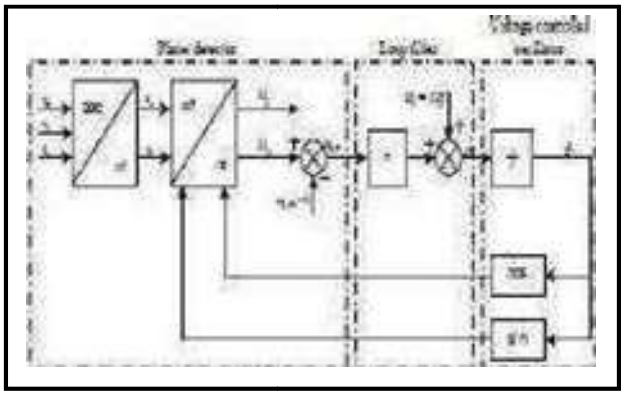

Fig. 2 Structure of three phase-locked loop

The principle consists in transforming the three phase voltages into their components V_d and V_q, set reference DC voltage of q-axis. Then the frequency will be got after PI controller and angle value after proposed controller. When utility voltage has only positive sequence fundamental components, the steady value of d-q coordinate is DC current, phase and frequency can be locked by controlling q-axis component zero and the mathematic expression is given by:

$$U_{abc} = U^{+}\begin{bmatrix}\cos wt \\ \cos(wt - 2\pi/3) \\ \cos(wt + 2\pi/3)\end{bmatrix} U^{-}\begin{bmatrix}\cos wt \\ \cos(wt + 2\pi/3) \\ \cos(wt - 2\pi/3)\end{bmatrix} \quad (7)$$

From the equation, U^{+}, U− shows positive and negative voltage amplitude separately, θ^{0}− shows negative sequence voltage initial phase angle relative to negative sequence voltage. After 3/2 conversion, the expressions of output voltage can be got in αβ static coordinate:

$$U = \begin{bmatrix}U & U\end{bmatrix}^T = T\ U_{abc} \quad (8)$$

Where,

$$T_{\alpha} = \frac{2}{3}\begin{bmatrix} 1 & \frac{1}{2} & \frac{1}{2} \\ 0 & \frac{\sqrt{3}}{2} & -\frac{\sqrt{3}}{2} \end{bmatrix} \quad (9)$$

After *dq* conversion to the synchronous coordinate system, we obtained:

$$\begin{cases} U'_{sd} = U_{sd}\cos(\theta) + U_{sq}\sin(\theta) \\ U'_{sq} = U_{sq}\sin(\theta) + U_{sq}\cos(\theta) \end{cases} \quad (10)$$

V. Simulation Results

The wind turbine, the characteristics of which are illustrated in Fig. 3, is connected to a distribution network supplying alternating loads. This being the case, the wind turbine follows a wind at variable speed such as the profile is illustrated by Fig 4. Then, the various measurements carried out on the installation are represented by figures 5 to 8, respectively, the speed of the synchronous generator permanent magnets as well as the offset angle of the turbine blades (see Fig 5 and Fig 6). In addition, the active and reactive powers are shown by figures7 and 8 and in turn the voltages and current of a network phase are represented by figure 9.

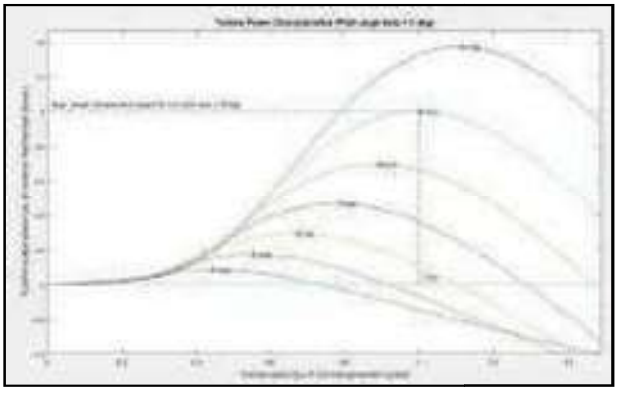

Fig. 3 Characteristics of the wind turbine

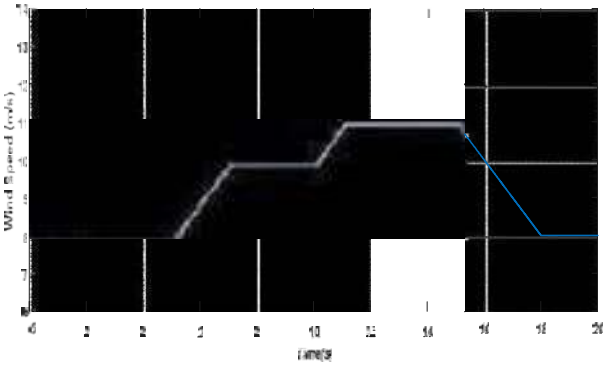

Fig. 4 Wind Speed

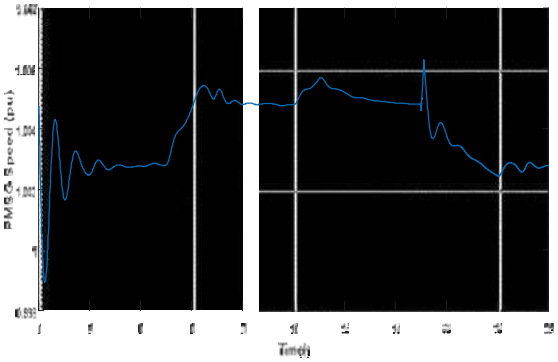

Fig. 5 PMSG Speed

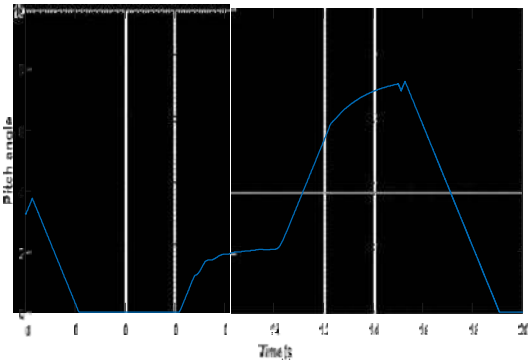

Fig. 6 Pitch angle

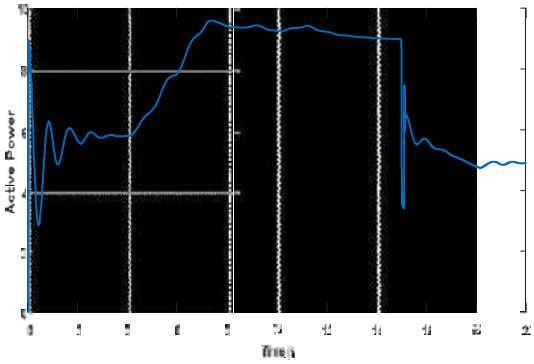

Fig. 7 Active Power waveforms

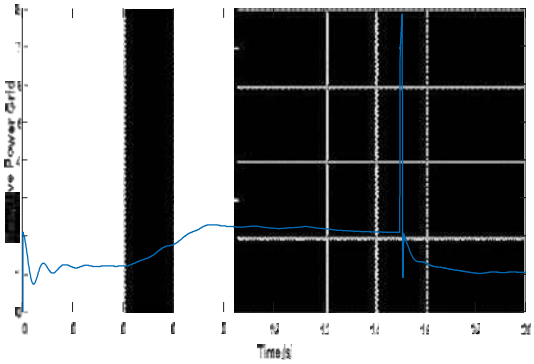

Fig. 8 Reactive Power waveforms

V. CONCLUSION

The analyze of control strategy or wind energy conversion system have been investigated in this work. The obtained simulations verify the efficiency of the used control. The different signals obtained and illustrated by this work have a behavior clearly influenced by the profile of the wind and the connection to the electrical distribution network as well as the control adopted.

REFERENCES

[1] Aditya Venkataraman ; Ali I. Maswood ; Nirnaya Sarangan ; Ooi H. P. Gabriel ,An Efficient UPF Rectifier for a Stand-Alone Wind Energy Conversion System, IEEE Transactions on Industry Applications, Volume: 50 , Issue: 2 , 2014.

[2] Venkata Yaramasu ; Apparao Dekka ; Mario J. Durán ; Samir Kouro ; Bin Wu ,PMSG-based wind energyconversion systems: survey on power converters and controls, IET Electric Power Applications, Volume: 11 Issue: 6 , 2017.

[3] F. Boukhili , A. Zaafouri, M.I. Dami, T. Bahi, Control of DFIG based wind turbine Connected to Grid, Proceedings of the International Conference on Recent Advances in Electrical Systems, Tunisia, 2018.

[4] Aditya Venkataraman ; Ali I. Maswood ; Nirnaya Sarangan ; Ooi H. P. Gabriel ,An Efficient UPF Rectifier for a Stand-Alone Wind Energy Conversion System, IEEE Transactions on Industry Applications, Volume: 50 , Issue: 2 , 2014.

[5] Yingjie Tan ; Kashem M. Muttaqi ; Phil Ciufo ; Lasantha Meegahapola, Enhanced Frequency Response Strategy for a PMSG-Based Wind Energy Conversion System Using Ultracapacitor in Remote Area Power Supply Systems, IEEE Transactions on Industry Applications, Volume: 53 , Issue: 1 ,2017

[6] Venkata Yaramasu ; Apparao Dekka ; Mario J. Durán ; Samir Kouro ; Bin Wu ,PMSG-based wind energy conversion systems: survey on power converters and controls, IET Electric Power Applications, Volume: 11 , Issue: 6 , 2017.

[7] M. Malinowski, « Sensorless control Strategies for Three- Phase PWM Rectifiers »; PhD Thesis, University of Technology, 2001.

[8] Shubham Khandelwal ; Ketan P. Detroja Controlled power point tracking for autonomous operation of PMSG based wind energy conversion system, Indian Control Conference (ICC), 2017

[9] Omessaad Elbeji, Mouna Ben Hamed, Lassaad Sbita, International Journal of Modern Nonlinear Theory and Application, 2014, 3, 88-97

[10] Yin, M., Li, G., Zhou, M. and Zhao, C. (2007) Modeling of the Wind Turbine with a Permanent Magnet Synchronous Generator for Integration. IEEE, Power Engineering Society General Meeting, Tampa, 24-28 June 2007, 1-6.

[11] Chen, X.F., Shu, Z.B. and Zhao, Y.K. (2005) Mathematic Model and Performance Analysis of PMSM, Based Servo System. Journal of Mechanism and Electronics, 1, 1-43.

[12] Carranza, O., Figueres, E., Garcera, G. and Gonzalez-Medina, R. (2013) Analysis of the Control Structure of Wind Energy Generation Systems Based on a Permanent Magnet Synchronous Generator. Applied Energy, 103, 522-538. http://dx.doi.org/10.1016/j.apenergy.2012.10.015.

[13] Song, Y.; Dhinakaran, B.; Bao, X. Variable speed control of wind turbines using nonlinear and adaptive algorithms. J. Wind Eng. Ind. Aerodyn. 2000, 85, 293–308.

[14] Ghodbane-Cherif, M.; Skander-Mustapha, S.; Slama-Belkhodja, I. An improved predictive control for parallel grid-connected doubly fed nduction generator-based wind systems under unbalanced grid conditions. Wind Eng. 2019, 43, 377–391.

[15] Sahri, Y.; Tamalouzt, S.; Lalouni Belaid, S.; Bacha, S.; Ullah, N.; Ahamdi, A.A.A.; Alzaed, A.N. Advanced Fuzzy 12 DTC Control of Doubly Fed Induction Generator for Optimal Power Extraction in Wind Turbine System under Random Wind Conditions, 2021, 13, 11593.

Le Dimensionnement Optimal pour la Production de l'Electricité dans les Mini-Réseaux de l'Algérie : Cas de Debdeb

Dahmani Souria[#1], Mouhoubi Aïssa[*2]

[#]*Département des Sciences Economiques, Université A. Mira de Bejaia*
Copmus Aboudaou, N9, Tala Hamza. Bejaia. Algérie

[1]souria.dahmani@univ-bejaia.dz
[2]aissa.mouhoubi@univ-bejaia.dz

Résumé— **L'énergie électrique produite dans les mini-réseaux des Réseaux du Grand Sud de l'Algérie est générée par des systèmes basés sur des centrales diesel et des turbines à gaz. Par ailleurs, le potentiel solaire important dont dispose le Sud et les difficultés techniques liés aux centrales conventionnelles, ont poussé les autorités à entreprendre des politiques énergétiques visant l'intégration des systèmes hybrides dans les localités reculées des 33 RGS. Les systèmes hybrides de production d'électricité dans les mini-réseaux des RGS est une solution d'électrification viable pour assurer une alimentation électrique sans interruption.**

Ce projet de thèse présente une étude de faisabilité d'une conception optimale d'un système hybride PV- diesel sans stockage pour améliorer le service d'accès à l'électricité dans la localité de Debdeb. Homer Pro est utilisé pour simuler la configuration la plus rentable, compte tenu des coûts de fonctionnement du système sur la durée de vie du projet en procédant à l'évaluation technico-économique de la solution optimale sélectionnée. Cette démarche consiste à minimiser le coût actualisé de l'énergie (LCOE).

L'analyse de sensibilité a été effectuée sur le système pour évaluer l'impact des variations des prix de carburant et du coût d'investissement du PV sur la capacité du PV optimale et le coût unitaire de l'électricité. Le LCOE au prix moyen à l'international du gasoil est de 0,0783$/ kWh et 0,283$/kWh aux prix national (subventionnée). L'analyse comparative entre le système diesel déjà existant et le système hybride obtenu, a montré que le système hybride est plus rentable et économise la consommation du gasoil en augmentant la durée de vie des DG.

Mots clés :

***Mots-clés*— l'énergie électrique, énergies renouvelables, RGS, mini-réseaux, systèmes hybrides.**

I. INTRODUCTION

L'accès médiocre à l'énergie et la limitation de la consommation électrique dans les régions reculées et isolées du monde font la nécessité de déployer une combinaison de solutions autonomes (Bustos & Watts, 2017, p. 206) afin d'améliorer la couverture des réseaux électriques et assurer une qualité de vie meilleure pour les populations. En 2020, environ 11% de la population mondiale, soit 640 millions, n'ont pas accès à cette énergie, particulièrement où l'électricité est requise pour satisfaire une demande locale (The World Bank, 2021). Une situation principalement prononcée dans les régions insulaires, les endroits arctiques et désertiques difficiles d'accès où les approvisionnements en énergie sont très coûteux, et les régions rurales des pays en développement. Selon l'AIE, 168 millions d'habitants indiens et 603 millions d'africains n'ont, carrément, pas accès à l'électricité (IEA, 2020).

Dernièrement, les réseaux autonomes, y compris les systèmes de mini-réseaux et de micros réseaux, sont devenus la meilleure solution d'électrification dans les régions isolées où l'extension du réseau principal n'est pas économiquement rentable. Ces systèmes ont pris de l'ampleur en tant qu'alternative plus viable et économique permettant la production en continue de l'énergie électrique et l'amélioration de la qualité de vie des habitants.

Dans la littérature, plusieurs études ont décrit les dimensionnements optimaux des systèmes hybrides dans les réseaux autonomes, et ont élaboré des stratégies de gestion de l'énergie pour des systèmes électriques autonomes utilisant des sources d'énergies renouvelables et le stockage. (Khan & al, 2017) ont présenté un examen approfondi de la production de l'électricité à partir de différents systèmes hybrides PV-éolien- diesel avec ou sans stockage pour les villes de Amritar, Ludhiana, Chandigarh, et Patiala à Pendjab en Inde. La plupart des travaux réalisés considèrent la réduction du coût total comme l'objectif principal. (Nasr & Nasr-Azadani, 2017) et (Rodríguez-Gallegos & al, 2018) ont évalué les performances de l'intégration d'une centrale PV dans un système diesel déjà existant et son impact sur la consommation du gasoil compte tenu de la contrainte de la réserve tournante, (Kellogg & al, 1998) ont présenté un algorithme dans le but de déterminer la capacité de production et le stockage optimaux nécessaires pour un système hybride PV- éolien pour un réseaux autonome dans la région de Montana.

(Yang & al, 2008) ont développé un dimensionnement optimal pour un système hybride PV- éolien accompagné d'un système de batterie. Le système autonome est basé sur l'algorithme de dimensionnement qui minimise le LCOE. (Kalinci & al, 2015), (Ipsakis & al, 2009) et (Blal & al, 2016)ont présenté une analyse technique et économique d'un

ISSN: 1737-9334

système hybride autonome à base d'énergie renouvelable avec une capacité de stockage d'hydrogène. (Rekioua & al, 2014) ont développé un système hybride PV avec une pile à combustible pour assurer la continuité de la production de l'électricité dans les zones isolées. (Khellif & al, 2012), (Khirennas & al, 2021) et (Berbaoui & al, 2020) ont proposé un algorithme d'ordonnancement pour optimiser le dimensionnement et le placement d'une centrale PV dans un système diesel autonome dans le Grand Sud de l'Algérie.

En l'Algérie, les Réseaux du Grand Sud (RGS) sont éloignés du réseau électrique national dont l'interconnexion est quasiment impossible vu les distances et le niveau de la demande. Ils sont alimentés en électricité par des mini-réseaux à base de turbines à gaz et des centrales diesel. Compte tenu des distances et des contraintes liées à l'environnement, des difficultés d'approvisionnement en combustible sont souvent observées, en plus de la nécessité d'escorter le gasoil par camions, sur des routes détériorées, souvent très longues, et le stocker de manière à assurer l'alimentation en continu des populations, engendrant par l'occasion un coût supplémentaire.

II. VUE D'ENSEMBLE SUR LES RGS

Les Réseaux du Grand Sud, constitués de multiples systèmes électriques autonomes, alimentant chacun une région du Grand Sud et atteignant les limites frontalières. Ils sont pourvus de centrales Diesel ou de gaz et de centrales solaires Photovoltaïques et desservent ces régions grâce à des réseaux moyenne et basse tensions (MT et BT). Ils alimentent à temps plein les localités dispersées du Grand Sud algérien avec une tension de distribution maximale de 30 KV (SKTM 2022).

A. Généralités sur les RGS

La loi N° 02-01 de 2002 apportant la règle de la suppression des monopoles publics exercé par SONELGAZ (Assoul, 2018), Shariket Kahraba wa Taket Moutadjadida, par abréviation SKTM, est la société de production d'électricité conventionnelle pour Réseaux du Grand Sud et des Energies Renouvelables pour le territoire national. Société par actions avec un capital souscrit en totalité par SONELGAZ et dont le siège social est situé à Ghardaïa, SKTM est chargée principalement du développement des infrastructures électriques du parc de production des Réseaux du Grand Sud, de l'engineering, de la maintenance et de la gestion des centrales électriques relevant de son champ de compétence. Elle est également chargée de la commercialisation de l'énergie produite pour les filiales de distribution, notamment, après le déploiement des énergies renouvelables sur le Réseau Interconnecté Nord (RIN).

Actuellement, les Réseaux du Grand Sud, comportent 33 localités non interconnectées (Fig. 1) alimentées par des turbines à gaz ou des groupes Diesel. Ces localités sont les suivantes :

− La région Sud-ouest (14 localités) : Ain Belbel, Bordj Badji Mokhtar, Béni Abbes, Oum Lassel, Site1, Site2, Site3, Site4, Tabelbala, Talmine, Tindouf, Timiaouine, Hassi Khebbi et Kerzaz.

− La région Sud Est (19 localités) : Afra, Bordj El Houas, Bordj Omar Driss, Debdeb, Djanet, El Goléa (El Menea), Idèles, In Guezzam, M'Guiden, Tamanrasset, Tinalkoum, Tinzaouatine, El Borma, Illizi, In Amenas, Tarat, Amguid, Moulaylahcen, Arak.

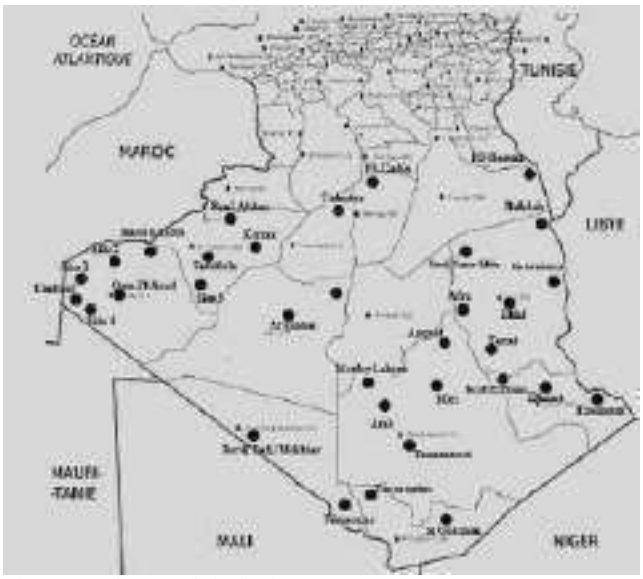

Fig 1 : carte des RGS de l'Algérie

Etant donnée la grande dispersion des agglomérations ainsi que les populations rurales du grand sud, les systèmes énergétiques dans les RGS reposent sur la production et la distribution d'énergie électrique localement par des groupes électrogènes diesel et des mini-réseaux. Cette solution est d'actualité car elle est moins coûteuse que le raccordement au réseau national (interconnecté).

B. Les Mini-Réseaux des RGS

Lorsque l'extension du réseau national n'est guère viable du point de vue économique, les principales options disponibles pour raccorder au réseau les populations privées d'accès à l'électricité sont le raccordement à de mini-réseaux distincts fonctionnant indépendamment du réseau principal et les systèmes de production autonomes qui alimentent les consommateurs individuels. De nombreux États dans le monde ont adopté la conception des systèmes hybrides/non hybrides pour la production de l'électricité et l'ont déployé dans des réseaux autonomes, particulièrement les mini-réseaux afin d'assurer un accès rentable à l'électricité pour les populations vivant dans des zones rurales, reculées ou isolées.

La technologie des sources d'énergies renouvelables déployées dépend de sa disponibilité. Le photovoltaïque solaire et l'éolienne sont les filières les plus développées dans les systèmes hybrides en raison de leur disponibilité dans les régions où ces communautés sont principalement situées, ainsi que de leurs coûts d'investissement en baisse rapide.

ISSN: 1737-9334

Les Réseaux du Grand Sud de l'Algérie sont alimentés en électricité par des mini-réseaux. Ils sont caractérisés par des capacités de production de faibles puissances et de petites infrastructures de transmission et de distribution consistantes qui peuvent couvrir la demande d'énergie électrique. Ces systèmes de réseaux indépendants sont appelé aussi systèmes horsréseau.

La demande d'électricité dans les RGS est principalement celle des ménages, des établissements publics et de petites entreprises. Elle progresse de 14,1% par an, principalement sous l'impulsion de la hausse de la demande des ménages (SKTM, 2022). Les centrales électriques diesel sont plus favorables pour alimenter à plein temps les RGS en raison de la facilité de leur conception et manipulation et du temps éphémère requis à leur démarrage. Malgré cela, elles sont incapables de satisfaire une surcharge pendant de longues périodes, ajoutant à ça, les coûts élevés d'exploitation et de maintenance, ce qui les rend non compétitives.

Les modes de production de l'électricité dans les RGS facilitent le déploiement des systèmes hybrides dans les mini-réseaux grâce à leur faible coût d'investissement par capacité de kilowatt et à leur grande fiabilité.

III. LA PRODUCTION DE L'ELECTRICITE DANS LES RGS

Le système d'agglomération du sud de l'Algérie se caractérise par une faible population et une charge d'électricité fluctuante au cours d'une journée, des saisons et de l'année. Pour répondre à la charge de pointe, les sites de production de l'électricité doivent sans cesse être approvisionnés. La capacité de production de chaque générateur diesel est limitée et le régime de fonctionnement de celui-ci influe grandement l'efficacité de la production en termes de kWh/litre. Les coûts de production varient en fonction de la station et du combustible utilisé, notamment danslesrégions des zones enclavées où le gasoil est utilisé.

A. Le Profil de Charge des Mini-Réseaux des RGS

Selon leur profil de demande, les localités du Grand Sud de l'Algérie sont presque toutes qualifiées de zones non industrialisées où les clients sont principalement des ménages, des bâtiments publics et de petites entreprises. De plus, les charges de pointe annuelles qui se produisent pendant la journée de la saison estivale sont beaucoup plus élevées que les charges moyennes.

L'évolution continuelle de la consommation dans une localité des RGS est présentée comme étant une courbe de charge (Fig. 2). Cette dernière retrace l'ensemble des puissances mesurées en valeur moyenne sur une durée déterminée (10 minutes par exemple) pendant un intervalle de temps défini.

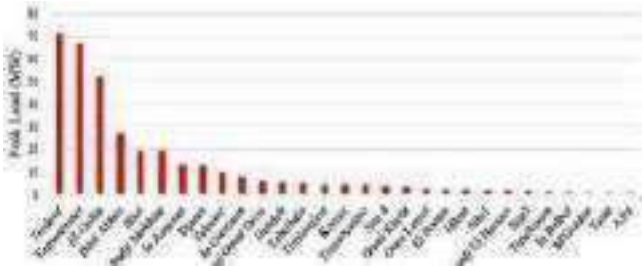

Fig. 2 : Charge de pointe en 2019 dans chacun des mini-réseaux des RGS.

Les charges de pointe atteintes au cours de l'année 2019 dans les mini-réseaux des RGS sont comprises entre 1 MW et 30 MW sauf pour les mini-réseaux d'Ain Belbel, M'guiden, Tarat et Afra où les pointes de charges ont été inférieures à 1 MW. Dans les localités de Tindouf, Tamanrasset et El-Goléa ces valeurs respectives ont dépassé 50 MW.

B. Le Parc de Production des RGS

L'électricité produite dans les mini-réseaux des RGS à l'exception des capacités photovoltaïques récemment installées, est assurée par des centrales électriques locales à base de combustibles fossiles composées de plusieurs unités de groupes diesel (DG) et/ou turbines à gaz (TG). Dans certaines localités et en cause d'anomalie, les turbines à gaz fonctionnent au diesel à la place du gaz naturel car le carburant n'est pas disponible.

La continuité de l'approvisionnement en électricité étant prioritaire, les systèmes de production d'électricité à base de combustibles fossiles sont dimensionnés pour répondre aux pics de charge avec une redondance suffisante qui tient compte de l'éloignement des localités. Par conséquent, les centrales sont continuellement renforcées avec des unités DG et/ou GT supplémentaires ; sinon de nouveaux sont construits.

Les centrales électriques composant les systèmes de production d'électricité des mini-réseaux du Grand Sud algérien sont exploitées par SKTM tandis qu'une autre filialeà 100 % de Sonelgaz, à savoir la Société Algérienne de Distribution de l'Electricité et du Gaz (SADEG), exploite les réseaux de distribution locale 30 kV-400/230 V et commercialise l'électricité auprès des clients.

La capacité totale installée dans tous les mini-réseaux du Grand Sud de l'Algérie est évalué en début de 2022 à 977 MW ; dont plus de la moitié (58 %) fonctionne au diesel, 38% en gaz. La partie de la source photovoltaïque est constituée de 4% de la capacité, autrement dit, des 37 MWc, entre autre, celles de Tamanrasset, Tindouf, Djanet, Timiaouine et Bordj Badji Mokhtar ajoutées aux systèmes de production d'électricité.

Environ 4% de la capacité installée en 2022 est représentée par l'énergie photovoltaïque, un pourcentage significativement faible d'autant plus que d'importantes capacités à base d'énergie fossile s'ajoutent chaque année pour

ISSN: 1737-9334

faire face à la croissance constante de la demande d'électricité dans les localités du Grand Sud de l'Algérie.

Le bilan de production de l'électricité de 2021 montre que le diesel représente 49% de l'électricité totale livrée, le gaz naturel contribue de 47 %, tandis que 4% provient de la capacité photovoltaïque installée.

Les systèmes hybrides dans les RGS de l'Algérie sont caractérisés par des systèmes PV- diesel sans stockage et à faible pénétration du PV. Ils sont composés de centrales diesel multi-unités avec des groupes électrogènes diesel (DG) de différentes tailles installées soit dans une salle des machines, soit dans des conteneurs extérieurs séparés et une centrale photovoltaïque (Khirennas & al, 2021, p. 3).

IV. LE MIX-ENERGETIQUE DANS LES MINI-RESEAUX DES RGS

L'objectif clé du programme national pour la promotion des énergies renouvelables et de l'efficacité énergétique lancé par le gouvernement algérien est l'exploitation du potentiel solaire et la diversification des sources de production d'électricité dans les mini-réseaux du grand sud ainsi que dans les deux autres réseaux.

L'expérience de l'intégration de systèmes photovoltaïques dans la production d'électricité des mini-réseaux des RGS a débouché sur des systèmes hybrides PV- diesel à l'échelle MW dans les localités de Tamanrasset, Tindouf et Djanet en tant que premiers projet réalisés.

A. Le Potentiel Renouvelable Solaire dans le Sud de l'Algérie

Dans tous les bassins méditerranéens, il existe un gigantesque réservoir d'énergie solaire dans le nord de l'Afrique et particulièrement dans la région sud de l'Algérie. Le potentiel de ce type d'énergie dans le grand sud de l'Algérie est le plus important (Tab. 1). La durée d'ensoleillement de la quasi-totalité du territoire national dépasse 2000 h annuellement et atteint 3900 h (hautes plaines et Sahara). L'énergie reçue quotidiennement sur une surface horizontale de 1 m2 est d'environ 5 kWh sur la majeure partie du pays, soit près de 1700 kWh/m2/an au nord et 2263 kWh/m2/an au sud.

TABLEAU 1 : Taux d'ensoleillement du Grand Sud de l'Algérie

Surface (%)	Durée d'ensoleillement quotidienne moyenne (h)	Durée moyenne d'ensoleillement (h/an)	Energie moyenne reçue (kwh/m^2/an)	Densité d'énergie solaire journalière (kwh/m^2)
86	9.59	3500	2650	7.26

La constante solaire représente la quantité d'énergie solaire que recevrait, par unité de temps, un mètre carré de surface à la limite de l'atmosphère à incidence normale. Elle correspond au flux solaire ramené à la distance Terre- Soleil. En Algérie, sa moyenne annuelle est estimée à 2 650 KWh/m2.

En raison de la grande superficie et de la diversité climatique, l'Algérie dispose d'un fort potentiel d'énergie solaire, en particulier dans la région saharienne qui convient aux applications de l'énergie solaire comme le photovoltaïque. Le nombre d'heures annuelles d'ensoleillement est équivalent à 3 500h/an, soit presque 145 jours, 19 heures et 55 minutes d'ensoleillement.

La productivité moyenne annuelle (potentiel solaire) d'un (01) kW installé en PV, est donnée par site de production des RGS comme suit :

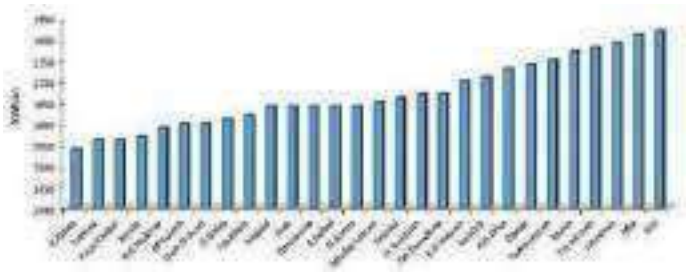

Fig. 3 : Potentiel solaire des RGS

Le potentiel solaire est quasiment disponible dans le grand sud de l'Algérie notamment dans les localités de la région du Sud-Est à l'exemple d'Illizi et Afra qui enregistrent de très hautes températures. Les températures très chaudes dans les RGS font que les systèmes de refroidissement (réfrigérateurs et climatiseurs) fonctionnent à plein temps, cela contribue à l'augmentation de la demande en électricité. Ceci dit, l'exploitation de l'énergie solaire dans ces zones permet la réduction de la consommation du diesel et l'économie d'énergie.

B. Le Déploiement des Systèmes Hybrides dans les RGS de l'Algérie

Les localités des RGS de l'Algérie sont alimentées en électricité par des systèmes de production d'électricité longuement constitués de centrales multi-unités de générateurs diesel et des turbines à gaz et cela jusqu'en 2015, l'année à laquelle trois centrales photovoltaïques ont été mises en service à Tamanrasset, Tindouf et Djanet. Ces centrales photovoltaïques dont les capacités installées respectives sont 13 MWc, 9 MWc et 3 MWc font partie du projet 343 MWc, qui constituent un extrait de la première phase de déploiement du programme national des énergies renouvelables (Fig. 4). SKTM a placé des contrats de réalisation de 23 centrales photovoltaïques dans les différentes régions du pays, réalisées entre 2015 et 2017 (SKTM, 2016).

ISSN: 1737-9334

L'hybridation des mini-réseaux du grand sud de l'Algérie, en l'occurrence, les trois centrales photovoltaïques fonctionnent avec succès en parallèle avec les centrales électriques à combustibles fossiles existantes. Ces systèmes hybrides imposent la tension et la fréquence du mini-réseau et les onduleurs PV s'auto-synchronisent avec eux et injectent autant de puissance photovoltaïque que disponible à moins que leur production ne soit volontairement réduite.

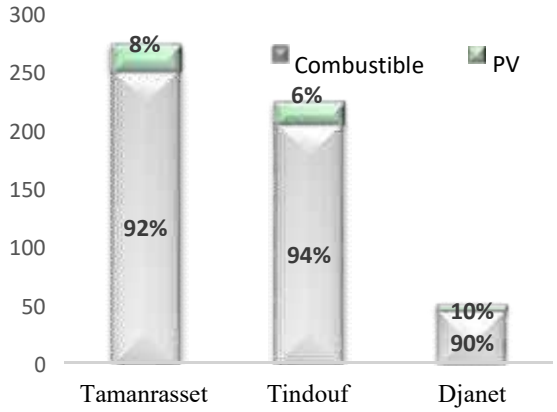

Fig. 4 : La part du PV dans l'électricité produite par les systèmes hybrides

La première centrale mise en service est celle de Djanet, le 19 février 2015. D'une puissance de 03 MWc, cette centrale est la première dans sa catégorie, elle est implantée dans la région de Tidjentouret, à l'entrée de Djanet dans la wilaya d'Illizi et s'étend sur une superficie de 5 hectares.

La centrale solaire de Tamanrasset est implantée sur une superficie de 26 hectares. Elle dispose de 4 092 panneaux photovoltaïques. L'investissement public alloué à la réalisation de ce projet est estimé à 2,6 Mds DZD (près de 19 M EUR).

La centrale électrique solaire de Tindouf a permis, depuis sa mise en service en janvier 2016, le renforcement de la production électrique générale dans la wilaya qui est passée à plus de 75 mégawatts tout en répondant à la demande locale en électricité de la population. D'une capacité de production de 9 mégawatts, celle-ci est implantée dans la région de Merkale (localité de Tindouf), et permis la rédaction les coûts de production de la principale centrale de Tindouf, fonctionnant au diésel et qui consomme quelque 6.000 litres/ jour de mazout (gasoil).

En 2019, environ 3% de la capacité installée est représenté par l'énergie photovoltaïque, un pourcentage significativement faible d'autant plus que d'importantes capacités à base d'énergie fossile s'ajoutent chaque année pour faire face à la croissance constante de la demande d'électricité dans les localités du Grand Sud algérien.

La production moyenne annuelle photovoltaïque des mini-réseaux hybrides de Tamanrasset, Tindouf et Djanet pour l'année 2019 sont respectivement de 8%, 6% et 10%. Leurs rendements énergétiques annuels spécifiques sont respectivement de 1 668 kWh/kWc, 1 532 kWh/kWc et 1 736 kWh/kWc. Des valeurs qui confirment l'énorme potentiel solaire des localités du Grand Sud de l'Algérie.

Par ailleurs, durant l'année 2019, 7 149 m3 du diesel et 7 542 615 m3 de gaz sont économisés grâce au fonctionnement de la centrale photovoltaïque de Tamanrasset. Plus encore, 5 400 m3 de gasoil ont été économisés à Tindouf. Quant à Djanet, la quantité du fossile économisée est 2 462 m3 de gasoil et 1 335 513 m3 du gaz naturel.

Au cours du troisième trimestre de 2021, deux autres centrales PV de 2 MWc et 10 MWc ont été installé dans les localités de Timiaouine et Bordj Badji Mokhtar. Ces centrales viennent s'ajouter au 8,4 MW et 61 MW des capacités des centrales fossiles existantes. La capacité totale des énergies renouvelables est évaluée au début de 2022 à 37 MWc.

V. MODERNISATION DU SYSTEME DE PRODUCTION D'ELECTRICITE A BASE DE DIESEL PAR UN DIMENSIONNEMENT OPTIMAL DU SYSTEME PV-DIESEL SANS STOCKAGE DANS LA LOCALITE DE DEBDEB

La faisabilité économique du système hybride est basée sur l'estimation des coûts d'installation, des coûts de remplacement, des coûts d'exploitation et d'entretien de tous les composants du système avec une grande fiabilité pour satisfaire la demande de charge. Le coût d'énergie par KW produit obtenu est considéré comme le prix minimum de l'électricité auquel le projet énergétique atteindra le seuil de rentabilité.

L'objectif d'optimisation est de minimiser le coût du système et de déterminer le dimensionnement optimal du système hybride en fonction de son coût unitaire. Les variables à optimiser compte tenu d'une très faible perte de charge sont : les capacités de la centrale PV, les générateurs diesel et les batteries de stockage si il y aura lieu et par conséquents les différents coûts de système.

Au sud de l'Algérie, le coût actualisé de l'électricité des centrales électriques au diesel est relativement très élevé en raison de son faible rendement par rapport aux autres centrales modernes. Les générateurs diesel (DG) consomment énormément de carburant, par conséquent, les coûts de maintenance et d'exploitation sont relativement élevés en raison des zones arides.

Dans ce qui suit, il est à étudier la faisabilité de l'hybridation de la centrale électrique diesel de la localité de Debdeb avec un système PV sans stockage dans lequel les performances des sous-systèmes sont simulées.

Debdeb est une commune appartenant à la daïra d'In Amenas. Située à 470 km au nord du chef-lieu d'Illizi et à proximité d'un poste frontière vers la Libye, elle est localisée dans le Sud-Est du Grand Sud. Debdeb est caractérisée par un climat désertique sec et chaud. Le nombre d'habitants à Debdeb est d'environ 5 481 habitants en 2020 avec une densité de 0,1 h/km². Comme tous les mini-réseaux du grand sud de l'Algérie, la localité de Debdeb est caractérisée par la particularité désindustrialisée de la zone. La consommation de

ISSN: 1737-9334

l'électricité est essentiellement celle des ménages avec les unités de ventilation et de climatisation comme poste le plus consommateur d'électricité principalement en saison estivale.

A. Simulation du Système Hybride Proposé

Afin de déterminer si le projet d'hybridation va être réalisé ou non, il faut estimer la création de valeur qu'il va générer. Lors de la réalisation d'un projet, les coûts d'investissement se distinguent de la simple dépense par le fait que ces derniers sont censés produire des effets positifs sur plusieurs années. Pour cela, il faut confronter les sommes qui vont être déboursés aux celles qui vont par la suite être encaissés et qui apparaitront à des dates différentes. Ceci impose d'avoir recours aux principes d'actualisation.

Les données météorologiques de l'emplacement de l'usine de production de l'énergie électrique de Debdeb ainsi que les données techniques liés à centrale diesel déjà existante sont utilisés comme des données d'entrée dans le logiciel de simulation « Hybrid Optimisation of Multiple Energy Ressources » HOMERPro par abréviation. Le logiciel a effectué des simulations horaires de toutes les combinaisons des composantes de la source d'énergie considérée et a évalué les coûts de fonctionnement des systèmes sur une période donnée.

Les données de l'irradiation solaire horaire utilisée dans HOMER sont fournies par le logiciel PV-GIS mis en place par la commission européenne en présentant des cartes d'ensoleillement (irradiation en kWh/m²) et de températures précises haute définition à travers les coordonnées géographiques du site étudié. Ensuite, une analyse technico-économique annuelle est appliquée pour tester la faisabilité de la centrale PV- diesel.

Le rayonnement solaire de Debdeb est bien réparti avec un rayonnement moyen de 6,25 kWh/m2/jour et un ensoleillement quotidien moyen de plusieurs heures sur le site.

Le rayonnement reçu est très élevé et peut dépasser 8,3 kWh/m2/jour pendant la période estivale, ce qui rend l'utilisation de systèmes hybrides dans la région très attrayante.

Dans le processus de simulation, Homer équilibre entre la demande et l'offre de l'énergie et calcule la faisabilité de toutes les configurations du système hybride pour optimiser le moindre coût d'électricité généré dans le système.

Le coût en capital initial d'un composant est le coût d'installation de ce dernier au début du projet. Pour les trois composantes (générateurs diesel, PV, et onduleurs), le coût d'investissement en ($/kW) est exprimé en fonction de la capacité du système (en kW) par une loi de puissance.

L'optimisation des systèmes hybrides implique la conception et la planification de l'exploitation de ce dernier, la formule du coût actualisé de l'énergie traduit en anglais de Levelized Cost Of Energy (LCOE) développée ci-après englobe à la fois les coûts fixes et les coûts variables des composants, tous ramenés à la première année en utilisant un taux d'intérêt réel (%) qui prend en compte le taux d'inflation.

Le coût actualisé de l'énergie (LCOE) est définit comme le coût moyen par kWh d'énergie électrique utile produit par le système. Dans la formulation du LCOE, les paramètres macroéconomiques doivent préalablement être définis intrinsèquement ; la durée de vie du projet (années), le taux d'intérêt nominal en %, le taux d'inflation annuel en %, les coûts d'acquisition, d'exploitation et de remplacement des différentes composantes du système hybride à simuler.

B. Les Résultats de Simulation

Le système hybride proposé est un système PV- diesel sans capacité de stockage et les capacités des générateurs pris en compte sont liées à la charge de pointe enregistrée à Debdeb en 2020 et qui est de 5400 kW.

Afin d'assurer la circulation de l'énergie entre les composants du système hybride, l'onduleur est utilisé pour convertir l'énergie électrique du courant continu (CC) en courant alternatif (CA).

L'efficacité de l'onduleur est de 95% pour toutes les tailles des composants.

Basés sur le coût actualisé de l'énergie le plus bas, les résultats de simulation sont classés et filtrés par type de système et répertoriés dans le tableau des résultats d'optimisation de toutes les simulations réalisables pour le cas de sensibilité sélectionné. En se basant sur le prix non subventionnée du gasoil fixé au prix moyen à l'international de 1,2$, le tableau retrace la simulation pour le prix du gasoil de 1,2$/l sans compter les coûts de transport.

Dans le processus d'optimisation, chaque configuration des 31 configurations du système est simulée. Le résultat optimal obtenu est lorsque le système se compose d'une centrale PV de 6500kW (6,5 MW) couplée aux cinq générateurs diesel de 800 kW, 1000 kW, 1000 kW, 1000 kW et 1800 kW.

La configuration optimale obtenue pourrait alimenter la localité de Debdeb et couvrir la demande de la population d'électricité tout au long de l'année.

Le coût actualisé de l'électricité (LCOE) et le coût actuel nette total (NPC) pour le système hybride PV- diesel sont de 0,28 $/kWh et 93,7 M$, respectivement. Le résultat montre que les deux coûts sont moins élevés par rapport au système diesel déjà existant.

Homer utilise le système diesel comme référence pour apprécier les avantages du système hybride. D'après le logiciel, le système diesel consomme 5 979 183 litres du gasoil par an (TAB. 2), soit 1 280 085 litres de plus que le système hybride.

TABLE II: consommation annuelle du gasoil par les deux systèmes.

Quantity	Value	Units	Quantity	Value	Units
Total fuel consumed	5 979 183	L	Total fuel consumed	4 694 478	L
Avg fuel per day	16 381	L/day	Avg fuel per day	10 971	L/day
Avg fuel per hour	683	L/hour	Avg fuel per hour	457	L/hour

Les générateurs diesel de la centrale déjà existante (tableau à gauche) consomment environ 680 l/ heure du gasoil pour répondre à la demande de charge horaire de 2 375,7 kWh. Des pics de consommation sont atteints pendant la saison estivale pour répondre à la hausse de la demande de charge. Le système hybride PV- diesel obtenu pourrait épargner 2,4 M$ du gasoil chaque année. Cela est dû au remplacement des DG par la centrale photovoltaïque pour la production de l'électricité. Les DG ne fonctionnent que quelques heures pendant la nuit et avant le lever du soleil.

Les résultats obtenus montrent que l'électricité totale annuelle produite est de 20 811 420 kWh. Le surplus annuel d'électricité (l'excès d'électricité) qui se produit est extrêmement faible, il est de 60kWh/ an, soit, 0,0003% du total produit. Du côté du système hybride PV-diesel sans stockage, environ 14,2 GWh de l'électricité annuelle est générée par la centrale PV, le reste est assuré par la source d'énergie conventionnelle (la centrale diesel). Le fonctionnement annuel des DG est réduit par rapport au système diesel seul, cela s'explique par la réduction de la puissance de sortie de ces derniers, dû à la baisse du nombre d'heures de leur fonctionnement.

Les résultats économiques obtenus montrent que les coûts liés à la consommation du gasoil de la centrale diesel seule sont très élevé couvrant 93% des coûts totaux du système diesel. Le coût net actuel total du système diesel sur la période des 25 ans est évaluée à 121,59 M$. Le coût total actualisé de remplacement du système est nul. Cela revient à l'annulation des coûts des remplacements des DG qui est lié au nombre d'heures de fonctionnement de ces derniers. Toutefois, les coûts d'O&M représente environ 8M$, soit, 37% du total, dont la moitié est générée par le DG de 1800 kW avec 4,3 M$. La valeur de récupération est de 435 mille de $.

L'électricité journalière moyenne produite par la centrale PV est de 39,1 MWh/jour. Les pics de production de l'électricité sont atteints durant les trois premiers mois de l'année. En revanche les hausses températures en été, aboutissent à une diminution du rendement de la centrale et réduisent la puissance des cellules photovoltaïques. La puissance maximale générée par la centrale PV est de 6 802 kW et le nombre d'heures annuelles de son fonctionnement est de 4 090 h/an. La puissance de sortie PV est entièrement utilisée dans les périodes de demande de charge élevée. Le rendement moyen de la centrale PV est de 68,6% et le coût d'un kWh de l'électricité généré par cette dernière est de 0,053 $/kWh, soit, 8% de moins par rapport au coût moyen mondial (0,057$/kWh) (IRENA, 2021, p. 14).

L'intégration de la centrale PV permet la réduction des coûts de fonctionnement. Les coûts d'O&M des DG ont chuté de 30%, 44%, 66%, 33% et 2% sauf pour le DG de 800 kW dont les coûts d'O&M ont connu une augmentation de 32%. La valeur de récupération connait une augmentation de 329%, en raison de la réduction des coûts.

VI. CONCLUSION

La technologie solaire photovoltaïque est la plus déployée dans les systèmes hybrides des RGS en raison de sa disponibilité et de son faible coût d'investissement. Les systèmes hybrides PV- diesel déployés pour la production de l'électricité dans les mix-énergétiques des RGS de l'Algérie jouent un rôle important dans l'approvisionnement futur de l'électricité et garantissent la stabilité de la consommation de l'électricité et améliore la qualité de l'électricité desservie. Les systèmes hybrides ont pour but de rentabiliser les centrales diesel et de garantir la sécurité d'approvisionnement du carburant gasoil pour améliorer les conditions socioéconomiques des populations rurales du Grand Sud de l'Algérie.

L'algorithme de planification du système hybride s'est appuyé sur les simulations de toutes les combinaisons des composants du système à l'aide des variables de décision. Les résultats de simulation ont montré que la solution du PV optimal pour le prix de 1,2$/l du gasoil est de 6,5MWc et que le coût de l'énergie totale produite diminue de 33%, marquant un revenu annuelle de 1,76 M$. Grâce à la contribution de la centrale PV dans la production de l'électricité, la quantité du gasoil épargnée est de 226 l/j.

Les pertes d'énergie générées par le système hybride PV-diesel sans stockage constituent des quantités d'électricité produites mais pas consommées. Pour résoudre ce problème du surplus, la conception d'une capacité de stockage pourrait absorber l'excès d'électricité.

REFERENCES

1. Blal, M., & al. (2016). Study of hydrogen production by solar energy as tool of storing and utilization renewable energy for the desert areas. international journal of hydrogen energy, 1-19.
2. Bouraiou, A., & al. (2019). Status of Renewable Energy Potential and Utilization in Algeria. Journal of Cleaner Production.
3. Bustos, C., & Watts, D. (2017). Novel methodology for microgrids in isolated communities: Electricity cost-coverage trade-off with 3-stage technology mix, dispatch & configuration optimizations. Applied Energy N° 195, 204-221.
4. IEA. (2020). Electricity Access Database.
5. Ipsakis, D., & al. (2009). Power management strategies for a stand-alone power system using renewable energy sources and hydrogen storage. International Journal of Hydrogen Energy, 7081-7095.
6. Kalinci, Y., & al. (2015). Techno-economic analysis of a stand-alone hybrid renewable energy system with hydrogen production and storage options. International Journal of Hydrogen Energy, 7652-7664.
7. Kellogg, W., & al. (1998). Generation unit sizing and cost analysis for stand-alone wind, photovoltaic, and hybrid wind/PV systems. IEEE Trans. Energy Convers. 13, 70-75.
8. Khan, M., & al. (2017). Techno economic feasibility analysis of different combinations of PV-Wind-Diesel-Battery hybrid system for telecommunication applications in different

cities of Punjab, India. Renewable and Sustainable Energy Reviews, 577-607.

9. Khelif, A., & al. (2012). Feasibility study of hybrid Diesel–PV power plants in the southern of Algeria: Case study on AFRA power plant. Electrical Power and Energy Systems N° 43, 546–553.

10. Khirennas, A., & al. (2021). A new optimal sizing methodology of storage-less PV system for retrofitting existing diesel-based power generation system within mini-grids. Energy Conversion and Management N° 250.

11. Nasr, M., & Nasr-Azadani, E. (2017). 'System performance in microgrids based hybrid. IEEE Power & Energy Society General Meeting.

12. Rekioua, D., & al. (2014). Development of hybrid photovoltaic-fuel cell system for stand-alone application. International Journal of Hydrogen Energy, 1604-1611.

13. Rodríguez-Gallegos, C., & al. (2018). A multi-objective and robust optimization approach for sizing and placement of PV and batteries in off-grid systems fully operated by diesel generators: An Indonesian case study. Energy, 410-429.

14. SKTM. (2016). Energies renouvelables . Récupéré sur Projet 343 MWc: https://www.sktm.dz/12/projet-343-mwc

15. The World Bank. (2021). Data. Récupéré sur Access to electricity (% of population): https://data.worldbank.org/indicator/EG.ELC.ACCS.ZS

16. Yang, H., & al. (2008). Optimal sizing method for stand-alone hybrid solar–wind system with LPSP technology by using genetic algorithm. Solar Energy, 354-367.

Dynamique spatio-temporelle de la Tourbière de Dar Fatma (AIN Draham) et conséquence sur la végétation du site

RABIAA MOUHBI
Laboratoire des Ressources Sylvo-Pastorales. *Institut Sylvo-Pastoral de Tabarka, Université de Jendouba*
Tabarka, Tunisie
mouhbirabiaa@gmail.com

SANA DALLALI
Laboratoire de Recherches en Systèmes de Production Agricole et de Développement Durable, Ecole,Supérieure d'Agriculture, Mograne, Zaghouan Tunisie,
sanadallali02@gmail.com

HANENE BOURAOUI
Laboratoire des Ressources Sylvo-Pastorales. *Institut Sylvo-Pastoral de Tabarka, Université de Jendouba*
Tabarka, Tunisie
hanenebouraoui@yahoo.fr

HOUCINE SELMI
Laboratoire des Ressources Sylvo-Pastorales. *Institut Sylvo-Pastoral de Tabarka, Université de Jendouba*
Tabarka, Tunisie
houcine_selmi@live.fr

***Résumé*— La zone humide de Dar Fatma fait partie du gouvernorat de Jendouba, de la délégation d'Ain Draham. Elle fait partie de la VI eme série forestière d'Ain Draham. Elle est classée depuis 1993 comme réserve naturelle. La tourbière est située à une altitude de 770 m. Elle se compose de 5 tourbières de diamètre entre 2 et 8 m. Le site de Dar Fatma, vieux depuis ans, sa végétation est de type hydrophile. La tourbière est une vaste accumulation de matière organique non décomposée. Le mouvement massif de la population forestière des zones montagneuses vers les zones urbaines en 1960, àcause du glissement répétitif de la terre dans le secteur de l'Atatfa, a influé directement l'espace de la tourbière et sur sasuperficie qui a régressé de 200 ha en 1960 à 7 ha en 2019. La végétation qui existe dans la tourbière est aussi influencée par les actions anthropiques (la surexploitation du milieu, le pâturage du cheptel, la pollution) et certaines espèces ont totalement disparu.**

Mots clé—: tourbière, Dar Fatma, Série forestière, matière organique, action anthropique

I. INTRODUCTION

Les tourbières sont des zones humides accumulant une quantité importante de matière organique sous forme de tourbe sur une épaisseur d'au moins 30 cm à plusieurs mètres de profondeur (Gorham, 1991). La tourbe est constituée majoritairement de débris végétaux peu décomposés contenant au moins 30% de matière organique (MO) Joosten and Clarke, 2002). Cette accumulation de MO permet le stockage d'une grande quantité de carbone (C). En effet, les tourbières auraient stocké depuis le début de l'Holocène entre 270 et 547 Gt C représentant 15 à 30% du C des sols mondiaux alors que leur superficie ne représente que 3% des terres émergées (Turunen et al., 2002). Cette accumulation de C est possible grâce à un déséquilibre important entre la production primaire et la décomposition (Bragazza et al., 2009). Dans ces milieux, le C est davantage assimilé par la photosynthèse qu'émis lors de la décomposition et ce, malgré une faible production primaire. L'accumulation de la tourbe s'y opère grâce à la faible décomposition de la MO avec une activité réduite des décomposeurs de par les conditions environnementales particulières du milieu et une végétation caractéristique.

Une des conditions environnementales majeures déterminant la création d'une tourbière est un bilan hydrique positif avec des apports d'eau supérieurs à leurs pertes. Ceci permet de créer et maintenir des conditions anoxiques qui, associées à d'autres facteurs (oligotrophie, acidité des eaux), limitent la décomposition de la MO. La Tunisie contient 2 tourbières, la tourbière de Dar Fatma et la tourbière de bini M'tir. Dans ce cadre nous étudions l'influence spatio-temporelle sur la tourbière et leur conséquence sur sa végétation. Les tourbières de Dar Fatma, aujourd'hui, est menacée par plusieurs facteurs, de part, les facteurs anthropiques, on site la ruralité des habitants vers les zone agricoles, le pâturage, la pollution, d'autre par, les facteurs climatiques, comme le changement climatique. Le but de ce travail est mettre le doit sur la valeur et l'importance de cette réserve naturelle et étudier ces facteurs pour la protéger et conserver de dépriser.

II. MATERIEL ET METHODES

A. Materiel

1. La tourbière de « Dar Fatma »

La tourbière de dar fatma est située à une altitude de 770 m, elle fait partie du TF n° 196 S2 Béja, couvre une superficie de 15.30 ha et se compose de 5 petits tourbières d'un diamètre compris entre 2 et 8 m et de profondeur n'excédent pas 10m et dont la plus intéressante sur les plans scientifiques écologiques, historique et dynamique est celle qui a livre 10 m de sédiments essentiellement tourbeuse (Karem. A *et al*., 2007). Elle est considérée parmi les plus anciens écosystèmes naturels (est âgée de 33000 ans) (photo 1). Cette tourbière est d'une profondeur de 10 et a été formée au cours de l'holocène. Sa végétation est de type hydrophile, est constamment engorge d'eau issue des sources et chabets voisines. La tourbière est une vaste accumulation de matière organique peu ou pas décomposée appelée tourbe. La flore de la tourbière de dar fatma

ISSN: 1737-9334

comprend des espèces de sphaignes et d'hépatiques. Les sphaignes représentent la strate muscinale d'une tourbière et son à l'origine de la tourbification par leur accroissement continu et leur capacité à acidifier le milieu (DGAT, 2012). La zone humide de Dar Fatma se situe à l'extrême nord-ouest de la Tunisie et fait partie de l'ensemble de chainons montagneux de direction générale SSW - NNE, culminant à Dj El Ghorra à 1203 m, sur la frontière Tunis-Algérienne et qui porte le nom de la Kroumirie (coordonnée géographiques, 36°48' nord, 08°05' est).

Source : Google CNES/Airbus

Photo 1: photo satellite de la tourbière Dar Fatma

La zone humide de Dar Fatma fait partie du gouvernorat de Jendouba, de la délégation d'Ain Draham et Imadat d' Atatfa. Elle est géré par l'arrondissement forestier d'Ain Draham et soumise au régime forestier et fait partie de la VI éme série des forêts d'Ain Draham, est titrée domaine de l'état (titre foncier 196S2 Béja) (Karem A. *et al.,* 2007).
Ce site est classé depuis 1993 comme réserve naturelle (arrêté du ministère de l'agriculture du 18/12/1993 paru au JORT N° 100) (Karem A. *et al.,* 2007).

2. *Cadre d'etude*

Présentation de la VI^{ème} série forestière d'Ain Draham

La série forestière est incluse dans le massif forestier qui ceinture la ville d'Ain Draham et qui est constitué de 10 séries forestières numérotées de 1 à 10 dont Ain Draham VI qui est limitée au nord par des terres agricoles et le foret de Houamdia série unique, à l'Est par la série au nord d'Ain Draham VIII et Oued Ezzene II et III et en partie Ain Draham VIII. Administrativement la série appartient au gouvernorat de Jendouba, la délégation d'Ain Draham et le secteur de Dar Fatma principalement et en parétien à l'ouest par le secteur d'Ouled Sedra (la carte2). La localité de Dar Fatma et de Fej Errih constituent les principaux regroupements humains en petits hameaux, la vallée d'El Atatfa et une partie de la vallée de Babbouch constituent l'espace agricole principal à l'échelle de la série. Vers l'Est d'Ain Draham la route goudronnée entre Ain Draham et Boussalem qui traverse la série jusqu'à Etbeinia. La route goudronnée allant vers Dar Fatma constitue aussi en partie un accès à la série (Arrondissement de forêt, 2018).

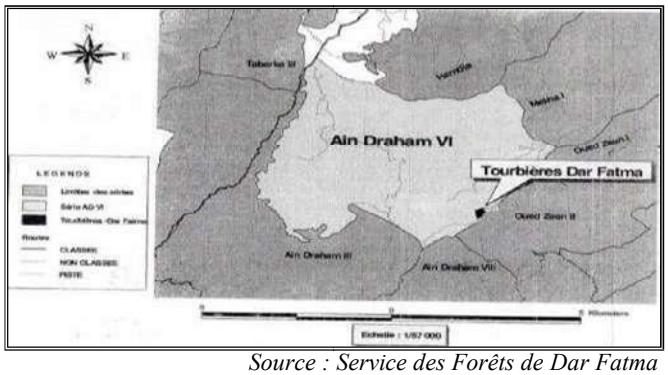

Source : Service des Forêts de Dar Fatma

Figure 1: Situation de la tourbière par rapport à la VI^{ème} série forestière Ain Draham

Conditions bioclimatiques

La zone est donc située dans l'étage humide entre 800 mm et plus de 1500 mm/an. C'est la zone la plus humide du pays. C'est la zone la plus humide du pays.
Le volume et la régularité des fortes précipitations sont une caractéristique climatique de la zone jusqu'à 1500 mm sur les sommets au dessus de 800m, donc ces fortes précipitations et la fraicheur en altitude donnent un étage bioclimatique méditerranéen humide supérieur, variante à hiver tempéré (Bonvallot, 1982). La tendance à la diminution des précipitations annuelles (mm) est très légère et non significatives statistiquement, entre 1900 et 2004 soit sur 105 années. Le moyenne annuelle est estimé à 1590 mm et a varie entre un minimum de 5774 mm en 1943 et un maximum de 2436 mm en 2003.

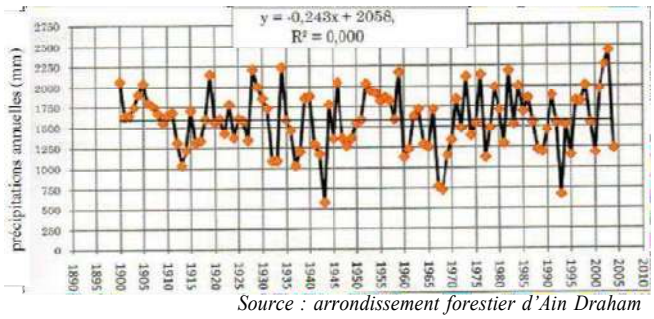

Source : arrondissement forestier d'Ain Draham

Figure 2 : Variation des précipitations annuelles à Ain Draham entre 1900 et 2004

En se référant aux données météorologiques d'Ain Draham, la répartition des températures moyenne mensuelles est illustrée dans le tableau 1

Tableau 1: Températures mensuelles moyennes

Mois/station		J	F	M	A	M	Jn	Jt	A	S	O	N	D
Ain Draham	**M** en °C	9 ,4	10,4	13,8	16,8	20,8	25,7	29,8	31	27,3	21,3	15,3	10,5
	Moy en °C	6,6	7,2	9,8,	12,3	15,9	20,2	23,7	24,7	21,9	16,9	11,8	7,9
	m en °C	3,9	4	5,9	7,9	11	14,7	17,7	18,5	16,5	12,5	8,4	5,3

Source: arrondissement forestier d'Ain Draham

Condition physiques

La zone du PDC est un versant de pentes moyennes à fortes : elle couvre le versant de Djebel Sra, direction sud-nord. Cette zone est composée des deux vallées Atatfa et de Babouch séparées par ligne de hauteurs échancrées en gorges, formée par les Dj .Bounouela et Ain fallous. La

caractéristique principale du relief est sa vigueur représentée par des pentes fortes, encaissements des vallées dans les argiles et les marnes à des altitudes comprises entre 100 et 300m, séparées par des lignes de crête dans les formations gréseuses du Numidien. Les pentes sont supérieures à 15% sur plus des ¾ de la zone des Atatfa, ce qui s'ajoute aux facteurs favorisant les processus d'érosion. Sur les replats recouverts de colluvions, des sols bruns hydro-morphes occupent de faible superficie. Ces sols présentent des traces d'hydro-morphe entre 20 et 40 cm de profondeur, ce qui perturbe ou empêche la croissance des végétaux. L'excès d'eau en hiver favorise les phénomènes de solifluction pelliculaire, et la sécheresse estivale provoque la formation de larges fentes de retrait qui détruit le réseau racinaire des plantes cultivées.

Les sols des replats recouverts de colluviaux sablo-graveleux sont plus favorables à l'agriculture mais exigent un constant un constant effort de drainage d'hiver et d'irrigation en été (Bonvallot J., 2016). Le réseau hydrographique est dense et se compose de deux oueds importants : oued renaga et ses affluents (oued mouxnet loudeze (avec deux chabet : chabet Hassalou et chabet El Malleh) et oued Beidha (drainant le mont de Dar Fatma).

L'oued El Mellah (affluent d'oued El Kebir) constitue la limite ouest et nord de la zone d'étude. Sur ce dernier (oued El Kèbir) le barrage El Khdhairia a été érigé.

Ce réseau hydrique est très dense avec les autres chabets sansnom précis, correspondant au relief très accidenté.

B. METHODE

1. Délimitation de la zone d'étude

La tourbières de dar fatma est localisée à 7°55' de longitude est et de 31°74' de latitude nord. Elle est accessible par la route de Ain Draham- Tebainia en passant par Sra Rabeh-Dar Fatma .elle fait partie de la série VI du foret de Ain Draham. Son relief est plutôt une dépression plate située entre deux versants escarpés : ceux d'Atatfa au nord et de oued zeen au sud. Ce plateau se trouve entre le synclinal de Babouch et synclinal de Béni M'tir (Tbini M., 2004).

2. La végétation

La végétation présente dans la réserve est l'expression la plus concrète liée directement aux conditions hydriques et édaphiques de celle-ci. La zone humide de Dar Fatma renferme essentiellement diverses espèces de graminées à savoir : *Spharagnum plumosum, S. Subsecundun, Eleocharis mulicaulis, Montia fontana ; Hypericum afrus, Anagallis crassipes, Bellis annua, Isoetes hustrix, Asphodelus microcarpus.* L'*Erica arborea*, espèce plutôt du maquis occupé l'espace entre les tourbières et signe par sa présence l'assèchement avancé de la zone. En plus suite à cet assèchement et à l'arrêt provoqué du fonctionnement des tourbières, certaines espèces de la flore holocène ont trouvé refuge dans l'autre site humides de la région : Alnus *glutinosa, Fraxinus excelsoir, Salix pedicellata* (TBINI M. , 2004).

3. Valeurs sociales et culturelles

Le nom de dar fatma « maison de fatma » en arabe – viendrait du souvenir d'une jeune mariée romane noyée ou embourbée dans la zone humide. L'origine du nom témoigne de la reconnaissance profonde et ancienne du caractère humide des lieux. La clairière de Dar Fatma a toujours représenté un lieu de pacage et de repos pour les troupeaux et les bergers locaux, car elle offre une biomasse importante pour le bétail (c'est une prairie naturelle graminéenne). La surexploitation du pâturage a donné lieu dans un passé récent à un certain assèchement du site, aggravé par le drainage, le défrichement illicite et même la pratique, les années pluvieuses, de la céréaliculture (TBINI M., 2004).

4. Impact de la population sur la tourbière

La zone humide de Dar Fatma est limitrophe au village Dar fatma (12 km à Ain Draham) et du poste forestier (800 m). La plupart des habitats de la région sont des petits éleveurs constituant la population locale et sont essentiel de la main d'œuvre utilisée pour exécuter les travaux prévus dans le cadre de l'aménagement forestier . L'élevage des bovins surtout de race locale et des ruminants surtout des caprins est pratiqué sur les parcours forestiers environnants et sur les quelques prairies réduites dans la zone. (D.G.F, 2018).

Tableau 2: le secteur agricole au niveau de la forestière AD VI

Douar/ Agglomeration	Nombre Ménages	Nombre Exploitations agricoles	Nombre Eleveurs	Nombre d'Unités Zootechniques Bovine	Nombre d'Unités Zootechniques Ovines	Nombre d'Unité Zootechniques Caprines
Sra Rabeh	220	150	150	60	150	300
Sidi M'mamed	230	160	160	120	100	400
Dar Fatma	150	105	105	70	250	100
Chehida	0	15	15	15	50	50
Total serie forestière AD VI	600	430	430	265	550	850
Total secteur El atatfa	700	500	500	300	600	900

Source : Arrondissement des Forêts d'Ain Draham, 2018

L'intensité du surpâturage causé par le troupeau bovin est très importante. En effet, la densité de la bouse des vaches ainsi que les pieds de vache et l'étendue en surface de leurs reposoirs justifient l'ampleur de l'action destructrice causée par ce facteur notamment sur les tapis que forment les sphaignes ,très vulnérables et fortement affectés du fait que ces bryophytes sont appréciées par le bétail (Geluck *et al*., 1993).

Le troupeau (bovin, ovin et caprin) endommage d'une part le semis et les touffes de sphaigne qui n'est pas conseiller du pâturer, par son piétinement et d'autre par, la végétation herbacée par sa consommation accélérée des plantes avant même quelles forment les réserves et les pousses de l'année suivante. Les animaux consomment que les végétations les plus appétant, ce qui permet de limitation des certain espèces. Les habitats locaux rejettent les déchets domestiques dans la tourbière ce qui provoque la modifie le milieu et diminue la diversité végétales et animales. De part, d'autre part ces rejets provoquent la toxicité du sol et de nappe d'eau.

III. RESULTATS ET DISCUSSION

A. Etat actuel de la tourbiere

Le site présente une valeur conservatoire exceptionnelle avec une grande richesse en hydrophytes patrimoniales pour

la Tunisie. Il fait l'objet du statut de réserve naturelle depuis 1993, et de site RAMSAR depuis 2007.

La tourbière de dar fatma est située à une altitude de 770 m, elle fait partie du TF n° 196 S2 Béja. La principale clairière a été clôturée, le défrichement interdit, et le pâturage sévèrement limité. Dans la deuxième clairière en aval, de telles mesures n'ont pas encore été effectuées et la zone est toujours soumise à une pression de pâturage très forte.

La première tourbière : Dar Fatma qui se compose de 5 tourbières d'un diamètre compris entre 2 et 8 m, la deuxième tourbière : Bir Gaid qui se compose par 2 tourbières (image 3). La deuxième tourbière est moins importante que la première à cause de l'impacte de facteurs topographie.

La tourbières hébergent des espèces végétales importantes pour le maintien de la biodiversité .ce sont d'une part les graminées, d'autres parts des plantes aquatiques très rares tel que les sphaignes. Plus ce qu'elle a une valeur écologique, elle a une valeur économique puise qu'elle est la 2 ^{éme} tourbière dans monde, elle est lieu de visite pour les chercheurs, les étudiants et les touristes, et une valeur esthétique.

La tourbière est menacée par des problèmes comme la chasseresse, la pollution et la surexploitation, sur fréquentation humaine .ce derniers menacent actuellement la survie de la tourbière.

B. Dynamique de la population forestiere de Dar Fatma et leur cheptel

1. Historique de la zone d'Atatfa

Le village de dar fatma a commencé à être mis en œuvre depuis 1962. L'état est intervenu pour l'aider les gens dont les habitations étaient menacées par les glissements dans la vallée. Il y a eu les premiers glissements en 1950 dans les zones d'Araoufia à coté de Gueltat El Mellah (dans la vallée d'Atatfa). Après ces glissements, une partie des populations ont été transférées en 1965 à Dar Fatma. Dans l'année 1970, l'état a voulu rassembler les populations de vallée d'Atatfa dans le village de Sra Rabeh avec une aide de l'Etat à la construction de logements à Sra Rabeh : avec le programme de la SNTT, pour créer le village de Sra Rabeh. Apres l'année 1970, le village de Sra Rabeh se développe âpres construction de la route Ain Draham- Sra Rabeh en prévision de l'électrification et de l'amenée de l'eau potable. Les gens sont alors venus s'installer à Sra Rabeh en venant de la vallée d'Atatfa pour ceux don les terres étaient menacée par l'érosion et les glissements. en 1978, le début d'intervention l'association APPEL a Dar Fatma.

2. Dynamique de la population forestière de dar fatma

La population totale de la délégation d'Ain-Draham était en 1975, dernière source officielle accessible de 34 057 habitants, la densité s'établissant à 68 h au km^2, chiffre moyen pour la Kroumirie dont certains secteurs supportent jusqu'à 120 h au km^2.La zone des Atatfa, plus spécialement étudiée ici, apparaît come assez peu peuplée avec une densité de 56. Mais ce chiffre global ne traduit qu'imparfaitement la réalité car, si l'on considère non plus la surface totale mais celle qui est exploitée par l'agriculture, la densité correspondante fait un bond prodigieux et passe 238 h au km ^{2} pour une population totale de 3 097 h regroupés en 8 douars. Le tableau 3 présente l'évolution de population locale dans les années 1960-2019.

Tableau 3: Evolution de la population forestière de Dar Fatma

Année	1960	1970	1980	1990	2000	2010	2019
Population	873	910	1012	904	789	593	317

Une l'augmentation progressive de population forestière jusqu'à atteint 1012 habitants, en 1980. Ce mouvement massif des habitants est dû au glissement de la terre de la zone montagneuse de secteur Atatfa. Apres l'année 1985, l'effectif de la population diminue. Cette diminution est causée par l'exode rural vers les villes ou les zones urbaines. Les habitats locaux de cette région sont de petits éleveurs. Leurs productions sont pour subsistance.

Âpres les pertes en terre par érosion et la rareté de ressources et médiocricité du niveau de vie, les habitants se sont enfuit pour l'installation définitive et l'emploi.

3. Dynamique de cheptel

Le tableau 4 présente l'évolution du cheptel de Dar Fatma entre les années 1960 et 2019.

Tableau 4: Evolution du cheptel de Dar Fatma

Année	1960	1970	1980	1990	2000	2010	2019
Bovin	512	435	389	207	178	114	98
Ovin	839	967	1020	739	456	198	136
Caprin	216	534	1265	876	510	267	156

Source: notre enquête (2019)

D'après la figure 4, on remarque que l'effectif du cheptel est très important en 1980. Cette élévation est due au mouvement massif de la population dans la même période. Cet effectif diminue progressivement dans les années jusqu'à atteindre en 2019, 156 têtes caprine, 136 têtes ovine et 98 têtes bovine.

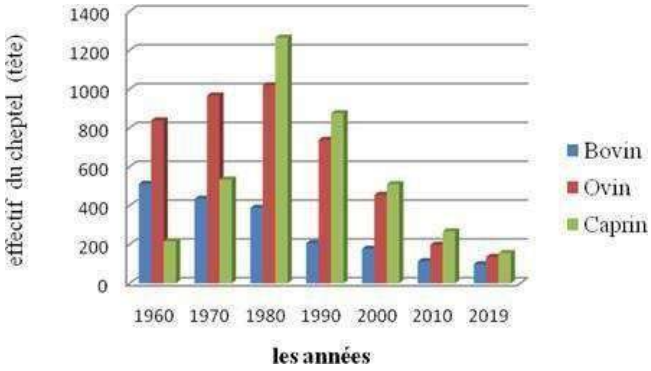

Figure 4: dynamique de cheptel de Dar Fatma entre les années 1960 et 2019

C. Dynamique spatio-temporelle de la tourbiere de Dar Fatma

La zone d'Atatfa a connu d'importants problèmes depuis les années 80 : avec la survenue d'importants mouvements de masse sur leurs terrains agricoles et aires d'habitats (versants d'Atatfa). Le mouvement massif de la population dans les zones forestières provoque la réduction de la superficie du site étudiée. La figure 5 porte la dynamique de la superficie de la tourbière de Dar Fatma depuis les années 1960 à 2019.

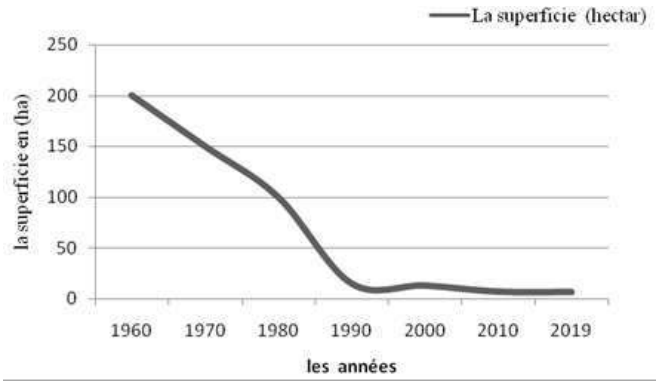

Figure 5: Dynamique de la superficie depuis les années 1960 à 2019.

Avant la migration de la population, vers les zones forestières. La superficie de la tourbière en 1960 était 2 km^2. Après le mouvement massif des habitants, cette superficie diminue progressivement jusqu'à atteindre 15 ha en 1993. Dans les années 1994-2000, les maisons des habitants de Saidia sont écroulées à cause du glissement de terre. Les habitant0s se sont installés dans une partie de la tourbière par force. Malgré les demandes répétitifs du chef de service forestier compétent de changer vers un autre locale la population a y resté. Toutes les tentatives sont ratées avec les habitants.

En 2007, l'arrondissement forestière a sauvegardé la tourbière par une clôture de 1131 ml mais qui n'as pas tenu un bon moment. Au temps où la tourbière de Dar Fatma entre dans la convention de site de RAMSAR le 7 novembre 2007 jusqu'à 2011 la superficie de la réserve a été stable, de 13 ha grâce à la clôture qui protège la réserve. Suite au relâchement sécuritaire après la révolution de 2011, la clôture a été détruite par la population locale qui n'a jamais été impliquée dans les programmes de conservation et de gestion de cette réserve. Actuellement, la superficie de cette réserve, naturelle est environ 7 ha (photo 2).

Photo 2: la superficie de la tourbière de Dar Fatma.

Le site est pollué par les rejets de déchets domestiques ce qui provoque la toxicité du sol. Cette toxicité influe sur la typologie de la végétation et du sol donc perturbation de l'écosystème (photo 3).

Photo 3: pollution dans la tourbière

D. Les conséquences sur la végétation

La tourbe accumulée à Dar Fatma depuis des milliers d'années, constitue une véritable boite d'archives naturelles permettant de reconstituer le climat, la dynamique des paysages et de la végétation, et l'impact humain de cette région. Les enjeux conservatoires de la tourbière, sont aujourd'hui d'autant plus importants. L'influence humaine directe paraît incontestable. Mais elle joue également de façon indirecte. En effet, l'accroissement des surfaces cultivées, l'augmentation de l'effectif des troupeaux responsable d'un éclaircissement du tapis végétal, conduisent à une augmentation du ruissellement et Dégradation de la végétation comme présente dans le tableau 5.Certain espèce étaient présenter dans la tourbière en 1960 comme *Lotus corniculatus, Carex sp, Biscutella didyma, Daucus setifolius, Hypericum sp, Juncus funtanesii* et d'autre.

Aujourd'hui, ces espèces qui sont disparus. Selon l'étude de Pautou *et al*. (1991), dans le marais de Lavours (Ain), le piétinement accélère la décomposition de la litière et favorise les végétaux de petite taille. Sur la tourbe aérée, *Potentilla reptans* progresse. Par contre *Frangula alnus* régresse car ses feuilles sont appréciées par les bovins ; ces dernières ont un goût douceâtre par rapport à celles d'*Alnus glutinosa* qui sont amères et refusées par le bétail. Aussi, les bourgeons de *Salix cinerea* sont plus appréciés par rapport à

ISSN: 1737-9334

Cladium mariscus peu recherché par les animaux bien que les bovins consomment en hiver la partie inférieure de la plante enfoncée dans le sol (Pautou *et al*., 1991). Par ailleurs, la fructification ainsi que la production des graines des végétaux annuels (Thérohytes) sera également empêchée. Ainsi, la matière végétale prélevée par les animaux comme le signale (Lezreg, 1983) devient ainsi supérieure à la production annuelle des végétaux. Ceci a pour conséquence une disparition des espèces les moins résistantes et une réduction du couvert végétal.

Au cours du siècle, l'homme a augmenté de manière croissante son emprise sur le milieu naturel en exploitant de plus en plus les espèces dont certaines se disparaissent, on cite *Lotus corniculatus, Carex sp, Biscutella didyma, Daucus setifolius, Hypericum sp, Juncus funtanesii, Juncus conglomeratus, Mentha aquatica, Silene colorata, Vicia sativa. Calycotome villosa.* Le rythme actuel de consommation des ressources naturelles par l'humanité excède leur rythme de renouvellement.

Tableau 5: Démembrement des espèces ; dégradation de la végétation entre 1960-2019

Les années	1960	2019
Strate herbacée	*Anagallis crassifolia* *Asphodelus sp* *Bellis repens* *Isoètes sp* *Lotus corniculatus* *Sphagnum sp* *Carex sp* *Biscutella didyma* *Daucus setifolius* *Hypericum sp* *Juncus funtanesii* *Juncus conglomeratus* *Mentha aquatica* *Silene colorata* *Vicia sativa*	*Sphagnum plumosum,* *Subsecundun* *Eleocharis mulicaulis* *Montia fontana* *Hypericum afrus* *Anagallis crassipes* *Bellis annua* *Isoètes hustrix* *Asphodelus microcarpus*
sous-bois	*Erica arborea* *Agrimonia eupatoria* *Calycotome villosa* *Cistus sp* *Genista aspalathoïdes*	*Erica arborea* *Alnus glutinosa* *Fraxinus excelsoir* *Salix pedicellata*
Strate arborée	*Quercus suber*	

La pollution provoquée par l'homme, à crée un réchauffement climatique qui est la cause du changement climatique de la terre. Cette dernière influe sur le métabolisme de la végétation, dont absence et apparence des autres espèces végétale.

La photo 4 présente l'impact des animaux sur la végétation du site. La clairière de Dar Fatma a toujours représenté un lieu de pacage et de repos pour les troupeaux et les bergers locaux, car il offre une biomasse importante pour le bétail (c'est une prairie naturelle graminéenne). La surexploitation du pâturage a donné lieu dans un passé récent à un certain assèchement du site, aggravé par le drainage, le défrichement illicite et même la pratique, les années pluvieuses, de la céréaliculture.

Actuellement, la tourbière de Dar Fatma a connu une pression anthropique considérable et farouche et qui a provoqué une régression de l'espace depuis les années soixante jusqu'aujourd'hui et à ce niveau on a pu enregistrer une variation de l'espace de 200 ha à 7 ha en 2019.

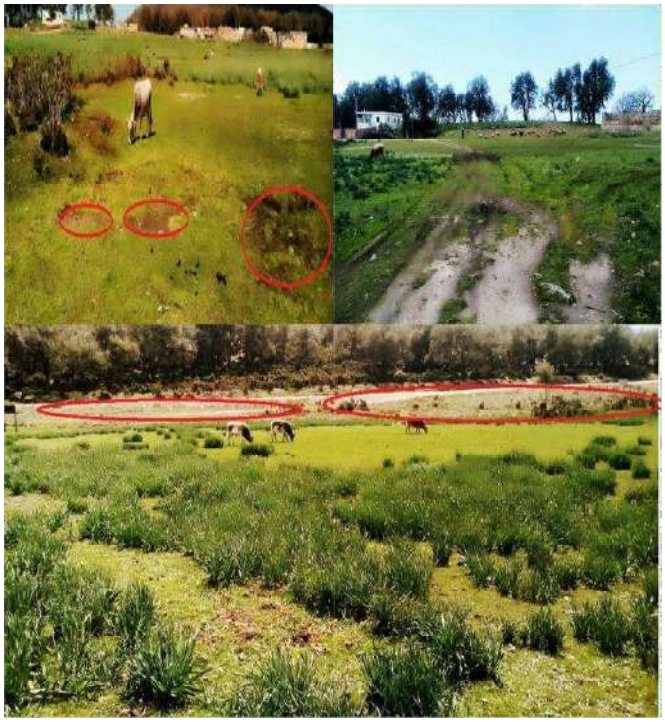

Photo 4: Dégradation de la végétation ; l'influence d'animaux sur la tourbière

IV. CONCLUSION

La végétation actuelle du site est l'expression la plus concrète des conditions hydriques et édaphiques. Elle s'est appauvrie par rapport aux périodes antérieures (par exemple l'aulne *Alnus glutinosa*, le frêne *Fraxinus excelsior* et le saule *Salix pedicellata* ont disparu à cause de l'assèchement progressif), mais certaines espèces ont pu résister, notamment celles citées au point 12. Elles persistent sur le site et sont inféodées à des conditions relativement plus sèches et plus chaudes. Aux alentours des tourbières existaient autrefois dans la forêt de la Kroumirie le lion de l'Atlas, le léopard et le serval, mais les derniers individus ont été abattus au début du vingtième siècle. Actuellement la faune est caractérisée par la présence, entre autres mammifères, du cerf de Barbarie (*Cervus elaphus barbarus)* (sous-espèce endémique), du sanglier (*Sus scrofa)* et du renard (*Vulpes vulpes)*. La végétation a connu aussi une pression énorme causée par le cheptel et a engendré la disparition de beaucoup d'espèces herbacées rares et propres pour la tourbière et à ce niveau on a enregistré la disparition des espèces végétales suivantes : *Lotus corniculatus, Carex sp, Biscutella didyma, Daucus setifolius, Hypericum sp, Juncus funtanesii, Juncus conglomeratus, Mentha aquatica, Silene colorata, Vicia sativa. Agrimonia eupatoria, Calycotome villosa, Cistus sp, Genista aspalathoïdes*.

Les habitants ont pris place tout autour de la tourbière et ont construit des maisons en dur sans se soucier de l'importance du site.

V. REFERENCES

Aerts R Verhoeven JTA, Whigham DF. (1999). Plant-mediated controls on nutrient cycling in temperate fens and bogs. Ecology, 80: 2170–2181

BELOUAHEM-ABED Djamila, 2012 : Etude écologique des peuplements forestiers des zones humides dans les régions de SKIKDA, ANNABA et EL TARF (Nord-Est algérien)

Ben Tiba B (1996) : Des tourbières de Dar Fatma, Tunisie septentrionale. In : Management of

Berendse F., Van Breemen, N., Rydin, H., Buttler, A., Heijmans M., Hoosbeek M. R., Lee J.A., Mitchell E., Saarinen T., Vasander H., & Wallén B. (2001). Raised atmospheric CO2 levels and increased N deposition cause shifts in plant species composition and production in Sphagnum bogs. Global Change Biology, 7(5), 591-598.

Bonvallot J., « glissements de terrain et aménagement du milieu naturel dans une montagne méditerranéenne humide. Casdes Atatfa, Kroumirie, Tunisie septentrionale »,27p, géographe ORSTOM , téléchargé en juin 2016.

Boon,A.,chapman,D. ,Evans,M. g. ,Holden,J. Reed,M.S. et Worrall,F. (2009). Can carbon offsetting pay for upland ecological restoration? Science of the total environemme nt, vol. 408, p.26-36.

Breeuwer A., Heijmans M. M., Robroek B. J., & Berendse F. ,(2008). The effect of temperature on growth and competition between Sphagnum species. Oecologia, 156(1), 155-167.

Buttler, A., Robroek, B. J., Laggoun-Défarge, F., Jassey, V. E., Pochelon, C., Bernard, G., et al., (2015). Experimental warming interacts with soil moisture to discriminate plant responses in an ombrotrophic peatland. Journal of vegetation science, 26(5), 964-974

Buxton R. et Winhaù J. (1997). Sphagnum peatlands of Australia: an assessment of harvesting sustainabilitu. Biological conservation,n° 82,p. 21-29.

Cojocaru C. ,crestescu I. et macoveani M. (2011). Peat-based sorbents for the removal of oil spills from water surface: application of artificial neural network modeling. Colloids and surfaces: physicochical and engineering aspects, vol. 384, p. 675-684.

Cornelissen JHC., van Bodegom PM, Aerts R. et al (2007). Global negative vegetation feedback to climate warming responses of leaf litter decomposition rate in cold biomes. Ecol Lett, 10:619–627

Coulson JC. et Butterfield J. (1978). An investigation of the biotic factors determining the rates of plant decomposition on blanket bogs. Journal of Ecology, 66: 631–650.

DGAT « atlas numerique du gouvernorat Jendouba » juin 2012, apport de 1 ere phase ,112p.

Dieleman C. M., Branfireun B. A., McLaughlin J. W., & Lindo, Z. ,(2015). Climate change drives a shift in peatland ecosystem plant community: implications for ecosystem function and stability. Global change biology, 21(1), 388-395.

Duflos G. , 2015 : la tourbiere du Mont Bar, Végétation_tourbière_France.pdf

Fabien Leroy 4 Oct 2018 : Effets des changements de végétation dans les tourbières à sphaignes sur le cycle du carbone Université d'Orléans, 2017. Français. .

Fatima Laggoun-Défarge,2012 : fonctionnement et dynamiqye des tourbières ,impact de l'anthropisation et du changement climatique. Géochimie. université d'Orléans, 2011.<tel-00603695v2>.

Fenner N., Ostle N. J., McNamara N., Sparks T., Harmens H., Reynolds B., & Freeman C. ,(2007). Elevated CO2 effects on peatland plant community carbon dynamics and DOC production. Ecosystems, 10(4), 635-647.

Freléchoux F., Buttler A., Schweingruber F. H., & Gobat J. M., (2000). Stand structure, invasion, and growth dynamics of bog pine (Pinus uncinata var. rotundata) in relation to peat cutting and drainage in the Jura Mountains, Switzerland. Canadian Journal of Forest Research, 30(7), 1114-1126.

Gibbs,J.P. ,(2000). Wetland loss and biodiversity conservation. Society for conservation biology, vol. 14n°1, p.314-317.

Heijmans M., Klees H., de Visser W., & Berendse F. ,(2002). Response of a Sphagnum bog plant community to elevated CO2 and N supply. Plant Ecology, 162(1), 123-134.

Hood G.,(1999). Canadian peat harvesting and its effects on the environment. Acta horticulturae, vol. 481, p598-602.

Jaquin A., 2010 : Dynamique de la végétation des savanes en lien avec l'usage des feux à Madagascar. Analyse par série temporelle d'images de télédétection. Thèse de Doctorat, Université de Toulouse, 141p.

Jassey, V. E., Chiapusio, G., Binet, P., Buttler, A., Laggoun-Défarge, F., Delarue, F., et al., (2013). Above-and belowground linkages in Sphagnum peatland: climate warming affects plant-microbial interactions. Global Change Biology, 19(3), 811-823

Johnson LC, Damman AWH. (1993). Decay and its regulation in Sphagnum peatlands. Advances in Bryology, 5: 249–296.

Lezreg A., (1983) : Etude des changements de la végétation à l'embouchure de l'Oued Reghaïa. Thèse d'Ingéniorat d'Etat en Agronomie. INA d'El Harrach. 84 p.

Limpens J., Berendse F. ,(2003). How litter quality affects mass loss and N loss from decomposing Sphagnum. Oikos, 103: 537–547.

Limpens, J., Berendse, F., Blodau, C., Canadell, J. G., Freeman, C., Holden, J., et al. (2008). Peatlands and the carbon cycle: from local processes to global implications–a synthesis. Biogeosciences, 5(5), 1475-1491

Mediterranean Wetlands III, Case Studies 2, 69-80, eds C. Morillo and J.L. Gonzales,

Mediterranean Wetlands III, Case Studies 2, 69-80, eds C. Morillo and J.L. Gonzales,

MedWet/Ministerio de Medio Ambiente, Madrid.

MedWet/Ministerio de Medio Ambiente, Madrid.

Minayeva, T. Y., & Sirin, A. A. (2012). Peatland biodiversity and climate change. Biology Bulletin Reviews, 2(2), 164-175.

Myers-Smith, I. H., Forbes, B. C., Wilmking, M., Hallinger, M., Lantz, T., Blok, D., et al. (2011). Shrub expansion in tundra ecosystems: dynamics, impacts and research priorities. Environmental Research Letters, 6(4), 045509.

Parish, F., Sirin A., Charman D., Joosten H., Minaeva T., & Silvius M. ,(2008). Assessment on peatlands,

biodiversity and climate change. Global Environment Centre, Kuala Lumpur and Wetlands International Wageningen, 179.

Pautou G., Majchrzak Y., Manneville O., Gruffaz R., Moreau D., (1991) : Dynamique de la végétation et gestion de la réserve naturelle du marais de Lavours (Ain). Revue de géographie de Lyon. Vol. 66 n°1, pp. 61-70.

Payette, S.et Rochefort, L., (2001).introduction. In Payette, S.et Rochefort, L. Ecologie des tourbières du Québec-Labrador (introduction, p.1-5). Saint- Nicolas, Les presses de l'Université Laval.

Pearson, R. G., Phillips, S. J., Loranty, M. M., Beck, P. S., Damoulas, T., Knight, S. J., & Goetz, S. J. ,(2013). Shifts in Arctic vegetation and associated feedbacks under climate change. Nature Climate Change, 3(7), 673- 677.

Pellerin,S. et poullin, m., (2001). La conservation. in payette, S. et Rochefort, L. écologie des tourbières du Québec-labrador (chap. 24,p. 505-518). Sait- Nicolas, les presses de l'université Laval.

Plamondon, A. , Prévost,M. et Roy, V. (2001). La production forestière. In payette, S. et Rochefort, L. écologie des tourbières du Québec-labrador (chap. 22,p. 423-447). Saint- Nicolas, les presses de l'université Laval.

Price, J. ,(2001). L'hydrologie. In Payette, S. et Rochefort, L., écologie des tourbières du québec-Labrador (chap. 5, p. 141-158). Saint-Nicolas, les presses de l'université Laval.

Robert Nègre ,(1952) Note phytosociologique sur quelques mares et tourbières de Kroumirie, Bulletin de la Société Botanique de France, 99:10, 16-22, DOI: 10.1080/00378941.1952.10836507

ROCHE E. et BOUZID S., 2007 : Evolution de la végétation et du climat dans le Nord-ouest de la Tunisie au cours des 40 derniers millénaires. Géo-Eco-Trop, 2007, 31: 171 - 214

Rochefort, L. (2001). Restauration écologique. In payette,S. et rochefort.L., écologie des tourbières du Québec-labrador (chap. 23, p. 449-504). Saint – Nicolas, les presses de l'université Laval.

Selmi H., 2015-2016 : conception et mise en place d'une carte web des aires protégées en tunisie.

Strack, M. (2008). Executive summary for policymakers: peatlands in Global charge. In strack, M. peatlands and climate (p. 9-12). Vapaudenkatu, international peat society, 223p

Tbini M., 29-06-2004 :chef de service des forets d' Ain Draham, arrondissement des foréts , Ain Draham : la zone humide de Dar Fatma

THOMAS Jacques - Les tourbières de Midi – Pyrénées : comment les conserver ? – CREN Midi-Pyrénées, 1999, 116 pages

Thormann M.N., Szumigalski A.R., Bayley S.E. ,(1999). Aboveground peat and carbon accumulation potentials along a bog-fen-marsh wetland gradient in southern boreal Alberta, Canada. Wetlands, 19: 305-317.

Turetsky, M. R. ,(2003). The role of bryophytes in carbon and nitrogen cycling. The Bryologist, 106(3), 395-409.

Turetsky, M. R., Donahue, W. F., & Benscoter, B. W. ,(2011). Experimental drying intensifies burning and carbon losses in a northern peatland. Nature Communications, 2, 514.

Van Breemen N. ,1995. How Sphagnum bogs down other plants. Trends in Ecology and Evolution, 10: 270-275.

Attribution Optimale des D-STATCOM dans un Réseau Electrique avec l'Algorithme PSO

K. Ifrah[#1], W. Ifrah[#2], S. Benachour[#3] ,O. Bendjeghaba[#4]

[1, 3,4#] *Automatisation et Électrification des procédés,* [2#] *Génie Mécanique, Université M'Hamed Bougara de Boumerdes, LREEI*

[2#] *Génie Mécanique, Université M'Hamed Bougara de Boumerdes, LEMI*

55 avenue de l'indépendance, 35000, Boumerdes, Algérie

[1]k.ifrah@univ-boumerdes.dz

[2]w.ifrah@univ-boumerdes.dz

[3]so.benachour@univ-boumerdes.dz

[4]bendjeghaba@univ-boumerdes.dz

***Résumé* — Dans cet article nous allons optimiser les attributions des D-STATCOM dans un réseau électrique. Il existe plusieurs stratégies qui permettent de faire l'attribution des D-STATCOM et dont la diffusion peut être classifiée en cinq méthodes : « la méthode analytique », « la méthode réseau de neurones artificielles », « la méthode métaheuristique », « la méthode approche sensible », la dernière étant la combinaison entre l'approche sensible et la méthode métaheuristique. Dans ce travail nous avons opté pour la méthode métaheuristique en utilisant l'algorithme PSO et un réseau électrique radial avec un jeu de barres de IEEE 33 « IEEE bus system 33 ».**

Avec le logiciel Matlab nous allons simuler le système et les résultats seront présentés, analysés et discutés.

***Mots clés*— Optimisation, Métaheuristique, D-STATCOM, Réseau Electrique.**

I. INTRODUCTION

Avec l'augmentation de la charge et l'exigence d'efficacité des réseaux électriques, la production, le transport et la distribution d'électricité sont très importants pour le système d'alimentation électrique, qu'il soit régi par différents organismes ou par une seule entité [8]. Le but du système de distribution est de fournir une énergie adéquate à partir du transport jusqu'aux consommateurs [10]. Le système de distribution a une combinaison de différents types de charges industrielles qui ont une résistance élevée au rapport de réactance (R/X) [1] [4]. Avec l'augmentation de ces charges, la perte de puissance atteint une valeur élevée et entraîne une mauvaise régulation de la tension et une chute de cette tension. La réduction de la perte de puissance est considérée comme l'un des problèmes importants dans les réseaux électriques pour optimiser l'efficacité du système. Par conséquent, il est nécessaire d'utiliser un équipement de haute précision avec un rendement élevé pour réduire les pertes et augmenter la tension. Il existe des équipements traditionnels tels que des batteries de condensateurs, un compensateur série synchrone statique (SSSC), [6] un régulateur de tension automatique (AVR), des réacteurs série et shunt pour améliorer le profil de tension, réduire les pertes, diminuer l'écart de tension et améliorer l'efficacité du système [5]. Les condensateurs shunt D-STATCOM sont utilisés pour la compensation de puissance réactive dans un réseau de distribution radiale.

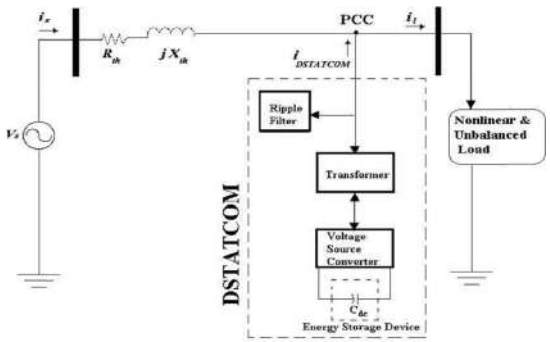

Fig. 1 La configuration d'un D-STATCOM dans un réseau électrique.

Parmi les nombreuses stratégies d'attribution des D-STATCOM, les métaheuristiques sont généralement les méthodologies les plus utilisées pour résoudre les problèmes d'attribution. Fig.1.

II. METHODOLOGIE

Pour ce travail nous avons opté pour l'utilisation de l'algorithme PSO qui est l'un des métaheuristiques les plus robustes. Cet algorithme nous permet d'optimiser l'emplacement ainsi que le nombre nécessaire des D-STATCOM dans un réseau électrique standard le IEEE 33 BUS, l'optimisation est basé sur ces deux index ; l'index de sensibilité de tension (VSI : Voltage Sensivity index) ainsi que l'index de perte de puissance (PLI : *Power Loss index*).

A. IEEE 33 BUS

Le système de distribution radiale de bus IEEE-33 Fig.2. se compose de 33 bus et de 32 branches. Les valeurs de base sont de 100 MVA et 12,66 kV et les charges totales de puissance réelle et réactive de ce système sont de 3715 kW et 2300 kVAR. La perte totale de puissance active et réactive pour le cas de base est de 202,51 kW et 135,03 kVar [3]. Le bus numéro 1 dans ce système est considéré comme l'alimentation électrique d'un réseau de production/transmission. Le reste des bus est considéré comme emplacement candidat de D-STATCOM [7].

ISSN: 1737-9334

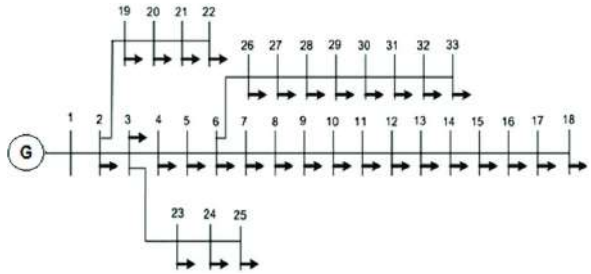

Fig. 2 The IEEE-33 bus radial distribution system

B. D-STATCOM

La puissance réactive est une énergie oscillante bidirectionnelle qui transite entre les réseaux électriques et les charges ; cependant, de nombreuses charges telles que les moteurs ont besoin de puissance réactive dans leur fonctionnement. DSTATCOM peut fournir cette énergie réactive améliorant la puissance qualité du réseau électrique. La figure 1 illustre l'énergie réactive de compensation fournie par un D-STATCOM [12]. Dans ce cas le réseau, la charge et le D-STATCOM sont en parallèle, ayant la même tension (tension de réseau vG). iG, iL, iD sont respectivement les courants de réseau, de charge et D-STATCOM. Fig.3.

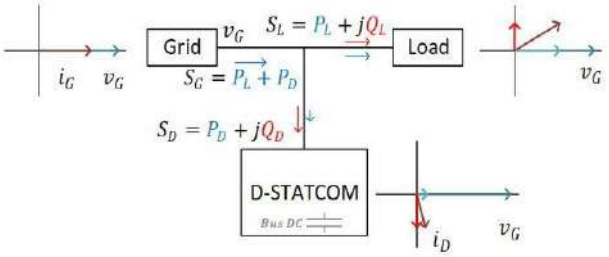

Fig. 3 D-STATCOM opération.

C. L'algorithme PSO

L'optimisation des essaims de particules (PSO) est l'un des algorithmes bio-inspirés et il est simple à lui rechercher des solutions optimales dans l'espace des solutions [9]. Il est différent des autres algorithmes d'optimisation en ce sens que seule la fonction objective est nécessaire et qu'elle ne dépend pas du gradient ou de toute forme différentielle de l'objective. Fig.4.

L'algorithme PSO proposé pour résoudre le dimensionnement ainsi que leur attribution optimale du D-STATCOM afin de minimiser la perte de puissance totale est réalisé par :

- Etape 1 : Lire les données du système de distribution (données de bus, données de ligne, limites de tension min et max, limite d'intensité de lignes, limites de puissance active et réactive), limites minimales et maximales de la taille D-STATCOM et les paramètres PSO.
- Etape 2 : Déterminer les bus candidats selon PLI et VSI et le nombre de candidats selon la marge acceptable spécifiée.
- Etape 3 : Générer aléatoirement la population de particules, leurs vitesses et pour chaque flux de charge de particules pour connaître les pertes de puissance et la chute de tension.
- Etape 4 : Évaluer l'aptitude de la fonction objective de chaque particule et trouver le meilleur personnel (P_{best}) de toutes les particules et la meilleure particule globale (G_{best}) à partir de leurs valeurs d'aptitude.
- Etape 5 : Mettre à jour la vitesse, la position des particules et exécuter le flux de charge pour connaître les pertes de puissance à la recherche de la meilleure solution.
- Etape 6 : Obtenir la combinaison D-STATCOM ; la taille D-STATCOM optimale ainsi que leur attribution avec la fonction objective minimale et la perte de puissance totale correspondante, le profil de tension, les charges de lignes.
- Etape 7 : Répéter les étapes 3 à 6 pour chaque candidat de combinaison D-STATCOM et enregistrer les valeurs de la fonction objective de l'essaim pour chaque combinaison afin de trouver le nombre optimal de D-STATCOM.
- Etape 8 : Imprimer la solution optimale correspondante à la combinaison D-STATCOM optimale, y compris (nombre optimal d'appareils D-STATCOM, leurs tailles et leurs attributions).

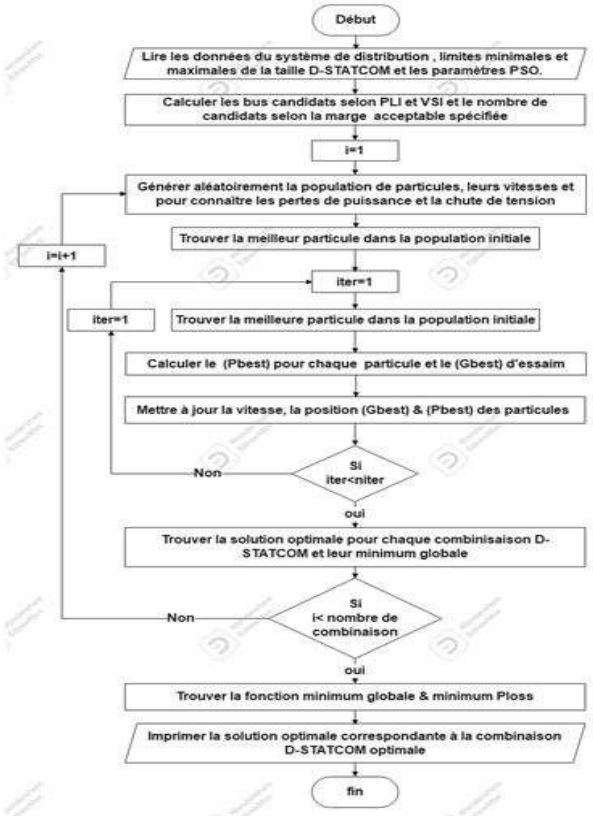

Fig. 4 Organigramme de l'algorithme PSO.

D. Attribution optimale des D-STATCOM

Le problème de dimensionnement de D-STATCOM peut être exprimé mathématiquement comme un problème d'optimisation avec une fonction objective soumise à certaines contraintes d'égalité et de non-égalité [11]. Les sections suivantes illustrent la fonction objective et les contraintes appliquées dans cet article.

La fonction objective est une fonction non linéaire. Elle minimise la chute de tension et la perte de puissance dans le système de distribution [6] [2]. La fonction objective peut s'écrire comme suit :

$$\{F = min(w_1 \times obj_1 + w_2 \times obj_2) \quad (1)$$

Ou :

- obj_1 et obj_2 : désignent respectivement la minimisation des chutes de tension et l'amélioration de l'indice de sensibilité à la tension (VSI) et la minimisation des pertes de puissance (PLI).
- w_1 et w_2 : représente la vélocité de la fonction.

$$\{obj_1 = \frac{1}{TVSI} \quad (2)$$

$$TVSI = \sum_{i=1}^{32} VSI_{i+1} \quad (3)$$

Dans cet article, VSI est utilisé pour déterminer le bus qui a le plus de chance de chute de tension [7] [1]. Le bus avec une faible valeur VSI a plus de chances d'être sélectionné comme bus candidat pour l'installation du D-STATCOM. Le VSI à chaque bus est calculé :

$$VSI_{i+1} = |V_i|^4 - 4[P_{i+1}X_i - Q_{i+1}R_i]^2 - 4|V_i|^2[P_{i+1}R_i + Q_{i+1}X_i] \quad (4)$$

Les valeurs PLI de tous les bus sont calculées Eq. 5. Le bus ayant la valeur PLI la plus élevée étant le plus favorable est donc sélectionné comme bus candidat pour le placement DSTATCOM [4].

$$obj_2 = PLI[g] = \frac{M[g]-Mn}{Mx-Mn} \quad for\ g = 2,3,4,\ldots,n \quad (5)$$

Où :

- N : nombre total de jeux de bars
- M : réduction des pertes de puissance
- Mx : maximum perte de puissance
- Mn : minimum perte de puissance

III. RESULTATS ET ANALYSE

A l'aide du logiciel Matlab nous avons effectué des simulations en nous basant sur les modèles prédéfinis. Cette simulation est faite pour deux cas.

A. Cas 1 :

Dans ce cas, D-STATCOM ne sont pas installés dans le système (ce cas est appelé cas de base). Ici, les résultats obtenus montrent que les pertes de puissance active et réactive sont respectivement de 210,98 kW et 143,13 kVAR. La tension minimale obtenue dans ce cas est de 0,9038 p.u et elle se situe dans le bus 18. Les résultats obtenus sont présentés dans le tableau 1.

B. Cas 2 :

Dans ce cas, D-STATCOM sont placés à des emplacements optimaux pour réduire les pertes de puissance et pour améliorer le profil de tension du système, et les résultats obtenus sont présentés dans le tableau 1. Cependant, trois D-STATCOM peuvent être installés dans ce système. L'attribution optimale de D-STATCOM est dans le 6ème, 15ème et 2ème bus et la taille optimale est 349 kVAr, 928 kVAr et 2065 kVAr. La perte de puissance optimale obtenue dans ce cas est de 174,3214 kW, soit 13,99 % de moins que la perte de puissance du cas de base. La tension de profile minimale est de 0,92922 p.u. située dans le 33ème de ce système.

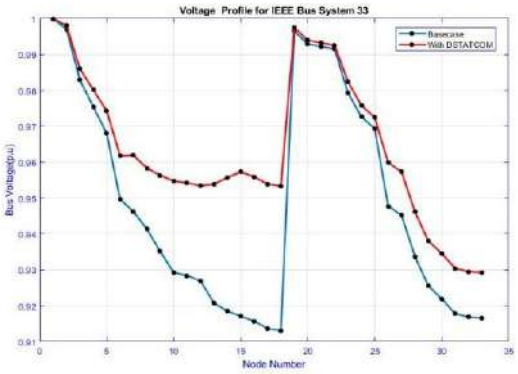

Fig. 5 La tension de profile

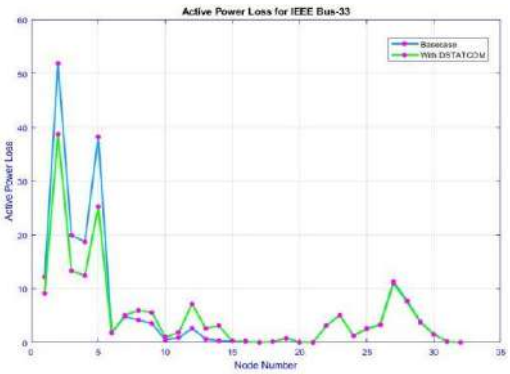

Fig. 6 Pertes puissances active

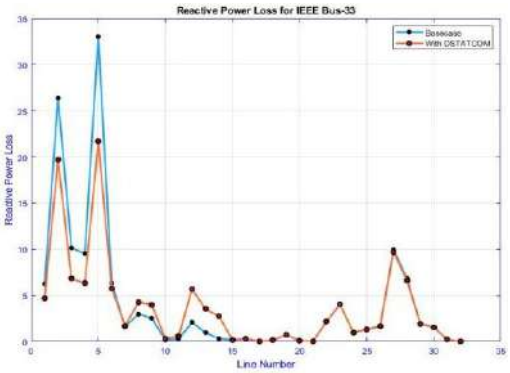

Fig. 7 Pertes des puissances réactive

TABLE I
LES RESULTATS DE LA SIMULATION SUR LE BUS 33-IEEE

PARAMETERS	BASECASE	WITH_DSTATCOM
Total Power Loss (kW)	202.6771	174.3214
Minimum Voltage	0.91306	0.92922
Minimum Voltage Bus Number	18	33
Maximum Voltage	0.99703	0.99803
Maximum Voltage Bus Number	2	2
DSTATCOM Location	NIL	6 15 2
DSTATCOM Size (kVar)	NIL	349 928 2065
VSI (p.u)	25.595	27.2722
Execution Time (sec)	3.4741	3.0948

IV. CONCLUSION

Cet article présente une nouvelle méthodologie pour déterminer l'attribution optimale des (D-STATCOM) dans un réseau électrique de distribution radiale. L'approche des indices de stabilité de la tension ainsi que l'indice de perte de puissance (VSI) et (PLI) sont utilisés pour trouver l'emplacement optimal des D-STATCOM. L'objectif du problème d'optimisation proposé est de minimiser les pertes de puissance réelles totales dans le système tout en satisfaisant plusieurs égalités et inégalités contraintes. L'algorithme d'optimisation (PSO) est utilisé pour déterminer la taille optimale des D-STATCOM. Les résultats de simulation sur 33 bus systèmes de distribution radiale montrent qu'il y a eu une réduction significative des pertes de puissance et une amélioration la tension de profile du système.

REFERENCES

[1] [De, S., & Electrique, G. (2018). Optimisation multi-critères du placement d'un D-STATCOM dans un réseau de Distribution par les Colonies de Fourmis. (Sge), 3–5.

[2] Pujara, A. J., & Vaidya, G. (2011). Voltage stability index of radial distribution network. 2011 International Conference on Emerging Trends in Electrical and Computer Technology, ICETECT 2011, 5(6), 180–185.

[3] Eminoglu, U., & Hocaoglu, M. H. (2007). A voltage stability index for radial distribution networks. Proceedings of the Universities Power Engineering Conference, 408–413.

[4] Gupta, A. R., Jain, A., & Kumar, A. (2016). Optimal D-STATCOM placement in radial distribution system based on power loss index approach. 2015 International Conference on Energy, Power and Environment: Towards Sustainable Growth, ICEPE 2015, 0–4.

[5] Balamurugan, P., Yuvaraj, T., & Muthukannan, P. (2018). Optimal Allocation of DSTATCOM in Distribution Network Using Whale Optimization Algorithm. Engineering, Technology & Applied Science Research, 8(5), 3445–3449.

[6] Salkuti, S. R. (2019). Optimal location and sizing of DG and D-STATCOM in distribution networks. Indonesian Journal of Electrical Engineering and Computer Science, 16(3), 1107–1114.

[7] Ponoćko, J. (2020). Data Analytics-Based Demand Profiling and Advanced Demand Side Management for Flexible Operation of Sustainable Power Networks. Springer, 191–197.

[8] Benavides Córdoba, S., Ortiz Castrillón, J. R., Muñoz Galeano, N., Cano Quintero, J. B., & López Lezama, J. M. (2019). Implementation of a Distribution Static Compensator D-STATCOM: Hardware and Firmware Description. Scientia et Technica, 24(4), 555–565.

[9] Sirjani, R., & Rezaee Jordehi, A. (2017). Optimal placement and sizing of distribution static compensator (D-STATCOM) in electric distribution networks: A review. Renewable and Sustainable Energy Reviews, 77(April), 688–694.

[10] Sedighizadeh, M., Dakhem, M., Sarvi, M., & Kordkheili, H. H. (2014). Optimal reconfiguration and capacitor placement for power loss reduction of distribution system using improved binary particle swarm optimization. International Journal of Energy and Environmental Engineering, 5(1), 1–11.9

[11] Sambaiah, K. S., & Jayabarathi, T. (2021). Optimal reconfiguration and renewable distributed generation allocation in electric distribution systems. International Journal of Ambient Energy, 42(9), 1018–1031.

[12] Arya, A. K., Kumar, A., & Chanana, S. (2019). Analysis of Distribution System with D-STATCOM by Gravitational Search Algorithm (GSA). Journal of The Institution of Engineers (India): Series B, 100(3), 207–215.

ISSN: 1737-9334